Conference Proceedings of the Society for Experimental Mechanics Series

G.P. Tandon · Srinivasan Arjun Tekalur · Carter Ralph
Nancy R. Sottos · Benjamin Blaiszik *Editors*

Experimental Mechanics of Composite, Hybrid, and Multifunctional Materials, Volume 6

Proceedings of the 2013 Annual Conference on Experimental and Applied Mechanics

Springer

Conference Proceedings of the Society for Experimental Mechanics Series

Series Editor
Tom Proulx
Society for Experimental Mechanics, Inc.,
Bethel, CT, USA

For further volumes:
http://www.springer.com/series/8922

G.P. Tandon • Srinivasan Arjun Tekalur • Carter Ralph
Nancy R. Sottos • Benjamin Blaiszik
Editors

Experimental Mechanics of Composite, Hybrid, and Multifunctional Materials, Volume 6

Proceedings of the 2013 Annual Conference on Experimental and Applied Mechanics

Springer

Editors
G.P. Tandon
University of Dayton Research Institute
Dayton, OH
USA

Srinivasan Arjun Tekalur
Michigan State University
East Lansing, MI
USA

Carter Ralph
Southern Research Institute
Birmingham, AL
USA

Nancy R. Sottos
University of Illinois
Urbana, IL
USA

Benjamin Blaiszik
Argonne National Laboratory
Center for Nanoscale Materials
Argonne, IL
USA

ISSN 2191-5644 ISSN 2191-5652 (electronic)
ISBN 978-3-319-00872-1 ISBN 978-3-319-00873-8 (eBook)
DOI 10.1007/978-3-319-00873-8
Springer Cham Heidelberg New York Dordrecht London

Library of Congress Control Number: 2013942489

Printed on acid-free paper

Springer is part of Springer Science+Business Media (www.springer.com)

Preface

Experimental Mechanics of Composite, Hybrid, and Multifunctional Materials, Volume 6: Proceedings of the 2013 Annual Conference on Experimental and Applied Mechanics represents one of eight volumes of technical papers presented at the SEM 2013 Annual Conference & Exposition on Experimental and Applied Mechanics organized by the Society for Experimental Mechanics and held in Lombard, IL, June 3–5, 2013. The complete Proceedings also includes volumes on: *Dynamic Behavior of Materials; Challenges in Mechanics of Time-Dependent Materials and Processes in Conventional and Multifunctional Materials; Advancement of Optical Methods in Experimental Mechanics; Mechanics of Biological Systems and Materials; MEMS and Nanotechnology; Fracture and Fatigue; Residual Stress, Thermomechanics & Infrared Imaging, Hybrid Techniques and Inverse Problems*.

Each collection presents early findings from experimental and computational investigations on an important area within Experimental Mechanics, Composite, Hybrid, and Multifunctional Materials being one of these areas.

Composites are increasingly the material of choice for a wide range of applications from sporting equipment to aerospace vehicles. This increase has been fueled by increases in material options, greater understanding of material behaviors, novel design solutions, and improved manufacturing techniques. The broad range of uses and challenges requires a multidisciplinary approach between mechanical, chemical, and physical researchers to continue the rapid rate of advancement.

New materials are being developed from natural sources or from biological inspiration leading to composites with unique properties and more sustainable sources, and testing needs to be performed to characterize their properties. Existing materials used in critical applications and on nanometer scales require deeper understanding of their behaviors and failure mechanisms. New test methods and technologies must be developed in order to perform these studies and to evaluate parts during manufacture and use. In addition, the unique properties of composites present many challenges in joining them with other materials while performing multiple functions.

This volume on the Experimental Mechanics of Composite, Hybrid, and Multifunctional Materials presents new research on the wide-ranging topics connected by the composites thread. Topics include: Failure Behavior of Polymer Matrix Composites, Microvascular and Natural Composites, Nanocomposites for Multifunctional Performance, Composite/Hybrid Characterization Using Digital Image Correlation, Joints/Bonded Composites, Non-Destructive Testing of Composites, Characterization of Energy Storage Materials, and Composite Test Methods.

Dayton, OH, USA — G.P. Tandon
East Lansing, MI, USA — Srinivasan Arjun Tekalur
Birmingham, AL, USA — Carter Ralph
Urbana, IL, USA — Nancy R. Sottos
Argonne, IL, USA — Benjamin Blaiszik

Contents

Chapter 1
Prediction of Properties of Coir Fiber Reinforced Composite by ANN

G.L. Easwara Prasad, B.S. Keerthi Gowda, and R. Velmurugan

Abstract In the present study the mechanical properties of coir reinforced epoxy resin composite is predicted by using ANN approach. The experimental study by using short coconut coir fibers reinforced with Epoxy LY556 resin composite is reported in earlier studies. The coir fibers collected from Orissa, India, used in lengths of 5, 20 and 30 mm with 30 % fiber and 70 % matrix are used. Experiments conducted as per ASTM standards, and results of tensile, flexural, and impact strengths are reported. It is also reported that the fiber length is having significant effect on the properties of composites. The traditional experimental methods used in obtaining the properties of composites is expensive, require human resources, time consuming and human errors may occur. To reduce the above drawbacks, the present study is under taken to develop a weighted matrix between input (Fiber Length) and output (properties). ANN's training and its testing are adopted to fix the appropriate weighted matrix which in turn prognosticates the appropriate mechanical properties of coir fiber reinforced epoxy resin composites. Similar trend in the variation of tensile strength, flexural strength and impact strength were obtained in the prediction using ANN and they compared well with the experimental results reported.

1.1 Introduction

The advantages of composite materials over conventional materials stem largely from their higher specific strength, stiffness and fatigue characteristics, which enable structural design to be more versatile. By definition, composite materials consist of two or more constituents with physically separable phases [1, 2]. Composites are materials that comprise strong load carrying material i.e., fibers (known as reinforcement) embedded in weaker material (known as matrix). Reinforcement provides strength and rigidity, and supporting structural loads. The matrix or binder (organic or inorganic) maintains the position and orientation of the reinforcement. Significantly, constituents of the composites retain their individual, physical and chemical properties; yet together they produce a combination of qualities which individual constituents would be incapable of producing alone. The reinforcement may be platelets, particles or fibers and are usually added to improve mechanical properties such as stiffness, strength and toughness of the matrix material.

Natural fibers such as jute, sisal, pineapple, abaca and coir [3–12] have been studied as a reinforcement and filler in composites. Growing attention is nowadays being paid to coconut fiber due to its availability. The coconut husk is available in large quantities as residue from coconut production in many areas, which is yielding the coarse coir fiber. Coir is a lingo-cellulosic natural fiber. It is a seed-hair fiber obtained from the outer shell, or husk, of the coconut. Because of its hard-wearing quality, durability and other advantages, it is used for making a wide variety of floor furnishing materials, yarn, rope etc. [13]. Hence, research and development efforts have been underway to find new use areas for coir, including utilization of coir as reinforcement in polymer composites [14–20].

G.L.E. Prasad (✉)
Manglore Institute of Technology and Engineering, Mudbidre, Karnataka, India
e-mail: gle.prasad@gmail.com

B.S.K. Gowda
Civil Engg dept, D A C G Government Polytechnic, Chickmaglur, Karnataka, India

R. Velmurugan
Aerospace Engineering Dept, I I T Madras, Chennai, India

G.P. Tandon et al. (eds.), *Experimental Mechanics of Composite, Hybrid, and Multifunctional Materials, Volume 6*, Conference Proceedings of the Society for Experimental Mechanics Series, DOI 10.1007/978-3-319-00873-8_1,

It is found that for 5 mm length, 20 mm length and 30 mm length of coir fiber embedded with the epoxy resin as matrix at the ratio of 30: 70, micro hardness increased from 15 to 16.9 Hv, Tensile strength increased from 3.208 to 13.05 MPa, Tensile modulus increased from 1.331 to 2.064 GPa, Flexural strength increased from 25.41 to 35.42 MPa, Impact energy increased from 16 to 17.5 KJ/m^2 [21]. In the present study these experimental results [21] are compared with the results obtained from ANN analysis and it is found that the trend is similar.

1.2 Experimental Programme

Following are the material properties and casting procedure adopted in earlier studies "Study on Mechanical Behavior of Coir Fiber Reinforced Polymer Matrix Composites" [21].

Materials The fabrication of the various composite materials is carried out through the hand lay-up technique. Short coconut coir fibers are reinforced with Epoxy LY 556 resin, chemically belonging to the 'epoxide' family is used as the matrix material. Its common name is Bisphenol A Diglycidyl Ether. The low temperature curing epoxy resin (Araldite LY 556) and corresponding hardener (HY951) are mixed in a ratio of 10:1 by weight as recommended.

Mixing and casting Three different types of composites are fabricated with three different fiber lengths such as 5, 20 and 30 mm. Each composite consisting of 30 % of fiber and 70 % of epoxy resin. The mix is stirred manually to disperse the fibers in the matrix. The casting of each composite is cured under a load of about 50 kg for 24 h before it is removed from the mould. Then the casted specimens are cured in the air for another 24 h after removing them from the mould. Specimens of suitable dimension are cut using a diamond cutter for mechanical testing. Utmost care has been taken to maintain uniformity and homogeneity of the composite.

Test procedure Test specimens were subjected to various mechanical tests as per ASTM standards. The tensile test and three-point flexural tests of composites were carried out using Instron 1195. The ASTM standard test method for tensile properties of fiber resin composites has the designation D 3039–76. Micro-hardness measurement is done using a Leitz micro-hardness tester. Low velocity instrumented impact tests are carried out on composite specimens. The test results are reported as per ASTM D 256 using an impact tester. The charpy impact testing machine has been used for measuring impact strength.

1.3 Artificial Neural Network

Artificial neural network(ANNs) are similar to the biological neural networks in the sense that functions are performed collectively and in parallel by the units, rather than there being a clear delineation of subtasks to which various units are assigned [22, 23]. Currently, the term artificial neural network tends to refer mostly to neural network models employed in statistics, cognitive psychology and artificial intelligence. Neural network models designed with emulation of the central nervous system (CNS) in mind are subject to theoretical neuroscience and computational neuroscience. Artificial neural network models are specified by topology, node characteristics and training or learning rules. These rules specify that initial set of weights should be adopted during improvement of convergence performance. Broadly there are two types of ANN models namely supervised and unsupervised. In case of supervised both input patterns and output patterns are known during training. The present paper adopts feed forward supervised ANN model for prediction of 'Characteristic compressive strength'. The possible training parameters are number of iterations (epoch), learning rate, error goal and number of hidden layers. These parameters are varied until a good convergence of ANN training is obtained and there by fixing the optimal training parameters. These optimal parameters are used for testing and validation process. However the number of neurons in input layer and output layer are determined based on the problem domain depending up on number of input variables and number of output or target variables. The number of hidden layers and neurons in hidden layer are fixed during the training process. The specific ANN topology model adopted in this study is shown. A significant number of reports have been published in application of ANN for the prediction of future events in civil engineering problems. These reports and papers have been varied from, A fuzzy-Neuro Model for Conventional CSC particulate composite mix design (Nataraj et al. [24]), Reducing prediction error by transforming input data (Bhattacharya and Solomatine [23]).

1.4 Results and Discussion

Figure 1.1 depicts the topology adopted to predict the Micro Hardness, Tensile strength, Tensile modulus, Flexural strength and Impact energy of coir fiber reinforced epoxy resin composite. Table 1.1 shows the values predicted from ANN analysis for all the above mentioned mechanical properties of coir fiber reinforced epoxy resin composite for different values of coir fiber length of fiber to resin ratio 30:70 the value within the parenthesis are the results reported in the experimental study [21]. Figure 1.2 shows the training convergence curve generated during the prediction process.

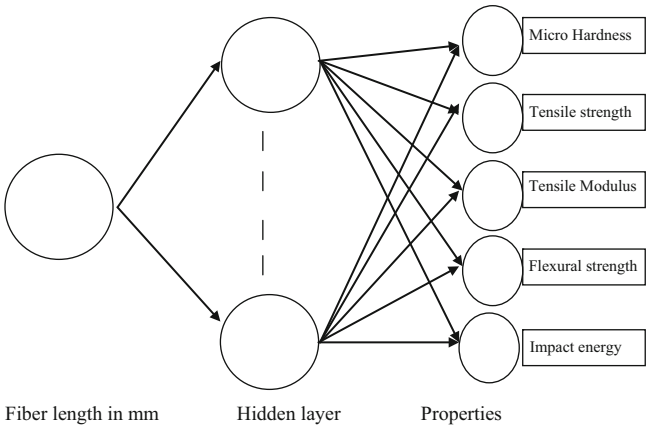

Fig. 1.1 Topology to predict properties of coir fiber reinforced epoxy resin composite (1-4-5)

Table 1.1 Properties of coir reinforced epoxy resin composite

Fiber length (mm)	Micro hardness (Hv)	Tensile strength (MPa)	Tensile modolus (GPa)	Flexural strength (MPa)	Impact energy (KJ/m^2)
1	15.465	3.1483	1.1582	24.4285	15.7681
3	15.2574	3.2988	1.1522	24.8518	15.9364
5	15.0133 (15)	3.6091(3.21)	1.1675(1.33)	25.4158(25.41)	16.0006(16)
6	14.8696	3.8147	1.1784	25.7509	16.0288
8	14.5405	4.3355	1.2048	26.5153	16.0901
10	14.1711	5.0079	1.2363	27.3668	16.1594
12	13.793	5.8131	1.2712	28.239	16.2335
14	13.4474	6.6963	1.3084	29.0654	16.3082
16	13.1789	7.5836	1.3481	29.8092	16.3817
18	13.0386	8.4175	1.3955	30.4843	16.4581
20	13.0974(12.6)	9.1892(9.16)	1.4633(1.52)	31.1605(31.28)	16.5506(16.5)
22	13.4524	9.9449	1.574	31.9397	16.6803
24	14.1683	10.7424	1.7509	32.865	16.8622
26	15.131	11.5582	1.986	33.8126	17.0782
28	16.05	12.283	2.2247	34.6077	17.2888
30	16.7868(16.99)	12.9238(13.05)	2.4341(2.56)	35.3416(35.42)	17.5272(17.5)

1.5 Conclusion

It can be observed from Table 1.1 and Figs. 1.3, 1.4, 1.5, 1.6, and 1.7 the properties like Micro Hardness, Tensile strength, Tensile modulus, Flexural strength and Impact energy can be obtained for a particular composite of designated fiber length. Investigation demonstrates feed forward ANN model could be very good mathematical tool for prediction of mechanical properties of coir fiber reinforced epoxy resin composites, using data pattern rather than complicated experimental procedures. ANN approach avoids memorization of equation, procedures, much involvement of manual activity and generalizes the problem domain. In the results reported in Table 1.1 and Figs. 1.3, 1.4, 1.5, 1.6, and 1.7 the values predicted for various properties of coir fiber reinforced composite are closely matching with the experimental values reported in the earlier studies.

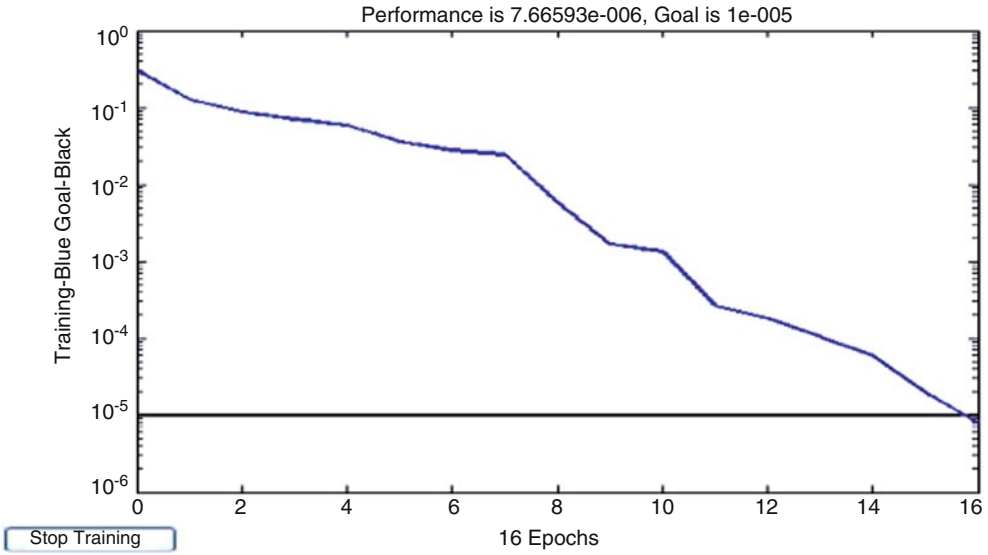

Fig. 1.2 Training convergence curve

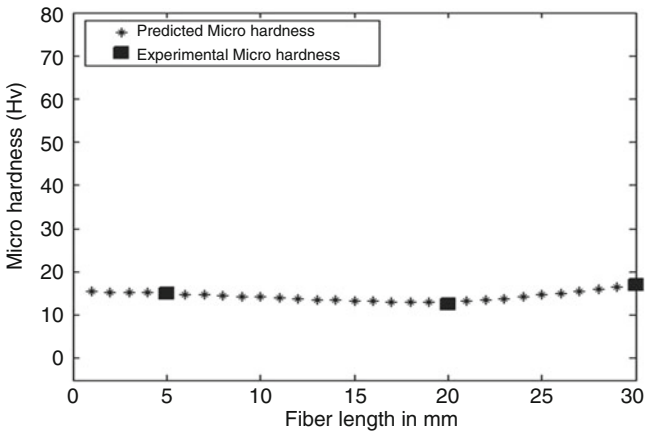

Fig. 1.3 Variation of micro hardness of the composites with fiber length

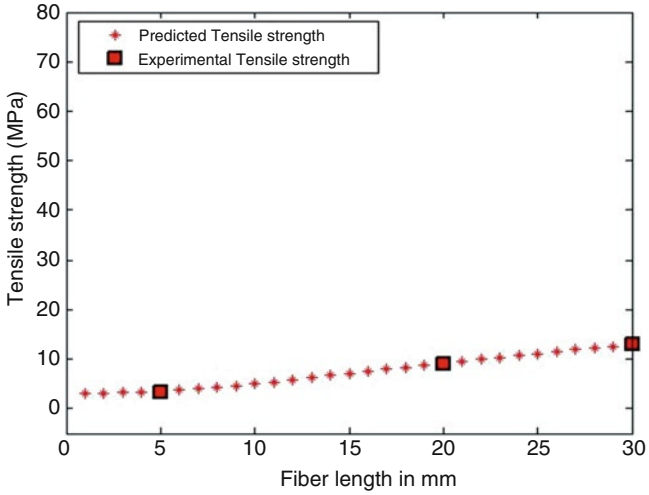

Fig. 1.4 Variation of tensile strength of the composites with fiber length

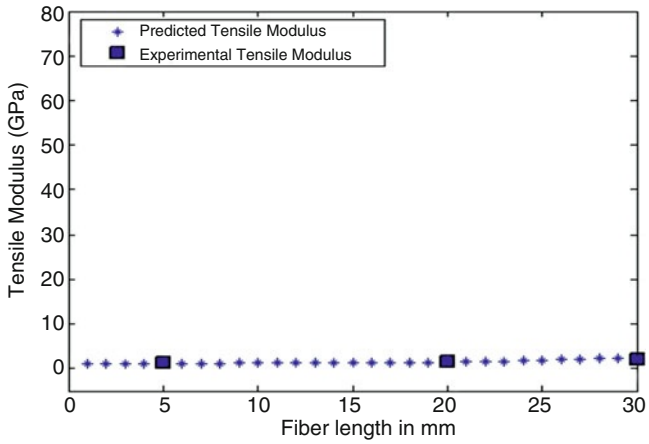

Fig. 1.5 Variation of tensile modulus of the composites with fiber length

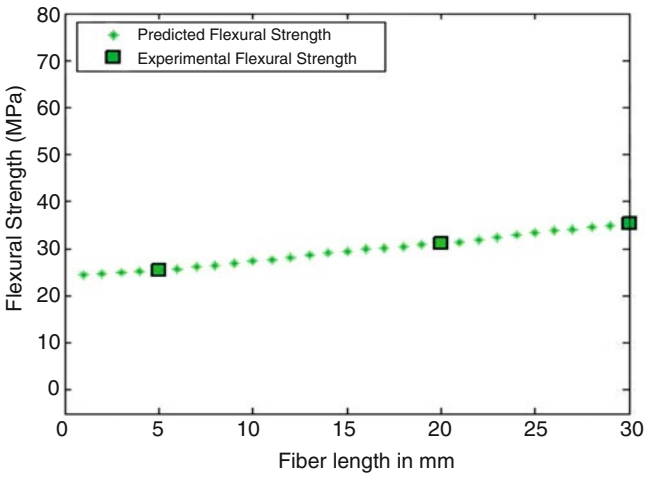

Fig. 1.6 Variation of flexural strength of the composites with fiber length

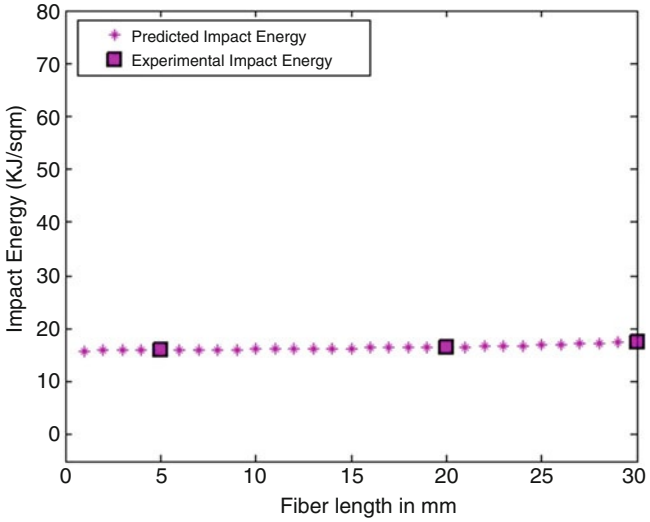

Fig. 1.7 Variation of impact energy of the composites with fiber length

References

1. Mueller DH, Krobjilowski A (2003) New discovery in the properties of composites reinforced with natural fibers. J Ind Text 33(2):111–129
2. Lilholt H, Lawther JM (2000) Natural organic fibres. In: Comprehensive composite materials, (6 vols) Kelly A, Zweben C (Eds) Elsevier Science, Oxford, Vol 1, chap 10, pp 303–325
3. Mohanty AK, Khan MA, Hinrichsen G (2000) Influence of chemical surface modification on the properties of biodegradable jute fabrics-polyester amide composite. Compos Part A 31:143–150
4. Mohanty AK, Khan MA, Hinrichsen G (2000) Surface modification of jute and its influence on performance of biodegradable jute-fabric/biopol composites. Compos Sci Technol 60:1115–1124
5. Li XH, Meng YZ, Wang SJ, Rajulu AV, Tjong SC (2004) Completely biodegradable composites of poly(propylene carbonate) and short, lignocellulose fabric hildegardia populifolia. J Polym Sci Part B Polym Phys 42(4):666–675
6. Shibata M, Takachiyo K, Ozawa K, Yosomiya R, Takeishi H (2002) Biodegradable polyester composites reinforced with short abaca fiber. J Polym Sci 85(1):129–138
7. Iannace S, Nocilla G, Nicolais L (1999) Biocomposites based on sea algae fibers and biodegradable thermoplastic matrices. J Polym Sci 73(4):583–592
8. Shibata M, Ozawa K, Teramoto N, Yosomiya R, Takeishi H (2003) Biocomposites made from short abaca fiber and biodegradable polyester. Macromol Mater Eng 288(1):35–43
9. Luo S, Netravali AN (1999) Interfacial and mechanical properties of environment-friendly 'green' composites made from pineapple fibers and poly(hydyoxybutyrate-co-valerate) resin. J Mater Sci 34:3709–3719
10. Rout J, Misra M, Tripathy SS, Nayakand SK, Mohanty AK (2001) The influence of fibre treatment on the performance of coir-polyester composites. Compos Sci Technol 61:1303–1310
11. Bisanda ETN (2000) The effect of alkali treatment on the adhesion characteristics of sisal fibres. Appl Compos Mater 7:331–339
12. Gassan J, Bledzki AK (1999) Possibilities for improving the mechanical properties of jute/epoxy composites by alkali treatment of fibres. Compos Sci Technol 59(9):1303–1309
13. Satyanarayana KG, Pillai CKS, Sukumaran K, Pillai SGK, Rohatgi PK, Vijayan K (1982) Structure and properties of fibers from different parts of coconut tree. J Mater Sci 17:2453–2472
14. Owolabi O, Czvikovszky T, Kovacs I (1985) Coconut fibre reinforced thermosetting plastics. J Appl Polymer Sci 30:1827–1836
15. Varma DS, Varma M, Varma IK (1985) Coir fibres II: evaluation as a reinforcement in unsaturated polyester resin composites. J Reinf Plast Compos 4(4):419–431
16. Varma DS, Varma M, Varma IK (1986) Coir fibers. 3. Effect of resin treatment on properties of fibers and composites. Ind Eng Chem Prod Res Dev 25(2):282–289
17. Prasad SV, Pavithran C, Rohatgi PK (1983) Alkali treatment of coir fibres for coir-polyester composites. J Mater Sci 18:1443–1454
18. Geethamma VG, Thomas Mathew K, Lakshminarayan R, Thomas S (1998) Composite of short coir fibres and natural rubber: effect of chemical modification, loading and orientation of fibre. Polymer 39(6–7):1483–1491
19. Paul A, Thomas S (1997) Electrical properties of natural-fiber-reinforced low density polyethylene composites: a comparison with carbon black and glass-fiber-filled low density polyethylene composites. J Appl Polymer Sci 63(2):247–266
20. Abdul Khalil HPS, Rozman HD (2000) Acetylated plant-fiber reinforced polyester composites. A study of mechanical, hygrothermal and aging characteristics. Polym Plast Technol Eng 39(4):757–781
21. Sanjay Kindo (2010) Study on mechanical behavior of coir fiber reinforced polymer matrix composites. B.Tech. dissertation thesis, Department of Mechanical Engineering National Institute of Technology Rourkela – 769008

22. Kurup PU, Dudani NK (2002) Neural networks for profiling stress history of clays from PCPT data. J Geotech Geoenviron Eng 128(7):569–578
23. BattacharyaB, Solomatine DP (2005) Machine learning in soil classification. In: Proceedings of the international joint conference on neural networks, Montreal Canada, 31 July, 4 Aug 2005, pp 2694–2699
24. Natraj MC et al (2006) A fuzzy-neuro model for conventional concrete mix design. Engineering letters 132EL_13_2_8 (advance online publication: 4 Aug 2006)

Chapter 2
Impact of Semi-rigidity of Joint on Timber Composite Truss Beam

Sebastian Fuentes, Eric Fournely, Rostand Moutou Pitti, and Abdelhamid Bouchair

Abstract The DOREAN design system is based on a wood structure made with girder trusses. This paper quantifies the contribution of the OSB panels on the load carrying capacity of the trusses in the DOREAN house structure. On the one hand, by experimental tests carried out on double shear specimens, and on the other hand by modelling a T-beam including the stiffness of the assembly between the panel and the truss beam. The connexion between the OSB panel and the upper chord of the lattice beam is realized by staples. Shear tests are performed varying the number of fasteners with three thicknesses of panel and three different orientations of the staples. This last parameter is of high importance because of the short loaded edge distance in the narrow wood element of the chords. Strength and stiffness of the stapled joint are obtained from tests and the interaction between fasteners is analysed. The T-beam obtained by the connexion between the OSB panels and the DOREAN lattice beam is modelled using beam elements. The semi-rigid behaviour is taken into account for all the connexions between the lattice beam elements and the OSB panels. Conditions of serviceability and ultimate strength are analysed with the influence of the variability of the T-beam parameters.

2.1 Introduction

It is known that the use of wood material in the construction has a significant contribution to the stability of the ecosystem. More again, the wood material has a positive impact in the thermic regulation of industrial buildings, small and collectives' houses [1, 2]. Due to the economic demand and to the fact that the energy costs represent a significant part of household expenses, it appears necessary to improve the composition and the assembly of structural elements in timber building [3]. According to its assembly and building mode, the DOREAN's beam can contribute to solving a part of this problem.

Figure 2.1 presents the dimensions of a typical truss beam and the equipment used to realise the assembly of the truss members. These beams are generally built from low-size timber members, assembled by nails, by plates with metal teeth or by adhesives. The efficiency of this assembly is obtained by the control of the manufacture process and the knowledge of the joints behaviour [4, 5]. These beams can be used in the frame systems or slabs in combination with OSB panels.

The present investigation is focused on the semi-rigid behaviour of the nailed and glued connexion between the lattice beam members and the OSB panels. In the literature framework, few authors have discussed the influence of these connections in the global behaviour of the structures and especially timber structures. Among them, Zhu et al. [6] have proposed numerical study of OSB webbed timber I-beams with interactions between openings and Feraboli [7] has performed experimental test of notched response of OSB wood composites.

S. Fuentes • E. Fournely • A. Bouchair
Clermont Université, Université Blaise Pascal, Institut Pascal, BP 20206, F-63000 Clermont-Ferrand, France

CNRS, UMR 6602, Institut Pascal, F-63171 Aubiere, France

R.M. Pitti (✉)
Clermont Université, Université Blaise Pascal, Institut Pascal, BP 20206, F-63000 Clermont-Ferrand, France

CNRS, UMR 6602, Institut Pascal, F-63171 Aubiere, France

CENAREST, IRT, BP 14070, Libreville, Gabon
e-mail: rostand.moutou_pitti@univ-bpclermont.fr

G.P. Tandon et al. (eds.), *Experimental Mechanics of Composite, Hybrid, and Multifunctional Materials, Volume 6*, Conference Proceedings of the Society for Experimental Mechanics Series, DOI 10.1007/978-3-319-00873-8_2,

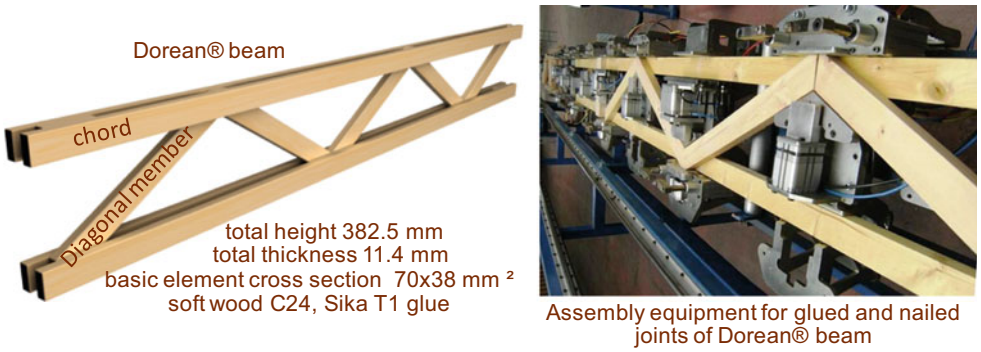

Fig. 2.1 DOREAN beam

The experimental tests performed on push-out specimens provide the load–displacement curves of the connections between the wood members and the OSB panels. Thus, various configurations of connections are tested changing the thickness of the panels and the connection type (number and orientation of staples, glue, panel thickness). The experimental results are used as input data in a simple numerical finite element model. The comparison of experimental test and simulation are presented and discussed.

2.2 Experimental Program

Previous experimentations on lattice beams [2] provided the ultimate and the serviceability mechanical properties of Dorean beams without OSB panels. In this paper, a new experimental program is performed to obtain the strength and the rigidity of the connection between the two parts of a T-beam composed by Dorean beam and OSB panels. This T-beam is used in slab application with composite effect due to the association of truss beam and OSB panels. Tests are carried-out on double shear push-out specimens with glued, nailed or glued and nailed joints (see Table 2.1).

2.2.1 Specimen Dimensions and Set-up

The push-out specimens are tested in universal press under compression loading to obtain the shear load on the connection. Figure 2.2 shows a shear specimen loaded in the direction parallel to grain and its load–displacement curve. The static loading history (Fig. 2.3) includes a preloading phase, a partial unloading and finally a re-loading phase until failure or excessive displacement. The specimens are loaded in the direction parallel to grain or perpendicular to grain of the wood members. The first plateau after preloading (Fig. 2.3) is defined as 1,200 N and 600 N for the specimens loaded in the directions parallel to grain or perpendicular to grain, respectively. The second plateau, after unloading phase, is defined as 200 N in both cases. The dimensions of the two types of specimens loaded in the directions parallel and perpendicular to grain with the measurement devices of load and displacements are shown in Fig. 2.3. The relative displacements between the OSB panels and the wood member are measured on four points around the wood member using LVDT sensors. Thus, for each test, the mean value of displacement measured by the two transducers for each interface between OSB panel and wood member is considered to represent the behaviour of the connection. The orientation of the staple is defined as the angle between the longitudinal axis of the staple and the longitudinal axis of the timber element.

The configurations of specimens tested are summarized in Table 2.1. Three specimens are tested in each configuration. For all the specimens the staples are positioned on one line parallel to the wood member. The spacing between the staples is equal to 150 mm (see Fig. 2.4) for all the specimens except for the configurations “2” and “6–3” respectively with 7 or 3 staples and a half spacing.

Table 2.1 Various configurations of connections between the panels and the wood member of lattice beam

	Specimen orientation	Staples	Number of staples	Glue	Staple orientation	OSB thickness
1-1	//	Yes	4	No	45	18
1-2	//	Yes	4	No	90	18
1-3	//	Yes	4	No	0	18
2	//	Yes	7	No	0	18
3	//	No	0	Yes	0	18
4-1	//	Yes	4	No	0	15
4-2	//	Yes	4	No	0	10
5	//	Yes	4	Yes	0	18
6-1	⊥	Yes	2	No	0	18
6-2	⊥	Yes	2	Yes	0	18
6-3	⊥	Yes	3	No	0	18

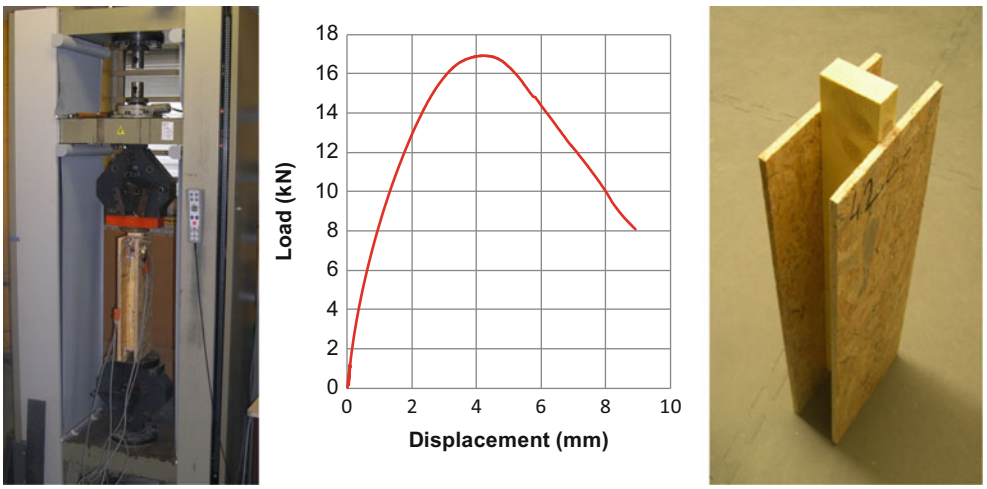

Fig. 2.2 Universal press, load–displacement curve and push-out shear specimen

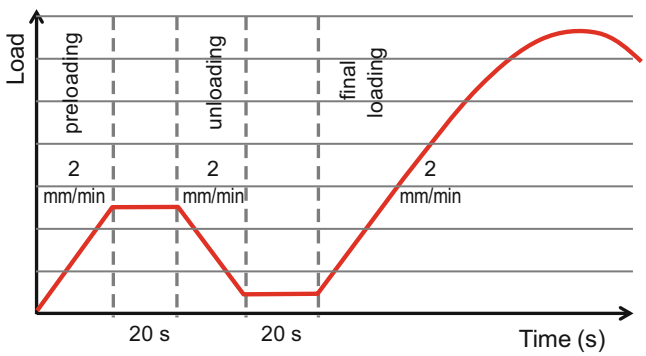

Fig. 2.3 Loading history used for the experimental program

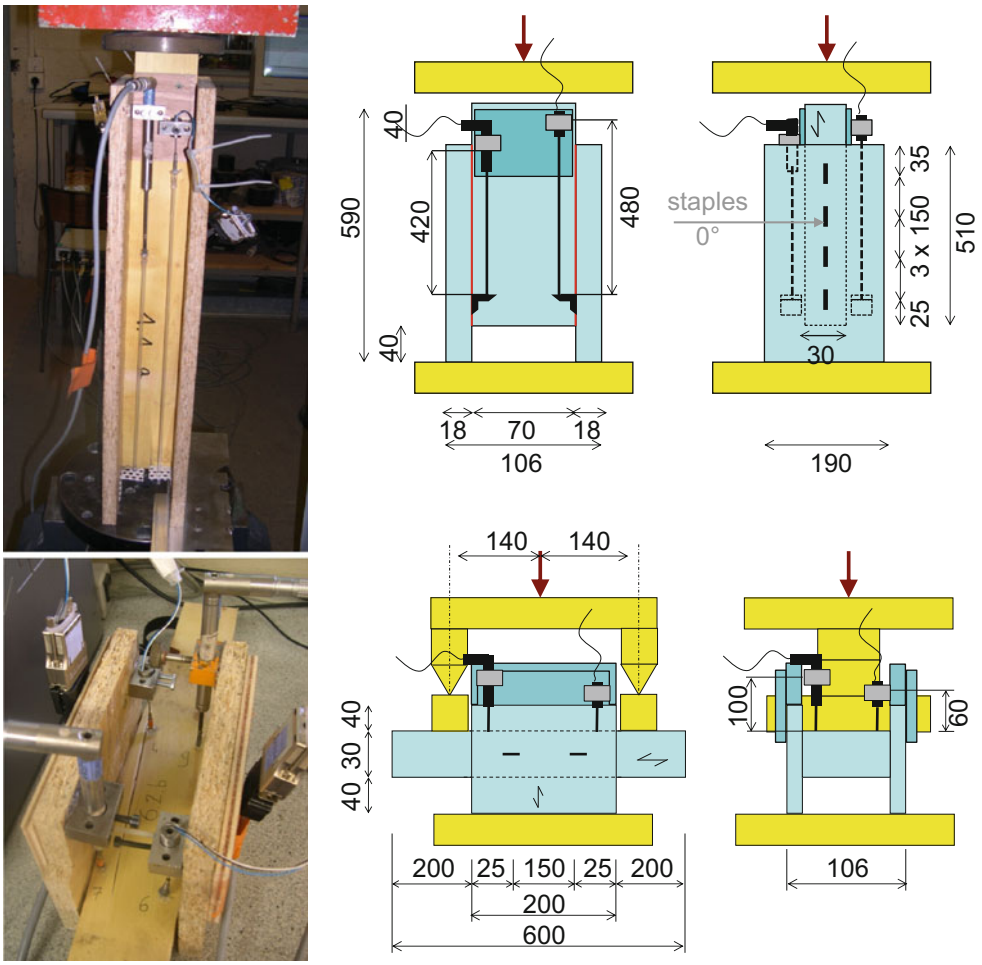

Fig. 2.4 Dimensions of specimens with the measurement devices of load and displacement

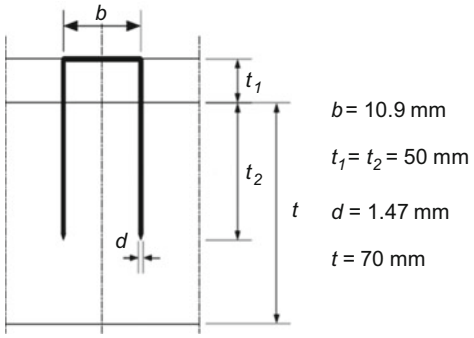

Fig. 2.5 Dimensions of the staples

2.2.2 *Material Characteristics*

Timber elements are made of spruce of C18 class resistance [8, 9]. The mean value of density is 435 kg/m^3 (standard deviation of 15 %) with average value of moisture content equal to 7.2 % (standard deviation of 12 %). The panels are made of OSB3 [10] with an average density of 640 kg/m^3 [11]. The staples defined on Fig. 2.5 are made from steel with ultimate stress f_u equal to 540 MPa. The shear strength of such staple using the Eurocode 5 requirements is about 0.5 kN for the 3 thicknesses of panels used in the tests. This strength is given for one staple and one shear plan between the wood member and the wood OSB panel. The polyurethane glue used in the tests is characterized by a shear strength of 1.2 MPa.

2.3 Discussion of Experimental Results

Examples of load- displacement relationship are plotted on Fig. 2.6. The displacement for each index a, b and c is the mean value of the four LVDTs around the wood member. The indexes a, b and c represent the three specimens tested for each configuration. The zoom on the beginning of the curve with the effect of unloading and reloading is illustrated for one specimen (index a). This figure allows comparing the mechanical behaviour between the 45° and 90° orientation of staples. Table 2.2 gives a synthetic overview of experimental results on the whole set of specimen. The parameters defined in the Table 2.2 can be defined as follows: F_{max} is the maximum load during test, F_y and dep_y are defined by the intersection between the lines tangent to the initial and final phases (1/6 of initial tangent) of the load–displacement curves, F_u is the ultimate value of the force and dep_u is defined as the lowest value between the displacement for F_u and the displacement corresponding to a decreasing of 20 % of the load compared to F_{max}, the ductility is the ratio dep_u/dep_y, the rigidity is defined by the initial phase of the load–displacement curve.

- Shear in the direction parallel to the main axis of timber element

The strength of mechanically connected joints (without glue) is between 6.8 and 8.5 kN for 4 staples. The higher values of strength are obtained for OSB 18 and the lower values for OSB 10. The best orientation of staple is an angle of 90 ° (staples perpendicular to the grain direction of timber element). Doubling the number of staples with half spacing induces an increasing of strength of about 75 %. With the same number and orientation of staples, the presence of glue allows reaching strength between 17.3 and 19 kN, but the static ductility is slightly reduced in comparison with the staples. For these configurations of joints in shear, the values of rigidity is between 5.3 and 13.9 kN/mm.

- Shear in the direction perpendicular to the main axis of timber element

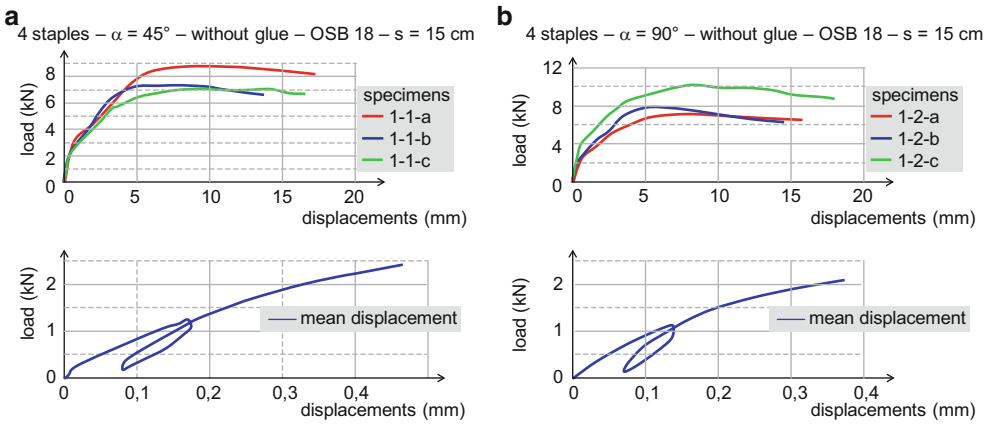

Fig. 2.6 Examples of push-out test in parallel configuration (whole curves and zoom on the initial phase of specimen "a"). (**a**) Specimens 1-1, α = 45°, (**b**) specimens 1-2, α = 90°

Table 2.2 Synthetic table of results

	Specimen orientation	Staples	Number of staples	Glue	Staple orientation	OSB thickness	F_{max} (kN)	F_y (kN)	F_u (kN)	dep_y (mm)	dep_u (mm)	Rigidity (kN/mm)	Ductility
1-1	//	Yes	4	No	45	18	7.7	3.2	6.9	0.6	>18	5.3	>30
1-2	//	Yes	4	No	90	18	8.5	4.1	6.8	0.7	>18	5.9	>26
1-3	//	Yes	4	No	0	18	7.3	3.7	5.9	0.6	>18	6.2	>30
2	//	Yes	7	No	0	18	12.8	7.3	10.2	0.8	>18	9.1	>23
3	//	No	0	Yes	0	18	19	15.9	15.2	1.4	5.8	11.4	4
4-1	//	Yes	4	No	0	15	7.8	2.5	6.3	0.3	>18	8.3	>60
4-2	//	Yes	4	No	0	10	6.8	3.7	5.5	0.9	8.8	4.1	10
5	//	Yes	4	Yes	0	18	17.3	12.5	13.1	0.9	6.8	13.9	8
6-1	⊥	Yes	2	No	0	18	3.8	1.8	3.1	0.7	10.3	2.6	15
6-2	⊥	Yes	2	Yes	0	18	10.7	5.8	8.5	1.2	7.2	4.8	6
6-3	⊥	Yes	3	No	0	18	6	2.8	4.8	0.6	10.2	4.7	17

The strength obtained with 2 staples is around 4 kN and that of 3 staples is about 6 kN. With the same number and orientation of staples, the presence of glue increases the strength to reach more than 10 kN with a significant decrease of the static ductility. For these configurations of joints in shear, the values of rigidity are between 2.6 and 4.8 kN/mm.

2.4 Composite Beam Simulation

In order to take into account the composite behaviour of a T-beam realized with a Dorean lattice beam and OSB panels connected by staples or glue, a finite element model is realized using beam elements. The mechanical properties of the Dorean beam, obtained in a previous study [1, 3], are used in the numerical simulation of the present study. Thus, simple beam elements are used. Truss elements with semi-rigid behaviour at the end of the members and between the wood member and the OSB panel are considered (Fig. 2.7).

2.4.1 FEM Model

Truss assumptions are considered for Dorean beam, with or without semi-rigidity of the joints between chord and diagonal elements. The span of the beam considered in the model is equal to 3.60 m as the one tested in a previous study concerning a truss beams without OSB panels [3]. A modulus of elasticity of 10,000 MPa is assumed for wood in the lattice beam. The analysis of the influence of semi-rigid connections in the lattice beam on its stiffness determined by inverse analysis on bending test showed that the initial stiffness of the connection varies between 4.1 and 10 kN/mm. The vertical and diagonal elements are with a cross section of 38×70 mm^2, the chord is with a cross section of $2 \times (38 \times 70)$ mm^2. OSB panel cross section is equal to (10, 15 or 18) $\times$ 625 mm^2. Its MOE is taken equal to 2,000 MPa corresponding to the low boundary value from standards. This low value is coherent with complex modelling including contact between panels along the span of the floor.

The mesh is illustrated on Fig. 2.7 and the loading is a uniformly distributed force applied on the panel elements. The interface between panels and the Dorean beam is modelled by three beam elements as shown on Fig. 2.8. AB and CD elements are rigid beam in order to assume Navier-Bernoulli hypothesis. BC element is rigid in bending and semi-rigid in longitudinal direction. This rigidity K is defined as following:

$$F_V = K \cdot \delta \Rightarrow K = \frac{F_V}{\delta} = \frac{E_C \cdot A_C}{l_C} \tag{2.1}$$

with, K the value obtained from experiments with a spacing between connectors equal to the connected length on push-out specimens.

To represent the composite effect between the upper chord of the truss beam and the OSB panel, short beam element is used to represent the semi-rigid behaviour between the panel and the wood member (Fig. 2.8). The initial stiffness of the connection is obtained from the tests on shear specimens. The OSB panel is represented by equivalent beam element.

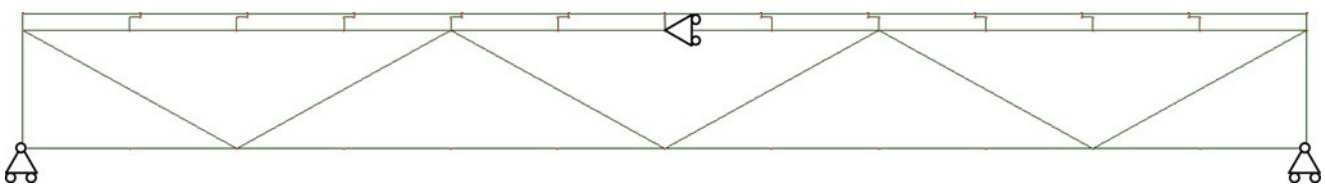

Fig. 2.7 DOREAN beam's mesh with shear connection (panel to upper chord)

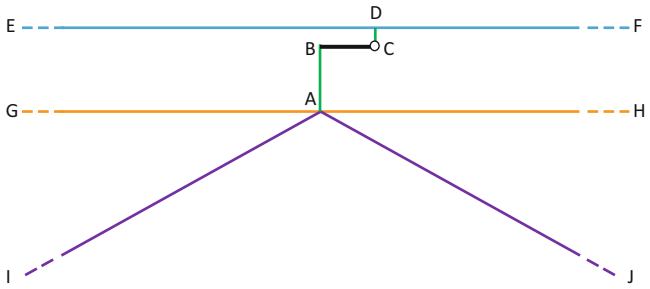

Fig. 2.8 Mechanical characteristics of the elements, boundary conditions

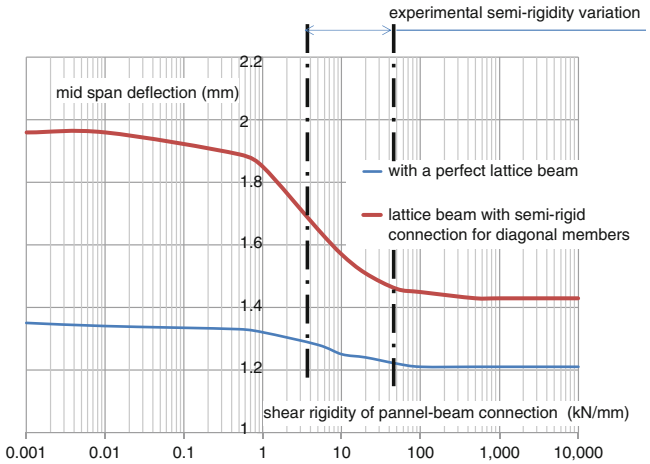

Fig. 2.9 Comparison of experimental and numerical results

2.4.2 Comparison of Experimental and Numerical Results

The simple finite element model is performed to analyse the influence of the axial semi-rigid behaviour at the end of the members and the shear semi-rigid behaviour at the interface between the OSB panels and the upper chord of the lattice beam. Figure 2.9 shows the influence of the shear semi-rigidity at the interface on the global deflection, at linear phase, of a T-beam combining lattice beam and OSB panel. The axial connections at the end of the truss members are considered rigid or semi-rigid. The comparison shows that the lattice beam with axial semi-rigidity at the end of the members is more sensitive to the evolution of the shear semi-rigidity at the interface between the panel and the upper chord. Besides, the increase of the shear rigidity increases the global stiffness of the T-beam. Here, for a span of 3.36 m, this increase is equal to 12 % and 37 % respectively for the perfect lattice beam and for the truss beam with semi rigid shear connection between the panel and the upper chord. This increase reaches 41 % for a span of 4.45 obtained adding 2 diagonals.

2.5 Conclusion

The tests on lattice timber beams (DOREAN®) manufactured with various techniques of connections showed the influence of the connection on the beam behaviour. This beam is associated with OSB panels to obtain a wooden floor. Tests realized on push-out shear specimens between OSB panels and beam members using staples and glue provided the load-slip curves at the interface between the two materials. In comparison with the connections using only staples, the glue showed an increase of the strength and the stiffness of the connection with a decrease of the ductility. The test provided the load-slip curves used in the simple finite element model. The results of the simple simulations illustrate the effects of shear semi-rigidity on the global behaviour of the T-beam combining lattice beam and OSB panels. This preliminary study will be extended to analyse different ratios of stiffness between the truss beam and the panels. The stiffness at the interface will be analysed considering real non-linear behaviour of materials and connections.

References

1. Fournely E, Moutou Pitti R, Bouchair H, Dubois F (2012) Experimental analysis of the semi-rigidity joint in the standardized timber beam. Springer; 34:357–366. doi:10.1007/978-1-4614-4226-4_42
2. Moutou Pitti R, Fournely E, Bouchair H (2010) Comportement d'une poutre treillis en bois avec assemblages semi-rigides. 28ème Rencontres Universitaires de Génie Civil, AUGC, La Bourboule, 02–04 Juin 2010, pp 1297–1306
3. Fournely E, Moutou Pitti R, Bouchair A (2012) Behaviour of timber lattice beam with semi-rigid joints: analytical and experimental study. Pro Ligno 8(3):19–41
4. AFNOR, NF EN 408 (2004) Structures en bois, Bois de structure et bois lamellé collé, détermination de certaines propriétés physiques et mécaniques. Mars 2004, p 32
5. AFNOR, Eurocode 5 (2005) Conception et clacul des structures en bois – généralités, règles communes et règles pour les bâtiments, NF EN 1995–1.1
6. Zhu EC, Guan ZW, Rodd PD, Pope DJ (2005) Finite element modelling of OSB webbed timber I-beams with interactions between openings. Adv Eng Softw 36:797–805
7. Feraboli P (2008) Notched response of OSB wood composites. Compos Part A 39:1355–1361
8. CTBA (2007) Panneaux OSB, Application Bois Construction (ABC), Centre Technique du Bois et de l'Ammeublement, Paris
9. CTBA (2006) Panneaux dérivés du bois, Panneau 21.01, Centre Technique du Bois et de l'Ammeublement, Paris
10. AFNOR, NF EN 300 (2006) Panneaux de lamelles minces, longue et orientées – OSB définitions, classification et exigences, Eurocode 5
11. Krono France (2010) Technical specification of Kronoply – physical and technical characteristics, Krono France, Paris

Chapter 3
Prediction of Properties of CRPCSC Particulate Composite by ANN

G.L. Easwara Prasad, B.S. Keerthi Gowda, R. Velmurugan, and M.K. Yashwanth

Abstract Determining the properties of Crushed Rock Powder, Cement, Sand and Coarse Aggregate (CRPCSC) particulate composite in a conventional way by conducting the experiments is time consuming and requires men and material. In the present study an effort is made to predict the spilt tensile strength and slump values of M20 and M35 grade CRPCSC particulate composite using artificial neural network (ANN). ANN is a computational model that is inspired by structure and functional aspects of biological neural network. ANN is used in many areas of research and development. In this study experimental results reported by earlier researchers are used. In the present study the spilt tensile strength and slump values of M20 and M35 grade CRPCSC particulate composite with different percentages of crushed rock powder replacement for sand is predicted. The results are also compared with conventional particulate composite (CSC) to find the optimum percentage of CRP replacement to sand. In the analysis, mix design proportion of CRPCSC particulate composite is used as input data to obtain the predicted values of split tensile strength and slump as output from ANN. Analysis of input and output data, network training, network testing and their validation is conducted and the results obtained from ANN analysis were comparable with the experimental results of CRPCSC report.

3.1 Introduction

CSC particulate composite has been the most preferred constructional material for over decades. It is being increasingly used day by day all over the world due to its versatility and mould ability of the material and its compressive strength. River sand is one of the constituents used in production of conventional CSC particulate composite. It has become highly expensive and also good quality material is not available. The non availability of sufficient quantity of natural sand for making CSC particulate composite is affecting the growth of construction industry. Recently several researchers have used manufactured fine aggregates as a partial replacement of natural sand and investigated its effect on major CSC particulate composite properties. Similarly Crushed Rock Powder (CRP) could be alternative to natural sand. CRP (stone dust) is a byproduct generated from quarrying activities involved in the production of crushed coarse aggregate.

It is found that CSC particulate composite of M20 grade has shown the split tensile strength as 2.55 N/mm^2 at 28 days and for 20 % replacement of stone dust, split tensile strength increased to 3.16 N/mm^2 [1]. Similarly the strength increases up to 40 % replacement and decreases gradually up to 60 % replacement of stone dust. In the study reported, workability is measured by means of slump cone method. The value of slump with constant water/binder ratio for CRP concrete and normal concrete is maintained around 65–75 mm by adding an admixture which complies with IS: 9103:-1999[1]. It is found

G.L.E. Prasad (✉)
Manglore Institute of Technology and Engineering, Mudbidire, Karnataka, India
e-mail: gle.prasad@gmail.com

B.S.K. Gowda
Civil Engg Dept, D A C G Government Polytechnic, Chickmaglur, Karnataka, India

R. Velmurugan
Aerospace Engineering Dept, I I T Madras, Chennai, India

M.K. Yashwanth
Civil Engg Dept, PESCE, Mandya, Karnataka, India

G.P. Tandon et al. (eds.), *Experimental Mechanics of Composite, Hybrid, and Multifunctional Materials, Volume 6*, Conference Proceedings of the Society for Experimental Mechanics Series, DOI 10.1007/978-3-319-00873-8_3,

that inclusion of CRP in concrete results in reducing the workability of concrete due to the presence of flaky particles of CRP. Sahu A.K (2003) [2] studied the suitability of crushed stone dust as fine aggregate for CSC particulate composite, it has been assessed by comparing its basic properties with those of conventional CSC particulate composite. It is observed that there is significant increase of about 10–15 % in split tensile strength for CSC particulate composite mixes when sand is partially replaced by stone dust. In the present study the results are compared with the results obtained from ANN analysis and it is found that the trend is similar.

3.2 Experimental Programme

The following are the material properties and results of the studies "strength and durability properties of concrete containing CRP and Fly ash" [1].

Materials: For preparing test specimens 53 grade OPC confirming to IS 12269:1987, coarse aggregates, Natural sand, CRP were used. The maximum size of coarse aggregate was limited to 20 mm to get maximum increase in compressive strength, admixtures like plasticizers and super plasticizers confirming to IS: 9103: 1999 are used. The CRPCSC particulate composite mix proportion for M20 and M35 are shown in the Tables 3.1 and 3.2.

Mixing and casting: Cement, CRP were mixed dry and kept separately. Then coarse aggregate and dry mix of cement and CRP kept in three layers and appropriate amount of water was sprinkled on each layer and mixed thoroughly. Then the plasticizers or super plasticizers were added and the materials were mixed thoroughly. Then cylindrical specimen of standard 150 mm diameter and 300 mm long specimens conforming to IS: 10086-1982 was casted. Each layer was compacted with 25 blows using 16 mm diameter steel rod, specimens were cured for 28 days in fresh water after 24 h of their casting, and tested in their experimental study.

Table 3.1 Mix proportion of M20 CRPCSC particulate composite

			Mix proportion(weight in kg/m^3)								
				Aggregates							
				Fine			Coarse				
Sl. no.	CSC particulate composite	Designation	Cement	Sand	CRP	Total fine	20 mm	12.5 mm	Total coarse	Water (kgs)	Plasticizers (kgs)
1	Conventional CSC particulate composite	CSC	348.3	695.03	–	695.03	662.27	441.5	1,130.7	191.6	0.697
2	CRP particulate composite	CRPCSC 20	348.3	559.64	139.9	699.54	662.27	441.5	1,130.7	191.6	0.697
3		CRPCSC 40	348.3	422.92	281.95	704.87	662.27	441.5	1,130.7	191.6	0.87
4		CRPCSC 60	348.3	281.95	422.92	704.87	662.27	441.5	1,130.7	191.6	0.87
5		CRPCSC 80	348.3	140.6	562.41	703.01	662.27	441.5	1,130.7	191.6	1.045
6		CRPCSC 100	348.3	–	713.66	713.66	662.27	441.5	1,130.7	191.6	1.045

Table 3.2 Mix proportion of M35 CRPCSC particulate composite

			Mix proportion(weight in kg/m^3)								
				Aggregates							
				Fine			Coarse				
Sl. no.	CSC particulate composite	Designation	Cement	Sand	CRP	Total fine	20 mm	12.5 mm	Total coarse	Water (kgs)	Super plasticizers (kgs)
1	Conventional CSC particulate composite	CSC	369.6	688.46	–	688.46	729.66	486.44	1,216.1	157.08	1.848
2	CRP particulate composite	CRPCSC 20	369.6	554.29	138.57	692.86	729.66	486.44	1,216.1	157.08	1.848
3		CRPCSC 40	369.6	418.89	279.26	698.15	729.66	486.44	1,216.1	157.08	2.033
4		CRPCSC 60	369.6	279.26	418.89	698.15	729.66	486.44	1,216.1	157.08	2.218
5		CRPCSC 80	369.6	139.26	557.04	696.3	729.66	486.44	1,216.1	157.08	2.402
6		CRPCSC 100	369.6	–	706.85	706.85	729.66	486.44	1,216.1	157.08	2.587

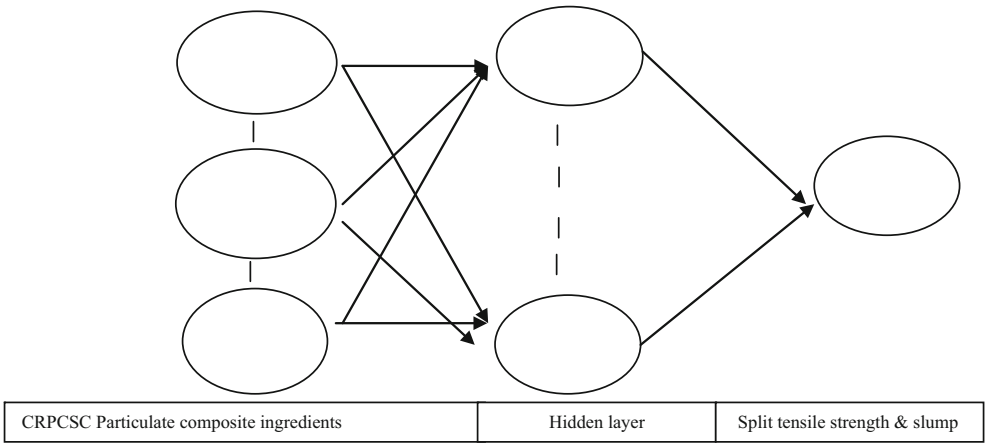

Fig. 3.1 Illustrative topology to predict split tensile strength and slump of CRPCSC particulate composite

Test procedure: The specimens are tested for their strength properties. The cylindrical specimens (150 mm diameter and 300 mm long) were tested in compression testing machine of capacity 2,000KN capacity. The test specimens were loaded at constant rate of loading at 1.20 N/cm^2/min to 2.40 N/cm^2/min as per the standard procedure explained in IS 516:1999[1]. The concrete mix are tested as per standard procedure adopted to slump cone test.

3.2.1 Artificial Neural Networks

Artificial neural network(ANNs) are similar to the biological neural networks in the sense that functions are performed collectively and in parallel by the units, rather than there being a clear delineation of subtasks to which various units are assigned [3, 4]. Currently, the term artificial neural network tends to refer mostly to neural network models employed in statistics, cognitive psychology and artificial intelligence. Neural network models designed with emulation of the central nervous system (CNS) in mind are subject to theoretical neuroscience and computational neuroscience. Artificial neural network models are specified by topology, node characteristics and training or learning rules. These rules specify that initial set of weights should be adopted during improvement of convergence performance. Broadly there are two types of ANN models namely supervised and unsupervised. In case of supervised both input patterns and output patterns are known during training. The present paper adopts feed forward supervised ANN model for prediction of 'split tensile strength and slump values'. The possible training parameters are number of iterations (epoch), learning rate, error goal and number of hidden layers. These parameters are varied until a good convergence of ANN training is obtained and there by fixing the optimal training parameters. These optimal parameters are used for testing and validation process. However the number of neurons in input layer and output layer are determined based on the problem domain depending up on number of input variables and number of output or target variables. The number of hidden layers and neurons in hidden layer are fixed during the training process. The specific ANN topology model adopted in this study is shown in Fig. 3.1. A significant number of reports have been published in application of ANN for the prediction of future events in civil engineering problems. These reports and papers have been varied from, A fuzzy-Neuro Model for Conventional CSC particulate composite mix design [5]. Reducing prediction error by transforming input data [4].

3.2.2 Results and Discussion

Figures 3.2, 3.3, 3.4, and 3.5 shows the variation of split tensile strength and slump of M20 and M35 grade particulate composite with different CRP levels. By increasing the percentage of CRP replacement in CSC particulate composite, the split tensile strength goes on increasing upto 40 % replacement of natural sand by CRP and gradually reduces till 100 % replacement, though the strength at 100 % replacement is higher than conventional CSC particulate composite.

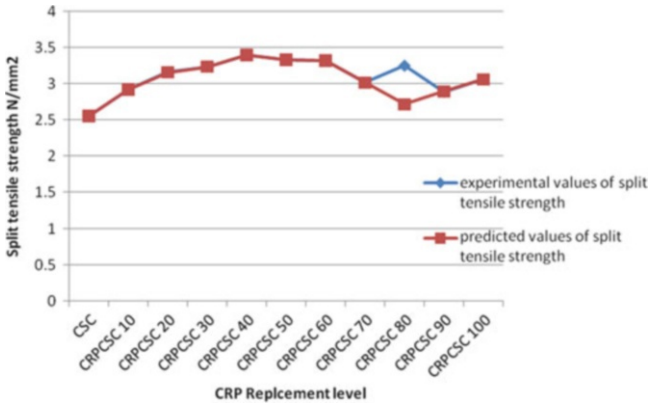

Fig. 3.2 Variation of split tensile strength for M20 particulate composite for different replacement levels of CRP

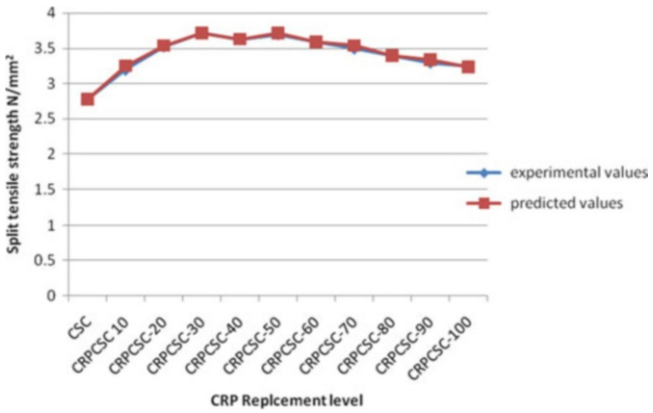

Fig. 3.3 Variation of split tensile strength for M35 particulate composite for different replacement levels of CRP

Fig. 3.4 Variation of slump for M20 particulate composite for different replacement levels of CRP

At 100 % replacement the split tensile strength is greater for CRPCSC particulate composite in comparison with conventional CSC particulate composite. The slump value of normal concrete is 74 mm for M20 grade and it decreased to 70 mm for 100 % replacement. Similar variation has been observed in M35 grade CRPCSC particulate composite. It has also been observed that inclusion of CRP in concrete results in reducing the workability of concrete due to the presence of flaky particles of CRP. The results are predicted for all the above cases by using ANN approach and same pattern of results are found. Split tensile strength at 28 days and slump values of M20 and M35 grade particulate composite are shown in the Tables 3.3 and 3.4. The values shown with in the parenthesis are the results predicted from ANN analysis. Figures 3.2, 3.3, 3.4, and 3.5 represent the variation of split tensile strength and slump values for M20 and M35 grade particulate composite for different replacement levels of CRP.

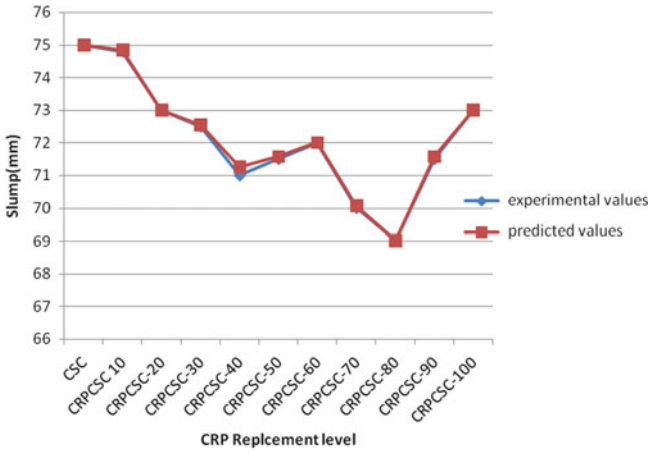

Fig. 3.5 Variation of slump for M35 particulate composite for different replacement levels of CRP

Table 3.3 Split tensile strength and slump values of M20 particulate composite

		Sand and crushed rock powder content		Split tensile strength (N/mm^2)	
Sl. no.	Designation	Sand (%)	CRP (%)	28-days	Slump(mm)
1	CSC	100	0	2.55(2.5499)	74(74.000)
2	CRPCSC 10	90	10	(2.9185)	(73.4957)
3	CRPCSC 20	80	20	3.16(3.159)	73(72.999)
4	CRPCSC 30	70	30	(3.2335)	(72.1151)
5	CRPCSC 40	60	40	3.40(3.401)	70(69.999)
6	CRPCSC 50	50	50	(3.3325)	(69.0625)
7	CRPCSC 60	40	60	3.32(3.32)	68(68.001)
8	CRPCSC 70	30	70	(3.015)	(70.0499)
9	CRPCSC 80	20	80	3.25(2.7126)	71(71.5145)
10	CRPCSC 90	10	90	(2.892)	(71.6693)
11	CRPCSC 100	0	100	3.06(3.0599)	70(70.0003)

Table 3.4 Split tensile strength and slump values of M35 particulate composite

		Sand and crushed rock powder content		Split tensile strength (N/mm^2)	
Sl. no.	Designation	Sand (%)	CRP (%)	28-days	Slump (mm)
1	CSC	100	0	2.78(2.777)	75(74.9956)
2	CRPCSC 10	90	10	(3.2535)	(74.8432)
3	CRPCSC 20	80	20	3.53(3.539)	73(72.9999)
4	CRPCSC 30	70	30	(3.7208)	(72.5467)
5	CRPCSC 40	60	40	3.63(3.7352)	71(71.2503)
6	CRPCSC 50	50	50	(3.7156)	(71.5732)
7	CRPCSC 60	40	60	3.59(3.59)	72(71.9999)
8	CRPCSC 70	30	70	(3.5429)	(70.067)
9	CRPCSC 80	20	80	3.40(3.399)	69(69.000)
10	CRPCSC 90	10	90	(3.3401)	(71.5690)
11	CRPCSC 100	0	100	3.25(3.2391)	73(73.000)

3.2.3 Conclusion

The variation of split tensile strength and slump values with different replacement levels of CRP is similar for both the grades M20 and M35. As the replacement of CRP in place of sand increases, the split tensile strength increases gradually up to 40 % replacement and decreases thereafter. At replacement level of 100 % the split tensile strength is greater for CRPCSC particulate composite in comparison to conventional CSC particulate composite. Similar trend has been observed in the

ANN prediction. Up to 40 % replacement of CRP for M20 grade particulate composite split tensile strength at 28 days increases to 3.40 N/mm^2 and for 60 % replacement split tensile strength decreases to 3.32 N/mm^2. Similar variation is observed in both M20 and M35 grade CSC particulate composite with different replacement levels of CRP. From our study it is observed that ANN could be a good mathematical tool for prediction of properties of particulate composite, using data pattern rather than time consuming laboratory procedures.

It demonstrates that whenever conventional method is tedious and time consuming to estimate properties of particulate composite, ANN model supports to predict the properties.

References

1. Sayyid Maheboob (2011) Strength and durability properties of concrete containing crushed rock powder and fly ash. M.Tech. dissertation thesis, UVCE, Bangalore University, Jnanabharathi, Bangalore
2. Sahu AK, Sunil Kumar, Sachan AK (2003) Crushed stone waste as fine aggregate for concrete. Indian Concrete J 845–848, January 2003
3. Kurup PU, Dudani NK (2002) Neural networks for profiling stress history of clays from PCPT data. J Geotech Geoenviron Eng 128(7):569–578
4. Battacharya B, Solomatine DP (2005) Machine learning in soil classification. In: Proceedings of international joint conference on neural networks, Montreal, 31 July, 4 Aug 2005, pp 2694–2699
5. Natraj MC et al (2006) A fuzzy-neuro model for conventional concrete mix design. Eng lett 132EL_13_2_8 (advance online publication), 4 Aug 2006

Chapter 4
Lithium-Ion Battery Electrode Inspection Using Flash Thermography

Nathan Sharp, Douglas Adams, James Caruthers, Peter O'Regan, Anand David, and Mark Suchomel

Abstract Pulse thermography was used to experimentally evaluate lithium-ion battery electrode quality. Lab manufactured electrodes with gross defects, thickness variation, and composition variation all were detectable with this method. Thickness variation was shown to have a one to one ratio percent change in thickness to percent change in thermal response. A thickness difference of 4 μm (4 % of total) was detectable with the method. Lab electrodes were compared with commercial electrodes with comparable results. Both types of electrodes showed a significant thickness oscillation that has not previously been reported regarding lithium-ion battery electrodes.

4.1 Introduction

The strong push towards increased renewable energy production and consumption is highlighting the need for rechargeable batteries that are inexpensive, light, and durable. Lithium ion batteries have become very popular because they have a high energy density, but are currently being held back by their high price [1, 2]. They allow for a rechargeable electrochemical potential by transferring lithium ions back and forth between the anode and cathode electrodes. These two electrode surfaces are made of porous materials that allow the ions to intercalate. Lithium ion batteries are constructed by fabricating and assembling hundreds or thousands of layers of anode–cathode pairs to generate the desired amount of current.

The amount of charge that can be stored in an electrode surface is determined by the material properties and dimensions of the surface. If these properties are homogeneous across the electrode surface, then the electrochemical potential from the lithium ions will be constant in the direction parallel to the surface of the electrode surface and the only gradient in potential will occur in a direction that is perpendicular to the surface. However, if there are areas on the electrode that vary in thickness or composition, potential and current gradients will develop parallel to the electrode surface. These undesired potential gradients can create regions that have a voltage potential that is higher than the overall voltage of the battery. If the voltage exceeds a critical value then undesirable and irreversible reactions can occur which eventually can cause battery failure. Electrode surfaces degrade through extensive use and will eventually fail regardless of the initial quality of those surfaces. However, the greater the inhomogeneity that is introduced into the electrode surface during manufacturing, the more likely it is that the battery will fail before its design life is reached [3]. Also, failure on only a small part of one electrode surface will cause failure of the entire battery. Because there are so many anode–cathode layers stacked in each battery cell, even a very small percentage of defects could significantly affect battery life.

N. Sharp (✉)
Mechanical Engineering Department, Purdue University, 1500 Kepner Dr, 47906 West Lafayette, IN, USA

Purdue University, 1500 Kepner Dr, 47905 West Lafayette, IN, USA
e-mail: nsharp@purdue.edu

D. Adams
Mechanical Engineering Department, Purdue University, 1500 Kepner Dr, 47906 West Lafayette, IN, USA

J. Caruthers • P. O'Regan • A. David • M. Suchomel
Chemical Engineering Department, Purdue University, 47906 West Lafayette, IN, USA

G.P. Tandon et al. (eds.), *Experimental Mechanics of Composite, Hybrid, and Multifunctional Materials, Volume 6*, Conference Proceedings of the Society for Experimental Mechanics Series, DOI 10.1007/978-3-319-00873-8_4,

Current quality control strategies of lithium ion manufacturing involve six sigma statistical tools. These are sound strategies that should be continued; however, quality control could be greatly improved if the electrode surfaces could also be objectively monitored during the manufacturing process. This type of process monitoring tool could improve battery quality with only minimal additional manufacturing cost, leading to an overall potentially significant cost savings.

4.2 Materials and Methods

Sample anodes and cathodes were used in the experimental thermography testing. It was desirable to use electrodes that were as similar as possible to electrodes used in commercial batteries, so the primary goal in the selection of electrode materials was to replicate commercial electrodes as closely as possible. In order to perform the necessary experiments, it was required to manufacture the electrodes for testing instead of purchasing them commercially.

The exact composition of electrodes in commercial batteries is unknown since this information is considered a trade secret by manufacturers, but research on the subject is widely available [4–6]. Electrode compositions and percentages were chosen based on literature. Lithium cobalt oxide ($LiCoO_2$) was used for the active cathode material and graphite was used for the active anode material. The electrodes are made of 94 % active material, 3 % carbon black, and 3 % binder (PVDF). All anode films were backed with a copper current collector and all cathode films were backed with aluminum; both copper and aluminum are standard current collector materials for lithium ion batteries.

All sample electrodes that were tested were manufactured at Purdue University in the School of Chemical Engineering in the battery laboratory in Forney 2,184 unless otherwise noted. The electrode films were made to replicate electrodes that are used in commercial batteries to the greatest extent possible. Figure 4.1 shows a finished cathode and anode film such as the ones used in the pulse thermography testing. The electrodes were cut to the desired size, between 50 and 150 mm^2, at which point they were ready for testing.

A Flir Systems A325 infrared camera was used to measure the infrared radiation from the specimens at 60 frames per second with a 320 by 240 pixel resolution while a Flashpoint 2420A flash lamp with a xenon bulb was used to provide a pulse of heat to the current collector surface. The pulse provides a short burst of light (about 1 ms) and infrared radiation which quickly heats the copper or aluminum current collector. The camera uses microbolometers to measure the amount of infrared radiation emitted from the electrode surface in the spectral range of 7.5–13 μm. The flash, electrode, and camera were mounted onto a custom rigging, which ensured consistency in the experimental test setup. A picture of the test setup is shown in Fig. 4.2.

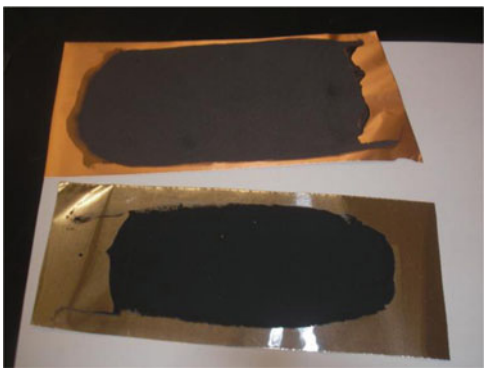

Fig. 4.1 Samples of finished electrodes

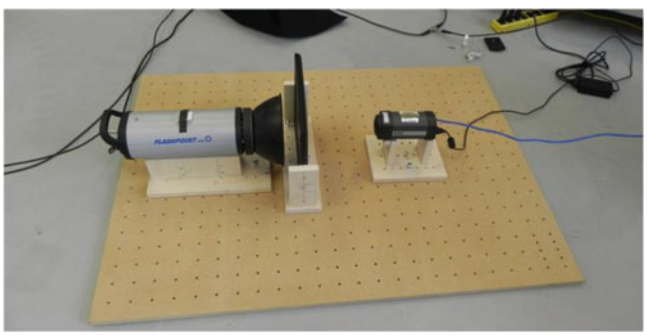

Fig. 4.2 Test setup used to ensure consistency

4.3 Results and Discussion

There are many potential types of defects that can occur in lithium ion battery electrodes. The results involving the detection of many of these defects will be discussed in this section.

4.3.1 Gross Defects

There are several possible sources of gross defects on battery electrode surfaces during the manufacturing process. Contaminants could affect the current collector surface, scratches could be introduced into the electrode surface from an imperfection in the coater blade or calendaring process, or bubbles could develop in the slurry during the mixing process. These defects were tested to ensure that they are detectable with flash thermography.

4.3.1.1 Contaminants

Two types of contaminants on the current collector surface were tested: oil and graphite. Both materials are used in the battery electrode manufacturing process and therefore have a possibility of contaminating the electrodes. Figure 4.3 includes a photo image of the current collector (the photo image was mirrored so that the photo and thermal image could be compared more easily) and Fig. 4.4 includes the accompanying thermal image. Both the oil and graphite show up clearly on the thermographic image, likely due to an increase in the absorptivity of the material.

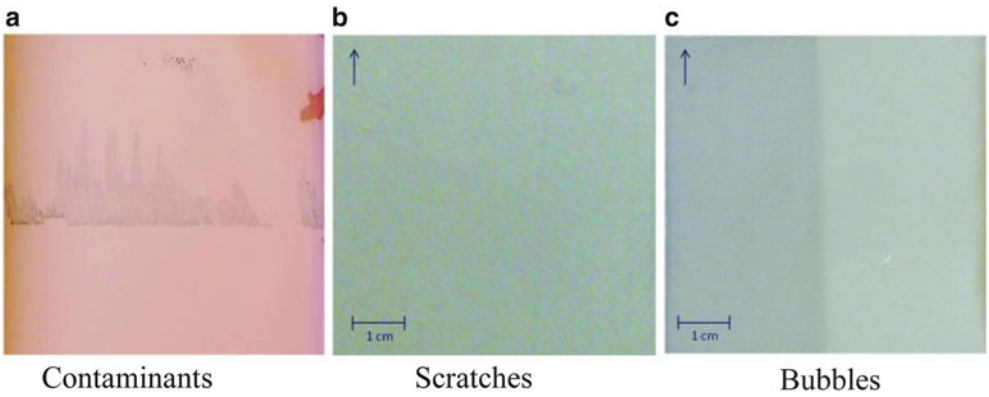

Fig. 4.3 Photo images for gross defect electrodes

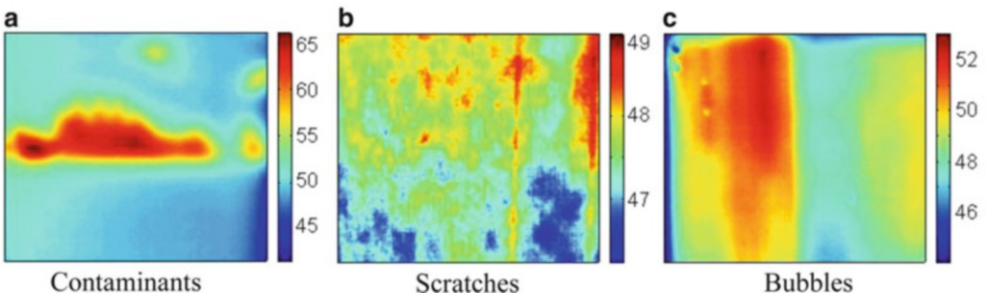

Fig. 4.4 Thermography images for gross defect electrodes

Table 4.1 Thickness testing results

	Test 1	Test 2	Test 3
Thickness range (μm)	103–107	107–118	115–135
Percentage thickness change	4	10	17
Percentage temperature rise difference	4.8	9.2	19.2

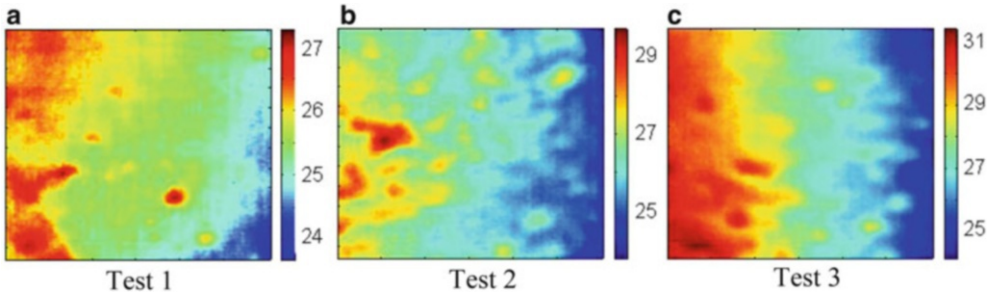

Fig. 4.5 Thickness testing thermography images

4.3.1.2 Scratches

During the manufacturing process, scratches could be introduced into the electrode surface if a particle became stuck on the coater blade or some sort of irregularity in the flow of the slurry occurred as it was scraped under the coater blade. Figure 4.3 includes a photo image and Fig. 4.4 includes the accompanying thermal image of a film with two slight scratches that were made incidentally during the manufacturing process. The two vertical scratches on the right side of the image are barely visible in the photo image but appear as obvious streaks in the thermal image.

4.3.1.3 Bubbles

The slurry mixing process is, in part, used to mix the slurry in such a way as to "defoam" it, or to eliminate all of the bubbles. Even so, occasionally bubbles become trapped in the slurry while it is being coated and these bubbles create air pockets in the electrode. Figure 4.3 includes a photo image and Fig. 4.4 includes the accompanying thermal image of an electrode with three bubbles that incidentally formed under the surface of the electrode film. These bubbles are less than a millimeter in diameter and difficult to detect visually, yet they can be easily detected with a thermal image.

4.3.2 Thickness Variation

Thickness variations in the electrode will occur to some degree no matter what manufacturing or quality control mechanisms are in place. The tighter the range in the uncertainty of the thickness, however, the more spatially uniform the electrode will be and, therefore, the more efficient and the more durable it likely will perform in a battery. Three films, each with a different magnitude of thickness gradient, were manufactured and tested to estimate the method's sensitivity to changes in thickness. Table 4.1 shows the thickness ranges for each electrode, the associated percentage thickness change, and the resulting percentage temperature rise difference; the results show close to a one to one correlation between percentage thickness change and percentage temperature rise difference. The results also show that the method can clearly detect thickness gradients of as low as 4 %. Figure 4.5 shows the thermal images from tests 1 through 3, respectively. The temperature gradient is seen to be roughly linear for all three cases. Also note that for this section the initial temperature before the test was subtracted from the data so the temperature results reflect only the rise in temperature, not the measured temperature. The temperature was compensated in this manner to facilitate percentage rise comparisons.

Table 4.2 Composition test settings

	Percentage by weight			
Material	Control	Test 1	Test 2	Test 3
$LiCoO_2$	96	94	96	96
PVDF	2	3	1	3
Carbon black	2	3	3	1

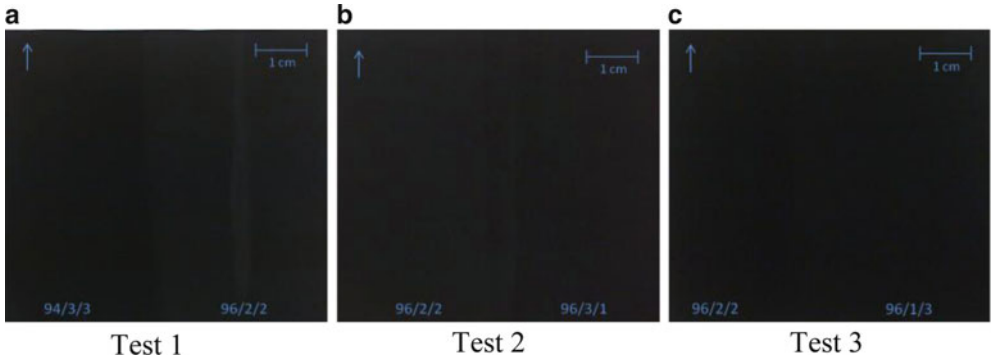

Fig. 4.6 Composition test photos

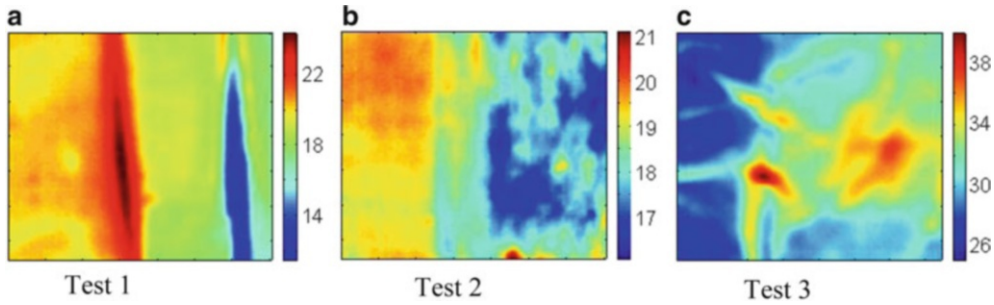

Fig. 4.7 Composition test thermography images

4.3.3 Composition Variation

Another possible cause of temperature variation in the response is if the composition of the electrode material is not uniform. If the composition varies in this way, the thermal conductivity should vary as well. This type of defect was also experimentally studied. Electrodes were manufactured with different compositions on each half of the surface. The different percentages of each material are listed in Table 4.2. The amount of NMP was held constant in all compositions.

Figure 4.6 shows the photo images of each of the 3 electrodes tested with the compositions of each side labeled; Fig. 4.7 shows the accompanying thermal images. Based on the results of the three tests together, it can be concluded that the amount of PVDF dominates the thermal response of the electrodes. The sensitivities of each ingredient to thermal response were not calculated. However, the thermal response difference is significantly higher than it would be if it were only due to emissivity difference, validating the previous assumption that emissivity difference is negligible. Table 4.3 shows results from the composition test.

4.3.4 Commercial Electrodes

An important test for this method is to verify that the results from the electrodes manufactured in the lab are consistent with results obtained for electrodes that are being used inside of commercial lithium ion batteries. To this end, electrodes were purchased from a commercial battery supplier and tested. Figure 4.8 shows the photo image and thermography image for a

Table 4.3 Composition test results

	Ctrl 1	Test 1	Ctrl 2	Test 2	Ctrl 3	Test 3
% $LiCoO_2$	96	94	96	96	96	96
% PVDF	2	3	2	1	2	3
% Carbon black	2	3	2	3	2	1
Avg temperature rise	18.9	20.2	19.5	17.4	27.4	32.6
% Diff vs control	–	6.9	–	−10.8	–	19.0

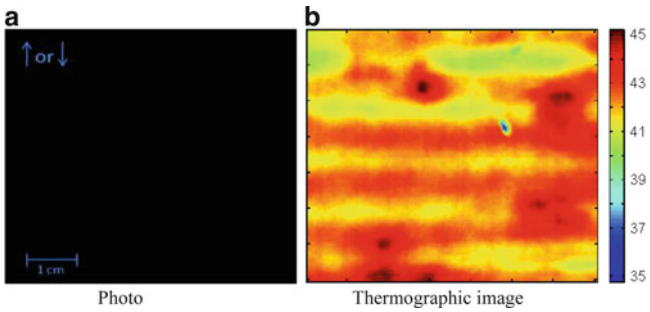

Fig. 4.8 Photo and thermographic image of commercial electrode

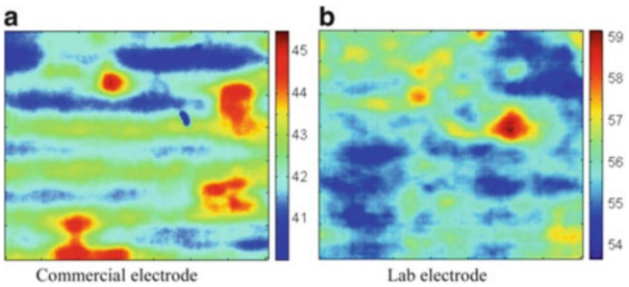

Fig. 4.9 Commercial electrode and lab electrode thermography images

purchased electrode. The results show that it is not close to perfectly uniform. The temperature range of the image is dominated by the presence of a bubble; Fig. 4.9 shows the same electrode with the range readjusted as well as an electrode of similar quality which was manufactured at the lab. These results show that both electrodes have a wave pattern as well as random hot spots that indicate areas of either reduced thickness or different material properties. The commercial electrode was not selectively chosen but was just a random sample, yet it shows significant spatial variability. This result shows that this method is not just a tool to prevent random errors in the manufacturing process, but that it can help to improve manufacturing processes such that the battery electrodes are consistently higher quality. This improvement in quality could potentially provide a large boost in battery performance and longevity without requiring large amounts of time and money invested in long term research or more expensive materials.

4.3.5 Wave Pattern

The results of the commercial film testing were consistent with findings from the lab manufactured electrode films in that both films showed a consistent wave pattern with the wave acting along the direction of the coating. This result was not anticipated. There have not been any findings in the literature that discuss this phenomenon. Due to the magnitude and nature of this phenomenon, it is almost certain that there is a periodic change in thickness occurring on the electrode films on the order of 10 % of the thickness of the electrode. Also, the fact that the phenomenon is identical on both the lab manufactured and commercial films indicates that it is due to some unknown effect of the process or materials. It appears that there is an as

yet unknown phenomenon causing a significant thickness variation. It is likely due to an effect from the fluid being forced under the coater blade or a vibration in the coater blade itself, although further testing would need to be performed to conclude the source of this effect.

4.4 Conclusion

Currently there is no way to assess lithium-ion battery electrode quality during the manufacturing process. Having the means to quantitatively determine electrode quality in situ could prevent the use of electrodes with defects, which could reduce battery life and efficiency.

Several types of defects types were tested. Gross defects such as contaminants, scratches, and bubbles were all detected clearly in the thermal image with the temperature range reaching as much as 10° for these defects, depending on the severity. Thickness gradients were also tested and found to have a sensitivity of 1 % change in temperature value for a 1 % change in thickness. Based on the measurement uncertainty and signal strength, this leads to detectable thickness gradients of as small as 4 %. Composition differences were tested and the results showed that the percentage of PVDF dominates the thermal response and that thermography can also detect a change in thickness. Testing also showed that many films exhibit a previously unknown periodic fluctuation in thickness parallel to the draw direction. This unknown phenomenon was found to be present in lab manufactured electrodes as well as electrodes which were purchased from a commercial battery manufacturer.

Testing showed that this method is a viable method to assess lithium-ion battery electrode quality. The method also has the advantages of being relatively inexpensive, fast, and robust. Everything found in the testing suggests that this method can be a successful quality control method. Work is currently being done to quantify predictions of the affect on battery life and performance from the irregularities in battery electrodes.

References

1. Daniel C (2008) Materials and processing for lithium-ion batteries. JOM 60:43–48
2. Delucchi M, Lipman T (2001) An analysis of the retail and lifecycle cost of battery-powered electric vehicles. Transport Res D 6:371–404
3. Smith M, Garcia R, Horn Q (2009) The effect of microstructure on the galvanostatic discharge of graphite anode electrodes in $LiCoO_2$-based rocking-chair rechargeable batteries. J Electrochem Soc 156:A896–A904
4. Marks T, Trussler S, Smith A, Xiong D, Dahn J (2011) A guide to Li-Ion coin-cell electrode making for academic researchers. J Electrochem Soc 158:A51–A57
5. Yang C, Wang Y, Wan C (1998) Composition analysis of the passive film on the carbon electrode of a lithium-ion battery with an EC-based electrolyte. J Power Source 72:66–70
6. Zhuang G, Ross P (2003) Analysis of the chemical composition of the passive film on Li-Ion battery anodes using attentuated total reflection infrared spectroscopy. Electrochem Solid-State Lett 6:A136–A139

Chapter 5
In-Situ Characterization of Strain in Lithium Ion Battery Anodes

Jubin Chen and Thomas A. Berfield

Abstract Anode material expansion and cracking is a well-known issue with high-capacity, rechargeable lithium ion battery systems. Substantial strains develop within the anode during both the lithium ion infusion and removal processes. In this work, a custom configuration of the standard CR2032 coin cell battery is used to allow in-situ monitoring of in-plane strain development within the anode via digital image correlation. An anode thin films consisting of amorphous silicon deposited on a metal substrate is tested to determine the influence of film adhesion and battery cycling parameters on the strain-to-failure behavior.

5.1 Introduction

Currently there is a large demand for high performance lithium ion batteries fueled by strong growth in the consumer electronics, power tools, and automotive industries. Lithium-ion batteries are highly desirable for these applications due to their outstanding energy-to-weight ratios, lack of memory effects, and slower charge loss rates than most alternative battery technologies.

Graphite materials have been used as lithium ion battery anodes starting approximately three decades ago [1]. The theoretical specific capacity of graphite is 372mAhg -1, which is fairly low compared to many alternative anodes for lithium ion battery. Researchers are continuously exploring alternative anode materials of lithium ion batteries include pure elements, alloys, composite materials, metal oxides and so on. Nanostructure composite material electrode has been vastly developed in recent years. Higher specific capacity means more electric charge cell can store, so the portable devices can be more light and convenient, electrical cars can cover longer road within one charge. Silicon, the theoretical specific capacity is over 4,000 $mAhg^{-1}$, is the highest to date among all the materials.

Due to the relatively low capacity with the commonly used anode graphite, silicon has a huge advantage over the graphite as the candidate electrode. However, silicon anode has its own limitations, because silicon thin film tends to crack and have volume changes during the insertion and extraction of lithium [2]. Silicon and Lithium forms alloys such as Li12Si7, Li7Si3, Li13Si4 and Li17Si5 [3]. Silicon volume will expand as large as four times and cannot deliver all the capacities [4, 5]. Capacity will fade dramatically after several hundred cycles.

Several methods have been used to reduce the volume expansion problems, including adding conductive materials, binders, surface modification, and introducing nanostructures. Binders and conductive additive powers can be added to the electrode to improve battery capacity. Li [6] et al. investigated using sodium carboxymethyl cellulose (CMC) as binder to Si powder, which vastly improved cycling performance.

Surface modifications are another method used to improve cell capacity. Fu [7] et al. showed that modification of the surface structures by mild oxidation, deposition of metals or metal oxides, coating with polymers or other kinds of carbons can make substantial electrochemical performance improvements. Reducing thickness of silicon thin film is another way to control the volume expansion and crack while remains more capacity [8]. Additionally, nanostructured electrodes are another promising method that can be used to improve cell capacity, cycling performance and battery life. Many nanostructure electrodes types have been investigated, including nanowires [9], nanoparticles [10], or nano-patterned electrodes [11].

J. Chen (✉) • T.A. Berfield
Department of Mechanical Engineering, University of Louisville, 40292 Louisville, KY, USA
e-mail: j0chen20@louisville.edu

G.P. Tandon et al. (eds.), *Experimental Mechanics of Composite, Hybrid, and Multifunctional Materials, Volume 6*, Conference Proceedings of the Society for Experimental Mechanics Series, DOI 10.1007/978-3-319-00873-8_5,

A number of works have attempted to directly measure the development of strain of anode materials within rechargeable lithium ion battery systems. The majority of these studies use a custom battery arrangement that incorporates a window to allow visual access to the anode electrode. Most recently, V. Sethuraman, et al., [12, 13] analyzed a silicon thin film anode system by using a laser optical detection method to determine in situ stress and mechanical property changes during charging/discharging. In a similar way, Qi and Harris [14] used a custom battery fixture to observe deformation and cracking of a graphite electrode. In that study, the graphite was deformation was determined using digital image correlation.

Developed originally in the 1980s by Sutton, et al., [15], digital image correlation (DIC) uses numerical algorithms performed on optically recorded images taken of a specimen surface during an applied loading. The outputs of a DIC experiment are the surface displacements and strains over the full imaged field (in-plane for 2D versions). Given the difficulties presented by the experimental mechanics measurement of anode strain development, DIC offers several advantages. These advantages include: (1) providing full-field displacement measurements; (2) the non-contact measurement allows wide range of specimen dimensions and scales; (3) it is fairly inexpensive to implement; (4) it is adaptable to many materials and loading methods.

5.2 Experimental Details

In this work, a custom version of the CR2032 Li-ion coin cell using an amorphous silicon thin film as the anode was developed. The custom cell allowed optical imaging of the anode throughout the process of battery cycling. A DIC analysis was then performed on the images to determine strain changes within the silicon layer.

For the battery anode, amorphous Si thin films were deposited by RF magnetron sputtering onto a 0.025 in. thick flat copper disk (Technics 4604 Sputter Coating System). A 4 in diameter round target of pure Si (99.99 %, Kurt J. Lesker) was used for the sputtering deposition. A 5 min pre sputtering procedure was used to remove any native silicon dioxide before the final sputtering. Si thin films were deposited by a 300 W RF power supply a duration typically between 30 min and 60 min, depending on the desired thickness. During deposition, the chamber pressure was set at 25 mTorr with Argon flow. Film thickness was measured by (Veeco Dektak 8 M profilometer) to be 500 nm–1,000 nm. The initial silicon thin film weight was approximately 1.0 mg.

The optical window was constructed by, first, using a mechanical punch to create a 0.25 in. diameter hole in the coin cell cap. Fine grit sand paper was used to remove any rough edges. A 12 mm diameter round, 0.15 mm thick glass cover slip (Ted Pella, INC) was then attached to the top surface of the cell cap by applying CRL 349 ultraviolet adhesive (Loctite Impruv) followed by a 2 min UV exposure to cure. The additional cell pieces, including the lithium metal cathode and polypropylene separator, had through-holes formed in them using a gasket punch while housed under the assembly glove box.

The custom CR2032 coin cell, Fig. 5.1, was assembled in an Argon filled glove box. All parts, including cell cap, gasket, spring (Hohsen) were put into a 80 °C heated chamber (Buchi glass oven B585) and connected to a vacuum pump for 8 h to

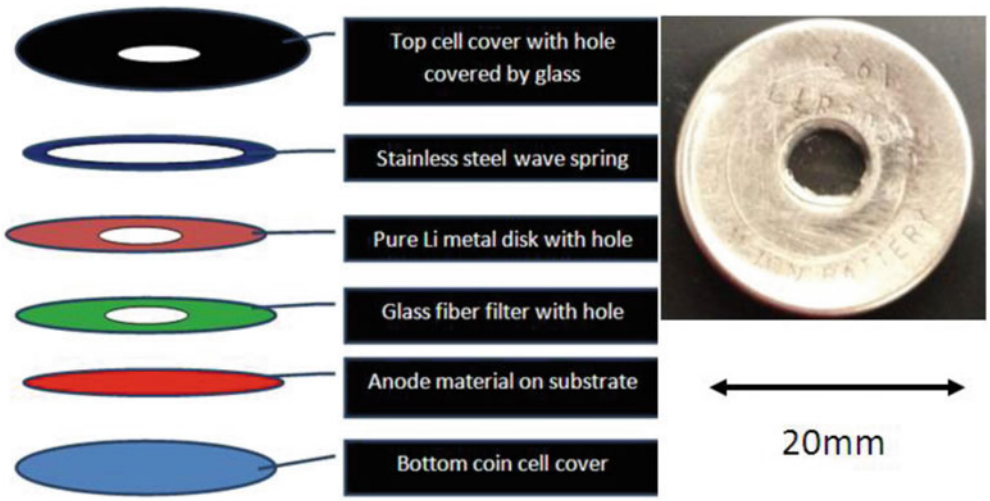

Fig. 5.1 Coin cell structure diagram (on the *left*) and a typical actual coin cell (on the *right*)

remove all possible water moisture and evaporated solvent before assembly. Amorphous silicon thin film on copper was used as the anode while a pure Lithium metal (5 mm thick from Sigma Aldrich) disk served as the cathode. The positive and negative electrodes were separated by glass fiber filter (Advantec) and the amount of the electrolyte was ca. 0.5 mL. The electrolyte was 1 M LiPF6-EC:DMC (1:2 by volume). Finally, a hand-operated crimping tool (Hohsen) was used to close and seal the coin cell. The detailed schematic and the actual coin cell are shown below in Fig. 5.1.

5.3 Results

Electrochemical characterization of the custom CR-2032 coin-type cell performance was conducted in an Arbin BT2000 battery tester. After the initial discharge of the battery, a constant current of 0.1 mA constant current was applied to cell during the charging cycles until a battery potential of 2 V was reached. During discharge cycles, a cut-off voltage set at 0.02 V for the battery was used, Fig. 5.2. After a short rest period upon reaching the discharge cut-off, the charging cycle was begun again (0.1 mA constant current applied). After charging, the battery maintained a 2 V open-circuit potential until the next discharge cycle began.

During the battery cycling, a Leica DMR microscope mounted with a Retiga 4000R digital camera from QImaging (2,048 × 2,048 pixels) was used to capture images of silicon thin film anode surface through the coin cell window, Fig. 5.3. Images were taken before cycling at several different spots, and at different magnifications using long working distance objectives ranging from 10X–50X. The inherent surface roughness of the substrate was found to provide a suitable pattern for performing digital image correlation.

A digital image correlation analysis was performed on a number of the images taken of the silicon anode surface. The most significant changes in the in-plane strain observed for the anode corresponded with images correlated between the fully charged and fully discharged states. For the sample data shown in Fig. 5.2a, the largest observed strain differential occurred between states **C** and **D** with an average magnitude of 1.34×10^{-3}. Comparatively, strain measurements on the very first cycle (corresponding to states **A** and **B** in Fig. 5.2a) between the initial image of the "as fabricated" anode and an image at the time of the first complete discharge, yielded an average strain differential of only 5.0×10^{-4}. For both cases, the strains reported were found by differentiating the displacement fields. These values were averaged over the field of view in both the "x" and "y" directions, and compared favorably with the direct DIC computed strains.

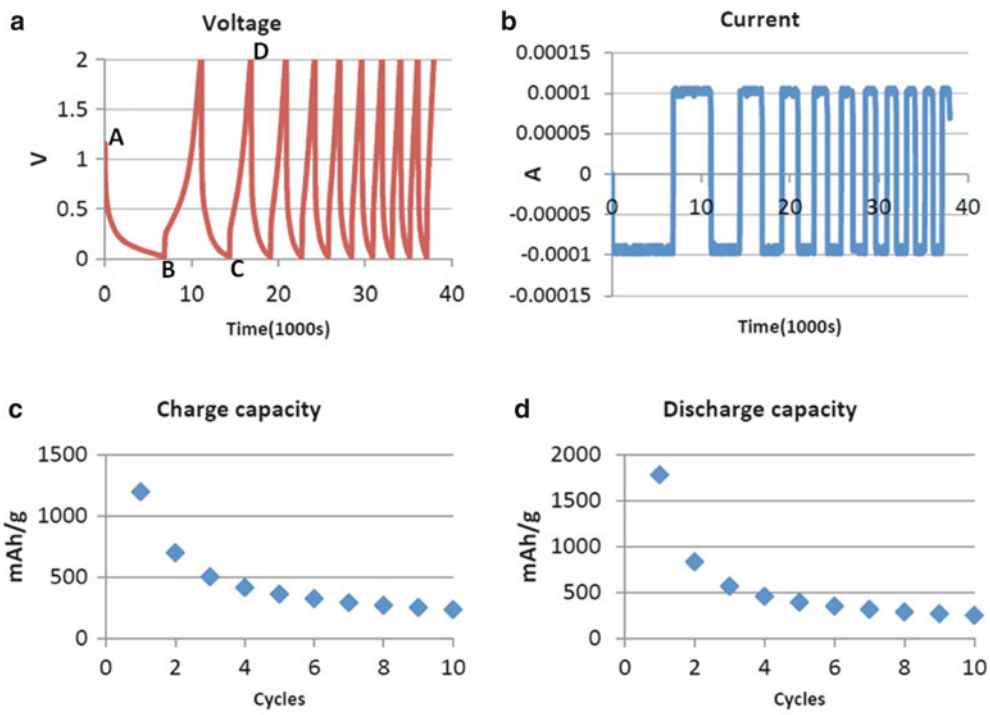

Fig. 5.2 Voltage (**a**) and current curves (**b**) during the battery cycling, and the overall charge (**c**) and discharge (**d**) capacities with respect to number applied cycles

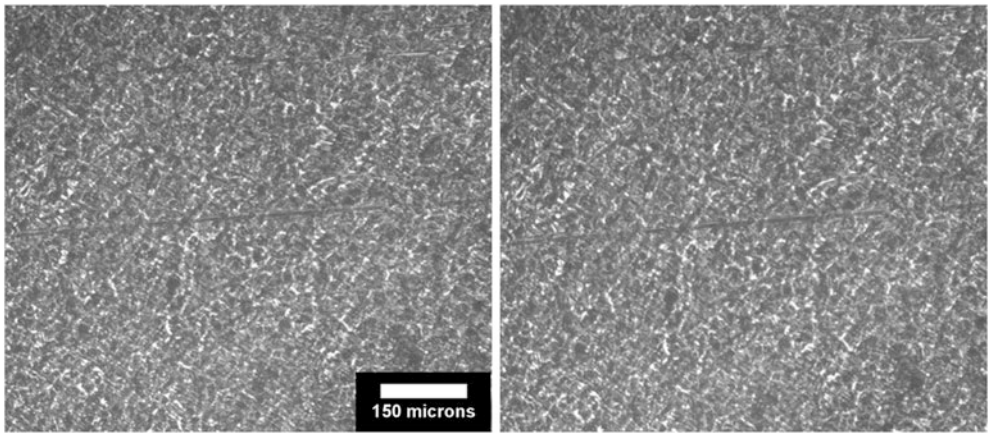

Fig. 5.3 Image taken before cycling (*left*) and after first discharge (*right*)

At later cycles, the average strains measured dropped, but eventually became difficult to substantiate due to degradation of the anode material (cracking). This degradation of the anode material corresponded with reduced charge/discharge capacities and produced increasing changes in the surface appearance, giving a non-ideal pattern for DIC measurements.

5.4 Discussion

As would be expected, the largest strain differential was observed to occur between the peak lithiation and delithiation states of the anode. It should be noted that the strain magnitudes measured represent in-plane deformations of the anode, which are greatly affected by the substrate constraint conditions. In this case, a thin copper substrate is used, only slightly thicker than a foil. This should allow greater in-plane expansions and contractions than some other potential common substrate options (e.g. a thick silicon wafer), but is still far from an unconstrained boundary. Significant out-of-plane deformations also likely occur, but appeared fairly uniform over the field of view.

Later in the battery lifetime, lower strains are expected as anode cracking begins and less volumetric expansion occurs, which coincided with diminished capacity. Cracking of the thin amorphous silicon layer is likely driven by inadequate adhesion with the substrate. For certain silicon layer thicknesses and sputter coating deposition conditions (higher temperatures and rates), it was also observed that the residual film stresses that developed were sufficient to cause delamination. Current work in progress with regards to this area is examining the roles of adhesion and substrate compliance on the rate of capacity degradation.

5.5 Conclusions

The DIC analysis of the lithium ion battery anode yielded two significant results. First, in situ characterization of displacement and strain of the amorphous silicon surface showed behavior consistent with the expected large volumetric deformations associated with Li ion implantation and removal. Secondly, as the anode surface degraded with cycling, the charge and discharge capacities decreased correspondingly.

References

1. Nagaura T, Tozawa K (1990) Lithium ion rechargeable battery. Prog Batteries Solar Cells 9:209
2. Boukamp BA, Lesh GC, Huggins RA (1981) All-solid lithium electrodes with mixed-conductor matrix. J Electrochem Soc 128:725–729
3. Obrovac MN, Christensen L (2004) Structural changes in silicon anodes during lithium insertion/extraction. Electrochem Solid State Lett 7(5): A93–A96
4. Park CM, Kim JH, Kim H, Sohn HJ (2010) Li-alloy based anode materials for secondary batteries. Chem Soc Rev 39(8):3115–3141

5. Kasavajjula U, Wang CS, Appleby AJ (2007) Nano- and bulk-silicon-based insertion anodes for lithium-ion secondary cells. J Power Sources 163(2):1003–1009
6. Li J, Lewis RB, Dahn JR (2007) Sodium carboxymethyl cellulose – a potential binder for Si negative electrodes for Li-ion batteries. Electrochem Solid State Lett 10(2):A17–A20
7. Fu LJ, Liu H, Li C, Wu YP, Rahm E, Holze R, Wu HQ (2006) Surface modifications of electrode materials for lithium ion batteries. Solid State Sci 8(2):113–128, February
8. Maranchi JP, Hepp AF, Kumta PN (2003) High capacity, reversible silicon thin-film anodes for lithium-ion batteries. Electrochem Solid State Lett 6(9):A198–A201
9. Chan CK, Peng HL, Liu G, McIlwrath K, Zhang XF, Huggins RA, Cui Y (2008) High-performance lithium battery anodes using silicon nanowires. Nat Nanotechnol 3(1):31–35
10. Kim H, Seo M, Park MH, Cho J (2010) A critical size of silicon nano-anodes for lithium rechargeable batteries. Angew Chem Int Edit 49(12):2146–2149
11. Xiao X, Liu P, Verbrugge MW, Haftbaradarab H (2010) Gao HImproved cycling stability of solicon thin film electrodes through patterning for high energy density lithium batteries. J Power Sources 196(3):1409–1416
12. Sethuraman VA, Chon MJ, Shimshak M, Srinivasan V, Guduru PR (2010) *In situ* measurements of stress evolution in silicon thin films during electrochemical lithiation and delithiation. J Power Sources 195:5062–5066
13. Sethuraman VA, Chon MJ, Shimshak M, Van Winkle N, Guduru PR (2010) *In situ* measurements of the biaxial modulus of Si anode for Li-ion batteries. Electrochem Commun 12:1614–1617
14. Qi Y, Harris SJ (2010) In situ observation of strains during lithiation of a graphite electrode. J Electrochem Soc 157(6):A741–A747
15. Sutton MA, Wolters WJ, Peters WH, Ranson WF, McNeill SRS (1983) Determination of displacements using an improved digital correlation method. Image Vis Comput 1(3):133–139, August

Chapter 6
Fracture Toughness and Fatigue Behavior of Nanoreinforced Carbon/Epoxy Composites

Joel S. Fenner and Isaac M. Daniel

Abstract In this study, the objective was to develop, manufacture, and test hybrid nano/microcomposites with a nanoparticle reinforced matrix and demonstrate enhancements to damage tolerance properties in the form of fracture toughness and fatigue life. The material employed was a woven carbon fiber/epoxy composite, with multi-wall carbon nanotubes (CNT) as a nano-scale reinforcement to the epoxy matrix. A direct-mixing process, aided by a block copolymer dispersant and sonication, was employed to produce the nanoparticle-filled epoxy matrix. Initial tests were performed on cast epoxy sheets (neat and with nanotubes) to determine effects of nanotubes on the matrix alone. Specimens were tested in Mode I three point bend, showing a 20 % increase in critical stress intensity factor K for nanotube-filled epoxy over neat resin. Woven carbon fiber performs were then infused with epoxy (neat and with nanotubes) by a wet layup process to produce flat composite plates. Composite specimens cut from these plates were subjected to Mode I double cantilever beam (DCB) tests (straight and tapered) showing nearly a 200 % increase in Mode-I fracture toughness G for nano-reinforced composite over reference composite. Fatigue tests were then performed on the woven carbon fiber composite in the form of cyclic short-beam three point bend to produce interlaminar shear fatigue. Stress-life curves obtained from cyclic short-bearm three point bend showed an increase of more than an order of magnitude in cyclic life at a given cyclic load between reference and nano-reinforced composite. Fatigue-fracture tests were performed on interlaminar Mode-I tapered double cantilever beams to produce Mode-I interlaminar fatigue-crack growth. The results of cyclic interlaminar Mode-I testing showed a much lower crack growth rate for nano-reinforced composite than for reference material. SEM micrographs of failed specimens also showed significant differences in fracture surface morphology between nano-reinforced and reference composite.

6.1 Introduction

The effect of nanoparticles on the mechanical properties of composite materials has been an important topic of recent composites research [1–13]. The motivation for these studies, namely the surprising enhancements that can be obtained from the introduction of relatively small quantities of nanoparticles, has considerable bearing on the applications of these materials and promotes their wider use.

Damage tolerance enhancements are to be expected from the addition of nanoparticles to a composite material owing to additional energy-absorbing mechanisms that arise. In the case of carbon nanotubes, mechanisms such as nanotube pullout from matrix, nanotube fracture, and nanotube stretching cause additional energy absorption at the nanoscale (Fig. 6.1) [2]. These mechanisms contribute to bulk macroscopic energy absorption, which in turn improves overall fracture toughness and fatigue life, as well as related properties such as compressive & shear strength and impact damage tolerance.

This objective of this study was to examine the effect of nanoparticles, namely carbon nanotubes (CNT), on the damage tolerance and energy-absorption properties of composites. Techniques were developed to develop and process the nanoparticle-reinforced composite, as well as to provide more robust methods of testing.

J.S. Fenner (✉) • I.M. Daniel
Center for Intelligent Processing of Composites, Northwestern University, Evanston, IL 60208, USA
e-mail: JoelFenner2012@u.northwestern.edu; imdaniel@northwestern.edu

G.P. Tandon et al. (eds.), *Experimental Mechanics of Composite, Hybrid, and Multifunctional Materials, Volume 6*, Conference Proceedings of the Society for Experimental Mechanics Series, DOI 10.1007/978-3-319-00873-8_6,

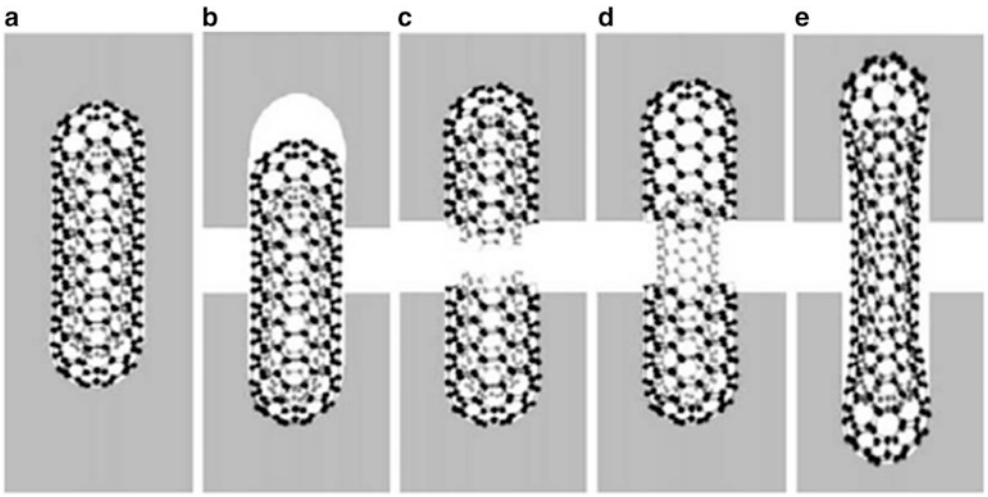

Fig. 6.1 Illustration of possible energy-absorbing mechanisms of CNTs embedded in matrix: (**a**) initial state, (**b**) pullout following CNT/matrix debonding, (**c**) fracture of CNT, (**d**) telescopic pullout-fracture of outer layer and pullout of inner layer, (**e**) partial debonding and stretching [2]

6.2 Material Processing

The material employed in this investigation was a woven carbon fiber/epoxy composite with matrix reinforcement provided by short multi-wall carbon nanotubes. The major mechanical reinforcement was provided by a 5-harness satin weave carbon fabric dry preform (Hexcel, AGP370-5H, AS4 fibers, 6 k tows). The matrix was a typical Bisphenol-A epoxy resin (DGEBA, Huntsman GY 6010) cured with an anhydride hardener (Methyltetraphthalic anhydride, Huntsman HY 917) and an additional amine accelerator (1-Methylimidazole, Huntsman DY 070). The nominal mixture ratio was 100:90:1 (resin: hardener:accelerator) by weight. The resin was reinforced with short multi-wall carbon nanotubes (Helix Material Solutions) of 1–2 μm in length and 10–30 nm in outer diameter. A polyester block copolymer supplied in solution with a weakly volatile organic solvent (Disperbyk-2150, BYK Chemie) was used to facilitate dispersion of the CNTs.

Preparation of the nanoparticle enhanced matrix was carried out primarily by simple mixing and sonication. A weighed amount of DGEBA was mixed with 0.5 %wt of nanotubes and 0.5 %wt of copolymer solution. The materials were mixed together thoroughly and then vacuum degassed at an elevated temperature (80 °C) to remove the organic solvent. The anhydride hardener was then added and mixed thoroughly, followed by a repeat vacuum degassing. The resulting mixture was subjected to sonication (90 W at 20 kHz for 30 min) to disperse the nanotubes. Just prior to composite infusion, the accelerator amine was then added, and the resin mixture infused into the carbon fiber preform, layer by layer, in a wet layup process. The wetted perform stack was subjected to final degassing and then brought to elevated temperature (150 °C) in a mold to achieve full cure. The construction of the mold (Fig. 6.2) allowed for careful control of finished laminate thickness and controlled removal of excess resin during curing. This process was developed and adapted to avoid previously encountered problems related to a marked increase in resin viscosity due to the presence of nanotubes and a filtration effect on nanotubes encountered in VARTM processing. The same procedure was used for the reference and nano-reinforced (hybrid) composites. After curing, composite plates were rough cut into specimens by means of diamond-abrasive cutting wheels, and wet-polished with SiC abrasive papers to final dimensions and smoothness.

6.3 Interlaminar Fracture Toughness

The neat and CNT- modified matrices were characterized by measuring their fracture toughness in Mode I. The Mode I toughness was determined by means of a notched beam specimen under three-point bending (ASTM 399). The measured critical stress intensity factor K_{IC} for plane strain conditions was found to be 763 kPa-$m^{1/2}$ for neat epoxy resin and 911 kPa-$m^{1/2}$ for nanotube-reinforced epoxy resin, showing an increase of nearly 20 % due to the presence of nanotubes.

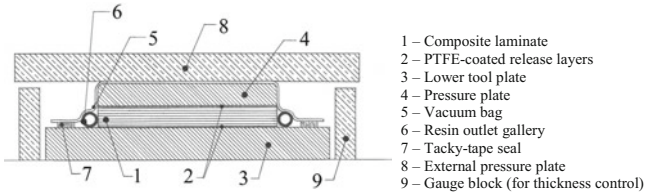

Fig. 6.2 Schematic diagram of composite fabrication mold

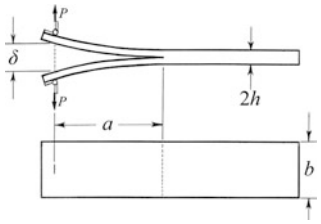

Fig. 6.3 Specimen geometry of fixed-width double cantilever beam specimen

The most critical property of the composite with a great impact on fatigue life is the interlaminar fracture toughness, for both Mode I and Mode II. The Mode I energy release rate of the reference and hybrid composites was measured by means of double cantilever beam (DCB) tests [14]. The typical fixed-width double-cantilever beam specimen (DCB) (Fig. 6.3) is often employed in fracture toughness testing due to its general simplicity of fabrication [13–15]. Fixed-width DCB specimens were machined from cast plates of both reference and nano-reinforced composite, utilizing a segment of PTFE film cast into the plate during fabrication as an interlaminar 'starter' crack at the loaded end of the beam.

Specimens of this type have a compliance C obtainable from simple beam theory as

$$C = \frac{\delta}{P} = \frac{8a^3}{Ebh^3} \tag{6.1}$$

where δ is the end deflection

P is the load
E is the elastic modulus along the beam axis
a is the crack length
b is the specimen width
2h is the specimen thickness

By the compliance method, the strain energy release rate G_I is then

$$G_I = \frac{1}{2}\frac{P^2}{b}\frac{dC}{da} = \frac{3P^2a^2}{4Ebh^3} \tag{6.2}$$

Performing tests of this type, under displacement-controlled conditions, on multiple specimens of hybrid nano-reinforced composite and reference material produced load–displacement curves as in Fig. 6.4. Nominal specimen dimensions were b = 25 mm and 2 h = 2.8 mm (8 plies).

An obvious increase in fracture toughness is apparent from the higher loads during crack extension of the hybrid nano-reinforced composite compared to the reference composite. Fracture toughness for these fixed-width specimens was computed by two approaches: by application of Eq. 6.2 at points where crack length measurements were taken and by numerically integrating the work of fracture from the load–displacement curves and measuring crack extension from beginning to end of test.

Due to difficulties associated with accurate measurement of the crack length during testing, and a desire to achieve greater accuracy in computed values of fracture toughness, width-tapered DCB specimens were considered (Fig. 6.5). Specimens of this type have a compliance of

$$C = \frac{\delta}{P} = \frac{6a^2k}{Eh^3} \tag{6.3}$$

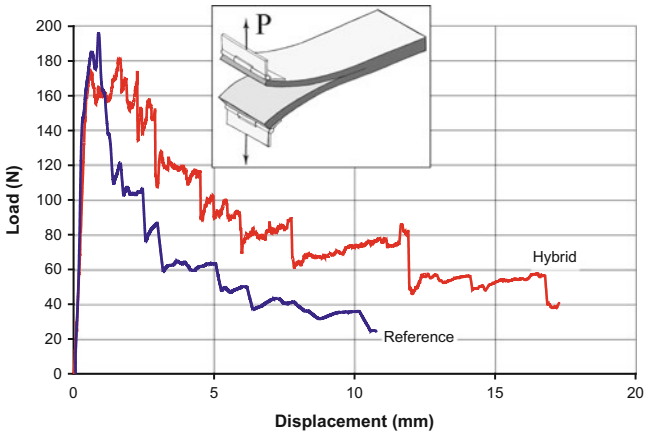

Fig. 6.4 Load–displacement curves from fixed-width double cantilever beam fracture toughness tests

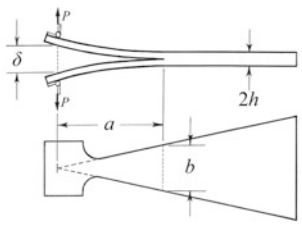

Fig. 6.5 Specimen geometry for width-tapered double cantilever beam specimen

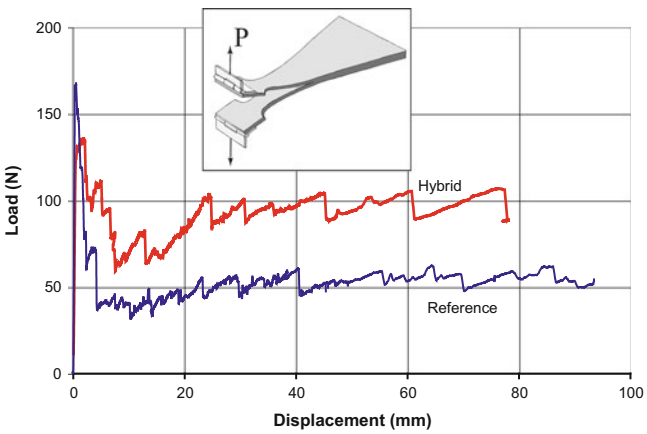

Fig. 6.6 Load–displacement curves from width-tapered double cantilever beam fracture toughness tests

where $k = \frac{a}{b}$, consequently giving a strain energy release rate of

$$G_I = \frac{1}{2}\frac{P^2}{b}\frac{dC}{da} = \frac{12P^2k^2}{Eh^3} \tag{6.4}$$

It is readily noted that this geometry removes the dependence of strain energy release rate on crack length a. Multiple specimens of this type were prepared and tested similarly under displacement-controlled conditions, giving load–displacement curves as in Fig. 6.6. Nominal specimen dimensions were k = 2.33 and 2h = 2.8 mm (8 plies) with $V_f = 0.63$.

As with the fixed-width specimens, the difference in load during crack extension is indicative of a higher fracture toughness in the hybrid nano-reinforced composite than in reference material. Also of note is the stepwise form of the load–displacement curve, indicative largely of crack propagation over woven fiber crimps, but also showing greater 'step' magnitudes in the hybrid composite than in the reference material. Fracture toughness for these width-tapered specimens was computed by two approaches, by the mean load from the load–displacement curves during stable crack growth using

Eq. 6.4, and by numerically integrating the work of fracture from the load–displacement curves and measuring crack extension from beginning to end of test. Both fixed-width and width-tapered DCB approaches were in good agreement. The interlaminar fracture toughness was determined to be 176 J/m^2 for the reference material and 498 J/m^2 for the hybrid nano-reinforced material, for an increase of 182 % in the nano-reinforced composite over reference material.

6.4 Interlaminar Shear Fatigue

Preliminary fatigue testing was conducted utilizing short beams in cyclic three point bending to produce cyclic interlaminar shear stress. Stress-life curves (Fig. 6.7) were produced for both the reference composite and hybrid nano-reinforced material. Nominal specimens were 25 mm in length, 10 mm in width, and 5.5 mm in thickness (16 plies), with $V_f = 0.63$. Utilizing a relation based on Paris Law, the experimental data were fitted to an empirical relation of the form

$$\tau_{max} = AN^{-1/m} \tag{6.5}$$

where τ_{max} is the maximum cyclic shear stress

N is the number of cycles
A is a stress parameter related to the static strength
m is a parameter related to the rate of damage accumulation

The parameters for the two materials tested were:

$A = 58.8$ MPa and $m = 20.47$ for the reference composite
$A = 66.2$ MPa and $m = 22.17$ for the hybrid nano-reinforced composite

The difference in the stress parameter, A, is closely tied to the observed increase in static strength of the nanoparticle-enhanced material over the reference one. The difference in the slope parameter, m, is also significant, as it implies a more gradual fatigue life rate, resulting in further separation of fatigue life curves between the reference and nanoparticle-enhanced materials at higher numbers of cycles.

6.5 Mode-I Interlaminar Fatigue Fracture

In the case of the fixed-width DCB specimen the ease of manufacture is offset by a more demanding protocol for data collection, namely the accurate measurement of crack length a during the test. This proved mildly inconvenient in the case of static fracture-toughness tests, as it demanded somewhat frequent crack length measurements. The difficulty in observing the crack tip and accurately measuring the crack length along a deformed specimen, introduced some additional error

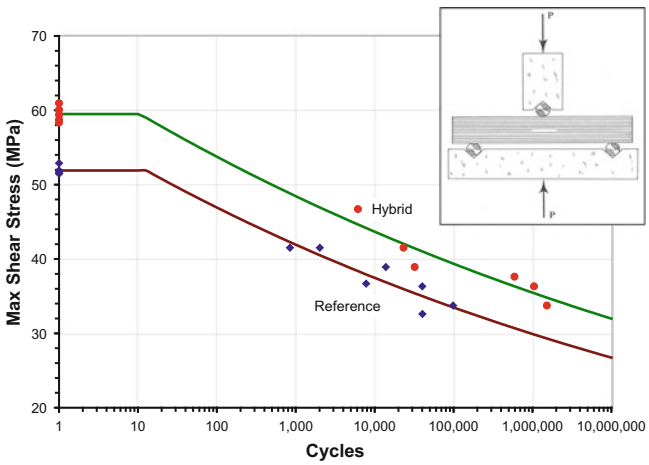

Fig. 6.7 Stress-life curves for interlaminar shear fatigue of reference and hybrid nano-reinforced composites

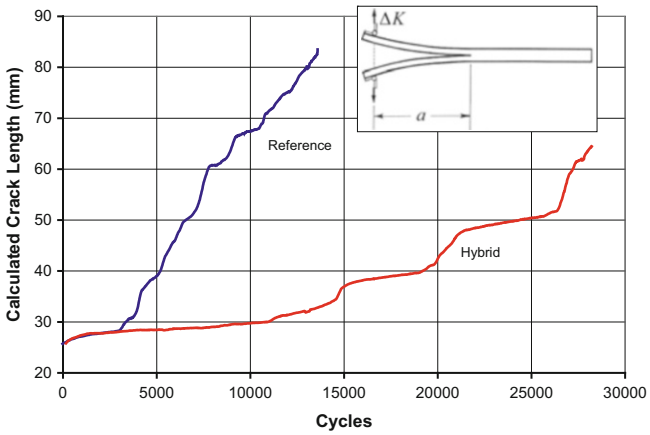

Fig. 6.8 Representative plot of computed crack length versus cycles for reference and hybrid nano-reinforced composite, $\Delta K = 2.59$ MPa-m$^{1/2}$ for both specimens

in crack length. This proved increasingly troublesome in the case of cyclic fatigue-fracture tests as the test would need to be halted periodically to take crack length measurements. Rather than endure a needlessly-complicated and tedious regimen of measurements, as is still often the case in such experiments [15], the width-tapered DCB was employed for greater simplicity.

One of the primary advantages of the width-tapered double-cantilever beam specimen already noted was that altering the mathematical relationship between specimen compliance and crack length potentially eliminated the need to measure the crack length directly. In the case of a static fracture-toughness test under displacement control, the immediate consequence was that critical crack growth occurs essentially at a fixed load regardless of crack length (Eq. 6.4). Looking at the same equations from a different standpoint, it is possible to calculate the crack length from machine-measured compliance by rewriting Eq. 6.3 as

$$a = \sqrt{k\left(\frac{\delta}{P}\right)\frac{Eh^3}{12}} \tag{6.6}$$

Likewise, the stress-intensity factor due to an applied load may be calculated from Eq. 6.4 as

$$K_I = \sqrt{EG_I} = Pk\sqrt{\frac{12}{h^3}} \tag{6.7}$$

or, for the case of cyclic fatigue-fracture under load-control

$$\Delta K = (P_{\max} - P_{\min})k\sqrt{\frac{12}{h^3}} \tag{6.8}$$

Introducing the Paris Law semi-empirical model for fatigue-fracture crack growth

$$\frac{da}{dN} = C(\Delta K)^m \tag{6.9}$$

where C & m are the empirical Paris Law coefficient and exponent, respectively, the immediate benefit is that it becomes possible to conduct a test under load-control with a single, constant cyclic stress intensity ΔK and expect a single, constant cyclic fatigue-crack growth rate da/dN. This is otherwise impossible with a fixed-width DCB. Fully automated and continuous indirect measurement of the crack length from typical testing machine data also becomes possible (since testing machine stroke and load are readily acquired by computer DAQ), allowing uninterrupted testing.

Testing width-tapered DCB specimens at fixed cyclic load amplitude produced plots of calculated crack length (Eq. 6.6) and cycle count as in Fig. 6.8. The load amplitude ratio ($P_{max}/P_{min} = R$) was set at $R = 0.1$ for all tests. Of note is the fact that, once crack length becomes sufficient to neglect the effect of the 'tab' (where hinges are attached) and transitional fillet, the cyclic crack growth becomes essentially linear, allowing a simple linear regression fit to the data to determine da/dN for a given test.

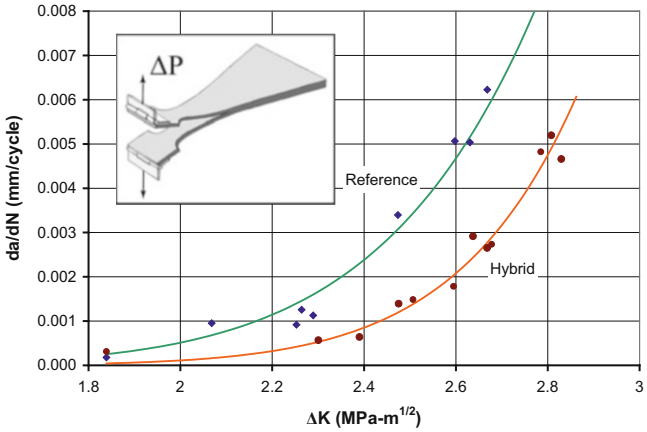

Fig. 6.9 Crack growth rate versus cyclic stress intensity for Mode-I interlaminar fatigue

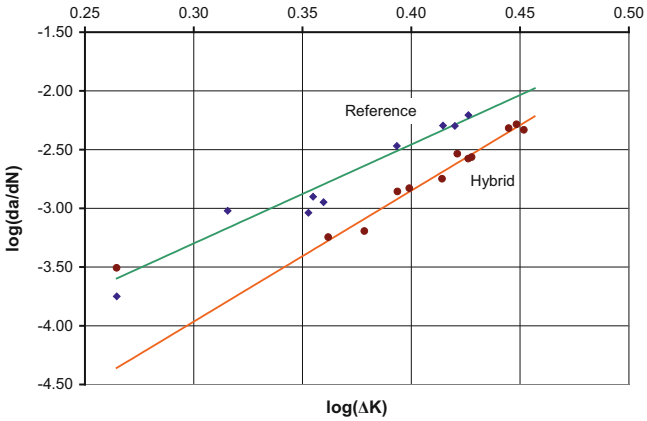

Fig. 6.10 Crack growth rate versus cyclic stress intensity (log-log scale)

Performing many such tests at different cyclic load amplitudes produced sufficient data to apply a Paris Law fit as plotted in Figs. 6.9 and 6.10. The Paris Law fit parameters for the two materials are

$$C = 1.491 \times 10^{-6} \quad \text{for reference composite}$$
$$m = 8.425$$

$$C = 4.890 \times 10^{-8} \quad \text{for hybrid nano} - \text{reinforced composite}$$
$$m = 11.153$$

with ΔK in MPa-m$^{1/2}$ and da/dN in mm/cycle. It is evident from the crack growth rate data and Paris Law parameters that the hybrid nanocomposite exhibits a lower crack growth rate than the reference material, and that the onset of crack growth is somewhat delayed or shifted in the case of hybrid nanocomposite.

6.6 Fractographic Observations

Failed specimens from interlaminar Mode-I static testing and Mode-I fatigue-fracture testing were machined into suitable samples for scanning electron microscopy. Surface conductivity for imaging was improved by plasma-depositon of metallic Osmium at a thickness of approx. 5 nm. Figure 6.11 shows typical images of fracture surfaces of statically-tested width-tapered DCB specimens, while Fig. 6.12 shows typical images from fatigue-fracture width-tapered DCB specimens.

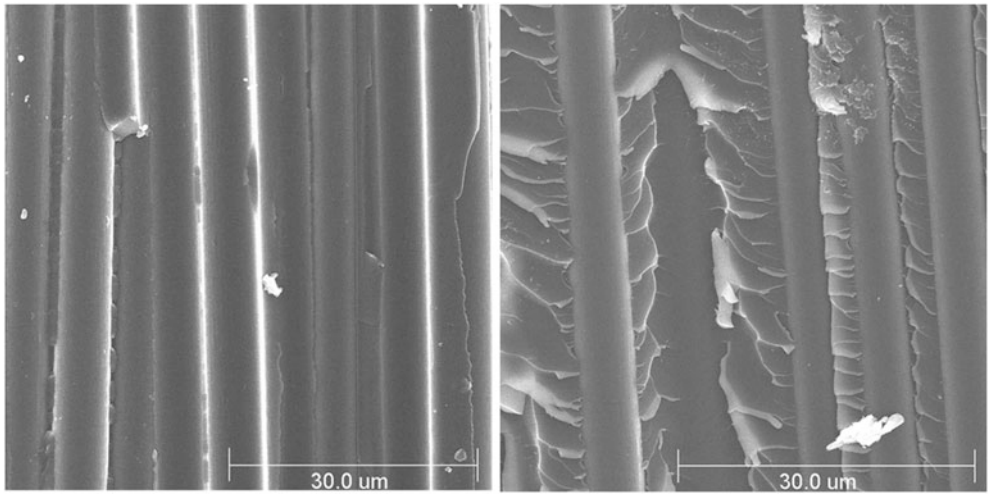

Fig. 6.11 Scanning electron micrographs of fracture surfaces from static fracture toughness tests: *Left*: reference composite; *Right*: hybrid nano-reinforced composite

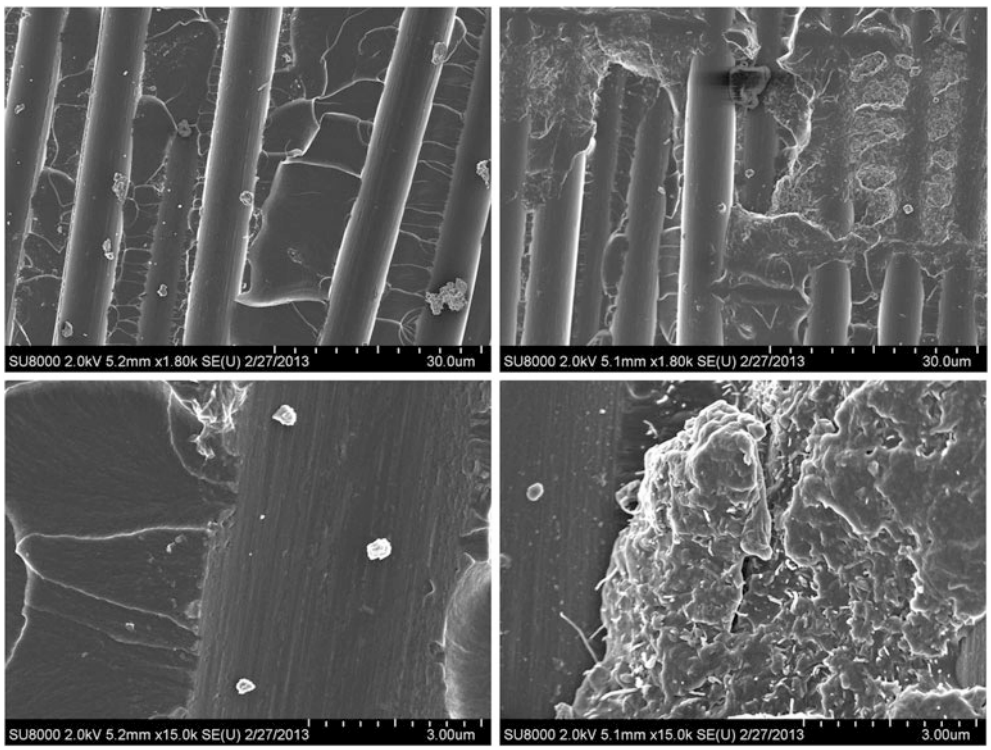

Fig. 6.12 Scanning electron micrographs of fracture surfaces from fatigue-fracture tests. *Left*: reference composite; *Right*: hybrid nano-reinforced composite ($\Delta K = 2.64$ MPa-m$^{1/2}$ for both specimens, crack propagation is from top to bottom of image)

From the images, it is evident that the morphology of the fracture surfaces between reference and hybrid nano-reinforced composite are rather different. The reference material with its neat epoxy matrix typically exhibits a smoother fracture surface than that of hybrid material with nanotubes reinforcing the matrix. Fatigue-fracture images also show a more sharply contoured or 'fractal' form of fracture surface than static fracture, further highlighting the effect of nanotubes on the composite properties. Nanotube pullout is evident in the pitting and protruding nanotube ends seen in the fatigue-fracture images in Fig. 6.12 but with a great deal more complicated fracture surface texture.

6.7 Conclusions

This study demonstrated that damage tolerance and energy absorption properties of fiber-reinforced composites can be significantly improved by nanoparticle reinforcement of the matrix. While the presence of nanoparticles in the matrix offers a modest improvement in fracture toughness to the matrix alone, the overall fracture toughness of the composite employing that matrix is improved much more dramatically. The interlaminar shear fatigue life of hybrid nano-reinforced composite showed an improvement of an order of magnitude due to nanotube reinforcement, attributable both to a modest increase in static shear strength and an increased fracture toughness of the material. Interlaminar fatigue-fracture crack growth rate was also reduced nominally by a factor of 2 due to the presence of nanotubes in the composite matrix.

Nanoparticles also evidently increase the 'roughness' or fractal dimension of a composite crack surface, regardless of whether crack growth is sudden (static loading) or incremental (cyclic loading). Nanotube pullout appears to be a more prevalent mechanism than others. Carbon fibers appear more likely to remain coated with matrix, when the matrix is reinforced with nanotubes as opposed to debonding 'cleanly' at a fracture surface.

The findings of this research are significant in that they show how a multitude of damage tolerance and service life properties of a composite material may be enhanced substantially by the introduction of a fairly modest quantity of nanoparticles and additional material processing. This not only translates to the possibility of developing more durable or robust composite materials for a broader range of applications, but also for materials that will survive significantly longer in a given application, as in high-cost systems (aircraft, wind turbines, etc.).

Acknowledgment This work was supported in part by ISEN (Initiative for Sustainability and Energy at Northwestern) and the Office of Naval Research with Dr. Y. D. S. Rajapakse as Program Manager.

References

1. Iwahori Y, Ishiwata S, Sumizawa T, Ishikawa T (2005) Mechanical properties improvements in two-phase and three-phase composites using carbon nano-fiber dispersed resin. Compos A 36:1430
2. Gojny FH, Malte MHG, Fiedler B, Schulte K (2005) Influence of different carbon nanotubes on the mechanical properties of epoxy matrix composites-a comparative study. Comp Sci Technol 65:2300–2313
3. Dean D, Obore AM, Richmond S, Nyairo E (2006) Multiscale fiber-reinforced nanocomposites: synthesis, processing and properties. Compos Sci Technol 66:2135
4. Subramaniyan AK, Sun CT (2006) Enhancing compressive strength of unidirectional polymeric composites using nanoclay. Compos A 37:2257
5. Siddiqui NA, Woo RSC, Kim JK, Leung CCK, Munir A (2007) Mode I interlaminar fracture behavior and mechanical properties of CFRPs with nanoclay-filled epoxy matrix. Compos A 38:449
6. Cho J, Chen JY, Daniel IM (2007) Mechanical enhancement of carbon fiber/epoxy composites by graphite nanoplatelet reinforcement. Scripta Mater 56:685
7. Qiu JJ, Zhang C, Wang B, Liang R (2007) Carbon nanotube integrated multifunctional multiscale composites. Nanotechnology 18 275708
8. Bekyarova E, Thostenson ET, Yu A, Kim H, Gao J, Tang J, Hahn HT, Chou TW, Itkis ME, Haddon RC (2007) Multiscale carbon nanotube-carbon fiber reinforcement for advanced epoxy composites. Langmuir 23:3970
9. Cho J-M, Daniel IM (2008) Reinforcement of carbon/epoxy composites with MWCNTs and dispersion enhancing block copolymer. Scripta Mater 58:533–536
10. Daniel IM, Cho J-M (2010) Multiscale hybrid nano/microcomposites-processing, characterization, and analysis, Chapter 12. In: Gilat R, Banks-Sills L (eds) Advances in mathematical modeling and experimental methods for materials and structures. Springer, pp 161–172
11. Manjunatha CM, Sprenger S, Taylor AC, Kinloch AJ (2010) The tensile fatigue behavior of a glass-fiber reinforced plastic composite using a hybrid-toughened epoxy matrix. J Compos Mater 44:2095–2109
12. Davis DC, Whelan BD (2011) An experimental study of interlaminar shear fracture toughness of a nanotube reinforced composite. Compos B 42:105–116
13. Joshen SC, Dikshit V (2011) Enhancing interlaminar fracture characteristics of woven CFRP prepreg composites through CNT dispersion. J Compos Mater 46:665–675
14. Argüelles A, Vina J, Cantelli AF, Lopez A (2011) Influence of the matrix type on the Mode I fracture of carbon-epoxy composites under dynamic delamination. Exp Mech 51:293–301
15. Daniel IM, Ishai O (2006) Engineering mechanics of composite materials, 2nd edn. Oxford University Press, New York

Chapter 7
Design of Multifunctional Energetic Structural Composites: A Preliminary Study on an Epoxy-Rubber Matrix with Exothermic Mixture Reinforcements

Emin Bayraktar, Diana Zaimova, Ming Jen Tan, and Ibrahim Miskioglu

Abstract A new multifunctional energetic structural composite was designed in the frame of a common research project for potential applications as structural energetic materials in aeronautical engineering. A mixture of structural and energetic functions can be achieved using different reinforcements in rubber-epoxy composites and this type of design give an exigent task. The mechanical and physical properties of the various composite systems containing Nickel and extremely fin aluminium and powders in a epoxy-rubber matrix were studied to investigate their mechanical physical properties. Dynamic (impact choc) tests and static compression tests have been carried out to understand failure response of these composites. Microstructural characterization can reveal that micro-sized Ni and Al stayed on homogeneously and intimately mixed within the epoxy matrix. Dielectric properties and dielectric loss angle tangent (tan delta) were investigated using a Dielectric Thermal Analyzer (DETA). Viscoelastic properties have been evaluated by microindentation tester and also surface wear resistance were measured by scratch test device.

7.1 Introduction

Multifunctional energetic structural composite materials offer the new prospect to come together differing properties and design materials for industrial applications requiring numerous functionalities (special requirements of electronic components). A mixture of structural and energetic functions can be achieved through use of reactive reinforcements in polymer-matrix composites, but the differing requirements for reactivity and strength make design of such materials a challenging task. Composites with polymeric matrices and hard, non-dissipative fillers can possess high stiffness and high damping, which is ideal for structural properties [1–10]. As well, epoxy groups are thermosetting polymers for which an important structural length scale, molecular weight between crosslinks (M_c), influences physical and mechanical properties. Addition of polymers to Ni + Al intermetallic-forming mixtures and Al + Fe_2O_3 termite powder mixtures has been shown to significantly affect the energetic of the reaction between the powders [3, 4, 8–10].

Mixture of these characteristics can potentially result in a material with desirable structural and energetic properties. The present paper gives preliminary results determined on design of multifunctional energetic structural materials (MESMs) based on use of highly exothermic Ni + Al powder mixture ($\Delta Hf < -2.0$ MJ/kg) [4] in a matrix of epoxy resin-scrap rubber. The main component of these scrap rubber is styrene–butadiene rubber (SBR) [11]. These static and dynamic structural/mechanical properties of Ni + Al-reinforced epoxy resin-scrap rubber composites (20 wt% scrap rubber-SBR) are needed to give detail analysis on the dielectric properties and dielectric loss angle tangent (tan delta) investigated using a Dielectric Thermal Analyzer (DETA). Finally, viscoelastic properties have been evaluated by microindentation tester and also surface wear resistance were measured by scratch test device.

E. Bayraktar (✉) • D. Zaimova
Supmeca-LISMMA-Paris, School of Mechanical and Manufacturing Engineering, Paris, France
e-mail: bayraktar@supmeca.fr

M.J. Tan
School of Mechanical & Aerospace Engineering, Nanyang Technological University, Nanyang, Singapore

I. Miskioglu
Michigan Technological University ME-EM Department, Houghton, MI, USA

G.P. Tandon et al. (eds.), *Experimental Mechanics of Composite, Hybrid, and Multifunctional Materials, Volume 6*, Conference Proceedings of the Society for Experimental Mechanics Series, DOI 10.1007/978-3-319-00873-8_7,

7.2 Experimental Conditions

7.2.1 Materials Processing and Dynamic Impact Behaviour of the Composite

A new multifunctional energetic structural composite was prepared in two stages. At the first stage, dry very fine epoxy resin and scrap rubber (20 wt%) was mixed and chemically treated by using toluene and acrylic acid and dried after treatment in the oven to eliminate entirely the trace of the chemicals. This mixture was milled 2 h to make a homogenous compound after heated at 110 °C for 2 h. At the second stage, dry Nickel and Aluminum in fine micro size was doped by mixing and put in the oven for heating during 2 h at 110 °C to prevent the humidity.

All of these compounds were then mixed in a blender and milled for 4 h. The specimens were then obtained by hot compacting (uniaxial) under pressure of 50 kN at the temperature of 180 °C for 15 min. The post curing was performed in the isothermal at 80 °C for 48 h. Only a series of pure epoxy-rubber matrix specimen have been prepared to compare the fracture beahviour with the composite. Preliminary static (compression) and dynamic (impact choc) tests have been carried out as previously described [3] to evaluate damage behaviour of this composite. Six samples were used for both of two different tests.

Microstructure and surface damage evaluations were made by means of optical (OM) and scanning electron microscopy (SEM). The accurate composition of this new designed material was given in Table 7.1 as wt%.

7.2.2 Evaluation of Viscoelastic Properties by Microindentation

CSM (Swiss company) indentation Tester device with a sphero-conical diamond indenter was used for measuring microindentation. Nine tests were performed and then averaged. The samples' thickness was approximately 5 mm. The maximum indentation loads (F_{max}) were 250 and 450 mN, the maximum load is reached in 30 s. The load was held at maximum for 400 s. The indentation hardness (H_{IT}), indentation modulus (E_{IT}) and the stiffness (S) were determined by using the Oliver and Pharr method [14]. Apart from the conventional microindentation test, another type of mode was used called multicycle constant load which gives the opportunity to examine the evolution of indentation hardness, indentation modulus and the stiffness of the composite material as a function of number of indentation cycles. Two different maximum loads were used for these measurements; 250 and 450 mN. The loading – unloading rate was 750 mN/min for an applied maximum load of 250 mN and 1,350 mN/min for an applied maximum load of 450 mN. The load was held at maximum for 50 s (dwell-creep time). Fifty cycles were performed for each maximum load.

The hardness test measurements were also carried out on Shore D scale tester. Twenty measures have been taken and then given as a unique averaged value.

7.2.3 Dielectric Properties

Dielectric properties (Permittivity (ε')) and dielectric loss angle tangent (tan delta) were investigated using a Dielectric Thermal Analyzer (DETA-Rheometric Scientific) at three different frequencies (1, 10, 100 kHz) for a long interval going on from room temperature up to 280 °C. The sample used for this type of test had a diameter of approximately 30 mm and was 1.5 mm thick.

Table 7.1 Composition of the epoxy-nickel based composite material

	Components (wt%)					
Composition	Epoxy	Nickel	Aluminum	Scrap rubber	PVA	Glass fiber
ENR	matrix	60	20	20	2	2

7.2.4 Surface Wear Resistance

Scratch tests have been carried out by using a LISMMA-Paris Micro-Scratch Tester Device with a Vickers diamond indenter. Test conditions are arranged as 2.06 N normal load with the frequency of 10 Hz in two different number of cycles; 50,000 and 100,000. Tangential and normal forces were controlled by software of LISMMA during the test that gives also coefficient of friction. After the test, damaged zone were measured by 3D optical roughness meter to characterize damage occurred after the scratch test.

7.3 Results and Discussion

7.3.1 Microstructure and Evaluation of Fracture Surface

Microstructures of the composite material that we have designed are shown in Fig. 7.1a–d. Figure 7.1a shows an example of macro picture of the cylindrical specimens and Fig. 7.1b and c show the microstructure (surface and transversal side) of the specimen that has a relatively homogeneous structure and uniform distribution of both particle types of nickel and aluminum (white particles: Nickel, dark particles Al and gray areas "epoxy-rubber" matrix).

Experimental measurement of the density for pure "Epoxy-Rubber" was found at the level of 1,285 kg/m^3 whereas the density of the composite (Ni + Al+"Epoxy-Rubber") was found at the level of 2,320 kg/m^3. It seems that these results arrive approximately 80 % of the theoretical density. It is only a remark that doping of epoxy-rubber and then the mixture of the entire elements play important role to approach the high density for the composite designed here.

As explained just in former section, pure epoxy-rubber samples were also tested and to compare with the composite structure (Ni + Al+"Epoxy-Rubber") designed here. According to the preliminary results of the dynamic-impact choc tests; the results from the six measures, one can be deduced an average energy of 4.11 kJ/m^2 with a standard deviation measures 0.589 kJ/m^2. And also, according to the preliminary results of the static compression tests; the results from the six measures, one can be deduced an average value of 350 N/mm with a standard deviation measures 11 N/mm

Finally, SEM micrographs taken from the fracture surface (Fig. 7.1d) of Ni + Al + epoxy + scrap rubber composite were evaluated after dynamic impact choc test. They indicate that there is a certain percentage of plastic deformation (about 15–20% of the fracture section) due to doped and treatment of "epoxy-rubber" with homogenous mixture. It is believed that if the mixture of "epoxy-rubber" matrix can be improved with additional chemical pretreatment, percentage of the plastic deformation can be increased. In general meaning, all other composite samples (Ni + Al+"Epoxy-Rubber") showed partially plastic deformation fractured following damage.

In fact, the microstructure shows very clearly that the importance of the dispersion of the small particle in the matrix. It means that the dispersion of the small additive particles throughout the epoxy matrix can supply physical entanglements because interaction of small particles with "epoxy-rubber" matrix can introduce to a loss in mobility of the chain segments [14, 15]. Because very small particles have a large surface area by increasing contacts with the "epoxy-rubber matrix", the strength level of the "epoxy-rubber" can increase and give higher mechanical strength of the interfaces [4]. This reason probably is partially due to the mechanical interlocking resulting from the extensive contact between the "epoxy-rubber" matrix and the small reinforced particles [4, 10–14]. In the literature, there are many results show that an increment in

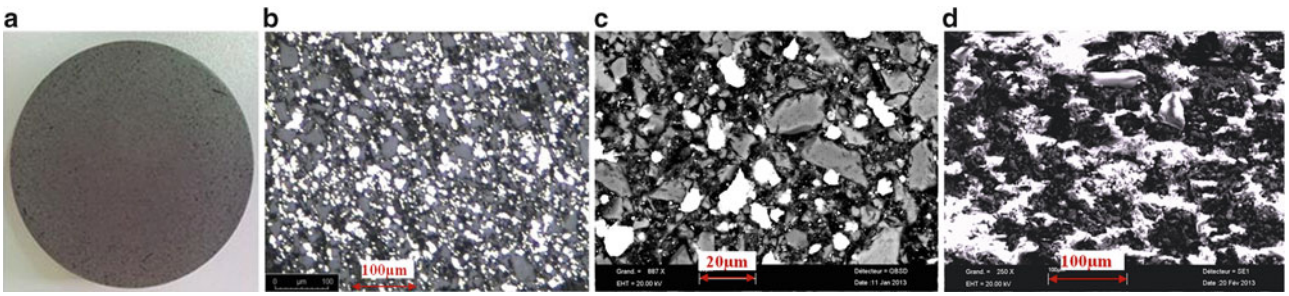

Fig. 7.1 OM and SEM micrographs showing the microstructure of the composite materials: (**a**) macrograph of the sample after compacting and post curing, (**b**–**c**) micrograph of polished (Ni + Al + epoxy-rubber) section showing the particles with a homogeneous distribution, (**d**) fracture surface after dynamic impact test showing partially plastic deformation

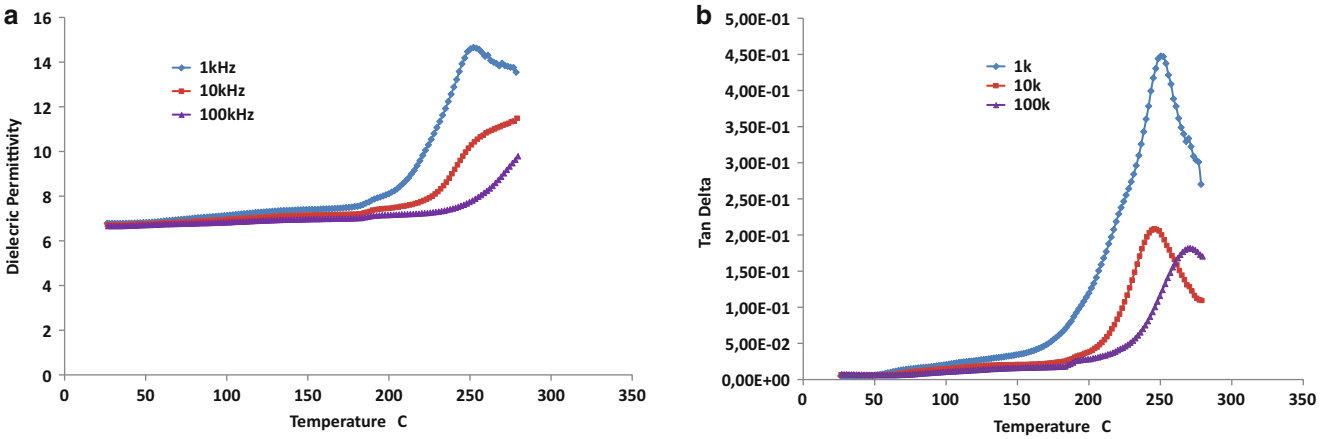

Fig. 7.2 (**a**) Dielectric permittivity and (**b**) dielectric loss angle tangent (tan delta) as a function of temperature

strength value has also been observed with increasing cross-linking density [4, 10–14]. It seems also from general appearance of the fracture surfaces (in dynamic-impact and even static compression tests) that this fracture type (partially mixture; brittle-ductile) likely to be stimulated by the entanglements and interlocking caused by the dispersion of small particles (Nickel-Aluminum) in the "epoxy-rubber" matrix.

7.3.2 Dielectric Response of the Composite Structure

Dielectric properties (Permittivity (ε')) and dielectric loss angle tangent (tan delta) were investigated using a Dielectric Thermal Analyzer (DETA-Rheometric Scientific) at three different frequencies (1, 10, 100 kHz) for a long interval going on from room temperature up to 280 °C. The sample used for this type of test had a diameter of approximately 30 mm and was 1.5 mm thick. It is important to know dielectric response of the composite with different filler contents at room temperature. At the first stage, some preliminary results were plotted in Fig. 7.2. Dielectric permittivity and also dielectric loss angle tangent (tan delta) for the composite (Ni + Al+"Epoxy-Rubber") are compared as a function of temperature. It can be seen then, that the dielectric permittivity was strongly dependent on frequency and filler concentration. Higher values obtained at low frequencies because of the low resistivity of magnetite, which generated electric charge conversion. The peaks obtained for three frequencies give more and less very close temperature values (these values are around 250 °C for 1 kHz and for 10 and 100 kHz 275 °C (Fig. 7.2a)). The same observation is seen in Fig. 7.2b, dielectric loss angle tangent (tan delta) is found around the 250 °C. These peaks corresponded to a relaxation process and started to be evidenced at high temperatures [14–17].

However, these results are not sufficient and they show some preliminary results and these tests actually continue should be detailed in the frame of the certain parameters such as temperature interval and increasing of the number of the frequency etc. But actual results can be well as indicative results for understanding the dielectric response of the composite discussed in this work.

7.3.3 Surface Wear Resistance by Scratch Test

Scratch tests results give useful information on the wear resistance of the composites designed in the current research. Tangential and normal forces were controlled by software – LISMMA during the test that gives also coefficient of friction. After the test, damaged zone was investigated by 3D optical roughness meter to measure, scratch depth, and average scratch roughness. Figure 7.3a shows the scratch test device designed by LISMMA-Paris. All of the data discussed here are controlled with special scratch test software-LISMMA. Frictional contact between the slipping diamond indenter and the surface of the composite material during scratch test was evaluated here.

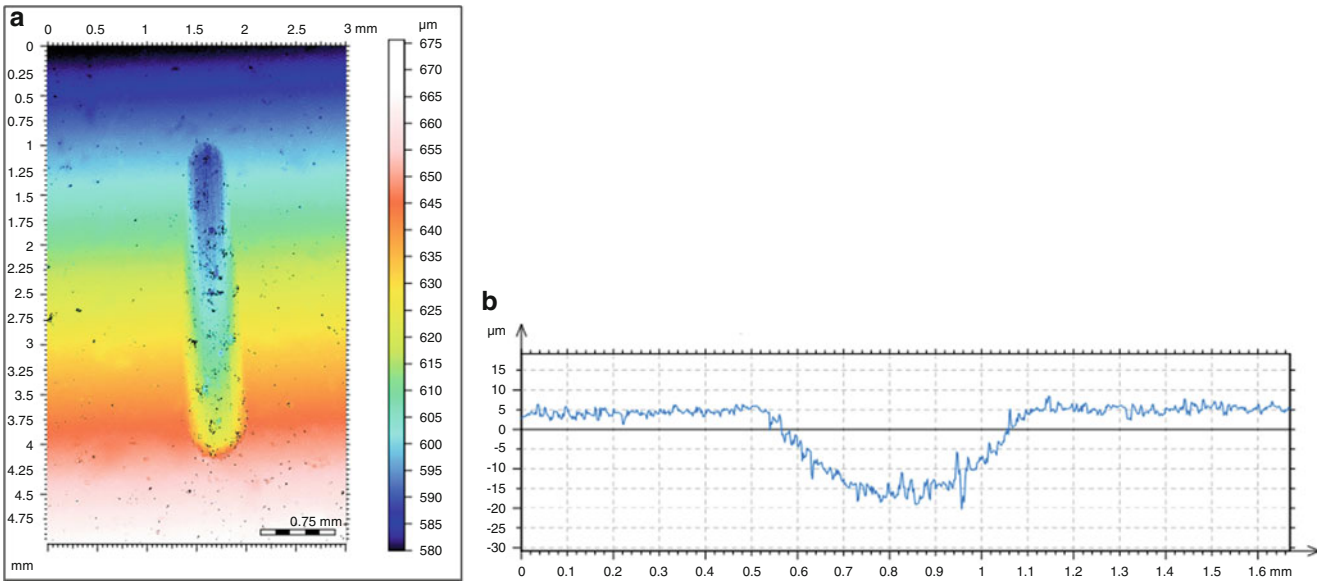

Fig. 7.3 (**a**) Damage traces obtained in the direction of width and length by scratch test after 50,000 cycles, (**b**) maximum depth profile (direction X-axis) obtained by scratch test after 50,000 cycles

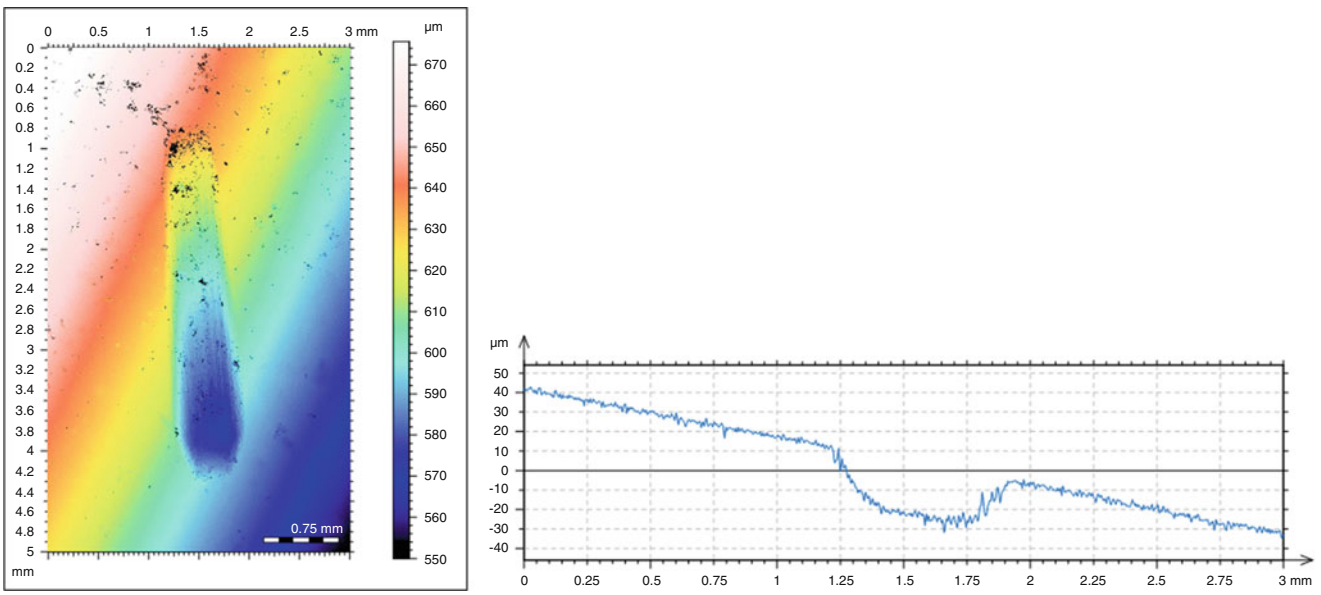

Fig. 7.4 Damage traces obtained in the direction of width and length by scratch test after 100,000 cycles Maximum depth profile (direction X-axis) obtained by scratch test after 100,000 cycles

In reality, because of the high shear stress at the interfaces the interfacial shear stress should probably be the main reason for damage of the matrix and reinforced filler interfaces [3, 10–18]. When the indenter is slipping, tangential tensile stress is caused on the surface behind the indenter, while in front of the indenter the tangential stress is compressive.

In the frame of this present work wear resistance was evaluated only under two test conditions (50,000 and 100,000 number of cycles for the composite presented here). Figures 7.3 and 7.4 indicate scratch damaged zone and characteristic parameters obtained by 3D optical roughness meter after the test conditions carried up to 50,000 and 100,000 number of cycles respectively.

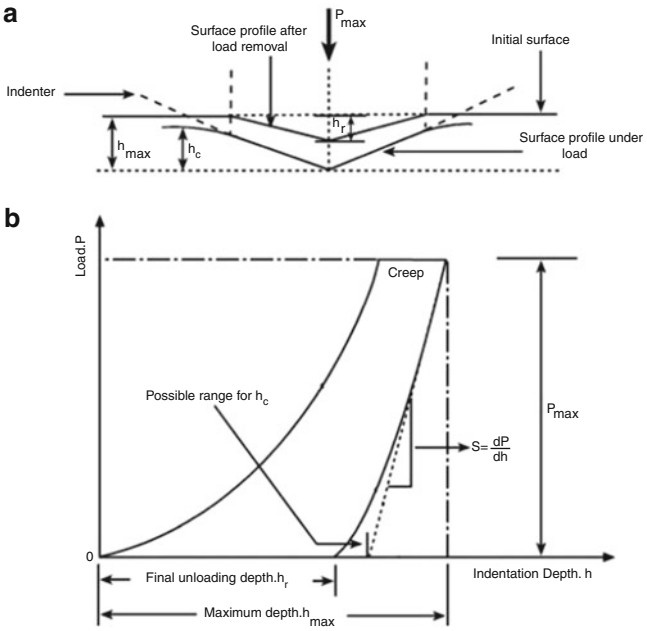

Fig. 7.5 Schematic plots of (**a**) cross-section of an indentation and (**b**) a typical load-indentation depth curve generated during a micro-indentation experiment, indicating key parameters needed for analysis

As observed from the Figs. 7.3 and 7.4, for the test after 50,000 cycles, the values for the maximum width and the maximum depth are found −0.617 mm; −23 μm respectively and also for the test after 100,000 cycles, the values for the maximum width and maximum depth are found −0.717 mm and −32.5 μm respectively.

More detail tests are required for the complete evaluation of wear resistance under different service conditions.

7.3.4 Microindentation Test

The microindentation test is a popular technique due to its simplicity and to the fact that it provides valuable information about the morphology and mechanical properties of polymeric materials. The indentation method has been also successfully employed to investigate the glass transition temperature of polymers. Recently, microindentation appears as a promising tool for micromechanical and microstructural investigation of polymer blends [3, 11].

Microindentation differs from classical measurement of hardness, where the impressions are first generated and then imaged with a microscope. Load and associated penetration depths are recorded simultaneously during both loading and unloading, producing a force-depth diagram (Fig. 7.5).

The Oliver and Pharr Method (Power Law Method) [18] recognizes the fact that the first portion of unloading curve may not be linear, and can be described by a simple power law relationship:

$$F = k(h - h_p)^m \tag{7.1}$$

Where k is a constant and m is an exponent which depends on indenter geometry. A power low function is used to describe the upper part of the unloading data.

$$F = F_{max}\left(\frac{h - h_p}{h_m - h_p}\right)^m \tag{7.2}$$

where the constants m and h_p are determined by a least of square fitting procedure. The contact stiffness S = (1/C) is given by the derivative at peak load:

$$S = \left(\frac{dF}{dh}\right)_{max} = mF_{max}\left[\frac{(h_m - h_p)^{m-1}}{(h_m - h_p)^m}\right] = mF_{max}(h_m - h_p)^{-1} \tag{7.3}$$

Table 7.2 Microindentation properties of composition ENR calculated at to different maximum loads−250 and 450 mN and creep time of 400 s

Property and maximum load	Indentation hardness (MPa)	Indentation modulus (GPa)	Stiffness (mN/nm)
250 mN	444.37	7.61	0.24
450 mN	374.12	6.76	0.30

and the tangent depth, h_r, is thus given by:

$$h_r = h_m - \frac{F_{max}}{S} \tag{7.4}$$

The contact depth, h_c, is then:

$$h_c = h_m - \varepsilon(h_m - h_r) \tag{7.5}$$

where ε now depends on the power law exponent m.

The tangent is found by differentiating the unloading curve and evaluating at maximum load (F_{max}). The intercept of this tangent with the displacement axis yields h_r.

The indentation hardness (H_{IT}) and indentation modulus (E_{IT}) were determined by using the Oliver and Pharr method transformed in the following relations:

$$A_p = f(h) \tag{7.6}$$

where A_p is projected contact area.

$$H_{IT} = \frac{F_{max}}{A_p(h_c)} \tag{7.7}$$

$$E_{IT} = \frac{1-\nu_s^2}{\frac{1}{E_r} - \frac{1-\nu_i^2}{E_i}} \tag{7.8}$$

$$E_r = \frac{\sqrt{\pi}S}{2\beta\sqrt{A_p(h_c)}} \tag{7.9}$$

where:

E_i – elastic modulus of the indenter (1,141 GPa)
ν_i – Poisson's ratio of the indenter (0.07)
E_r – reduced modulus of the indentation contact
ν_s – Poisson's ratio of the sample (0.35)

In the frame of the present work, we have carried out two different tests to understand viscoelastic behaviour of the composite (Ni + Al+"Epoxy-Rubber") under different test conditions.

Firstly, simple cycle conventional microindentation tests were made for two different maximum loads; 250 and 450 mN respectively. Creep (dwell time) for microindentation depths at two maximum loads were held as 400 s. From these basic test results, it can be deduced that even the very rich small particles (Nickel, Aluminum in the "epoxy-rubber" matrix) this composite show partially nonlinear viscoelastic behaviour. Experimental results for indentation hardness, and modulus and also stiffness were summarized in Table 7.2 and in Fig. 7.6.

Secondly, a typical microindentation test in multi-cycle constant load mode were carried out for obtaining more information and detail comparison of the values such as indentation hardness, and modulus and also stiffness by means of this type of test (Figs. 7.7 and 7.8). Here, indenter applications occur on the same point with certain cycle at constant load and should create damage on this zone exactly. By this way, it is interesting to see evolution of the indentation hardness, and modulus and also stiffness values as a function number of cycle for the same number of load cycle (Figs. 7.9 and 7.10).

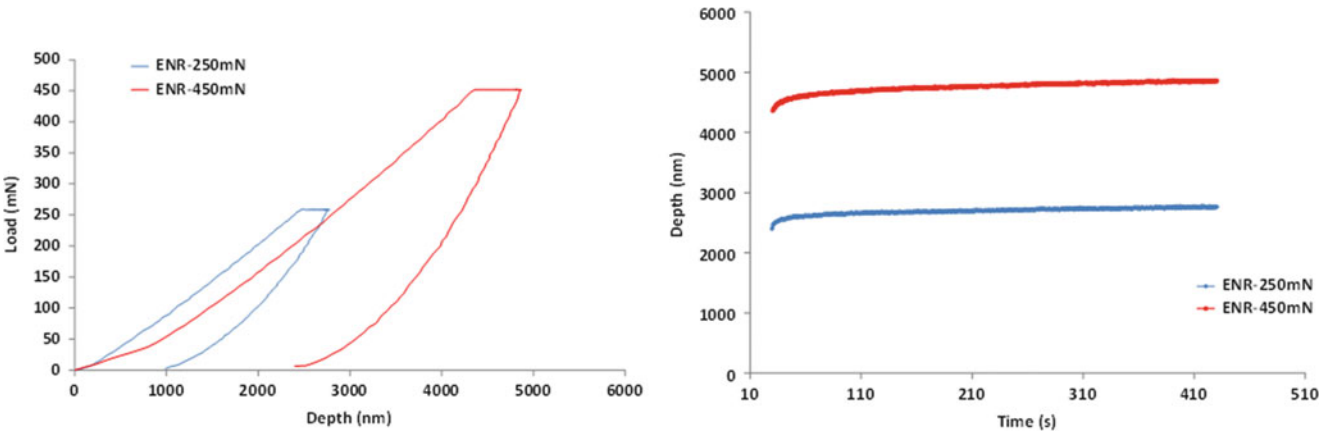

Fig. 7.6 Comparison of loading-unloading curves obtained by microindentation at two different maximum loads −250 and 450 mN. The creep time is 400 s for both loads. Microindentation depth at maximum loads 250 and 450 mN held for 400 s

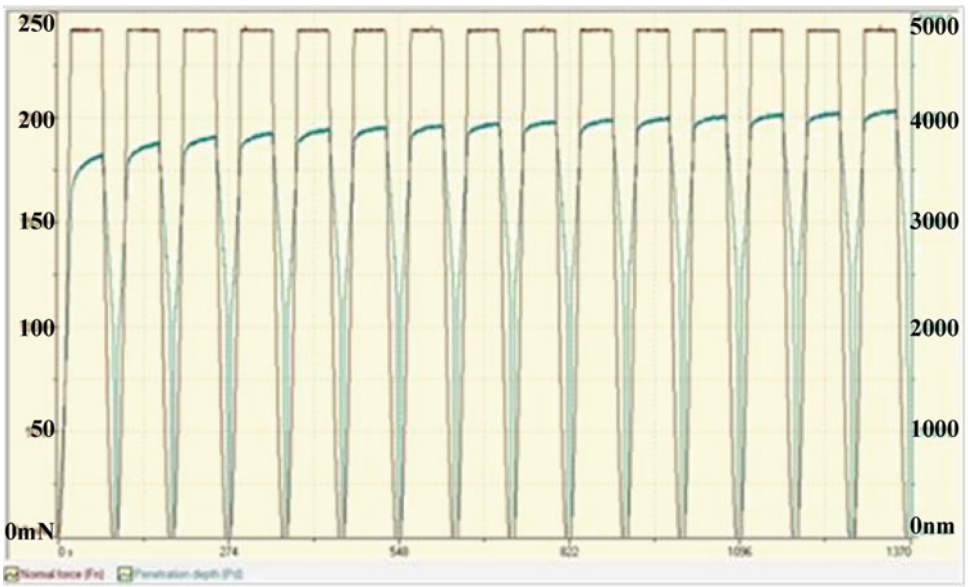

Fig. 7.7 Load (*red curve*) and depth (*blue curve*) profile as a function of time for showing only the first 15 cycles of multicycle microindentation at constant load 250 mN

The values presented in Figs. 7.9 and 7.10 are more reliable because load application by indenter arrive a stable condition and give more outlined results. An interesting result is observed here: evolution of the stiffness values does not show considerable differences. However evolutions of indentation hardness and modulus confirm the mechanical test results discussed in the section of 3.1. It means that there is no considerable strain hardening even if plastic deformation occurs partially on the applied point but most of the part of plastic part can be relaxed under the successive load on the same area. In our knowledge, this plastic zone is very limited area occurred at the end (bottom part) of the indentation depth.

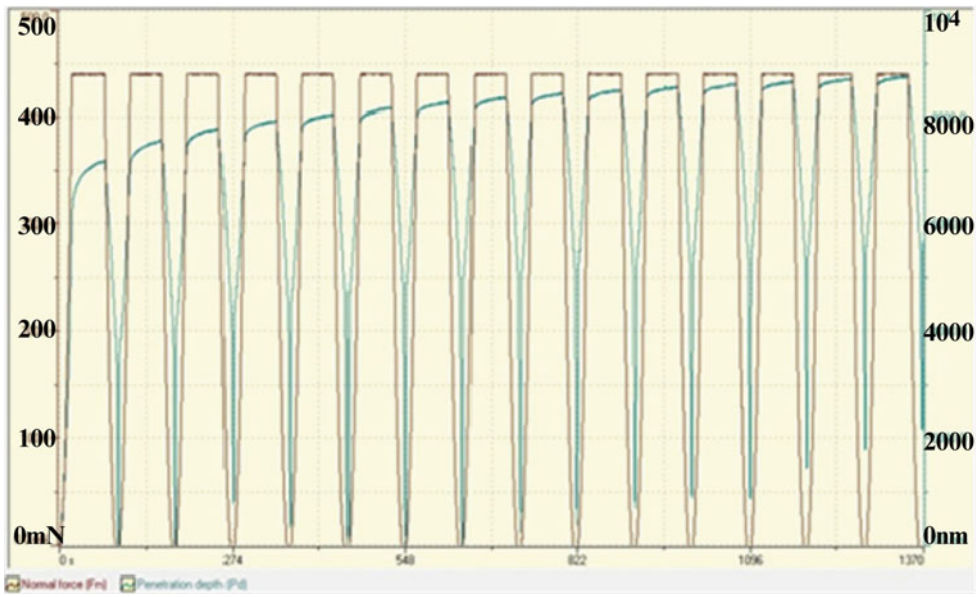

Fig. 7.8 Load (*red curve*) and depth (*blue curve*) profile as a function of time for showing only the first 15 cycles of multicycle microindentation at constant load 450 mN

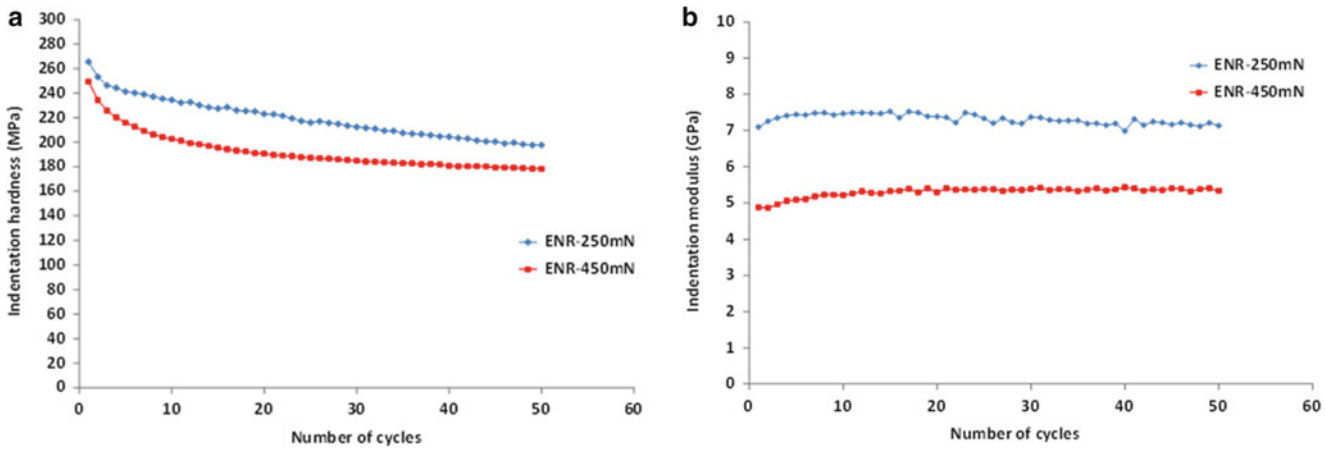

Fig. 7.9 (**a**) Comparison of indentation hardness as a function of number of cycles calculated from multicycle microindentation test at maximum loads 250 and 450 mN. (**b**) Comparison of indentation modulus as a function of number of cycles calculated from multicycle microindentation test at maximum loads 250 and 450 mN

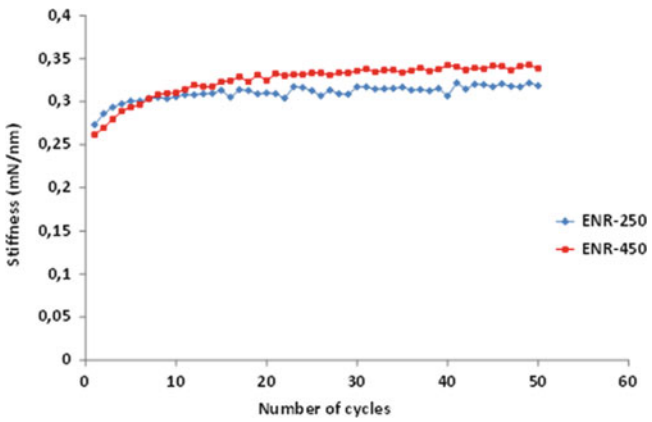

Fig. 7.10 Comparison of stiffness as a function of number of cycles calculated from multicycle microindentation test at maximum loads 250 and 450 mN

7.4 Conclusions

The structural behaviour of "Ni + Al+"Epoxy-Rubber" composites were evaluated under static compression tests and dynamic-impact choc test. Viscoelastic behaviour was evaluated by conventional and modified microindentation (constant multicycle test). Additional information about wear resistance was made by scratch test.

Partially plastic deformation and partially ductile damage were observed on the fracture surfaces and improved mechanical properties exhibited by new designed composite can be explained by increased network density caused by physical entanglements from the dispersion of small particles in the epoxy-rubber matrix. This case should be improved by making special treatment and doping epoxy and scrap rubber.

The dielectric response of this composite has been studied in the frequency range of 1, 10, 100 kHz for a long interval going on from room temperature up to 280 °C. Higher values obtained at low frequencies because of the low resistivity of magnetite, which generated electric charge conversion.

The present work is going on and a comprehensive study needs more detail experimental tests to make final evaluation of this composite. This part will be in the next volume of the present work.

References

1. Thadhani NN (1993) Shock-induced chemical reactions and synthesis of materials. Progress Mater Sci 37:117–126
2. Makino A, Law CK (1994) SHS combustion characteristics of several ceramics and intermetallic compounds. J Am Ceram Soc 77(3):778–786
3. Ouali N, Oppici A-C (2012) Elastomer toughened epoxy based composites, AMPT-Wollongong-Sydney, NSW-Australia, 23–26 Sept 2012
4. Martin M, Hanagud S, Thadhani NN (2007) Mechanical behaviour of nickel + aluminum powder-reinforced epoxy composites. J Mater Sci Eng A 443:209–218
5. Hunt EM, Plantier KB, Plantoya ML (2004) Nano-scale reactants in the self-propagating high temperature synthesis of nickel aluminide. Acta Materiala 52(11):3183–3191
6. Woody DL, Davis JJ, Miller PJ (1996) Mater Res Soc Symp Proc 418, 445
7. Thadhani NN, Armstrong RW, Gash AE, Wilson WH (Eds) (2006) Multifunctional energetic materials. MRS Symp Proc 896
8. Bai Y, Cheng Z-Y, Bharti V, Xu HS, Zhang QM (2000) High-dielectric-constant ceramic powder polymer composites. Appl Phys Lett 25:3804–3806
9. Kuo D-H, Chang C-C, Su T-Y, Wang WK, Lin B-Y (2001) Behaviours of multi-doped BaTiO3/epoxy composites. J Eur Ceram Soc 21:1171–1177
10. Wong CP, Bollampally RS (1999) Thermal conductivity, elastic modulus, and coefficient of thermal expansion of polymer composites filled with ceramic particles for electronic packaging. J Appl Polym Sci 74:3396–3403
11. Zaimova D, Bayraktar E, Katundi D, Dishovsky N (2012) Design of new elastomeric composites used in manufacturing engineering. 14th international materials symposium – IMSP'2012. Pamukkale-Denizli Turkey, vol 1, pp 1–13
12. Xu Y, Chung DDL, Mroz C (2001) Thermally conducting aluminum nitride polymer matrix composites. Compos A 32:1749–1757
13. Ramajo L, Reboredo MM, Castro MS (2007) Characterization of epoxy/BaTiO3 composites processed by dipping for integral capacitor films (ICF). J Mater Sci 42:3685–3691
14. Wernik JM, Meguid SA (2011) Multiscale modeling of the nonlinear response of nano-reinforced polymers. Acta Mech 217(1–2):1–16
15. Psarras GC (2006) Hopping conductivity in polymer matrix–metal particles composites. Compos A 37:1545–1553
16. Ultracki LA (1990) Polymer alloys and blends: thermodynamic and rheology. Hanser, New York
17. Psarras GC, Manolakaki E, Tsangaris GM (2002) Electrical relaxations in polymeric particulate composites of epoxy resin and metal particles. Compos A 33:375–384
18. Oliver WC, Pharr GM (1992) An improved technique for determining hardness and elastic modulus using load and displacement sensing indentation experiments. J Mater Res 7:1564–1583

Chapter 8
Experimental Measurement of the Energy Dissipative Mechanisms of the Kevlar Micro-fibrillar Network for Multi-scale Application

Quinn P. McAllister, John W. Gillespie Jr., and Mark R. VanLandingham

Abstract The study presented in this paper is a subset of the research described in a manuscript by the authors that was accepted for publication. In this study, nanoindentation tests were conducted on the surfaces of Kevlar 49 single fibers under a variety of contact conditions (i.e., probe geometry, indentation depth, and effective strain). The total, absorbed, and recovered energies of indentation were measured and associated with the observed deformation mechanisms of the Kevlar fibrillar network. To directly compare the energies of indentations made with the different probe geometries, the total energy of indentation was normalized by probe volume (i.e., specific energy). In general, the total energy, the percentage of the total energy that was absorbed, and specific energy of indentation increased as indentation depth and/or the effective strain increased, which correlated with the onset of additional fibril deformation mechanisms.

8.1 Introduction

Kevlar fibers have a diameter of ~12–13 μm that consists of a network of axially oriented microfibrils [1–8]. The average diameter of the surface microfibrils of the Kevlar 49 fibers studied herein was ~ 30 nm [9]. In this study, the energies (W) of indentations conducted on the surface of a Kevlar 49 fiber (see Fig. 8.1) were measured for indentations made with a variety of probe geometries resulting in a range of contact conditions. The probe geometry governs the "effective strain" and the volume of probe penetration during an indentation. The effective strain during an indentation acts as a qualitative ranking mechanism to compare probes. For indentation by a cone, the effective strain is related to the probe attack angle, ω – i.e., the relative angle between the probe surface and the sample surface [10–12]. Strain increases with increasing ω. In the case of indentation by a sphere, the effective strain is related to the ratio of contact radius to probe radius, a_c/r_{tip} [10–12]. Strain increases as a_c/r_{tip} increases. Therefore, indentations made by probes exhibiting either higher attack angles or decreased radii (i.e., increased probe sharpness) result in greater effective strains on the sample. Probe volume was considered as a normalization factor for the indentation energies made with the different probe geometries. Herein, the total, absorbed, and recovered energies of indentation, and the total specific energy of indentation (i.e., the total energy per probe penetration volume) were considered with respect to the effective strain of indentation and the corresponding deformation mechanisms of the Kevlar fibrillar network.

Q.P. McAllister (✉)
Center for Composite Materials, Department of Materials Science and Engineering, University of Delaware, Newark, DE 19716, USA

Weapons & Materials Research Directorate – Materials and Manufacturing Sciences Division, U.S. Army Research Laboratory, ATTN: RDRL-WMM-B, Aberdeen Proving Ground, MD 21005-5069, USA

J.W. Gillespie Jr.
Center for Composite Materials, Department of Materials Science and Engineering, University of Delaware, Newark, DE 19716, USA

M.R. VanLandingham
Weapons & Materials Research Directorate, U.S. Army Research Laboratory, ATTN: RDRL-WM, Aberdeen Proving Ground, MD 21005-5069, USA

G.P. Tandon et al. (eds.), *Experimental Mechanics of Composite, Hybrid, and Multifunctional Materials, Volume 6*, Conference Proceedings of the Society for Experimental Mechanics Series, DOI 10.1007/978-3-319-00873-8_8,

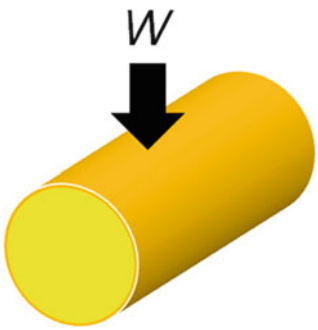

Fig. 8.1 Orientation of indentation used to measure the energy of indentation on single Kevlar fibers

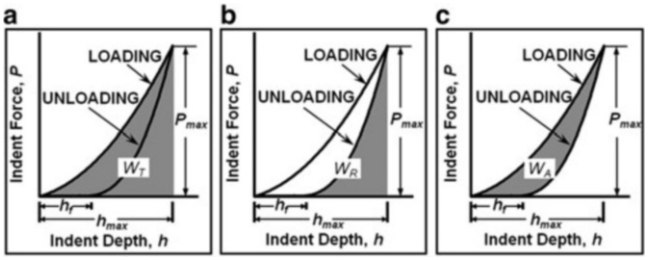

Fig. 8.2 Indentation energies determined from *P*-*h* curves (Modified and reprinted from McAllister et al. 2013 [20] with kind permission from Springer Science and Business Media)

8.1.1 Measuring Indentation Energies

The energies, or work (W), of indentation are measured using the experimental force (P) versus displacement (h) curve. The total energy of indentation (W_T) is given by Eq. 8.1 or the area beneath the loading portion of the *P*-*h* curve (see Fig. 8.2a); the recovered energy of indentation (W_R) is given by Eq. 8.2 or the area beneath the unloading portion of the *P*-*h* curve (see Fig. 8.2b); and, the absorbed energy (W_A) is given by Eq. 8.3 or the area between the loading and unloading portions of the *P*-*h* curve (see Fig. 8.2c). In Eqs. 8.1, 8.2, and 8.3 and Fig. 8.2, h_{max} is the maximum depth of indentation and h_f is the final depth of indentation after unloading.

$$W_T = \int_0^{h_{\max}} P dh \tag{8.1}$$

$$W_R = \int_{h_f}^{h_{\max}} P dh \tag{8.2}$$

$$W_A = W_T - W_R \tag{8.3}$$

In prior work, the energy of indentation was used to examine material behaviors [13–17] and depended on the volume of the probe [18, 19]. In general, the indentation energy per volume, or specific energy of indentation ($\overline{W}_T$), is a measure of resistance to overall deformation. Therefore, probe volume is used herein in an attempt to normalize the total energy of indentation for indentations made by different probe geometries. A complete derivation of the indentation volume for indentations made on a cylindrical fiber by each probe used in this study is given elsewhere [20]. The specific probe geometries and experimental indentation parameters are discussed in the following section.

8.2 Experimental

8.2.1 Materials and Sample Preparation

In this study, the energies to indent Kevlar 49 (diameter = 12.7 ± 0.7 μm) single fibers were measured. The fibers were prepared for indentation using a single fiber mounting technique that is described in detail in a prior publication by the authors [21]. The process results in the bottom of the fiber being embedded in a polystyrene film (with a thickness of ~1–4 μm)

that secures the fiber to a glass substrate. After additional surface preparation steps, described in detail elsewhere [9], the indentation measurements were made directly on the fiber surface.

8.2.2 Indentation Probe Geometries and Nanoindentation Procedure

The indentations were conducted using a Ti-950 TriboIndenter (Hysitron, Inc.) in displacement control mode with three different probe geometries: a three-sided, pyramidal Berkovich probe and two sphero-conical probes with 60° cone angles and tip radii of 213 and 357 nm, respectively. The indentation volume and effective strain depended on probe geometry and indentation depth. In general, for a given depth, the Berkovich probe exhibited the greatest volumes and lowest effective strains, the 213 nm radius probe exhibited the lowest volumes and highest effective strains, and the 357 nm radius probe exhibited intermediate values of volume and strain. The total specific energy of indentation ($\overline{W}_T$) for indentations made by each probe was calculated using Eq. 8.4:

$$\overline{W}_T = \frac{W_T}{V} = \frac{\int_0^{h_{\max}} P dh}{\left[\left(\int_0^{h_c} A_N dh_c\right)\left(\int_0^{h'_c} A_N dh'_c\right)\right]^{1/2}} \tag{8.4}$$

In Eq. 8.4, h_c is the indentation contact depth, A_N is the normal projected probe area, h'_c is the contact height in the transverse plane on the curved fiber surface, and V is the indentation volume [20].

At each testing position, the TriboIndenter's surface probe microscopy capability was used to locate the top of the fiber. Indentations were then conducted on the top of the fiber at a constant rate of 50 nm/s (with no hold period before unloading) to depths of 50, 100, 200, and 400 nm. At least 4 indentations were made at each depth with each probe. P, h, h_c, and A_N were measured or calculated using the traditional Oliver-Pharr analysis [22].

Subsequently, a Dimension 3100 atomic force microscope (AFM, Bruker AXS) was used to image at least 2 residual indentation impressions resulting from each contact condition (i.e., depth, probe). The images were acquired with a resolution of <8 nm per pixel using a NanoScope V controller, NanoScope 7 software, and a variety of tapping mode, etched silicon probes (TESP, RTESP, or TESPA). The observed deformation mechanisms of the fiber surface were then correlated to the measured absolute and specific energies.

8.3 Results and Discussion

The indentation force and energy curves presented in this section are average curves from at least 4 measurements, and are a subset of the results of a study by the authors that was accepted for publication [20]. The deformation micrographs/schematics portrayed in this section are from a mixture of indentations made on Kevlar 49 and Kevlar KM2, but are believed to be representative of the deformations of either fiber under the applicable contact conditions. The applicable contact conditions on Kevlar 49 are specified throughout this section.

8.3.1 The Energies and Deformation Mechanisms of Indentation

W_T-h curves are plotted in Fig. 8.3 for indentations made with each probe to a depth of 400 nm. At the greater indentation depths ($h \geq 200$ nm), indentation energy increased with probe volume; i.e., indentations made with the Berkovich probe exhibited the greatest indentation energy, indentations made with the 213 nm probe the lowest energy, and the energies of the indentations made with the 357 nm probe were in between those of the Berkovich and 213 nm radius probe. At indentation depths below 200 nm, the energy to indent the 213 nm radius probe increased above the energy to indent the 357 nm radius probe. At lower depths of indentation, in particular, the effective strain associated with indentation by the sphero-conical probes depends primarily on the tip radius. Therefore, the 213 nm radius probe likely imparts greater effective strain than the 357 nm radius probe. The effective strain therefore potentially affects the magnitude of W_T and the deformation mechanisms of the fibrillar network.

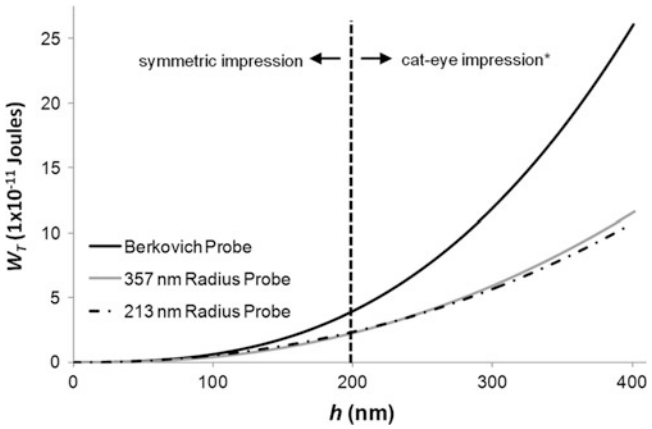

Fig. 8.3 $W_T - h$ plots for indentations made to 400 nm with each probe geometry. The *vertical dashed line* approximates the necessary indentation depth for the onset of cat-eye deformation (the "*" indicates that the cat-eye impression was only observed for indentations made with the sphero-conical probes). Modified and reprinted from McAllister et al. 2013 [20] with kind permission from Springer Science and Business Media

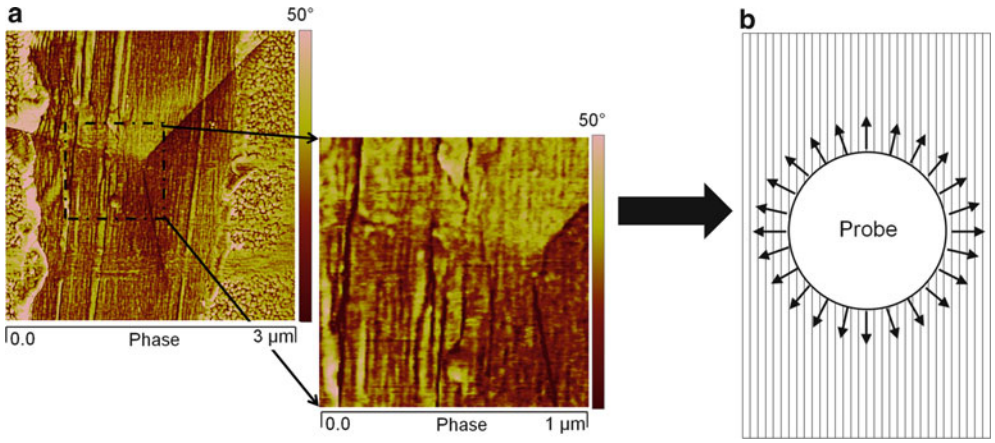

Fig. 8.4 (**a**) Phase channel image from an AFM scan of a 400-nm deep indentation of a Kevlar 49 fiber surface with a Berkovich probe. The zoomed region shows the fibrillar structure of the Kevlar surface remained intact through the contact zone of the probe during indentation (Reprinted from McAllister et al. 2013 [9] with kind permission from Springer Science and Business Media). (**b**) Schematic representation of the deformation associated with a general, axi-symmetric probe imparting low levels of strain. The *black arrows* indicate outward compression perpendicular to the probe surface. Fibrils within the contact area will undergo axial tensile/shear strains (Reprinted from McAllister et al. 2013 [20] with kind permission from Springer Science and Business Media)

The observed deformation mechanisms of the fibrillar network could generally be separated into two distinct regimes: (1) low effective strain: outward fibril compression resulting in a symmetric impression, as portrayed in Fig. 8.4; and (2) high effective strain: additional axial extension of the deformation zone, potentially due to axial fibril splitting or higher strain towards the probe apex, that led to a residual "cat-eye" impression, as portrayed in Fig. 8.5. The low strain deformation was observed for all indentations made with the Berkovich probe and indentations made to depths of 50 and 100 nm with the sphero-conical probes. The high strain deformations were observed for indentations made to depths of 200 and 400 nm with the sphero-conical probes.

The magnitude of W_T that was absorbed and recovered also depended on the level of effective strain (remember that effective strain generally increased with indentation depth for each probe). W_A and W_R were normalized by W_T (i.e., as a percentage of W_T) and are plotted versus h in Fig. 8.6. At lower depths and/or lower effective strains, where the fibrillar network was deformed primarily be outward compression, the energy of indentation was primarily recoverable. The indentations made on Kevlar 49 with the Berkovich probe resulted only in the low strain deformations, and the percentages of the indentation energy that was absorbed and recovered appeared to plateau, such that under these conditions, W_T will always be primarily recoverable (see Fig. 8.6c). In the case of indentations made with the sphero-conical probes,

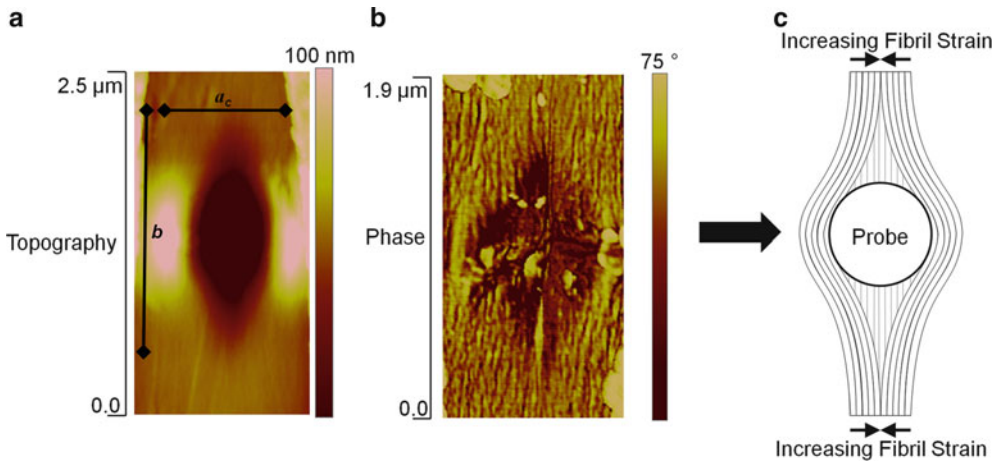

Fig. 8.5 (**a**) Z-sensor (topography) channel image from an AFM scan of a 400-nm deep indent of a Kevlar KM2 fiber made with the 357-nm radius probe. The height contrast is enhanced to highlight the elliptical nature of the residual indentation impression. (**b**) Phase channel image from an AFM scan of a 400-nm deep indent of a Kevlar KM2 fiber made with the 213-nm radius probe. The contact zone exhibits considerable fibrillar network disruption in the form of re-orientation and failure ((**a**) and (**b**) are reprinted from McAllister et al. 2013 [9] with kind permission from Springer Science and Business Media). "a_c" is the contact radius of the probe, and "b" indicates the extension of the deformation zone axially, along the fiber. (**c**) Schematic representation of (**a**) and (**b**) for a general, axi-symmetric probe exhibiting higher levels of strain. The *black arrows* indicate increased levels of axial tensile strain acting on the microfibrils towards the probe apex (Reprinted from McAllister et al. 2013 [20] with kind permission from Springer Science and Business Media)

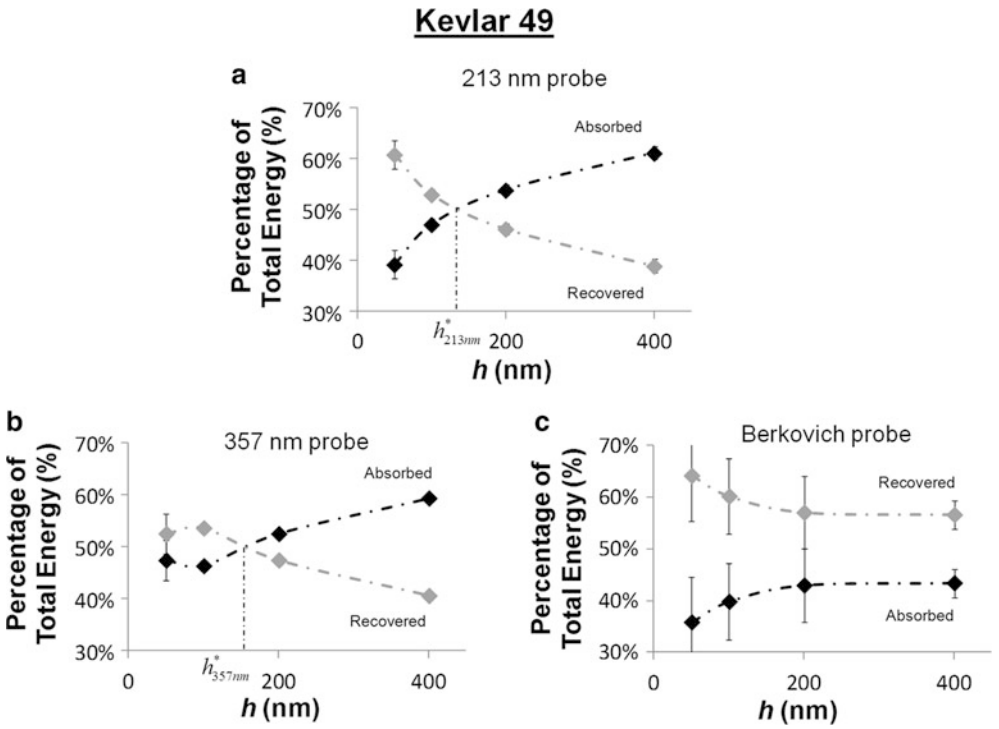

Fig. 8.6 The relative percentages of the absorbed and recovered energies of indentation for each probe at different depths on Kevlar 49 (Reprinted from McAllister et al. 2013 [20] with kind permission from Springer Science and Business Media)

as indentation depth increased so did the effective strain and the percentage of the indentation energy that was absorbed. At the lowest depths ($h \leq 100$ nm), indentation with the sphero-conical probes also primarily resulted in outward fibril compression and the W_T was primarily recoverable. The cat-eye deformation was observed at indentation depths of 200 nm and greater, and coincided with the additional forms of fibril deformation (i.e., axial splitting, fibril reorientation, fibril failure)

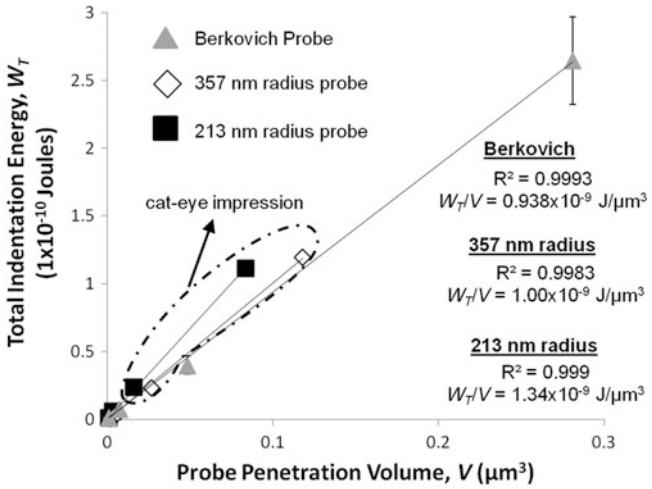

Fig. 8.7 The measured total indentation energy versus probe penetration volume for the three probes on Kevlar 49. The R^2 values and slopes of the linear fit trend lines (*black lines*) are given (Reprinted from McAllister et al. 2013 [20] with kind permission from Springer Science and Business Media)

that resulted in W_T being primarily absorbed (see Fig. 8.6a, b). In the next section, the absolute magnitudes of the total energy of indentation for indentations made with the different probe geometries are compared by normalizing the indentation energy by probe volume.

8.3.2 Normalizing Indentation Energy by Volume

The total energy of indentation (Eq. 8.1) of a Kevlar 49 fiber by each probe is plotted as a function of probe penetration volume in Fig. 8.7. The slope of the linear curve trend lines (solid black lines) is a measure of the total specific energy of indentation ($\overline{W}_T$). Increasing slope corresponds to a greater $\overline{W}_T$. $\overline{W}_T$ was not constant for different probe geometries and appeared to depend on the level of effective strain (i.e., probe sharpness) and the operable fibril deformation mechanisms. The highest value of $\overline{W}_T$ was realized for indentations made with the 213 nm radius probe. Indentations made with the 213 nm radius probe resulted in the highest levels of effective strain and the most prominent cat-eye deformation, fibril reorientation, and potential fibril failure. The lowest value of $\overline{W}_T$ was associated with indentations made with the Berkovich probe. Indentations made with the Berkovich probe imparted the lowest levels of effective strain and resulted primarily in outward fibril compression, perpendicular to the probe surface. The indentations made with the 357 nm probe resulted in strains that were generally in between the Berkovich and 213 nm radius probe and, consequently, an intermediate value of $\overline{W}_T$. Therefore, in summary, indentations made at higher levels of strain resulted in additional mechanisms of fibrillar deformation (i.e., cat-eye, reorientation, and failure) that increased the percentage of W_T that was absorbed and increased $\overline{W}_T$.

8.4 Conclusions

In this study, the total, absorbed, and recovered energies required to indent a single Kevlar 49 fiber were measured for a variety of contact conditions (i.e., probe geometries and indentation depths). The probe geometry and indentation depth governed the effective strain imparted by the probe on the Kevlar fibrillar network. The energies of indentation for each probe were therefore correlated to the effective strain and the operable deformation mechanisms of the fibrillar network. At lower effective strains, the fibrillar network deformed primarily by outward compression, perpendicular to the probe surface, and generally remained intact. As a result, the total indentation energy was primarily recoverable. At higher effective strains, an elliptical cat-eye deformation was observed that corresponded with fibrillar reorientation and failure and an increase in the percentage of the total indentation energy that was absorbed relative to the energy that was recovered. The total specific energy of indentation (i.e., the energy per volume) also depended on strain. The highest specific energy of indentation was realized for indentations made with the 213 nm radius probe, which imparted the highest effective strains and the most prominent cat-eye deformation. A more comprehensive investigation, including identification of specific fibrillar deformation mechanisms and indentation of Kevlar KM2 fibers, is provided in a manuscript by the authors that was accepted for publication [20].

Acknowledgments QM and JWG gratefully acknowledge sponsorship by the Army Research Laboratory under cooperative agreement W911NF-06-2-0011. The views and conclusions contained in this paper should not be interpreted as representing the official policies, either expressed or implied, of the Army Research Laboratory or the U.S. Government. The U.S. Government is authorized to reproduce and distribute reprints for Government purposes not withstanding any copyright notation herein.

References

1. Lee KG, Barton R Jr, Schultz JM (1995) Structure and property development in poly(p-phenylene terephthalamide) during heat treatment under tension. J Polym Sci Part B Polym Phys 33(1):1–14
2. Snetivy D, Vancso GJ, Rutledge GC (1992) Atomic force microscopy of polymer crystals. 6. Molecular imaging and study of polymorphism in poly(p-phenyleneterephthalamide) fibers. Macromolecules 25(25):7037–7042
3. Panar M, Avakian P, Blume RC, Gardner KH, Gierke TD, Yang HH (1983) Morphology of poly(p-phenylene terephthalamide) fibers. J Polym Sci Part B Polym Phys 21(10):1955–1969
4. Li SFY, McGhie AJ, Tang SL (1994) Comparative study of the internal structures of Kevlar and spider silk by atomic force microscopy. J Vac Sci Technol A 12(4):1891–1894
5. Sawyer LC, Chen RT, Jamieson MG, Musselman IH, Russell PE (1993) The fibrillar hierarchy in liquid crystalline polymers. J Mater Sci 28(1):225–238
6. Morgan RJ, Allred RE (1989) Aramid fiber reinforcements. In: Lee SM (ed) Reference book for composites technology. Technomic Publishing, Lancaster, pp 143–166
7. Dobb MG, Robson RM (1990) Structural characteristics of aramid fibre invariants. J Mater Sci 25(1):459–464
8. Li SFY, McGhie AJ, Tang SL (1993) Internal structure of Kevlar ® fibres by atomic force microscopy. Polymer 34(21):4573–4575
9. McAllister QP, Gillespie JW Jr, VanLandingham MR (2013) The influence of surface microstructure on the scratch characteristics of Kevlar fibers. J Mater Sci 48(3):1292–1302
10. Johnson KL (1985) Contact mechanics. Cambridge University Press, Cambridge
11. Bowden FP, Tabor D (1950) The friction and lubrication of solids. Oxford University Press, Oxford
12. Tabor D (1951) The hardness of metals. Oxford University Press, Oxford
13. Attaf MT (2003) A unified aspect of power-law correlations for berkovich hardness testing of ceramics. Mater Lett 57(30):4627–4638
14. Ni W, Cheng YT, Cheng CM, Grummon DS (2004) An energy-based method for analyzing instrumented spherical indentation experiments. J Mater Res 19(1):149–157
15. Krus TD, Juliano TF, Kecskes LJ, VanLandingham MR (2007) Initial plasticity onset in Zr- and Hf-rich bulk metallic glasses during instrumented indentation. J Mater Res 22(5):1265–1269
16. Bao Y, Zhou Y (2005) Assessing the elastic parameters and energy-dissipation capacity of solid materials: a residual indent may tell all. Acta Mater 53(18):4857–4862
17. He LH, Swain MV (2007) Energy absorption characterization of human enamel using nanoindentation. J Biomed Mater Res Part A 81(2): 484–492
18. Sakai M (1993) Energy principle of the indentation-induced inelastic surface deformation and hardness of brittle materials. Acta Metal Mater 41(6):1751–1758
19. Fischer-Cripps AC (2002) Nanoindentation. Springer, New York
20. McAllister QP, Gillespie JW Jr, VanLandingham MR (2013) The sub-micron scale energy dissipative deformation mechanisms of Kevlar fibrils. J Mater Sci. doi:10.1007/s10853-013-7422-6
21. McAllister QP, Gillespie JW Jr, VanLandingham MR (2012) Nonlinear indentation of fibers. J Mater Res 27(1):197–213
22. Oliver WC, Pharr GM (1992) An improved technique for determining hardness and elastic modulus using load and displacement sensing indentation experiments. J Mater Res 7(6):1564–1583

Chapter 9
Manufacturing and Damage Analysis of Epoxy Resin-Reinforced Scrap Rubber Composites for Aeronautical Applications

D. Zaimova, E. Bayraktar, I. Miskioglu, and N. Dishovsky

Abstract Simple methods to manufacture elastomer based composites using the styrene–butadiene rubber (SBR) recovered from scrap rubber pieces is proposed. These scraps are obtained basically from the manufacturing of the sport shoes. Epoxy resin is used as reinforcement along with other particles. The effect of combining the reinforcements with recycled SBR is studied by a series of experiments to evaluate the response of these materials to mechanical and thermal loading. Preliminary results on hardness, wear, storage modulus, loss angle tangent, creep response are presented. The results presented are part of an on-going project to design elastomer based composites utilizing recycled SBR for different engineering applications

9.1 Introduction

In many different engineering applications, there are very large usages of scrap tyres and most of them are in building market. In fact, European energy regulation actually considers a high standard of thermal protection in buildings with reasonable energy consumption, with low operational costs [1]. Other most important areas such as the aerospace and microelectronics industries have enourmous demand for high performance (ductile and high toughness) structural adhesive systems like epoxy and/or elastomers reinforced composites. Mainly for the microelectronics industry, the curing of such thermo setting systems have become the restricted access of the whole production process [2, 3]. Although the rubber waste accounts only 2 % of the total amount of solid waste, their production scraps increases becoming an inclusive industrial waste problem. In Europe, the annual cost for management of waste rubber tires is estimated at €600 million. Today, "The World Rubber" Industry announces that countries of the European Union generate 3,300,000 t of waste rubber tires per year. Additionally, the main component of these waste rubber tires is styrene–butadiene rubber (SBR) and, in spite of the different uses for recycling it, the research for new applications is still a need because of the extremely high amount of waste rubber tyres generated every year [4–6].

In recent years, some of the uses for waste rubber were in road pavements as asphalt-concrete mixtures and, in floor mats as an aggregate replacement. The rubbers for tire manufacturing must have high elasticity and frictional properties as well as the high load bearing capacity. Additionally, these materials are commonly used for long term applications at ambient or at moderately elevated temperature conditions. Conforming to these needs, elastomers (rubbers) should be used by simple processing with various materials in different conditions by addition of new alloying elements [7–11].

This paper formulate enquiries manufacturing facilities of scrap elastomers (SBR-rubbers) composites with different proportions of filler particles and also epoxy resin reinforcements by using of the simple curing methods. For this reason,

D. Zaimova (✉)
University of Chemical Technology and Metallurgy, Sofia, Bulgaria

Supmeca/LISMMA-Paris, School of Mechanical and Manufacturing Engineering, Paris, France

E. Bayraktar (✉)
Supmeca/LISMMA-Paris, School of Mechanical and Manufacturing Engineering, Paris, France

I. Miskioglu (✉)
ME-EM Department, Michigan Technological University, Houghton, MI, USA

N. Dishovsky
University of Chemical Technology and Metallurgy, Sofia, Bulgaria

G.P. Tandon et al. (eds.), *Experimental Mechanics of Composite, Hybrid, and Multifunctional Materials, Volume 6*, Conference Proceedings of the Society for Experimental Mechanics Series, DOI 10.1007/978-3-319-00873-8_9,

phsyical-thermal-mechanical properties of cured samples should be evaluated and analyzed the causes in order to improve the resistance of these types of composites.

Naturally, the main objective of our current research was to determine the ductility and toughness of scrap elastomer (SBR rubber) matrix composites containing SiC, B, Al_2O_3, and glass powder as reinforcements. Such that the present paper contains some preliminary experimental results of the research project for French aeronautic industry going on at LISMMA-Paris. As the first stage preliminary study, certain dynamic and static properties (Scratch test, hardness – Shore-A), thermal analysis- DMTA, nanoindentation etc. were investigated. Scanning electron microscopy (SEM) was used to study the microstructure of these composites.

9.2 Experimental Conditions

In the present study, very fine scrap elastomer (SBR-rubber) powder was used as the matrix material reinforced with SiC, B, Al_2O_3, fine epoxy and glass powder. All of the composites were fabricated by mixing 4 h and then put in an ultrasonic dispersion for 1 h. The specimens from the final mixture were manufactured by hot mounting the powder compositions under pressure of 20 kN and a temperature 180 °C for 10 and 15 min heating time and followed by 15 min of cooling time. Four compounds were designated as SiC-10, B-10 and SiC-15, B-15 based on their heating times. The post curing of the specimens was done in an isothermal oven for 24 h at 80 °C. The general compositions of the specimens are given in the Table 9.1.

The hardness-"Shore A" scale measurements have been carried out. Five measurements were taken and averaged for each specimen. The duration of one measurement was chosen as 60 s according to the standard – ASTM D 2240–05 (2010).

Viscoelastic behaviour of the composites was investigated by nanoindentation. Load was increased to 25 mN in 5 s, and kept constant for 400 s, then unloaded. During unloading the modulus and hardness were calculated using the Oliver-Pharr method [12]. A Berkovich indenter was used and 16 indents were made on each sample on a 4 by 4 matrix. Each indent was 75 μm away from its neighboring indents. Creep compliance $J(t)$ was calculated using [13]:

$$J(t) = \frac{A(t)}{(1-\nu)P_0 \tan\theta} \tag{9.1}$$

where:

$A(t) =$ Contact area
$P_0 =$ Constant applied load
$\theta = 70.3°$ For a Berkovich indenter
$\nu = 0.36$ (Assumed)

The stress exponent n is obtained from the log-log plot of strain rate vs. stress based on the equation

$$\dot{\varepsilon} = K\sigma^n \tag{9.2}$$

where K is a constant.

Dynamic Mechanical Thermal Analysis (DMTA) was carried out on the Dynamic Mechanical Analyzer MK III system (Rheometric Scientific). As the mode of deformation, single cantilever bending was used, at a frequency of 5 Hz and deformation of 64 μm in temperature range −80 to 80 °C. The heating rate used was 2 °C/min.

Table 9.1 Composition of the waste elastomeric based composite compounds

	Components (weight %)					
Composition	Rubber	Al_2O_3	SiC	Epoxy	Boron	Glass powder
SiC-10	100	20	5	25	–	5
SiC-15	100	20	5	25	–	5
B-10	100	20	5	25	2	5
B-15	100	20	5	25	2	5

Scratch tests were carried out on the specimens using a LISMMA-Paris Micro-Scratch Tester Device with a Vickers diamond indenter. Test conditions were set as 240 g normal load at a frequency of 10 Hz for three different number of cyles; 5,000, 10,000 and 15,000. Tangential and normal forces were controlled by the software of LISMMA during the test that gives also coefficient of friction. After the test, damaged zone were measured by 3D optical roughness meter to characterize damage occurred after the scratch test.

9.3 Results and Discussion

9.3.1 Evaluation by Hardness Shore "A"

The hardness of the composites is presented on Fig. 9.1. The composite SiC-10 has superior hardness. It can also be observed that the compacting duration affected the hardness of the SiC compounds but had no effect on the hardness of the B-10 and B-15. Comparing the composition containing only SiC and the composition containing Boron it is found that higher hardness is obtained for the composition with SiC only. This is a little bit surprising because normally boron has very high hardness and it's supposed to increase the hardness of the material too. Probably the quantity of boron (only 2 %) is not enough to increase the hardness. On contrary-it has negative effect and decrease the hardness.

9.3.2 Dynamic Mechanical Thermal Analysis (DMTA)

The storage modulus (E′) and dynamic mechanical loss angle tangent (Tan Delta) for the four compounds manufactured were studied in the temperature interval from −80 °C to +80 °C. In general way, there were any considerable changes in the range of −80 °C to −40 °C occurred in the storage modulus (E′) and loss angle tangent (Tan Delta) (Fig. 9.2) between the four compounds. The decrease of storage modulus (E′) with the increasing temperature, in other words, the transition from the glass to the high elastic state occurs at about −25 °C for all compounds. In the interval from −80 to −40 °C, the high values of storage modulus (E′) can be explained by the limited mobility of rubber molecules. (The curves presented for (E′) on Fig. 9.2 have close values which means that the reinforcing effect of the filler is the same for all four compounds –considering all of the compounds tested here). The loss factor is known as related to the energy lost due to energy dissipation as heat under an oscillating force

The mechanical loss angle tangent is the ratio between the dynamic loss modulus (E″) and the dynamic storage modulus (E′) (Tan Delta = E″/E′). It represents naturally the macromolecules mobility of the chains and polymers phase transitions. It is accepted that the higher the Tan Delta is the greater the mechanical losses; these losses are related to high energy input required for the motion of the molecular chains of the polymer as the transition is being approached [3, 14–16]. The position of the Tan Delta peak in the loss factor versus temperature curve can be used to identify the Tg of the rubber based composite materials.

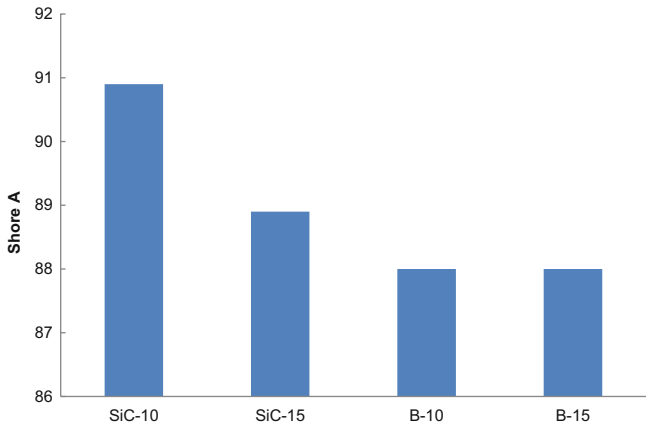

Fig. 9.1 Hardness test (Shore A) for compounds SiC-10 and SiC-15, B-10 and B-15

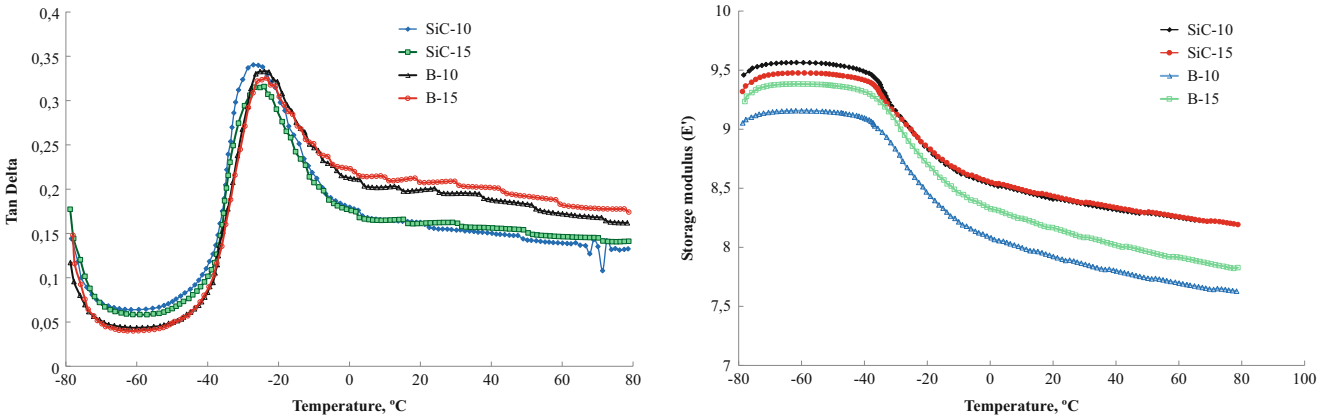

Fig. 9.2 Tan Delta (*left*) and storage modulus (*right*) as a function of the temperature for the compounds SiC-10, SiC-15, B-10 and B-15 under normal conditions

It is observed that T_g of the studied compounds does not change considerably (within the limits of 3–4 °C). The intensity of the peak is quasi similar. The results for Tan Delta suggest that despite the difference in the composition and the different compacting time, the interactions between the components are similar for all the compounds. There is slight increase in Tan Delta and storage modulus between 0 °C and 80 °C for both compounds containing boron comparing to those containing only SiC. This means that boron or boron in combination with the other additional reinforcements hinders the mobility of the rubber molecules and decreases the elasticity of the material. This claim is also supported by the hardness results, where compounds B-10 and B-15 has lower resistance to penetration and ability to recover after removal of the load.

9.3.3 Damage Analysis by Means of Scratch Test and 3D Optical Roughness Meter

Scratch tests results give a basic idea on the tribological behavior of the scrap elastomer based composites designed in the current research. Tangential and normal forces were controlled by software – LISMMA during the test that gives also coefficient of friction. After the test, damaged zone was investigated by 3D optical roughness meter to measure, scratch depth, and average scratch roughness. Figure 9.3a shows the scratch test device designed by LISMMA-Paris. All of the data discussed here are controlled with special scratch test software-LISMMA.

In fact, the frictional contact between the slipping diamond indenter and the surface of the composite material during scratch test was analyzed here. The normal and tangential force on indenter, the tangential stress on the surface and the interfacial stresses should be obtained. Further detail results and discussion will be published in an upcoming paper with the Finite Element Analysis (FEM) [16].

In reality, because of the high shear stress at the interfaces the interfacial shear stress may be the main reason for damage of the matrix and reinforced filler interfaces [2, 17–23]. As well known, when the indenter is slipping, tangential tensile stress is caused on the surface behind the indenter, while in front of the indenter the tangential stress is compressive.

To simplify the evaluation, only two test conditions (10,000 and 15,000 number of cycles for all of the composition was presented here). Figures 9.3, 9.4, 9.5, and 9.6 indicate scratch damaged zone and characteristic parameters obtained by 3D optical roughness meter after the test conditions carried up to 10,000 and 15,000 number of cycles respectively.

Additionally, the filler particle size at a constant weight fraction has a significant influence on the scratch resistance of the composites. This is also confirmed with micro indentation tests. It means that certain fillers play an important role for the scratch resistance that they were used as reinforcement elements here (the size of Al_2O_3 was under the 1 μm, Boron 2 μm, SiC 2 μm and waste rubber powder used as a matrix was variable between 5 and 10 μm and also fine glass powder was added with a powder diameter was ~1 μm).

Most probably, here Al_2O_3 and SiC can play fulfillment scratch resistance. For additional information, coefficient of friction for each compound determined after the scratch test are summarized in the Table 9.2. The scratch test conditions reveal that the compositions heated 15 min during molding and compacting have shown higher increment in the scratch resistance values when compared to the other composition heated 10 min during molding and compacting.

As indicated in the previous section, these results are only preliminary and for final and detailed evaluation, more comprehensive study and more intensive experimental test should be carried out.

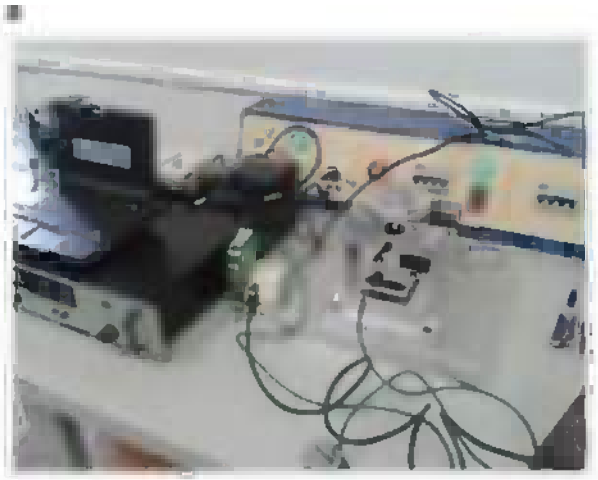

Scratch test device

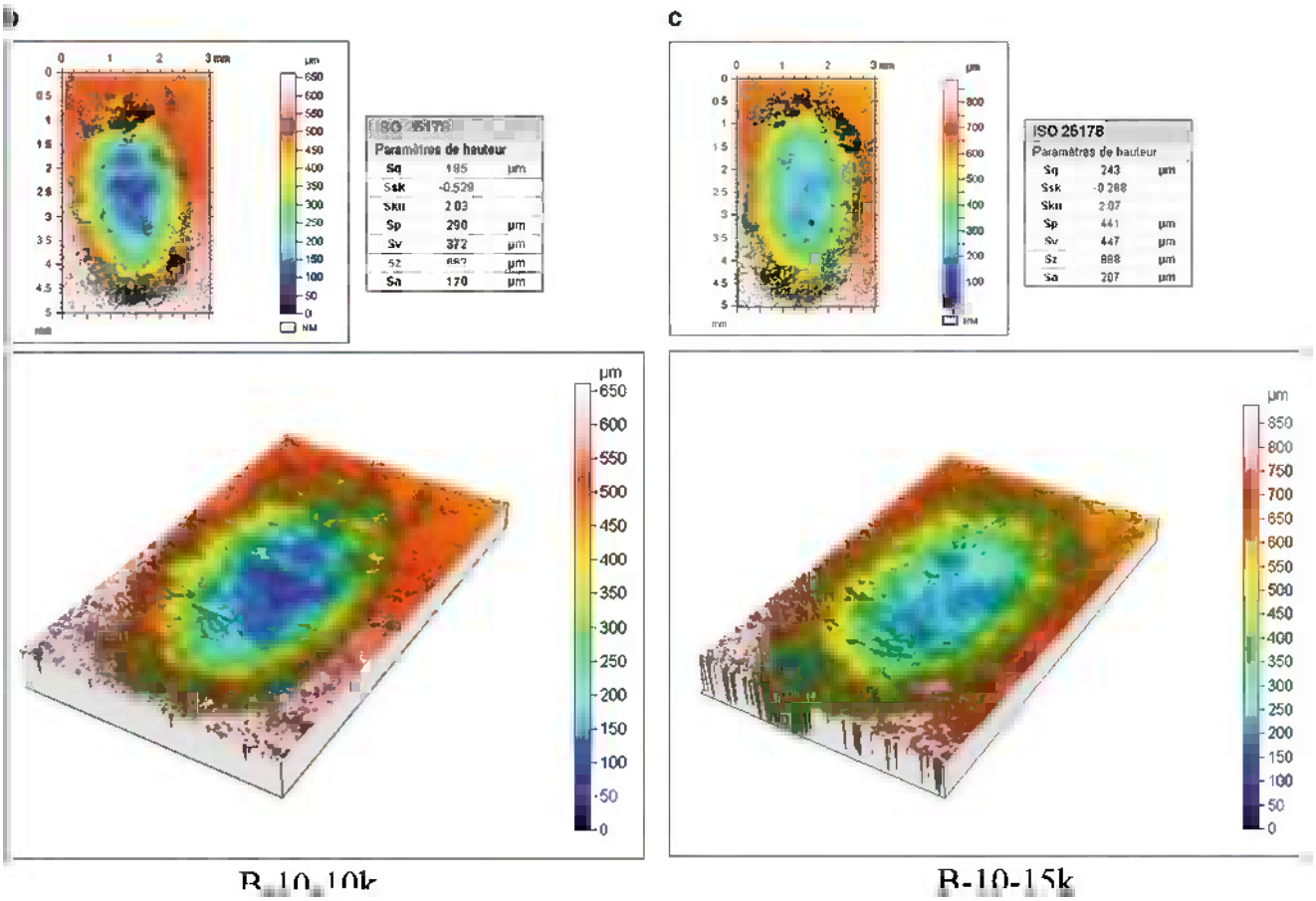

Fig. 9.3 (**a**) Scratch test measurement device designed by LISMMA, (**b**) damage traces obtained in the direction of width and length for the specimen B-10 for the number of cycle 10,000 and (**c**) for the number of cycle 15,000

9.3.4 Nanoindentation Characterisation: Creep Compliance Analysis

The principal goal of nanoindentation testing is to extract elastic modulus and hardness of the specimen material from experimental readings of indenter load and depth of penetration. In a typical test, force and depth of penetration are recorded as load is applied from zero to some maximum and then from maximum force back to zero. If plastic deformation occurs,

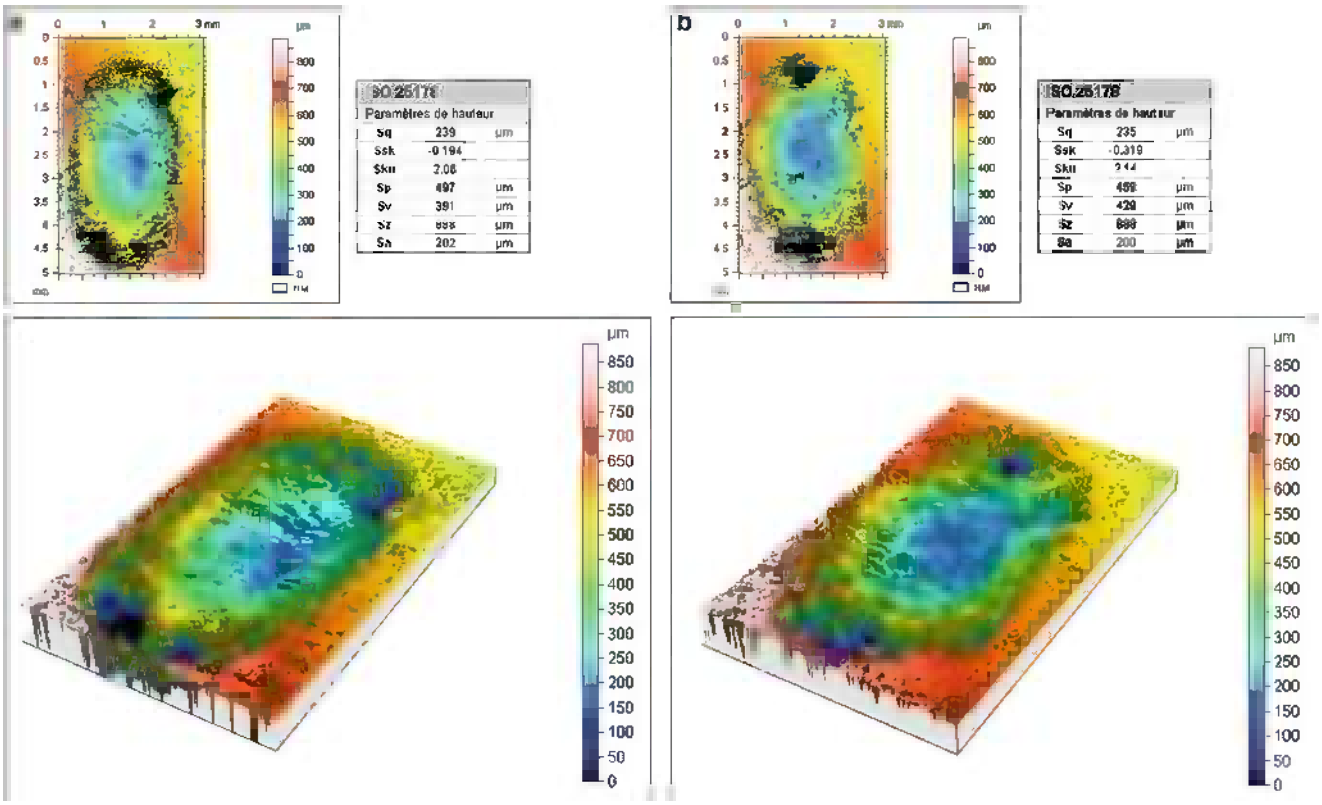

Fig. 9.4 (**a**) Damage traces obtained in the direction of width and length for the specimen B-15 for the number of cycle 10,000 and (**b**) for the number of cycle 15,000

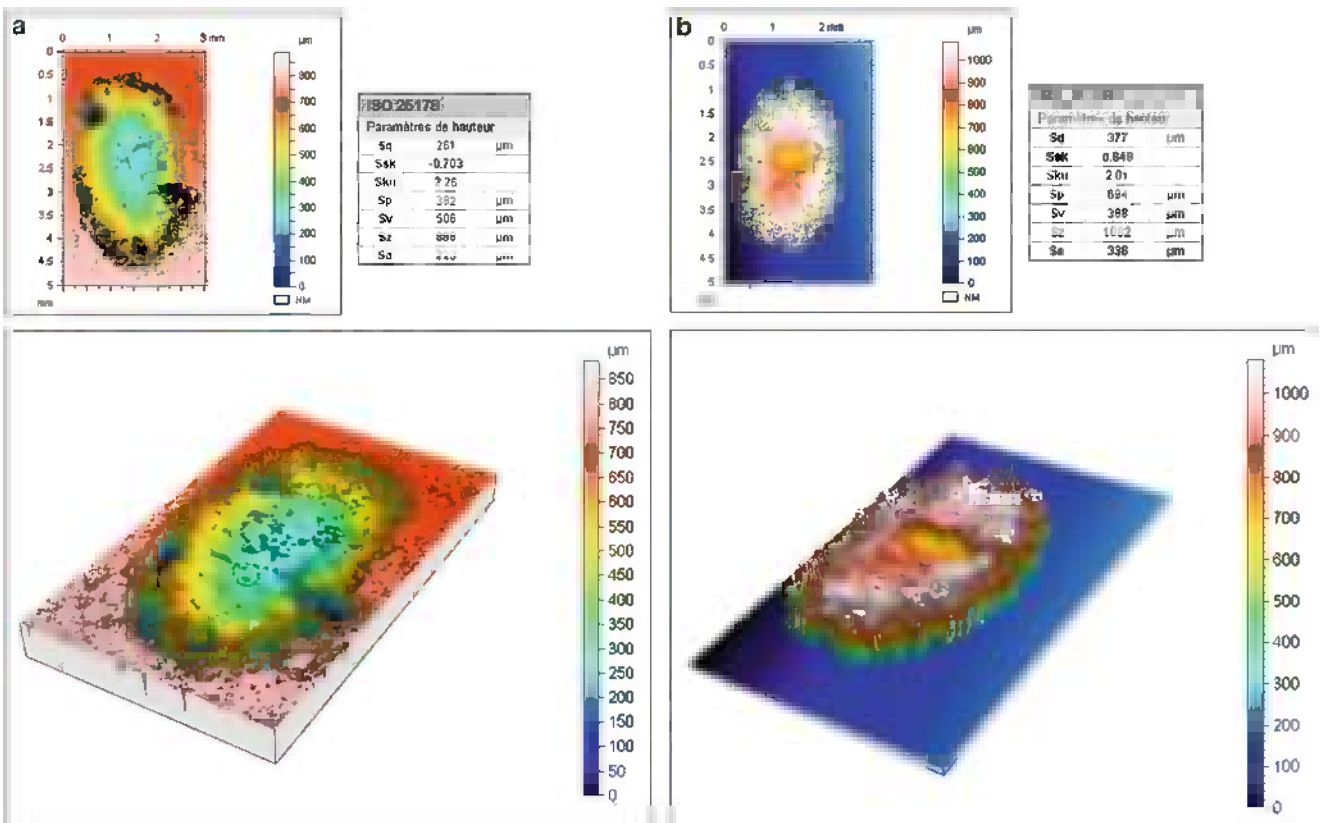

Fig. 9.5 (**a**) Damage traces obtained in the direction of width and length for the specimen SiC-10 for the number of cycle 10,000 and (**b**) for the number of cycle 15,000

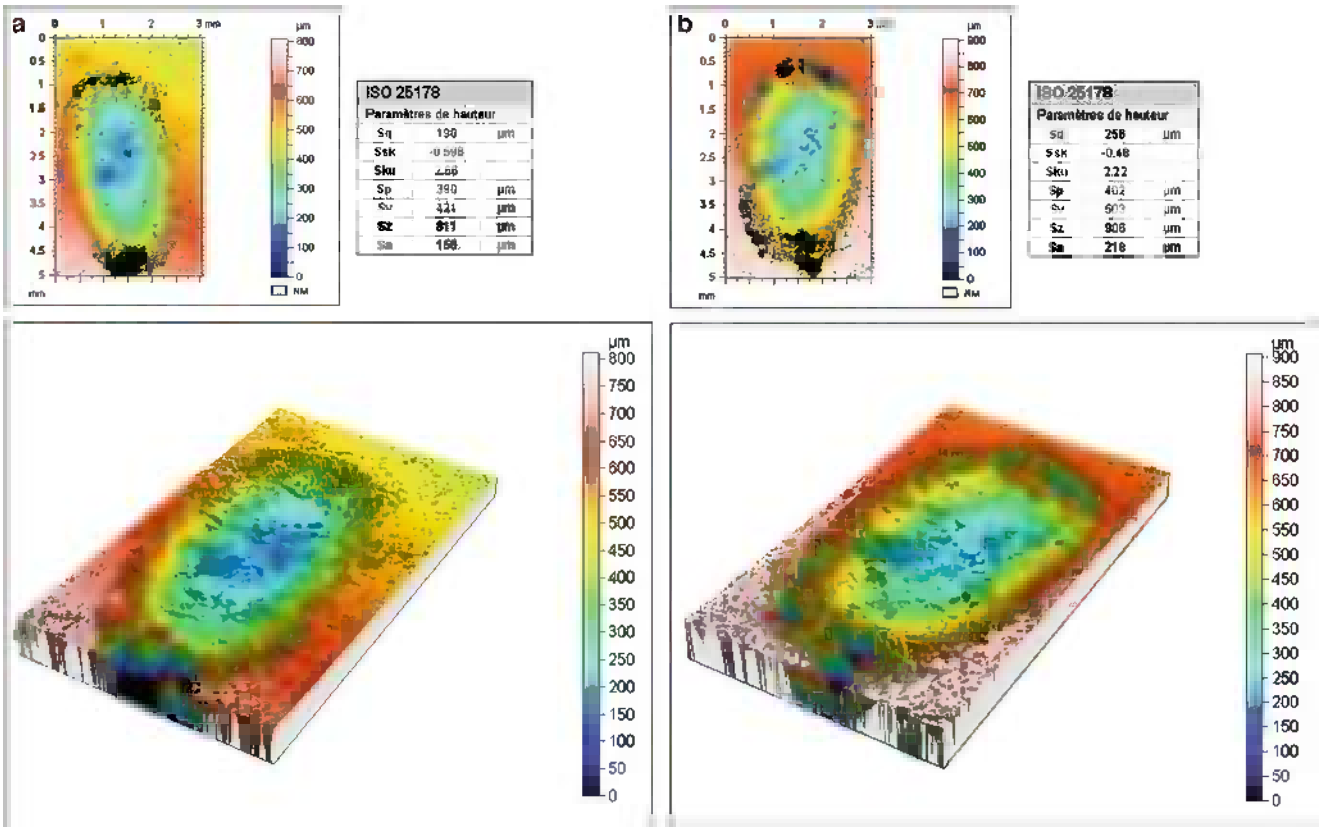

Fig. 9.6 (**a**) Damage traces obtained in the direction of width and length for the specimen SiC-15 for the number of cycle 10,000 and (**b**) for the number of cycle 15,000

Table 9.2 Friction coefficient after scratch test carried for the designed compositions

Number of cycles	SiC-10	SiC-15	B-10	B-15
5 k (5,000)	0.74	0.71	0.94	0.94
10 k (10,000)	0.81	0.80	0.90	0.87
15 k (15,000)	0.76	0.90	0.84	0.88

then there is a residual impression left in the surface of the specimen. Unlike conventional indentation hardness tests, the size (and hence the projected contact area) of the residual impression for nanoindentation testing is too small to measure accurately with optical techniques.

The depth of penetration together with the known geometry of the indenter provides an indirect measure of the area of contact at full load, from which the mean contact pressure, and thus hardness, may be estimated. When load is removed from the indenter, the material attempts to regain its original shape, but it prevented from doing so because of plastic deformation. However, there is some degree of recovery due to the relaxation of elastic strains within the material. An analysis of the initial portion of this elastic unloading response gives an estimate of the elastic modulus of the indented material [19–23].

Load and associated penetration depths are recorded simultaneously during both loading and unloading, producing a force-depth diagram (Fig. 9.7).

The Oliver and Pharr Method (Power Law Method) [12] recognizes the fact that the first portion of unloading curve may not be linear, and can be described by a simple power law relationship:

$$F = k(h - h_p)^m \tag{9.3}$$

Where k is a constant and m is an exponent which depends on indenter geometry. A power low function is used to describe the upper part of the unloading data.

$$F = F_{max}\left(\frac{h - h_p}{h_m - h_p}\right)^m \tag{9.4}$$

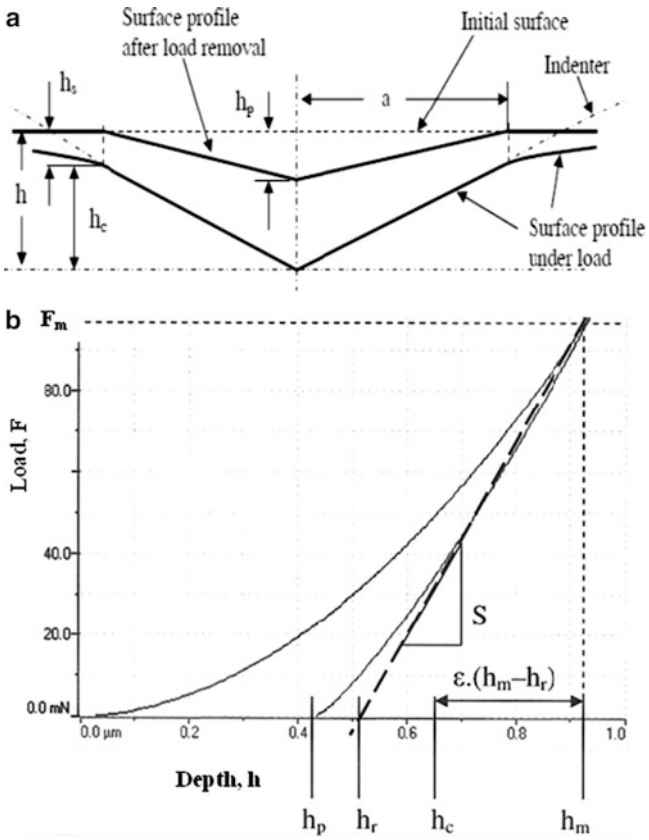

Fig. 9.7 Schematic plots of (**a**) cross-section of an indentation and (**b**) a typical load-indentation depth curve generated during a nanoindentation experiment, indicating key parameters needed for analysis [22]

where the constants m and h_p are determined by a least of square fitting procedure. The contact stiffness S = (1/C) is given by the derivative at peak load:

$$S = \left(\frac{dF}{dh}\right)_{max} = mF_{max}\left[\frac{(h_m - h_p)^{m-1}}{(h_m - h_p)^m}\right] = mF_{max}(h_m - h_p)^{-1} \tag{9.5}$$

and the tangent depth, h_r, is thus given by:

$$h_r = h_m - \frac{F_{max}}{S} \tag{9.6}$$

The contact depth, h_c, is then:

$$h_c = h_m - \varepsilon(h_m - h_r) \tag{9.7}$$

where ε now depends on the power law exponent m.

The tangent is found by differentiating the unloading curve and evaluating at maximum load (F_{max}). The intercept of this tangent with the displacement axis yields h_r.

The indentation hardness (H_{IT}) and indentation modulus (E_{IT}) were determined by using the Oliver and Pharr method transformed in the following relations:

$$A_p = f(h) \tag{9.8}$$

where A_p is projected contact area.

$$H_{IT} = \frac{F_{max}}{A_p(h_c)} \tag{9.9}$$

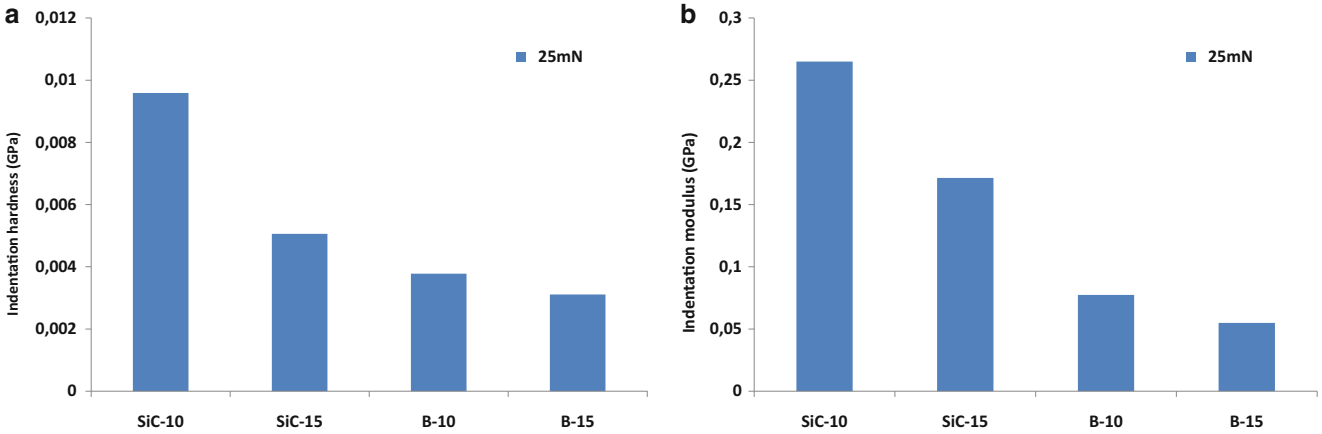

Fig. 9.8 Comparison of indentation hardness (**a**) and indentation modulus (**b**) obtained by nanoindentation test at maximum load 25 mN for compounds of SiC-10, SiC-15, B-10 and B-15

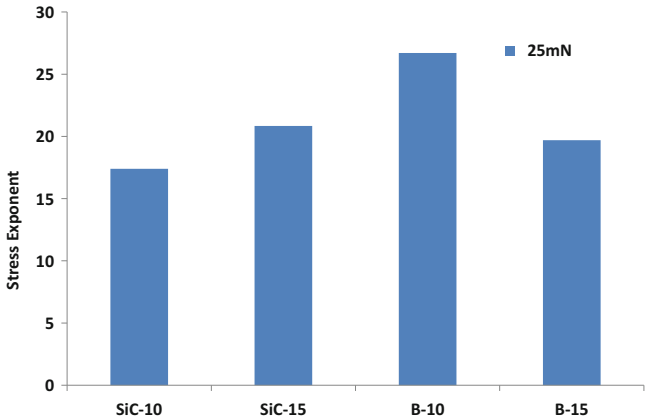

Fig. 9.9 Comparison of stress exponent calculated from the data obtained by nanoindentation test at maximum load 25 mN for compounds SiC-10, SiC-15, B-10 and B-15

$$E_{IT} = \frac{1-\nu_s^2}{\frac{1}{E_r} - \frac{1-\nu_i^2}{E_i}} \tag{9.10}$$

$$E_r = \frac{\sqrt{\pi}S}{2\beta\sqrt{A_p(h_c)}} \tag{9.11}$$

where:

E_i – elastic modulus of the indenter (1,141 GPa)
ν_i – Poisson's ratio of the indenter (0.07)
E_r – reduced modulus of the indentation contact
ν_s – Poisson's ratio of the sample (0.35)

Under experimental conditions of the present work, nanoindentation tests were carried out to measure mechanical properties of the four composites to optimize the composition of the production and to improve mechanical performance and durability of the composites. Figures 9.8a, b and 9.9 summarize the findings drawn from nanoindentation tests, essentially basic results from creep compliance evaluation for the four composites. A detailed comparison of indentation hardness, indentation modulus and stress exponent evolution was made in case of a maximum load 25 mN for the

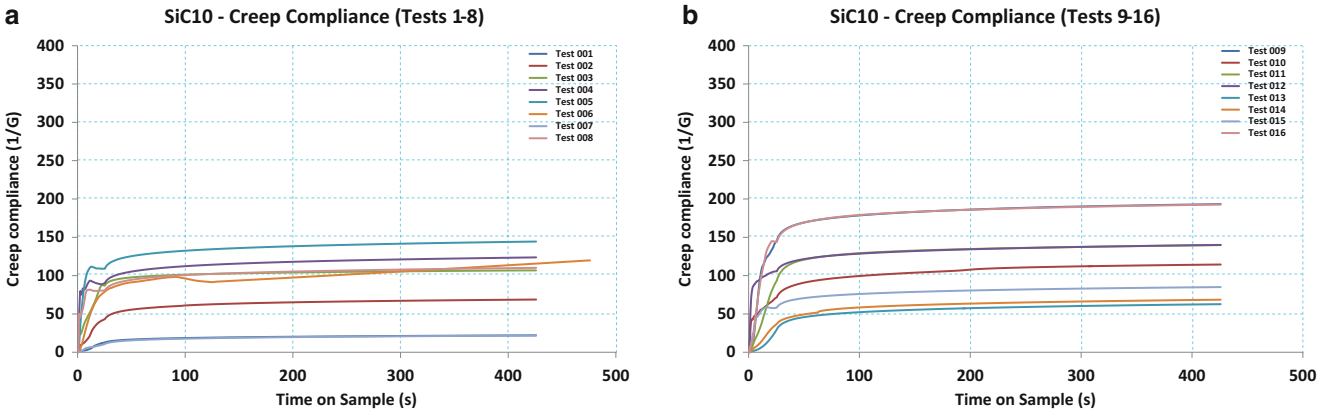

Fig. 9.10 Creep compliance (calculated from nanoindentation data) as a function of time for compound SiC-10

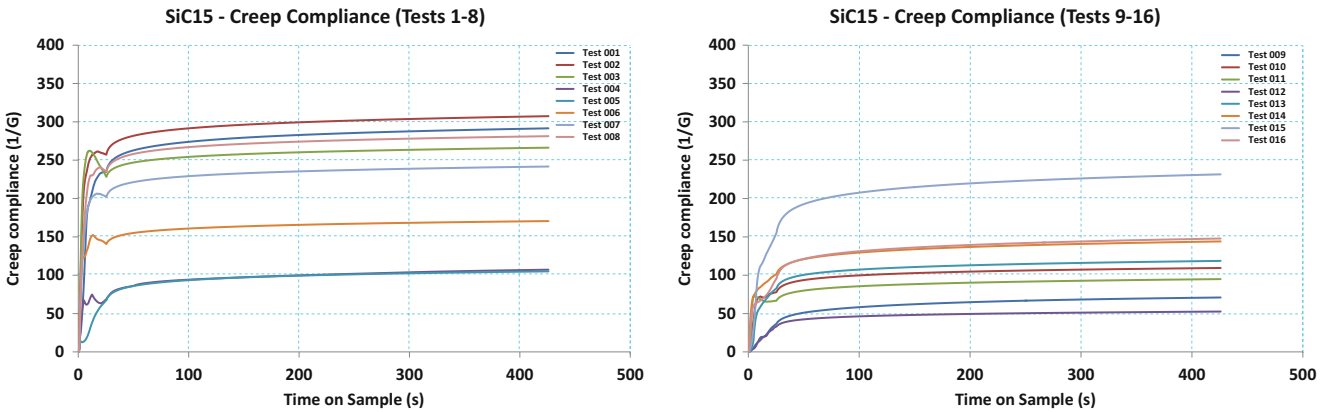

Fig. 9.11 Creep compliance (calculated from nanoindentation data) as a function of time for compound SiC-15

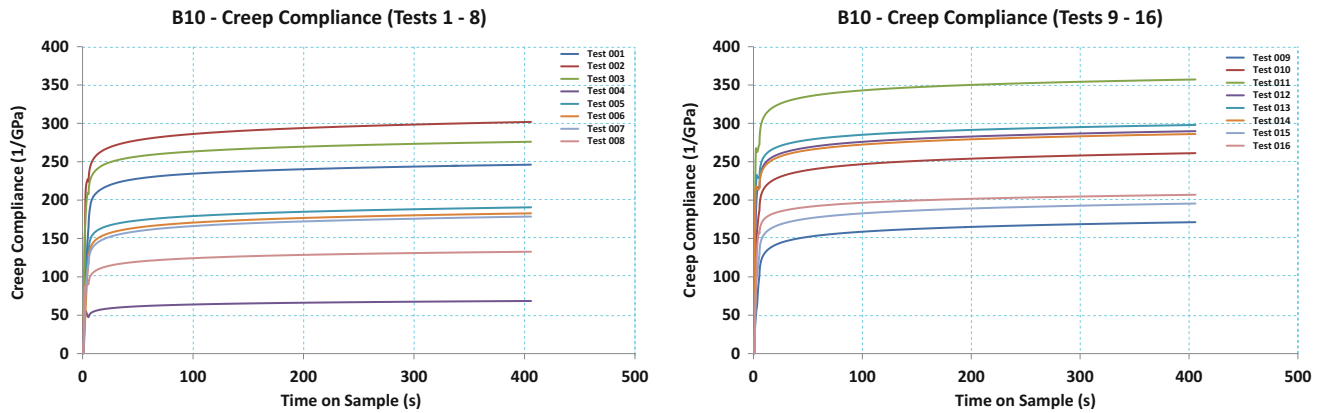

Fig. 9.12 Creep compliance (calculated from nanoindentation data) as a function of time for compound B-10

compounds of SiC-10, SiC-15, B-10 and B-15. At the first evaluation, it can be recognized the most useful composition called SiC-10 regarding to other composition.

In the frame of the present work, a sharp indenter (Berkovich indenter) was used. However, numerous studies have incorporated conical and/or spherical indenters in order to accomplish the linear viscoelastic deformation establishment.

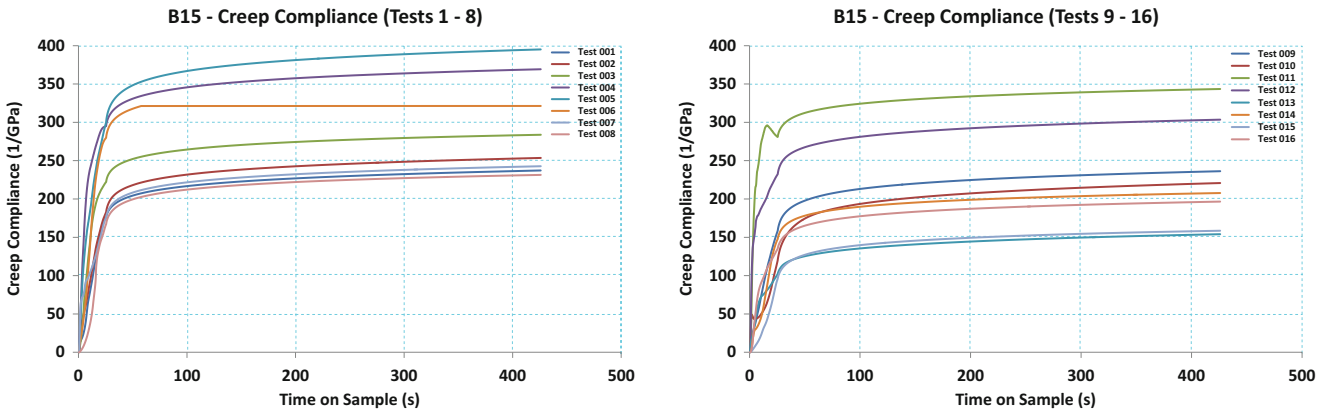

Fig. 9.13 Creep compliance (calculated from nanoindentation data) as a function of time for compound B-15

During indentation creep mainly polymer based materials [19, 22, 23]. Only a single maximum load was also used in our analysis such that load cannot be excluded. Four different compositions designed in the present work are very heterogeneous.

Structures as demonstrated in Figs. 9.10, 9.11, 9.12, and 9.13 with considerable differences in measured values. These results demonstrate that these materials cannot conform to the idealized linear viscoelastic behaviour under the contact creep conditions used here. It means that there is no linear path during loading and unloading.

9.4 Conclusions

In the frame of common research project going on, we try to design new composites from scrap elastomers (SBR) matrix powders essentially reinforced with SiC, B, Al_2O_3, fine epoxy and glass powder. For most useful chemical composition to optimize the structure, certain experimental results given on the four different compositions were discussed in the present work. Mechanical and tribological properties and thermal analysis of these composites were evaluated under different test conditions (Hardness Shore A, Scratch test, DMTA, etc.).

Scratch tests results gave a very useful data for the tribological (wear) behaviour of the waste elastomers based composites designed here in the present work. Dynamic Mechanical Thermal Analysis (DMTA) was useful for the determination of storage modulus (E′) and dynamic mechanical loss angle tangent (Tan Delta) for certain composites designed here. Analysis was carried out in the temperature interval from −80 °C to +80 °C. It was measured that there were any considerable changes in the range of −80 °C to −40 °C occurred in the storage modulus (E′) and loss angle tangent (Tan Delta) between the four composites.

In addition to these characterization tests, a detailed study has been carried out by nanoindentation to evaluate viscoelastic behaviour of the four composites developed in this project. Evaluation of creep compliance as a function of time at a maximum load has been carried out by nanoindentation test. These tests give more reliable results to understand the viscoelastic behaviour and real damage analysis at nano-scale of these composites under different service conditions.

These issues indicate that nanoindentation test is a valuable tool to evaluate both the mechanical and time-dependent properties of the composite materials used in this study. Even if, the analysis of the creep compliance is theoretically simple in the context of linear viscoelastic deformation, it should be taken account of numerous requirements. The measured compliance for the Berkovich tip was mostly nonlinear. The observed non constant creep compliance is a strong indication of deformation driven by the non-linear viscoelasticity. These analyses require further refinement to account for well-defined viscoelastic behviour of these composites.

Acknowledgments Authors gratefully acknowledge support from to CNAM-Paris, Arts et Metiers – Chair of industrial materials and Michigan Technological University, MI-USA, Engineering Mechanics Department, Houghton for using of their laboratory facilities.

References

1. The European Parliament and the Council of the European Union, Council Directive of 2002/91/EC: the energy performance of buildings, issued on 16 Dec 2002 (new form will be changed in 2012)
2. Ouali N, Oppici A-C (2012) Elastomer toughened epoxy based composites. AMPT-Wollongong, Sydney, 23–26 Sept 2012
3. Zaimova D, Bayraktar E, Katundi D, Dishovsky N (2012) Elastomeric matrix composites: effect of processing conditions on the physical, mechanical and viscoelastic properties. J Achiev Mater Manuf Eng 50–2:81–91
4. Papadopoulos AM (2005) State of the art in thermal insulation materials and aims for future developments. Energ Build 37:77–86
5. Turgut P, Yesilata B (2008) Physico-mechanical and thermal performances of newly developed rubber-added bricks. Energ Build 40:679–688
6. Kaynak C, Sipahi-Saglam E, Akovali G (2001) A fractographic study on toughening of epoxy resin using ground tyre rubber. Polymer 42:4393–4399
7. Yesilata B, Turgut P (2007) A simple dynamic measurement technique for comparing thermal insulation performances of anisotropic building materials. Energ Build 39:1027–1034
8. Bessri K, Montembault F, Bayraktar E, Bathias C (2010) Understanding of mechanical behaviour and damage mechanism in elastomers using x-ray computed tomography at several scales. Int J Tomogr Stat 14:29–40
9. Bayraktar E, Antholovich S, Bathias C (2006) Multiscale observation of fatigue behviour of elastomeric matrix and metal matrix composites by x-ray tomography. Int J Fatigue 28:1322–1333
10. Bayraktar E, Isac N, Bessri K, Bathias C (2008) Damage mechanisms in natural (NR) and synthetic rubber (SBR): nucleation, growth and instability of the cavitations. Int J Fatigue Fract Struct Mater 31(1):1–13
11. Luong R, Isac N, Bayraktar E (2007) Damage initiation mechanisms of rubber. J Arch Mater Sci Eng 28(1):19–26
12. Oliver WC, Pharr GM (1992) An improved technique for determining hardness and elastic modulus using load and displacement sensing indentation experiments. J Mater Res 7:1564–1583
13. Tehrani M, Safdari M, Al-Haik MS (2011) Nanocharacterization of creep behavior of multiwall carbon nanotubes/epoxy nanocomposite. Int J Plast 27:887–901
14. Zaimova D, Bayraktar E, Dishovsky N (2011) State of cure evaluation by different experimental methods in thick rubber parts. J Achiev Mater Manuf Eng 44(2):161–167
15. Hay J (2009) Introduction to instrumented indentation testing. Experimental techniques, SEM: Society for Experimental Mechanics, pp 66–71, November, December 2009
16. Botelho DS, Bayraktar E (2009) Experimental and numerical study of damage initiation mechanism in elastomeric composites-double cantilever beam specimens-DCB. J Achiev Mater Manuf Eng 36(1):65–71
17. Zaimova D, Bayraktar E, Katundi D, Dishovsky N (2012) Damage analysis of elastomeric based composites. AMPT-Wollongong, Sydney, 23–26 Sept 2012-b
18. Dasari A, Misra RDK, Rohrmann J (2004) Scratch deformation characteristics of micrometric wollastonite-reinforced ethylene-propylene copolymer composites. Polym Eng Sci 44(9):1738–1748
19. Catherine AT, Krystyn JVV (2006) Contact creep compliance of viscoelastic materials via nanoindentation. J Mater Res 21(6):1576
20. Botelho DS, Isac N, Bayraktar E (2007) Modeling of damage initiation mechanism in rubber sheet composites under the static loading. Int J Achiev Mater Manuf Eng 22(2):55–59
21. Tolle LG, Craig RG (1978) Viscoelastic properties of elastomeric impression materials: polysulphide, silicone and polyether rubbers. J Oral Rehabil 5:121–128
22. Fischer-Cripps AC (2011) Nanoindentation, 3rd edn. Springer, New York, pp 29–30, Chapter 2
23. Juliano TF, Vanlandingham MR, Tweedie CA, Van Vliet KJ (2007) Multiscale creep compliance of epoxy networks at elevated temperature. Exp Mech SEM 47:99–105

Chapter 10
Compliant Multifunctional Wing Structures for Flapping Wing MAVs

Ariel Perez-Rosado, Alyssa Philipps, Eli Barnett, Luke Roberts, Satyandra K. Gupta, and Hugh A. Bruck

Abstract The flight time of miniature air vehicles (MAVs) is limited by the need for a portable, light weight power source. The development of multifunctional, power generating wings has the capability of extending flight time without compromising overall flight performance. This paper seeks to investigate the feasibility of integrating flexible solar cells onto the flapping wings of a MAV to create "compliant multifunctional wing structures". Data is collected for bird-inspired miniature air vehicle wings designed with carbon fiber spars, and for comparable wings designed with a monolithic compliant component. Both of the designs are tested with wing bodies composed of plain Mylar foil with flexible, lightweight solar cells integrated onto them. The test setup is designed to simulate MAV operation under zero forward velocity. A motor that controls the wing flapping scheme is fixed to a rigid test stand. A 6 degree of freedom (DOF) load cell is used to measure aerodynamic lift as a function of time for a synchronized flapping scheme during wind tunnel testing. A second experiment is conducted to verify the functionality of solar cells as a regenerative energy source in real flight. A single compliant wing and a single regular wing are consecutively fixed to the test setup used in the first experiment, and the test is conducted under direct sunlight. The voltage generated by the solar cells is collected as a function of time, while the wing is flapping. The lift data is used to estimate flight characteristics, while the voltage data is used to estimate the viability of energy harvesting.

10.1 Introduction

Interest in the development of miniature air vehicles is increasing, due to the need for air vehicles that are capable of flying undetected through small spaces. This is motivated primarily by military, surveillance, and search and rescue applications. Bio-inspired, flapping MAV designs are favorable for stealth applications for two main reasons. First, flapping MAVs is expected to emit less noise in flight than traditional rotary MAVs, due to the MAV's low operation frequency. Second, Bio-inspired MAV may be disguised as an actual flying animal during performance [1].

Several successful MAVs have already been developed; however, most MAV designs have a severly limited flight time due to battery limitations. Zdunich et al. [2] developed and characterized the Mentor, a flapping-wing MAV that achieved both hovering and forward flight. They used bioinspired design to achieve low frequency oscillation of flapping. The motor was powered by a 8×600 mAh NiCd cells battery back, but flight testing proved this to be insufficient. The total flight time maximized at 1.5 min, and "continuous hovering flights rarely exceeded 20 s before the power output of the batteries began to decline" ([2], p. 1708).

Bejgerowski et al. [3] develop and optimize a MAV drive mechanism shape and design. The design was intended to address the problem of limited flight time, among other issues. This work succeeded in increasing energy efficiency, but did not directly address the limited power source problem. Even as battery technology improves, it will not provide the MAV with sufficient life-time for long missions. This beckons the need for a light weight, regenerative energy source that can be incorporated into a successful MAV. Regenerative designs generally put a greater burden on the MAV. Thus, more efficient MAV structural designs must be explored.

One new area of design is the incorporation of compliant wing designs to maximize lift and energy efficiency of MAVs. Many researchers have developed compliant mechanisms for various dynamic applications. In some cases, these mechanisms

A. Perez-Rosado • A. Philipps • E. Barnett • L. Roberts • S.K. Gupta • H.A. Bruck (✉)
Department of Mechanical Engineering, University of Maryland, College Park, MD 20742, USA
e-mail: bruck@umd.edu

G.P. Tandon et al. (eds.), *Experimental Mechanics of Composite, Hybrid, and Multifunctional Materials, Volume 6*, Conference Proceedings of the Society for Experimental Mechanics Series, DOI 10.1007/978-3-319-00873-8_10,

have been successfully incorporated into MAV wing designs. Mueller and Gerdes [1] experimented with multiple compliant, folding wing design incorporated into a flapping MAV. Five different compliant wing designs were tested for lift and thrust characteristics, as well as the ability to harness flight. Compliant designs that folded in one spot did not significantly increase lift and did not succeed in supporting flight. A compliant wing design containing a carbon fiber spar with distributed bending was determined to be a successful method of reducing thrust and increasing lift, while maintaining stability in flight.

Tantanawat and Kota [4] discuss the use monolithic structures in compliant mechanisms for dynamic applications. After conducting a detailed case study, they designed a compliant mechanism that would use elasticity to increase energy efficiency. A monolithic, elastic compliant design was found to require a smaller peak power input than traditional rigid body spring designs. Lesieutre et al. [5] tested the stability and stiffness of a compliant structure subjected to aerodynamic loads. Finite Element Analysis was used to evaluate wings composed of six-noded octahedral unit cells with diagonal tendon actuation. The results showed that structures achieve ideal lift and energy efficiency characteristics with compliant that are stiff in the axial direction and soft in the bending direction.

Our goal is to reduce the overall MAV flight time, by developing multifunctional, power regenerating wings. To achieve this goal, we attempt to incorporate solar cells into the MAV wing design without compromising flight performance. We expect that incorporating compliant wing designs with counter-balance the added weight and rigidity of the wings. We have created a compliant wing design and a comparable non-compliant wing design. We have tested each design with and without the incorporation of OEM solar cells capable of generating 6 V of electricity. The design and performance characteristics of the various wing configurations will be summarized and discussed in this paper.

10.2 Wing Design

10.2.1 Overview

All wings have three main components: (i) the wing body, composed of Mylar foil or Mylar, (ii) flexible Powerfilm© Solar cells and (iii) the main and supporting spars. The wing is designed to form a rounded pocket in the upstroke. The pocket creates a beneficial pressure gradient that forms an airfoil which generates lift. The ability to form this pocket is influenced by the rigidity of the wing. The installation of flexible solar cells increases the rigidity of the wings. Ergo, the attached solar cells should decrease the lift generated by the wings. To address the decrease in lift that comes with a more rigid wing, a compliant spar design is explored. The complaint spar is designed to maximize the lift generation by increasing the net static lift. For regular wings with minimal compliance, the net static lift is expected to be close to zero, because the negative lift forces on the upstroke counter- balance the positive forces on the downstroke. The complaint spar is expected to have a positive static lift, by serving two functions. First, the spar folding on the upstroke intends to reduce the negative lift, while the straight downstroke motion should provide lift that is nearly equivalent to the regular spar downward lift. Second, the compliant wing shape forms a lift generating air pocket during the upstroke that would increase the upwards lift force.

10.2.2 Compliant Spar Wing Design

The compliant wing is composed of one complaint spar, two auxiliary spars, a main supporting spar, and a Mylar® foil body. The compliant spar is designed for ideal durability, size, and weight. The spar is composed of two, 1/8″ carbon fiber rods adjoined by a monolithic compliant section. All carbon fiber spars are manufactured by Midwest Products Co. Inc, and fall under stock number 5720. A laser cutter is used to manufacture the compliant section from a 1/4″ thick Delrin® sheet. Delrin® material was selected for its superior tensile strength, stiffness, creep resistance, and fatigue [6]. Another advantage of selecting Delrin® material is that it is easy to manufacture on the laser cutter. The inside carbon fiber rod is 5″ long, the compliant section is 6″ long, and the outside compliant spar is 7″ long. The total horizontal length of the fully assembled compliant spar is 18″. The compliant section of the spar weighs 9.2 g. The complaint section is cut to have an upward curve to counteract the compliance of Delrin® under weight. Several iterations of the design lead to the selection of a wing spar with each rounded section bent at an angle of 4.58° upwards, as shown in Fig. 10.1. This angle allows the wing to bend to a completely straight line position during the upstroke, while complying during the down-stroke.

Diagonal cuts and flexible joints on each rounded section increase the stability of the design. The slits that are cut through the bottom of the spar hold Mylar strips that attach the spar to the body of the wing. The attachment of the compliant wing spar to the Mylar wing body is shown in Fig. 10.2.

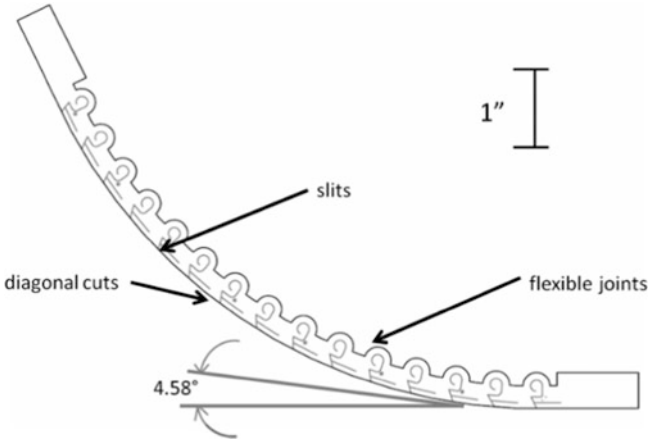

Fig. 10.1 CAD drawing of compliant wing design. The outline appears as it was cut into the laser cutter

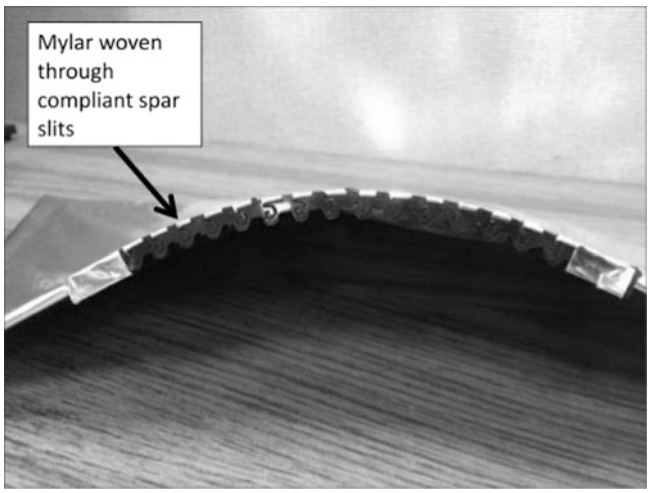

Fig. 10.2 Mylar slits woven through slits in the compliant section of compliant spar

The auxiliary spars and main supporting spar are composed of a .1″ diameter carbon fiber rod. Mylar foil is adhered to the spars with Gorilla Glue to form the wing fully assembled wing, shown in Fig. 10.3. The complete wing weighs 28.4 g without solar cells, and 29.0 g with solar cells. One auxiliary spar is 6 in. in length, and the other is 7 in. in length.

Powerfilm© MPT6-75 OEM solar cell modules, with a 6 V and 50 mA rating, are soldered together in series to amplify current. Three solar cells are adhered to the Mylar wing body using Gorilla Glue.

10.2.3 Regular Spar Wing Design

The regular wing is manufactured from the same materials as the compliant wing. The regular wing is designed with one main carbon fiber spar that is 1/8″ in diameter and 17″ length, one main supporting carbon fiber rod that is .1″ in diameter and 16″ length, and two auxiliary carbon fiber rods, each .08″ in diameter and 15″ and 14″ in length. The Mylar foil body and solar cell modules are adhered to the wing spar frame using UHU Por adhesive. The complete wing weighs 23.6 g without solar cells, and 26.4 g with solar cells. The fully assembled regular wing with solar cells is displayed in Fig. 10.4. The fully assembled MAV, composed of wings, a motor, and a carbon fiber frame, can be seen in Fig. 10.5. The flapping tail stabilizes the bird. The carbon fiber frame supports three, 3.7 V rated Lithium Ion Polymer Batteries, which powers the motor.

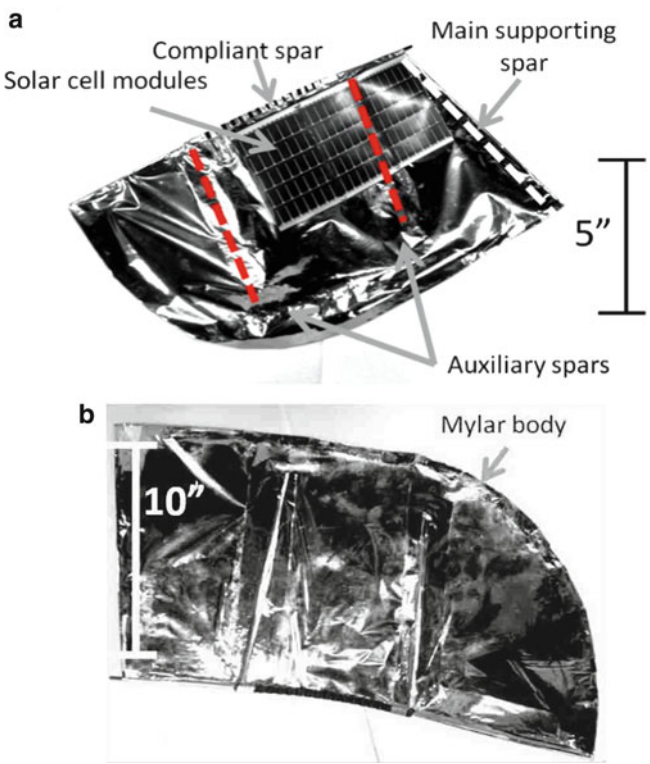

Fig. 10.3 Fully constructed compliant wing. (**a**) The *top* side of the compliant wing fixed with three powerfilm OEM flexible solar cell modules. (**b**) The *bottom* side of the compliant wing

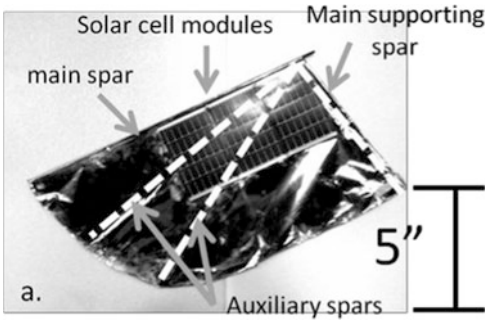

Fig. 10.4 Fully constructed regular wing. (**a**) The *top* side of the regular wing fixed with three Powerfilm© OEM flexible solar cell modules. The *bottom* side of the regular wing

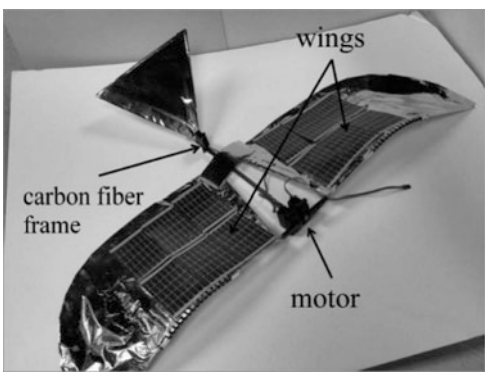

Fig. 10.5 Fully constructed MAV equipped for flight, with compliant wings, fixed with two rows of three OEM solar cells in series

10.3 Force Characterization and Experimental Results

10.3.1 Force Characterization Test

A test platform was developed to measure the static and aerodynamic forces on an MAV body in a wind tunnel at a speed of 5 m/s with a dynamic pressure of 12.5 kPa and angles of attack up to 20°. This test platform is similar to a previous test stand design that we developed [7, 8]. However, the new test stand utilized a 6 degree of freedom (DOF) load cell that was capable of measuring lift, thrust, and other forces simultaneously. The compliant and regular wing designs are each tested with solar cells integrated onto the Mylar wings. A schematic of the test stand is shown in Fig. 10.6. It is fixed with a motor, wings, and a carbon fiber frame. These three components comprise the main components of the completed MAV in flight, which is shown independently in Fig. 10.5. When the motor operates under a synchronized flapping scheme, both wings experience simultaneous up-strokes and down-strokes between 0° and 80°. The load cell voltage was measured as a function of time using the National Instruments' Measurement and Automation. Explorer software.

10.3.2 Force Characterization Results

Figure 10.7 shows lift profiles obtained from force measurements made during wind tunnel testing of the multifunctional wings. noticeable reduction in the downward lift component is observed in the compliant wing. Compliant spars also produce a slight increase in overall lift. Overall, the negative static lift was decreased by 50 % from nearly 400 g for the regular wing to nearly 200 g for the compliant wing. The positive static lift on the other hand remained about the same at slightly more than 300 g. However, when the wing was subjected to aerodynamic forces, the negative lift of the regular wing was decreased by 75 % to 100 g while the compliant wing observed only a slight decrease to just below 200 g. Furthermore, the changes in aerodynamic lift with angle of attack appeared consistent between the wing designs. Thus, it was concluded that the benefits of the current compliant wing design appear to be primarily in the reduction of negative static lift.

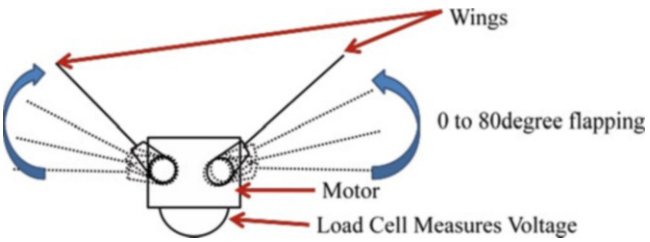

Fig. 10.6 Schematic diagram of test setup. The 6 DOF load cell is fixed to a rigid base in a wind tunnel, and the motor is directly attached to it

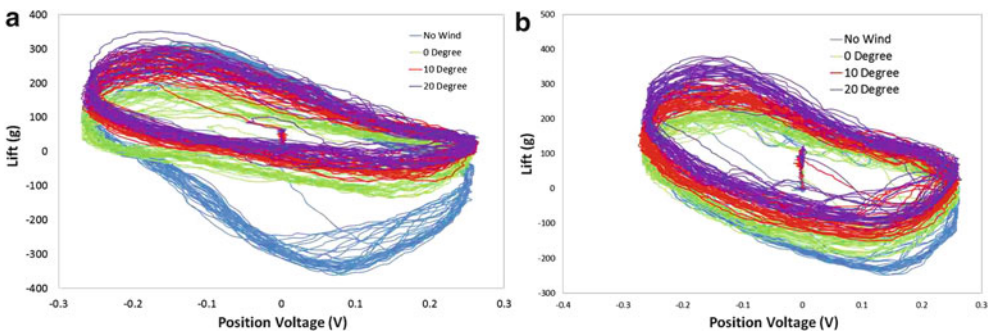

Fig. 10.7 Force measurements made in wind tunnel: (**a**) lift on regular wing, (**b**) lift on compliant wing

Fig. 10.8 Test setup for solar cells under full sunlight. Regular wing is shown on the *left* and compliant wing is shown on the *right*

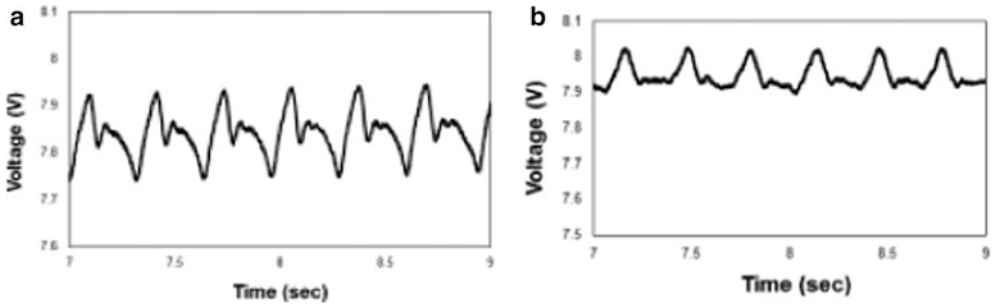

Fig. 10.9 Output voltage readings for solar cells integrated onto a: (**a**) regular wing and (**b**) compliant wing in full sunlight

10.3.3 Solar Cell Output Voltage Test

A second experiment is conducted to approximate the real-time voltage collection of the solar cells fixed to the bird wing. The solar cells are intended to charge three lithium ion polymer batteries, each individually rated at 3.7 V. The solar cells, which are individually rated at 6 V, are wired in series to maximize current. The fully constructed MAV requires a total of 7.14 V to operate effectively. The experimental setup for the compliant wing is shown in Fig. 10.8. The wing is attached to the same motor that was used in the flight characterization experiment. The test in conducted under direct sunlight, when the sun reaches its peak in the sky. During testing, the motor operates under the same synchronized flapping scheme used in the prior experiment. National Instruments' Measurement and Automation Explorer software is used to measure the voltage

Figure 10.9 displays the voltage measurements for the compliant and the regular wing during testing. The periodic voltage fluctuation exhibited in the graphs is due to the angle at which the sun strikes the solar cell modules. During the upstroke and down-stroke, the solar cell modules are fully exposed to the sun, and collect the peak amount of voltage. The solar cells is least exposed to the sun during the transition from an upstroke back to a down-stroke. This is when the voltage reaches a minimum on the graph. From these results, it appears that the compliant wing maintains more exposure to the sun with a max voltage of 8 V and minimum of 7.9 V as opposed to the maximum of 7.9 V and minimum of 7.7 V for the regular wing. Thus, it appears that the compliant wing can generate more voltage and therefore more power as opposed to the regular wing.

10.4 Conclusions

Solar cells were integrated into wings with and without a compliant front spars to create a multifunctional wing structure for flapping wing MAVs. Wing characterization data produced favorable results for the proposed compliant wing design. Static lift measurements revealed that the compliant wing design with solar cells may be more favorable than the compliant wing design without solacells. However, the aerodynamic lift produced from the compliant design with solar cells is not significantly better than for the regular wings.

Both wing configurations exhibit evidence of the ability to produce sufficient voltage to recharge three, 3.7 V batteries in flight during full sun conditions and while flapping. The voltage level for the compliant wing design appeared to be better than for the regular wing design, indicating better potential for energy harvesting. Though these test results appear promising, only the most ideal situations have been taken under consideration. Ergo, more tests must be conducted to determine if the current design is capable of flight.

Acknowledgements This research has been supported by Army Research Office through MAV MURI Program (Grant Number ARMY W911NF0410176), a NSF grant through the Research Experience for Undergraduates program, and by Dr. Byung-Lip "Les" Lee at AFOSR through grant FA95501210158. Opinions expressed in this paper are those of the authors and do not necessarily reflect opinions of the sponsors.

References

1. Mueller D, Gerdes J (2009) Incorporation of passive wing folding in flapping wing miniature air vehicles. Presented at the AMSE mechanism and robotics conference, San Diego, 30 Aug–2 Sept 2009
2. Zdunich P, Bilyk D, MacMaster M (2007) Development and testing of the mentor flapping wing micro-air vehicle. J Aircr 44(5):1701–1711, Sept–Oct 2007
3. Bejgerowski W, Ananthanarayanan A, Mueller D, Gupta SK (2009) Integrated product and process design for a flapping wing drive-mechanism. ASME J Mech Des 131(6):061006
4. Tantanawat T, Kota S (2007) Design if compliant mechanisms for minimizing input power in dynamic applications. J Mech Des 129:1064–1075
5. Lesieutre GA, Frecker M, Mehta V (2008) Compliant frame: a new paradigm to enable reconfigurable aircraft structures. AFOSR final report, Department of Mechanical and Aerospace Engineering, Pennsylvania State University, University Park
6. Clark ES (1996) Delrin material characteristics. Department of Materials Science and Engineering, University of Tennessee, Knoxville 37966–2200. J Heart Valve Dis 5(S2): S184–189. http://www.ncbi.nlm.nih.gov/pubmed/8905519
7. Mueller D, Bruck HA, Gupta SK (2010) Measurement of thrust and lift forces associated with drag of compliant flapping wing for micro air vehicles using a new test stand design. Exp Mech 50(6):725–735
8. Gerdes J, Cellon KC, Bruck HA, Gupta SK (2013) Characterization of the Mechanics of Compliant Wing Designs for Flapping Wing Miniature Air Vehicles. Exp Mech 1–13. doi:10.1007/s11340-013-9779-5

Chapter 11
Fabrication and Characterization of Bi-metallic, Structured Films with Ultra-low Thermal Expansion

Namiko Yamamoto, Eleftherios Gdoutos, and Chiara Daraio

Abstract We fabricate and characterize bi-metallic structured thin films (~1 um thick) with ultra-low effective coefficient of thermal expansion (CTE). The films consist of a periodic array of aluminum (Al) hexagonal plates attached to a titanium (Ti) frame. In this designed discontinuous geometry, the self-standing films present ultra-low effective CTE through local release of the thermal strains by relative rotation of the lattice elements. We fabricated this structured film by a combination of conventional micro-fabrication process steps, and we measured its CTE as ultra-low (-0.6×10^{-6}/°C) using 3D digital image correlation. This new thin film can lead to the creation of low-cost, adaptive structures that operate in extreme thermal environments, such as reflective layers for space telescopes.

11.1 Introduction

The ability to fabricate structured thin films with extremely low and tunable CTE is advantageous over conventional materials with ultra-low or negative CTE, because of their broad temperature range of operation, their scalability, and low-cost. Materials such as metal oxides, silica glasses, and invar exhibit low CTE values (~10^{-6} to 10^{-8}/°C), but these properties are temperature-dependent and thus the operation temperature range is limited [1, 2]. In addition, fabrication in bulk and machining of these materials are complex and expensive. On the contrary, the effective low CTE property of our bi-metallic film is achieved by a purely mechanical contrivance, and thus it is temperature independent. The structure of our thin films consists of a periodic array of unit cells. The unit cells are composed by a hexagonal plate of a higher CTE material (Al) combined with a frame of a lower CTE material (Ti, see Fig. 11.1a), based on the 2D truss design by Steeves et al. [3]. When heated, the thermal expansion of the Al hexagonal plate is accommodated by stretching and bending of the Ti frame into the open spaces, leaving the frame's connection nodes stationary, and resulting in the low effective CTE [4]. This local release of thermal strain is temperature-independent, and thus allows wide application temperature ranges. The fabrication of these structured films is relatively simple and scalable, and the constituent materials are low-cost.

11.2 Methods

11.2.1 Sample Fabrication

The bi-material lattice was designed based on pioneering work from Steeves et al. [3], and improved using 3D finite element simulations [4]. For the fabrication, we selected aluminum (23.1×10^{-6}/°C) for the hexagonal plates and titanium (8.6×10^{-6}/°C) for the frame because of their readiness and favorable CTE ratio. The ultra-low CTE of this particular

N. Yamamoto (✉) • E. Gdoutos
Graduate Aerospace Laboratories, California Institute of Technology, 1200 E. California Blvd, Pasadena, CA 91125, USA
e-mail: namikoy@caltech.edu

C. Daraio
Graduate Aerospace Laboratories, California Institute of Technology, 1200 E. California Blvd, Pasadena, CA 91125, USA

Department of Mechanical and Process Engineering, Swiss Federal Institute of Technology (ETH), Zürich, Switzerland

G.P. Tandon et al. (eds.), *Experimental Mechanics of Composite, Hybrid, and Multifunctional Materials, Volume 6*, Conference Proceedings of the Society for Experimental Mechanics Series, DOI 10.1007/978-3-319-00873-8_11,

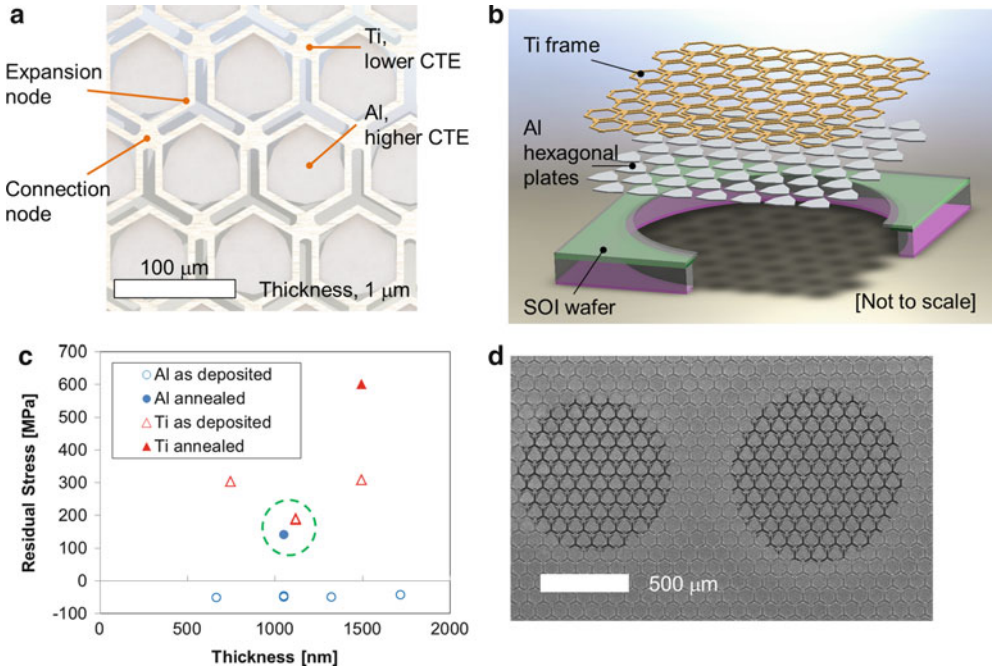

Fig. 11.1 Fabrication of the bi-metallic thin films: (**a**) schematic diagram of the lattice design, (**b**) schematic diagram showing the fabrication steps, (**c**) measured residual stresses, before and after annealing in the Al and Ti metal layers (the data points within the *dotted circle lines* shows the conditioning with the desired residual stress level), and (**d**) scanning electron microscope image of the self-standing films

design was simulated as 1.1×10^{-6}/°C [4]. The freestanding film was micro-fabricated following two steps (see Fig. 11.1b) using a Silicon-on-Insulator (SOI) wafer substrate. First, patterned Al and Ti films were deposited on the substrate by photolithography, electron-beam evaporation, and metal lift-off processes. Second, the 2D bi-metallic lattice film was released into circular sections by layer-by-layer etching of the substrate from the back side: deep reaction-ion etching for the bulk Si, reaction ion etching for the oxide layer, and then XeF_2 etching for the Si device layer. Due to the nature of the micro-fabrication processes selected, the hexagonal plates and frame are bonded by lap-joints. The final film thickness was measured to be ~1.2 μm (vs. 1 μm in design), and the crystalline orientation of the Al and Ti films was observed as [1 1 1] on the Si [1 0 0] substrate using X-ray diffraction. In order to release the film flat to be functional, the residual stress of the two metal layers need to be in the same tensile stress range. The residual stresses of the metal films were evaluated from the wafer curvature data (FLX, Tencor) before and after the metal film deposition, using Stoney's equation. As shown in Fig. 11.1c, as deposited, the Al layer presents residual compressive stress, while the Ti layer presents residual tensile stress (~200 MPa). The Al layer was annealed after deposition at 200 °C in a reduction gas atmosphere made of nitrogen and hydrogen; this annealing process relaxes impurities or dislocations within the Al film, resulting in the stress shift to tensile, conveniently in the same range as the as-deposited Ti film. As shown in Fig. 11.1d, this discontinuous lattice films were successfully released, with a high yield of 95 %.

11.2.2 CTE Measurement Using 3D Digital Image Correlation

The ultra-low CTE of the bi-metallic thin film was measured using a 3D digital image correlation (DIC) set-up with a stereomicroscope unit at Correlated Solutions Inc. (Columbia, SC). DIC is a computer-based process that provides full-field, real-time displacement measurement by tracking the motion of speckle patterns on a deforming sample [5–8]. Our thin film lattices were prepared with a ~4 μm speckle patterns by introducing an extra photolithography step just before the film release step. The samples were heated from room temperature to ~185 °C, and magnified images were recorded from two angles through a stereomicroscope. Displacements are calculated by minimizing the least-squares correlation coefficient of the grayscale intensity values before and after deformation. The correlation process and distortion were calibrated by

measurement on grid and speckle references. The measurement noise was evaluated by taking multiple images of a stationary sample; the noise is <2 nm (in-plane), while the expected displacement range is ~2 to 15 nm. The CTEs were calculated based on the changes of the distances between the points designed to be stationary: the distance between connection nodes on the frame and the distance between the centers of hexagons (see Fig. 11.1a). Data points were taken at scattered locations across the sample surface, at six set temperatures (room temperature, ~45 °C, ~80 °C, ~115 °C, ~150 °C, ~185 °C).

11.3 Results

11.3.1 Evaluation of the Measurement Technique

The accuracy of the 3D DIC measurement technique was evaluated using a Si wafer prepared with the same speckle pattern as a reference. Based on ~65 data points, the CTE of the Si wafer was calculated as 1.8×10^{-6}/°C (median), slightly off from the literature CTE value of [1 0 0] Si (2.6×10^{-6}/°C), as illustrated in Fig. 11.2a. In order to understand the source of variance, we sorted the measured CTEs in terms of the temperature rise (ΔT). As shown in Fig. 11.2b, scattering of the CTE data is significant with the smallest ΔT (at ~45 °C). With the smaller temperature increase, the thermal displacement is very small (~2 nm), and cannot be properly distinguished from the noise level. When the data points taken at ~45 °C are eliminated, scattering significantly decreased, and the new median was calculated as 3.3×10^{-6}/°C (see Fig. 11.2a).

11.3.2 Measured CTEs of the 2D Bi-metallic Lattice

The CTE measurements performed on the bimetallic thin films are summarized and compared with the reference and with the simulated data in Table 11.1. The measured CTE was calculated, excluding the data points taken at ~45 °C, as -0.6×10^{-6}/°C (median), significantly lower than those of Al (23.1×10^{-6}/°C) and of Ti (8.6×10^{-6}/°C), confirming the designed low-CTE mechanism as functional. However, this measured CTE value is slightly lower than the designed CTE value (1.1×10^{-6}/°C), and presents relatively large scatter. A similar discrepancy in the measured and predicted CTE values was also observed in the Si reference sample, within an error range of $\sim 0.5 \times 10^{-6}$/°C. This difference could also be attributed to the difference of the sample set-up in measurement and in simulation. The final in-plane and out-of-plane dimensions of the micro-fabricated samples are ~10 % to 20 % different from the design specifications. In addition, the micro-fabricated lattices are supported at the edges by the Si substrate, while the simulated lattices have free boundaries. We expect that these geometrical differences between the model and experiments and the boundary conditions influence the local lattice deformations, and thus the effective measured CTE.

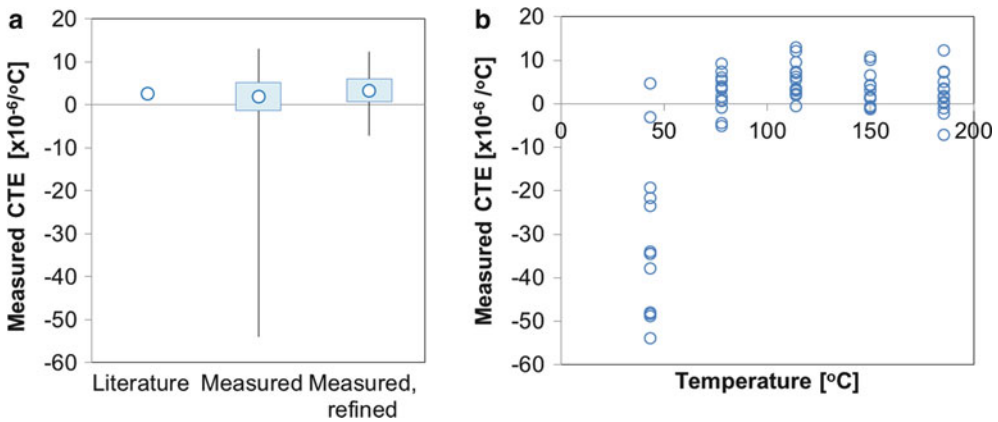

Fig. 11.2 CTE measurement on the Si reference sample. (**a**) Comparison of the literature and measured CTE values. The CTE from refined measurement is based on the data without the one taken at 45 °C. The *box plot* shows the following; *circles*, median; *lower edge of box*, 25th percentile; *upper edge of box*, 75th percentile; whiskers, extreme data points. (**b**) Measured CTE as a function of temperature

Table 11.1 Summary of CTEs of the bi-metallic lattice and its constituents. The measured CTE of the bi-metallic lattice is calculated excluding the data taken at ~45 °C

AI	Ti	Bi-metallic lattice	
Literature	Literature	Simulated	Measured (median)
$23.1 \times 10^{-6}/°C$	$8.6 \times 10^{-6}/°C$	$1.1 \times 10^{-6}/°C$	$-0.6 \times 10^{-6}/°C$

11.4 Conclusions

We designed and fabricated a self-standing thin film composed of a bi-metallic lattice of discontinuous elements. The thin film was designed to have a tunable, ultra-low coefficient of thermal expansion (CTE). The thin films were micro-fabricated controlling their residual stress, to ensure mechanical stability. The films presented an ultra-low effective CTE ($-0.6 \times 10^{-6}/°C$) measured via 3-D digital image correlation. The measured residual stresses and CTE of the samples agreed well with the values predicted by finite element simulations. These thermally stable thin films can be applied in high-precision devices operating in thermally harsh environments or in MEMS devices as buffer layers to minimize thermal fatigue and failure.

Acknowledgement The authors acknowledge Dr. Risaku Toda, Dr. Victor White, and Dr. Harish Manohara from Jet Propulsion Laboratory, and Ms. Elisha Byrne from the Correlated Solutions, Inc. for helpful discussions and technical assistance. This work was supported by the Keck Institute for Space Studies, and Center Innovation Funds (CIF) from NASA's Jet Propulsion Laboratory.

References

1. Miller W, Smith CW, Mackenzie DS, Evans KE (2009) Negative thermal expansion: a review. J Mater Sci 44(20):5441–5451
2. Roy R, Agrawal DK, McKinstry HA (1989) Very low thermal expansion coefficient materials. Ann Rev Mater Sci 19(1):59–81
3. Steeves CA, dos Santos e Lucato SL, He M, Antinucci E, Hutchinson JW, Evans AG (2007) Concepts for structurally robust materials that combine low thermal expansion with high stiffness. J Mech Phys Solid 55(9):1803–1822
4. Gdoutos E, Shapiro AA, Daraio C (2013) Thin and thermally stable periodic metastructures
5. Chu TC, Ranson WF, Sutton MA (1985) Applications of digital-image-correlation techniques to experimental mechanics. Exp Mech 25(3):232–244
6. Sutton MA, Ke X, Lessner SM, Goldbach M, Yost M, Zhao F, Schreier HW (2008) Strain field measurements on mouse carotid arteries using microscopic three-dimensional digital image correlation. J Biomed Mater Res A 84A(1):178–190
7. Sutton MA, Wolters WJ, Peters WH, Ranson WF, McNeill SR (1983) Determination of displacements using an improved digital correlation method. Image Vision Comput 1(3):133–139
8. Sutton MA, Yan JH, Tiwari V, Schreier HW, Orteu JJ (2008) The effect of out-of-plane motion on 2D and 3D digital image correlation measurements. Opt Lasers Eng 46(10):746–757

Chapter 12
Macro Fiber Composites and Substrate Materials for MAV Wing Morphing

Bradley W. LaCroix and Peter G. Ifju

Abstract This paper examines the application of a relatively new type of piezoelectric actuator, termed a Macro Fiber Composite, on small unmanned air vehicles with a wingspan of 0.61 m for the purpose of active flight control. The design is examined on a local–global level with the primary goals being to maximize curvature and load bearing capacity of the actuator-substrate component while also maximizing the effective roll and pitch moment when the actuator component is applied on the aircraft. Within this document the strain of the individual MFC is measured, the performance of various substrates and adhesives examined within a cantilever setup and a four point bend setup, and the overall performance of the MFC actuators evaluated when embedded on an innovative forward swept Micro Air Vehicle wing. The wing incorporates composite material bend-twist coupling to allow passive load alleviation while providing a planform for sufficient control authority using only two MFC actuators.

Nomenclature

AVL	Athena Vortex Lattice
CA	Cyanoacrylate
CG	Center of Gravity
DIC	Digital Image Correlation
FEA	Finite Element Analysis
MAV	Micro Air Vehicle
MFC	Macro Fiber Composite

12.1 Introduction

Micro air vehicles (MAVs) have been used for a wide variety of applications from search and rescue to military applications. Usually these missions are carried out in harsh environments with a large amount of sand, moisture, and heat. Traditionally, servo motors have been the device of choice for control surface actuation due to their relative low cost and reasonable dependability. However, a new type of solid state device, termed a Macro Fiber Composite (MFC), promises to increase reliability in harsh conditions, significantly decrease part count, and offer notably faster actuation. One such device is shown in Fig. 12.1a.

These devices utilize the piezoelectric effect to produce strain when actuated with an applied voltage (−500–1,500 V). Specific MFCs are quoted as being capable of producing 1,800 με with a blocking force of 454 N (102 lbf). When adhered to a substrate material, such as carbon fiber composite, the actuation of the MFC produces out-of-plane deflection in the form of curvature, similar to that of a bimorph, as seen in Fig. 12.1b. The curvature produced by the unimorph can be predicted using thermal expansion relations in Classical Laminate Plate Theory. By varying the elastic modulus and thickness of the

B.W. LaCroix (✉) • P.G. Ifju
University of Florida, 231 MAE-A, P.O. Box 116250, Gainesville, FL 32611, USA
e-mail: BradLaCroix@gmail.com

G.P. Tandon et al. (eds.), *Experimental Mechanics of Composite, Hybrid, and Multifunctional Materials, Volume 6*, Conference Proceedings of the Society for Experimental Mechanics Series, DOI 10.1007/978-3-319-00873-8_12,

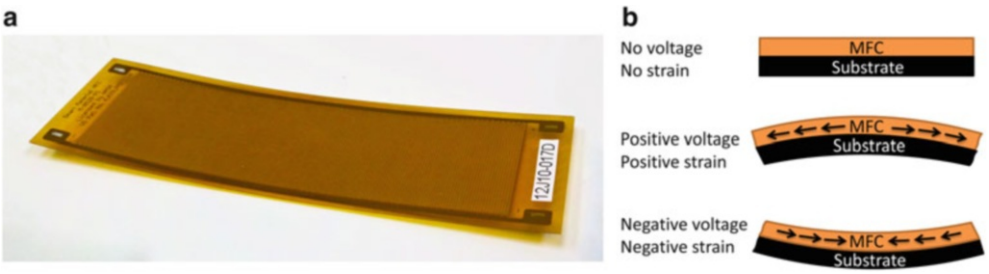

Fig. 12.1 (**a**) The M8528-P1 actuator fabricated by smart Materials Corporation with an active area measuring 85 mm by 28 mm (**b**) an illustration of the resulting curvature when adhering the MFC to a substrate

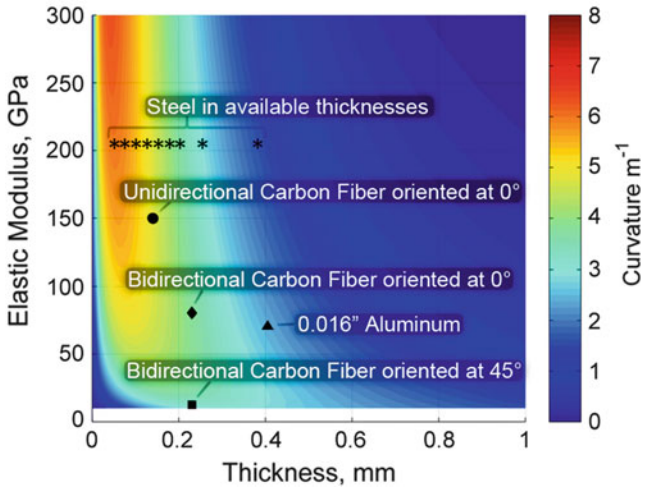

Fig. 12.2 The predicted curvature of the unimorph based on thickness and elastic modulus of the substrate as calculated by Classical Laminate Plate Theory (CLPT)

substrate while maintaining the properties of the MFC, the predicted curvature can be calculated for a range of materials as shown in Fig. 12.2. Experimental tests, shown in latter sections, demonstrate that the curvature trend follows that of Fig. 12.2, but with a scaling of magnitude.

Available in a variety of sizes, ranging from 3 to 57 mm in width to 25–140 mm in length, MFCs provide a new flexibility in small aircraft design due to their potential to replace traditional control mechanisms such as servomotors and the potential to be embedded into the wing. Significant research on the application of MFCs on Micro Air Vehicles (MAVs) has been conducted previously by individuals such as Bilgen [1–10], Wickramasinghe [11], Paradies [12], Vos and Barrett [13–19], and Ohanian [20, 21].

This research investigates innovative methods of applying MFCs on MAVs measuring 0.61 m (2 ft). Recent work has established a working prototype with proven flight time with only two actuators. Furthermore, this prototype, shown in Fig. 12.3a/b, benefits from the forward swept wing design which incorporates advanced bend-twist coupling of carbon fiber composites. Utilizing this unique layup, the wing will wash-out (twist down) in a load alleviating manner when aerodynamically loaded as opposed to an isotropic wing that would wash-in (twist up) when loaded and negatively affect the stability of the aircraft. The intent of this planform is to provide the opportunity for increased performance due to high maneuverability as well as the large distance between the MFCs and the aircraft's center of gravity.

Limiting the number of actuators is important for two reasons. Firstly, each M8528-P1 actuator costs in excess of $100, which is more than four times the cost of a traditional servomotor. Secondly, since the MFCs require high voltage input, each discrete channel requires nearly an N increase in electronics weight, where N is the weight of the high voltage electronics necessary for one channel. Therefore, a four channel system will require nearly double the electronics weight as a two channel system. Since this aircraft utilizes elevons, in which the ailerons and elevators are combined, only two channels are required. Roll and yaw are inherently coupled, thereby eliminating the need for a rudder.

Consequently, this research aims to optimize the performance of a two-channel, two MFC platform in order to minimize weight while maintaining a cost-effective flight system. A local–global approach is used to progress towards this goal and will

Fig. 12.3 (**a**) Top view of the forward swept wing aircraft, (**b**) bottom view of the aircraft with MFCs in view. (**c**) Out-of-plane deflection as measured by digital image correlation (DIC) when right MFC is actuated to 1,500 V

be explored in detail within this manuscript. Firstly, from a local respect, the independent performance of the MFC when bonded to a substrate is examined to improve the overall deflection capability of the MFC layup. Various materials such as steel, aluminum, and carbon fiber have been considered, as well as various adhesion techniques [22]. Two types of experiments have been conducted in this regard: A cantilever set-up coupled with Digital Image Correlation (DIC) in which the unimorph is held fixed at one end and loaded at the other end to measure tip deflection. The other experiment is composed of a four point bend test in which the unimorph load capability is measured as a function of displacement. Alternatively, a global approach is used to optimize the positioning, material selection, and overall design of the planform to enhance the overall performance of the aircraft. Workbench tests, where the MFCs were actuated and submitted to various loading, were conducted in conjunction with DIC to measure the wing deflection, as seen in Fig. 12.3c. These tests will be used to calibrate and validate the finite element model. Aerodynamic load software has also been coupled with the finite element model to predict the fluid–structure interaction and the resulting aerodynamic loads of the deformed structure. Wind tunnel tests with DIC are planned to occur in the near future to further calibrate the combined finite element model / aerodynamic loads program.

12.2 Detailed Experiments and FEA Models

A proprietary electronics board is used to power the actuators during flight. This board allows the MFCs to be actuated from −500 to 1,500 V using a typical 11.1 V battery and standard receiver. However, for workbench tests, a different set-up is used in order to generate a stable voltage at a desired level. Within this setup, shown in Fig. 12.4, a voltage divider is carefully devised to reduce the circuit voltage to a level within the limits of the multimeter while preventing excessive current draw which would affect the voltage to the MFC.

12.2.1 MFC Strain Quantification

One of the key aberrations of MFCs is the hysteresis encountered during actuation. Hysteresis has been reported in numerous publications [3, 9, 20, 23] and, while relatively modest, it must still be accounted for, especially within experiments. Furthermore, the precise strain that a particular MFC produces is a necessary property for validating finite element models. A DIC setup was constructed to determine the hysteresis in the M8528-P1 MFC and is shown in Fig. 12.5a. Since the layup of the MFC itself is slightly asymmetric, it will generate curvature when actuated. Consequently, the MFC would move relative to the plane of the DIC cameras if left unrestrained. Therefore, a small weight was placed at the free end of the MFC to prevent the MFC from deflecting out of the plane of focus. In addition, to insure sufficient resolution, the camera system was focused at a small portion of the MFC actuator, essentially maximizing the strain per pixel.

The resistance of the resistors in the voltage divider were measured prior to the experiments and then used to calculate the exact voltage applied to the MFC throughout each the experiment. The upper voltage limit was adjusted to 1,700 V, rather than the manufacturer specified 1,500 V due to literature suggesting that 1,700 V is a safe upper limit for this type of MFC [8, 4, 23]. As a result, all of the hysteresis tests are conducted from −500 to 1,700 V. The data extracted from this experiment is shown in Fig. 12.5b. Note that there is a significant level of strain in the transverse (y) direction, which indicates it should not be ignored in the FEA model. Also worth noting is the magnitude of the longitudinal strain range. The quoted value from Smart Materials Corporation is given as 1,800 με, whereas, the measured value is nearly 2,600 με. It is unclear whether the

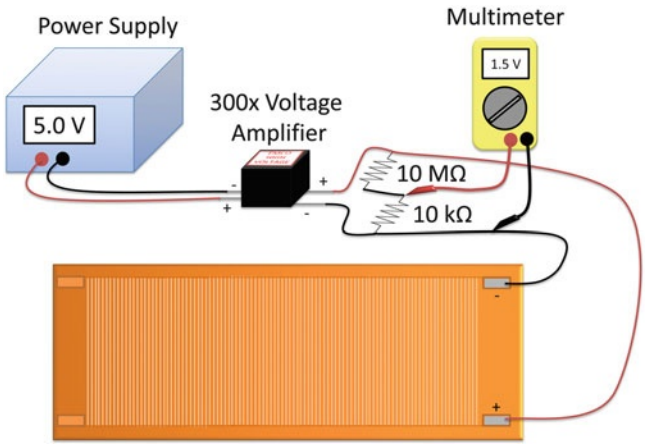

Fig. 12.4 An illustration of the electronics setup used for all of the workbench tests

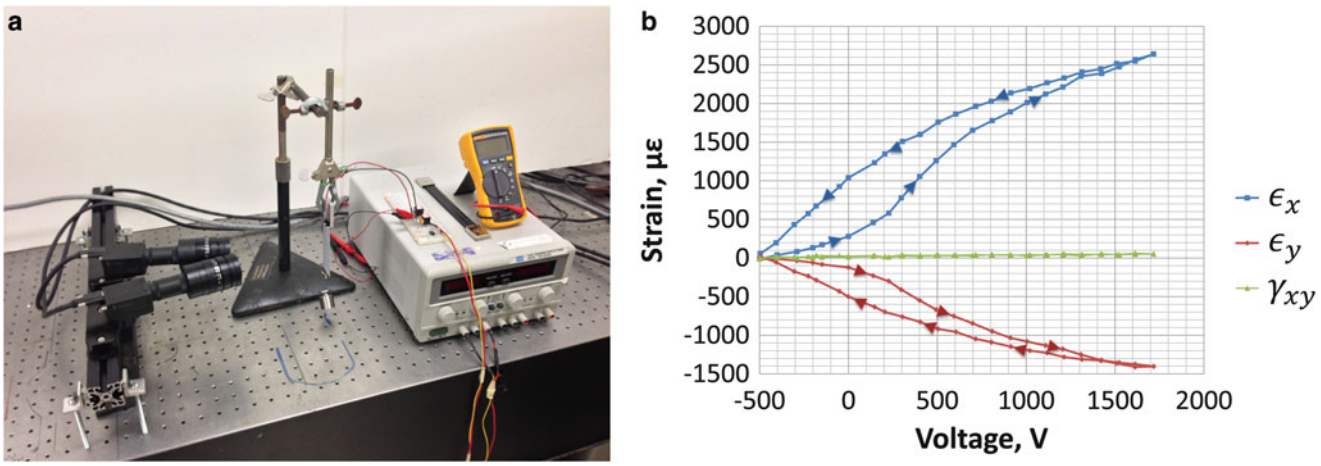

Fig. 12.5 (**a**) DIC set-up for the strain measurement of an M8528-P1, (**b**) strain components of the M8528-P1 actuator when actuated from −500 to 1,700 V and returning to −500 V

quoted 1,800 με pertains to the MFC strain from 0 to 1,500 V or from −500 to 1,500 V or how Smart Materials Corp. accounted for hysteresis, so this value may not deviate as much as it seems. To validate the experimental data, the DIC system was recalibrated and the experiment repeated. However, the same results were obtained.

12.2.2 Preliminary Unimorph Tests

In the initial set of experiments, two substrates were examined: bidirectional carbon fiber at 45° ($E = 12\ GPa$ and $t = 0.3\ mm$) and unidirectional carbon fiber aligned with the length of the MFC ($E = 110\ GPa$ and $t = 0.15\ mm$). In these experiments, one end of the unimorph was held fixed while the MFC was actuated from 0to 1,500 V and the relative displacement measured using DIC. These results are shown in Fig. 12.6 and reinforce the results shown in Fig. 12.2, where the higher modulus of the unidirectional carbon fiber outperforms the thicker, lower modulus bidirectional carbon fiber.

Similarly, Fig. 12.7 shows the results when comparing two adhesion techniques. The first method, co-cure, is achieved by laying the MFC on a layer of carbon fiber pre-impregenated with epoxy (pre-preg) and then curing the assembly under vacuum pressure in the oven at 260°F for approximately 6 h. The second method, utilizing a quick curing adhesive termed

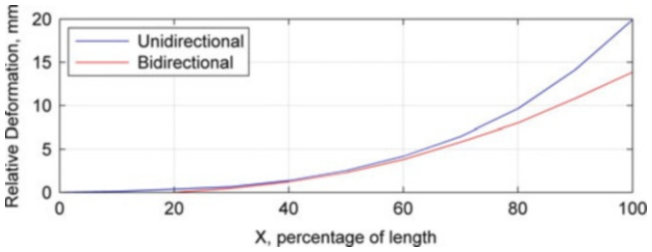

Fig. 12.6 Results comparing the deflection of the unidirectional and bidirectional carbon fiber unimorphs

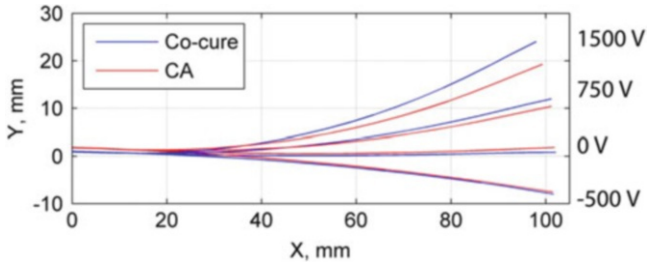

Fig. 12.7 Results comparing the deflection of a co-cured unimorph and a CA unimorph

Cyanoacrylate (CA), is performed by first curing the carbon fiber separately and adhering the MFC to the cured carbon fiber using the CA. Both of these tests were performed with the same type of unidirectional carbon fiber. The results show that the co-cure method produces a superior unimorph with larger deflections than the CA unimorph.

12.2.3 Cantilever Experiments

A cantilever setup was chosen as a test rig due to its similarity to most MAV wings which are composed of stiff leading edges. This test is well suited for FEA validation, but may not adequately test the unimorph structures under loading. Therefore, four point bend tests are also conducted and are presented in Sect. 12.2.5.

The cantilever tests were conducted by actuating the unimorph through various voltages while applying various loads to the tip of the cantilevered unimorph. An aluminum tube was adhered to the tip of the unimorph and a Kevlar string tied through the tube to allow precise application of various loads. Furthermore, the tube prevented excessive localized deformation from occurring. Figure 12.8a shows the cantilever setup with two 10 g masses attached to the free end. DIC images were taken at each interval of loading and/or actuation and meticulous care was taken to avoid the effects of hysteresis.

One of the primary interests in this set of experiments was to further compare substrate materials. The trend indicated in Fig. 12.2, predicts that thin steel should produce a larger degree of curvature than a standard layer of unidirectional carbon fiber. Since both the modulus is larger and the thickness is less (if less than 0.17 mm), the overall curvature should be more. This was confirmed when conducting tests comparing steel and unidirectional carbon fiber, the results of which are shown in Fig. 12.8b. In these experiments, the unimorphs were actuated from –500 to 1,500 V then returned to−500 V. DIC images and voltages were measured at intermittent points during this process.

An interesting aspect concerning the MFC actuation is the hysteresis due to loading. In other words, the order in which the loading is applied can affect the final displacement. Since the finite element model does not account for hysteresis, and rather is the average between the top and bottom portion of the hysteresis curve, the FEA displacement curve should fall somewhere in between the experimental DIC results. This is exemplified in the plots shown in Figs. 12.9 and 12.10. The details about the FEA models are presented in the following section. In regards to the experimental setup, if the loading is applied first, the MFC will be displaced to a lower position than if the loading is applied after actuation, in which case the MFC is better able to maintain its position. This is true for both up (1,500 V) and down (−500 V) actuation.

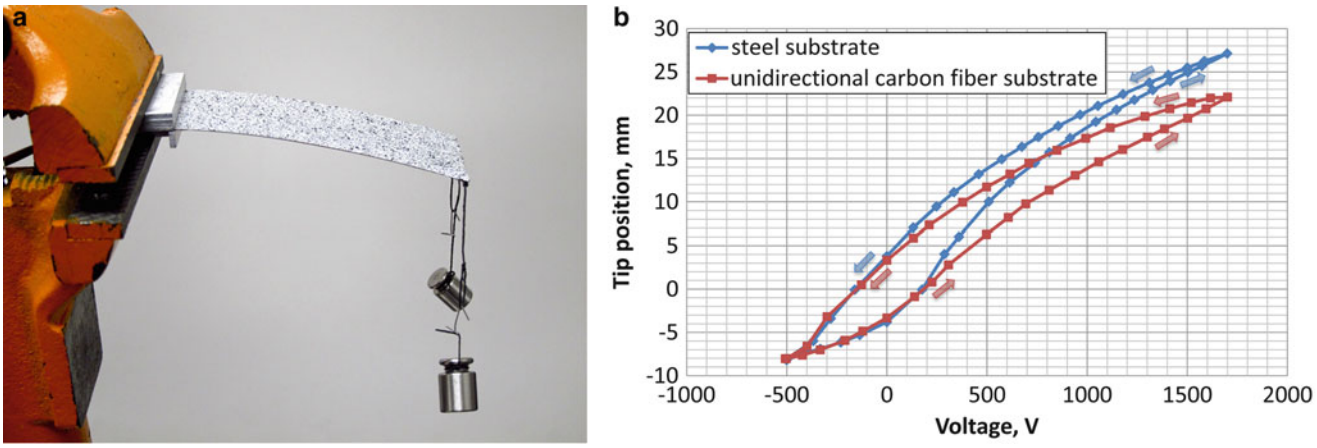

Fig. 12.8 (**a**) The cantilever setup with 10 g masses attached to the free end, (**b**) the hysteresis results when comparing the unloaded tip deflection of the 0.10 mm steel substrate to the 0.17 mm unidirectional substrate unimorph

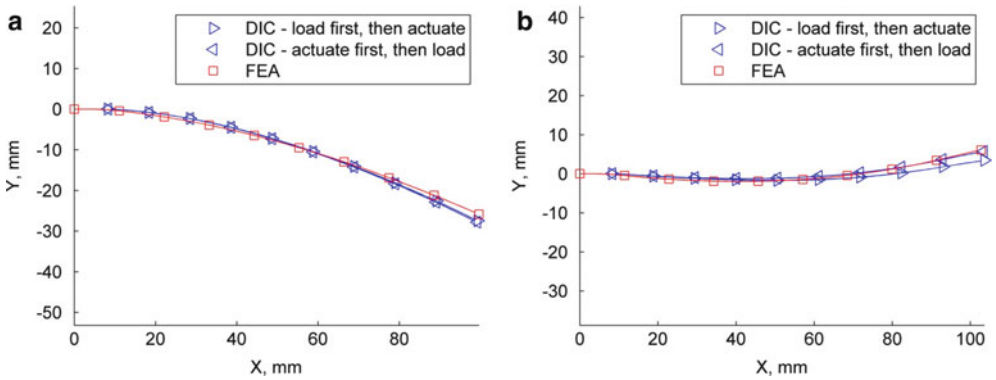

Fig. 12.9 Comparison between the DIC experimental results and the finite element model for the 0.17 mm unidirectional carbon fiber substrate. (**a**) –500 V actuation with 40 g load (**b**) 1,500 V actuation with 40 g load

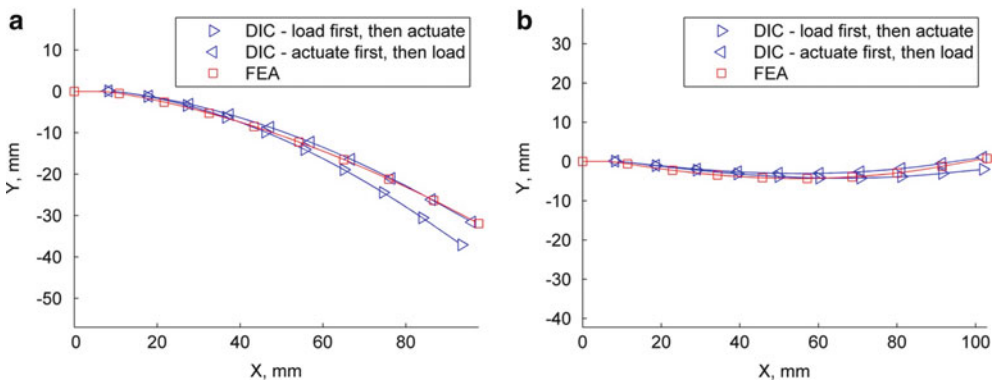

Fig. 12.10 Comparison between the DIC experimental results and the finite element model for the 0.10 mm steel substrate. (**a**) –500 V actuation with 40 g load, (**b**) 1,500 V actuation with 40 g load

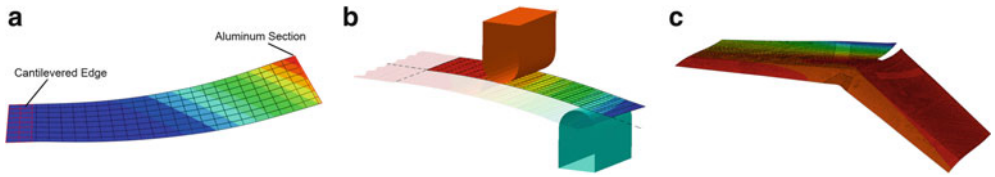

Fig. 12.11 (**a**) Cantilever FEA model, (**b**) four point bend quarter model, (**c**) complete wing model

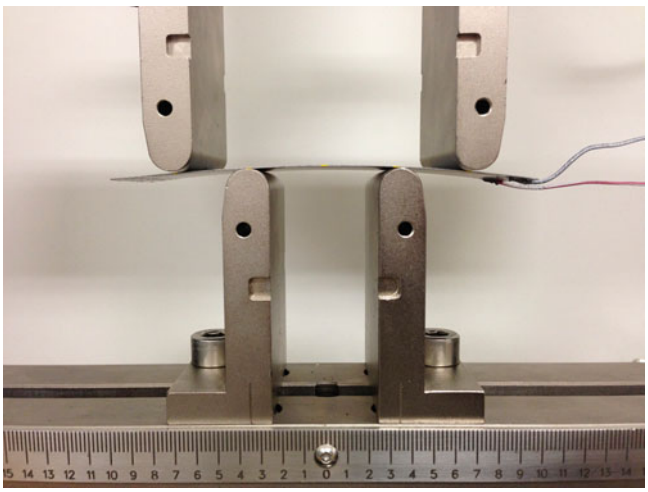

Fig. 12.12 Four point bend test setup

12.2.4 Finite Element Modeling

Finite element models were produced in Abaqus as a step towards a larger FEA model which encompasses an entire MAV wing with MFCs. All FEA models are composed of 3D shell elements composed of composite sections to simulate the layup of the unimorph, examples are shown in Fig. 12.11. Note, the cantilevered model incorporates an aluminum partition to represent the aluminum tube present in the experimental model. To replicate the linear strain actuation of the MFC in FEA, a detailed thermal expansion profile was created using the hysteresis plot of Fig. 12.5b. The profile input into FEA was a simplified curve that represented the mean between the two curves. This curve was then converted to the correct units (strain per degree temperature). This was a justifiable simplification since most of the analyses take place at the extreme voltage bounds, at −500 and 1,500 V. Therefore, unless a dynamic or intermediate analysis is conducted, the behavior of the MFC within the upper and lower bounds is unimportant.

12.2.5 Four Point Bend Tests

Another set of experiments were conducted using a four point bend experimental setup on a Test Resources electromechanical test machine using a 10 lb (~ 44 N) load cell. These experiments were considered to be a more ideal loading of the MFC unimorph since the primary output force of the unimorph is a bending moment while the four point bend fixture applies a pure bending moment within the interior supports. Therefore, this setup is expected to give more reliable quantifications of the load bearing capacity of the unimorphs and corresponding substrates. The experimental assembly for the four point bend setup is shown in Fig. 12.12. In the figure, the unimorph is actuated to 1,500 V while being constrained by the loading fixtures. The experiment is conducted in two different ways for each unimorph.

In the first experimental run (Positive Run):

1. The MFC is actuated to the −500 V position.
2. The loading fixtures are lowered until they make contact with the unimorph and a slight load is measured.
3. The MFC is actuated to the 1,500 V while the loading fixtures constrain it.

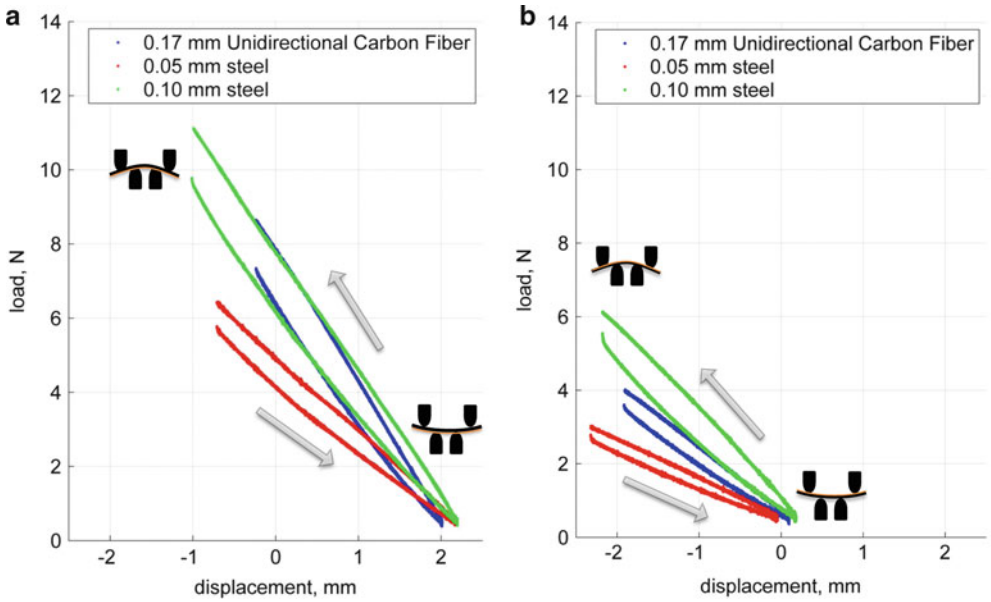

Fig. 12.13 Four point bend test results (**a**) positive run – loading as a function of displacement when the MFC is actuated to 1,500 V, (**b**) negative run – loading as a function of displacement when the MFC is actuated to −500 V

Test Begins

4. The load fixture is moved up at a rate of 0.11 mm/s (0.25 in/min) until the load is reduced to 0.44 N (0.1 lb).
5. The load fixture is moved downward at a rate of 0.11 mm/s (0.25 in/min) until the starting position is reached.

Test Ends

The second experimental run (Negative Run) is conducted in a similar manner, but the unimorph is placed face down on the loading fixtures and the following steps taken:

1. The MFC is actuated to the 1,500 V position.
2. The loading fixtures are lowered until the make contact with the unimorph and a slight load is measured.
3. The MFC is actuated to −500 V while the loading fixtures constrain it.

At this point, steps 4 and 5 are completed as above.

Multiple runs of the same experiment were conducted to insure that the method was repeatable. Very little variation was observed. Furthermore, an additional experiment was conducted with the 0.10 mm steel unimorph in which grease was applied to the contact points of the four point bend setup and the procedure repeated. These results were almost identical to the ungreased results, indicating that friction plays a nearly negligible role in the process.

These results indicate that the 0.10 mm steel substrate is superior to both the unidirectional carbon fiber substrate and 0.05 mm steel substrate in load bearing capacity. The 0.10 mm steel substrate unimorph is capable of producing approximately 10–11 N of force (2.3–2.5 lbf) while constrained. Early flight tests seemed to indicate that aerodynamic loads were affecting the actuated position of the MFCs, thereby decreasing the control authority at higher flight speeds and greater wing loadings. This suggests that the substrate that provides the highest load bearing capacity while maintaining large displacements is preferable to the substrate that provides the largest deflection but has very low load bearing capacity. Therefore, future iterations of MFC actuated MAVs will take advantage of these results by implementing the 0.10 mm steel.

Another interesting aspect of the unimorph actuation is that the load bearing capacity decreases significantly when actuating to the −500 V position, as demonstrated in Fig. 12.13b. The load bearing capacity is approximately halved when loading in the −500 V direction vs the 1,500 V direction. Therefore, it can be concluded that the MFCs exemplify nearly twice the actuation load output in the extensional 1,500 V actuation as compared to the −500 V actuation.

12.3 Forward Swept Wing Design

A unique, forward swept planform, was chosen for the application of the MFCs. This planform was chosen due to its high maneuverability and its anticipated performance when actuated using MFCs. Furthermore, the planform allows for the actuators to be placed at the inboard section of the wing where there is less probability for control reversal, which occurs when the wing is too compliant and a commanded maneuver results in an opposing maneuver. The actuators are also placed a significant distance, longitudinally, from the center of gravity (CG), thereby increasing their effectiveness for pitch control.

Forward swept wings are generally avoided due to their tendency to wash-in. This occurs when a wing made of isotropic or quasi-isotropic material is aerodynamically loaded and the load causes the wing to twist upwards, thereby further increasing the aerodynamic load. This can cause instabilities and also be structurally catastrophic. However, if composite materials are used, it is possible to design and manufacture the wing to incorporate bend-twist coupling, thereby producing washout. In this way, aerodynamic loading will effectively bend the wing which results in twist. Therefore, the torque created by the load will be negated or additionally offset by the bend-twist coupling. This effect is shown in Fig. 12.14.

A flat, uncambered wing was first manufactured to minimize the time investment in investigating such a radical MAV design. This wing incorporated specific fiber angles to generate the desired bend-twist coupling, but without camber. A complete tail with horizontal stabilizer, vertical stabilizer, elevator, and rudder were also part of this design. To minimize costs and to provide flexibility in design changes, servos were chosen as the actuating mechanism. This first iteration is shown in Fig. 12.15a.

Flight testing showed that once the CG was moved to the appropriate location, that the aircraft was stable and comparable in stability to most other aircraft of similar size. The large wing area and low payload weight resulted in a relatively low wing loading and therefore allowed for slower flight speeds. With a remarkable successful set of initial test flights, the decision was made to progress to the next iteration.

The next iteration, shown in Fig. 12.15b, incorporates the control surfaces into the trailing edge of the wing as elevons. A 3D wing design was created using in-house MATLAB software and the mold manufactured from tooling board using a CNC machine. With the proper reflex incorporated into the wing, the horizontal tail could be completely eliminated. A similar layup was used in the fabrication of the wing as the first iteration, but with fewer overall layers. Fewer layers were

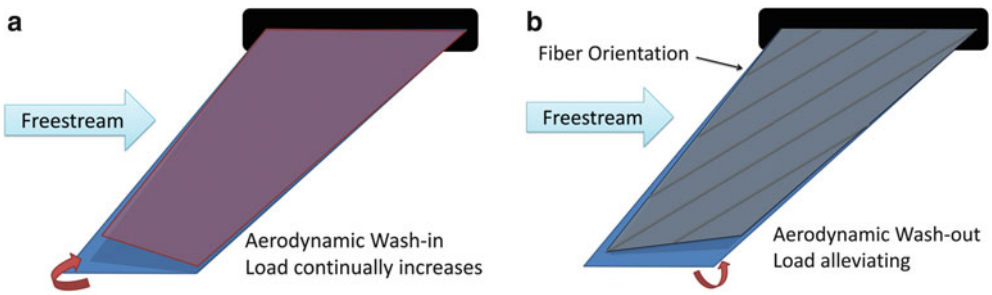

Fig. 12.14 An illustration of the bend-twist coupling when incorporated into wings. (**a**) Isotropic wing, (**b**) composite wing with bend twist coupling

Fig. 12.15 (**a**) First iteration of forward swept wing with servo actuated tail surfaces. (**b**) Second iteration of forward swept wing with servo actuated elevons on the trailing edge of the wing. (**c**) Third iteration of forward swept wing with exclusive actuation provided by MFC actuators

necessary due to the camber in the wing, which creates a higher moment of inertia cross-section. Finally, the fuselage was streamlined to reduce cross-sectional area and weight.

Flight testing showed that this aircraft performed even better than the first iteration with superb flight characteristics. Relatively little input was necessary from the pilot to keep the aircraft level and it was noted that the control surfaces provided sufficient control authority. At this point, it was decided that this was a promising planform for MFCs and the next step could be taken by incorporating MFCs into the wing in the next iteration.

The third iteration, complete with MFC actuators, is shown in Fig. 12.15c. The layup for this iteration is the same as the second iteration with the exception of the section of wing directly in contact with the MFCs. Since earlier testing showed that larger deflection was obtainable with unidirectional carbon, the bidirectional carbon fiber directly adjacent to the MFC was removed and unidirectional carbon fiber placed parallel to the longitudinal direction of the MFC. Therefore, the material directly underneath the MFC is one layer of unidirectional carbon fiber and the area around the MFC is bidirectional carbon fiber. The transition from unidirectional carbon fiber to bidirectional carbon fiber is evident in Fig. 12.15c. With respect to manufacturing, the entire wing was laid up as one part and co-cured with the MFCs in their respective locations.

The flight tests showed that once again the design was stable, necessitating minimal pilot input and exhibited sufficient pitch control. However, due to the inboard location of the MFCs and the minimal displacement exhibited by the actuation of the MFCs, there was insufficient roll authority. Nonetheless, the aircraft was still flight worthy and could execute large banking turns. Therefore, one of the primary goals for the next iteration is to improve the roll authority of the aircraft while maintaining sufficient pitch control.

12.4 Experimental Tests, FEA Models, and Future Research

A variety of loads were applied to the third aircraft to generate a set of data to verify the FEA model. Digital image correlation was used to measure the wing deformation while conducting the workbench tests. The experimental setup with all three loads applied is shown in Fig. 12.16. These loading points are precisely located at the wing tip leading edge, wing tip trailing edge, and trailing edge of the wing directly behind the center of the MFC actuator. An example of one experiment and its corresponding FEA model is shown in Fig. 12.17. To generate the FEA model, DIC was performed on the undeformed wing and the geometry recorded. This recorded geometry was then input into the FEA model thereby allowing for multiple analyses to be performed on the specific geometry and various MFC locations and layups examined.

The next iteration for the forward swept wing will utilize 0.10 mm steel substrate material embedded into the wing. This requires the combination of pre-preg carbon fiber for the wing as well as standard epoxy to bond the MFC to the steel. By using high temperature epoxy, the entire layup can be co-cured in the oven in one step, producing a single composite part. This layup method has been tested and the results shown in Fig. 12.18.

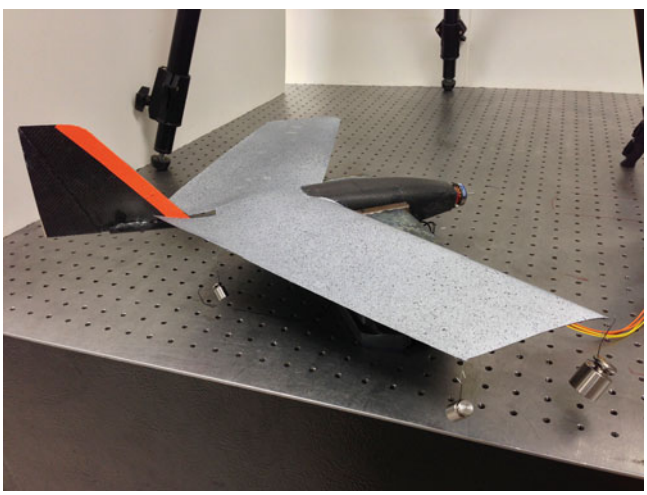

Fig. 12.16 Loading locations for the DIC experiments

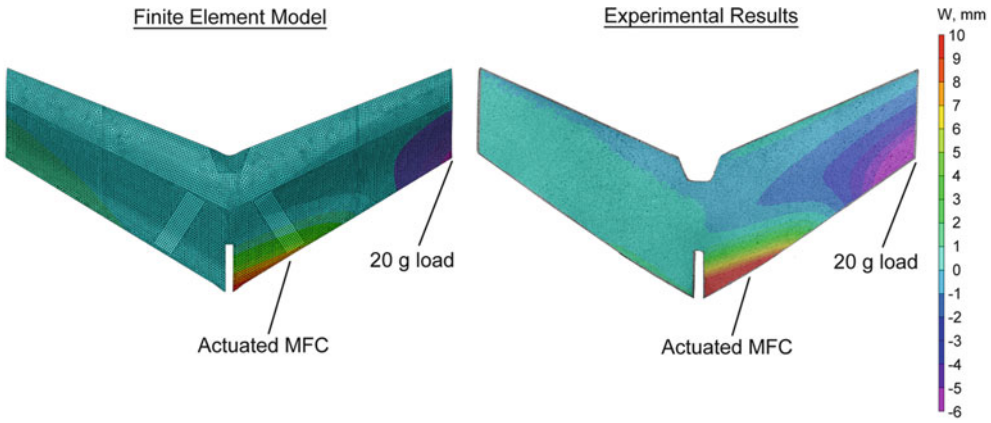

Fig. 12.17 Finite element model and DIC experimental results when applying a 20 g load at the wing tip trailing edge while actuating the MFC at 1,500 V

Fig. 12.18 (**a**) Top view of the steel embedded within the wing, (**b**) bottom view of the same wing, (**c**) rear view of the wing

The coupling between the Abaqus FEA and Athena Vortex Lattice (AVL) [24] is currently functional and is in its initial verification stages. AVL is a program developed at MIT for the aerodynamic and flight-dynamic analysis of rigid aircraft. Given that it is a rigid planform analysis tool, it is necessary to iterate between Abaqus and AVL to determine the deformed geometry upon which the aerodynamic loads are acting. MATLAB is used as the coordination program to run Abaqus and AVL and pass the results back and forth. The current MATLAB program allows for every aspect of the geometry to be altered, including layup orientations and MFC placement. After the geometry and other aircraft specifications are declared, MATLAB can generate the corresponding Abaqus (FEA) model and calculate the unloaded actuation of the MFCs. This deformed geometry is then passed from Abaqus into AVL where the aerodynamic loads are calculated across the surface of the wing. Finally, these aerodynamic loads are passed back to Abaqus where the pressure load is applied to the surface of the deformed wing. A new deformed geometry is calculated and the process continues until the maximum change in geometry is less than 0.1 mm. At this point, the pitch and roll moment coefficients can be studied to compare a variety of designs. An example of the AVL loads visualization is shown in Fig. 12.19.

Once the computer model has been verified, it will be possible to use it to optimize the positioning of the MFCs and overall layup of the wing by comparing the calculated roll and pitch moments for various designs. Initial flight testing has shown that the current test plane produces adequate pitching authority, but lacks sufficient roll authority to execute aggressive banking maneuvers. It seems reasonable that moving the MFC outboard would increase the roll moment produced by the actuator, but it is important to maintain sufficient pitching authority. The computer model predicts that moving the MFCs farther outboard, by approximately 12.7 mm (0.5 in.) and replacing the unidirectional carbon fiber with the 0.10 mm steel will maintain the same pitching authority but increase the roll moment capability. Wind tunnel testing will be used to confirm this prediction and to further calibrate the computer model. After proper validation, additional optimization will take place to further improve the design.

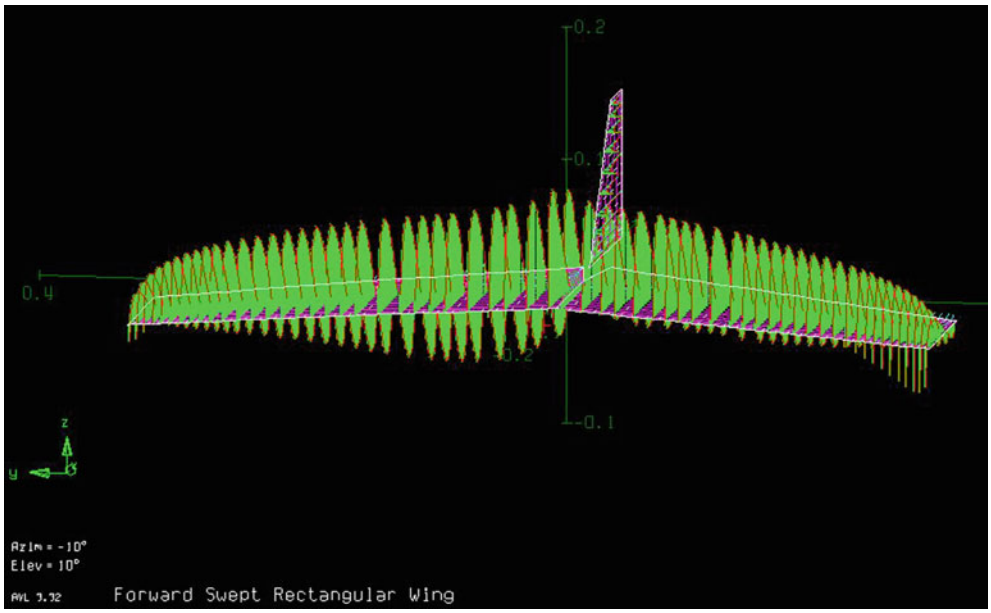

Fig. 12.19 An example of the forward swept wing geometry in AVL with loads applied and 1,500 V applied to the right actuator and −500 V applied to the left actuator

12.5 Conclusion

MFCs show great potential in the application to small unmanned air vehicles and MAVs. Their main advantages over traditional servos lie within their longevity, reduction in part count, bandwidth of actuation, and solid state layup. This makes them ideal candidates for harsh conditions and missions which require a significant number of cycles. This research has shown several important discoveries. First, the M8528-P1 actuators are capable of producing a range of strain in excess of 2,600 με when actuated from −500 to 1,700 V. Secondly, materials with higher elastic moduli tend to produce a larger and higher load bearing actuation, given the appropriate thickness. It has been established that 0.010 mm steel produces the largest load bearing capacity of the substrates tested while also producing a relatively large tip deflection. Finally, it has been shown that a forward swept wing design with bend-twist coupling provides a reliable platform for the implementation of a minimal number of MFCs, reducing costs and aircraft weight.

Future research will continue by improving the computer models of the forward swept wing design by completing wind tunnel testing and DIC. Once the computer model is properly validated, an optimization process will be used to determine the best design for the final aircraft.

References

1. Bilgen O, Friswell M, Park S, Kochersberger K, Inman D (2011) Surface actuated variable-camber and variable-twist morphing wings using piezocomposites. In: 52nd AIAA/ASME/ASCE/AHS/ASC structures, structural dynamics and materials conference, Denver, CO
2. Bilgen O, Kochersberger KB, Inman DJ (2009) Macro-fiber composite actuators for a swept wing unmanned aircraft. Aeronaut J 113 (3337):385–395
3. Bilgen O, Friswell M, Inman D (2011) Theoretical and experimental analysis of hysteresis in piezocomposite airfoils using Preisach model. J Aircraft 48(6):1935–1947
4. Bilgen O, Kochersberger K, Inman D, Ohanian O III (2010) Macro-fiber composite actuated simply supported thin airfoils. Smart Mater Struct 19(5):055010
5. Bilgen O, Kochersberger K, Diggs D, Kurdila A, Inman D (2007) Morphing wing micro-air-vehicles via macro-fiber- composite actuators. In: 48th AIAA/ASME/ASCE/AHS/ASC structures, structural dynamics, and materials conference, Honolulu, HI
6. Bilgen O, De Marqui C, Kochersberger KB, Inman DJ (2010) Macro-fiber composite actuators for flow control of a variable camber airfoil. J Int Mater Syst Struct 22(1):81–91
7. Bilgen O, Kochersberger K (2007) Morphing wing aerodynamic control via macro-fiber-composite actuators in an unmanned aircraft. In: AIAA 2007 conference and exhibit, Rohnert Park, CA

8. Bilgen O, Kurdila A, Inman D, Kochersberger K, Wicks A (2007) Macro fiber composite actuated unmanned air vehicles: design, development, and testing. Virginia Polytechnic Institute and State University, Blacksburg, VA
9. Bilgen O, Kochersberger K, Inman D, Ohanian O III (2010) Novel, bidirectional, variable-camber airfoil via macro-fiber composite actuators. J Aircraft 47(1):303–314
10. Bilgen O (2010) Aerodynamic and electromechanical design, modeling and implementation of piezocomposite airfoils. Virginia Polytechnic Institute and State University, Blacksburg, VA
11. Wickramasinghe V, Chen Y, Martinez M, Wong F, Kernaghan R (2011) Design and verification of a smart wing for an extreme-agility micro-air-vehicle. Smart Mater Struct 20(12):125007
12. Paradies R, Ciresa P (2009) Active wing design with integrated flight control using piezoelectric macro fiber composites. Smart Mater Struct 18(3):035010
13. Barrett R, Vos R (2008) Post-buckled precompressed subsonic micro-flight control actuators and surfaces. Smart Mater Struct 17(5):055011
14. Barrett R, Vos R (2010) Post-buckled precompressed techniques in adaptive aerostructures: an overview. J Mech Des 132(3):031004
15. Barrett R, Vos R, Tiso P, Breuker R De (2005) Post-buckled precompressed (PBP) actuators – enhancing VTOL autonomous high speed MAVs. In: 46th AIAA/ASME/ASCE/AHS/ASC conference, Austin, TX
16. Barrett R, Vos R, Breuker RD, Tiso P (2007) Post-buckled precompressed elements: a new class of control actuators for morphing wing UAVs. Smart Mater Struct 16(3):919–926
17. Barrett R, McMurtry R, Vos R, Tiso P, De Breuker R (2006) Post-buckled precompressed piezoelectric flight control actuator design, development and demonstration. Smart Mater Struct 15(5):1323–1331
18. Vos R, Gurdal Z, Abdalla M (2010) Mechanism for warp-controlled twist of a morphing wing. J Aircraft 47(2):450–457
19. Vos R, Gurdal Z, Abdalla M (2008) A novel mechanism for active wing morphing. In: 49th AIAA/ASME/ASCE/AHS/ASC structures, structural dynamics, and materials conference, Schaumburg, IL
20. Ohanian III O, Hickling C, Stiltner B (2012) Piezoelectric morphing versus servo-actuated MAV control surfaces. In: 53rd AIAA/ASME/ASCE/AHS/ASC structures, structural dynamics and materials conference, Honolulu, HI
21. Ohanian III O, David B, Taylor S, Kochersberger K, Probst T, Gelhausen P (2013) Piezoelectric morphing versus servo-actuated MAV control surfaces, Part II: flight testing. In: 51st AIAA aerospace sciences meeting including the new horizons forum and aerospace exposition, AIAA, Grapevine, TX
22. LaCroix B, Ifju P (2012) Utilization and performance enhancements of multiple piezoelectric actuators on micro air vehicles. In: 50th AIAA aerospace sciences meeting including the new horizons forum and aerospace exposition, Nashville, TN
23. Williams RB, Inman DJ (2004) Nonlinear mechanical and actuation characterization of piezoceramic fiber composites. Virginia Polytechnic Institute and State University, Blacksburg, VA
24. Drela M, Youngren H (2012) Athena vortex lattice (AVL). http://web.mit.edu/drela/Public/web/avl/. Retrieved 12 July 2011

Chapter 13
Experimental Characterization of Thermomechanically Induced Instability in Polymer Foam Cored Sandwich Structures

S. Zhang, J.M. Dulieu-Barton, and O.T. Thomsen

Abstract This paper presents a primarily experimental investigation of the instability behaviour of polymer foam cored sandwich structures loaded at elevated temperatures. An experimental setup was designed to induce the unstable behaviour using sandwich beam specimens subjected to four-point bending and by imposing a linear temperature gradient through the core thickness. A wavy deformation of the face-sheet was observed using high-speed imaging combined with digital image correlation (DIC) for the specimens tested at elevated temperatures over 70 °C, thus identifying the occurrence of face-sheet wrinkling. The face-sheet wavy deformation evolves to core crushing in tens of microseconds and thereby the high-speed imaging is essential in this work. The experimental results shows that the failure mode of the specific polymer foam cored sandwich beam specimens shifts from face-sheet yielding to face-sheet wrinkling as the temperature increases, and this is shown to agree well with analytical and numerical predictions.

13.1 Introduction

Polymer foam cored sandwich structures are used increasingly in for multiple industrial applications including e.g. marine structures and wind turbine blades. In service, such sandwich structure components are frequently exposed to solar radiation which results in elevated surface temperature in the range of 50–90 °C [1]. At such temperatures, the polymer foam core materials exhibit significant reduction of stiffness and strength [2, 3]. A common elevated temperature condition of sandwich structures is that only one face sheet is heated such that a temperature gradient exists through the thickness, e.g. solar radiation on the outer surface. Consequently, since the polymer foam generally conducts heat very poorly, a significant through thickness thermal gradient is generated. In this case, the polymer foam core becomes not only softer and weaker but will also display inhomogeneous mechanical properties in the through thickness direction. Hence, the commonly used classical sandwich panel theory (as described in [4]) that assumes homogeneous material properties in the through thickness direction becomes inadequate to model the mechanical behaviour. Recently, Frostig and Thomsen [5–7], using high order sandwich panel theory (HSAPT), demonstrated that bending, buckling and free vibration of sandwich structures can all be affected significantly when a foam cored sandwich structure is exposed to a through thickness temperature gradient. Particularly, Frostig and Thomsen predicted that at certain elevated temperatures the load-response of sandwich structures may shift from being linear and stable to nonlinear and unstable due to the core material degradation. The instability due to elevated temperatures was also predicted by Birman [8] using a modification of Hoff and Manter's wrinkling analysis. Although these predictions hitherto have not been experimentally validated, it has aroused concerns about the performance of foam cored sandwich structures at elevated temperatures. Thereby, a focused experimental study is required to confirm the thermomechanical interaction effects analysed in [5–8].

S. Zhang (✉)
Faculty of Engineering and Science, University of Southampton, Highfield, Southampton SO17 1BJ, UK

J.M. Dulieu-Barton • O.T. Thomsen (✉)
Faculty of Engineering and Science, University of Southampton, Highfield, Southampton SO17 1BJ, UK

Department of Mechanical and Manufacturing Engineering, Aalborg University, Aalborg East DK-9220, Denmark
e-mail: o.thomsen@soton.ac.uk

G.P. Tandon et al. (eds.), *Experimental Mechanics of Composite, Hybrid, and Multifunctional Materials, Volume 6*, Conference Proceedings of the Society for Experimental Mechanics Series, DOI 10.1007/978-3-319-00873-8_13,

The objective of the present research is to conduct an experimentally based investigation of the influence of elevated temperature on the stability of sandwich structures, aiming to assess if face sheet wrinkling or localised buckling may occur at lower mechanical load levels due to elevated temperatures such as 50–90 °C. The sandwich beam specimens are loaded in simply supported four-point bending, and a through thickness temperature gradient is introduced by heating the top face sheet using an infrared lamp while the bottom face sheet is exposed to ambient temperature. A novel technique is developed to identify the face sheet wrinkling by using high-speed imaging and DIC (digital image correlation [9]). The high-speed imaging provides an insight into the rapid evolution of the wrinkles and the DIC quantifies the shape of the wrinkles.

13.2 Experimental Arrangement

13.2.1 Loading Configuration

The four-point bending configuration used in this work is shown in Fig. 13.1. The top face sheet is heated to an elevated temperature and the bottom face sheet is exposed to ambient temperature to generate a temperature gradient through the specimen thickness. The sandwich beam specimen is simply supported which enables free thermal expansion of the sandwich beam specimen before loading, thus the thermally induced stress only results from a mismatch of the coefficients of thermal expansion of the face sheet and the core and can be considered as insignificant in the context of the present work. With a transverse load, P, the top face sheet carries a compressive stress and the bottom face sheet carries a tensile stress in the x direction, thus face sheet wrinkling can only occur at the top face sheet. To avoid local indentation at the loading points, stiff rubber loading pads with an aluminium alloy facing is used to distribute the concentrated transverse load.

13.2.2 Specimen Material and Geometry

Aluminium alloy (AA7075-T6) was selected as the face sheet material due to its good heat conduction making it easier to achieve a uniform temperature through the face sheet. Furthermore, the stiffness and strength of aluminium alloy is virtually independent of temperature over the range 25–90 °C, so that the influence of core stiffness reduction (softening) due to elevated temperature on the overall sandwich structure behaviour can be separately investigated. The mechanical properties of the aluminium alloy AA7075-T6 was tested at different temperatures in accordance with ASTM standard E8 [10]. The obtained Young's modulus, Poisson's ratio and yield strength are shown in Table 13.1. It was observed that both the Young's modulus and yield strength decreases slightly with increasing of temperature. At 90 °C, about 5 % of the Young's modulus and 8 % of the yield strength are lost in comparison to the corresponding values at 25 °C.

Divinycell H100 PVC foam with a nominal density of 100 kg/m^3 was chosen as the core material. Divinycell H100 foam core is representative of a very large range of cross-linked rigid PVC foam cores used in a wide range of structural applications. The temperature dependence of the elastic properties of Divinycell H100 foam has been characterised in [2, 3], and the test results shows that the Young's modulus and shear modulus depend on temperature according to:

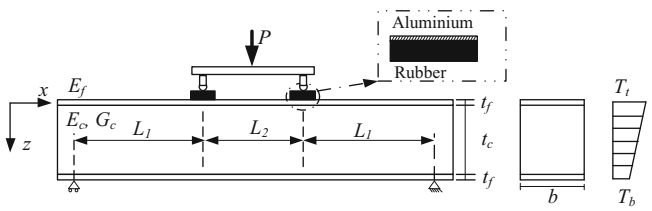

Fig. 13.1 Schematic of four-point bending test of sandwich beam with a through thickness temperature gradient

Table 13.1 Material properties at room temperature (25 °C)

Material	E_z (MPa)	E_x (MPa)	G_{zx} (MPa)	ν_{zx}	σ_y (MPa)
AA7075-T6	69,100	69,100	26,576	0.3	512
Divinycell H100	132 [2]	58 [2]	32 [3]	0.4 [2]	

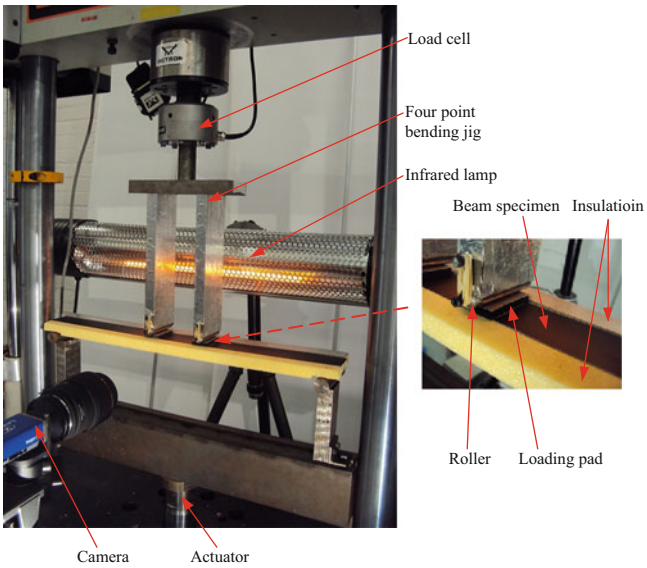

Fig. 13.2 Experimental set-up

$$\frac{E(T)}{E(T_0)} = \frac{G(T)}{G(T_0)} = -3.1943 * 10^{-6}T^3 + 4.2436 * 10^{-4}T^2 - 2.2653^{*}10^{-2}T + 1.3626 \tag{13.1}$$

where *E(T)* and *G(T)* represent the Young's and shear moduli of Divinycell H100 at temperature *T*, respectively. T_0 represents the room temperature (25 °C). Equation 13.1 shows that over half of the foam material stiffness has been lost at 90 °C in comparison with that at 25 °C. The Young's modulus and shear modulus at room temperature are listed in Table 13.1.

To eliminate core shear failure, specimens with a large aspect ratio (length to thickness) were used. Because of the restriction of the test machine used in the experimental work the length of the specimen was selected to be 600 mm. The thickness of the face sheet and core were chosen to be 0.3 and 15 mm, respectively. The loading span L_1 and L_2 (see Fig. 13.2) were chosen to be 275 and 100 mm, respectively. For this specific specimen geometry, at room temperature the critical wrinkling stress obtained using the Plantema's wrinkling analysis [11] is −547 MPa, which is larger than the yield strength of the face sheet, 512 MPa. This indicates that at room temperature the failure should be initiated by face sheet yielding. However, if the top face sheet is heated to elevated temperatures, the foam core becomes softer and consequently results in a smaller critical wrinkling stress thereby the specimen failure may be initiated by wrinkling.

13.2.3 Experimental Procedure and Deformation Measurement

The photograph of the experimental apparatus is shown in Fig. 13.2. The sandwich beam specimen was loaded by a four-point bending jig mounted on an Instron 8502 servo-hydraulic test machine. The top part of the bending jig was connected to the load cell, and the bottom part of the bending jig was connected to the actuator. The top face sheet was heated by an infrared lamp, while the bottom face sheet was exposed to the ambient temperature. During the heating process, two PVC foam blocks were positioned adjacent to the specimen side to reduce the heat convection from the specimen side surface to the ambient air. A linear temperature profile through the core thickness was observed after the specimen had reached the state of heat equilibrium (detailed data in [12]). DIC was used to characterise the overall deflection of the sandwich beam specimen as well as to quantify the wavy deformation of the wrinkles in face sheet. During the loading process, a 16 M pixel resolution camera was used to record the images of the side surface of the specimen, and the corresponding load (*P*) was recorded synchronously. The deformation of the specimen was calculated using the commercially available software Davis 8.0 by conduction image correlation between the recorded specimen images. To capture the occurrence of the predicted face sheet wrinkling, images were also recorded at a frequency of 60 kHz using a PHOTRON FASTCAM SA5 high-speed camera.

13.3 Results

Tests were conducted for top face sheet temperatures of 25 °C, 50 °C, 70 °C, 80 °C and 90 °C. All the specimens failed by a collapse near the mid-span (Fig. 13.3). The top face sheet folded into the core causing local core crushing, which again led to complete loss of overall sandwich specimen stiffness and collapse. A comparison between the experimental and expected failure stress is shown in Fig. 13.4. Here, the blue line represents the yield strength of the face sheet at different temperatures; the red line represents the critical wrinkling stress of the specimen obtained by a modified Plantema wrinkling theory [13]. It is clearly seen that, for the specimens tested at 25 °C and 50 °C the specimen failure was initiated by face sheet yielding, and that the failure stress reduces very slightly with increasing temperature of the top face sheet. For the specimens tested at 70 °C, 80 °C and 90 °C, respectively, the failure was initiated by face sheet wrinkling (local instability), and the failure stress dropped significantly with increasing top face sheet temperature.

To further examine the occurrence of top face sheet wrinkling for the specimen tested at 90 °C specimen images were recorded using the PHOTRON FASTCAM SA5 camera at a high frequency of 60 kHz. Image correlation was conducted on the images to view the specimen deformation during the specimen failure process. Figure 13.5 shows the specimen displacement in the through thickness direction at the initiation of specimen failure. At the starting point of the specimen failure, a full wave length wrinkle was clearly seen as shown in Fig. 13.5a. Only 17 μs later, the shape of the wavy deformation of the face sheet became irregular, where the magnitude of the wave crest is much larger than the wave trough, as can be seen from Fig. 13.5b. This must be caused by the core crushing at the wave crest due to development of large compressive stresses, which suggests that the wavy deformation triggered a very quick core crushing (within tens of μs) and this makes high-speed imaging essential and indeed necessary to capture the wrinkling behaviour.

The face sheet wavy deformation was observed not only for the specimens tested at 90 °C, but also for the specimens tested at 25 °C and 50 °C. This does not contradict the results shown in Fig. 13.4 which say that the specimen fails by face sheet yielding at 25 °C and 50 °C. The reason is that for the ductile face sheet material (AA7075-T6) significant stiffness reduction is encountered when yielding is initiated, and this together with the reduced core stiffness provoked wrinkling instability to occur post the yield initiation of the top face. To distinguish between the face sheet yielding and wrinkling, the compressive strain of the top face sheet was obtained using DIC. For a better measurement precision, the compressive strain was obtained as the average measured strain over a length of 50 mm of the top face sheet near the mid-span. The strain state of the top face sheet of sandwich beam specimens just before collapse is shown in Fig. 13.6, where the measured tensile stress–strain curves of AA7075-T6 at different temperatures are also plotted. It is seen that for the specimen tested at room temperature, the top face sheet was beyond the elastic limit before the specimen failed. This indicates that the specimen

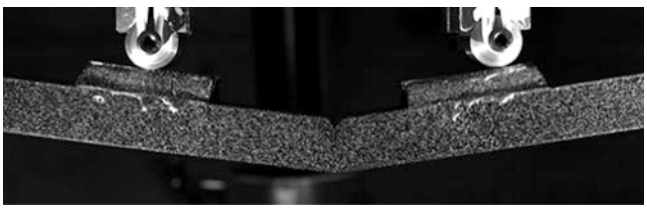

Fig. 13.3 Failure shape of the specimen

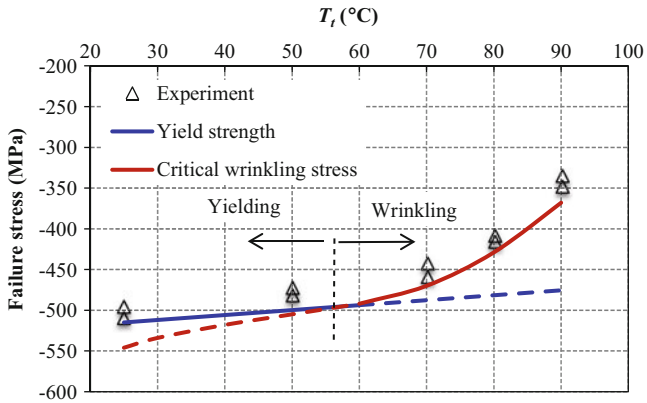

Fig. 13.4 Comparison between the predicted failure stresses and the experimental results

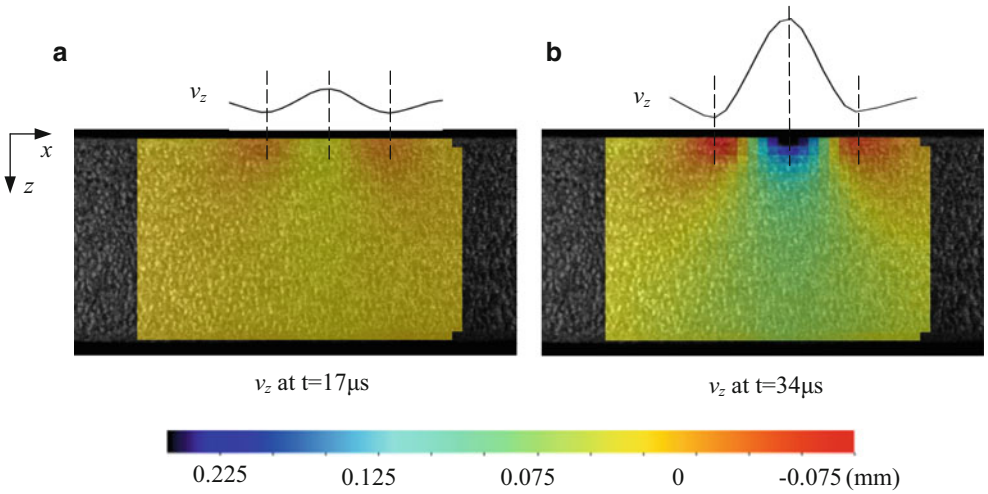

Fig. 13.5 z direction displacement contour of the specimen at times 17 and 34 μs

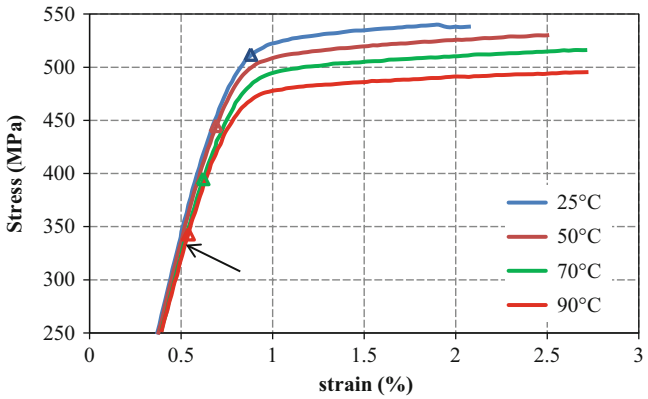

Fig. 13.6 Stress–strain state of the face sheets (aluminium alloy, AA7075-T6) of sandwich beam specimens before core collapse

failure was initiated by face sheet yielding followed by plastic instability. For the specimens tested at 70 °C and 90 °C, the top face sheet is still in the linear-elastic deformation region before the specimen collapse. This shows that the specimen failure was initiated by face sheet wrinkling (instability). Figure 13.6 re-confirms that the specimen failure shifts from face sheet yielding at low temperatures to face sheet wrinkling at elevated temperatures due to the thermal degradation of the polymer foam core.

13.4 Conclusion

An experimental apparatus was established to investigate the behaviour of polymer foam cored sandwich beam specimens subjected to a simultaneous simply supported four-point bending load and a linear temperature gradient through the thickness. High-speed imaging combined with DIC was adopted to assess the occurrence and rapid evolution of face sheet wrinkling. For the particular sandwich beam specimen considered, it was experimentally observed that the specimens failed by face sheet yielding at room temperature and by wrinkling (instability) when the top face sheet is heated to 70 °C or higher. This failure mode shift corresponds well with the predictions by Frostig and Thomsen [5], Birman [8], and Zhang et al. [13].

Acknowledgments The work presented was co-sponsored by the Chinese Scholarship Council, the Danish Council for Independent Research | Technology and Production Sciences (FTP), Grant Agreement 274-08-0488, "Thermal Degradation of Polymer Foam Cored Sandwich Structures", and the US Navy, Office of Naval Research (ONR), Grant Award N000140710227. The ONR programme manager was Dr. Yapa D. S. Rajapakse. The financial support received is gratefully acknowledged.

References

1. DATAFORTH (2012) Wind turbines today enhanced reliability with dataforth signal conditioners. http://www.dataforth.com/catalog/pdf/Wind_Turbines_Today.pdf. Accessed 3 Nov 2012
2. Zhang S, Dulieu-Barton JM, Fruehmann RK, Thomsen OT (2012) A methodology for obtaining material properties of polymeric foam at elevated temperatures. Exp Mech 52(1):3–15
3. Zhang S, Dulieu-Barton JM, Fruehmann RK, Thomsen OT (2011) Thermal degradation of polymeric foam core materials for sandwich structures. In: Proceedings of the 18th international conference on composite materials, Jeju
4. Zenkert D (1995) An introduction to sandwich construction. Chameleon Press, London
5. Frostig Y, Thomsen OT (2008) Non-linear thermal response of sandwich panels with a flexible core and temperature dependent mechanical properties. Compos B Eng 39(1):165–184
6. Frostig Y, Thomsen OT (2008) Thermal buckling and postbuckling of sandwich panels with a transversely flexible core. AIAA J 46(8):1976–1989
7. Frostig Y, Thomsen OT (2009) On the free vibration of sandwich panels with a transversely flexible and temperature dependent core material – Part II: numerical study. Compos Sci Technol 69(6):863–869
8. Birman V (2005) Thermally induced bending and wrinkling in large aspect ratio sandwich panels. Compos A Appl Sci Manufact 36(10):1412–1420
9. Sutton MA, Orteu J-J, Schreier HW (2009) Image correlation for shape, motion and deformation measurements. Springer Science + Business Media, New York
10. ASTM-E8 (2007) Standard test methods for tension testing of metallic materials, ASTM International. http://www.astm.org/Standards/E8.htm
11. Plantema FJ (1966) Sandwich construction. Wiley, New York
12. Fruehmann RK, Dulieu-Barton JM, Thomsen OT, Zhang S (2011) Experimental investigation of thermal effects in foam cored sandwich beams. In: Thermomechanics and infra-red imaging, vol 7. Springer, New York, pp 83–90
13. Zhang S, Dulieu-Barton JM, Thomsen OT (2012) The effect of temperature on the failure modes of polymer foam cored sandwich structures. Composite structures, Accepted for publication

Chapter 14
Characterization of Mixed-Mode Energy Release Rates for Carbon Fiber/Epoxy Composites Using Digital Image Correlation

Joseph Puishys III, Sandip Haldar, and Hugh A. Bruck

Abstract There is great interest in using advanced mechanical characterization techniques, such as Digital Image Correlation (DIC), to investigate complex fracture behavior of fiber-reinforced composites. In this study, unidirectional carbon fiber/epoxy composites were fabricated from the pre-preg carbon fiber epoxy tapes for the characterization of their energy release rates. Quasi-static mixed-mode fracture experiments were performed using a Wyoming Test Fixture. The crack tip response of the composite was determined by using the displacement fields obtained from DIC based on LEFM. The fracture parameters obtained from the DIC analysis have been compared to those determined from the global load displacement response using ASTM standard. The results show that the experimental investigation of the energy release rates using more local, near field displacements around the crack tip obtained by DIC provide accurate quantification of the crack tip response relative to the global loading conditions. Effects of global bending and fixture compliance on the global load–displacement response can also be eliminated by using full-field DIC measurements.

14.1 Introduction

The past four decades have seen remarkable changes in the manner in which industry utilizes materials. Particularly prevalent in the military industry, is a marked shift away from heavy, homogenous, and well understood metallic materials, to more versatile, and lightweight polymer matrix composites. Structures that were traditionally metal I beams are often replaced with composite sandwich structures. Structures which were sheet metal are now often replaced with laminates. The need for low cost and lightweight materials for use in aviation platforms, automotive industry, and marine vehicles has spurred tremendous advances in composite technology. Today, composites are a state of the art material; extremely versatile and offering limitless potential. In particular, carbon fiber has become an industry and high design favorite, often applied in weaves with high performance resins such as PEEK; carbon fiber has found itself in almost every imaginable application. Such tremendous advances in technology however, are not without disadvantage. Carbon fiber composites, by nature, are a highly directional material, and one which exhibits favorable characteristics in only discrete directions. Though good strength to weight ratios may be fundamentally positive characteristics of composite laminates, they are not without significant drawbacks. The directional nature of fiber reinforcement puts special emphasis on the engineers to properly design composite components for its expected load, and application. Unidirectional laminates are particularly weak when loaded transverse to the fiber direction, and take on the strength characteristics of the matrix only. This is predominantly troubling when a laminate is loaded in bending. Thus accurate characterization of fracture parameters is of utmost importance to fully utilize the potential of these materials [1]. The present study intends to use Digital Image Correlation (DIC) to determine the deformation fields around the crack tip and then quantify the fracture parameters of unidirectional carbon fiber/epoxy composites. Using DIC enables accurate detection and quantification of strain fields present in mixed mode fracture and correlate them to the microstructure associated with lower length scales. This work represents an attempt to utilize DIC to extract fracture parameters of composite laminate structures under mixed mode I and mode II loading conditions with the Wyoming test fixture. The analysis presented within this research affirms the successful use of DIC for applications with fracture mechanics, as well as the limitations of such techniques.

J. Puishys III • S. Haldar • H.A. Bruck (✉)
Department of Mechanical Engineering, University of Maryland, College Park, MD 20742, USA
e-mail: bruck@umd.edu

G.P. Tandon et al. (eds.), *Experimental Mechanics of Composite, Hybrid, and Multifunctional Materials, Volume 6*, Conference Proceedings of the Society for Experimental Mechanics Series, DOI 10.1007/978-3-319-00873-8_14,

14.2 Experimental Method and Materials

14.2.1 Experiment

The experimental characterization of fracture parameters of carbon fiber laminates has been performed under quasi-static load in Imada MX-500 load frame equipped with a Z2H-440 load cell to measure the load and a caliper to measure the displacement. Fracture experiments of carbon fiber laminate composite specimens at different mode I/II-mixity have been performed using the Wyoming Test Fixture (Fig. 14.1), especially designed to perform mixed mode bending. The required mode mixity can be obtained by changing the lever arm lengths. However, the mixed mode bending (MMB) using the present fixture is limited to maximum of around 20 % mode-I by the required arm length in the configuration. Thereby, in the present study the experiments have been performed for the mode-mixities of 22–100 % (pure mode-II) by the above mentioned test fixture. For the pure mode-I cases, double cantilever specimen has been used. The experiments have been performed using the ASTM Standard D6671 designed for unidirectional carbon fiber tape laminates. The correction parameters associated with the experiments using Wyoming Test Fixture are (i) Transverse modulus correction parameter $\Gamma = 1.18\dfrac{\sqrt{E_{11}E_{22}}}{G_{13}}$ and (ii) crack length correction parameter $x = \sqrt{\frac{E_{11}}{11\,G_{13}}\left[3 - 2\left(\frac{\Gamma}{1+\Gamma}\right)^2\right]}$.

The deformation fields in the specimen under mixed-mode loading have been determined by Digital Image Correlation (DIC). To this goal, imaging was conducted with digital cameras from Point Grey Optics with the aid of optical lenses for suitable magnifications. The specimens placed in the fixture were illuminated by fiber optic high intensity illuminator. The specimen surface was speckle patterned at different densities for DIC. Images were captured during the deformation of the specimen at several magnifications to quantify the deformation fields by using commercial DIC software Vic 2D from Correlated Solutions Inc, SC.

14.2.2 Material Fabrication

The unidirectional carbon fiber/epoxy composite laminates have been prepared from pre-impregnated carbon fiber tape from Composites Store Inc. Square tapes of the size of 6″ × 6″ were cut from the roll of the carbon fiber tape and 24 of these tapes were laid up (all of them in 0° orientation) to prepare around 3.11 mm thick unidirectional laminates. A 13 μm Teflon film was inserted in between 12th and 13th layer of the pre-preg tape to create a pre-crack. The pre-crack was of around 2″ in length. The layers 13th to 24th were inverted compared to the other layers to eliminate the micro residual stresses that may otherwise lead to wrapping of the laminate leading to curvature in the specimen after cure. The laid up plies were then covered between two thick Nylon plates from wither side to be placed in between fine polished aluminum plates for curing under 2,000 lbs load. The temperature cycle for curing was 200 °C for 1 h and then 2,300 °C for 2 h.

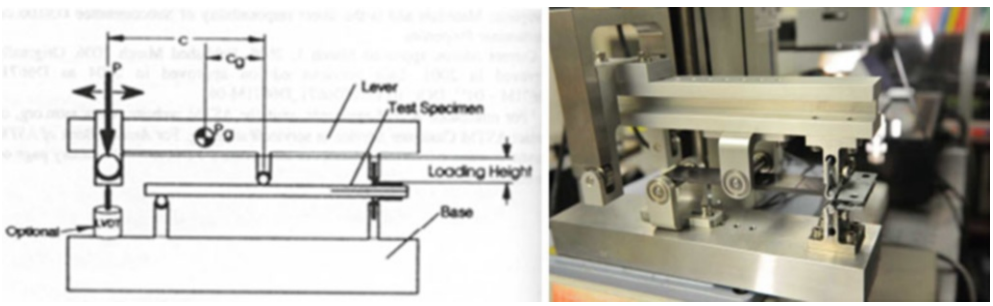

Fig. 14.1 Schematic of Wyoming test fixture developed for mixed mode loading and (*right*) a carbon fiber laminate composite placed in the fixture

14.3 Theoretical Background and Experimental Analysis

Linear elastic Fracture Mechanics (LEFM) theory has been employed as the baseline for the characterization of the unidirectional composite laminated fabricated from the pre-preg laminates. However, the Wyoming Test Fixture is designed to allow for direct determination of the modulus of a unidirectional composite in the fiber direction, E_{1f}, as follows:

$$E_{1f} = \frac{8(a_o + xh)^3 (3c - L)^2 + \left[6(a_o + 0.42xh)^3 + 4L^3\right] (c + L)^2}{16L^2bh^3\left(\frac{1}{m} - C_{sys}\right)} \tag{14.1}$$

correcting for the system compliance, C_{sys}, and using the geometric parameters of the test fixture and specimen (some of which can be seen in Fig. 14.1) as well as the slope of the specimen's load–displacement curve, m. This is then used to determine the mode-I and mode-II energy release rates, G_I and G_{II} respectively, as follows:

$$\begin{aligned} G_I &= \frac{12P^3(3c - L)^2}{16b^2h^3E_{1f}}(a + xh)^2 \\ G_{II} &= \frac{9P^3(c + L)^2}{16b^2h^3L^2E_{1f}}(a + 0.42\,xh)^2 \end{aligned} \tag{14.2}$$

The mode mixture is defined as $G_{II}/(G_I + G_{II})$, where 100 % mode-mixture implies pure mode-II loading condition.

Images captured during deformation were also used to determine the deformation fields around the crack tip in the unidirectional carbon fiber composite laminates using Digital Image Correlation (DIC). The displacement fields obtained from DIC were then compared to the displacement fields that are expected from the LEFM for transversely isotropic materials, for which the crack opening displacements (COD) and crack shearing displacement (CSD) are as follows:

$$\begin{aligned} COD &= \left[4(2)^{\frac{1}{4}} \frac{(a_{11}a_{22})^{\frac{1}{4}}}{\sqrt{\pi}}\left(\frac{2a_{12} + a_{66}}{2a_{11}} + \sqrt{\frac{a_{22}}{a_{11}}}\right)^{\frac{1}{4}}\right]\sqrt{G_I}\ \sqrt{r} \\ CSD &= \left[4(2)^{\frac{1}{4}}\sqrt{\frac{a_{11}}{\pi}}\left(\frac{2a_{12} + a_{66}}{2a_{11}} + \sqrt{\frac{a_{22}}{a_{11}}}\right)^{\frac{1}{4}}\right]\sqrt{G_{II}}\ \sqrt{r} \end{aligned} \tag{14.3}$$

Note that a_{11}, a_{22}, a_{12}, and a_{66} are all elastic constants for the unidirectional composite related to E_{11}, E_{22}, G_{12}, and v_{12}. To determine the energy release rate, the error minimization scheme was used with these expressions and the displacement data obtained with DIC.

14.4 Material Properties

The material constants required for the analysis using the LEFM had been experimentally verify to determine their consistency with values available in literature for similar material. The composite laminates being transversely isotropic, the moduli in two directions have been obtained from three point bend test of the specimens prepared in two directions. The moduli had been determined from the load–displacement response of the specimen using the relation $E = \frac{L^3}{4wh^3}\frac{\Delta p}{\Delta \delta}$ as listed below in Table 14.1.

Table 14.1 The measured material properties of the unidirectional carbon fiber/epoxy composites used for this study

E_{11}	Axial stiffness	138 GPa
E_{22}	Transverse stiffness	10.3 GPa
G_{12}	In plane shear stiffness	5.9 GPa
v_{12}	Major Poisson's ratio	0.3
v_{21}	Minor Poisson's ratio	0.0224

14.5 Experimental Results

14.5.1 Energy Release Rate from Load–Displacement Calculations and ASTM Relations

The load displacement response of the carbon fiber laminate composites under mixed-mode loading is depicted in Fig. 14.2. Compliance correction was applied to the experimentally obtained data to account for the load frame deformations. It is also important to note from Fig. 14.2 that for displacement values above 8 mm we begin to see a flattening of the load–displacement curve. This is due to the crack tip approaching the central loading point of the test fixture. This serves to arrest the crack growth and induce an artificially low value for G_{IC}, as a result, only the data between 6 and 8 mm of displacement should be considered for calculation of Mode I critical energy release rates. Using the load displacement data as depicted earlier from the fracture experiments of the carbon fiber laminates under the mode mixture cases of 22 %, 50 % and 100 %, the ASTM standards were utilized to determine the energy release rates under Mode-I (G_I) and Mode-II (G_{II}) at various loads for a standard sized test specimen. The resulting variations in energy release rates with load for specimens under mode mixities of 22 %, 50 % and 100 % determined using the ASTM standard can be seen in Fig. 14.3. The corresponding critical energy release rates are marked on the plots where the load for initial crack propagation occurred, which were determined from Fig. 14.2.

It is noted that when fracture is dominant in a mixed mode bending test, the highest critical fracture load may be expected and potentially the most unstable crack growth. For the 22 % mode mixture case, crack propagation occurred at 90 N, resulting in a critical energy release rate of only 271 J/m^2. The 50 % mode mixture case fractured at 301 N and had a critical energy release rate of 630 J/m^2. In the 100 % mode mixture case, the crack propagation occurred at 590 N, resulting in a critical energy release rate of 672 J/m^2. As the load lever arm length "c" is increased and the mode mixity decreases, the crack is grown at much lower load levels. Therefore, there is potentially a more controlled crack growth condition due to a substantially lower dG/da according to Eq. 14.2 and as evidenced in Fig. 14.2. So, for the purposes of future crack growth analysis using DIC, it was decided to focus attention on the more controlled crack growth observed in the 22 % mode mixity condition.

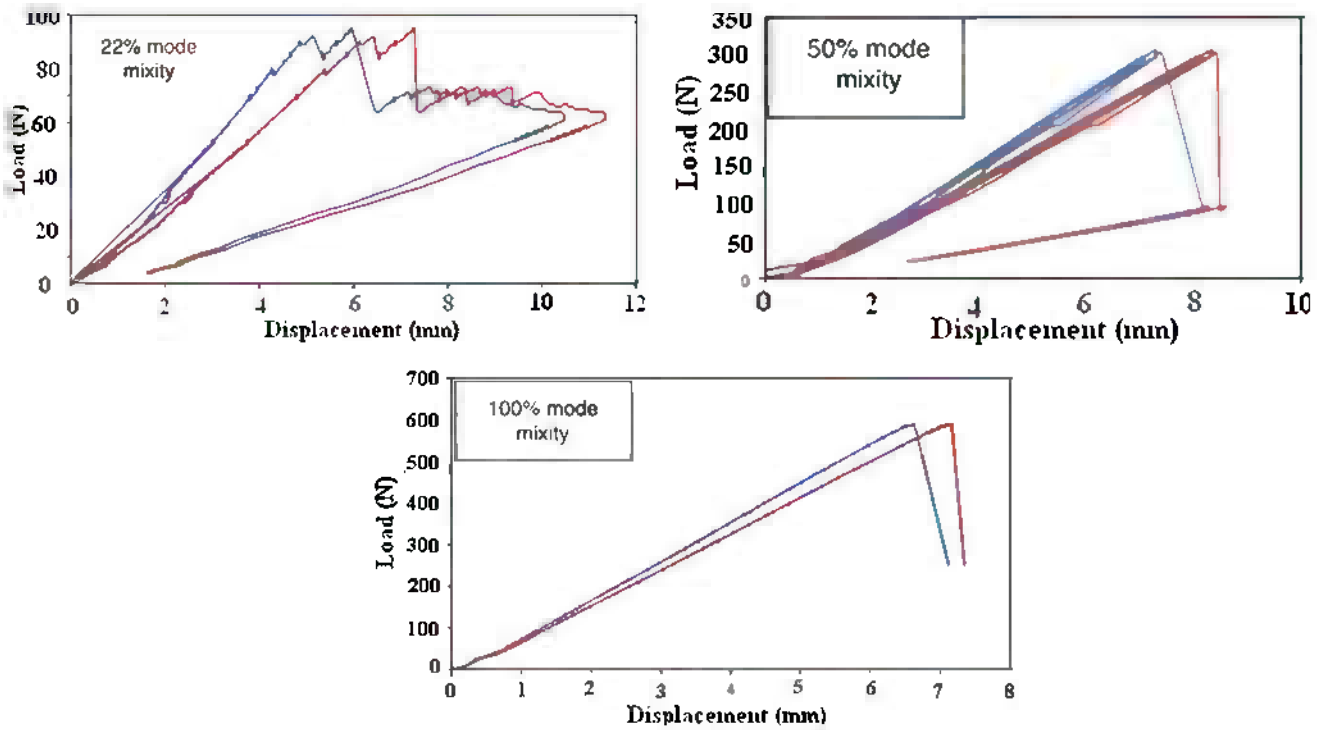

Fig. 14.2 Global load displacement response of the carbon fiber laminates under mixed-mode loading with (*red*) being measured and (*blue*) being compliance corrected

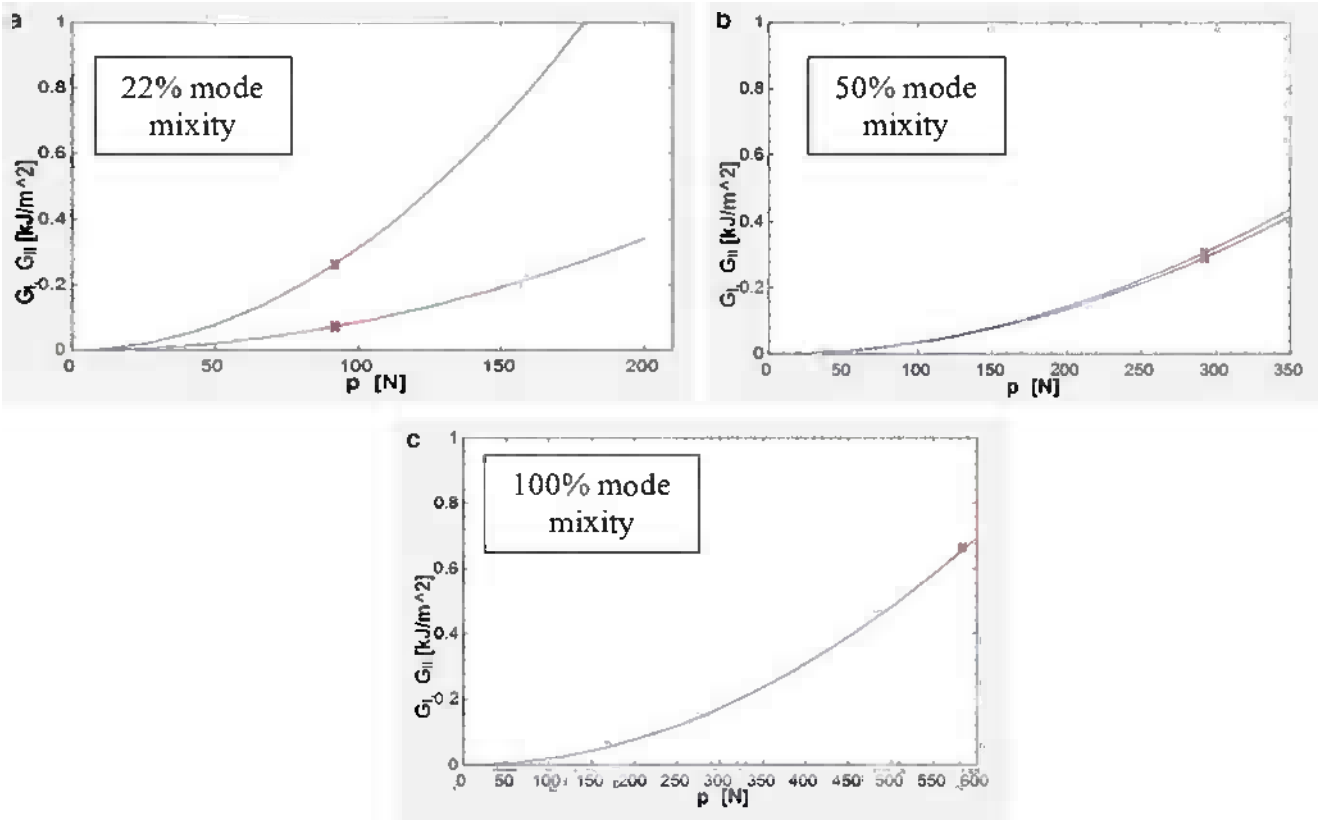

Fig. 14.3 Critical energy release rates for (**a**) 22 % mode mixture, (**b**) 50 % mode mixture and (**c**) 100 % mode mixture

14.5.2 Crack Tip Displacement Measurements Obtained from DIC

The load displacement obtained from experiment can be used to analytically determine the mixed-mode fracture parameters globally using the LEFM relations from ASTM standard. However, DIC can be better utilized to determine the displacement fields locally near the crack tip, thereby, facilitating the determination of a local measure of mode mixture and other fracture parameters. This technique believed to be of superior reliability due to its ability to quantify the displacement directly from the specimen image and its high accuracy up to sub-pixel resolution in measurement. Thus the direct measurement of deformation by DIC eliminates the compliance correction of fixture and load frame, effect of global bending of the specimen. The near-field crack tip displacements transverse to the crack can be seen in Fig. 14.4 for a 22 % mode mixture (pure mode-II) test. An example of the far-field shear strain is also depicted in Fig. 14.5. The CSD and COD were extracted from the displacement fields obtained by DIC. The fit of the analytical expressions from Eq. 14.3 to the DIC displacement fields can be seen in Fig. 14.5. Results matched the orthotropic equations rather well, in particular for CSD. Fitting COD required the use of higher order terms, without which a high quality fit was not attainable. This is indicative of the dominance of rotation due to cantilever bending.

14.5.3 Fit of Analytical Crack Tip Field Solutions to DIC Crack Tip Displacement Fields to Determine Mixed-Mode Energy Release Rates

In this approach, full field crack tip displacement has been used to determine the mixed-mode energy release rates. The complete expansion of the crack tip displacement field for full field analysis of an orthotropic material is developed by Liu et al. [2], Shukla et al. [3]. The detailed derivation of the full field equations may be found in reference [3].

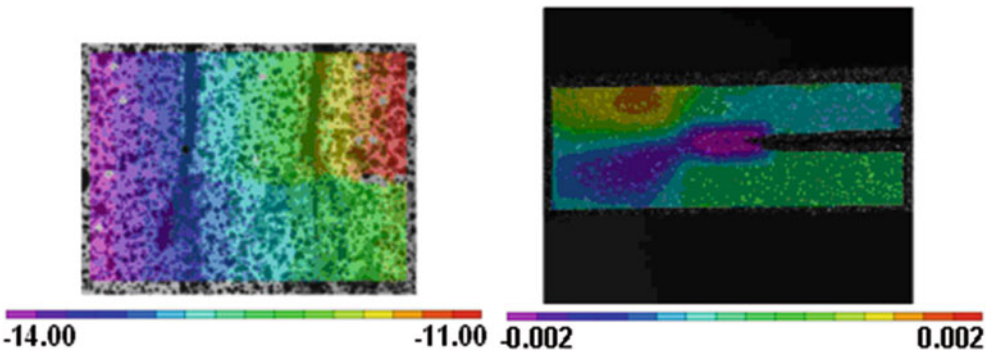

Fig. 14.4 DIC results showing (*left*) near-field displacements transverse to the crack, and (*right*) far-field shear strain at the crack tip with various length scales for 22 % mode mixity

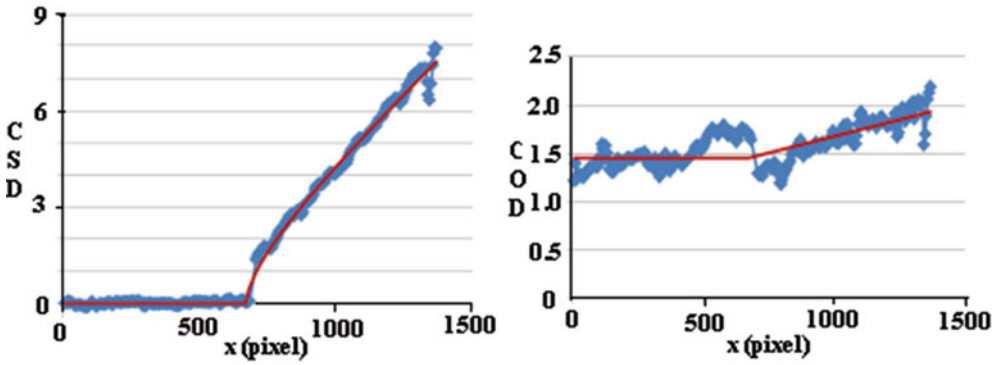

Fig. 14.5 COD (*top*) and CSD (*bottom*) extracted from 22 % mode mixity test using DIC and subsequent fits using Eq. 14.3

In this approach, the analytical LEFM crack tip field solutions for an orthotropic material (from which Eq. 14.3 is derived) are fit to the DIC displacement data in a least squares analysis so that the effect of any local noise in the DIC measurement can be minimized and the subsequent error in the determination of the energy release rates. The full field displacement fields have been corrected for global rotation that might occur due to global bending of the specimen. Using a numerical algorithm, the fracture parameters have been optimized to result the displacement fields similar to those determined by DIC. The displacement fields obtained from LEFM analytical fits and DIC measurements for a specimen under 22 % mode-mixture at various loading condition are depicted in Fig. 14.6 below. The resulting fracture parameters obtained from the optimization is list in Table 14.2. The results indicate good correlation between the values calculated using the ASTM relations from the global loading conditions and those obtained from the LEFM analytical fits to the DIC displacement fields, as well as the fits to the CSD and COD determined using DIC.

14.6 Conclusions

Experiments have been performed with unidirectional carbon fiber/epoxy composites prepared from the pre-preg tapes of carbon fiber under mixed-mode loading condition using a Wyoming test fixture. The global load displacement has been used to determine the energy release rates using the standard relations from the ASTM standard. The local near-field crack tip displacements have been determined by using DIC to the images captured during the test. The energy release rates have been determined by fitting the LEFM theory to the displacement fields determined by using DIC. The experimental results for a

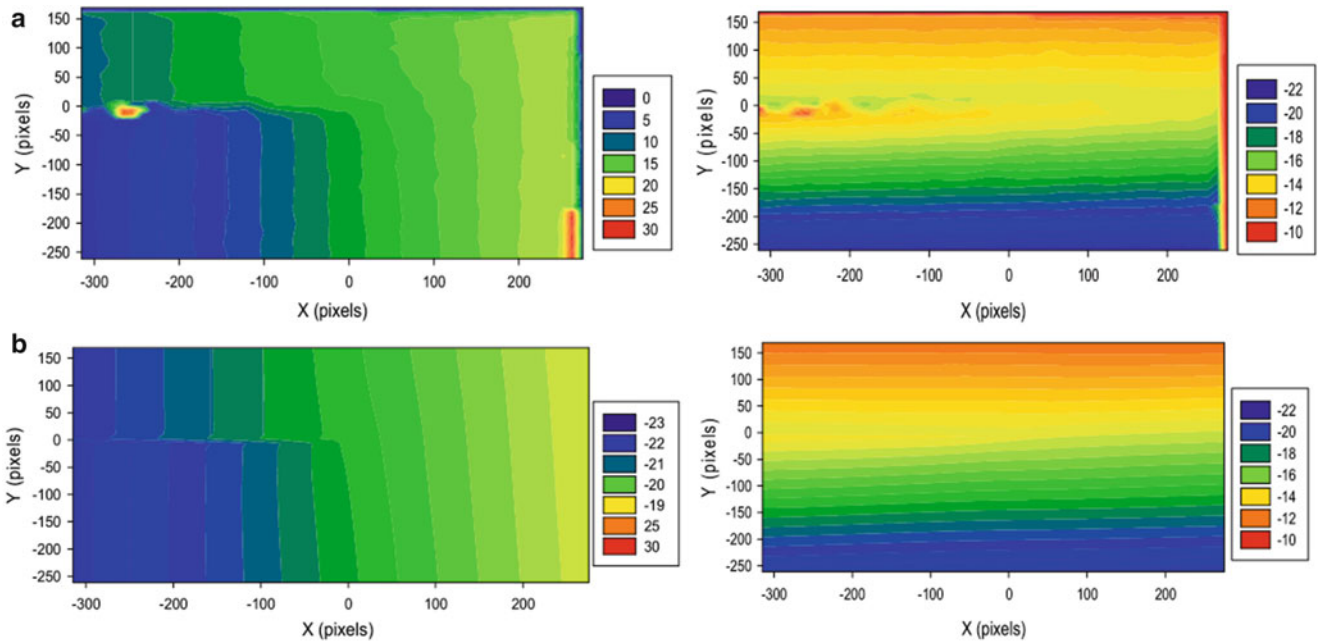

Fig. 14.6 (*Right*) U and (*left*) V displacement fields obtained from (**a**) DIC measurement and (**b**) LEFM analytical fits to the DIC displacements at a load level of 60 N and 22 % mode mixity

Table 14.2 Energy release rates obtained from full field DIC measurement compared to those determined from global response using the ASTM relations and from the CTD fields for a 22 % mode mixity

Method	G_I [J/m^2]	G_{II} [J/m^2]	G_c [J/m^2]	Mode mixture (%)
ASTM standard	212.1	58.56	270.66	21.6
CSD and COD [DIC]	254.55	72.41	326.97	22.1
Full field [DIC]	285.41	77.83	363.24	21.4

22 % mode mixity have indicated that both the full-field and CSD & COD displacements obtained by fitting analytical solutions to DIC displacement fields through a can be used to determine the fracture parameters of the laminate composite with reasonable accuracy. Effects of global bending and fixture compliance on the global load–displacement response can also be eliminated by using full-field DIC measurements.

Acknowledgements This work was supported by NAWCAD in Pax River, MD through cooperative agreement N00421-98-H-1116 with the University of Maryland.

References

1. Sih GC, Paris PC, Irwin GR (1965) On cracks in rectilinearly anisotropic bodies. Int J Fract Mech 1(3):189–203
2. Liu C, Rosakis AJ, Ellis RW, Stout A (1998) Study of the fracture behavior of unidirectional fiber reinforced composites using coherent gradient sensing. Int J Fract 90:335–382
3. Shukla A, Agarwal BD, Bhushan B (1989) Determination of stress intensity factor in orthotropic composite materials using strain gages. Eng Fract Mech 332:467–477

Chapter 15
Strain Rate Effects on Failure of a Toughened Matrix Composite

J.D. Schaefer, B.T. Werner, and I.M. Daniel

Abstract The objective of this study was to characterize the quasi-static and dynamic behavior of a toughened matrix composite (IM7/8552) and apply the Northwestern (NU) failure theory to describe its strain-rate dependent failure under multi-axial states of stress. Unidirectional and off-axis experiments were conducted at two strain rates, quasi-static (10^{-4} s^{-1}) and intermediate (~1 s^{-1}) using a servo-hydraulic testing machine. Stress–strain curves were obtained and the nonlinear response and failure were measured and evaluated based on classical failure criteria and the NU theory. Predicted failure envelopes were compared with experimental results. The NU theory was shown to be in excellent agreement with experimental data.

15.1 Introduction

As the use of composite materials expands into increasingly diverse applications, it is critical to characterize their behavior in order to efficiently employ them in design. This is especially true in cases where these materials are used as structural components with the potential to undergo dynamic and multi-axial states of stress. In such cases, composites undergoing shear and compression have been shown to exhibit non-linear behavior due to the plastic deformation of the polymer matrix. Additionally, such materials tend to exhibit altered mechanical properties according to strain rate [1–5].

Historically, thermosetting polymeric matrices have been primarily utilized in developing composite materials for structure applications; however, recently new thermoplastic reinforced thermosets have been developed. These modified matrix composites provide increased delamination resistance, fracture toughness, as well as increased matrix toughness [6–9].

Of further importance is the need to quickly ascertain new material constituent behavior so that it may readily be used in design. Many models have been proposed based on macroscopic material properties [5, 10–12]. However, models that require a fitting parameter to the data are inherently non-predictive and do not provide a simple model for material characterization.

In this paper, the steps to characterize a new thermoplastic-toughened epoxy matrix composite material are presented (IM7/8552). A discussion of the initial quasi-static experiments and specimens used to determine fundamental material properties is first presented, followed by the results for quasi-static and intermediate strain rate composite behavior. The results are compared to the classic failure envelopes as well as the NU theory [13].

J.D. Schaefer (✉) • B.T. Werner • I.M. Daniel
Northwestern University, Evanston, IL, USA
e-mail: Josephschaefer2011@u.northwestern.edu; imdaniel@northwestern.edu

G.P. Tandon et al. (eds.), *Experimental Mechanics of Composite, Hybrid, and Multifunctional Materials, Volume 6*, Conference Proceedings of the Society for Experimental Mechanics Series, DOI 10.1007/978-3-319-00873-8_15,

15.2 Experimental

15.2.1 Material Characterization

The investigated material is IM7/8552 from Hexcel, obtained in prepreg form. The plies were stacked in appropriate orientation and cured according to a standard autoclave process. The following procedures were used to determine the basic material properties (E_1, E_2, F_{1t}, F_{2t}, ν_{12}, F_6, G_{12}, V_f, F_{2c}).

The longitudinal Young's modulus (E_1), major Poisson's ratio (ν_{12}), and longitudinal tensile strength (F_{1t}) were determined using a tensile test of [0_6] coupons having 0.5″ wide × 9″ length. The coupons were tabbed to have a gage length of 6″, and strain gages were affixed to specimen surface in 0/90° rosette arrangement. Testing was performed according to ASTM specification D3039/D3039M-00, and the work of Daniel and Ishai [14].

The transverse Young's modulus (E_2) and transverse tensile strength (F_{2t}) were obtained from testing [90_{16}] coupons having dimensions 1″ × 10″ and a 7″ gage length. Strain gages were applied to the specimen surface along the loading axis, and the failure was brittle in nature. Testing was completed per [14].

An off-axis tension test was performed to determine the shear dependent material properties of the lamina. The shear modulus (G_{12}) and shear strength (F_6) were determined using a 10° off-axis specimen to minimize the effects of longitudinal and transverse stress components σ_1 and σ_2 on the shear response. The specimens were 0.5″ × 8″ with 1.25″ tabs and were cut from plates of 16 plies. The edges were carefully polished to reduce the effects of micro-cracks induced from cutting with the wet saw. Shear gages were applied along the fiber direction and the strain was recorded using the digital data acquisition setup. The material properties were determined according to the procedure listed in [14].

Transverse compression tests were performed to determine F_{2c}. 54 ply lamina plates (6″ × 4″) were prepared and cured according to the same cure cycle as for the thin plates, and samples were cut using an abrasive water lubricated grinder. The samples were then precision ground into prismatic specimens with geometry (0.3″ × 0.3″ × 0.9″). Before testing, it was ensured that the specimens had planar and perpendicular faces to ensure uniform loading and prevent premature specimen failure due to kinking. For testing, specimens were mounted onto steel blocks using epoxy adhesive, and gages were applied to the specimen surface aligned to the loading direction. For all basic material characterization tests, at least five samples were tested per property.

Off-axis specimens were prepared from thick plates (54 plies) with orientations of 15°, 30°, 45°, 60°, 75° to the loading axis. The coordinate scheme is presented in Fig. 15.1. These samples were mounted to rectangular steel blocks and tested per the transverse and longitudinal samples. The samples underwent axial loading that primarily provided transverse normal and in-plane shear stress states. Testing proceeded until catastrophic failure in which a failure plane formed splitting the sample. At least three specimens were tested per sample type, and the angle orientation was verified using an angle measurement software package. A sample with indicated off-axis fiber orientation and compression loading direction is shown in Fig. 15.2.

In considering material performance, the fiber volume fraction plays a significant role in determining the constitutive composite material behavior. In the current work, the fiber volume fraction was determined using gravimetric and micrograph analysis to ensure material uniformity between thick and thin lamina.

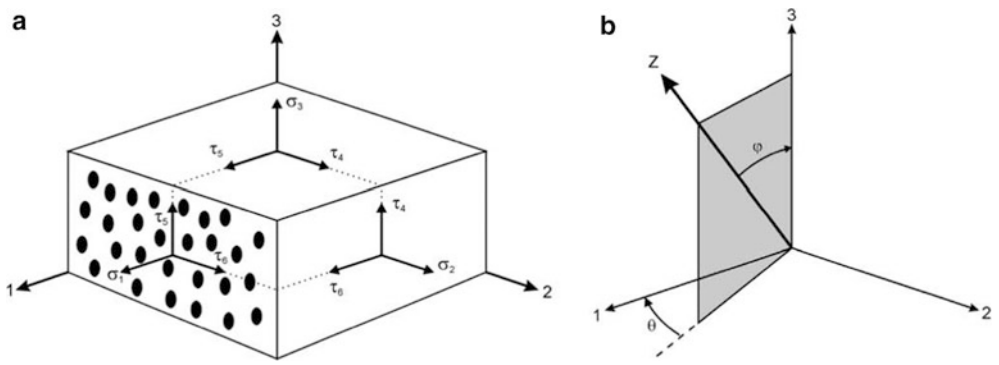

Fig. 15.1 (**a**) Unidirectional composite element loaded along principal material axes and (**b**) loaded along an off-axis direction

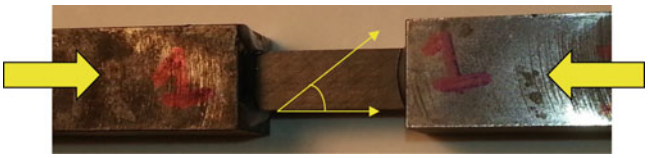

Fig. 15.2 30° off-axis compression sample; loading direction and fiber orientation indicated

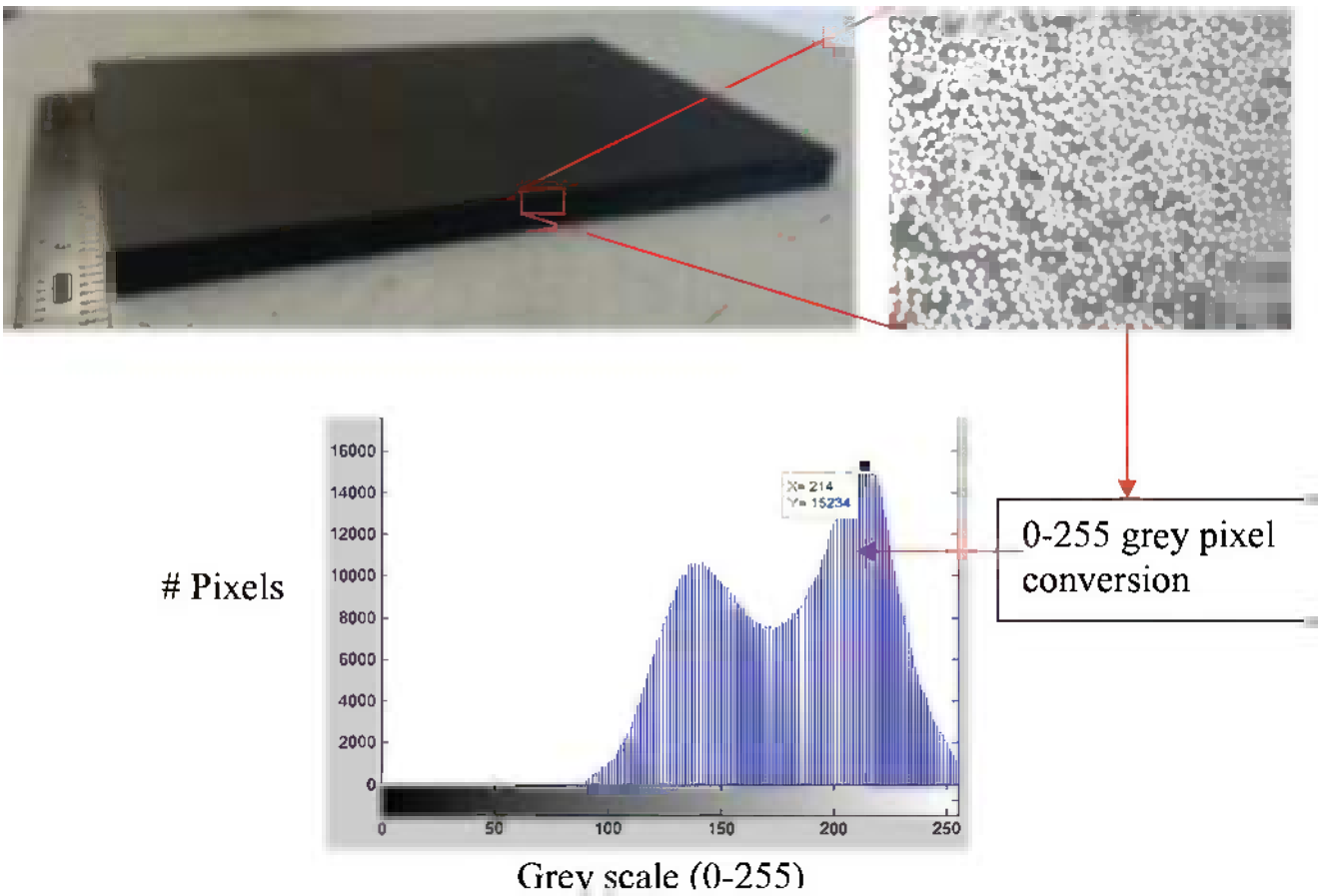

Fig. 15.3 Thick plate composite shown from which micrographs are obtained (*upper left*); a sample micrograph, 200× (*upper right*); a histogram of the grayscale pixel counts (*lower left*)

For the gravimetric approach,

$$V_f = \frac{p_c - p_m}{p_f - p_m}$$

Where p_c, p_m, p_f are the densities for the composite, matrix, and fibers, respectively.

The digitized micrograph method involves sectioning samples from various locations within the composite plate so that the cross section may be imaged on a microscope. The samples are cut perpendicular to the fiber direction, mounted in epoxy, and polished on a micro-grain rotating water sander. The grayscale images were then processed in a Matlab program that creates a histogram of the number of pixels of grey contrast from 0 to 255. The process is shown schematically in Fig. 15.3.

Table 15.1 Quasi-static and intermediate properties for IM7/8552

Property	10^{-4} s^{-1}	~1 s^{-1}	m_p
Fiber volume ratio, V_f	0.58	–	–
Longitudinal modulus, E_1, GPa (Msi)	154 (22.4)	–	–
Transverse modulus, E_2, GPa (Msi)	8.6 (1.25)	9.4 (1.4)	0.031
In-plane shear modulus, G_{12}, Gpa (Msi)	5.6 (0.81)	6.2 (0.9)	0.038
Major Poisson's ratio, ν_{12}	0.33	–	–
Longitudinal tensile strength, F_{1t}, Mpa (ksi)	2,650 (385)	–	–
Transverse tensile strength, F_{2t}, Mpa (ksi)	76.4 (11)	89.6 (13)	0.057
In-plane shear strength, F_6, Mpa (ksi)	89 (13)	109 (15.8)	0.075
Transverse compressive strength, F_{2c}, Mpa (ksi)	288 (42)	350 (51)	0.054

In the histogram, two clear peaks are visible separated by a trough. The peak on the right represents the counts for pixels inhabiting fiber, the trough the interface, and the lower peak represents pixels associated with the matrix. By comparing the relative peak and trough values to the total number of pixels, the fiber volume fraction is determined per [14]. Using these two approaches, the V_f was determined to be ~0.58 for all plates tested.

The determined static and intermediate rate material properties for IM7/8552 are listed in Table 15.1.

15.2.2 Quasi-Static and Intermediate Rate Testing

For the quasi-static tests, samples were gripped in the servohydraulic testing machine and tested at a rate of 10^{-4} s^{-1}. The intermediate tests were performed at ~1 s^{-1} rates, however a special fixture was used to provide a gap between the sample and the bottom crosshead to allow for the crosshead to accelerate (due to inertia) to a uniform speed before the load was applied to the specimen. This approach was performed to obtain a uniform strain rate in the samples during the tests.

Presented by Daniel et al. [1], the NU Theory is failure mode based and dependent on macroscopic material properties. As noted by the authors, the NU criteria are suitable for interfiber/interlaminar failure under transverse normal, and parallel to the fibers shear loading on the 1–2 or 1–3 planes. They are especially applicable to highly anisotropic composites with failure occurring due to a low interaction of modes.

The criterion for each of the three failure modes developed (compression, shear, and tension dominated) for the case of a unidirectional composite loaded in the 1–2 plane:

Compression Dominated

$$\left(\frac{\sigma_2^*}{F_{2c}}\right)^2 + \left(\frac{E_2}{G_{12}}\right)^2 \left(\frac{\tau_6^*}{F_{2c}}\right)^2 = 1 \quad \text{NUa} \tag{15.1}$$

Shear Dominated

$$\left(\frac{\tau_6^*}{F_6}\right)^2 + \left(\frac{2G_{12}}{E_2}\right)\left(\frac{\sigma_2^*}{F_6}\right) = 1 \quad \text{NUb} \tag{15.2}$$

Tension Dominated

$$\left(\frac{\sigma_2^*}{F_{2t}}\right) + \left(\frac{E_2}{2G_{12}}\right)^2 \left(\frac{\tau_6^*}{F_{2t}}\right)^2 = 1 \quad \text{NUc} \tag{15.3}$$

where

$$\sigma_i^* = \sigma_i \left(m_p \log \frac{\dot{\varepsilon}}{\dot{\varepsilon}_o} + 1\right)^{-1} \tag{15.4}$$

And $\sigma_i = \sigma_2$, τ_6, and m_p is the slope of the line created by plotting the normalized matrix dominated strength property verse the log of strain rate for the two given rates investigated. Developed by Daniel et al. [2], the final relation (Eq. 15.4) was found to accurately model the strain dependent material properties for the studied strain range.

15.3 Results and Discussion

The axial failure strengths for each of the tested samples were converted to the transverse and shear strengths associated with ply angle orientation accordingly:

$$\sigma_2 = sin^2(\theta) \cdot \sigma_x$$

$$\tau_6 = sin(\theta)cos(\theta) \cdot \sigma_x$$

Where θ is the angle in regards to the loading direction and σ_x is the axial failure stress.

The results for stress were plotted with the corresponding failure envelopes for the classical failure theories: maximum stress (noninteractive), Tsai-Hill, Hashin-Rotem, Tsai-Wu (fully interactive), and failure mode based/partially interactive (Sun, Daniel) [1, 14, 15]. As noted, the NU theory was previously developed to model the interfiber/interlaminar failure of brittle thermoset composite materials. In the case of the new thermoplastic toughened IM7/8552 results, the NU theory fits the data quite well (Fig. 15.4). Similarly, the results for the intermediate failure stresses are compared to the failure envelopes (Fig. 15.5). The lamina properties obtained from the intermediate rate tests were used to build the envelopes. Further, the quasi-static and intermediate results are shown together in Fig. 15.6 to indicate the significant influence of strain rate on the composite failure behavior. In all cases, the NU theory provides an excellent fit to the data, which indicates that the theory is able to appropriately model the toughened epoxy composite material.

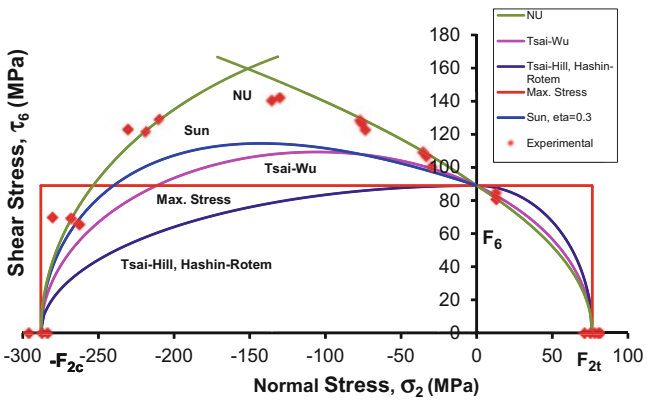

Fig. 15.4 Comparison of classical failure envelopes and experimental results for IM7/8552 composite under quasi-static transverse normal and shear stress

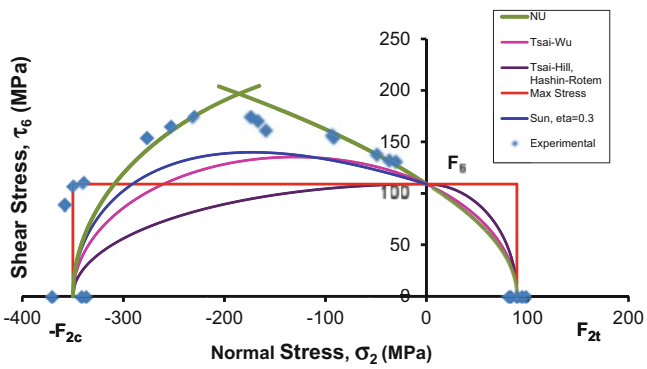

Fig. 15.5 Comparison of classical failure envelopes and experimental results for IM7/8552 composite under intermediate transverse normal and shear stress

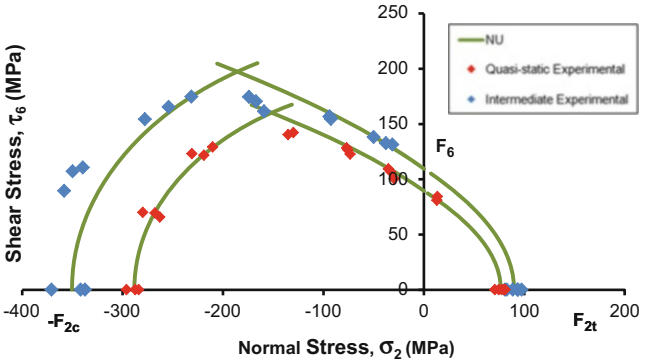

Fig. 15.6 NU failure envelopes compared to experimental results for IM7/8552 composite at quasi-static and intermediate strain rates

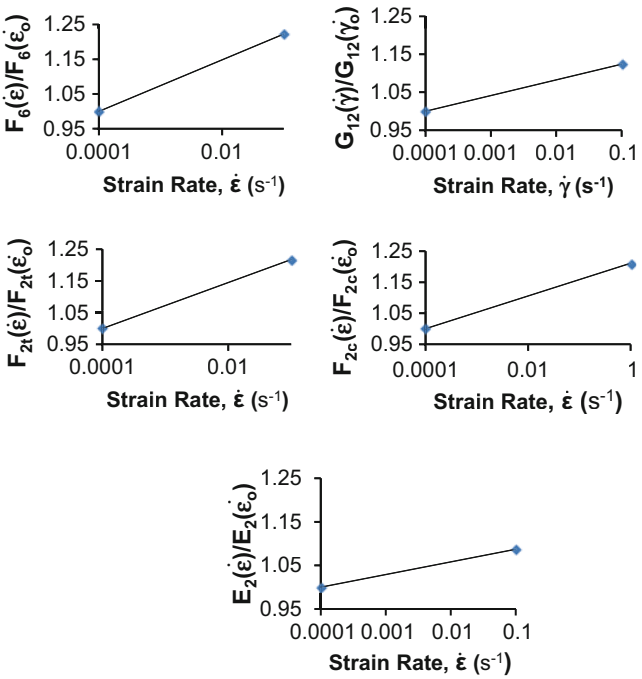

Fig. 15.7 Variation of material strength and moduli with strain rate

In order to model the strain rate dependent behavior of the material, the intermediate rate properties were normalized against the static values and plotted versus the logarithm of strain rate as shown in Fig. 15.7. For the two strain rates investigated, a linear relation is determined for the matrix dominated material properties:

$$P(\dot{\varepsilon}) = P(\dot{\varepsilon}_o)\left(m_p log_{10}\frac{\dot{\varepsilon}}{\dot{\varepsilon}_o} + 1\right) \tag{15.5}$$

Where $P(\dot{\varepsilon})$ is the property associated with a particular strain rate, $P(\dot{\varepsilon}_o)$ is the property associated with the static strain rate, and m_p is a scalar parameter derived from the given relationship. The determined m_p values are provided in Table 15.1.

Referring to the presented rate-dependent NU (a-c) relations, the stress was normalized using Eq. 15.4 and the scalar parameter m_p of the appropriate material property $(\sigma_2,\ \tau_6)$ Based on the criteria, the failure envelopes of Fig. 15.6 collapse into a normalized master envelope as shown in Fig. 15.8.

Thus, with only a few simple material characterization tests it becomes possible to accurately predict the failure behavior of off-axis specimens loaded in transverse normal compression and shear.

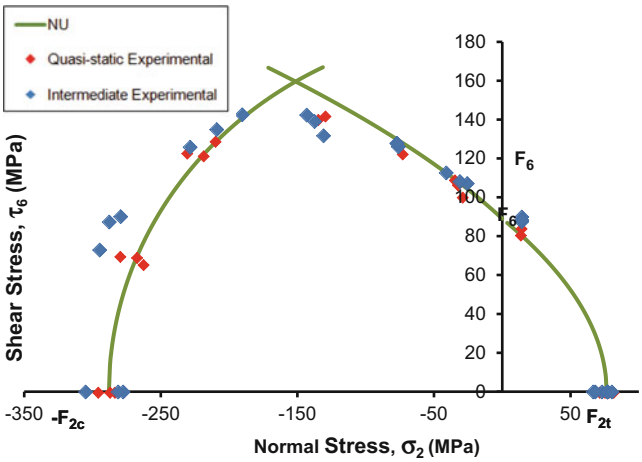

Fig. 15.8 Master failure envelop for IM7/8552 composite material for strain rates in the range of 10^{-4} to ~1 s^{-1}

15.4 Summary and Conclusions

The steps to characterize a new carbon/epoxy composite material are provided for static and intermediate testing rates (10^{-4} to 1 s^{-1}). IM7/8552 toughened carbon/epoxy lamina were tested at various biaxial states of stress combining transverse compression and shear. The material properties were found to vary linearly with the logarithm of strain rate for the tested range. The results were compared to new and classical failure theories, and the failure mode based NU theory was found to fit the date quite well. Using this theory, it is possible to perform relatively few tests to characterize the strain rate behavior of a material therefore decreasing time to potential implementation.

Acknowledgements The authors recognize sponsorship by the Solid Mechanics Program of the Office of Naval Research (ONR). We are grateful to Dr. Y. D. S. Rajapakse of ONR for his encouragement and cooperation, and to Joel Fenner assisting with developing the tooling required for this work.

References

1. Daniel IM, Luo J-J, Schubel PM, Werner BT (2009) Interfiber/interlaminar failure of composites under multi-axial states of stress. Compos Sci Technol 69:764
2. Daniel IM, Werner BT, Fenner JS (2011) Strain-rate-dependent failure criteria for composites. Compos Sci Technol 71:357
3. Koerber H, Camanho PP (2011) High strain rate characterisation of unidirectional carbon–epoxy IM7-8552 in longitudinal compression. Compos A Appl Sci Manuf 42:462
4. Koerber H, Xavier J, Camanho PP (2010) High strain rate characterisation of unidirectional carbon-epoxy IM7-8552 in transverse compression and in-plane shear using digital image correlation. Mech Mater 42:1004
5. Karim MR, Fatt MSH (2006) Rate-dependent constitutive equations for carbon fiber-reinforced epoxy. Polym Compos 27:513
6. Di Pasquale G et al (1997) New high-performance thermoplastic toughened epoxy thermosets. Polymer 38:4345
7. Jang K, Cho W-J, Ha C-S (1999) Influence of processing method on the fracture toughness of thermoplastic-modified, carbon-fiber-reinforced epoxy composites. Compos Sci Technol 59:995
8. Wilkinson SP, Ward TC, McGrath JE (1993) Effect of thermoplastic modifier variables on toughening a bismaleimide matrix resin for high-performance composite materials. Polymer 34:870
9. Arg et al (2011) Influence of the matrix type on the mode I fracture of carbon-epoxy composites under dynamic delamination. Exp Mech 51:293
10. Sun CT, Chen JL (1989) A simple flow rule for characterizing nonlinear behavior of fiber composites. J Compos Mater 23:1009, 1 Oct 1989
11. Thiruppukuzhi SV, Sun CT (2001) Models for the strain-rate-dependent behavior of polymer composites. Compos Sci Technol 61:1
12. Wang C, Sun CT, Gates TS (1996) Elastic/viscoplastic behavior of fiber-reinforced thermoplastic composites. J Reinf Plast Compos 15:360, 1 Apr 1996
13. Daniel IM, Cho J-M, Werner BT, Fenner JS (2011) Characterization and constitutive modeling of composite materials under static and dynamic loading. AIAA J 49:1658, 2011/08/01
14. Daniel IM, Ishai O (2006) Engineering Mechanics of Composite Materials. Oxford University Press, Oxford
15. Sun C (2000) Strength and analysis of unidirectional composites and laminates. In: Kelly A, Zweben C (eds) Comprehensive composite materials. Elsevier Science, Oxford

Chapter 16
HP/HT Hot-Wet Thermomechanical Behavior of Fiber-Reinforced High-Temperature Polymer Composites

Yusheng Yuan and Jim Goodson

Abstract High-temperature polymers and polymer composites have been used extensively in aerospace structures and critical industrial applications, including those in oilfield operations, where high-temperature performance or certain environmental resistant capability is demanded. However, when moisture or a wet condition is associated with the high temperature, the polymers, polymer composites, and even some reinforcement fibers, behave very differently from their original dry state because of severe hygrothermal and/or hydrolytic degradation. In many cases of oilfield downhole operations, service tools are required to perform in a hot-wet environment at a temperature above 204 °C and a pressure above 70 MPa. This presents a significant challenge to the polymers and polymer composites in their applications. Understanding the high-pressure/high-temperature (HP/HT) hot-wet thermomechanical behavior of the high-temperature polymers, reinforcement fibers and their composites is extremely important.

This study aims to investigate the HP/HT hot-wet thermomechanical behavior of the selected continuous fiber-reinforced high-temperature polymer composites based on various testing and analysis techniques associated with an HP/HT hot-wet exposure process. The HP/HT hot-wet environments affect the thermomechanical properties of most high-temperature polymers and their composites significantly. Mechanisms involve hygrothermal and/or hydrolytic degradations in resin matrix, reinforcement fibers and the fiber/resin interfaces. Relationships among mechanical properties, glass transition temperature, hygrothermal degradation and the HP/HT hot-wet exposure have been addressed. Critical issues with the conventional environmental-thermal-mechanical testing and analysis methods are discussed. An innovative HP/HT in-situ thermomechanical testing and analysis system is presented.

16.1 Introduction

High-temperature polymers, including polyimides, bismaleimides (BMI), cyanate esters, phenolics, high-temperature epoxies and thermoplastics, and their composites, have been used extensively in aerospace and numerous industrial applications, including in oilfield operations [1–3], where high-temperature performance and certain environmental resistant capability is demanded. However, when moisture or a wet condition is associated with high-pressure/high-temperature (HP/HT), polymers, their composites, and even some inorganic reinforcement fibers behave very differently from their original dry state because of severe hygrothermal degradation and hydrolytic attack from the destructive and corrosive superheated wet environment [4, 5].

Oilfield downhole operations, including drilling, logging, completion, production and workover, require equipment to perform in an extremely harsh environment in a deep well involving high-pressure, high-temperature and various corrosive fluids and gases. This requires the materials for downhole equipment to possess high strength with heat- and corrosion-resistant capabilities. Many completion and workover tools are set temporarily in a wellbore, and must be removed by drilling or milling immediately after certain operations. This requires easy cutting of the tool materials. Recently developed

Y. Yuan (✉) • J. Goodson
Baker Hughes, 14990 Yorktown Plaza Dr., Houston, TX 77040, USA
e-mail: yusheng.yuan@bakerhughes.com

G.P. Tandon et al. (eds.), *Experimental Mechanics of Composite, Hybrid, and Multifunctional Materials, Volume 6*, Conference Proceedings of the Society for Experimental Mechanics Series, DOI 10.1007/978-3-319-00873-8_16,

new technologies in oil and gas exploration and production, involving offshore deepwater extended-reach drilling and completion, further require lightweight and fatigue-resistant materials for downhole tubular components and equipment [1–3]. Advanced fiber-reinforced high-temperature polymer composites enable work at elevated temperatures in deep wells while offering the required advantages such as lightweight, corrosion resistance, long fatigue life and easy removal. Furthermore, non-conductive and non-magnetic high-temperature polymer composites are considered to be ideal materials for construction of resistivity and induction logging tools [2, 3].

Glass fiber-reinforced plastics (GRP) and other polymer-matrix composite products have been used in downhole operations since the 1970s for sucker rods, downhole tubing and casing, drill pipes, coiled tubing and well screens [1]. However, these applications are still very limited in temperature rating (mostly below 93 °C) and in long-term performance reliability [6, 7]. In many downhole operations, service tools must perform in an HP/HT hot-wet fluid condition at a temperature above 204 °C and a pressure above 70 MPa [2, 3, 8]. This presents a significant challenge to the applications of the high-temperature polymers and their composites in oil wells. Understanding the HP/HT hot-wet thermomechanical behavior of various high-temperature polymer resins, reinforcement fibers and their composites is extremely important.

Hygrothermal mechanical behavior of composite materials has been a critical research subject for high-performance composites and their applications since the 1960s. Early studies for aircraft structures and critical industrial applications involved moisture absorption and desorption [9–11], moisture-induced glass transition temperature (T_g) shift, swelling and damage in cured resins or resin phases [11–17], effects of temperature and moisture on mechanical properties of resin, fiber, resin/fiber interface and their composites, and the related damage or degradation mechanisms [17–22]. Major findings from these studies include: (1) Moisture absorbed in an epoxy resin or resin phase in a composite functions as a plasticizer that lowers the resin T_g and degrades the high-temperature mechanical properties of the resin and its composite [11, 13, 17]; (2) Moisture absorption causes swelling of the resins or resin composites and a moisture concentration gradient induces residual stresses that may lead to micro-cracking in the resins or composites [12–14]; (3) Boiling water causes resin phase swelling in a composite and produces tensile stress across the resin/fiber interfaces that may cause interface debonding [18, 19]; (4) Water immersion degrades the strength of glass fibers. The major mechanism for the strength loss in an aqueous environment was considered to be an ion-exchange process in the fiber surface regions where the water functions as a catalyst, accelerating the cracking process by reducing the fiber surface energy [20–22]; (5) Mechanisms for high-temperature property degradation of the resins and composites after exposure in a humid environment mainly involve reduction of the resin T_g, development of the internal micro-cracking due to the uneven swelling, and weakening of the fiber/resin interfaces during the exposure process [13, 19]. Since the environmental conditions applied in most of these studies were simulating a flying environment of a high-speed-aircraft, they were typically below 75–100 % relative humidity at 71–82 °C and ambient pressure, which were far less severe than the HP/HT hot-wet environmental conditions in oil wells. Because of lacking advanced DMA (dynamic mechanical analysis) thermal analysis technology in the early years, the reported T_gs were mostly determined by thermo-mechanical analysis (TMA) or heat distortion temperature test (HDT), where the valuable dynamic modulus transition information of the sample materials could not be revealed.

In the past two decades, research has focused on the durability of high-temperature polyimide resins and their carbon fiber composites for aircraft engine components and hypersonic reusable space vehicles. The research identified the failure sequence paths in the carbon fiber-reinforced polyimide composites under extreme conditions. The damage mechanisms include “imide” ring and “amide” group hydrolysis in a high-temperature hygrothermal environment [23–25]. Because of increased demands in HP/HT operations and technologies in global oil and gas industries, HP/HT environmental resistant materials for downhole equipment are critical, including HP/HT resistant polymers and composites. Since 1999, research within Baker Hughes has focused on HP/HT hot-wet resistant polymers and composites and their applications. The research included new materials search and development, experimental testing and characterization and HP/HT in-situ test method development [1–3, 26–29]. Research in this area also included publications [30–32] where the water absorption and mechanical tests were conducted in a pressurized hot-wet condition at relatively low temperatures.

This paper summarizes the results of the investigations in HP/HT hot-wet thermomechanical behavior of selected high-temperature polymers and their fiber-reinforced composites in a simulated HP/HT hot-wet environment using advanced thermal analysis, mechanical testing, microstructure examination and other analysis techniques. Based on the experimental and analytical results, the authors will update the existing knowledge and present new findings in these research areas, and will address further the relationships among the mechanical properties, resin glass transition, hygrothermal-induced damage and the HP/HT hot-wet exposure. Critical issues with the conventional environmental-thermal-mechanical test methods are discussed. An innovative HP/HT in-situ thermomechanical testing and analysis system and the associated test methods are presented.

16.2 Experimental

Constituent Materials and Laminate Systems Polyimides, bismaleimides (BMI), cyanate esters, phenolics and some high-temperature epoxies are commonly known as high-temperature thermosetting polymers with their dry T_gs ranging from 204°C to 400 °C. Thermoplastic polyaryletherketones (PAEK), including PEEK, PEK and PEKEKK, are also known as high-temperature resins with good chemical and moisture resistance. Although their dry T_gs are typically in the range from 144°C to 164 °C, they can work at a temperature much higher than their T_g because of their stable phenyl backbone chemistry and spherulitic semi-crystalline polymer morphology [33]. Although polyimide and cyanate ester resins with imide ring and ester linkage chemistry are susceptible to hydrolytic scission at a high-temperatures [4, 23–25], the authors still wanted to confirm their chemical stability in an immersed HP/HT hot-wet environment. These high-temperature resins will be included in this study. Glass fibers have been also identified to be susceptible to severe hydrolytic attack in a HT/HP hot-wet environment [27], but their composite products are still used extensively in oilfield operations for short-term applications at relatively lower temperatures. For comparison, E-glass, S2-glass and carbon fibers will be used as reinforcement fibers in composite laminates in this study.

An advanced polyimide resin (PI-1), a cyanate ester resin (CE-1), two tetra-functional epoxy resins (EP-1 and EP-2), a bi-functional epoxy resin (EP-3), two phenolic resins (PH-1 and PH-2), and a thermoplastic PEEK resin were selected as matrix resins incorporated with carbon fiber or E-glass or S2-glass fiber to form composite laminates for studies. These composite systems along with their processing methods, fiber volume fractions and dry T_gs are listed in Table 16.1. The aromatic amine-cured tetra-functional epoxy resin has a high T_g with excellent mechanical properties, and it has been used extensively as a matrix resin in composite downhole equipment. Consequently, the unmodified neat resin version, EP-1, was also included in the table.

HP/HT Downhole Environment Simulation The hostile wellbore condition often involves high temperatures, high pressures and highly corrosive fluid and gas environments, such as drilling mud, completion brine, crude oil, acid solution and CO_2 or H_2S gases. One major motivation for using composite materials downhole is their good corrosion resistance. Fiber-reinforced composites have been reported to be much less sensitive to CO_2 and H_2S gases and hydrocarbons [30, 31] compared with the conventional carbon steel and some rubber compounds. Among various downhole fluid and gas conditions, the most destructive to polymeric resins and their composites are the caustic water-based brine and the aqueous acid solutions under an HP/HT condition. Since the acid solutions are used only for special treatments in a short duration (typically a few hours) and a brine solution is the most commonly encountered fluid environment, the current HP/HT environmental exposure tests are designed to be conducted in a 3 % NaCl brine in a high-pressure autoclave at a temperature from 121 °C to 260 °C under a nitrogen pressure from 35 to 70 MPa for 3–10 days, simulating a class of short-term HP/HT downhole applications.

Water Absorption and Substance Leaching Standard mechanical test specimen-sized samples of the neat resin and the selected composites were used in exposure processes. Before exposure, all specimens were dried in a desiccator for 72 h. Weight and thickness of each sample were measured to 0.0001 g and 0.001 in., respectively, before and after the exposure. Since the superheated HP/HT exposure condition is extreme to the polymers, unbound substances or hydrolytic products inside the resin or laminate samples may be leached out or extracted by the exposure fluid during the exposure process [16]. Consequently, the neat weight change of a sample after the exposure should be considered to be a combination of the water

Table 16.1 List of neat resin and selected composite systems in studies

Composite system	Resin matrix	Reinforcement	Processing method	V_f (%)	Dry T_g (°C)
PI-1/T650	Polyimide	T650 carbon fabric	Prepreg lamination	57	388
CE-1/T300	Cyanate ester	T300 PW carbon fabric	Prepreg lamination	57	332
EP-1	Tetra-functional epoxy	None	Casting	None	230
Neat resin	Aromatic amine cured				
EP-1/7781E	EP-1	7781 E-glass fabric	Wet lamination	57	228
EP-1/6781S	EP-1	6781 S2-glass fabric	Wet lamination	57	228
EP-1/T300	EP-1	T300 PW carbon fabric	Wet lamination	58	230
EP-2/AS4	Tetra-functional epoxy	AS4 carbon UD [0/90]sn	Prepreg lamination	60	287
EP-3/T300	Bi-functional epoxy	T300 carbon UD [0/90]sn	Prepreg lamination	60	181
PH-1/6781S	Commercial resole phenolic	6781 S2-glass fabric	Prepreg lamination	59	295
PH-2/T300	Developmental phenolic	T300 PW carbon fabric	Prepreg lamination	54	302
TP-1/AS4	PEEK	AS4 carbon UD [0/90]sn	Autoclave lamination	61	144
TP-1/S2-G	PEEK	S2-glass UD [0/90]sn	In-situ tape-placement lamination	60	144

absorption and the substance leaching. To identify these two processes quantitatively, an additional drying process of the exposed wet samples was conducted at 100 °C in an oven.

Thermal Analysis Glass transition temperatures (T_g) and the related dynamic mechanical properties of the neat resin and the composite samples were determined by a dynamic mechanical analysis (DMA) method before and after the environmental exposure. In the DMA, an AR2000 rheometer was used as a DMA analyzer with a torsional oscillation mode. The analyses were conducted with a 51 × 12.7 × 3.2 mm (L × W × T) rectangular specimen with 1-Hz frequency, 0.05 % torsional strain and 3–5 °C/min. heating rate in a dry inert atmosphere. According to ASTM D7028, the T_g values were determined by the onset point of the measured storage modulus (G') curves. It was noted that the dry heating during the DMA procedure causes a drying process to the exposed wet samples, which affected the accuracy of the analysis of the exposed wet samples. However, in the current torsional DMA procedure with a relatively large specimen size for a dense and rigid solid material, the analysis results are still considered to be acceptable for practical engineering material selection and characterization per ASTM D7028.

Neat Resin Tensile Tests Tensile strength, modulus and strain at break of the neat resin specimens were determined at ambient and elevated temperatures, before and after the environmental exposure. The tensile tests were conducted at a servo-hydraulic testing machine with a set of mechanical wedge grips, an alignment fixture and a test oven according to ASTM standard D638. The D638 Type-1 tensile specimens with a gauge section of 63.5 × 12.70 × 3.00 mm were used in the tests, which were cut and machined from the neat resin panels prepared with a casting process. The panels were cured at 149 °C for 2 h and then at 204 °C for 2 h. In the high-temperature tests, the test specimens were preheated for 25 min in the fixture before running the tests. Because preheating during the elevated-temperature tests could generate additional hygrothermal damage in the exposed wet specimens, additional elevated-temperature tests were conducted for the exposed specimens after a drying process at 90 °C for further studies. Issues on high-temperature mechanical test methods for exposed neat resin and composite specimens will be discussed in a later section.

Composite Mechanical Tests Standard tensile and compression tests of the composite specimens were conducted at ambient and elevated temperatures, before and after the environmental exposure. The tensile and compression tests were conducted with a servo-hydraulic testing machine according to ASTM standards D3039 and D6641, respectively. The standard straight-side tensile specimens (254 × 25.40 × 3.20 mm) and compression specimens (140.0 × 12.70 × 3.20 mm) were cut and machined from the laminated composite panels. The laminate panels were fabricated by wet or prepreg lamination process in symmetric cross-ply or balanced bi-directional woven fabric construction with a thickness from 2.50 to 3.20 mm and cured in an autoclave or under a press per the manufacturer specified cure schedule.

Hygrothermal Cracking and Interface Examination To study the thermal and hygrothermal cracking resistance and the fiber/resin interface condition of the selected composites, microstructures of the laminate samples after the HP/HT hot-wet exposure and after an additional thermal impact process (by direct heating of the exposed wet samples in a dry oven at a high-temperature for 20–30 min) were examined under a high-magnification optical microscope with sectioned and polished laminate samples.

16.3 Results and Discussion

16.3.1 Water Absorption, Sample Leaching and Post-exposure Inspection

EP-1 Epoxy Neat Resin Measured net weight gains, water absorption, sample leaching and thickness changes of the EP-1 neat resin samples after exposure in 3 % NaCl brine at 149 °C, 177 °C and 204 °C, respectively, for 72 h are listed in Table 16.2. The test data showed that: (1) A trend of the water absorption increased with the exposure temperature, but the sample net weight gain after the exposure decreased with the exposure temperature significantly, and even became a negative value after the 204 °C exposure because sample leaching occurred during the high-temperature exposure; (2) Sample leaching was undetectable during the exposure at 149 °C, insignificant during the exposure at 177 °C, but severe during the exposure at 204 °C, indicating a leaching onset temperature between 149 °C and 177 °C in the current exposure condition. Accordingly, the EP-1 neat resin samples after 149 °C or 177 °C exposure showed no or minor internal damage as shown in Fig. 16.1b, c, respectively. The 204 °C exposure is beyond the resin's chemical stability even in a short-term duration. After exposure in the brine at 204 °C for 72 h, the EP-1 samples were blistered and cracked severely associated with high water absorption (4.18 %) and a high leaching (6.15 %), as shown in Figs. 16.1d and 16.2.

Table 16.2 Water absorption and related weight and dimensional changes of EP-1 neat resin and selected composites after HT/HP hot-wet exposure

Material systems	Exposure condition In 3 % NaCl brine	Net Wt. gain (%)	Water absorption (%)	Leaching (%)	Thickness change (%)	Post-aging examination
EP-1	@149 °C, 34.5 MPa for 72 h	3.95	3.75	Undetected	1.45	No visible cracks
Neat resin	@177 °C, 34.5 MPa for 72 h	2.78	3.65	0.87	1.71	No visible cracks
	@204 °C, 34.5 MPa for 72 h	−1.97	4.18	6.15	0.85	Severe blistering
EP-1/7781E	@Ambient T + P for 240 h	0.14			0.27	
	@121 °C, 0.34 MPa for 240 h	1.15			1.37	
	@121 °C, 34.5 MPa for 240 h	1.15			1.54	
	@177 °C, 34.5 MPa for 240 h	2.40			6.24	Interface debonding
EP-1/6781S	@Ambient T + P for 240 h	0.11			0.14	
	@121 °C, 0.34 MPa for 240 h	1.19			1.23	
	@121 °C, 34.5 MPa for 240 h	1.28			1.23	
	@177 °C, 34.5 MPa for 240 h	1.94			4.34	Interface debonding
EP-1/T300	@121 °C, 34.5 MPa for 240 h	1.21			0.74	Minor interface debonding
	@177 °C, 34.5 MPa for 240 h	1.47			1.63	Interface debonding
	@Ambient T + P for 72 h	0.14	0.14	Undetected	0.42	
	@121 °C, 0.34 MPa for 72 h	0.89	0.89	Undetected	0.85	
	@121 °C, 34.5 MPa for 72 h	0.80	0.80	Undetected	0.85	
	@121 °C, 69.0 MPa for 72 h	0.86	0.86	Undetected	0.85	
	@149 °C, 34.5 MPa for 72 h	1.48	1.48	Undetected	1.69	No visible cracks
	@177 °C, 34.5 MPa for 72 h	1.18	1.52	0.34	0.99	Minor interface debonding
	@204 °C, 34.5 MPa for 96 h	0.48	1.41	0.93	1.27	Interface debonding
EP-2/AS4	@204 °C, 34.5 MPa for 96 h	1.88	3.03	1.55	2.43	Severe delamination
EP-3/T300	@149 °C, 34.5 MPa for 72 h	1.36	1.36	Undetected	0.65	
PH-1/S2	@Ambient T + P for 240 h	1.06			0.26	
	@121 °C, 34.5 MPa for 240 h	1.65			1.00	
	@177 °C, 34.5 MPa for 240 h	1.64			1.17	
	@204 °C, 34.5 MPa for 96 h	1.65	3.29	1.64	1.05	Resin and interface cracking
HP-2/T300	@204 °C, 34.5 MPa for 72 h	0.67	1.73	1.06	−0.12	No major cracking
TP-1/AS4	@177 °C, 34.5 MPa for 240 h	0.79			0.59	
	@204 °C, 34.5 MPa for 168 h	0.76	0.70	Undetected	0.79	No cracking, no debonding
PI-1/T650	@204 °C, 34.5 MPa for 72 h					PI-1 resin totally dissolved
CE-1/T300	@204 °C, 34.5 MPa for 72 h					CE-1 resin mostly dissolved

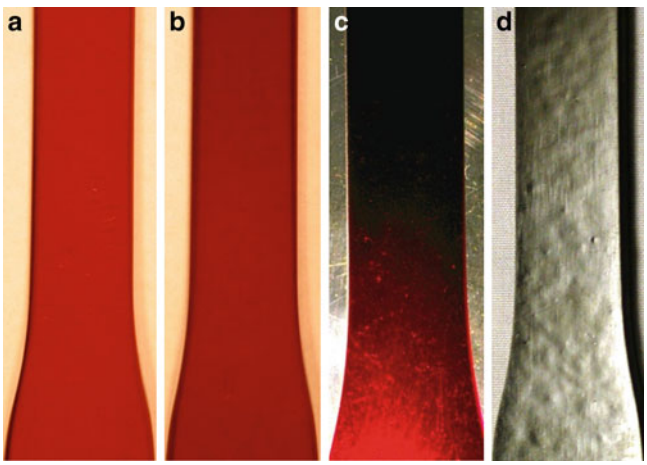

Fig. 16.1 EP-1 neat resin samples from *left*: (**a**) unexposed, (**b**) exposed in 3 % NaCl brine at 149 °C, 34.5 MPa for 72 h, (**c**) at 177 °C for 72 h, and (**d**) at 204 °C for 72 h

Based on these observations, severe leaching may reduce the sample dimensions and cause irreversible material structural damage. Besides water absorption, we may consider sample leaching as a major indication of hygrothermal or hydrolytic degradation in a superheated aqueous environment, which may involve both physical and chemical processes [16]. It is believed that water absorption in a high-temperature aqueous environment may not obey the common diffusion law because sample leaching and irreversible damage in the sample material are involved.

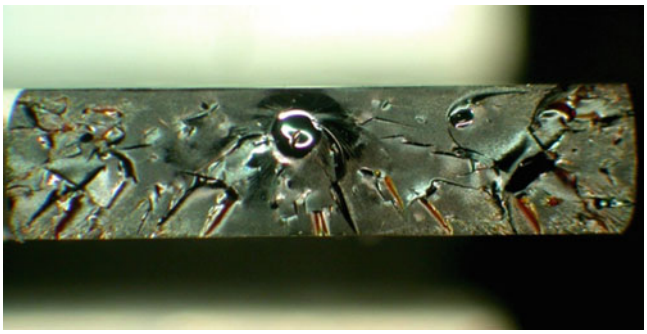

Fig. 16.2 Room-temperature tensile fracture surface of a EP-1 neat resin specimen after exposure in 3 % NaCl brine at 204 °C, 34.5 MPa for 72 h

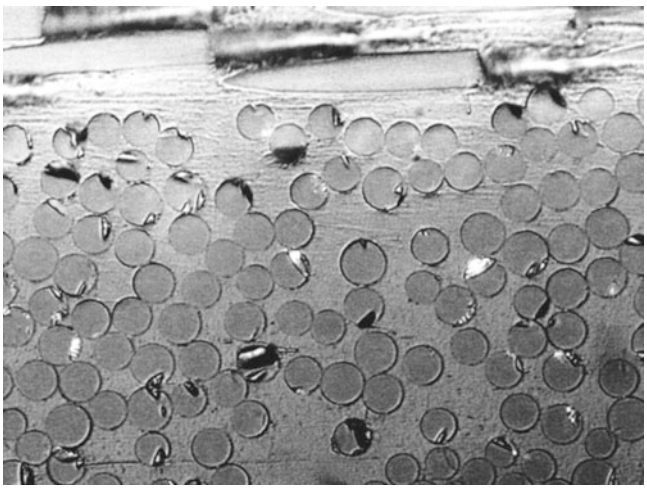

Fig. 16.3 Micrograph (×800) of a polished cross section of an EP-1/7781E sample after exposure in 3 % NaCl brine at 177 °C, 34.5 MPa for 96 h

Hot-wet Resistant Polymer Composites Measured net weight gains, water absorption, sample leaching and thickness changes of the selected glass fiber- and carbon fiber-reinforced high-temperature epoxy, phenolic and PEEK composites after exposure in 3 % NaCl brine under the specified temperature and pressure conditions are also listed in Table 16.2. To closely monitor the water absorption characteristics of the EP-1/T300 composite, the water absorption tests were conducted in a full range of exposure temperatures and pressures, from ambient to 204 °C and 69 MPa. Based on these studies, we have the following observations and discussion:

When the exposure temperature was at 149 °C or lower, no sample leaching was found from the EP-1 epoxy composites, and the water absorption and the related dimensional changes behaved regularly and were enhanced by a higher exposure temperature. When the exposure temperature increased above 149 °C, however, sample leaching was activated along with the possible damage initiation and development in the test samples. The sample net weight gain, water absorption and the related dimensional changes showed an irregular behavior, depending on the material system and the degree of leaching and the internal damage. When the exposure temperature reached 177 °C or above, damages were found in most high-temperature epoxy composite samples; fiber/resin interface debonding in wet-laminated EP-1/7781E, EP-1/6781S and EP-1/T300 samples after exposure in brine at 177 °C for 96 h, and severe delamination in a prepreg-laminated EP-2/AS4 sample after exposure in brine at 204 °C for 96 h, as shown in Figs. 16.3, 16.4, 16.5 and 16.6, respectively.

Comparing the measured data among the EP-1/7781E, EP-1/6781S and EP-1/T300 composite samples, we found that the glass fiber-reinforced EP-1 composites absorbed more water and had higher swelling than the carbon fiber-reinforced EP-1 composite, especially when the exposure temperature reached 177 °C. Mechanisms causing this difference may involve the hydrophilic nature of the glass fibers in the hot-wet condition, where the osmotic pressure built up by dissolution on the fiber surfaces during the fiber/resin interface debonding process in a high-temperature aqueous environment. This osmotic pressure may also generate microcracks in the resin phase surrounding the fibers, causing higher water absorption and expansion [18], as shown in Figs. 16.3 and 16.4, compared with the case with less interface debonding and less resin phase cracking in the carbon fiber-reinforced EP-1/T300 composite after 177 °C exposure, as shown in Fig. 16.5.

Phenolic resins are commonly known as a resin system with low moisture intake and good hot-wet resistance. However, PH-1/6781S samples were found to have much higher water absorption than its epoxy counterpart EP-1/6781S when they

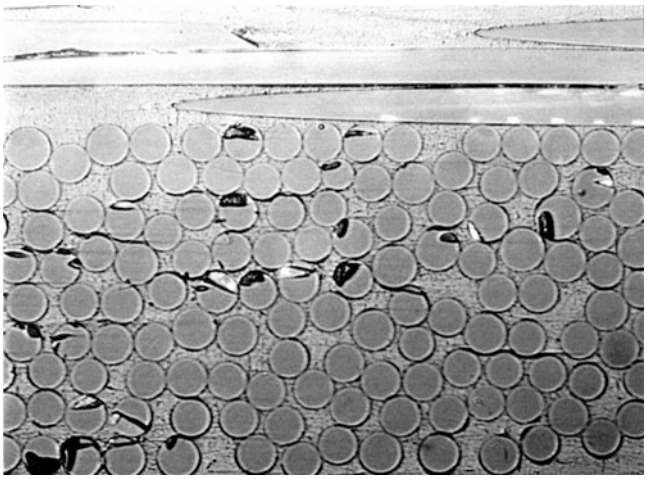

Fig. 16.4 Micrograph (×800) of a polished cross section of an EP-1/6781S sample after exposure in 3 % NaCl brine at 177 °C, 34.5 MPa for 96 h

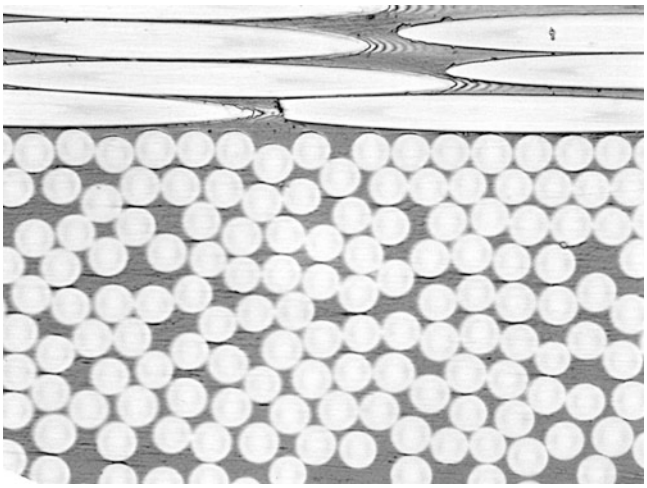

Fig. 16.5 Micrograph (×1,000) of a polished cross section of an EP-1/T300 sample after exposure in 3 % NaCl brine at 177 °C, 34.5 MPa for 96 h

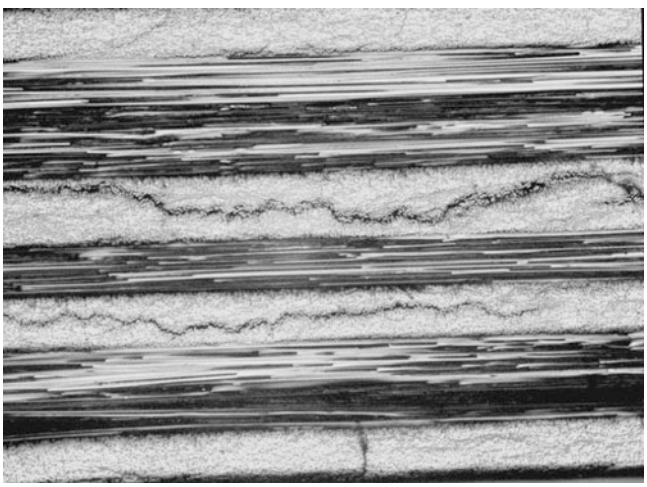

Fig. 16.6 Micrograph (×50) of a polished cross section of a EP-2/AS4 sample after exposure in 3 % NaCl brine at 204 °C, 34.5 MPa for 96 h

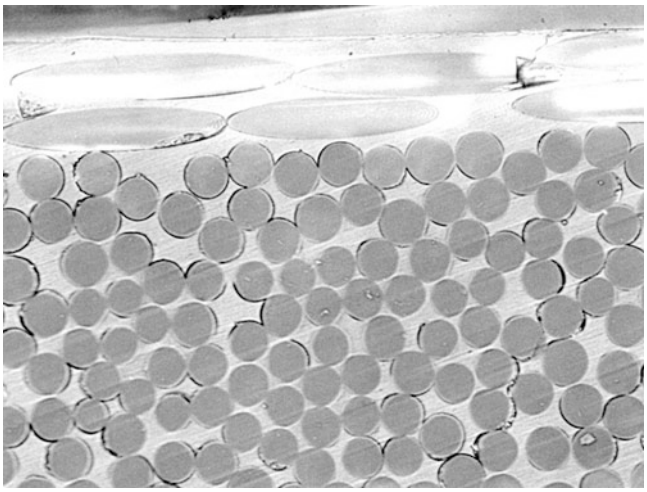

Fig. 16.7 Micrograph (×800) of a polished cross section of a PH-1/6781S sample after exposure in 3 % NaCl brine at 204 °C, 34.5 MPa for 96 h

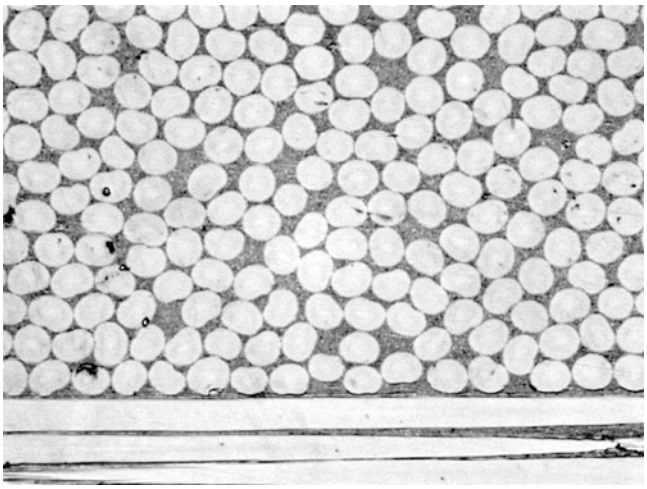

Fig. 16.8 Micrograph (×800) of a polished cross section of a PH-2/T300 sample after exposure in 3 % NaCl brine at 204 °C, 34.5 MPa for 96 h

were exposed in the 3 % NaCl brine in ambient conditions. This suggests that a higher void or microcrack content may exist in the unexposed phenolic composite samples due to the nature of the cured phenolic resin. After the 204 °C hot-wet exposure, the PH-1/6781S samples showed high water absorption due to extensive resin/fiber interface debonding and matrix cracking developed in the test samples, as shown in Fig. 16.7. The carbon fiber-reinforced developmental phenolic composite PH-2/T300 was found to possess low water absorption, low sample leaching, small dimensional changes and good hygrothermal cracking resistance when exposed at 204 °C because this phenolic resin is a toughened hot-wet resistant phenolic system. A micrograph of a PH-2/T300 sample after exposure in the brine at 204 °C, 34.5 MPa for 72 h is shown in Fig. 16.8.

Carbon fiber-reinforced thermoplastic PEEK composite, TP-1/AS4, was found to have the lowest water absorption and dimensional changes. No sample leaching and hygrothermal cracking were found in the test samples after the hot-wet exposure up to 204 °C, indicating that the semi-crystalline thermoplastic PEEK resin possesses the best HT/HP hot-wet environmental resistance capability and is able to maintain its composite structural integrity in hot-wet environment up to 204 °C. A micrograph of a TP-1/AS4 sample after exposure in the brine at 177 °C, 34.5 MPa for 240 h, shows perfect fiber/resin interfaces, as presented in Fig. 16.9. However, in the case of S2-glass fiber-reinforced PEEK composite, TP-1/S2-G, after exposure in the same hot-wet condition, the micrograph, presented in Fig. 16.10, shows interface debonding between the glass fibers and PEEK resin, indicating a week hot-wet resistance of the glass fiber and the fiber/resin interface, even with the hot-wet resistant PEEK resin. This fiber/resin microstructural degradation will further result in a mechanical degradation of the TP-1/S2-G composite in the exposure environment.

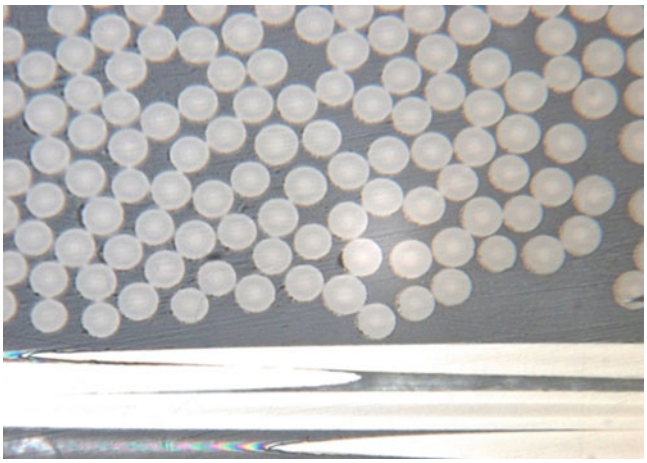

Fig. 16.9 Micrograph (×1,000) of a polished cross section of a TP-1/AS4 sample after exposure in 3 % NaCl brine at 177 °C, 34.5 MPa for 240 h

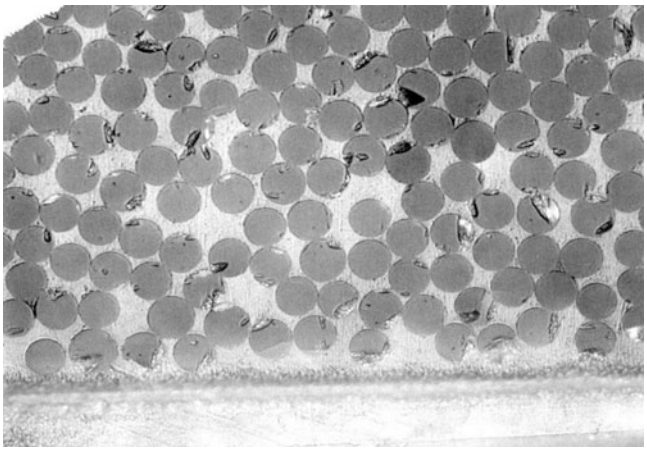

Fig. 16.10 Micrograph (×1,000) of a polished cross section of a TP-1/S2-G sample after exposure in 3 % NaCl brine at 177 °C, 34.5 MPa for 240 h

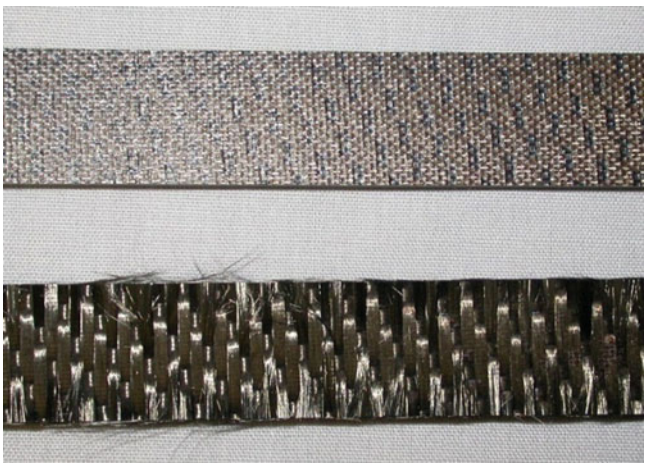

Fig. 16.11 PI-1/T650 tensile specimen before and after exposure in 3 % NaCl brine at 204 °C, 34.5 MPa for 72 h

No effect of the applied hydrostatic pressure on water absorption in EP-1/T300, EP-1/7781E and EP-1/6781S composites was observed in the current exposure tests at 121 °C under a hydrostatic pressure from near-ambient pressure to 69 MPa. This confirms further the similar observations by early researchers [30].

Hot-wet Degradable Polymers After exposure in 3 % NaCl brine at 204 °C, 34.5 MPa for 72 h, the polyimide resin in the PI-1/T650 laminate specimens was totally dissolved by the hot brine, as shown in Fig. 16.11 and the cyanate ester resin in

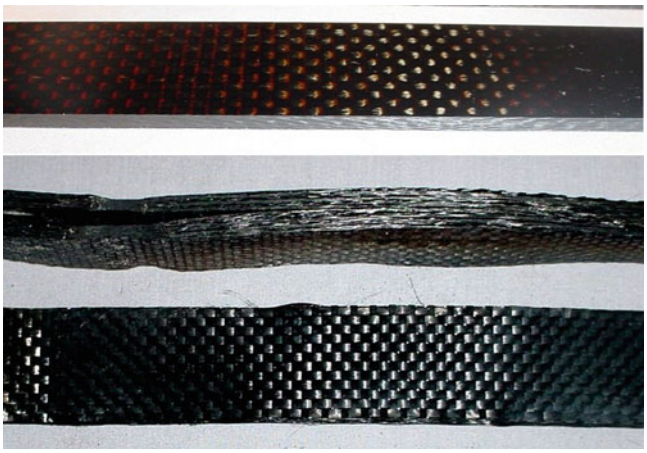

Fig. 16.12 CE-1/T300 tensile specimen before and after exposure in 3 % NaCl brine at 204 °C, 34.5 MPa for 72 h

Table 16.3 DMA results of EP-1 neat resin and selected epoxy-matrix composites

Material systems	Exposure condition In 3 % NaCl brine	First transition G′ onset/G′ drop (°C/%)	First transition T_g at G″ peak (°C)	Full transition G′ onset/G′ drop (°C/%)	Full transition T_g at G″ peak (°C)	Full transition T_g at tan δ peak (°C)
EP-1 neat resin	Unexposed – dry			231/~28	242	251
	@ 149 °C, 34.5 MPa for 72 h	174/~35	185	238/~80	233	244
	Exposed @149 °C and dried			230/~40	229	240
EP-1/T300	Unexposed – dry			221/23	228	239
	@ 149 °C, 34.5 MPa for 72 h	167/~30	181	228/~54	231	244
	@ 177 °C, 34.5 MPa for 240 h	135/~5	150	230/~30	241	247
	@ 204 °C, 34.5 MPa for 96 h	182/~10	196	250/~65	264	276
EP-2/AS4	Unexposed – dry				287[a]	
	@ 204 °C, 34.5 MPa for 96 h		193	248/~55	282	293
EP-3/T300	Unexposed – dry			189/~14	196	205
	@ 149 °C, 34.5 MPa for 72 h	83/~15	90	147/~90	151	160

[a]Manufacturer's data

the CE-1/T650 laminate specimens was almost totally dissolved by the hot brine, as shown in Fig. 16.12, although both the matrix resins are advanced high-performance aerospace resins with an extremely high T_g. This confirmed further the severe hydrolytic breakdown of the polymers containing the imide ring, amide group or ester linkage in their polymer chemistries in a superheated high-temperature hot-wet environment. The authors call this class of polymer resins "hot-wet degradable polymers". The hydrolysis onset temperatures of these polymers are varied depending on the type of the hot-wet degradable polymers and the chemistry of each grade of the hot-wet degradable resin.

16.3.2 Glass Transition and Transition Temperatures

EP-1 Epoxy Neat Resin Measured DMA curves and the T_g values of the EP-1 epoxy neat resin samples in dry condition and after the hot-wet exposure in 3 % NaCl brine at 149 °C and 177 °C under 34.5 MPa are presented in Table 16.3 and Figs. 16.13 and 16.14, respectively. Analysis results from the exposed and post-dried samples are also included. Based on the results presented, we have the following discussion:

Partial Transition and Full Transition In the DMA, a dry EP-1 neat resin sample in general gives only one major full transition in its storage modulus curve, where the modulus loss through the transition is usually greater than 80 %. Dry T_g of the EP-1 resin measured from an unexposed dry sample is around 231 °C (G' onset), and the typical DMA curves from this analysis are presented in Fig. 16.13. However, DMA curves determined from the exposed wet samples show commonly two transitions, a first partial transition and a final full transition that are shown typically also in Fig. 16.13 for a 149 °C-exposed sample. The first (partial) transition at a lower temperature (174–185 °C) gives about 50 % modulus reduction while the second transition at a higher temperature (233–238 °C) results in a further softening of the cured resin.

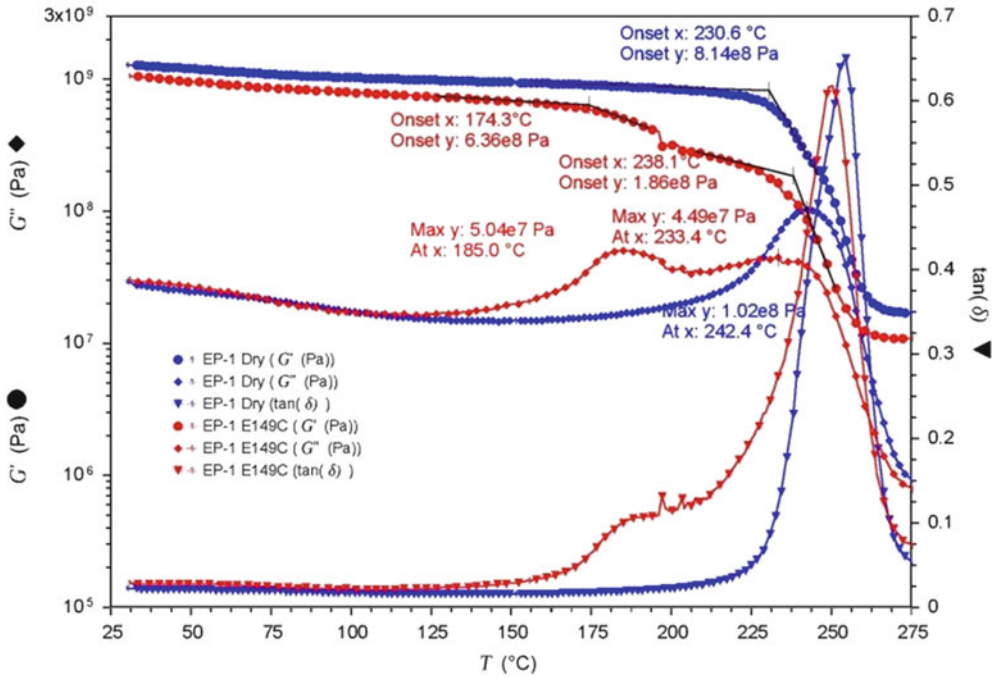

Fig. 16.13 DMA curves of EP-1 neat resin determined in dry and in wet condition after exposure in 3 % NaCl brine at 149 °C, 34.5 MPa for 72 h

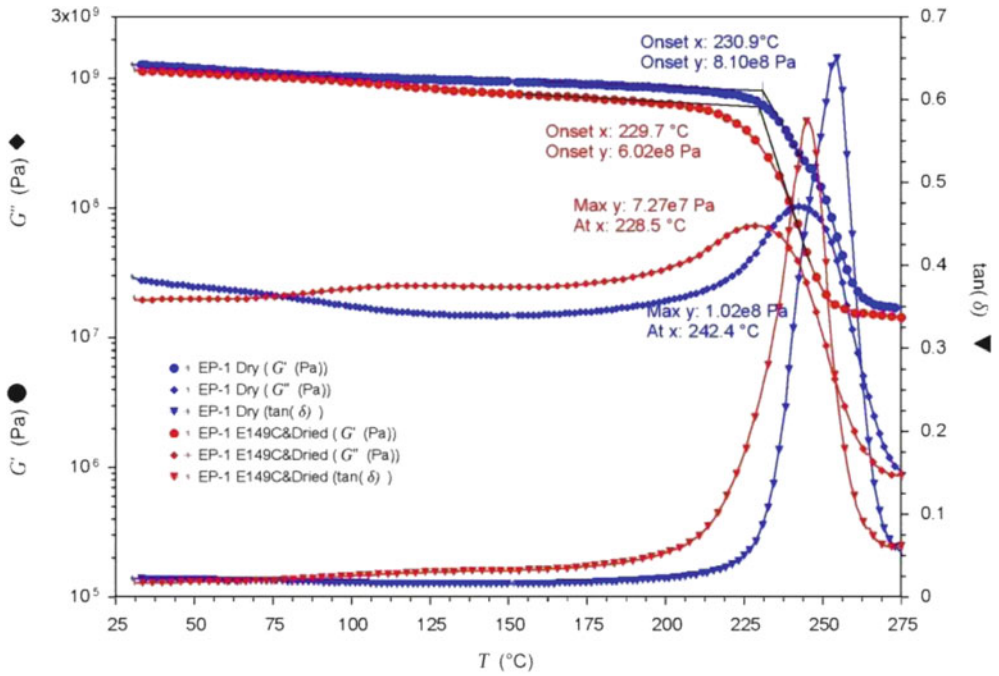

Fig. 16.14 DMA curves of EP-1 neat resin determined from a dry sample and an wet sample exposed in 3 % NaCl brine at 149 °C, 34.5 MPa for 72 h and then dried at 90 °C for 72 h

It is believed that the first transition at a lower temperature is a result of the moisture absorption in the exposed wet samples, and the measured transition temperature, 174–185 °C, is the wet T_g of the cured EP-1 resin after the hot-wet exposure. Since the first transition in modulus is only partial due to the highly cross-linked tetra-glycidyl methylene diamine network of the cured EP-1 resin, the residual material properties (stiffness and strength) of the exposed EP-1 resin may be still useful in some extent at a temperature near or above its wet T_g in a hot-wet environment. In fact, with a

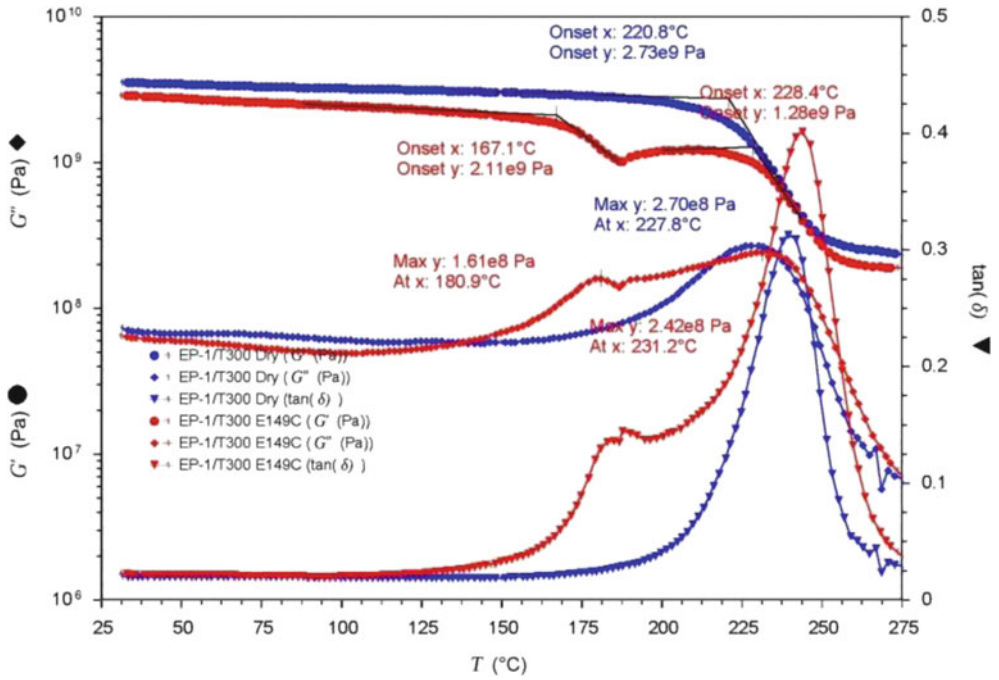

Fig. 16.15 DMA curves of EP-1/T300 composite determined in dry and in wet condition after exposure in 3 % NaCl brine at 149 °C, 34.5 MPa for 72 h

relatively thick wall design, this epoxy resin has been used as a matrix resin in composite downhole tools at 149–177 °C successfully for short-term services.

Reversible and Irreversible Processes The moisture-induced glass-transition temperature degradation is supported by the classical polymer science theories [34] and it is in general considered as a reversible, physical degradation. This can be confirmed further by recent DMA results of a 149 °C-exposed EP-1 neat resin sample after a post-drying process at 90 °C for 52 h. The DMA curves from this exposed and dried sample, presented in Fig. 16.14, show fairly good recovery in T_g and the storage modulus, and the recovered T_g are quite close to its initial dry T_g. However, any physical material structure damage introduced by the hot-wet environmental exposure will be considered as irreversible degradation that can be observed clearly from the EP-1 neat resin samples exposed at 177 °C and 204 °C, as shown in Figs. 16.1c, d and 16.2. It was observed that more extensive irreversible hygrothermal damage was introduced in the 177 °C-and 204 °C-exposed samples than in the 149 °C-exposed samples.

It is important to know that, in performing DMA for exposed wet EP-1 epoxy (or similar epoxy) samples, we should consider their overall transition behavior, including the first transition, full transition and the storage modulus drop at the onset of the transition. If one reports only the first transition temperature as the resin wet T_g, it may ignore some useful residual material properties near or above the first transition temperature and underestimate the material's performance. If one reports only the final full transition temperature as the resin T_g, it ignores the degradation from the first transition and the drying effect to the wet sample in the high heating test environment before the final transition, resulting in an overestimate of the material's performance.

Selected High-temperature Polymer Composites Measured T_gs of selected carbon fiber-reinforced epoxy composites, EP-1/T300, EP-2/AS4 and EP-3/T300, before and after the hot-wet exposure are presented in Table 16.3. Typical DMA curves measured from the EP-1/T300, EP-3/T300, PH-1/6781S, PH-2/T300, TP-1/AS4 and TP-1/S2-G composite samples before and after a HP/HT hot-wet exposure are presented in Figs. 16.15, 16.16, 16.17, 16.18, 16.19, 16.20. It is observed from the presented DMA data that the characteristics of glass transitions and the effects of moisture on the glass transitions of the composites are dependent on the type of the matrix resins.

Epoxy-matrix Composites Epoxy resins are characterized with moisture degradation in T_g and high-temperature performance. However, degree of the degradation depends on the epoxy chemistry, cure agents and other additives in resin formulations. Carbon fiber-reinforced, aromatic amine-cured tetra-functional epoxy-matrix composites, such as EP-1/T300 and EP-2/AS4, show similar glass transition behavior as that found from the EP-1 neat resin before and after the HP/HT

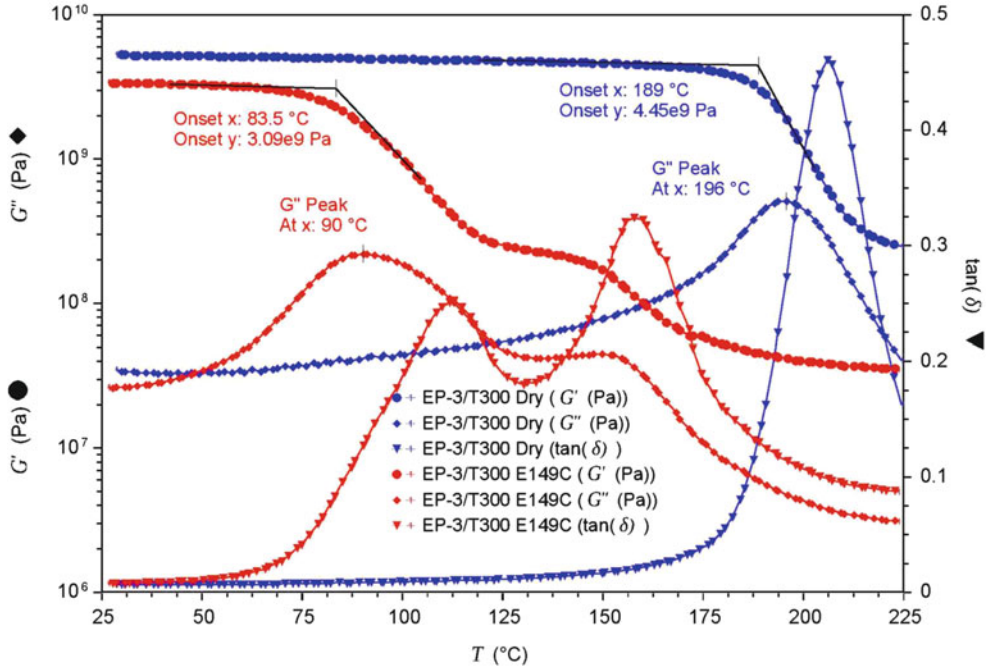

Fig. 16.16 DMA curves of EP-3/T300 composite determined in dry and in wet condition after exposure in distilled water at 149 °C, 34.5 MPa for 72 h

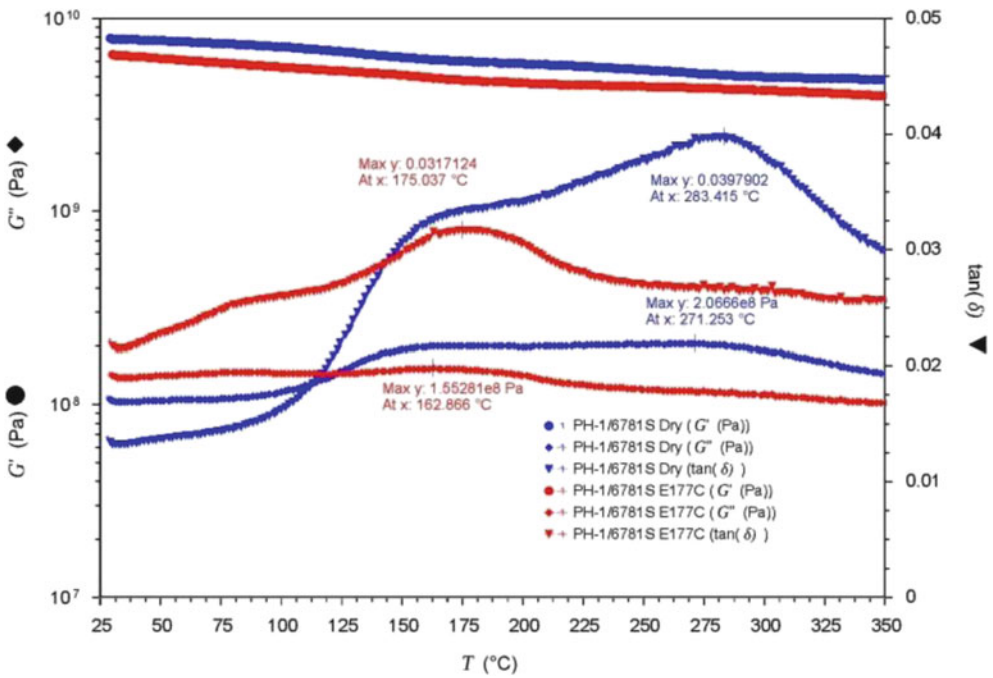

Fig. 16.17 DMA curves of PH-1/6781S composite determined in dry and in wet condition after exposure in 3 % NaCl brine at 177 °C, 34.5 MPa for 96 h

hot-wet exposure; that is, a dry sample shows only one full transition at a high temperature, while an exposed wet sample shows a partial transition at a low temperature and a full transition at a higher temperature. Typical DMA curves of EP-1/T300 composite samples before (in dry) after the hot-wet exposure at 149 °C, 34.5 MPa for 72 h are shown in Fig. 16.15, which are similar to those measured from the EP-1 neat resin sample in the same exposure and analysis conditions as presented in Fig. 16.13. Figure 16.16 presents the DMA curves measured from a carbon fiber-reinforced bi-functional,

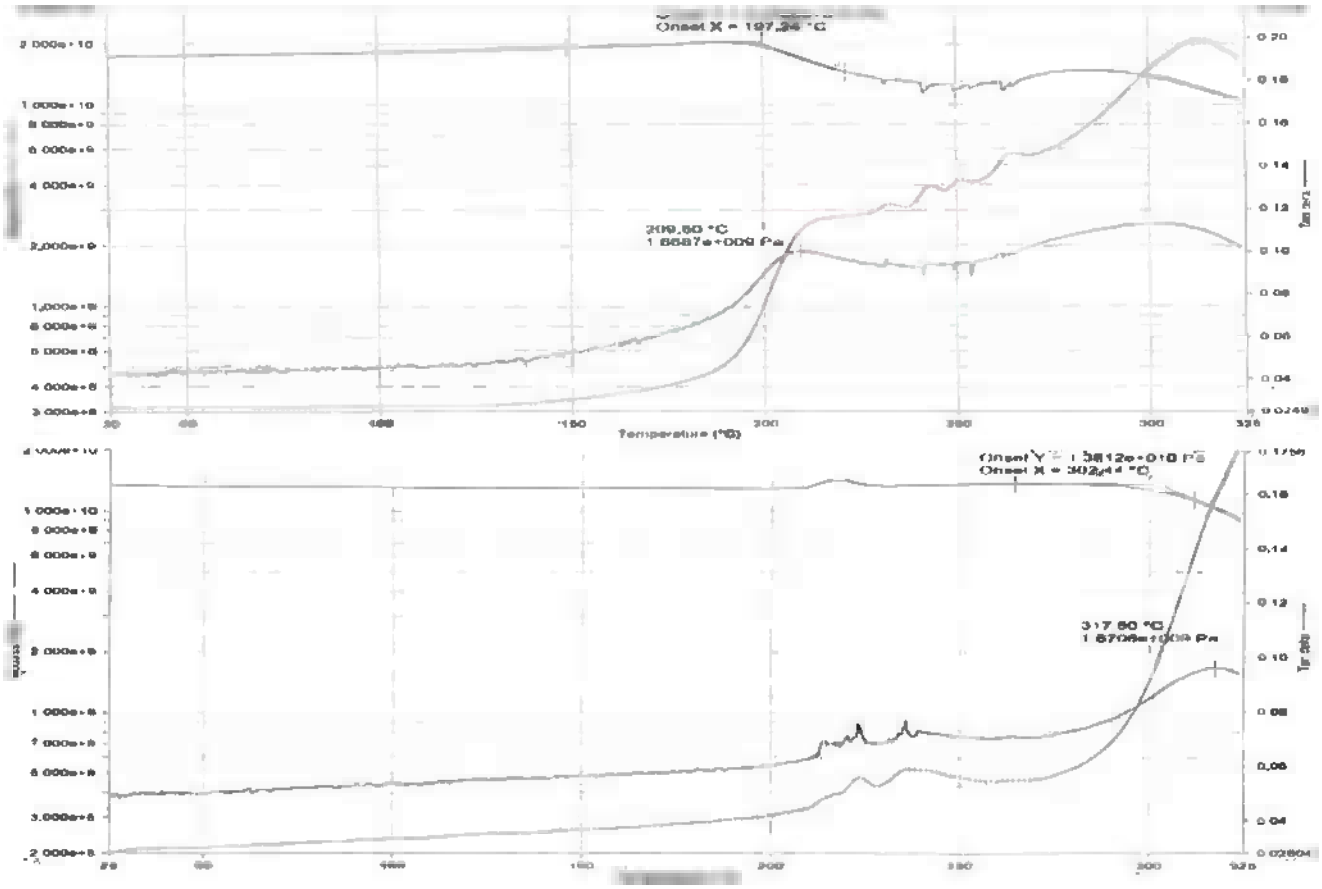

Fig 16.18 DMA curves of PH-2/T300 composite determined in dry (*top*) and in wet condition after exposure in 3 % NaCl brine at 204 °C, 34.5 MPa for 72 h

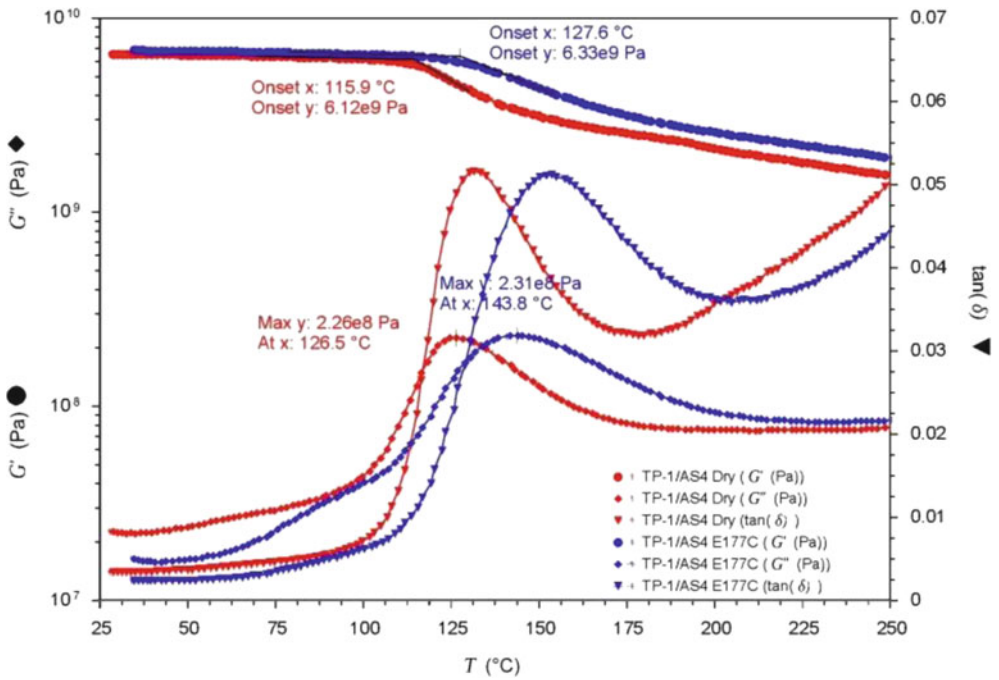

Fig. 16.19 DMA curves of TP-1/AS4 composite determined in dry and in wet condition after exposure in 3 % NaCl brine at 177 °C, 34.5 MPa for 240 h

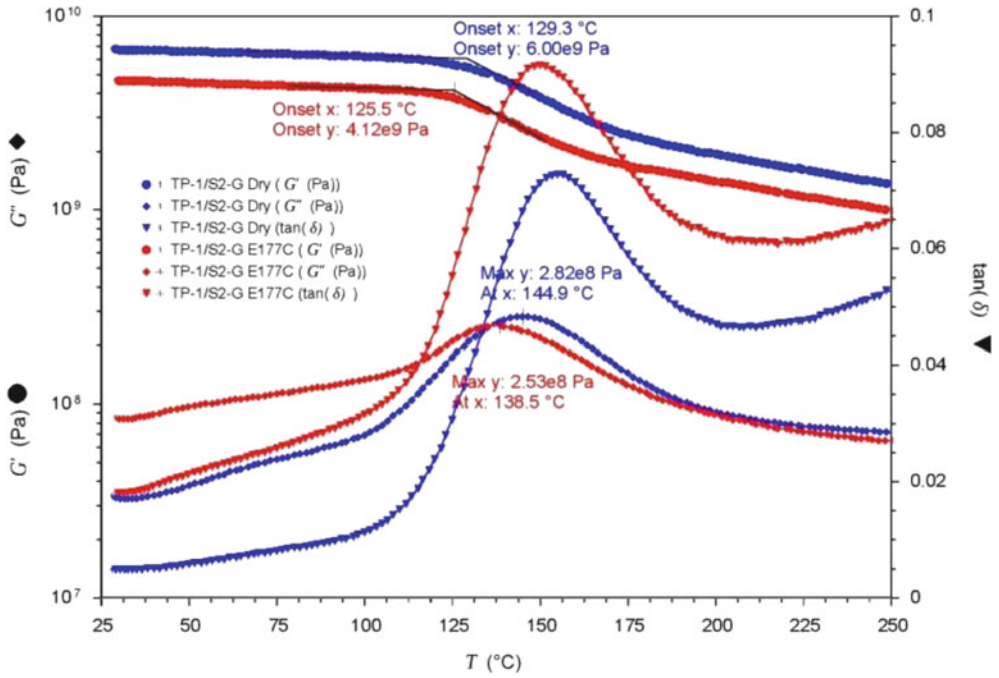

Fig. 16.20 DMA curves of TP-1/S2-G composite determined in dry and in wet condition after exposure in 3 % NaCl brine at 177 °C, 34.5 MPa for 240 h

hot-wet sensitive epoxy resin composite, EP-3/T300, before and after the hot-wet exposure in distilled water at 149 °C, 34.5 MPa for 72 h, where a very different glass transition behavior was observed with a big wet T_g shift (106 °C), deep modulus drop at the transition and no remaining mechanical properties after the transition.

Phenolic-matrix Composites Dynamic thermomechanical behavior of phenolic-matrix composites is found to be very different from that of epoxy-matrix composites. DMA T_g determination for a well cured phenolic composite has been very difficult because the measured storage modulus change with the temperature is minimal even during the "glass transitions". This behavior is shown clearly in Fig. 16.17, where the DMA curves were determined from the PH-1/6781S samples before (in dry) and after the hot-wet exposure in 3 % NaCl brine at 177 °C, 34.5 MPa for 96 h. Although we may report its dry T_g and wet T_g to be 271–283 °C and 163–175 °C, respectively, by using its loss modulus peak or tan (δ) peak, the storage modulus reduction during these transitions is minimal or undeterminable no matter the test samples were in dry or wet conditions. In the full temperature sweep range from 25 °C to 350 °C, the storage modulus reduction of the PH-1/6781S samples was less than 40 % in both dry and wet conditions. This indicates a superior high-temperature and HP/HT hot-wet environmental resistance of the cured phenolic resin network. The parallel discrepancy shown between the dry and wet storage modulus curves of the PH-1/6781S samples in Fig. 16.17 is an indication of fiber/resin interface debonding and resin phase cracking in the exposed wet sample, as shown in Fig. 16.7. Figure 16.18 presents the DMA curves of the carbon fiber-reinforced developmental phenolic composite PH-2/T300 in dry condition and wet condition after exposure in 3 % NaCl brine at 232 °C, 34.5 MPa for 72 h. Since this developmental phenolic resin was tried to be toughened by delaying its crosslink, the dry storage modulus curve showed a relatively low initial T_g at 197 °C or 209 °C and a continuous cure that raised its T_g to 302 °C. After exposure at 232 °C for 72 h, no low-level wet T_g was observed and the final T_g of the exposed sample increased to 317 °C. These test data indicated further that the HP/HT hot-wet condition would not degrade the glass-transition behavior of the phenolic composites, and served as a continuous cure process to the composites with increased glass-transition temperatures.

Thermoplastic PEEK-matrix Composites Thermoplastic PEEK resin is known to have good resistance to high heat and hygrothermal degradation because of their stable backbone chemistry and the spherulitic semi-crystalline polymer structures. The DMA curves of the carbon fiber-reinforced PEEK composite, TP-1/AS4, in dry condition and wet condition after exposure in 3 % NaCl brine at 177 °C, 34.5 MPa for 240 h are presented in Fig. 16.19. It is observed from the DMA curves that (1) the dry and wet storage modulus curves before their transitions are almost overlapping indicating a minimal material structural damage was introduced (good fiber/resin bonding maintained) during the hot-wet exposure; (2) the transitions are short and gradual and the storage modulus curves are relative flat, indicating certain mechanical properties

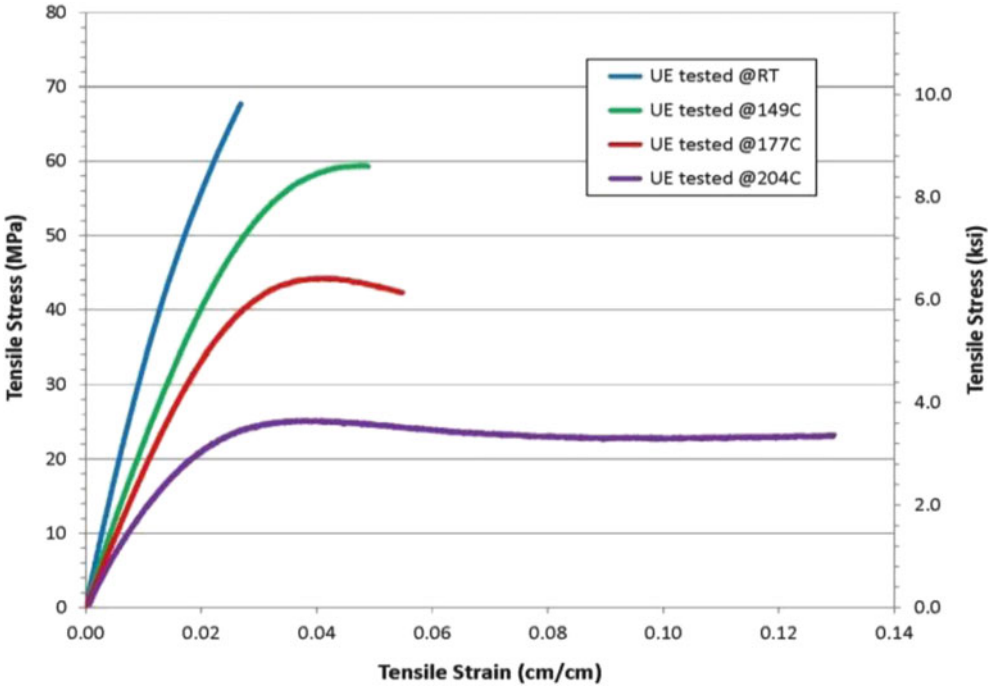

Fig. 16.21 Tensile stress–strain curves of unexposed EP-1 neat resin specimens tested at RT, 149 °C, 177 °C and 204 °C

remained after their dry and wet T_gs; (3) the wet T_g (G″ peak) was determined as 17 °C below its dry T_g at 144 °C and the wet storage modulus curve after the transition is still quite close to the dry storage modulus curve indicating an insignificant effect of the hot-wet condition on the thermomechanical performance. Figure 16.20 presents the DMA curves of the S2-glass fiber-reinforced PEEK composite, TP-1/S2-G, in dry and wet conditions before and after exposure in 3 % NaCl brine at 177 °C, 34.5 MPa for 240 h. Since the matrix resin in TP-1/S2-G is the same PEEK resin in TP-1/AS4 composite, the glass transition behavior of the TP-1/S2-G composite in dry and wet conditions is similar to that of the TP-1/AS4 composite with a small wet Tg shift and gradual or relatively flat transitions. However, unlike in the analysis for TP-1/AS4, the discrepancy between the dry and wet storage modulus started from the beginning of the analysis at ambient temperature and kept nearly parallel through the analysis. This indicates glass fiber/resin interface debonding in the TP-1/S2-G samples during the 240 h hot-wet exposure, as shown in Fig. 16.10 in previous section.

16.3.3 Mechanical Properties

Tensile Properties of EP-1 Epoxy Neat Resin Tensile tests of the cured EP-1 epoxy neat resin were conducted at room temperature (RT), 149 °C, 177 °C and 204 °C before and after the hot-wet exposure in 3 % NaCl brine under 34.5 MPa at 149 °C, 177 °C and 204 °C for 72 h, respectively.

Typical temperature-dependent tensile stress–strain curves of the unexposed EP-1 neat resin specimens are presented in Fig. 16.21. From these curves we can see that the tensile strength retention of the cured neat resin is excellent at 149 °C (~90 %), good at 177 °C (~68 %), and marginal at 204 °C (~38 %); and the cured neat resin shows its brittleness at RT with very limited tensile strain at break (2.6 %) and its ductility when the test temperature reaches 149 °C or higher.

Typical tensile stress–strain curves of the EP-1 neat resin specimens tested at RT and the corresponding exposure temperatures after exposure in the brine at 149 °C, 177 °C and 204 °C, respectively, along with the stress–strain curves of the unexposed specimens tested at RT, 149 °C and 177 °C, are plotted in Fig. 16.22. For easy comparison, the measured temperature-dependent tensile strengths at RT, 149 °C, 177 °C and 204 °C before and after the hot-wet exposure at 149 °C, 177 °C and 204 °C, along with the room-temperature tensile strengths of the exposed specimens are plotted in Fig. 16.23. According to the tensile test data presented in Figs. 16.22 and 16.23, the following discussion is given:

(1) The results show insignificant degradation in room-temperature tensile strength and modulus of the neat resin specimens after the 149 °C and 177 °C exposure, but severe degradation in tensile strength after the 204 °C exposure (25 % retention only) because of substantial leaching and severe hygrothermal cracking occurred in the specimens after

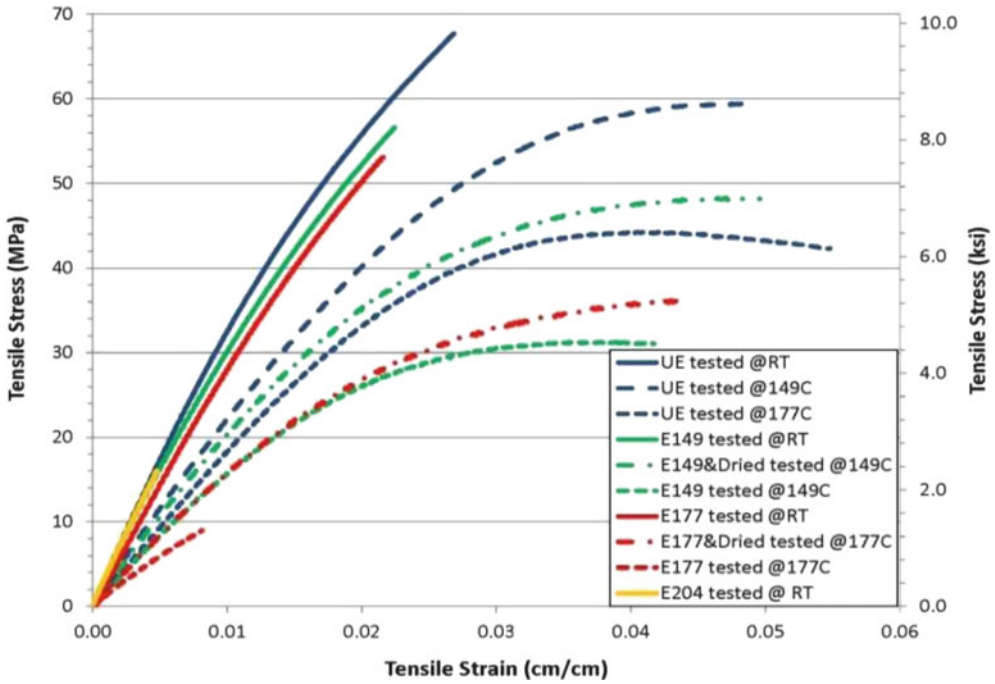

Fig. 16.22 Tensile stress–strain curves of unexposed and exposed EP-1 neat resin specimens tested at RT and the corresponding exposure temperatures

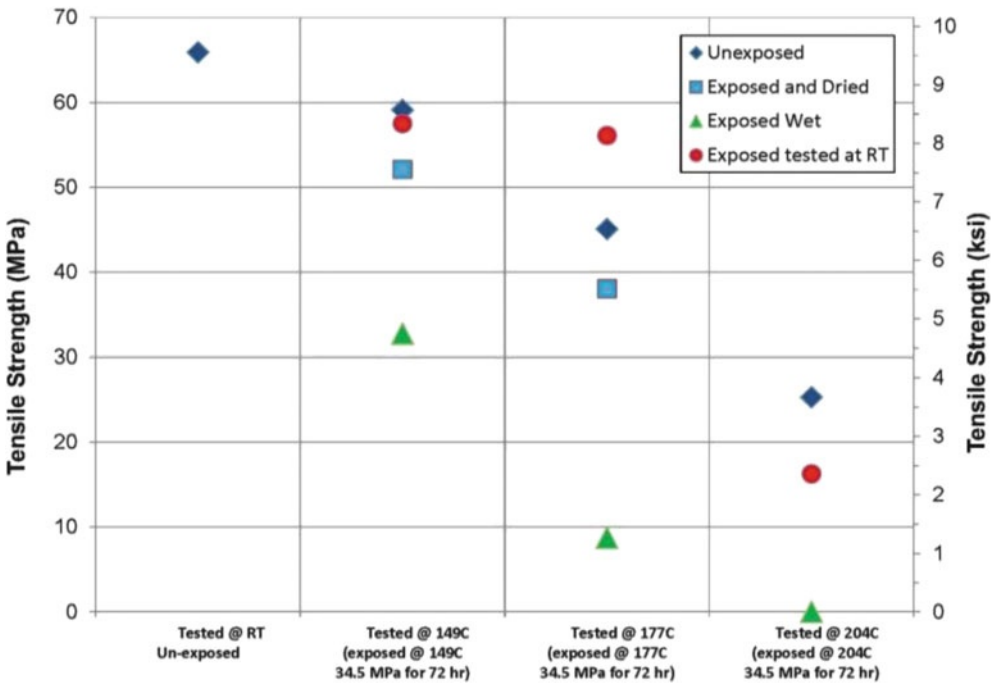

Fig. 16.23 Temperature-dependent tensile strengths of EP-1 neat resin before and after exposure in 3 % NaCl brine at 149 °C, 177 °C or 204 °C under 34.5 MPa for 72 h, with and without drying

204 °C exposure, as shown in Figs. 16.1d and 16.2. These results also suggest minimal structural damage was introduced in the test specimens after the 149 °C and 177 °C hot-wet exposures. (2) Specimens after 149 °C or 177 °C exposure show severe degradation in tensile strength when tested at 149 °C and 177 °C. Mechanisms for these high-temperature mechanical property loss of the EP-1 neat resin after the HP/HT hot-wet exposure may involve the reduction in resin T_g and the

Fig. 16.24 Through-thickness polarized photograph of two 177 °C exposed EP-1 neat resin specimens shows difference in internal cracking: *upper* – as exposed wet specimen; *lower* – exposed and then heated in an oven at 177 °C for 20 min

development of the micro damage in the test materials due to the uneven swelling and surface crazing from the hot-wet exposure [13, 19]. Besides these, severe hygrothermal blistering damage was identified in the 177 °C-exposed tensile specimens after the dry pre-heating in the 177 °C tests. Evidence of the blistering damage in a 177 °C-exposed specimen after 20 min dry heating in an oven at 177 °C is shown in Fig. 16.24. This additional damage introduced from improper test method reduced further the tensile strength of the 177 °C-exposed specimens**.** No blistering damage was identified with a careful examination in a 149 °C-exposed neat resin specimen after 20 min direct heating cycle in an oven at 149 °C.

To eliminate the blistering damage in the test specimens during the high-temperature tensile tests, the exposed wet specimens were first dried in an oven at 90 °C for 52 h, and then tested at the elevated temperatures. Tensile stress–strain curves and tensile strengths at 149 °C and 177 °C of the 149 °C- and 177 °C-exposed specimens after drying process are also presented in Figs. 16.22 and 16.23, respectively. From these test data we can see that the neat resin specimens after the 149 °C exposure lost their tensile strength at 149 °C by about 45 %, but a drying process recovered this loss by about 75 %. This may suggest that the degradation in mechanical properties at 149 °C of the EP-1 neat resin after the 149 °C exposure is basically a moisture-induced reversible process since no additional dry-heating-induced damage was identified in the 149 °C-exposed specimens. But for the test results at 177 °C of the specimens involving the 177 °C exposure, the same is not the case since sample leaching during the hot-wet exposure and the specimen hygrothermal blistering during the dry preheating in the 177 °C test were involved.

Tensile Properties of Selected Polymer Composites Measured tensile strength of the TP-1/AS4, TP-1/S2-G, EP-1/T300, EP-1/6781S, EP-1/7781E, HP-2/T300 and PH-1/6781S composites at RT, 177 °C and 204 °C before and after the HP/HT hot-wet exposure at 177 °C and 204 °C for 240 h or 168 h (except PH-2/T300 specimens exposed at 204 °C for 72 h) are plotted in Fig. 16.25, respectively. It is observed from the chart that the tensile strength retention of the carbon fiber-reinforced composites, TP-1/AS4, EP-1/T300 and PH-2/T300, are all fairly good at 177 °C and 204 °C before and after the hot-wet exposure since the tensile strength in a principal fiber direction of a continuous fiber-reinforced composite is a fiber-dominated property and the carbon fibers possess excellent high-temperature and hot-wet environmental resistance. In contrast to the carbon fiber-reinforced EP-1 and TP-1 composites, tensile strengths of the glass fiber-reinforced EP-1 and TP-1 composites, EP-1/6781S, EP-1/7781E and TP-1/S2-G, dropped 70–80 % and 45–55 %, respectively, after the hot-wet exposure at 177 °C, 34.5 MPa for 240 h. This indicates that the glass fibers in the EP-1- and even TP-1-matrix composites were attacked severely by the hot-wet environment through resin phase diffusion and fiber/resin interface capillary action, and consequently resulted in loss of tensile strength of the glass fiber-reinforced composites. After the HP/HT hot-wet exposure at 177 °C and 204 °C, similar degradation in tensile strength of the S2-glass fiber-reinforced phenolic composite, PH-1/6781S, is also observed from the chart in Fig. 16.25. This degradation, however, was found to be much less severe than that of the S2-glass fiber-reinforced epoxy composite EP-1/6781S in the same exposure and test conditions. It was observed that the tensile strength of the PH-1/6781S composite in initial unexposed condition was much lower than that of the EP-1/6781S composite, but found to be much higher than that of the EP-1/6781S composite after the 177 °C hot-wet exposure. These results may imply that the phenolic resin can provide more effective protection to the glass fibers in the composite than the epoxy resin, or when the glass fibers become very weak under a HP/HT hot-wet condition, the hot-wet resistant phenolic resin phase in the glass/phenolic composite may play a more important role.

Compression Properties of Selected Polymer Composites Measured compressive strengths are presented in Fig. 16.26 for the TP-1/AS4, TP-1/S2-G, EP-1/T300, EP-1/6781S, EP-1/7781E, HP-2/T300 and PH-1/6781S composites at RT, 177 °C and 204 °C before and after the HP/HT hot-wet exposure at 177 °C and 204 °C for 240 h or 168 h (except PH-2/T300

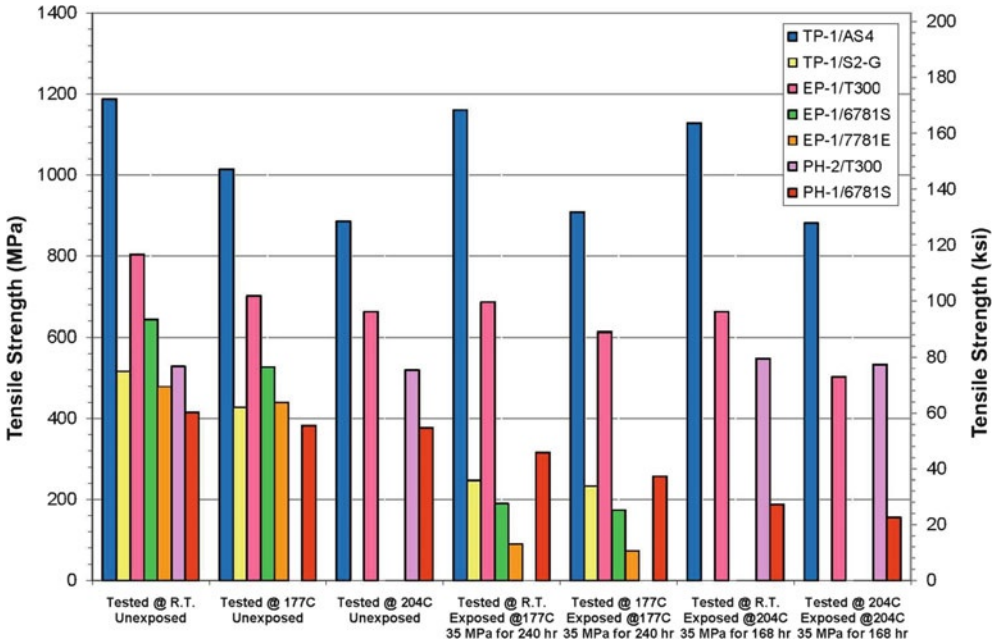

Fig. 16.25 Measured tensile strengths of selected composites TP-1/AS4, EP-1/T300, EP-1/6781S, EP-1/7781E, PH-2/T300 and PH-1/6781S at RT, 177 °C and 204 °C before and after the specified HP/HT hot-wet exposure

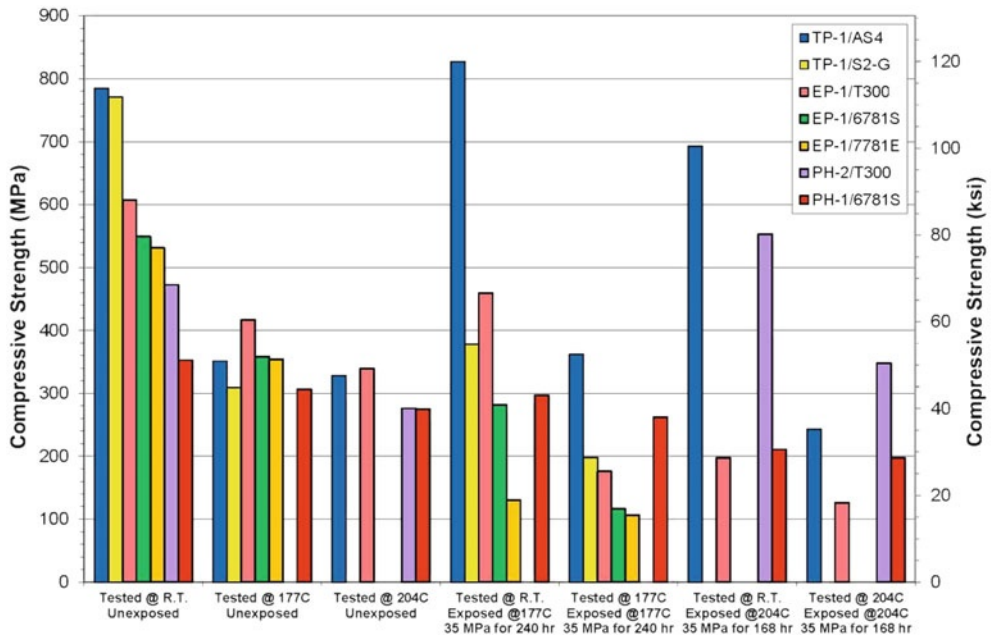

Fig. 16.26 Measured compressive strengths of selected composites TP-1/AS4, EP-1/T300, EP-1/6781S, EP-1/7781E, PH-2/T300 and PH-1/6781S at RT, 177 °C and 204 °C before and after the specified HP/HT hot-wet exposure

specimens exposed at 204 °C for 72 h), respectively. From the data presented in Fig. 16.26, we can see that the temperature effects on compressive strengths of the composites are more significant than the effects on tensile strengths and the effects are more dependent on the type of matrix resins since the compressive strength of a composite is a matrix-dominated property especially when tested at an elevated temperature.

It is noted that room-temperature compressive strength retention of the EP-1/T300 composite after the hot-wet exposure at 121 °C and 177 °C for 240 h was as high as 93 % (566 MPa) and 76 % (460 MPa), respectively. However, when the

exposed wet specimens were tested at 177 °C, the compressive strengths were reduced dramatically to only about 172 MPa (30 % retention) even if the composite is reinforced by the carbon fibers. The reason causing this phenomenon may involve that the moisture absorbed in the EP-1 epoxy resin phase in the exposed EP-1/T300 specimens reduced its T_g from about 221 °C in dry to about 167 °C in wet, and the test temperature at RT was far below its wet T_g, but the test temperature at 177 °C was above its wet T_g. This moisture induced degradation in T_g and mechanical properties may be considered as a reversible physical effect for certain material systems under a relatively low exposure and testing temperature. However, in the case of the EP-1/7781E and EP-1/6781S composites after the hot-wet exposure at 177 °C for 240 h and in the case of the EP-1/T300 composite after the exposure at 204 °C for 168 h, the room-temperature compressive strength retention was no longer high, only about 25 %, 50 % and 32 %, respectively. The exposure-induced compressive-strength losses will no longer be considered as reversible because significant irreversible hygrothermal or hydrolytic damage in glass fibers, epoxy resin phase or at the fiber/resin interfaces are involved as we discussed and illustrated in the previous sections. It is noted that, when the exposure temperatures and the mechanical test temperatures are at or above 177 °C, the dry preheating to the exposed wet EP-1/T300 test specimens serves as a thermal impact and generates additional hygrothermal structural damage in the test specimens [2], which affects reversely the test results. This is a test method issue associated with the current environmental-mechanical test method, and it is true with any brittle thermosetting polymer-matrix composites.

It is encouraging to see from the chart that although the initial room-temperature compressive strength of the glass fiber-reinforced phenolic composite, PH-1/6781S, was much lower than that of the carbon fiber-reinforced epoxy composite, EP-1/T300, after the 177 °C hot-wet exposure, its compressive strength at 177 °C became much higher than that of the EP-1/T300 composite with a retention rate about 75 %. This is obviously attributed to the outstanding HP/HT hot-wet resistance of the PH-1 phenolic resin matrix as illustrated in the previous sections. It is also encouraging to see that the carbon fiber-reinforced developmental phenolic composite PH-2/T300 shows a significant improvement in compressive strength at RT and 204 °C after the 204 °C HT/HP hot-wet exposure. This improvement may be resulted from the continuous curing effect of the PH-2 phenolic resin phase during the hot-wet exposure and the toughening effect of the wet condition to the phenolic resin matrix. It was the first time that the compressive strength of a polymer-matrix composite at 204 °C reached 50 ksi after exposure in 3 % NaCl brine at 204 °C, 34.5 MPa for 72 h even though the current test method may have introduced a reverse effect.

Finally, It can be seen from the chart that the carbon fiber-reinforced PEEK composite, TP-1/AS4, possesses a high compressive strength at room temperature and excellent hot-wet environmental resistance with no degradation in compressive strength at 177 °C after the 177 °C exposure and very limited degradation in compressive strength at 204 °C after the 204 °C exposure. This outstanding hot-wet mechanical performance is supported by the combined outstanding hot-wet resistance of PEEK resin, carbon fibers and their bonding interfaces. However, compressive strength retention of the TP-1/AS4 composite at 177 °C and 204 °C, no matter before or after the hot-wet exposure, was found to be only 35–47 % because of the relatively low T_g of the TP-1 resin that is way below the test temperatures. Compressive strengths at RT and 177 °C of the S2-glass reinforced PEEK composite, TP-1/S2-G, in dry condition are very similar to those of the carbon fiber-reinforced TP-1/AS4 composite; however, after the 177 °C hot-wet exposure, the compressive strengths of the TP-1/S2-G composite at RT and 177 °C are only 48–55 % of the ones of the TP-1/AS4 composite, also due to the week hot-wet resistance of the glass fibers and the relatively weak interface bonding between the glass fiber and PEEK resin.

HP/HT In-situ Thermomechanical Test System and Test Method It has been identified in the current environmental-mechanical tests that the dry preheating to the exposed neat resin and composite specimens in the high-temperature mechanical tests serves as a thermal impact and may introduce additional hygrothermal damage in the exposed test specimens prior to the mechanical tests. Besides this, additional thermal and pressure cycles during the specimen transfer between the environmental aging and post-aging mechanical testing may introduce additional damage in the test specimens. The mechanical test environment in a regular test machine is usually very different from the exposure condition, where the exposed test specimens are subjected to a drying process and the effect of the hydrostatic pressure is omitted. These issues are also found in the current DMA thermal analysis procedures for exposed wet samples. All these problems with the current environmental-thermal-mechanical test methods may produce inaccurate or incorrect test results. To eliminate all the problems with the current test method and to simulate the test environment more closely to the real HP/HT downhole condition, an innovative HP/HT in-situ thermomechanical test system has been developed and constructed and the associated HP/HT in-situ thermomechanical testing and analysis methods have been established at Baker Hughes [28, 29].

The HP/HT in-situ thermomechanical test system was designed to contain the HP/HT environmental chamber and the mechanical test load frame. This enables conducting various thermomechanical tests and analyses directly in a simulated HP/HT fluid and gas environment. As illustrated in Fig. 16.27, the HP/HT in-situ test system consists of an HP/HT autoclave, a controlled cell oven, a hydraulic driving system, a mechanical test load frame, a high-pressure gas source and a nitrogen pressure control system. The autoclave can accommodate the in-situ tensile load frame, standard or custom test fixtures

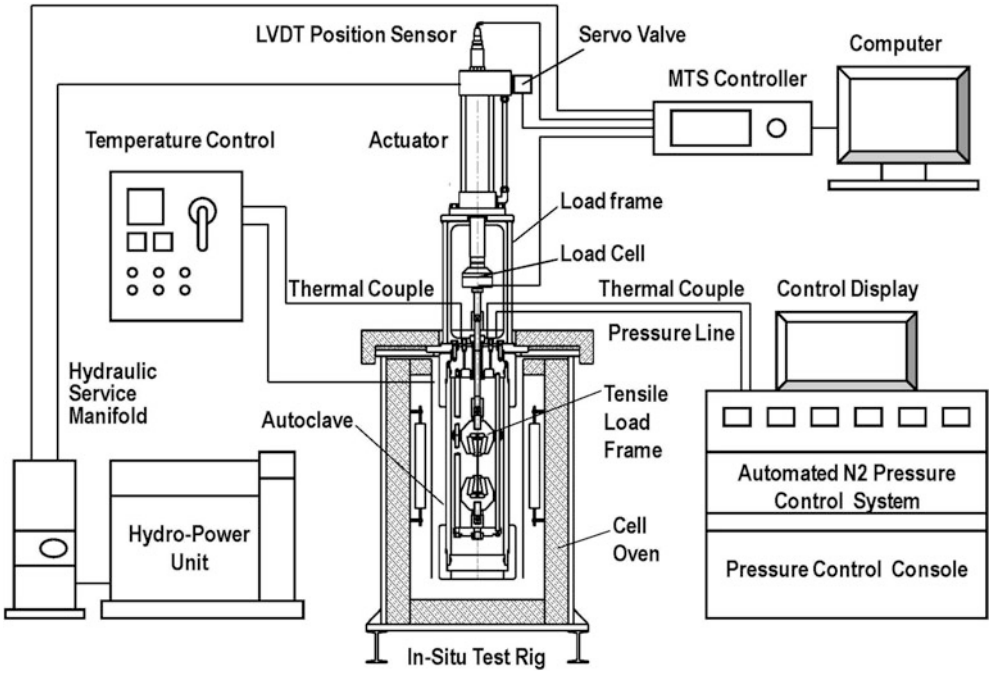

Fig. 16.27 Schematic of the HP/HT in-situ thermomechanical test system with the associated hydraulic, heating, gas pressure and control systems

for compression, shear and flexural tests, and the environmental medium under a HP/HT condition. The hydraulic driving system includes an actuator, a servo valve, a service manifold and a hydraulic power unit. The load frame connects the hydraulic actuator and the loading train. The hydraulic driving system and the mechanical test frame are controlled by a full-functional controller for operation and data acquisition. The nitrogen pressure control system can control the autoclave pressure accurately within ±0.035 Mpa. This HP/HT in-situ test system is capable of performing standard and custom tensile, compression, shear and flexural tests in a simulated HP/HT fluid and gas environment up to 260 °C and 70 MPa. It can also be used in dynamic oscillation mode as a dynamic mechanical-thermal analyzer to determining the wet T_gs of the high-temperature polymers and composites in a pressurized hot-wet environment. The HP/HT in-situ test system and the associated test methods can provide critical and accurate true test data for polymer and composite applications in HP/HT downhole environments and for related scientific investigations. Multiple HP/HT in-situ thermomechanical test systems are currently constructed and in operation at Baker Hughes and generating reliable HP/HT in-situ test data for various high-performance polymers and composites for various critical applications.

16.4 Summary and Conclusions

Comprehensive studies in water absorption, sample leaching, hygrothermal structural damage, thermal and mechanical properties of the selected neat resin and fiber-reinforced polymer composites were conducted associated with an HP/HT hot-wet environmental exposure process. Based on the experimental and analysis results, the following conclusions may be drawn:

1. Water absorption and moisture distribution in a polymer resin or polymer composite in an HP/HT aqueous environment may not obey the common diffusion law since sample leaching and irreversible hygrothermal structural damage in the sample material may occur during the high-temperature hot-wet exposure.
2. Besides water absorption, substance leaching is considered as another major indication of hygrothermal degradation of the polymer resins and composites in an HP/HT aqueous environment. Thermoplastic PEEK resin and its carbon fiber-reinforced composites were found to have minimal water absorption and no sample leaching after the hot-wet exposure up to 204 °C indicating a stable chemistry of the PEEK resin.
3. No effect of hydrostatic pressure on water absorption in composites was found in the current HP/HT hot-wet exposure condition up to 70 MPa.

4. Carbon fibers possess excellent resistance to high temperature and HP/HT hot-wet environments; they are the best reinforcement fibers for HP/HT hot-wet resistant composites providing high mechanical strength and long-term performance. Glass fibers are susceptible to hygrothermal and hydrolytic degradations and fail to resist HP/HT hot-wet environment; they can only be used in composites in hot-wet environment below 177 °C for short-term applications.
5. An HP/HT hot-wet environment presents significant challenges to most high-temperature polymers due to moisture-induced thermomechanical degradation, hygrothermal structural damage and hydrolytic scission. Polyimides and cyanate ester, as well as BMI, contain imide rings, amide group and ester linkages that are susceptible to hydrolytic scission. Epoxy resins, in general, are subject to substantial T_g shifting when contacting a hot-wet condition and lose their high-temperature mechanical properties. PEEK resin has excellent HP/HT hot-wet resistance and good mechanical retention in the hot-wet environment, but with limited temperature capability for composite structural applications. Phenolic resins are found to possess the best HP/HT hot-wet resistance and the best high-temperature capability. Carbon fiber-reinforced phenolic or PEEK composites are found to possess the best resistance to the HP/HT hot-wet environment.
6. Torsional DMA with a relatively large sample size is a valid analysis technique to determine the resin T_g and characterize the thermomechanical behavior of polymers and polymer composites involving wet conditions although some limitations are still present with the commercial DMA technology.
7. The conventional environmental-thermal-mechanical test procedure and the test methods have been identified with inherent drawbacks and may produce inaccurate or incorrect test results. To eliminate the problems with the current HP/HT environmental-mechanical test method, an innovative HP/HT in-situ thermomechanical testing and analysis system and the associated test methods have been developed and established.

Acknowledgements The authors would like to thank Baker Hughes Completions and Production Technology for their permission to publish this paper. The authors would like to express sincere appreciation to Bennett Richard, director research and technology for his constant support and encouragement to the research projects. Thanks also due to Chris Campo for his assistance in a part of the DMA work.

References

1. Yusheng Yuan, Goodson J (2001) Progress and challenges of composite applications in downhole operations. In: Proceedings of the third MERL conference on oilfield engineering with polymers, London, pp 99–112, 28–29 Nov 2001
2. Yusheng Yuan, Goodson J (2004) Advanced composite downhole applications and HP/HT environmental challenges. Paper 04616, corrosion-2004, NACE international 59th annual conference & exposition, New Orleans, 28 Mar–1 Apr 2004
3. Yusheng Y, Goodson J (2007) Hot-wet downhole conditions affect composite selection. Oil Gas J 105(34):52–63
4. Daniel RR (2001) Hygrothermal behavior. In: ASM handbook. Composites, vol 21. ASM International, Material Park, Ohio, pp 246–251
5. Siskin M, Katritzky A. Overview of the reactivity of organics in superheated water: geochemical and technology implications, pp 324–330
6. API 15HR (2001) Specification for high pressure fiberglass line pipe, third edition. American Petroleum Institute, Washington, DC 20005
7. Feechan M, Makselon C, Nolet S (2003) Field experience with composite coiled tubing. SPE 82045, the SPE/IcoTA coiled tubing conference in Houston
8. Mike P (2012) High-pressure/high-temperature challenges. SPE J Petrol Technol 64(4):120
9. Mckague EL Jr, Halkias JE, Reynolds JD (1975) Moisture in composites: the effect of supersonic service on diffusion. J Compos Mater 9:2–9
10. Shirrell CD, Halpin J (1977) Moisture absorption and desorption in epoxy composite laminates. Compos Mater Testing Design ASTM STP 617:514–528
11. DeIasi R, Whiteside JB (1978) Effect of moisture on epoxy resins and composites. In: Vinson JR (ed) Advanced composite materials-environmental effects, ASTM STP, ASTM, Philadelphia, PA 19103, vol 658, pp 2–20
12. Ashbee KHG, Frank FC, Wyatt RC (1967) Water damage in polyester resin. Proc Royal Soc London A 300:415–419
13. Browning CE (1976) The mechanisms of elevated temperature property losses in high performance structural epoxy resin matrix materials after exposure to high humidity environments. Ph.D. dissertation, University of Dayton, Dayton
14. Lee Mckague E Jr, Reynolds JD, Halkias JE (1978) Swelling and glass transition relations for epoxy matrix material in humid environments. J Appl Polymer Sci 22:1643–1654
15. Roger JM (1980) Structure–property relationships and environmental sensitivity of epoxies. In: Pritchard G (ed) Developments in reinforced plastics, vol 1, Chapter 7. Applied Science Publishers, London, pp 211–229
16. Abeysinghe HP, Edwards W, Pritchard G, Swampillai GJ (Nov. 1982) Degradation of crosslinked resins in water and electrolyte solutions. Polymer 23:1785–1790
17. Browning CE, Husman GE, Whitney JM (1977) Moisture effects in epoxy matrix composites. Compos Mater Test Des ASTM STP 617:481–496
18. Ashbee KHG, Wyatt RC (1969) Water damage in glass fiber/resin composites. Proc Royal Soc London A 312:553–564
19. Ishai O, Mazor A (1974) The effect of environmental-loading history on longitudinal strength of glass-fiber reinforced plastics. Rheologica Acta 13:381–394
20. Robert EL (1964) Glass fibers for high-strength composites. In: Broutman LJ, Krock RH (ed) Modern composite materials, Chapter 11. Addison-Wesley, Reading, Massachusetts

21. Metcalfe AG, Gulden ME, Schmitz GK (1971) Spontaneous cracking of glass filaments. Glass Technol 12:15–23
22. Jones FR, Rock JW, Bailey JE (1983) The environmental stress corrosion cracking of glass fiber-reinforced laminates and single E-glass filaments. J Mater Sci 18:1059–1071
23. Morgan RJ, Shin EE, Lincoln JE, Zhou J, Drzal LT, Wilenski MS, Lee A, Curliss D (1998) Durability characterization of bismaleimide and polyimide-carbon fiber composites, In: Proceedings of the 43rd international SAMPE symposium, Anaheim, pp 106–119, 31 May–4 June 1998
24. Morgon RJ, Shin EE, Zhou J, Zhou J (1999) High-temperature polymer matrix-carbon fiber composites – performance issues and future needs. In: Proceedings of the 44th international SAMPE symposium, Long Beach, pp 1098–1110, 23–27 May 1999
25. Shin EE, Morgon RJ, Zhou J, Sutter JK, Meador MA (1999) High-temperature polymer matrix-carbon fiber composites – critical degradation mechanisms and test methodologies. In: Proceedings of the 44th international SAMPE symposium, Long Beach, pp. 2382–2396, 23–27 May 1999
26. Yusheng Y, Goodson J, Rihong F (2013) HP/HT Hot-wet resistance of thermoplastic PEEK and its composites. In: Composite materials and joining technology for composites, vol 7 – proceedings of the 2012 annual conference on experimental mechanics. Springer, New York, pp 161–177
27. Yusheng Yuan, Goodson J, Sequera D, Zhu J (2013) Advanced HP/HT hot-wet resistant composites for extreme downhole applications. In: Proceedings of Smithers Rapra 2013 high-performance polymers for oil & gas, Houston, 9–11 Apr 2013
28. Yusheng Yuan, Goodson J (2007) HT/HP hot-wet thermomechanical properties and HT/HP in-situ mechanical test method of high-temperature polymer composites. In: Proceedings of the 52nd international SAMPE symposium and exhibition, Baltimore, 3–7 June 2007
29. Yusheng Yuan, Goodson J (2008) HTHP in-situ mechanical test rig and test method for high-temperature polymers and composites. In: SPE 113516, proceedings of the 2008 SPE Europec/EAGE annual conference and exhibition, Rome, 9–12 June2008
30. Avena A, Bunsell AR (1988) Effect of hydrostatic pressure on the water absorption of glass fiber-reinforced epoxy resin. Composites 24:355–357
31. Hale JM, Gibson AG (1998) Coupon tests for fibre reinforced plastics at elevated temperatures in offshore processing environments. J Compos Mater 32(4):387–404
32. Hale JM, Gibson AG, Speake SD (1998) Tensile strength testing of GRP pipes at elevated temperatures in aggressive offshore environments. J Compos Mater 32(10):969–985
33. Rose JB, Staniland PA (1982) Thermoplastic aromatic polyetherketone. US Patent # 4,320,224, 16 Mar 1982
34. Bueche F (1962) Physical properties of polymers. Interscience, New York

Chapter 17
Effect of Ply Dispersion on Failure Characteristics of Multidirectional Laminates

B.T. Werner, J.D. Schaefer, and I.M. Daniel

Abstract The influence of layer thickness and ply interdispersion was investigated on the failure characteristics of multidirectional laminates. The composite material investigated was a high strength carbon fiber composite with a toughened epoxy matrix (IM7/8552). The basic unidirectional material was fully characterized in a previous study under static and dynamic loading conditions. In this study the investigation was extended to angle-ply laminates with varying layer thickness while including the effects of residual stresses. Intralaminar and interlaminar failure mechanisms were observed and found to be strongly related to the layer thickness for the same layup. For thin layer thicknesses failure modes included fiber breaks resulting in higher ultimate strengths. For thicker layers consisting of multiple stacked parallel plies, more matrix dominated intralaminar and interlaminar failures were observed resulting in lower ultimate strengths. This trend reaches a lower limiting plateau as the layer thickness increases. Failure modes and ultimate strengths were further investigated as a function of strain rate. All results were evaluated by the recently developed Northwestern (NU) failure theory.

17.1 Introduction

Classical lamination theory makes the assumption that all of the layers within a laminate are in a state of plane stress, therefore all out-of-plane stress components are zero, $\sigma_z = \tau_{xz} = \tau_{yz} = 0$. However, for composite parts that contain geometric discontinuities, such as free edges, interlaminar stresses can develop from mechanical or hygrothermal loadings. These interlaminar stresses can cause delaminations which may severely reduce the strength of the laminate [1]. In $[\pm \theta]_s$ angle-ply laminates under axial tensile stress $\bar{\sigma}_x$, each layer is subjected to the same axial stress, $\sigma_x = \bar{\sigma}_x$. Due to the off-axis orientation of adjacent layers, θ and-θ, and the resulting shear coupling from the axial stress, each layer will undergo shear deformations of opposite sign (Fig. 17.1). When bonded into a laminate, each layer must have zero shear strain so significant interlaminar shear stress, τ_{xz}, is developed to counteract the shear strain introduced by the shear coupling from the axial stress.

This shear stress forces the layer into alignment with the laminate and varies across the width of the specimen where it is zero over much of the interior while peaking near the edges (Fig. 17.2). The moment produced by τ_{xz} is equilibrated by the intralaminar shear stress τ_{xy} which acts on the transverse cross section of the layer. The intralaminar stresses are constant over most of the central region and drop to zero at the edges (Fig. 17.2) [3, 4].

By adjusting the normalized layer thickness of the laminate, the effects of the interlaminar stresses on failure can be mitigated. The magnitude of τ_{xz} is related to the layer thickness as the dimension d in Fig. 17.2 is on the order of the layer thickness. The objective of this study was to investigate the effect of normalized layer thickness on the failure strength and failure mode of a $[20/\text{-}20]_s$ carbon/epoxy composite subjected to uniaxial tension. Results are compared with the Northwestern (NU) failure theory prediction and the effect of strain rate on strength were measured.

B.T. Werner (✉) • J.D. Schaefer • I.M. Daniel
Northwestern University, Evanston, IL, USA
e-mail: bwerner@u.northwestern.edu; josephschaefer2011@u.northwestern.edu; imdaniel@northwestern.edu

G.P. Tandon et al. (eds.), *Experimental Mechanics of Composite, Hybrid, and Multifunctional Materials, Volume 6*, Conference Proceedings of the Society for Experimental Mechanics Series, DOI 10.1007/978-3-319-00873-8_17,

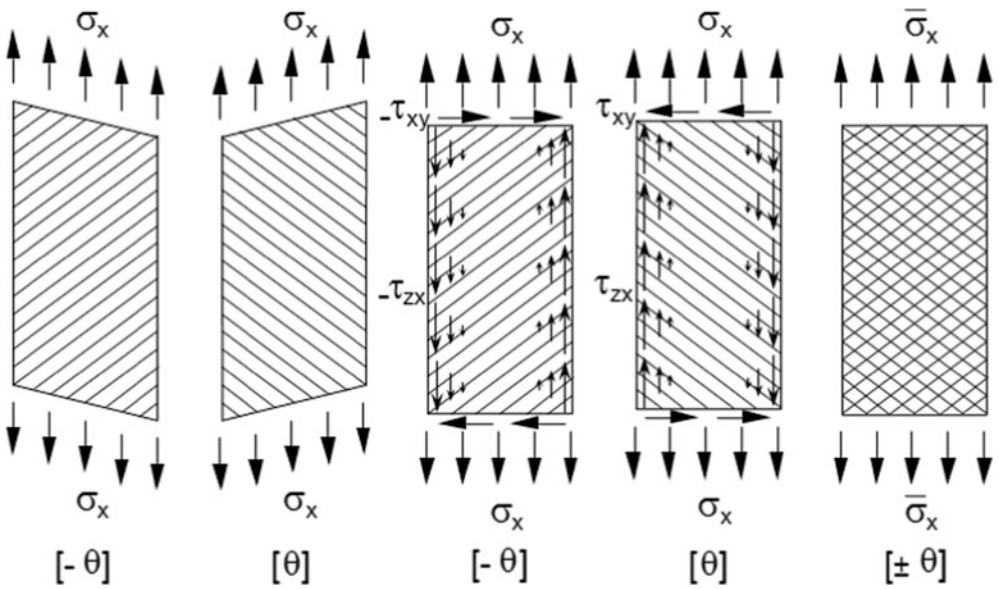

Fig. 17.1 Illustration of generation of interlaminar and intralaminar shear stresses in angle-ply laminate under axial tension [2]

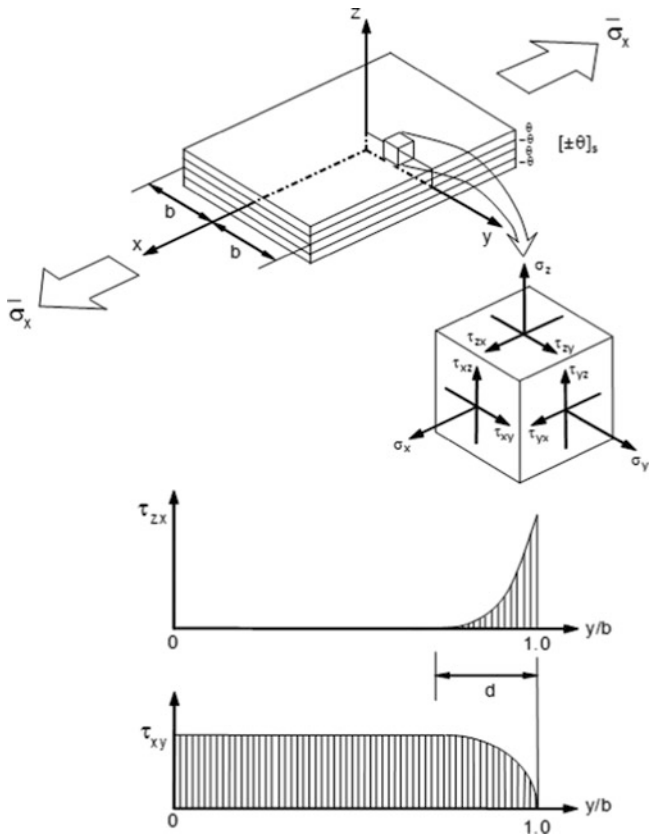

Fig. 17.2 Distribution of interlaminar (τ_{zx}) and intralaminar (τ_{xy}) shear stresses in θ-layer of $[\pm\theta]_s$ angle-ply laminate under axial tension [2]

17.2 Experimental Procedure

17.2.1 Material and Specimen Preparation

In this study a unidirectional high stiffness, high strength carbon epoxy composite was used (IM7/8552) to produce $[20_k/-20_k]_{ms}$ angle-ply laminates, where k represents the number of plies per layer and m is half the number of layers per laminate. The total number of plies, n = 4 km. The IM7/8552 prepreg was cured in a two step bleederless process where one layer of separator was used on either side of the layup. This produced a consistent composite laminate with a fiber volume fraction, $V_f = 0.58$ and a ply thickness, t = 0.14 mm (0.0055 in).

Glass/epoxy (G-10) tabs are bonded to the ends of the tension coupon of length 6.35 cm (2.5 in.) and the coupons are cut to have a 19 mm (0.75 in.) width and a gage length of 11.4 cm (4.5 in). This provides an aspect ratio of 6:1. By keeping the width of the coupon constant, any change in the interlaminar strength is due to altering the normalized layer thickness and not due to a decrease in peak interlaminar shear stress from a wider coupon. After cutting with a diamond blade, the ends are hand polished to ensure a consistent cross section.

Four different layups were tested to investigate the effect of normalized layer thickness on laminate strength. The normalized layer thickness is determined by dividing the layer thickness, kt, by the total thickness of the laminate, h. The layup configurations of the laminates tested are shown in Table 17.1.

The thickness of each layer was varied from 1 ply thick to 4 plies thick in a 16 ply laminate. To differentiate between normalized layer thickness and simple layer thickness, a fourth laminate was tested with a layer thickness of 3 plies but a normalized layer thickness similar to the laminate with a layer thickness of 4 plies.

17.2.2 Testing and Results

The tensile coupons were tested in a servo-hydraulic testing machine (Instron 8500) at a constant displacement rate. Axial strains were measured using an extensometer while transverse strains were measured with an electrical resistance strain gage. Three specimens from each different layup configuration were tested. The extreme cases of a normalized layer thickness of 0.0625 and of 0.25 were tested at both quasi-static (1.7×10^{-5} s^{-1}) and intermediate (1.7×10^{-2} s^{-1}) strain rates to determine the strain rate effect on laminate strength. The average strengths for the different layup configurations and strain rates are shown in Table 17.2.

There is a trend which shows that as the normalized layer thickness decreases, the strength increases at the quasi-static rate. This suggests that as the normalized layer thickness shrinks, the interlaminar shear stress does not have to be as high to realign the layer with the laminate so it plays a smaller role in the failure. It was also observed that there is a strengthening of the laminate as the strain rate increases when the normalized layer thickness is high. Since the shear strength and stiffness of a carbon epoxy composite has been shown to increase with increasing strain rate, this suggests that there is an enhancement in the interlaminar shear strength at higher strain rates [5, 6].

Table 17.1 Tested layup configurations

Layup	Number of plies, n	Normalized layer thickness
$[20/\text{-}20]_{4s}$	16	0.0625
$[20_2/\text{-}20_2]_{2s}$	16	0.125
$[20_4/\text{-}20_4]_s$	16	0.25
$[20_3/20_3]_s$	12	0.25

Table 17.2 Laminate strengths

Layup	Strain rate (s^{-1})	Average strength (MPa)	Strain rate (s^{-1})	Average strength
$[20/\text{-}20]_{4s}$	1.8×10^{-5}	919	1.7×10^{-2}	917
$[20_2/\text{-}20_2]_{2s}$	1.7×10^{-5}	625	–	–
$[20_4/\text{-}20_4]_s$	1.7×10^{-5}	462	1.8×10^{-2}	517
$[20_3/20_3]_s$	1.7×10^{-5}	443	–	–

17.3 Discussion

As the normalized layer thickness changes, the laminate strength varies between two extremes: the strength of a plate of infinite width where there are no edge effects and the strength of a unidirectional 20° off-axis specimen (Fig. 17.3).

In a plate of infinite width, the interlaminar shear stress approaches zero so it has no impact on the failure strength. This means that there is no interlaminar component to the failure so the failure must be intralaminar. This corresponds nicely with the Northwestern (NU) failure theory prediction (Fig. 17.4) [7] which is based on the lamina strengths and stiffnesses for IM7/8552 reported in Schaefer, et al. [8]. The experimental points presented in the figure are the lamina stresses at failure, including the residual stresses that were generated during the cure. When the normalized layer thickness becomes large, the interface between opposite angled plies fails through interlaminar shear immediately and the layers each act like an unconstrained 20° lamina.

As seen in Table 17.2, the strength of the laminate with thicker layers shows strain rate dependence (Fig. 17.5).

For every decade increase in rate, the strength of the thicker layer laminate is increased by 4 %. This is on the order of the strain rate dependence of the lamina. As shown in Schaefer et al., the in-plane shear stiffness in in-plane shear strength increases by 3.8 % and 7.5 % respectively with each decade increase in strain rate. The laminate with thinner layers does not show the same strength enhancement with increasing strain rate. This is most likely due to the failure mode observed in the different types of specimen.

As shown in Fig. 17.6, for thicker layered laminates the failure is clearly interlaminar. There is a single intralaminar crack in each layer but there is a large amount of delamination. Each layer is distinct and no fibers are broken. This lends support to

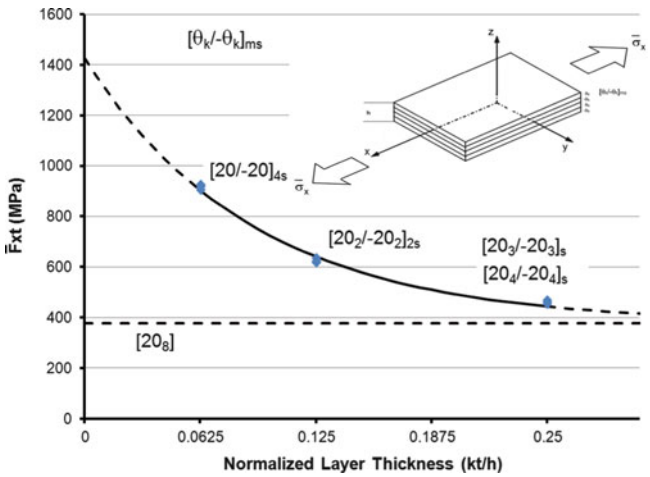

Fig. 17.3 Variation in laminate strength as a result of normalized layer thickness, kt/h

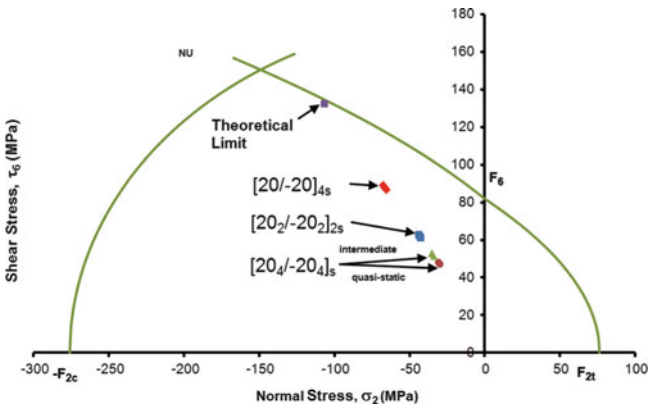

Fig. 17.4 Laminate strengths compared to Northwestern (NU) failure theory lamina strength envelope

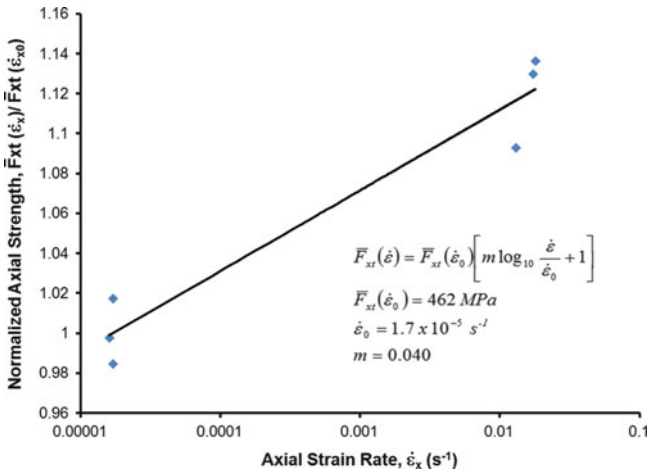

Fig. 17.5 Increase in laminate strength due to increasing strain rate for interlaminar shear failures $[20_4/-20_4]s$

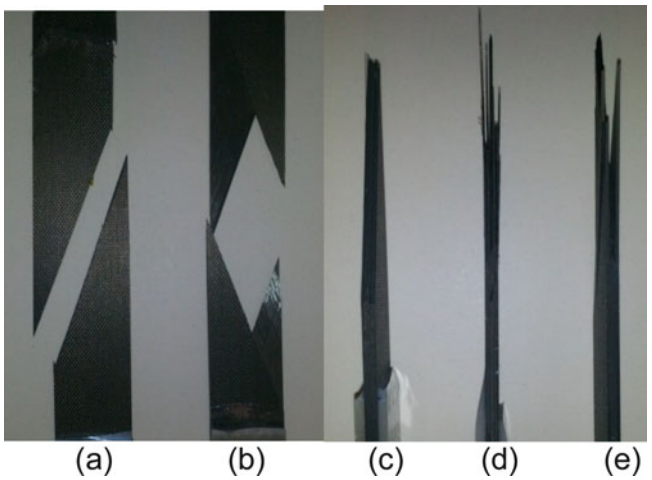

Fig. 17.6 Failure surfaces of thinner layer (**a**), (**c**), thicker layer (**b**), (**e**), and middle thickness layer (**d**) laminates

the proposed mechanism for strengthening of the laminate with increasing strain rate. For the thinner layer thickness laminate, there is no delamination seen in the failure surface. Half of the plies fail through intralaminar shear while the other plies have fibers broken parallel to the shear slip plane. The interlaminar stresses may contribute to the initiation of the failure, but the amount of strain energy stored within the laminate is enough to break fibers once cracks start to form.

The nature of the failure mechanisms can be further explained by looking at SEM images of the failure surfaces. In the thick layer laminate (Fig. 17.7), the exposed fibers are very smooth while the matrix shows significant microcracking. This shows that the matrix was subjected to significant damage prior to failure while the fibers show no noticeable signs of plasticity or cracking.

The SEM images of the thinner layer laminate show a much different failure surface. While there are fibers that run parallel to the failure surface, they appear much rougher and look as if some of them have fractured during failure. The matrix looks similar to the images above of the interlaminar failure where there is significant cracking. This suggests that the matrix was forced to carry a high stress from a combination of inter and intralaminar stresses. The most significant difference is the fiber breakage shown at high magnification in Fig. 17.8c. The fibers which do not run parallel to the failure surface clearly fractured near the failure plane.

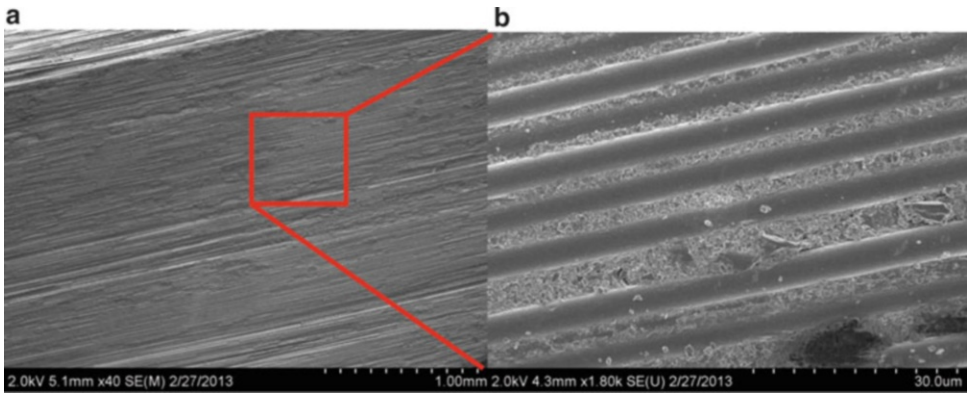

Fig. 17.7 SEM images of interlaminar failure surface for thicker layer laminate

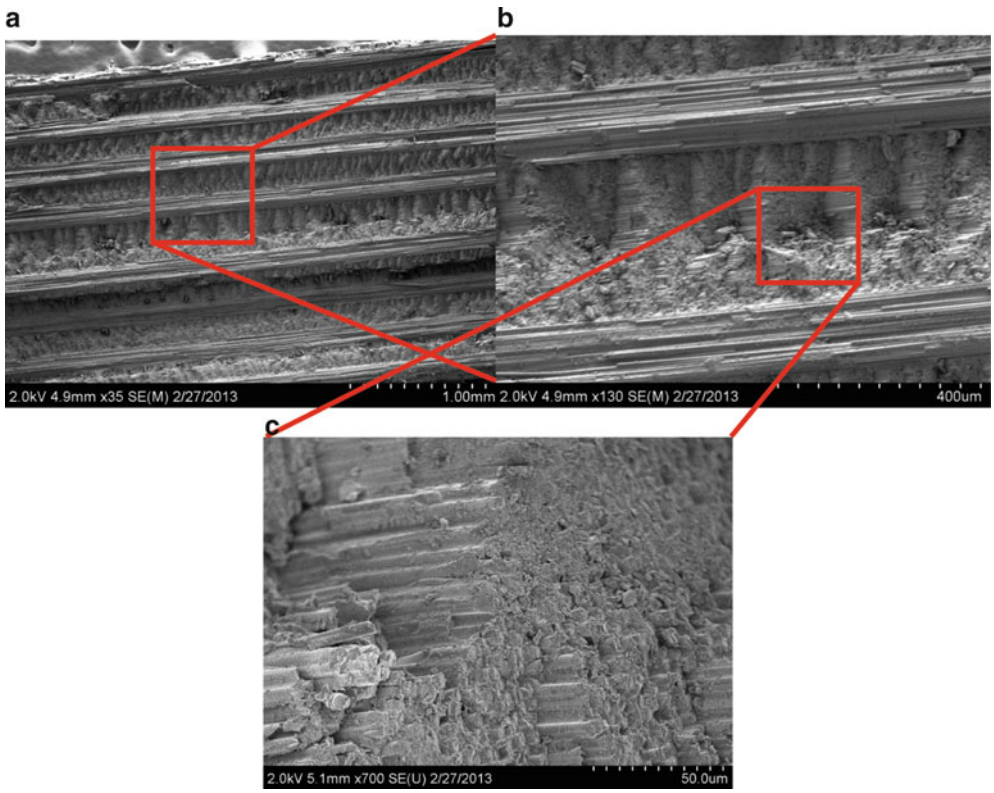

Fig. 17.8 SEM images of intralaminar failure surfaces for thinner layer thickness laminate

17.4 Conclusions

It was shown in this study that the dispersion of plies within a laminate can have a significant impact on its interlaminar strength. For any laminate that has free edges, interlaminar stresses can cause failure well below the strength predicted by classical failure theories. Strain rate can also impact the stress at which delaminations initiate. While grouping similarly oriented plies together in a laminate or introducing thicker plies can simplify composite production, it can dramatically alter performance. Further study is necessary to attempt to quantify the impact of interlaminar stresses and improve the predictive abilities of failure theories.

Acknowledgement The work described in this paper was sponsored by the Solid Mechanics Program of the Office of Naval Research (ONR). We are grateful to Dr. Y. D. S. Rajapakse of ONR for his encouragement and cooperation.

References

1. Altus E, Ishai O (1986) Transverse cracking and delamination interaction in the failure process of composite laminates. Composites Sci Technol 26(1):59–77
2. Daniel IM, Ishai O (2006) Engineering mechanics of composite materials, 2nd edn. Oxford University Press, New York, p 411, xviii
3. Pipes RB, Pagano NJ (1970) Interlaminar stresses in composite laminates under uniform axial extension. J Composite Mater 4:538
4. Pipes RB, Daniel IM (1971) Moire analysis of interlaminar shear edge effect in laminated composites. J Composite Mater 5(Apr):255
5. Daniel IM et al (2011) Characterization and constitutive modeling of composite materials under static and dynamic loading. Aiaa J 49 (8):1658–1664
6. Daniel IM, Werner BT, Fenner JS (2011) Strain-rate-dependent failure criteria for composites. Composites Sci Technol 71(3):357–364
7. Daniel IM et al (2009) Interfiber/interlaminar failure of composites under multi-axial states of stress. Composites Sci Technol 69(6):764–771
8. Schaefer J D, Werner B T,Daniel I.M (2013) Strain rate effects on failure of a toughened matrix composite, in SEM 2013 annual conference & exposition on experimental and applied mechanics 2013. Lombard

Chapter 18
Optimization and Service Life Prediction of Elastomeric Based Composites Used in Manufacturing Engineering

D. Zaimova, E. Bayraktar, I. Miskioglu, and N. Dishovsky

Abstract Lifetime prediction of the polymer materials have been an active field of research in recent past. An understanding in the polymer degradation mechanisms and their stabilization has lead to creation of composite materials for advanced applications. It is important to know the service life deterioration kinetics of materials with good accuracy for designing critical applications. The present paper discusses comprehensive test results carried out in the frame of a basic research project. First of all, a detailed analysis is presented on the influence of accelerator-vulcanizing agent system on the mechanical properties and viscoelastic behaviour. As a first design parameter for the new compositions (for example: the mixture of Natural and Butadiene Rubbers (NR-BR) vulcanized at the temperatures of 140 °C and 160 °C) were evaluated and secondly the effect of reinforcements and their interactions with the matrix are discussed. Preliminary results on a study of nanoindentation characterisation to predict viscoelastic behaviour of the elastomeric based composite sheets is also presented.

18.1 Introduction

Elastomer is a unique material that is both elastic and viscous. Elastomeric parts can therefore function as shock and vibration isolators and/or as dampers. Although the term rubber is used rather loosely, it usually refers to the compounded and vulcanized material. In the raw state it is referred to as an elastomer. Vulcanization forms chemical bonds between adjacent elastomer chains and subsequently imparts dimensional stability, strength, and resilience [1]. Elastomers have elastic properties similar to those of a metallic spring and have energy absorbing properties like those of a viscous liquid. These viscoelastic properties allow rubber to maintain a constant shape after deformation, while simultaneously absorbing mechanical energy.

The viscosity (which varies with different elastomers) increases with reduced temperature. The elasticity follows Hooke's law and increases with increased strain, while the viscosity follows Newton's law and increases with increased strain rate. Therefore, when applying a strain, the resultant stress will increase with increasing strain rate. Recently nanoindentation method has been applied to study the creep response of various materials. Creep is the increase in strain or deformation of a material with time when the material is subjected to a constant load for an extended period of time (i.e. time-dependent deformation).

D. Zaimova (✉)
University of Chemical Technology and Metallurgy, Sofia, Bulgaria

Supmeca/LISMMA-Paris, School of Mechanical and Manufacturing Engineering, Saint-Ouen, France
e-mail: diana.zaimova@gmail.com

E. Bayraktar
Supmeca/LISMMA-Paris, School of Mechanical and Manufacturing Engineering, Saint-Ouen, France
e-mail: bayraktar@supmeca.fr

I. Miskioglu
ME-EM Department, Michigan Technological University, Houghton, MI, USA

N. Dishovsky
University of Chemical Technology and Metallurgy, Sofia, Bulgaria

G.P. Tandon et al. (eds.), *Experimental Mechanics of Composite, Hybrid, and Multifunctional Materials, Volume 6*, Conference Proceedings of the Society for Experimental Mechanics Series, DOI 10.1007/978-3-319-00873-8_18,

The change of strain at any time increases with load, temperature and relative humidity. Viscoelastic materials, such as rubber, can undergo creep deformation at relatively low stress levels (well below the ultimate strength of the material) and low temperatures (i.e. room temperature – referred to as cold flow). This can lead to considerable reduction in life expectancy of the component. The nanoindentation test results also provide information on the elastic modulus, hardness, strain-hardening, cracking, phase transformations, and energy absorption. The specimen size is very small and the test can in many cases be considered non-destructive [2–13].

In this study along with the classical methods for characterizing elastomeric composites (vulcanization characteristics, swelling, tensile test before and after aging and so on) we have applied the nanoindentation method to obtain an idea for the viscoelastic behaviour of the materials which are the subject of our investigation. The nanoindentation method gives the opportunity to make modelling of creep behaviour respectively the life service of rubber articles [4–6, 8, 10, 11, 14, 15]. In what follows, partial results of a French-Bulgarian cooperative research on elastomeric based composites will be discussed.

18.2 Experimental Procedure

In the frame of the research project, two basic compositions were mixed in our laboratory using two rolling mixer. The moulding conditions were determined from torque data using moving die rheometer MDR 2000 (Alpha Technologies) at temperatures of 140 °C and 160 °C. Four compounds (A, B, C, D) based on sulphur vulcanized Natural rubber/ Polybutadiene rubber blends were prepared containing certain fillers (carbon black) and/or reinforcements in order to investigate their deformation behaviour. Two ratios of accelerator to sulphur were used for preparation of the compounds also known as conventional vulcanization system (CV) in which the quantity of sulphur is higher, and efficient vulcanization system (EV) in which the quantity of accelerator is superior. Compounds A and B are vulcanized using conventional vulcanization system (CV) at vulcanization temperatures of 140 °C and 160 °C respectively. Compounds C and D are vulcanized using efficient vulcanization system (EV) at 140 °C and 160 °C respectively. The exact composition of the blends is not reported in this paper because of confidentiality matters.

Cured sheets of 2 mm thickness were prepared by compression moulding. The moulding took place at 140 °C and 160 °C and pressure 100 kg/cm^2. The behaviour of these compounds in detrimental environmental conditions were tested by means of swelling experiments. The swelling tests were carried out by submerging the molded samples in toluene at room temperature. After these tests, the crosslink densities for each compound were calculated according to the molecular mass between two crosslinks. All of the crosslink densities were calculated according to Fory-Rehner relation [3]:

$$\frac{1}{2M_c} = \frac{1}{2\rho V_0}\left[\frac{ln(1-V_r)+V_r+\mu V_r^2}{V_r^{1/3}-\frac{1}{2}V_r}\right] \tag{18.1}$$

$$\nu = \frac{1}{2M_c} \tag{18.2}$$

where;

M_c-molecular mass between crosslinks;

ρ-Density of the rubber;

V_0-molar volume of the solvent;

V_r-volume fraction of the swollen rubber;

μ-interaction parameter between the rubber sample and the solvent;

ν-Crosslink density.

The mechanical properties were determined in accordance with ASTM D 412a$^{\varepsilon 2}$ (2010). The aging test was performed in air flow oven at 70 °C for 21 days. Second type of aging was performed in ultraviolet box for 21 days. The samples were cut from the moulded sheets in dumbbell shape. The sample length and thickness were measured. Tensile tests were performed using an Instron model 4507. A minimum of 3 specimens were tested for each compound. Testing was done at room temperature with a cross head speed of 500 mm/min^{-1}.

Nanoindentation characterisation was carried out to determine the visco-elastic behaviour of these composite materials by creep phenomenon. For each specimen 16 indents are taken. Each indent is 50 μm away from its neighbouring indents. The load was increased from zero to the maximum at a rate of 1 mN/s. Then load was held at the maximum load for 400 s then unloaded. During unloading the modulus and hardness were calculated using the Oliver-Pharr method.

A Berkovich indenter is in all the tests. Poisson's ratio was assumed to be 0.36 for all samples. Using the data collected during typical creep test creep compliance $J(t)$ was calculated using [4]:

$$J(t) = \frac{A(t)}{(1-\nu)P_0 \tan\theta} \tag{18.3}$$

where:

$$A(t) = \text{Contact area}$$

$$P_0 = \text{Constant applied load}$$

$$\theta = 70.3^\circ \text{ For a Berkovich indenter}$$

$$\nu = 0.36 \text{ Assumed}$$

The stress exponent n is obtained from the log-log plot of strain rate vs stress based on the equation

$$\dot{\varepsilon} = K\sigma^n \tag{18.4}$$

where K is a constant.

In final stage, a multi-cycle wear test analysis was also performed. The type of indenter tip was conical with 90° apex angle. The loads on sample were respectively 10 mN and 20 mN and wear distance of 500 μm. The wear test Speed is 50 μm/s. Twenty wear cycles per wear set were performed. On one sample wear tests were performed along 5 different paths (parallel paths separated by 50 μm).

18.3 Results and Discussion

18.3.1 Vulcanization Characteristics

The rheometer, a convenient instrument to evaluate the effects of carbon black-rubber interactions on rate of cure and cross-linking, was employed for the purpose of characterizing critical parameters related to the vulcanization process. Table 18.1 shows vulcanization characteristics of the four compounds studied here.

The minimum torque (M_L) in a rheograph measures the viscosity of the vulcanizates, and the maximum torque (M_H) is generally correlated with the stiffness and crosslink density.

It is well known that the difference between maximum (M_H) and minimum (M_L) torque is a rough measure of the crosslink density of the samples and usually known as ΔM. From the table it is noticed that the highest value of ΔM is for compound A. Hence the crosslink density is maximum for compound "A" compared with the other three compounds. This is also confirmed by the results for the crosslink density obtained by the equilibrium swelling (Fig. 18.1). The highest crosslink density is registered for compound "A". But the carbon black particles whose surfaces are covered by entangled rubber chains can be considered as physical crosslinks. The physical crosslinking hinders the mobility of rubber chains and restrains the deformation of rubber therefore increases the torque. However, swelling cannot detect the type of the crosslinks although the high maximum torque for compound "A" can be considered also as sign for superior number of physical crosslinks.

The scorch time (Ts_2) is the time required for the minimum torque value to increase by two units and measures the premature vulcanization of the material. What makes an impression is that the CV system exhibited shorter Ts_2 values than the EV therefore more crosslinks are formed in shorter time.

These results should be expected because the greater quantity of the accelerator (essentially in the compounds "C" and "D") should provide superior values for Ts_2.

In fact, it is possible this anomaly to be due to the nature of sulphenamide class accelerators (delayed action in the beginning of vulcanization) and on the other hand the higher content of sulphur in compound "A" and "B". But the overall rate (V) of vulcanization is slightly in favour of the compound cured with EV. Detailed studies on the vulcanization and chemical structures of the compounds created within the framework of this research were reported in our earlier papers [3, 7, 9, 12, 13].

Table 18.1 Vulcanization characteristics of four compounds studied in this research project

Blend number				
Characteristics	A	B	C	D
ML, dNm	2.98	2.71	2.73	2.53
MH, dNm	36.46	33.97	32.27	31.67
$\Delta M = MH - ML$	33.48	31.26	29.54	29.14
T_{90}, min:s	17:22	4:47	17:24	5:43
T_{s2}, min:s	6:18	1:23	9:34	2:41
V, %min	9	31	13	33

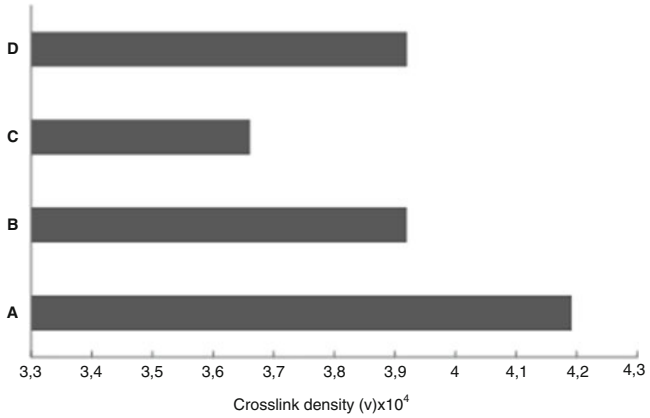

Fig. 18.1 Crosslink density determined by swelling

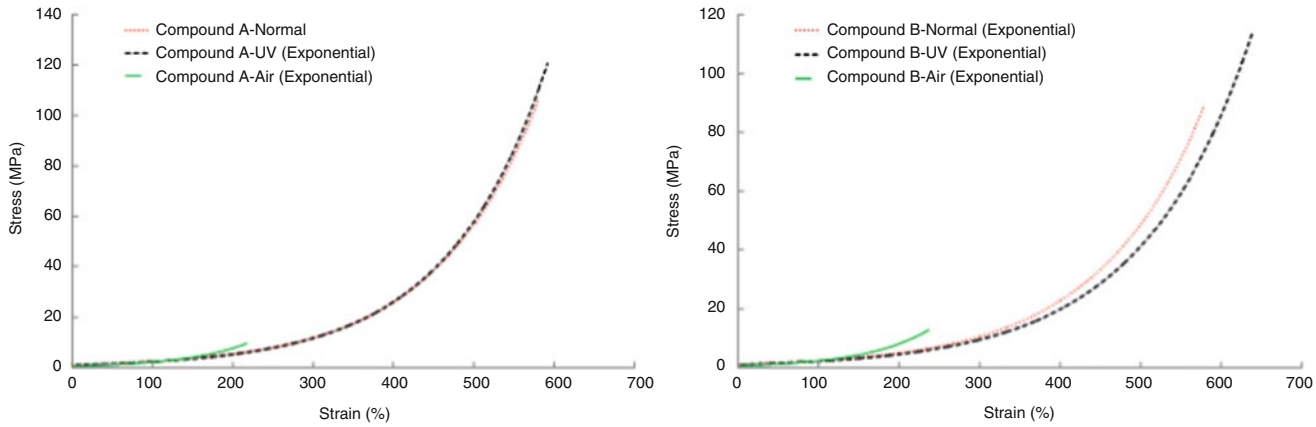

Fig. 18.2 Stress–strain curves for the compounds A (*left*) and B (*right*) in normal and aging conditions

18.3.2 Mechanical Properties Before Aging

Tensile properties are commonly used to measure the degradation behaviour of elastomers. This basic information is absolutely necessary to understand the damage behaviour of the elastomer based composites under different solicitation conditions (normal, aging ultraviolet and aging under air flowing with certain humidity) as explained in the former session. Typical stress–strain curves for compounds A, B, C and D are illustrated in the Figs. 18.2 and 18.3 respectively.

First basic mechanical property from these curves can be drawn for determining modulus values in case of 100 % and 300 % deformation rates. As indicated on Figs. 18.4a and 18.4b, all of the four compounds show similar values of modulus at 100 % (M_{100}) and modulus at 300 % (M_{300}) deformation. Although the compounds vulcanized with EV (C and D) give

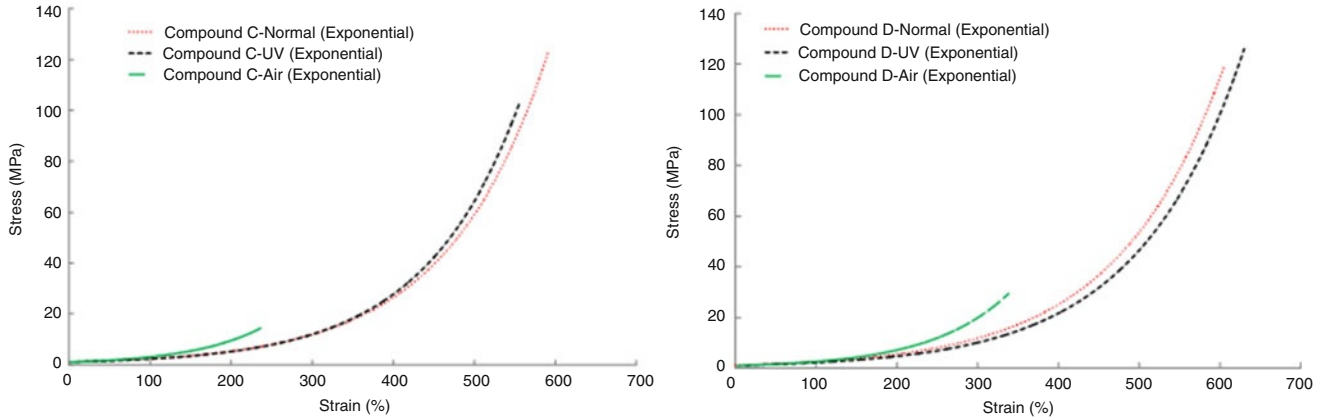

Fig. 18.3 Stress–strain curves for the compound C (*left*) and D (*right*) in normal and aging conditions

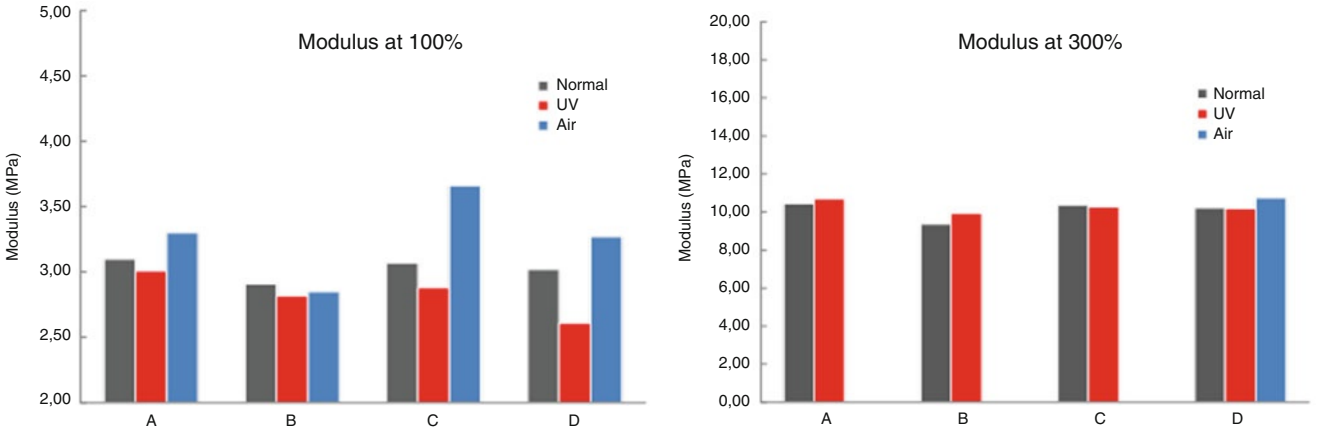

Fig. 18.4 Comparison of $M_{100\%}$ (*left*) and $M_{300\%}$ (*right*) for the compounds A, B, C, D in normal and aging conditions

slightly better results than those vulcanized with CV (A and B). These results are showing that compounds D and C poses better stiffness in low deformation than the other two. This is probably due to the different nature of the network structure obtained during vulcanization. The superior number of mono- sulphide and C-C bonds, typical for EV, are characterized with higher strength especially under low deformation explains this phenomenon. Obviously the temperature of vulcanization does not affect significantly on M_{100} and M_{300}.

On the other hand, the tendency is not the same for tensile strength (Fig. 18.5a) and the elongation at break (Fig. 18.5b). The higher values are for the compound vulcanized with CV. All compounds have the ability to exhibit crystallization under stress thanks to NR but according to literature the superior number of di- and poly- sulphide linkages (result from CV) improves the elasticity of the compound which explains the higher values of elongation at break. In addition CV gives more homogeneous structure which plays positive role for the strength of vulcanizates. Once more the temperature of vulcanization does not play significant role for the tensile strength and elongation at break.

18.3.3 Mechanical Properties After Aging

The mechanical properties of the compounds after aging are also evaluated in detail. As discussed just in the previous section (Figs. 18.2 and 18.3), a detailed comparison of the stress–strain curves before and after 21 days of aging (in air oven and under UV light). It can be seen that UV light does not affect significantly the mechanical properties of the studied compounds. The same relation is observed for M_{100}, M_{300}, tensile strength and elongation at break.

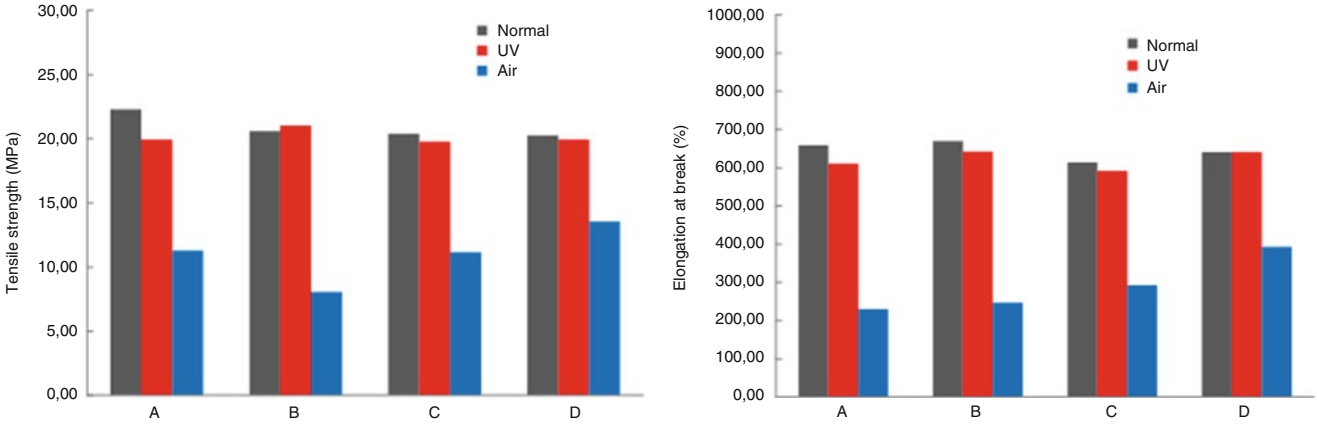

Fig. 18.5 Comparison of tensile strength values (*left*) and elongation at break (*right*) for the compounds A, B, C, D in normal and aging conditions (UV and air flowing with certain humidity)

These results can be explained with the ability of rubber compound to form additional crosslinks under the influence of temperature and UV light. Although the over-crosslinking makes the vulcanizates brittle and reduces its elasticity apparently the period of exposure was not sufficient to create over-crosslinked vulcanizates. Probably the number of crosslinks created during UV aging compensates the number of the chains destructed by aging effect. The thermal aging however (21days in air oven at 70 °C) causes more severe damage on the studied compounds. Under low level of deformation (100 %) thermal aging has positive effect. At this stage, crosslink scissions and the formation of new crosslinks into the networks affected these properties. But under high stress and deformation the process of destruction of the crosslinks is much more significant and leads to failure of the specimen.

Concerning the type of vulcanization system, the values of all mechanical properties given in Figs. 18.4 and 18.5 for the four studied compounds (A, B, C, and D) presenting the resistance to UV aging are similar. The CV system vulcanizates (A and B) has a high content of polysulphide linkages with low bond strength. By contrast, monosulphide linkages have relatively strong bond strength and are dominant in the EV system vulcanizates [5, 7, 9, 12, 13]. As a result, the CV system exhibits a weaker thermal aging resistance than polysulphide crosslinks. For all compounds the extended period of heating, the excessive main chain scission and/or modification resulted in a reduced tendency to crystallize at high elongation. It is observed that the effect of the temperature of vulcanization is not significant for aging resistance.

18.3.4 Nanoindentation Characterisation: Creep Compliance and Wear Track

Nanomechanical creep testing has significant potential for interpreting the mechanical responses of polymer because the material response inherently includes time-dependent deformation. Although the conventional measurement for mechanical compliance (J_t) include macro scale tensile or simple shear test, researchers have increasingly interpreted an analogous creep compliance using nanoindentation creep. For nanoindentation creep the load is maintained constant and J_t should measure the relation between displacement and time [4, 6].

Figures 18.6 and 18.7 present comparison of creep compliance as a function of time at four different maximum loads. The results for J_t obtained for load of 5 mN (Fig. 18.6) show similar values for compounds A, B and D. The lower values of compound C is contrary to the results found in literature [4, 7, 10, 11], It means that lower crosslink density correlates with increased mechanical compliance, compound C shows exactly the opposite behaviour. From swelling data (Fig. 18.1) is clearly seen that compound C has the lowest crosslink density and should give maximum values for J_t. It cannot be considered as a mistake because the same behaviour is observed for maximum loads of 10, 15 and 20 mN as indicated in Figs. 18.6 and 18.7.

Moreover the creep behaviour of compound A, which has the highest crosslink density is also opposite to what is found in the literature. It gives the highest values of J_t at maximum loads of 10 and 15 mN. This could be a result of chain scissions during the holding period at maximum load. As mentioned before the data from swelling test gives information for the quantity of the crosslinks but not for their type (chemical, physical and so on). If we consider that the superior number of crosslinks in compound A are of physical character (weaker than the chemical ones) or polysulfide (because of the CV vulcanization system) it is possible part of them to be destroyed or weakened under the influence of the higher load.

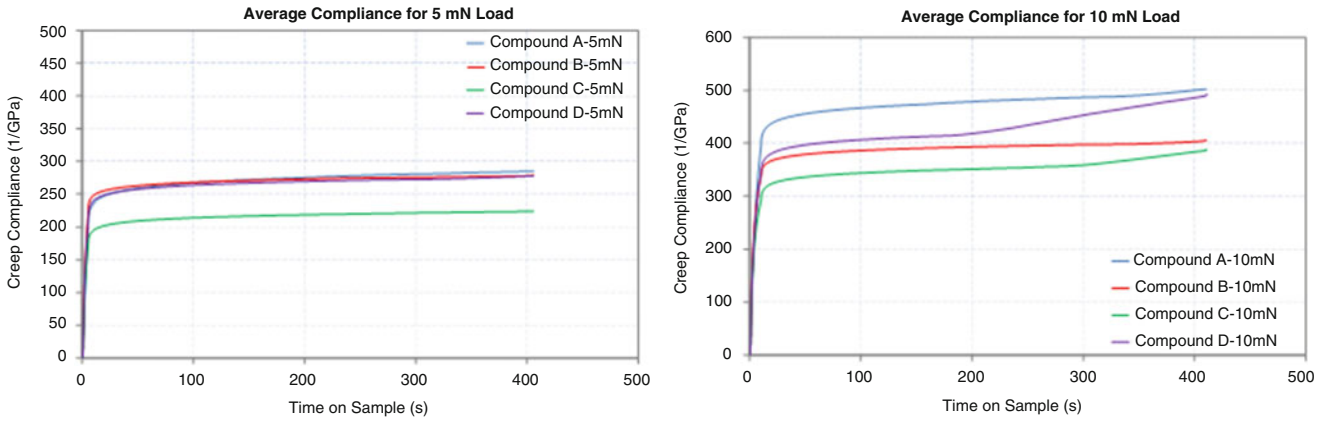

Fig. 18.6 Comparison of creep compliance as a function of time for the compounds A, B, C, D at maximum loads of 5mN (*left*) and 10mN (*right*)

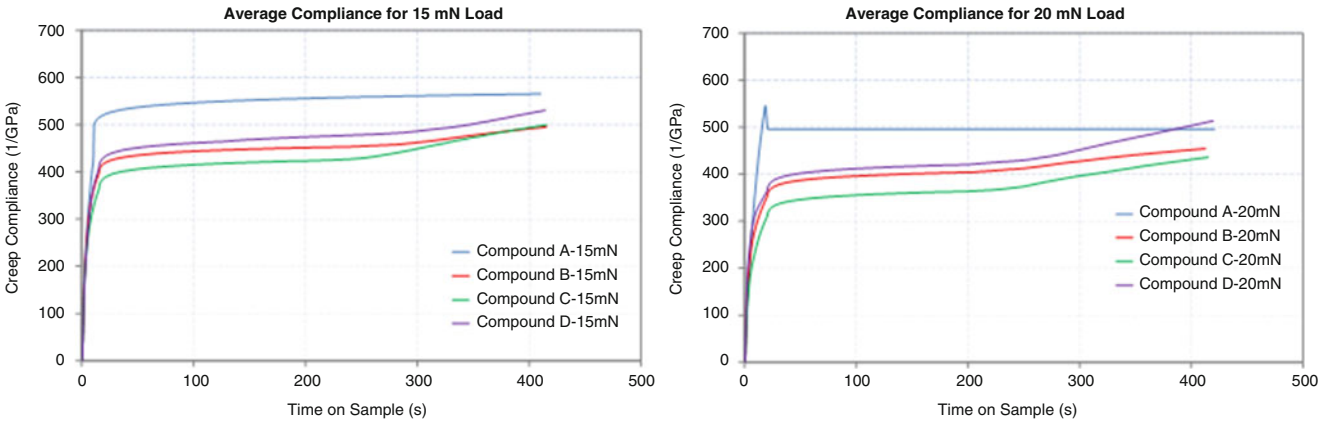

Fig. 18.7 Comparison of creep compliance as a function of time for the compounds A, B, C, D at maximum loads of 15mN (*left*) and 20mN (*right*)

This claim is also supported by the results obtained for compound A at maximum load of 20 mN where the material shows particular behaviour which makes the creep data impossible to use. These curves display clearly that the load, 20 mN is a limit for the maximum load which can be use in the case of the investigated compounds. The lowest creep compliance values for compound C still stay obscurity.

To observe the effect of the size of the maximum load the four compounds are analyzed separately. Figures 18.8 and 18.9 present the creep compliance depending on the different maximum loads (5 mN, 10 mN, 15 mN) for all of the four compounds. As expected higher loads result in higher creep compliance.

Figure 18.10 (left) shows the indentation hardness calculated from the load–displacement curve at different loads. For maximum load of 5 mN a small difference can be detected once depending on the vulcanization system and once depending on vulcanization temperature. This is an interesting result because in our previous studies [3, 9, 12, 13] we have found that in macro scale hardness (shore A) there is any effect of both temperature and vulcanization system, which is also confirmed by the results of nanoindentation at 10, 15 and 20 mN. Obviously under very low stress on the nano scale it is possible to see the effect of vulcanization system and vulcanization temperature. Our results show that compounds A and C, vulcanized at 140° have higher hardness (measured at 5mN) than those vulcanized at 160° probably due to more homogeneous structure which gives higher resistance of the material subjected to stress. Regarding the vulcanization system compounds A and B (CV) give better results than compounds C and D (EV). It can result of higher elasticity of compounds A and B (observed also from stress–strain results) and the possibility to recover more quickly during unloading period.

In the same way, a detail comparison of stress exponents are given in Fig. 18.10 right by calculating from the data obtained by nanoindentation tests for all of the four compounds A, B, C, D. Results are given on the same figure at four

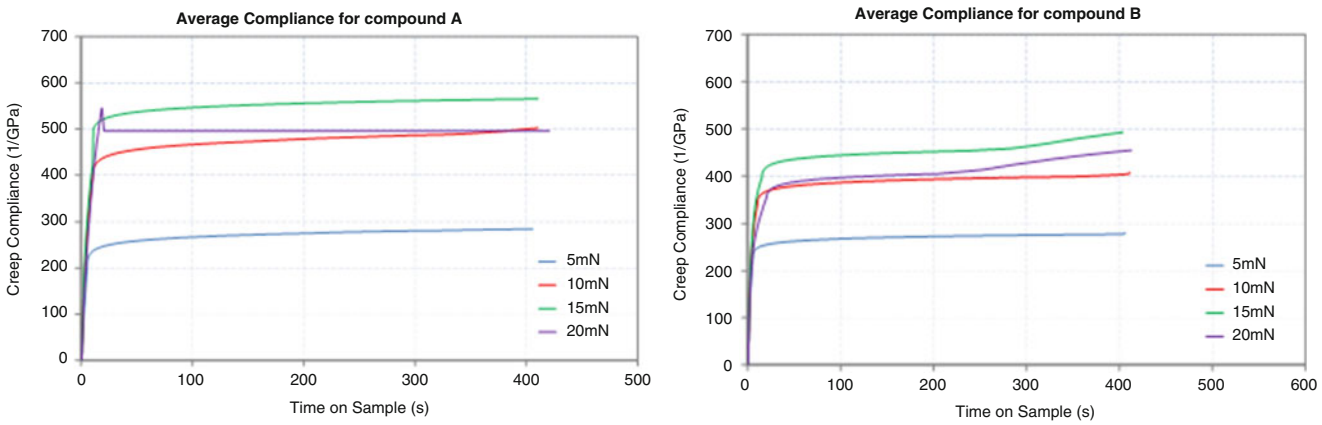

Fig. 18.8 Comparison of creep compliance evolution as a function of time for the compounds A (*left*) and B (*right*) at four different maximum loads (5mN, 10mN, 15mN, 20mN)

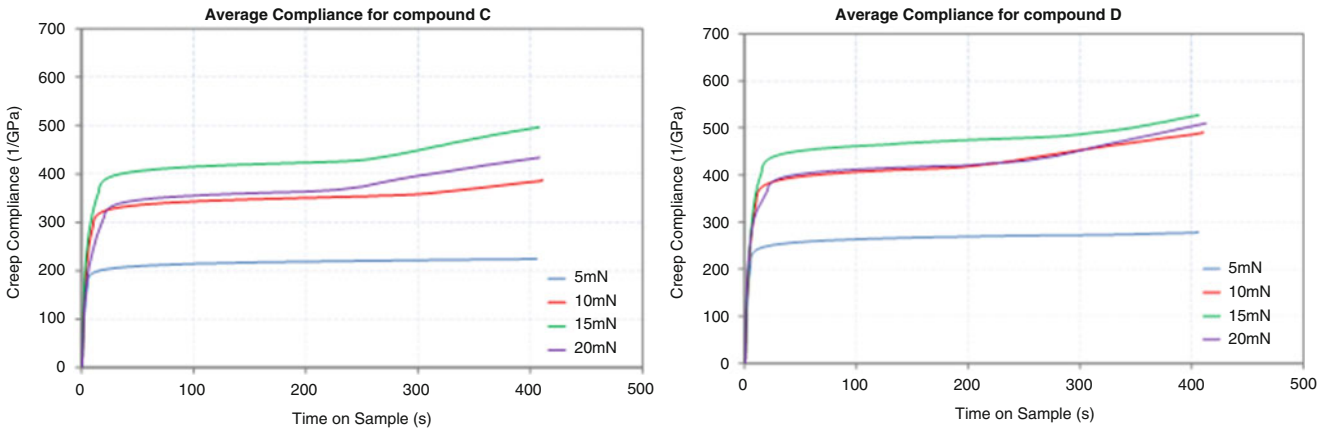

Fig. 18.9 Comparison of creep compliance evolution as a function of time for the compounds C (*left*) and D (*right*) at four different maximum loads (5mN, 10mN, 15mN, and 20mN)

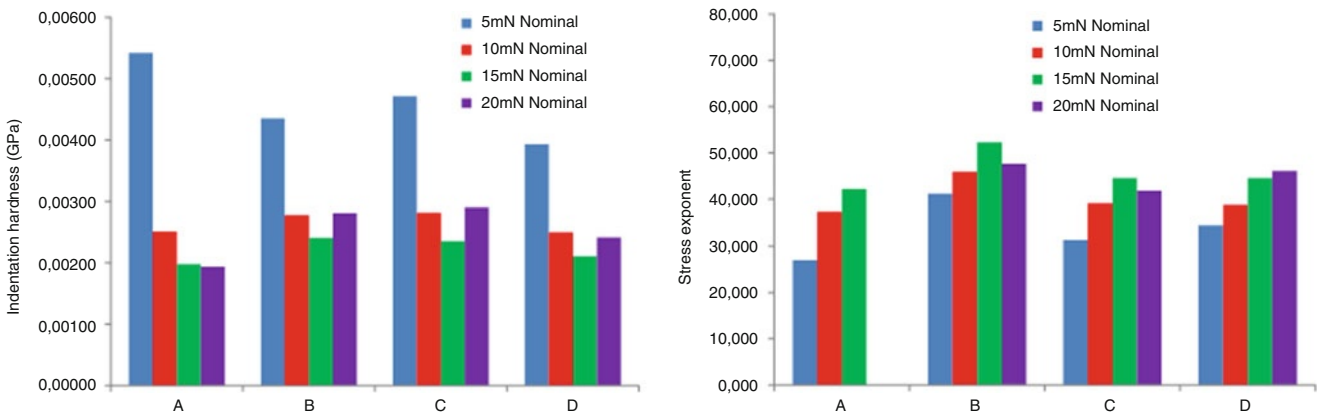

Fig. 18.10 *Left* comparison of indentation hardness obtained by nanoindentation test for Compounds A, B, C, D at four different maximum loads (5mN, 10mN, 15mN, 20mN) and *right* comparison of stress exponent calculated from the data obtained by nanoindentation test for Compounds A, B, C, D at four different maximum loads (5mN, 10mN, 15mN, 20mN)

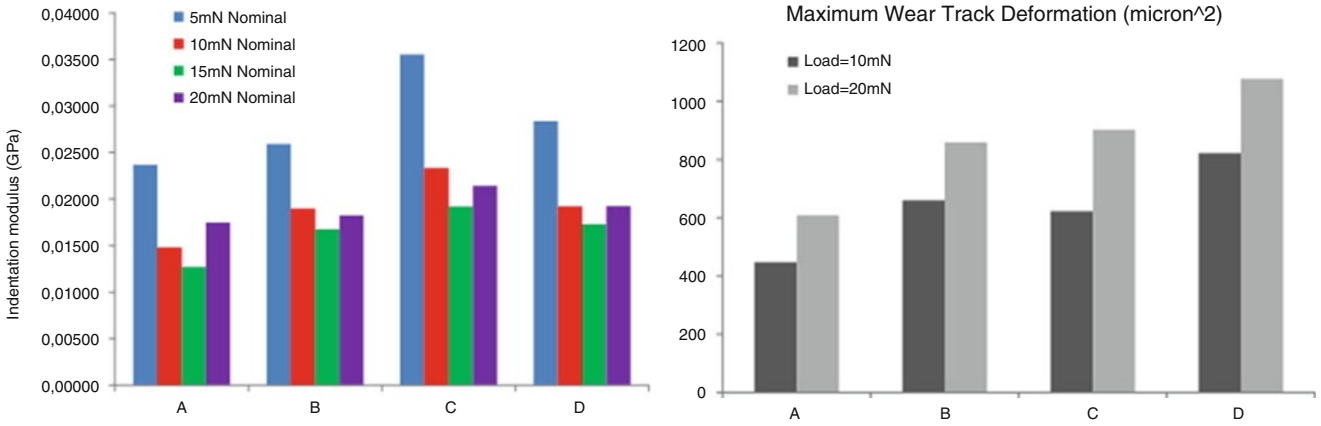

Fig. 18.11 *Left* comparison of indentation modulus obtained by nanoindentation test for Compounds A, B, C, D at four different maximum loads (5mN, 10mN, 15mN, 20mN) and *right*; comparison of maximum wear track deformation obtained by multi-cycle wear test at two different maximum loads; 10 and 20mN

different maximum loads (5mN, 10mN, 15mN, 20mN). Very similar conclusion can be drawn from this evaluation. The compound C gives optimal stress exponent results regarding to the three other compounds.

Other important evaluation from nanoindentation test was made on the indentation modulus of the four compounds as presented in Fig. 18.11 left. Unlike the hardness results, for indentation modulus the effect of temperature can't be seen. Only the effect of vulcanization system is observed mostly for maximum load of 5mN. The higher values are in favour of EV (compounds C and D). These results are surprising because of the indentation hardness results. Normally the indentation modulus and indentation hardness are connected. If the hardness is high it's supposed to have high indentation modulus because both properties are connected with the stiffness of the material i.e. a measure of the resistance offered by an elastic body to deformation. In previous works [11] has been found that the type of crosslinks doesn't have effect on the tensile modulus of rubber materials but in our case a different effect is seen for both hardness and indentation modulus. It cannot be easily explained easily why such behaviour is observed.

Results of multi-cycle wear test analysis were summarised in Fig. 18.11. Here, only the maximum wear track deformation is presented at two different loads (10 and 20 mN). At the first approach, the applied load doesn't seem to affect significantly the evolution of the wear track deformation values. The same dependence is observed for both loads by the temperature of vulcanization and vulcanization system. Once again compound A and C have superior resistance to deformation thanks to their homogeneous structure. As concerning the effect of vulcanization system, two compounds A and B (CV) display lower deformation than compounds C and D (EV). These results demonstrate similar behaviour to those given in case of hardness evaluation. But, in our experimental knowledge, the question still remains to be answered; why they are not confirmed by indentation modulus results? This discussion will be given in the next publication.

18.4 Conclusion

In the frame of common research project going on, we try to design new elastomeric based composites. For most useful chemical composition to optimise the structure, certain experimental results given on the four different compounds were discussed in the present work. Mechanical behviour of these compounds were evaluated under different tensile test conditions (normal, aging with UV and aging with air flowing in humidity).

Additional to the tensile tests, more comprehensible study has been carried out by nanoindentation test to evaluate visco elastic behaviour of the elastomeric based composites developed in this project. Evaluation of creep compliance as a function of time at four different maximum loads and also wear track deformation behaviour at two different applied loads has been carried out by nanoindentation. These tests give more reliable results to understand the viscoelastic behaviour and real damage analysis at nano-scale of these composites under different service conditions. Actually, in the present work, nanoindentation characterisation for the four compounds was discussed only under normal conditions. Nanoindentation analysis for the compounds subjected to aging with ultraviolet and air flowing with certain humidity will be discussed in the next publications in detail and after a total comparison will be given for all of the compounds.

Acknowledgments Authors thank to CNAM-Paris, Arts et Metiers and Michigan Technological University, ME-EM Houghton MI-USA for the using of laboratory facilities.

References

1. Harris C, Piersol A (2002) Harris' shock and vibration handbook, vol Mechanical properties of rubber, 5th edn. McGraw-Hill, New York, chapter 33
2. Woishnis WA, Wright DC (1994) Select plastics to avoid product failure. Adv Mater Process 146(6):39–40
3. Zaimova D, Bayraktar E, Dishovsky N (2011) State of cure evaluation by different experimental methods in thick rubber parts. JAMME, J Achievements Mater Manufacturing Eng 44(2):161–167
4. Tehrani M, Safdari M, Al-Haik MS (2011) Nanocharacterization of creep behaviour of multiwall carbon nanotubes/epoxy nanocomposites. Int J Plast 27:887–901
5. Morrison NJ (1984) The reaction of cross-link precursors in natural rubber. Rub Chem Tech 57:86–96
6. Van Tweedie CA, Vliet KJ (2006) Contact creep compliance of viscoelastic materials via nanoindentation. J Mater Res 21(06):1576–1589
7. Zaimova D, Bayraktar E, Katundi D, Dishovsky N (2012) Design of new elastomeric composites used in manufacturing engineering. In: 14th international materials symposium – IMSP'2012, 10–12 October, Pamukkale-Denizli Turkey, Proceedings of IMSP' 2012:1048–1056
8. Plazek DJ (1966) Effect of crosslink density on the creep behaviour of natural rubber vulcanizates. J Polym Sci 4:745–763, A-2 Polym Phys
9. Zaimova D, Bayraktar ED, Katundi, Dishovsky N (2012) Elastomeric matrix composites: effect of processing conditions on the physical, mechanical and viscoelastic properties. J Achievements Mater Manufacturing Eng, JAMME 50(2):81–91, WAMME-Academy of Science, 2012 ISSN 1734–8412
10. Farlie ED (1970) Creep and stress relaxation of natural rubber vulcanizates. Part I. Effect of crosslink density on the rate of creep in different vulcanizing systems. J Appl Polym Sci 14:1127–1141
11. Juliano TF, VanLandingham MR, Tweedie CA, Van Vliet KJ (2007) Multiscale creep compliance of epoxy networks at elevated temperatures. Exp Mech 47(1):99–105
12. Zaimova D, Bayraktar E, Katundi D, Dishovsky N (2012) Applications of elastomeric based composites in industrial applications. International conference on advanced materials processing, AMPT-2012, Wollongong-Australia 1(1): 8–16, ed. AMPT-Editions, 2012, 23–26 Sept 2012
13. Zaimova D, Bayraktar E, Berthout G, Dishovsky N (2013) Design of new elastomeric matrix composites: comparison of mechanical properties and determining viscoelastic parameters via continuous micro indentation. Composite Mater Joining Technol Composites 7(1):227–234, ed. Springer, 2013
14. Wood LA, Bullman GW, Roth FL (1974) Long-time creep in a pure-gum rubber vulcanizate: influence of humidity and atmospheric oxygen. J Res Notional Bureau Standards A Phys Chem 78A(5):623–629
15. Tolle LGY, Craig RG (1978) Viscoelastic properties of elastomeric impression materials: polysulphide, silicone and polyether rubbers. J Oral Rehabil 5:121–128

Chapter 19
Deformation and Failure of Angle-Ply Composite Laminates

B.T. Werner, J.D. Schaefer, and I.M. Daniel

Abstract Angle-ply carbon/epoxy composite laminates were tested under uniaxial compression at two strain rates (10^{-4} and 1 s^{-1}). In this study, failure is defined as maximum ply damage. This is determined by noting where the stress–strain curve of the laminate reaches a characteristic damage state and the stress–strain behavior reaches a terminal modulus. The characteristic damage state stress is compared to predictions from the recently introduced Northwestern (NU) theory at each strain rate. Residual and interlaminar stresses were considered in the analysis and experiment design. Most classical theories fail to predict the exact failure behavior of the laminates. The NU theory is in good agreement in most cases with the exception of cases where the state of stress includes a non negligible stress component in the fiber direction. However, for determining lamina failure due to matrix dominated failure modes, the NU theory is in excellent agreement with experimental results.

19.1 Introduction

Failure within a laminate may be caused by failure of individual laminae within the laminate (intralaminar failure) or by separation of contiguous laminae (interlaminar failure). This study seeks to investigate intralaminar failure of a high stiffness high strength carbon/epoxy (IM7/8552) laminate. Failure of a laminate may be defined as the initiation of failure when the first layer fails, which is called first ply failure (FPF). In determining FPF, lamination theory is used to determine the state of stress acting on each layer and applying a selected failure criterion to determine whether the lamina's strength has been met or exceeded. This relies upon the assumption that an embedded lamina within a laminate shows the same in situ properties as the layer in isolation. Residual stresses from fabrication can also affect the performance of a layer within a laminate. Designs that use FPF as a failure criterion tend to be conservative as the failure of one ply does not necessarily translate into the failure of the structure.

Another approach to determining the ultimate strength of a laminate is to study failure progression. This way of looking at composite design is more useful in designing energy dissipating structures. Once a layer fails within a laminate it is discounted and the structure is reanalyzed without the damaged layers. In order to effectively use this approach, a well defined method for determining ply failure must be developed.

In this study, angle-ply laminates, $[\pm\theta]_{14s}$, were tested under uniaxial compression (Fig. 19.1). This produces various levels of biaxial stress within the lamina for different angles, θ. A similar approach was used in developing the Northwestern (NU) failure theory for lamina properties [1–3]. The NU theory outperforms classical failure theories in predicting the strength of a unidirectional lamina, so it is used to predict the characteristic damage state stress, σ_{cds}, in the angle-ply laminates. Daniel, et al. also showed that for matrix dominated failures of the composite lamina there is a significant strain rate effect on the lamina strengths [2, 3]. For this reason, the characteristic damage state stress found experimentally for the various angle-ply laminates in compression is compared to the NU theory prediction.

B.T. Werner (✉) • J.D. Schaefer • I.M. Daniel
Center for Intelligent Processing of Composites, Northwestern University, Evanston, IL 60208, USA
e-mail: bwerner@u.northwestern.edu; josephschaefer2011@u.northwestern.edu; imdaniel@northwestern.edu

G.P. Tandon et al. (eds.), *Experimental Mechanics of Composite, Hybrid, and Multifunctional Materials, Volume 6*, Conference Proceedings of the Society for Experimental Mechanics Series, DOI 10.1007/978-3-319-00873-8_19,

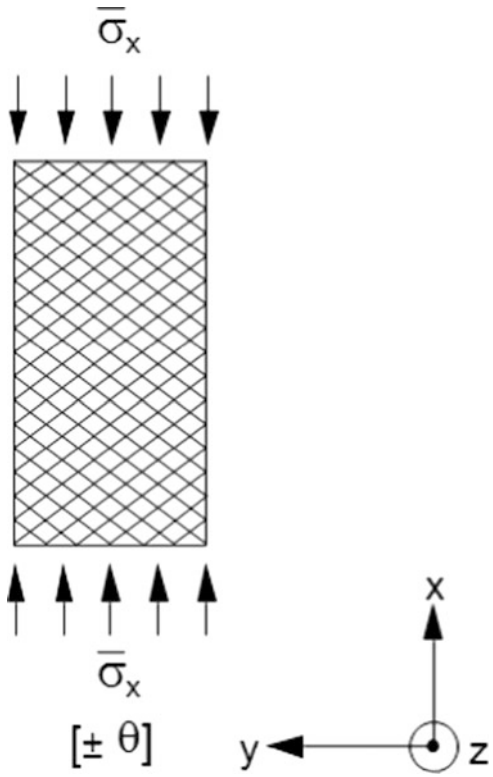

Fig. 19.1 Uniaxial compression of an angle-ply laminate [4]

19.2 Experimental Procedure

19.2.1 Material and Specimen Preparation

In this study a unidirectional high stiffness, high strength carbon epoxy composite was used (IM7/8552) to produce $[\pm\theta]_{14s}$ angle-ply laminates, where $\theta = 15°, 30°, 45°, 60°, 75°, 90°$. By alternating the orientation of the layer after each ply during layup, the effect of interlaminar stresses is kept to a minimum [5]. The $\pm 90°$ laminate is simply a unidirectional plate tested in the direction transverse to the fibers. The IM7/8552 prepreg was cured in a two step bleederless process where four layers of separator were used on either side of the layup. This produced a consistent composite laminate with a fiber volume fraction, $V_f = 0.58$ and a ply thickness, $t = 0.14$ mm (0.0055 in.).

Prismatic block compression specimens were cut from the plate of dimension 7.82 × 7.82 × 25.4 mm (0.31 × 0.31 × 1 in.) using a diamond blade. After cutting, the machined sides are polished using an abrasive grinder to ensure the pararellism of the loading faces. The specimen ends are then coated with a layer of graphite and bonded to steel loading blocks using an epoxy adhesive (Hysol 9430). The graphite prevents the fiber ends from bonding to the adhesive and allows the layers to deform in shear freely.

19.2.2 Testing and Results

The specimens are tested in a servo-hydraulic testing machine (Instron 8500). The tests are displacement controlled to ensure a consistent axial strain rate. The quasi-static tests are run at a displacement rate of 0.1524 mm/min (0.006 in/min) to produce an axial strain rate of 10^{-4} s^{-1}. The faster rate tests are performed at a displacement rate of 1.52 m/min (5 ft/min) to produce an axial strain rate of 1 s^{-1}. Strains are measured by bonding an electrical resistance strain gage to the in-plane face of the specimen. Data is recorded via the GPIB connection on a custom Labview program for the quasi-static rate tests and via an oscilloscope for the higher rate tests. For the higher rate tests, a channel is formed in the lower grip to allow the loading block to slide freely in the machine axis direction while having lateral support. This allows the crosshead to overcome its inertia and move at a constant displacement rate before the specimen is loaded. The stress–strain curves for the six cross-ply laminates and unidirectional transverse tension and compression are presented in Fig. 19.2.

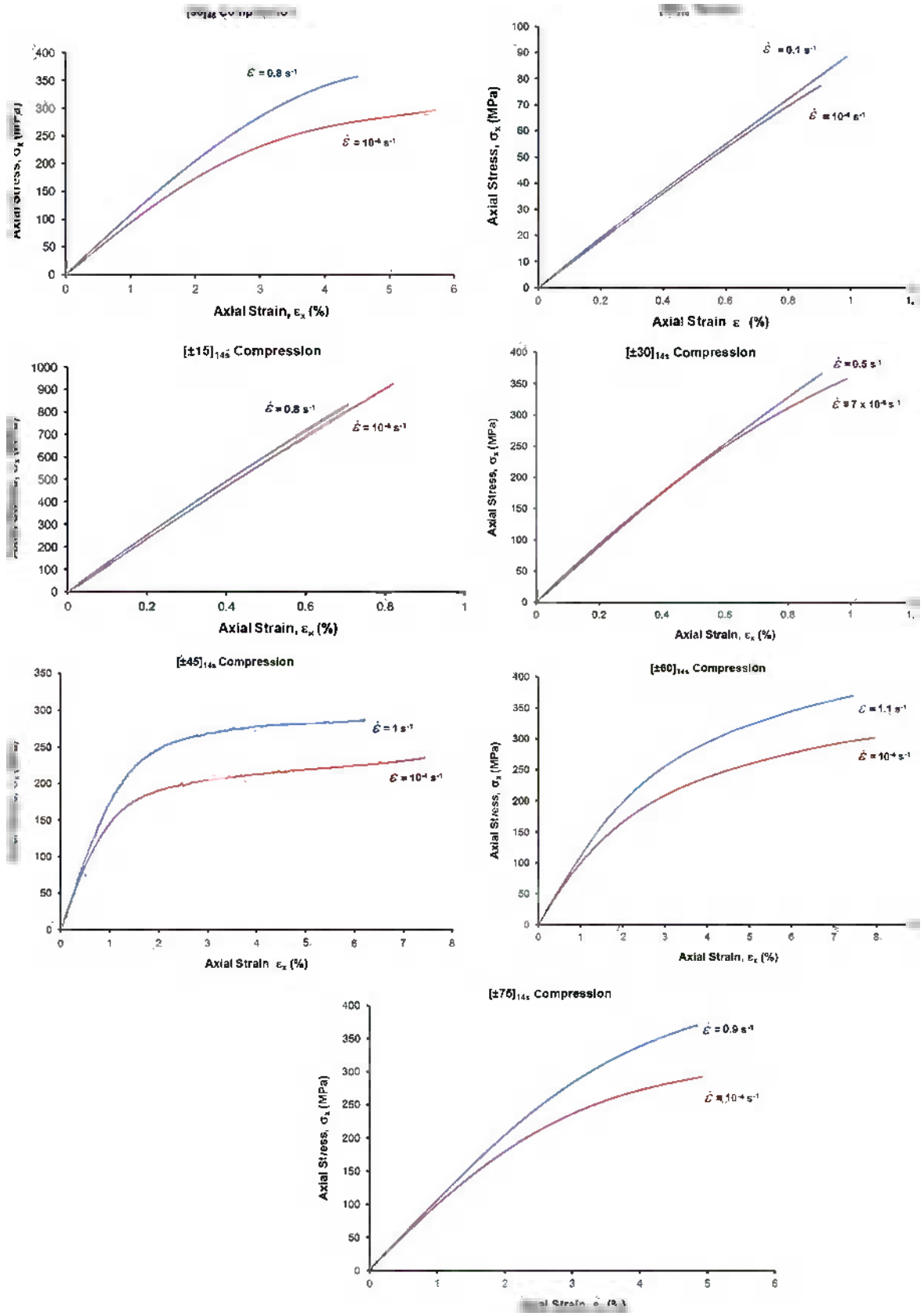

Fig. 19.2 Stress–strain curves for transverse compression, tension and angle-ply compression for IM7/8552

19.3 Analysis

As mentioned earlier, for multidirectional laminates the maximum stress level seen does not reflect the first ply failure. Once a ply fails, damage can continue to expand until the entire laminate fails. The goal of this study is to determine when maximum ply damage occurs. Reifsnider and Masters showed that for a $[0/90]_s$ crossply laminate the weaker 90° plies continue to crack until there is a minimum crack spacing where any additional applied stress cannot increase the axial stress in the layer to the failure level F_{2t}. This is called the characteristic damage state (CDS) of the laminate [6]. In a crossply this state is achieved when the stress–strain curve reaches a terminal modulus, E_t. The stress level at this point is the characteristic damage state stress, σ_{cds}. It is at this point that the layer has reached maximum ply damage and, in an angle-ply laminate, it has reached the maximum stiffness reduction.

For the stress–strain curves shown in Fig. 19.2, the characteristic damage state stress can be determined by drawing a tangent to the terminal modulus and determining the laminate stress when this modulus is reached as shown in Fig. 19.3.

Using the characteristic damage state stress, the residual stresses, and lamination theory, the lamina stresses can be plotted against the NU theory maximum ply damage envelope for both the quasi-static and higher strain rates (Fig. 19.4). The NU theory is dependent on the matrix dominated properties for the composite lamina: the stiffnesses, E_2 and G_{12}, and the strengths F_{2c}, F_{2t}, and F_6. When developing the NU theory for isolated lamina, a 10° off-axis tension test was used to determine the in-plane shear strength. However, to account for the effect of embedding the lamina within a laminate, the ±45° compression characteristic damage state stress was used for F_6 [7]. This definition of in-plane shear strength tends to be higher than what is given by the 10° off-axis test. For the direct transverse tension and compression strengths, the maximum stress shown by specimen is used. This is because the fibers are fully aligned and do not form a net which increases the ultimate strength of the angle-ply laminates.

As shown above, the NU theory does an excellent job of predicting when maximum ply damage occurs for both strain rates. The ±15º laminate does not fit the NU theory prediction very well. This is most likely due to the high stress component in the fiber direction. Improvements must be made to the NU theory to either include a fiber failure branch or to incorporate the effect of σ_1 into the current theory.

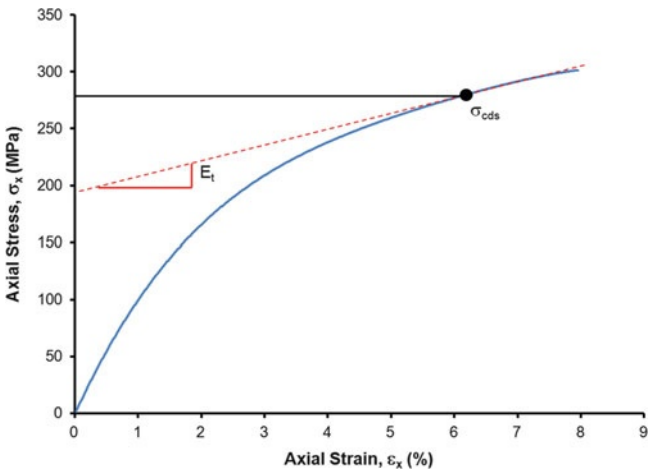

Fig. 19.3 Determination of characteristic damage state stress

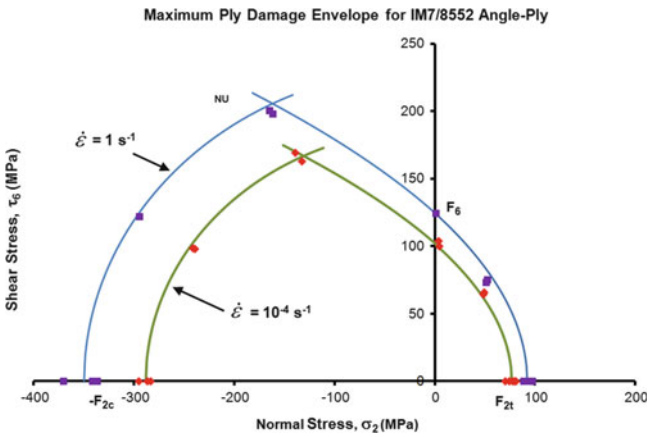

Fig. 19.4 NU theory prediction for characteristic damage state of various angle-ply laminates at different strain rates

19.4 Conclusions

When looking at progressive failure of multidirectional laminates it is important to determine the maximum amount of damage that an individual layer can tolerate. The NU theory does an excellent job of predicting the stress at which that occurs at any given strain rate. Angle-ply laminates, when interlaminar stresses do not initiate failure, restrict the failure modes to only act in the lamina plane. This may also hold true for more complex laminates and it appears that using the characteristic damage state of the lamina is an excellent starting point for investigating progressive failure.

Acknowledgement The work described in this paper was sponsored by the Solid Mechanics Program of the Office of Naval Research (ONR). We are grateful to Dr. Y. D. S. Rajapakse of ONR for his encouragement and cooperation.

References

1. Daniel IM et al (2009) Interfiber/interlaminar failure of composites under multi-axial states of stress. Compos Sci Technol 69(6):764–771
2. Daniel IM, Werner BT, Fenner JS (2011) Strain-rate-dependent failure criteria for composites. Compos Sci Technol 71(3):357–364
3. Schaefer JD, Werner BT, Daniel IM (2013) Strain rate effects on failure of a toughened matrix composite. In: SEM 2013 annual conference and exposition on experimental and applied mechanics, Lombard
4. Daniel IM, Ishai O (2006) Engineering mechanics of composite materials, 2nd edn. Oxford University Press, New York, xviii, 411 p
5. Werner BT, Schaefer JD, Daniel IM (2013) Effect of ply dispersion on failure characteristics of multidirectional laminates. In: SEM 2013 annual conference and exposition on experimental and applied mechanics, Lombard
6. Reifsnider KL, Masters JE (1982) An investigation of cumulative damage development in quasi-isotropic graphite/epoxy laminates. In: Reifsnider KL (ed) Damage in composite materials. American Society for Testing and Materials, West Conshohocken, pp 40–62
7. Rosen BW (1972) Simple procedure for experimental determination of longitudinal shear modulus of unidirectional composites. J Compos Mater 6:552–554

Chapter 20
Progressive Failure of a Unidirectional Fiber-Reinforced Composite

Pascal Meyer and Anthony M. Waas

Abstract A set of experimental results in support of developing a three-dimensional, Integrated Finite Element Method (IFEM) to capture progressive failure within the constituents of a three phase composite material is presented. Periodic Boundary Conditions (PBC) are used to apply macroscopic strains on a Representative Unit Cell (RUC) containing fiber, interface, and matrix with a fixed volume ratio. An orthotropic failure model has been implemented to introduce damage on the constituent level. The applicability of this code in a multi-scale framework is demonstrated and results are verified against experimental data.

20.1 Introduction

With the demand for faster but at the same time more efficient air transportation, new materials will have to be introduced into future propulsion systems. In an effort to make aero engines more efficient, the temperatures of the turbine sections will be raised to a level which exceeds the limit of current metallic materials.

New materials will have to be tested at very high temperatures that surpass 1,300 °C. New techniques that allow the observation of material behavior and damage evolution at these elevated temperatures need to be developed.

Strain measurements using extensometers can be applied at very-high temperatures but only provide a single value averaged over a large volume. Especially for non-metallic composites this technique will not capture the damage initiation and will subsequently lead to inaccurate proportional limits with no meaning in terms of damage initiation. Digital Image Correlation (DIC), principally developed by Sutton et al. [5], is a good tool to measure full-field displacement maps and in theory has no limitation at very high temperatures provided the image quality and speckle contrast are sufficient. DIC is an optical method to measure deformation on an object surface by correlating images of the deformed and undeformed imaged surface. This technique has been proven for applications at slightly elevated temperatures but faces several issues at very high temperatures that have to be considered in order to measure displacement fields. Black-body radiation emanating from the heated sample makes it impossible with standard lighting and camera equipment to image the surface of the test specimen. Speckle-techniques, usually in form of paint, that is applied to the surface tends to de-bond within a short amount of time at very-high temperatures. It also requires additional steps to be carried out before testing and results might be error-prone due to poor adhesion between the paint and sample. Precautions have to be in place to account for heat haze. Lui et al. [1] used aluminum-oxide and boron nitride ceramic coatings to create a speckle pattern on the sample surface. The maximum temperature that was demonstrated to achieve good DIC results was 704 °C. Novac and Zoc [2] employed a CO_2 Laser to locally heat up a test specimen. An air knife was positioned to blow across the sample surface in an effort to minimize thermal turbulence. A speckle pattern, using alumina or zirconia paints, was applied with an airbrush. They showed analytically that blue light illumination and filtering systems could provide contrast at temperatures up to 1,700 °C.

P. Meyer (✉)
Department of Aerospace Engineering, The University of Michigan, 2045 FXB Building, 1320 Beal Avenue, Ann Arbor, MI 48109, USA
e-mail: pasmey@umich.edu

A.M. Waas
Department of Aerospace Engineering, The University of Michigan, 3044 FXB Building, 1320 Beal Avenue, Ann Arbor, MI 48109, USA

G.P. Tandon et al. (eds.), *Experimental Mechanics of Composite, Hybrid, and Multifunctional Materials, Volume 6*, Conference Proceedings of the Society for Experimental Mechanics Series, DOI 10.1007/978-3-319-00873-8_20,

Grant et al. [3] showed that blue light illumination could be used for DIC measurements up to 1,000 °C. The authors measured Young's modulus and coefficient of thermal expansion for RR1000 samples. However, the reference image was updated frequently during the cross-correlation which may introduce strain errors. Lyons et al. [4] demonstrated DIC at temperatures up to 650 °C. The specimens were heated in a box furnace equipped with a window. Boron nitride- and aluminum oxide-based ceramic coatings were used to create the speckle pattern.

The present paper describes a simple, yet effective setup for room and high-temperature DIC measurements which employs the technique of blue light illumination with an appropriate bandpass filter used in combination with a two zone furnace for accurate and stable temperature control over a wide area of the tested sample. It is shown that this technique can be used to detect the onset of damage, appearing as regions of high strain gradients. These surface strain concentrations can result from interior damage that manifests as high strain fields on the surface, or because of cracks occurring on the surface. Final determination requires post-experiment inspections to ascertain the origin of surface strain gradients.

A detailed description of the setup is presented with details on illumination, filtering, and heating mechanism. Heat haze issues are addressed and a new speckling technique suitable for very-high temperatures is described and demonstrated, first at room and subsequently elevated temperature. Full field strain-measurements of a notched tensile test at 1,300 °C are presented.

20.2 Experimental Method

The thermo-mechanical testing was performed on a hydraulic test frame where both the bottom and top grip are displacement controlled. This configuration is preferable since the specimen center, when aligned correctly, will not show any rigid body movement relative to the camera which will allow for a lower correlation error when performing DIC on recorded images. Figure 20.1 shows the load frame and camera set-up. Hydraulic grips with 1 in. (25.4 mm) wide smooth wedges were employed and a grip pressure of 1,000 lbs was used to clamp the specimens. Aluminum mesh was used between the smooth grip surfaces and the rough specimen surface to ensure uniform loading. Heating was accomplished with a 3.5 in. tall two-zone hot rail furnace with horizontal sliding action supplied by Amteco Incorporated. An especially for visual very-high temperature application manufactured viewing port was incorporated in the center of the furnace. The viewing port consisted of an alumina housing and a window holder with a thin glass window about 3 in. away from the specimen surface. Figure 20.2 visualizes the path of the light from the LED assembly to the specimen from which it reflects back to the camera. This setup ensures easy specimen access and good temperature control over a large volume due to the two heating zones. The small window, good insulation properties of the viewing port, and proper insulation of all gaps minimized turbulent air caused by temperature differences.

Each heating zone was individually controlled under feedback from a type-R thermocouple. The thermocouples were placed about 2.5 mm above and below the center of the sample at a distance of about one tenth of millimeter away from the surface. Heating of the sample was split into three steps. First, the sample was heated to 1,000 °F (538 °C) at a ramp rate of

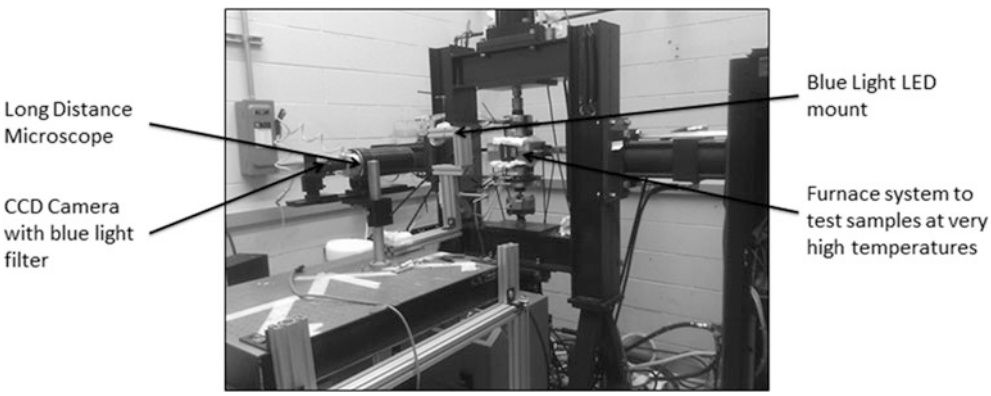

Fig. 20.1 Experimental setup

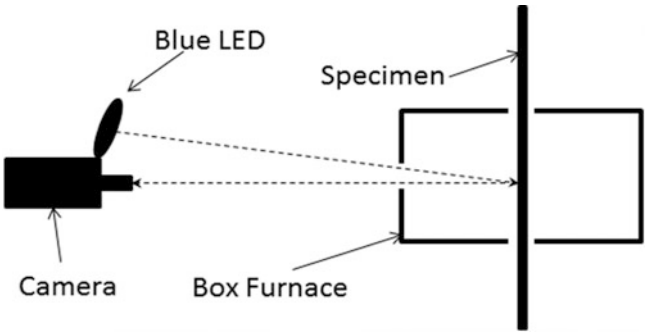

Fig. 20.2 Schematic view of the experimental setup

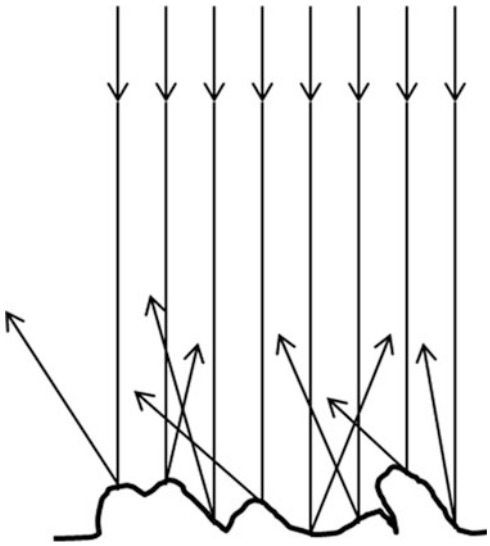

Fig. 20.3 Diffuse reflectance on surface features larger than the wavelength of the coherent illuminating source

60 °F per minute. A 5 min dwell time at 1,000 °F was included to allow the temperature to fully stabilize. Second, the temperature was ramped up to 2,000 °F (1,093 °C) at 50 °F (50 °C) per minute followed by a 5 min dwell time. Finally, the specimen was heated to 2,400 °F (1,315 °C) at 30 °F per minute. To allow the specimen to be in a thermally equilibrated state a dwell time of 15 min at 2,400 °F followed the last ramp-up.

The specimen was then loaded to failure in a displacement controlled test. The combined (bottom & top grip) displacement rate was set to 0.16 mm per minute. Compressed air in combination with air amplifiers were used during heat-up to avoid overheating of the grips. It is turned off for the duration of the testing procedure to avoid any air circulation around the furnace which would lead to heat haze and subsequently to a higher DIC correlation error.

The specimen was illuminated by two 447.5 nm wavelength Luxeon Star LED assemblies. Each assembly contains seven LXML-PR01-0500 LEDs with a total output of 6,370 mW each. The assemblies were mounted slightly above the optical setup. Images for correlation were acquired using a high-resolution digital camera. The camera used was a LaVision Imager E-Lite 5M with 2,448 × 2,050 pixel resolution. Two 2x magnifying lenses and a 200 mm focal length Nikor lens were connected to the camera. Best depth of field for the measurements was achieved with the F stop set to 8.

This camera-lens combination yielded in a field of view of 10 × 10 mm. The camera assembly was mounted on a precision alignment stage which allowed for easy adjustments. In order to minimize vibrations, the camera setup was mounted on an optical table. A blue light band-pass filter, with a center wavelength of 450 nm and a bandwidth of 80 nm, was built into the system. Images were post-processed with LaVision's DIC correlation software DaVis. This software is based on a Fourier-transform cross-correlation algorithm to determine the relative displacement of sub regions of the images. The proposed method will not use any artificial speckle pattern but rather rely on the natural surface architecture. The tested samples contain a "rough" surface as a result of the manufacturing process. That is, the typical wave-length of surface undulations are much larger than the wave length of the illumination source. As a results, the image of the surface on the image plane, due to diffuse reflection at the surface, results in a speckle pattern due to destructive interference as illustrated in Fig. 20.3.

This pattern is perfectly suited for full field small strain measurements as found in the tested samples. Artificial speckle patterns for high temperature applications often suffer from adhesion and degradation problems after a short period of time. Both result in correlation errors or even the complete loss of correlation. The pattern used in this work could be used for long periods of time, provided no oxidation or other surface changes occur.

20.3 Experimental Results

Both room- and high temperature experiments were conducted on cross-ply Ceramic-Matrix-Composite (CMC) specimens with a total length of 8 in., a gauge width of 0.4 in., and a thickness of 0.08 in.. A notch with a radius of 0.012 in. and a depth of 0.036 in. was cut horizontally on one side. The notch corresponded to a stress intensity factor of 3.6. The experiments were conducted as displacement controlled tests. Both the top and bottom grip were displaced at a constant rate of 0.08 mm (0.0031″) per minute each, which results in a combined displacement of 0.16 mm (0.0062″) per minute.

20.3.1 Room Temperature Tests

In support of the Integrated Finite Element model, room temperature tests on single edge notch tensile samples were conducted. Load was measured with a 2,000 lbs load cell. Full field strain maps were computed with DaVis DIC software. Selected images are shown in Fig. 20.6. Two cracks, propagating from the notch outward, were always observed at room temperature with the described notch geometry. Ultimately, final fracture occurred along one of these cracks.

20.3.2 Very-High-Temperature DIC

In order to verify the proposed method, high-temperature quasi-static uniaxial tests at 2,400 °F (1,315 °C) were conducted on the single edge notch ceramic specimens as described above. The grip section of the specimen plus an additional 0.5 in. protruded the furnace. Two thermocouples, as described above, were used to ensure a constant temperature of 2,400 °F (1315 °C) in the vicinity of the notch. After positioning the equipment in place and completing the heating cycle the temperature of the sample was equilibrated over a period of 15 min. Subsequently, the bottom grip was closed. It had been kept in the open position during the heating cycle to avoid loading of the sample due to thermal expansion. All air amplifiers, which were used for grip cooling, were turned off in order to minimize turbulent air in the line of sight between the furnace and camera. The grip temperature was closely monitored during the test to assure that the temperature stayed within its limitation during the test. Two images per second were recorded during the experiment and subsequently processed using DaVis DIC software. Fig. 20.4 shows two selected vertical (ε_{yy}) strain plots with the corresponding location on the normalized Stress-time curve. Stress and time were normalized by its maximum values. Damage initiation is clearly visible at a relative Stress of 0.7. The crack propagation is captured until final fracture.

20.4 Multi-scale FEM Approach

It is well known that failure of fibrous materials is driven by mechanisms on the microscopic scale. Interactions of fibers and matrix for example cannot be captured with homogenized material models. Multi-scale methods, as described by Galvanetto and Aliabadi [6], on the other hand are suitable to predict the behavior of these materials. Stress and strain fields can be accurately resolved for each constituent. This gives these type of methods the advantage to predict failure for each constituent separately and not in a homogenous sense. For this work a finite element code was developed that is completely

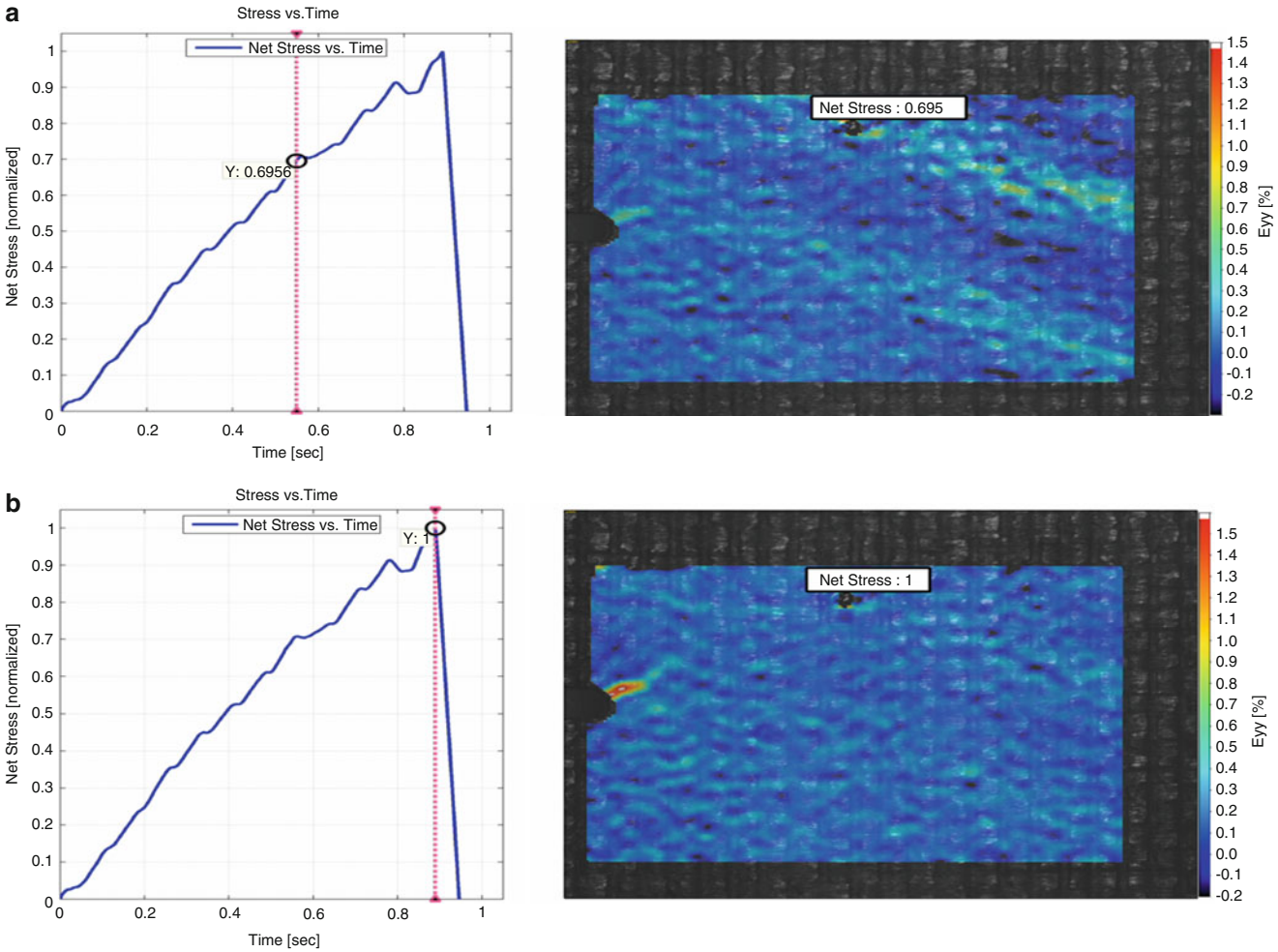

Fig. 20.4 (**a**) DIC results at 0.7 relative stress (**b**) DIC results at peak load

integrated in a user material subroutine (UMAT) of the commercial FEM software package ABAQUS. A macroscopic model, e.g. single edge notch tensile specimen, is created and run in ABAQUS. The material law for the macroscale is supplied by a sub-scale representative volume element (RVE) model that contains microstructural features of the composite. It is noted that the RVE is not the smallest geometrical repeat unit cell (RUC) that represents the microstructure. Instead, the RVE is the smallest volume of material, which accurately represents the physical mechanisms of deformation response and subsequent failure that needs to be accounted for in a given analysis.

In the IFEM, displacement fields at a particular integration point of the macroscopic model is passed on to the microscale and applied on the boundary of a Subcell which contains all constituents (for instance, Fiber, Matrix and Interface). Four main steps can be identified within the IFEM code. First, the element matrices are calculated and then assembled to form a global system of equations. In a second step Periodic Boundary Conditions are utilized to apply the macroscopic displacement fields on the boundaries of the Subcell. Next, the nodal displacements are calculated and the solution is used in a third step to calculate the element strains and stresses. Finally, a failure criterion is checked for each element within the Subcell. If the failure criterion is satisfied the element stiffness is reduced and the stress and strain fields are re-equilibrated. In the final step, the volume averaged stresses and the Jacobian matrix are calculated and passed back to Abaqus in order to update the stress state of the particular integration point in the macroscopic model.

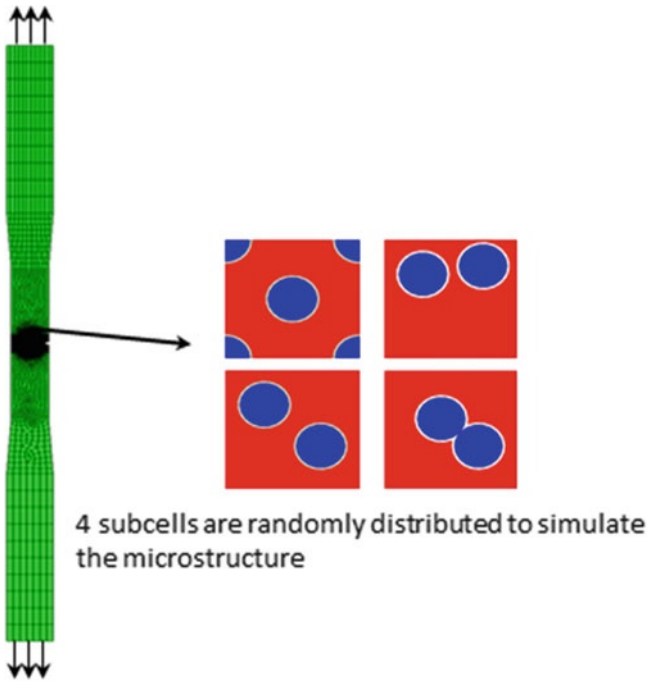

Fig. 20.5 Single edge notch tensile model with four 2 Fiber subcells

Four subcells containing two fibers each (as shown in Fig. 20.5) were randomly distributed throughout the macroscopic model in order to capture microstructural features as observed in the real specimen. With this technique, anomalies like fiber touching, varying fiber diameter, or fibers in close proximity to each other, can be captured. Maximum principle strain was chosen for the failure criterion which is well suited for brittle materials. The criterion was checked for each constituent separately.

Furthermore, strain to failure and fracture toughness are needed. Mesh objectivity is preserved on the Subcell level through a energy preserving failure method. In this method a fixed volume around an element which exceeded the failure criterion is subject to changes in the stiffness, rather than the single element. The fixed volume is calculated based on fracture mechanics according to Eq. 20.1, which provides a characteristic length scale first described by Bazant and Cedolin [7],

$$l = \frac{E^* G_{IC}}{\sigma_{cr}^2} \tag{20.1}$$

The characteristic volume associated with failure corresponds to l^3, E is Young's modulus, G_{IC} is the fracture toughness, σ_{cr} is the cohesive strength of the material.

Figure 20.6 shows a comparison of crack propagation as observed in experiments and IFEM predictions. The crack path in the single edge notch tensile simulation is part of the solution and unknown prior to the simulation. Two cracks were observed in all single edge notch experiments. This behavior was accurately captured with the multi-scale method.

20.5 Conclusions

In this work an experimental technique feasible for conducting room as well as very high temperature experiments was demonstrated. Experimental results at room temperature showed crack propagation on CMC specimens. Two cracks were observed for the tested notch geometry. It was demonstrated that this method in combination with a box furnace was well suited for very high temperature DIC measurements. One advantage of a box furnace compared to other heating techniques

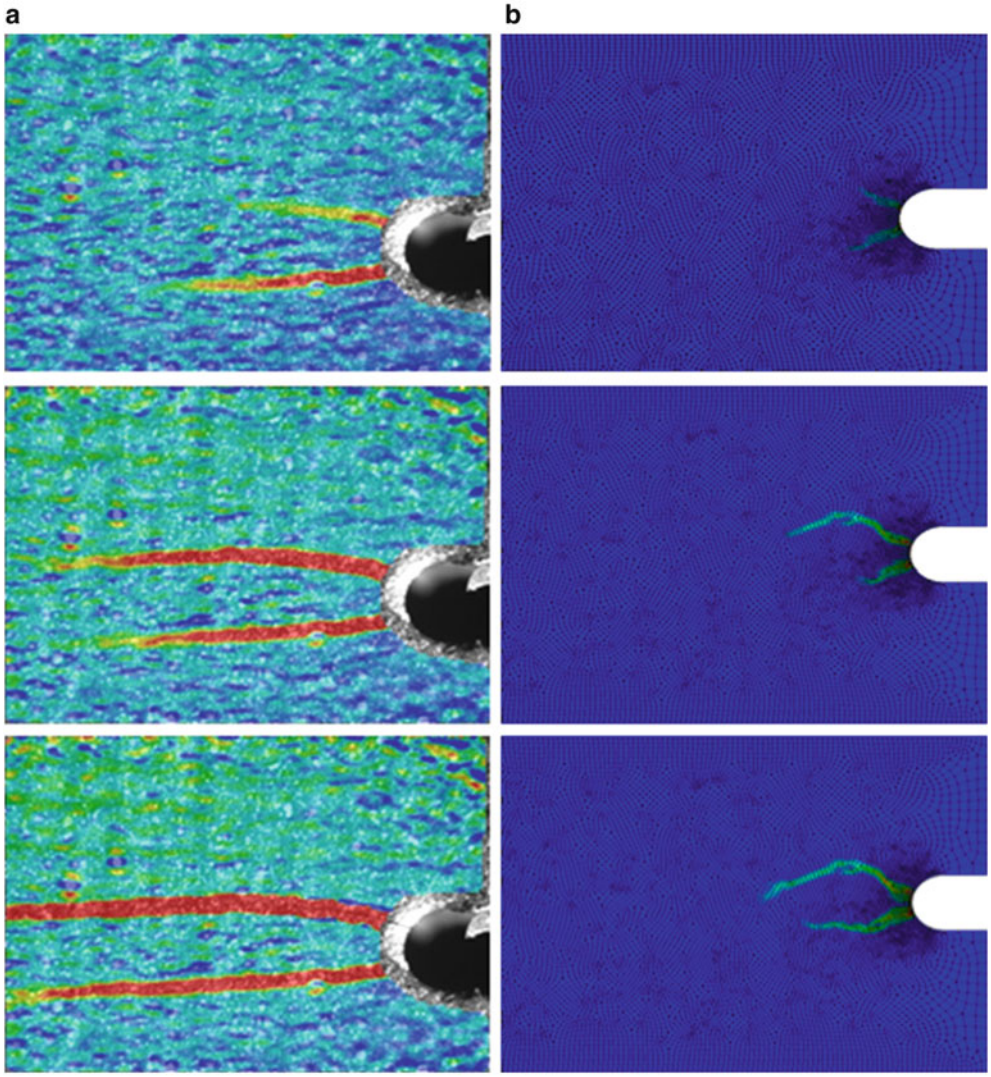

Fig. 20.6 (**a**) Crack propagation as observed in experiment (**b**) IFEM crack propagation prediction

is the ability to keep temperature fluctuations within a very small range of only a few degrees Fahrenheit. Turbulent air influences, which are generally problematic for DIC measurements at high temperature, were minimized with this setup.

A multi-scale finite element method (IFEM) was developed for predicting failure in fibrous materials. A macroscopic model was run in ABAQUS. IFEM was used to update the material law inside a user subroutine (UMAT). It was demonstrated that the experimentally observed failure schemes were captured with this multi-scale approach.

References

1. Liu J, Lyons J, Sutton MA, Reynolds A (1998) Experimental characterization of crack tdformation fields in alloy 718 at high temperatures. J Eng Mater Technol 120:1
2. Novac M, Zok FW (2011) High-temperature materials testing with full-field strain measurement: experimental design and practice. Rev Sci Instrum 82:115101
3. Grant BMB, Stone HJ, Withers PJ, Preuss M (2009) High-temperature strain field measurement using digital image correlation. J Strain Anal Eng Des 44:4
4. Lyons JS, Liu J, Sutton MA (1996) High-temperature deformation measurements using digital-image correlation. Exp Mech 36:64

5. Sutton MA, Wolters WJ, Peters WH, Ranson WF, McNeill SR (1989) Determination of displacements using an improved digital correlation method. Exp Mech 29:261–267
6. Galvanetoo U, Aliabadi MHF (2010) Multiscale modeling in solid mechanics – computational approaches. Imperial College Press, London
7. Bazant ZP, Cedolin L (1991) Stability of structures – elastic, inelastic, fracture, and damage theories. Oxford University Press, New York

Chapter 21
Process Optimization by Direct Integration of the RFID Chips During the Manufacturing of the Composite Parts Used in Aeronautical Engineering

H-A. Alhas, E. Bayraktar, C. Nizam, and J. Khalil

Abstract Basically, an RFID chip (Radio-frequency identification) is a very small memory chip, very much like a memory chip in a computer in function. It is the use of a wireless non-contact system that uses radio-frequency electromagnetic fields to transfer data from a tag attached to an object, for the purposes of automatic identification and tracking. When the small size RFID chips are integrated in the composites parts during manufacturing processes, the chips can transmit all of the information in every stage of manufacturing of the pieces even they keep all the information after the production.

Today, several RFID integrated systems are commercially used in certain applications such as transportation, supply chain in numerous sectors etc. However, RFID Chips, if we can integrate them directly in the composite parts, from the beginning of the production process, can improve the efficiency of the process and also decrease the lead time and processing time of the manufacturing process. In the frame of the common research project, the present paper concentrate on the direct integration of the RFID chips into the composite parts used in aeronautical industry during the manufacturing (laminating) process of these composite parts in order to develop a better and safety process and accelerate the operational excellence by decreasing extremely the delivery time. It means that it makes the intelligent composite parts via RFID chips during the manufacturing of the composites used in aeronautical engineering.

21.1 Introduction

Radio-frequency identification (RFID) is the use of a wireless non-contact system that uses radio-frequency electromagnetic fields to transfer data from a tag attached to an object/product, with the aims of automatic identification and tracking. Some tags require no battery and are powered by the electromagnetic fields used to read them. Others use a local power source and emit radio waves (electromagnetic radiation at radio frequencies). The tag contains electronically stored information which can be read from up to several meters away. Unlike a bar code, the tag does not need to be within line of sight of the reader and may be embedded in the tracked object.

RFID use has been steadily grooving but its most widespread adaption has been the result of powerful organizations such as Wal-Mart and the U.S. Department of Defence (DoD) that employ the technology in supply management. The DoD uses RFID technology to identify shipping containers and the products within them to ensure appropriate material control within the theatre of war. The DoD learned hard logistic lessons during the 1991 Gulf War and the DoD subsequently mandated its 30,000 suppliers to adapt RFID technology in 2003 [1–5]. With RFID technology, it is very easy to give brainpower to the materials during their manufacturing processes to be controlled from outside and from a distance without touching materials.

H-A. Alhas
Supmeca-LISMMA-Paris, Mechanical and Manufacturing Engineering School, ST Quen, France

Eurocopter, Quality & Business Improvement, Paris, France
e-mail: alhas10@hotmail.com

E. Bayraktar (✉)
Supmeca-LISMMA-Paris, Mechanical and Manufacturing Engineering School, ST Quen, France
e-mail: bayraktar@supmeca.fr

C. Nizam • J. Khalil
Airbus Headquarter – Value Chain Visibility, Toulouse, France

G.P. Tandon et al. (eds.), *Experimental Mechanics of Composite, Hybrid, and Multifunctional Materials, Volume 6*, Conference Proceedings of the Society for Experimental Mechanics Series, DOI 10.1007/978-3-319-00873-8_21,

With just using radio frequency, we are be able to take data saved on the previous step about product' quality and related info without stopping the production line in order to accelerate the process, because waiting is waste. Actually, the role of RFID is mainly a communication and information transfer technology.

Therefore, we can use these behaviours of the RFID technology to improve the process. Moreover, RFID technology is a wireless and powerless. From the wireless system, sensor and to the tags, RFID provides many new opportunities. Finally, using of RFID Technology effectively throughout production can enhance the competitive abilities of the companies and provide strategic advantages in the global market world.

In the frame of the common research project, the present paper concentrate on the direct integration of the RFID chips into the composite parts used in aeronautical industry during the manufacturing process of these composite parts in order to develop a healthier and safety process and accelerate the operational excellence by decreasing extremely the delivery time. It means that it makes the intelligent composite parts via RFID chips during the manufacturing of the composites used in aeronautical engineering. At the first stage, we will give detail information on the following aspects: Application of RFID technology, integration of an RFID chip into the composite parts, expected progress. We will give the preliminary simulated test results at the laboratory scale and we will inform the real test results in industrial scale carried out in the manufacturing department of the French aeronautic company (Paris) by integrating RFID chips in an aeronautical composite part.

21.2 Application of RFID Technology: RFID Integrated Systems

RFID is contactless and wireless. RFID Technology is ranked among the top 10 of dominant future technologies. The technical optimal solution would be the storage of data in a silicon chip. The most common form of electronic data-carrying device in use in everyday life is the smart card based upon a contact field (telephone smart card, bank cards). However, the mechanical contact used in the smart card is often impractical. A contactless transfer of data between the data-carrying device and its reader is far more flexible. In the ideal case, the power required to operate the electronic data-carrying device would also be transferred from the reader using contactless technology. Because of the procedures used for the transfer of power and data, contactless ID systems are called RFID systems (Radio Frequency Identification) [3].

A smart card is an electronic data storage system, possibly with additional computing capacity (microprocessor card), which is incorporated into a plastic card the size of a credit card. The first smart cards in the form of prepaid telephone smart cards were launched in 1984. Smart cards are placed in a reader, which makes a galvanic connection to the contact surfaces of the smart card using contact springs. Data transfer between the reader and the card takes place using reader via the contact surfaces. Smart cards make all services that relate to information or financial transactions simpler, safer and cheaper [3–7].

For this reason, RFID systems are closely related to the smart cards described above. Like smart card systems, data is stored on an electronic data-carrying device (the transponder). However, unlike the smart card, the power supply to the data-carrying device and the data exchange between the data-carrying device and the reader are achieved without the use of galvanic contacts, using instead magnetic or electromagnetic fields. The underlying technical procedure is drawn from the fields of radio and radar engineering. The abbreviation RFID stands for radio frequency identification, i.e. information carried by radio waves. Due to the several advantages of RFID systems compared with other identification systems, RFID systems are now beginning to conquer new mass markets. One example is the use of contactless smart cards as tickets for short-distance public transport [3–11].

The Information on an RFID chip is an Electronic Product Code (EPC). While the Universal Product Code (UPC) information of a barcode provides manufacturer and product information, the information provided by an EPC is vastly more comprehensive. When scanning an EPC at a checkout, the tag communicates to the inventory management system when and where the scanning took place; and not only does it identify that it was a particular type of product, it also identifies the individual occurrence of that product type. With an EPC, every product has a unique serial number and it is possible to track millions of trillions of distinct items [4–10].

21.3 Components of an RFID System

An RFID System is composed of only a few separate components: a tag; an RFID tag reader; an antenna; and a host computer that equipped with necessary software. Reader has radio frequency module to receive and transmit the data, and is able to forward the data to another system like a PC. Transponder is called data-carrying device, and has an electronic microchip.

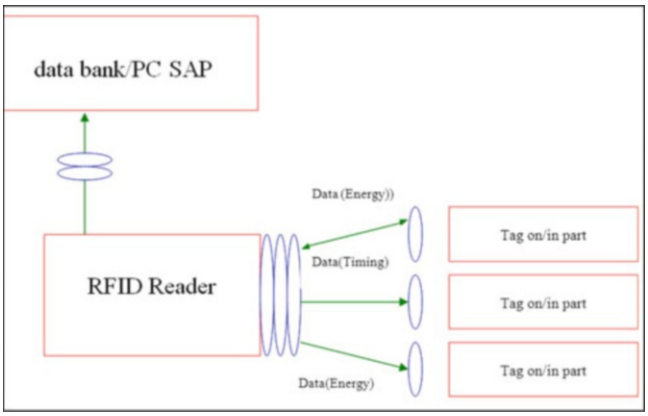

Fig. 21.1 Structure of the RFID-system

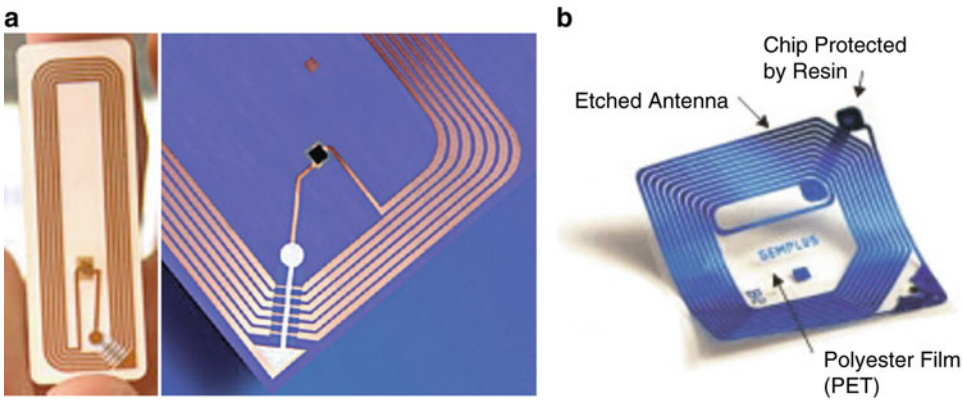

Fig. 21.2 Image of actual tag RFID (**a**) and detail of tag (**b**) [6–12]

Figure 21.1 show simply the structure of an RFID system that we have used as an application during the manufacturing of the composites used in aeronautical application. General idea as will be explained in the next section is to reduce the manufacturing time by entering RFID chips in the composites parts that these RFID chips contain all of the information related to the manufacturing processes and keep these information after the manufacturing.

Detail information on the image of actual tag RFID chip is shown in the Fig. 21.2 [6–8]. Thanks to special characteristics of these chips, we have carried out to keep all of the information related to the manufacturing of the composites parts. We believe that a successful operation has been carried out direct Integration of the RFID chips during the manufacturing of the composites used in Aeronautical Engineering.

In fact, the tag, also known as a transponder, is the basis of the RFID system and every product or shipment is equipped with an individually-identifiable tag. It is a device/chip without wire which is attached to a satellite/an antenna for communication, navigation, and identification and which is able to transmit and receive radio signals and has ability to transmit identification information, data from Reader, or transmitting data to Reader.

All tags require energy to operate them. There are two types of tags defined by the source of the energy: passive and active. Passive tags acquire energy from the incoming radio frequency waves, while active tags use power from a battery or an external energy source.

Passive tags have many advantages regarding to active tags. They are typically smaller, cheaper and last almost indefinitely, as there is no battery to wear out. Passive tags can operate on incredibly low power levels; however, they have short transmission ranges and do not perform well in electromagnetically-noisy environments. Passive tags can take almost any form and are commonly available as adhesive tags or moulded into car keys [9, 12]. Passive tags can operate in temperatures of −155 °C to +150 °C under 194 hPa maximum. RFID chip protects the data on itself during 30 years. For this reason, we will use passive tags in our experimental work. As an example, the main principle of data flow in a typical RFID System is presented in the Fig. 21.3. In reality, this is a reader that it is a device which is able to read data from a tag or transmitting data to a RFID tag [12–19].

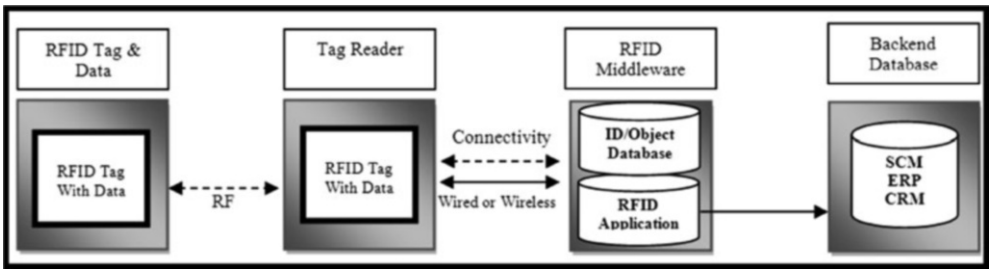

Fig. 21.3 Data flow in a typical RFID system

21.4 Experimental Conditions

In the frame of the common research project, we have directly integrated RFID chips (containing passive tags) into the composite parts used in aeronautical industry during the manufacturing (laminating) process of these composite parts in order to develop a healthier and safety process and accelerate the operational excellence by decreasing extremely the delivery time. It means that these intelligent composite parts via RFID chips during the manufacturing of the composites used in aeronautical engineering in order to make process optimization. Our basic and simple objective can be summarized as follows;

Improve the production process and decreasing the lead time by direct integration RFID Chips at the beginning of the lamination stage. Optimize and control of the composition of the epoxy matrix composite material during all of the manufacturing stages by this way. At the first stage, we have prepared five different compositions in the laboratory scale in order to simulate industrial manufacturing conditions (Table 21.1)

After that, we have introduced each of these compositions in the RFID chips by means of the portable readers and we have manufactured five pieces by direct integration of these RFID chips in the pieces by following the same procedure used aeronautical industry. For example, lamination of a composite product starts with the lamination and then sent it to the high pressured vessel between 120 °C and 180 °C for cooking operation and then waited minimum 24 h in an isothermal oven for finishing of the final thermosetting reaction during this stage. Composite parts are laid up on special tools in a manually intensive laminating process. These parts are then cured in very long pressured vessels before being removed from the tools, sent for mill work and off to final assembly. There are many vacuum vessel cycles, each typically requiring many hours to complete.

After all of the final manufacturing stage, we have controlled all of the pieces by using again the same portable reader to receive initial information on the pieces (composition, manufacturing stages etc.). The same operation has been carried out at the industrial scale as a preliminary application of RFID chips by direct integration in the industrial parts during their manufacturing stage. This industrial application has been carried out in the manufacturing department of the French aeronautic company (Paris) by direct integrating RFID chips in an aeronautical composite part. We have respected all of the manufacturing rules and followed all of the manufacturing stages after the integration of the RFID chips in the composite part.

21.5 Results and Discussion of the Process Optimisation

In the present work, we have implemented a new and low cost methodology in an industrial composite production that is used as usually in the aeronautical applications and we have obtained a considerable decrease in the production time. It means that the application of the RFID chip by direct integration, it is very easy to make all of the control of the pieces; at all of the stages of the manufacturing and the composition and also the evolution of the composition of the pieces during the process due to the pressure, temperature and others, etc. In other word, the control is possible in a very short time across the production processes from the initial design to the final assembly line from supplier to the end of the customer and also after the delivery to the customers to get high customer satisfaction. In spite of all of the improved processes we need simplifying, improving and accelerating our whole production processes to take under control all supply chains from supplier up to the end customer. This is a reality for the French aerospace manufacturing company that produce the composite parts as daily production process (Fig. 21.4). All of the manufacturing stages of the composite parts produced in this French aeronautic company were shown in this figure in detail.

Table 21.1 Compositions of the pieces introduced in the RFID chips

	Composition								
Specimen no	Al_2O_3	Epoxy	Fe_2O_3	B	SiC	TiO_2	Fe	Glass-fibre	Rubber
Chip I	20%	67%			1%		1%		
Chip II	20%	53%	10%	5%					
Chip III	20%	45%	10%	1%		20%			
Chip IV	20%	45%	10%	1%		20%		5%	5%
Chip V	20%	49%	10%	3%		10%		10%	5%

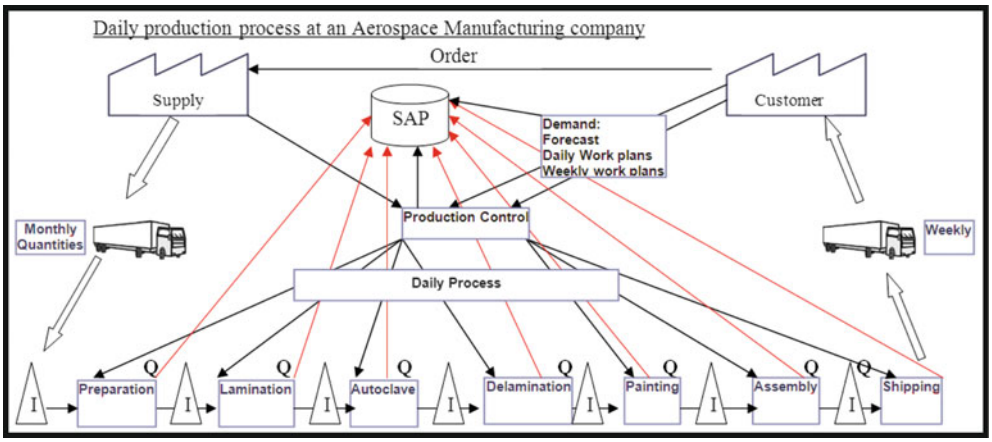

Fig. 21.4 Production process in an aeronautic company (*I* inventory, *Q* quality gates)

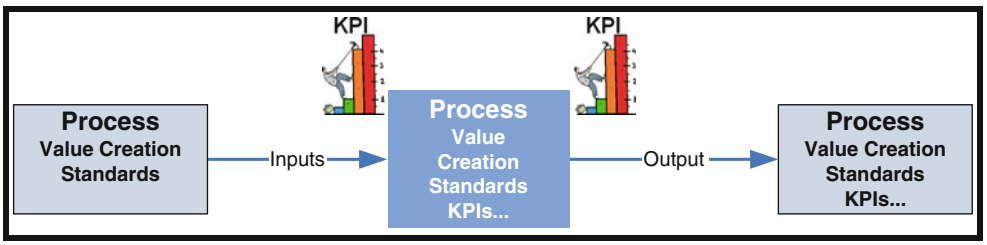

Fig. 21.5 Process flow during manufacturing in an aeronautic company

In aerospace manufacturing companies, the most difficult and crucial processes that we have determined are production processes. They are very complex and processing time due to the data control which is very long stage during manufacturing of the composite pieces. In a simple way, process can be identified as shown in the Fig. 21.5. Here, each process X has a supplier (internal or external) X-1 and a customer X + 1 (internal or external), it takes inputs from Supplier/internal customer X-1 and send products/service to the customer X + 1. A procedure describes the activities of a process and its relations with its interfaces X-1 and X + 1.

The essential performance measurement is based on different indicators, but the most important performance measurement indicators are on-time delivery, cost, and quality [15–22].

In the flow of the process (Fig. 21.5), the Key Performance Indicators (KPIs) are very important in the companies to give everyone in the organization a clear picture of what is important, of what they need to make happen [20–39]. For this reason, it is meaning to manage performance for reporting and monitoring all problems found during the production processes and is being reviewed to define the core problems, then to take actions preventive and corrective actions to reduce and eliminate the problems for the future. And also these are followed during the production cycle and after the delivery of the products as well as. All of the stages with together each quality gate are very well controlled by direct integration of the RFID chips that will give a considerable time reduction.

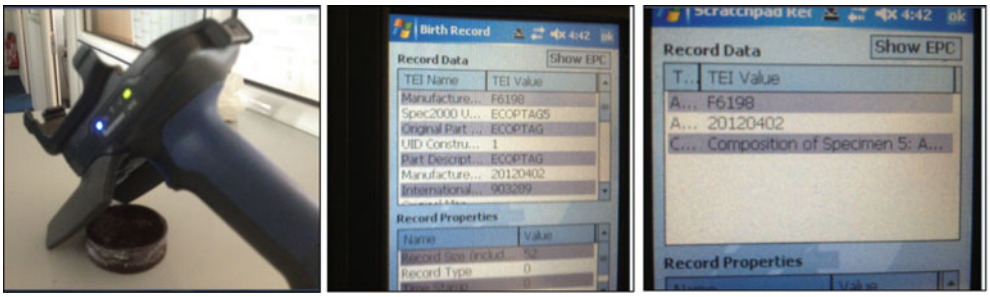

Fig. 21.6 Portable RFID chip reader used and passive RFID tags reader data collector

Fig. 21.7 Portable RFID chip reader to check the chip integrated in the composite samples

In summary, the products should be produced with minimum costs (essential for the low cost engineering), it means that they should be produced with a targeted cost, not much than targeted, should be pushed to the internal customers and then finally up to the end customers, and of course with the desired quality and delivery stage on time.

In fact, rewriteable RFID chips demonstrate a cost effective solution. For this reason, the original contribution of the present work to decrease the processing time by direct integration of the RFID chip at the beginning of the manufacturing stage of the pieces. In this way, these aeronautical pieces can be controlled very easily in a very short time and in any moment during the manufacturing stages and even under the service conditions when they are used in different application areas.

Figures 21.6 and 21.7 show the produced composite parts containing RFID chips and data collector results obtained by means of portable reader before and after the final manufacturing stage.

This new methodology is a very useful approach for low cost engineering in order to reduce processing time that allows us a quick data acquisition, product testing, data update, and quick processing, because the visibility of the products and all related data can be enhanced by using this RFID integration methodology across production.

21.6 Conclusion

This preliminary research on the direct integration of RFID chip in the composite parts during the manufacturing has given us very optimistic results to reduce production time that can be strategically traced across the supply chain to minimize time for each processing cycle and the final cost for the company as a whole. In manufacturing engineering, generally it is too difficult to imagine how reducing the controlling steps can reduce manufacturing lead time and cost. Costs can be minimized due to increased visibility and elimination of unnecessary steps across process. Decreasing of delivering at every step in the process “On-Time” and “On-Quality” will greatly support “On Cost” performance. For this reason, using RFID Technology by direct integration in the composites parts intends to measure and reduce “Process Variation”. The idea given here is not moved the tasks, but optimizing and eliminating the non-value added tasks by using RFID Chips in manufacturing stage.

This is a new an original approach that we have applied for the low cost engineering during the manufacturing of the composite parts in aeronautical company to reduce processing time that allows us a quick data acquisition, testing of the produced parts, data update, and quick processing, because the visibility of the products and all of the related data can be enhanced by using this RFID methodology across production. By this way, in the increment the visibility of the production, the costs and delivery time decrease automatically. Actually, in ordinary production of the composite parts, inspectors spend their approximately 2 h out of 8 h (daily working time) to examine products and materials for defects or deviations. Because all of the data should be documented and specially printed as attached to the products shift to the next process. An industrial application has been carried out in the manufacturing department of the French aeronautic company (Paris) by direct integrating RFID chips in an aeronautical composite part. We have respected all of the manufacturing rules and followed all of the manufacturing stages after the integration of the RFID chips in the composite part. Thanks to this new approach, all of excess waste steps have been completely eliminated and earned a very huge waste of time by savings quality improvements in the production system as explained just before in the Fig. 21.4.

References

1. Bhuptani M, Mordapour S (2005) Sun microsystems-practical book. Sun Microsystems, Santa Clara, CA, pp 78–94
2. Shepard S (2005) "RFID". McGraw Hill, New York. ISBN -10: 0071442995
3. Finkenzeller K (2003) RFID handbook: radio-frequency identification fundamentals and applications. pp 1–7. ISBN-13: 978–0471988519
4. Sweeney P (2005) RFID book for dummies. Wiley, Hoboken, pp 271–275
5. Garfinkel S, Rosenberg B (2005) Addison-Wesley. Sun Microsystems, Santa Clara, CA
6. (2005). http://newsimg.bbc.co.uk/media/images/
7. (2005). http://www.computerworld.com/computerworld/records/images/story
8. (2005). http://www.rfida.com/weblog/blogger.html
9. Thornton F, Haines B, Das A, Bhargava H, Campbell A, Kleinschmidt J (2008) In: Proceedings of the first ACM conference on wireless network security, pp 140–147. RFID security: techniques, protocols and system-on-chip design, Springer (2008). ISBN 978-1-59593-814-5
10. Lin Chin-Sen, Chen Long-Sheng, Hsu Chun-Chin (2011) An innovative approach for RFID product functions development. Expert Syst Appl 38(12):15523–15533
11. Baudin M (2005) RFID applications in manufacturing. MMTI – Manufacturing Management & Technology Institute, *Palo* Alto, California, pp 1–12
12. Susy d'Hont (2002) The cutting edge of RFID technology and applications for manufacturing and distribution. Texas Instrument TIRIS, MA, USA, pp 1–13
13. Rockwell Automation (2004) "RFID in manufacturing", a practical guide on extracting measurable value from RFID implementations in plant and warehousing operations, pp 2–20
14. Holloway S (2006) EMEA manufacturing industry solutions architect. Microsoft EMEA, Redmond, WA 98052-6399, USA
15. Ko J-M, Kwak C, Cho Y, Kim C-O (2011) Adaptive product tracking in RFID-enabled large-scale supply chain. Exp Syst Appl 38:1583–1590
16. Huang George Q, Zhang YF, Jiang PY (2007) RFID-based wireless manufacturing for walking-worker assembly islands with fixed-position layouts. Robot Comput Integr Manuf 23(4):469–477
17. Ngai EWT, Chau DCK, Poon JKL, Chan AYM, Chan BCM, Wu WWS (2012) Implementing an RFID-based manufacturing process management system: lessons learned and success factors. J Eng Technol Manag 29(1):112–130
18. Lu W, Huang G-Q, Li H (2011) Scenarios for applying RFID technology in construction project management. Automat Constr 20(2):101–106
19. Leimeister S, Leimeister J-M, Knebel U, Helmut K (2009) A cross-national comparison of perceived strategic importance of RFID for CIOs in Germany and Italy. Int J Info Manag 29(1):37–47
20. Makris S, Michalos G, Chryssolouris G (2012) RFID driven robotic assembly for random mix manufacturing. Robot Comput Integr Manuf 28(3):359–365
21. Huang Y, Williams Brian C, Zheng L (2011) Reactive, model-based monitoring in RFID-enabled manufacturing. Comput Ind 62(8–9):811–819
22. Lee J-Y, Seo D, Song B-Y, Gadh R (2010) Visual and tangible interactions with physical and virtual objects using context-aware RFID. Expert Syst Appl 37(5):3835–3845
23. Lin C-S, Chen L-S, Hsu C-C (2011) An innovative approach for RFID product functions development. Expert Syst Appl 38(12):15523–15533
24. Thevissen PW, Poelman G, De Cooman M, Puers R, Willems G (2006) Implantation of an RFID-tag into human molars to reduce hard forensic identification labor, part I: working principle. Foren Sci Int 159:S33–S39
25. Tsai M-C, Lee W, Wu HC (2010) Determinants of RFID adoption intention: evidence from Taiwanese retail chains. Info Manag 47:5–6, 255–261
26. Ilie-Zudor E, Kemény Z, van Blommestein F, Monostori L, van der Meulen A (2011) A survey of applications and requirements of unique identification systems and RFID techniques. Comput Ind 62:3
27. Kim HS, Sohn SY (2009) Cost of ownership model for the RFID logistics system applicable to u-city. Eur J Oper Res 194(2):406–417
28. Parlikad A-K, McFarlane D (2007) RFID-based product information in end-of-life decision making. Control Eng Pract 15(11):1348–1363
29. Ranasinghe Damith C, Harrison M, Främling K, McFarlane D (2011) Enabling through life product-instance management: solutions and challenges. J Netw Comput Appl 34(3):1015–1031

30. Tu Yu-Ju, Zhou W, Piramuthu S (2009) Identifying RFID-embedded objects in pervasive healthcare applications. Decis Support Syst 46(2):586–593
31. Meyer Gerben G, Främling K, Holmström J (2009) Intelligent products: a survey. Comput Ind 60(3):137–148
32. Roussos G (2008) Computing with RFID: drivers, technology and implications. Adv Comput 73:161–217
33. Gasco F, Paolo F, Braun J, Smith J, Stickler P, DeOto L (2011) Wireless strain measurement for structural testing and health monitoring of carbon fiber composites. Appl Sci Manuf 42(9):1263–1274
34. Roussos G, Kostakos V (2009) RFID in pervasive computing: state-of-the-art and outlook. Pervasive Mobile Comput 5(1):110–131
35. Maina JY, Mickle MH, Michael RL, Sch. Laura A (2007) Application of CDMA for anti-collision and increased read efficiency of multiple RFID tags. J Manuf Syst 26(1):37–43
36. Leung YK, Choy KL, Kwong CK (2010) A real-time hybrid information-sharing and decision support system for the mould industry. J High Technol Manag Res 21(1):64–77
37. Tsai W-C, Tang L-L (2012) A model of the adoption of radio frequency identification technology: the case of logistics service firms. J Eng Technol Manag 29(1):131–151
38. Holmström J, Främling K, Ala-Risku T (2012) Agent-based model for managing composite product information. J Eng Technol Manag 29(1):131–151
39. Bergquist B (2012) Traceability in iron ore processing and transports. Miner Eng 30:44–51

Chapter 22
Fiber Bragg-Grating Sensor Array for Health Monitoring of Bonded Composite Lap-Joints

Mahmoodul Haq, Anton Khomenko, Lalita Udpa, and Satish Udpa

Abstract The detection and characterization of defects in adhesively bonded composite joints is of special interest for determining the load carrying capacity and structural integrity of resulting components for automobile, marine and aerospace applications. Embedded fiber Bragg-grating (FBG) sensors are being increasingly used to monitor the bonded region in adhesive joints as they do not affect the intrinsic bonding properties. This paper presents a highly reliable system that uses embedded FBG sensors for health monitoring in glass-fiber composite joints. Particularly, an array of strategically placed FBG sensors characterizes the extent and location of defects in the joints studied. Experimental data from the embedded FBGs can be further used to develop experimentally validated simulations (EVS) which can be used as a design tool and also to evaluate residual capacity of damaged joints. Preliminary results demonstrate potential of the developed technique for a wide variety of bonded joints with similar and dissimilar adherends.

22.1 Introduction

Composites are being increasingly used in aerospace, marine, and automotive sectors because of their light weight, high corrosion resistance, and excellent mechanical properties at elevated temperatures [1, 2]. Adhesively bonded joints are gaining popularity in place of conventional fasteners as they provide light weight designs, reduce stress concentrations, enable joining of dissimilar materials, and are often cheaper than conventional fasteners. Bonded joints provide larger contact area than bolted joints thereby providing efficient stress distribution enabling higher efficiency and improved fatigue life [3–5]. Nevertheless, the quality of adhesively bonded joints depends on various factors including manufacturing techniques, manufacturing defects, physical damage and deterioration due to accidental impacts, moisture absorption, improper handling, etc. These factors can significantly affect the strength of resulting bonded joints and a successful monitoring technique that can provide information about the adhesive layer and its resulting joint is essential.

Strain distribution inside the adhesive layer can provide valuable information on the damage initiation, progression and health deterioration for in-service structures. Additionally, if the sensors can be incorporated prior to manufacturing, it can enable quality control of the resulting manufacturing processes. Ideally, the strain measuring sensors must be embedded in the adhesive and should not influence the intrinsic behavior of the adhesive or act as a damage initiator. In the past decade FBG sensors have become a promising tool to address this issue as they can be easily embedded inside the adhesive layer without affecting the resulting bonding properties [6–8].

In this study, an array of FBG sensors was embedded into the adhesive layer of single-lap joints. Similar to the study in reference [9], the array consists of several FBG sensors placed in the inspected area transverse to the joint direction, thereby allowing monitoring of the entire joint. Proposed technique allows identification of the defect location and its severity. Since FBG sensors can measure the strain distributions only in local area, the difference between measurements of reference FBG sensors in healthy region and those in vicinity of defected area provides us information about the defect position and severity. Also, since reference measurements within the same bonded area are used, the need for separate baseline or control data is not required.

M. Haq (✉) • A. Khomenko • L. Udpa • S. Udpa
Composite Vehicle Research Center, Michigan State University, 2727 Alliance Drive, Lansing, MI 48910, USA
e-mail: haqmahmo@egr.msu.edu

G.P. Tandon et al. (eds.), *Experimental Mechanics of Composite, Hybrid, and Multifunctional Materials, Volume 6*, Conference Proceedings of the Society for Experimental Mechanics Series, DOI 10.1007/978-3-319-00873-8_22,

Using this technique defects can be successfully located and their severity can be estimated based on the measurements of strain distributions in healthy and defective areas under static load. Also, strain distributions inside the adhesive during every step of manufacturing process can also be monitored. Moreover, accurate information about the adhesive obtained from these sensors can be used to develop and validate realistic and robust numerical simulations. Once validated experimentally, such simulations can be used as a powerful design and residual-life prediction tools. A similar effort on development of experimentally validated simulations through experimental data from embedded sensors has been attempted using single FBG sensors in Pi/T-joints [10]. This work follows the recommendations from [10] and includes an array of sensors instead of a single sensor. Furthermore, the array of strategically embedded FBG sensors can also be combined with other NDE modalities to develop reliable and robust data fusion techniques for precise structural evaluations.

22.2 Specimen Manufacturing and Sensor Installation

In this section, the principle of FBG sensor operation, strategic placement of sensors, details of materials used and the manufacturing process for adherends and single-lap joints are provided.

22.2.1 FBG Sensor Principle and Strategic Embedding of FBG Sensors in Array

Fiber Bragg-grating is a sandwich-like distributed reflector with periodically changed refractive index that is embedded into the optical fiber [11]. Such a structure acts as an optical filter that transmits the entire spectrum of the light source and reflects back the resonant, Bragg wavelength. Bragg wavelength is given by the following Eq. 22.1:

$$\lambda_B = 2n_{eff}\Lambda \tag{22.1}$$

where n_{eff} is the effective refractive index of the core and Λ is the period of Bragg-grating. The spectrum bandwidth of back reflected radiation also depends on the effective refractive index of the fiber core and Bragg-grating period. As one can see the perturbation of Bragg-grating period results in the shift of Bragg wavelength: the strain response arises due to both the physical elongation of the sensor and the change in fiber effective refractive index due to photoelastic effects, whereas the thermal response arises due to the inherent thermal expansion of the fiber material and the temperature dependence of the refractive index.

Wavelength-encoded nature of the FBG output provides a built-in self-referencing capability for the sensor. Since the wavelength is an absolute parameter, the output does not depend directly on the total light levels, losses in the connecting fibers and couplers, or source power. Moreover, the fiber and sensor have relatively small dimensions; therefore embedding in the composite structure does not affect the intrinsic properties of the host. These advantages of FBG sensors along with its immunity to electromagnetic interference, lightweight, high sensitivity, and ease in implementing multiplexed or distributed sensors make it very appealing for many areas of NDE applications, such as strain and temperature, vibration measurements, etc. [12].

However, FBG provides status of the region in the vicinity of sensor. Therefore in order to evaluate the entire area of interest an array of FBG sensors is used [9]. Each FBG sensor in the array can use the readings of other sensors as reference, which increases the robustness and adds the redundancy to the proposed technique. This will allow to overcome the thermal response of the FBG sensors and to compensate global strains of the in-service composite structure.

22.2.2 Glass-Fiber Composite Adherend Manufacturing

The vacuum assisted resin transfer molding (VARTM) technique was used to manufacture the composite adherends for the lap joints. The reinforcement used for the adherend was Owens Corning ShieldStrand S, S2-glass plain weave fabric with areal weight of 818 g/m^2. The distribution medium was AIRTECH Advanced Materials Group Resinflow 60 LDPE/HDPE blend fabric. The resin used was two part toughened epoxy, namely SC-15 obtained from Applied Poleramic SC-15 resin. A steel mold (609.6 mm $\times$ 914.4 mm) with point injection and point vent was used to fabricate 508.0 mm $\times$ 609.6 mm plates. After the materials were placed, the mold was sealed using a vacuum bag and sealant tape. The mold was then infused under vacuum with a pressure of 1 atm. The resin infused panel was cured in a convection oven at 60 °C for 2 h and post cured at 94 °C for 4 h.

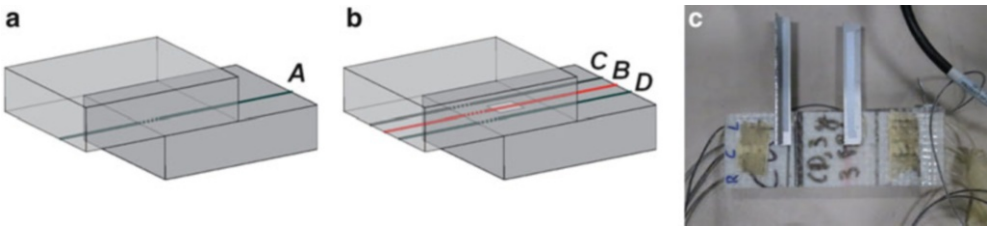

Fig. 22.1 (**a**) Healthy lap-joint with side-placed baseline FBG sensor A, (**b**) lap-joint with manufacturing defect, two reference side-placed FBG sensors C and D and the signal FBG sensor B and (**c**) actual photo of the lap-joint with manufacturing defect and 3 FBG sensors

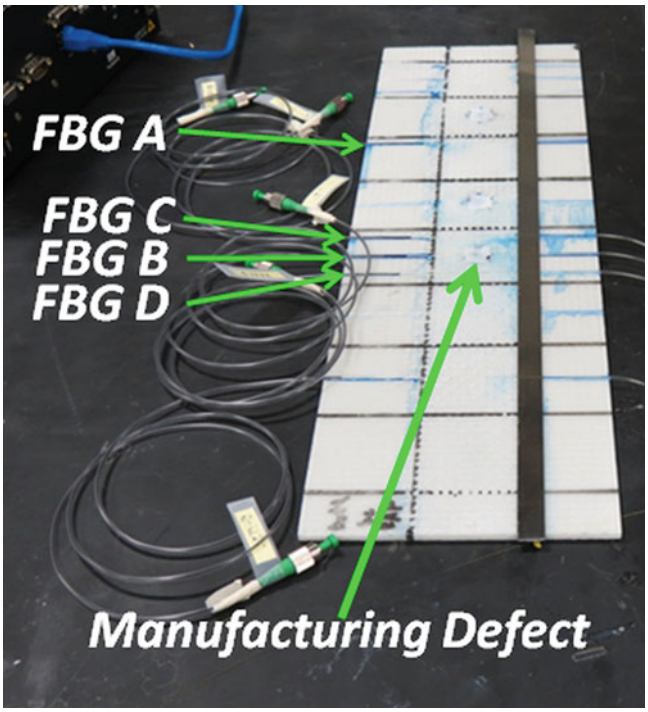

Fig. 22.2 Manufacturing of composite single-lap joints with embedded FBG sensors

22.2.3 Composite Single-Lap Joint Manufacturing and Sensor Placement

In this study, lap-joints were made from the glass-fiber reinforced plates manufactured by the above described process. The bonding area was sand-blasted and cleaned with acetone. Pseudo-disbond, or pseudo-damage representing a manufacturing flaw, was created by placing a teflon sheet of 15 mm × 15 mm at the center of the bonded area. Two single-lap joints were manufactured: (a) baseline joint with no initial disbond, and (b) pseudo-disbond joint with disbond in the center of bonded area (see Fig. 22.1). The manufacturing of single-lap joints with embedded FBG sensors and pseudo-disbond is represented in Fig. 22.2.

Each lap joint has a bonding area of 50.8 mm × 50.8 mm. The adhesive bond-line thickness was ensured to be 0.76 mm per ASTM D5868 by placing Teflon-coated steel strips at the end of the bonded area. These spacers were placed strategically such that it did not influence the resulting performance, and were removed prior to testing. The FBG sensors employed in this study had a 10 mm grating length, varying Bragg wavelengths and were obtained from Micron Optics, Inc, Atlanta, USA. It should be noted that the initial Bragg wavelength of the sensor does not affect strain coefficient which is 1.2 pm/με for each FBG sensor. The tensile and fracture properties of adhesive were obtained experimentally per ASTM standards. The experimentally obtained adhesive properties along with the experimental data from the sensors can be further used to develop realistic and accurate numerical models. These models are a part of a parallel effort by the authors and are currently in development and are not included in this paper.

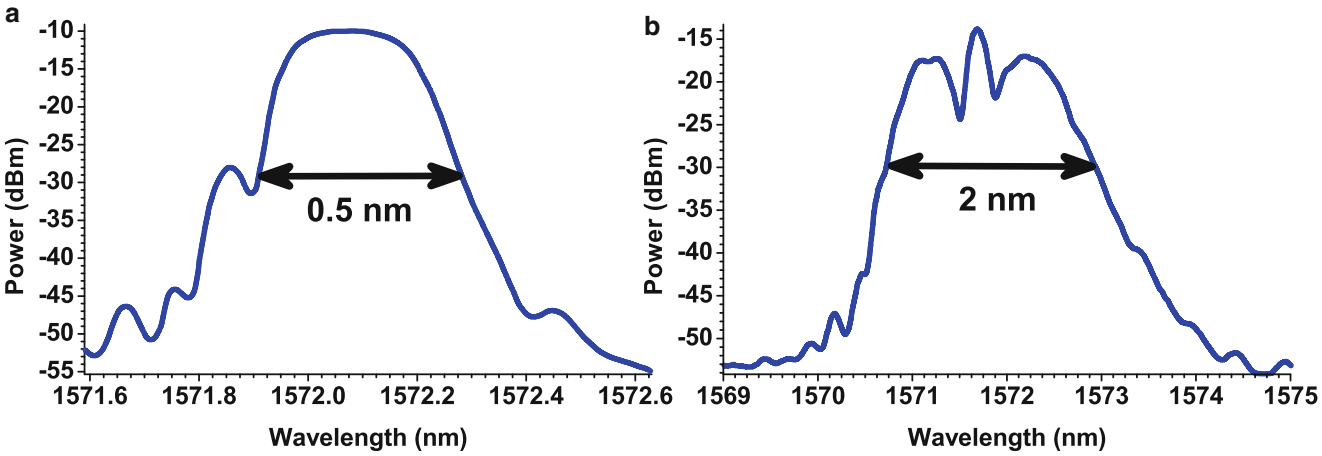

Fig. 22.3 Spectral response of the embedded in composite single-lap joint FBG sensor: (**a**) after infusing the resin in composite single-lap joint and (**b**) after the resin cured in composite single-lap joint

For the first healthy/baseline composite single-lap joint FBG sensor A with Bragg wavelength 1,532 nm was placed 7.5 mm away from the side edge; edge effects were found to be negligible in preliminary simulations. The second composite single-lap joint contained the manufacturing defect and three FBG sensors. Two reference sensors C and D with Bragg wavelength 1,572 nm were placed 7.5 mm away from the side edge, similar to FBG sensor A in the baseline joint. The central, FBG sensor B with Bragg wavelength 1,512 nm was placed in the middle, on the same level with reference sensors C and D.

After embedding the array of strategically placed FBG sensors in composite single-lap joints FBG responses were monitored throughout every step of manufacturing process. It was observed that after resin cures the spectral response of FBG sensor is changed from narrow-band single peak to wide-band multi-peak spectrum. An example of the actual spectral change for reference side-placed sensor D is shown in Fig. 22.3.

This may be caused by non-uniform stress distribution in adhesive layer due to resin shrinkage during the curing. It is known that in the vicinity of the defect the spectrum of FBG response splits to separate peaks that start to shift independently [13]. In this study we propose to use multi-peak feature of the FBG spectrum: peak shifts were tracked individually and corresponding strain values compared for the same FBG sensor and other FBG sensors. It is expected that for baseline sensor A and reference sensors C and D the variation of strain values should be lower than those of signal sensor B.

22.3 Composite Single-Lap Joint Evaluation

In this section, the experimental setup used for static tension-shear testing of composite single-lap joints and the experimental methodology are provided.

22.3.1 Experimental Setup and Methodology

The experimental test setup is shown in Fig. 22.4. Testing was performed as per ASTM D5868 in displacement control with a rate of 0.25 mm/min. The displacement and applied load from MTS were recorded. Additionally, an external laser extensometer (LE-05 Epsilontech Laser Extensometer) was used to obtain precise relative displacements between the adherends. Spectral responses of FBG sensors embedded in composite single-lap joints were logged in PC using Micron Optics Optical Sensing Interrogator sm125-700. All measurements from FBG sensors and extensometer were synchronized with MTS data.

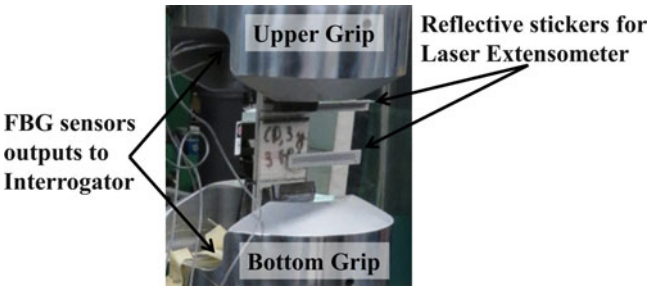

Fig. 22.4 Experimental setup for composite single-lap joint evaluation

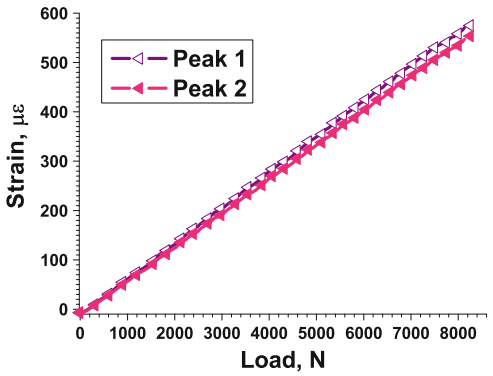

Fig. 22.5 Internal strain dependence on the applied load for baseline FBG sensor A

22.3.2 Experimental Results

In the first set of experiments, healthy lap joint with baseline FBG sensor A (see Fig. 22.1a) was evaluated. Static tensile-shear test was performed. The displacement and internal strain dependence on the applied load were recorded. To monitor internal strains the shift of the spectrum consisting of two peaks was tracked. The relationship between measured internal strain and applied load from both peak shifts is shown in Fig. 22.5. As one can see the deviation of internal strain values is insignificant therefore the entire spectrum shifts uniformly.

In the second set of experiments lap joint with manufacturing defect, two reference FBG sensors C and D and signal sensor B (see Fig. 22.1b) was evaluated. The displacement and internal strain dependence on the applied load was measured similar to the baseline joint. To monitor internal strains the shift of the spectral peaks for all FBG sensors was tracked and recorded. Spectral response of reference FBG sensors C and D had one and three peaks respectively and central FBG sensor B spectrum contained five peaks. The comparison of internal strains at varying applied loads calculated from spectral peak shifts for reference FBG sensors C and D is shown in Fig. 22.6a. A magnified, zoomed-in region of Fig. 22.6a is shown in Fig. 22.6b. Similar to the baseline FBG sensor A, the deviation of internal strain values is insignificant for reference sensors hence the entire spectrum shifts uniformly. This suggests that the manufacturing defect does not affect the local strain distribution in the vicinity of reference FBG sensors. Moreover the responses of reference sensors are identical which means they can be used to compensate thermal response of the Bragg-grating and global strains of the composite single-lap joint.

However spectral response of signal from FBG sensor B is different. One can see that the manufacturing defect affects the local strains: it adds more non-uniform stress distribution in adhesive layer and causes the peaks in the spectrum to shift separately and the spectrum begins to spread out (see Fig. 22.7a). This feature can be used as the health indicator of the composite structure. For comparison spectral responses from reference FBG sensors C and D and signal FBG sensor B are plotted together in Fig. 22.7b. It is obvious that in the vicinity of defects, the spectral response of the FBG sensor changes significantly: it does not shift uniformly and local strain values increase substantially.

The overview of measured results is represented in Fig. 22.8. The displacements of healthy and defected composite single-lap joints measured by laser extensometer at different applied loads are shown in Fig. 22.8a. Actual measurements do not start from zero as the grip closure introduces an initial compressive load of approximately 1,000 N. Local strain dependence on the applied load for baseline, reference and signal FBG sensors are represented in Fig. 22.8b. Initially at very low loads all FBG sensors behave similarly. As the applied load increases the response of the signal sensor B with manufacturing defect starts to deviate from reference and baseline FBG sensors. As it is well known, defects introduces

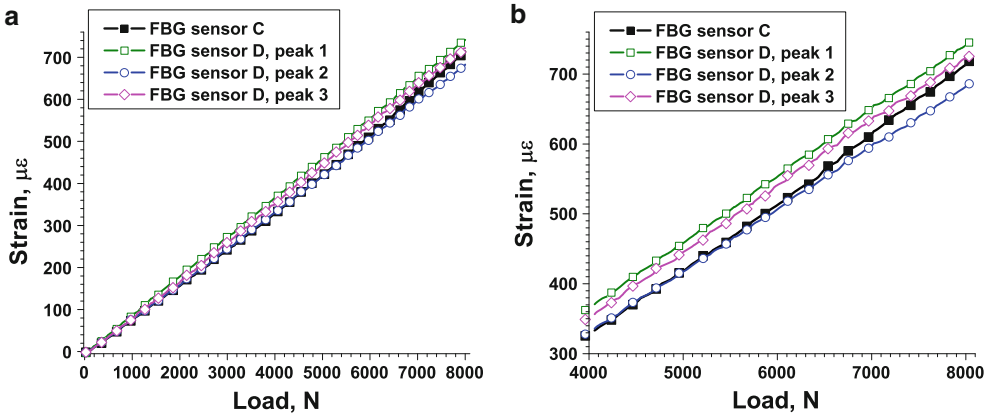

Fig. 22.6 (**a**) Internal strain dependence on the applied load for reference FBG sensors C and D and (**b**) zoomed-in region

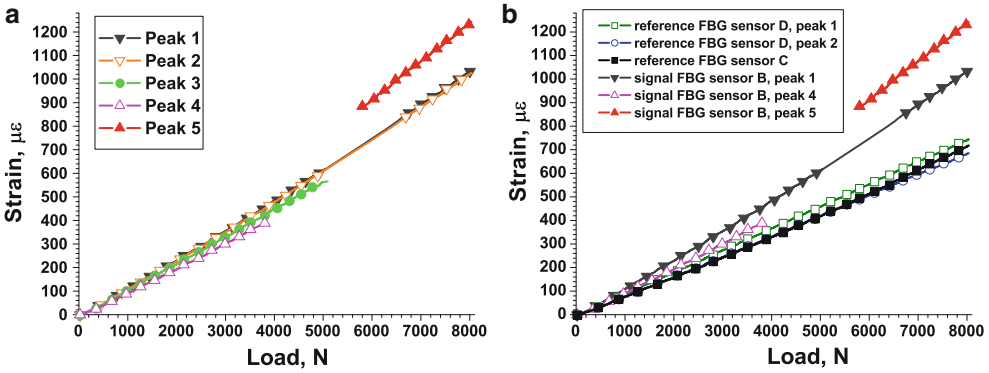

Fig. 22.7 (**a**) Internal strain dependence on the applied load for signal FBG sensors B and (**b**) comparison of internal strain dependence on the applied load for reference FBG sensors C and D and signal FBG sensors B

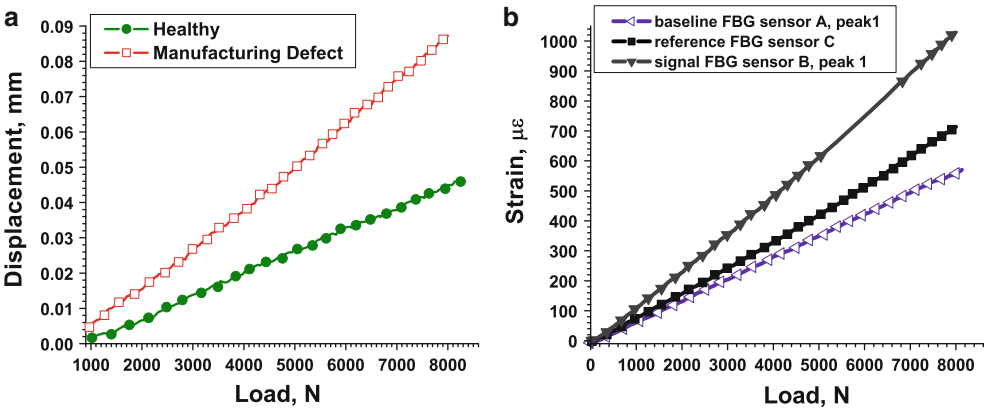

Fig. 22.8 (**a**) Comparison of the displacement versus load curves for healthy and defected single-lap joints and (**b**) comparison of strain versus load curves for baseline, reference and signal FBG sensors

stress concentrations that are very well captured by FBG sensor B that is in direct vicinity of the defect. The baseline and reference FBG sensors still agree very well. Upon further load increase (loads greater than 1,500 N), the response of reference sensors C and D is also influenced by the defect and starts to deviate from baseline response of sensor A. Overall, the variation of strains in the defective joint, namely, strains in B relative to C and D provide valuable information on the defect within that joint, and the location of the defect. Moreover, comparisons of strains from sensor

A corresponding to baseline, pristine joints and sensors C, D and B reveal the variation of strains in a defective joint at various loading conditions. A similar approach can be extended to a wide array of sensors to fully characterize the location and extent of defects.

22.4 Conclusions

An array of strategically embedded FBG sensors in the composite lap-joints with and without manufacturing defects was successfully implemented. The response of various sensors throughout the manufacturing process and during experimental static tension-shear loading conditions was studied. The spectral response of the sensors changed from a narrow-band single peak to a wide-band multi-peak during the curing process, which is attributed to the non-uniform stresses introduced due to resin shrinkage. During mechanical loading, the multi-peaks were found to shift together in pristine joints, while the peaks shift separately in the vicinity of the defect. This feature can be used as a stand-alone indicator for presence of defect. Additionally, the strategic placement of an array of sensors within the defective joint allowed for temperature, global strain compensations, and eliminated the need for additional baseline data. Furthermore, the effect of stress concentrations in the vicinity of defects was well captured by the array of sensors, with the sensor closest to defect being active at lower loads while the sensors away from the defect active at higher loads. Overall, this technique shows potential in the detection of defect location inside the adhesives and allows estimation of damage severity. Since the strain distributions are dependent on various factors including joint geometries, failure modes, operative conditions, the distance between sensor and defect, the sensor arrangement, monitoring parameters, etc., further research on robust diagnosis methods based on fiber Bragg-grating sensors is needed. Also, statistically significant experimental tests need to be performed before any strong conclusions are made. Nevertheless, the proposed technique shows great potential in defect detection and health monitoring of bonded joints. The proposed system can be further enhanced by combining with other NDE modalities to create reliable and robust data fusion based techniques for health monitoring of composite structures.

Acknowledgements This work was supported by US Army under TACOM/MSU Cooperative Agreement No. W56HZV-07-2-0001 and under ARL/MSU Cooperative Agreement No. ARL CA #W911NF-11-2-0017. The authors also acknowledge the cross-disciplinary collaboration with Dr. Alfred Loos and Dr. Nicholas Gianaris of Composite Vehicle Research Center, Michigan State University.

References

1. Windhorst T, Blount G (1997) Carbon-carbon composites: a summary of recent developments and applications. Mater Des 18(1):11–15
2. Park S-J, Seo M-K (2012) Carbon fiber-reinforced polymer composites: preparation, properties, and applications. Polym Compos 1:135–183
3. Khalili SMR, Shokuhfar A, Hoseini SD, Bidhkhori M, Khalili S, Mittal RK (2008) Experimental study of the influence of adhesive reinforcement in lap joints for composite structures subjected to mechanical loads. Int J Adhes Adhes 28(8):436–444
4. Lin W-H, Jen M-HR (1999) The strength of bolted and bonded single-lapped composite joints in tension. J Compos Mater 33(7):640–666
5. Kweon J-H, Jung J-W, Kim T-H, Choi J-H, Kim D-H (2006) Failure of carbon composite-to-aluminum joints with combined mechanical fastening and adhesive bonding. Compos Struct 75(1–4):192–198
6. Okabe Y, Mizutani T, Yashiro S, Takeda N (2002) Detection of microscopic damages in composite laminates with embedded small-diameter fiber Bragg grating sensors. Compos Sci Technol 62(7–8):951–958
7. Murayama H, Kageyama K, Uzawa K, Ohara K, Igawa H (2012) Strain monitoring of a single-lap joint with embedded fiber-optic distributed sensors. Struct Health Monit 11(3):325–344
8. Bernasconi A, Carboni M, Comolli L (2011) Monitoring of fatigue crack growth in composite adhesively bonded joints using fiber Bragg gratings. Procedia Eng 10:207–212
9. Fan Y, Kahrizi M (2005) Characterization of a FBG strain gage array embedded in composite structure. Sens Actuator A Phys 121(2):297–305
10. Haq M, Drzal L, Patterson E (2010) Health monitoring of composite Pi-joints using fiber optic sensors. In: Proceedings of 25th technical conference of the American Society for Composites and 14th US-Japan conference on composite materials, vol 1, pp 198–209
11. Kersey AD, Davis MA, Patrick HJ, LeBlanc M, Koo KP, Askins CG, Putnam MA, Friebele EJ (1997) Fiber grating sensors. J Lightwave Technol 15(8):1442–1463
12. Lee B (2003) Review of the present status of optical fiber sensors. Opt Fiber Technol 9(2):57–79
13. Hackney D, Peters K (2011) Damage identification after impact in sandwich composites through embedded fiber Bragg sensors. J Int Mater Syst Struct 22(12):1305–1316

Chapter 23
Semi-experimental Investigation of Bridging Tractions in Delamination

Ebrahim Farmand-Ashtiani, Joël Cugnoni, and John Botsis

Abstract Bridging by intact fibers is well recognized as an important toughening mechanism that accompanies delamination propagation in fibrous laminates. However, direct measurement of the bridging tractions is a challenging task. In this work, an iterative methodology based on internal strain measurements and parametric finite element modeling is employed to identify the contribution of fiber bridging to delamination resistance of unidirectional carbon fiber/epoxy laminates. Double cantilever beam specimens with integrated arrays of wavelength-multiplexed fiber Bragg gratings (FBG) are subjected to mode I loading. Non-uniform strain distribution in the vicinity of the interlaminar crack plane is locally monitored by means of the several embedded FBG sensors of 1 mm gauge length. Employing an inverse identification procedure, the measured strain data are used to determine the bridging tractions associated with delimitation growth. It is shown that such an iterative procedure can be effectively applied for characterization of the energy release rate due to the fiber bridging in specimens of different thicknesses.

23.1 Introduction

Laminated composites are used in a variety of structural applications such as aeronautics, aerospace, marine engineering and energy infrastructures. Inherent heterogeneity of laminated composites provides significant specific properties that can be tailored in specific directions and locations according to the structural design requirements. However, despite the aforementioned benefits, heterogeneity of composite materials is also a limiting parameter in predicting their service life expectancy [1].

Main failure mechanisms of fibrous laminates can be classified to the failure of an individual lamina (e.g. fiber failure, matrix failure, fiber/matrix interface failure) and loss of adhesion between two consecutive lamina, namely delamination. Among these failure mechanisms, the later is of special concern since the interface between the plies is weaker than an individual lamina itself. Impacts of falling objects, out of plane loads, drilling during the manufacturing processes, moisture or temperature variations and structural discontinuities are considered as typical causes of delamination. Since delamination often lies between the laminas, it can be unnoticeable by visual inspection of the external surface. Propagation of such damage in response to the service loads reduces the structural stiffness and may lead to a premature collapse of the structure [1–3].

Delamination tests based on fracture mechanics concepts, such as double cantilever beam (DCB) test, are frequently used to measure the strain energy release rate (ERR) associated with delamination growth (i.e. interlaminar fracture toughness). Delamination propagation in DCB test is often accompanied by fibers that cross the delamination crack from one surface to the other (i.e. fiber bridging). This phenomenon is important toughening mechanism as it leads to increasing ERR by crack growth and is usually described by the so-called R-curves [4–6].

Significant progress has been achieved on the analysis of fiber bridging and its contribution to fracture in various materials [7–11], However, a complete characterization of bridging tractions in monotonic and fatigue delamination has not been achieved especially in the case of large scale bridging where the effects of specimen dimensions can play a an important role.

Approaches for identification of traction-separation relations can be generally categorized in direct and iterative methods [12]. Direct methods, are mainly based on experimentally measured crack opening displacement (COD) and do not rely on extensive numerical analysis. However, the accuracy of traction-separation relations using the direct method can be limited

E. Farmand-Ashtiani • J. Cugnoni • J. Botsis (✉)
École Polytechnique Fédéral de Lausanne (EPFL), LMAF-STI, Lausanne CH-1015, Switzerland
e-mail: john.botsis@epfl.ch

G.P. Tandon et al. (eds.), *Experimental Mechanics of Composite, Hybrid, and Multifunctional Materials, Volume 6*, Conference Proceedings of the Society for Experimental Mechanics Series, DOI 10.1007/978-3-319-00873-8_23,

by resolution issues in measuring the COD that consequently affects the accuracy of the calculated bridging tractions. In the iterative methods the traction-separation parameters are determined by comparing numerical simulations and experimental data [12–17].

In this work, an iterative methodology based on internal strain measurements with fiber Bragg grating (FBG) sensors and parametric finite element (FE) modeling is employed to identify the effects of specimen thickness on bridging tractions encountered in mode I delamination of carbon fiber laminates.

23.2 Materials and Methods

23.2.1 Materials and Specimen

The composite material used in this work is fabricated by hand-lay-up of a unidirectional carbon/epoxy prepreg system (SE 70 from *Gurit SP*™ with cured thickness of 0.2 mm). A 60 mm long, 20 μm thick release film (A6000 from Aerovac®) is introduced in the mide-plane of each plate to create an initial crack. Composite plates are produced with two different thicknesses of 4 and 8 mm. The number of prepreg layers is proportionally increased with the specimen thickness (i.e. $[0_{20}]$ and $[0_{40}]$, respectively) so that the composite plates of different thicknesses have the same fiber volume fraction. The both layups are cured under vacuum at 78 °C for 10 h in an autoclave.

During the fabrication process, optical fibers (SM-28, 125 μm in diameter) with arrays of multiplexed FBG sensors are aligned in the reinforcing carbon fiber direction and placed at a distance of one prepreg layer above the crack plane. Prior to fabrication, the polymeric coating of the optical fibers is removed with sulfuric acid from the sensors zone and adjacent 10 mm length. The employed FBG arrays consist of 8 sensors with the gauge length of 1 mm that are equally spaced at 3 mm apart. Each sensor has a reflectivity of 50 % and a bandwidth (FWHM) of 1.5 nm. The corresponding Bragg wavelengths are located between 1,525 and 1,565 nm spaced by 5 nm. The precise position of the optical fiber through the thickness of the cured laminates is determined by optical microscopy of the transverse sections of the specimens. Longitudinal position of each sensor is determined by the optical low coherence technique (HP 8504B reflectometer) using a step length of 20 μm for the mirror moving.

The cured plates are cut into 25 mm wide beams with a length of 320 mm to prepare DCB specimens. Steel loading blocks ($10 \times 10 \times 25$) are glued onto each specimen's end with Araldit®, a rapid two component epoxy adhesive. To monitor crack propagation, the specimens' side face is painted white and marked with dark thin lines at every millimeter. The mechanical properties used in the numerical analysis is summarized as follows: $E_{zz} = 98$ GPa for the longitudinal modulus, $E_{yy} = E_{xx} = 9$ GPa for the transverse modulus, $G_{yx} = 5.2$ GPa, $G_{zx} = G_{zy} = 5$ GPa for the transverse modulus and Poisson ratios $v_{zx} = v_{zy} = 0.30$, $v_{xy} = 0.45$. The longitudinal modulus is obtained from four-point bending test and the other properties are calculated using the micromechanics model of Vanyin [18].

23.2.2 Monotonic Tests

A servo-hydraulic Instron® testing machine equipped with a 2 kN load cell is employed for conducting the monotonic delamination tests. Specimens are loaded under displacement control with a constant rate of 2 mm/min. A high resolution CCD camera is used to follow the crack length using the marks on the specimen's side surface. To obtain sufficiently smooth data for subsequent analysis, the measured crack length and corresponding compliance values are fitted to the following power law expression:

$$C = c_0 a^n \tag{23.1}$$

where C is the compliance of the specimen, a is the experimentally measured crack length and c_0 and n are empirical fitting parameters. Employing a linear elastic fracture mechanics approach, the energy release rate is determined using the following expression:

$$G = \frac{P^2}{2b}\frac{dC}{da} \tag{23.2}$$

where P is the applied load, b is the width of the specimen and the derivative dC/da is obtained by differentiating Eq. 23.1.

The response of the embedded multiplexed FBGs to the interlaminar crack propagation is monitored during the test using the Micron Optics SM130® interrogator that allows acquisition of the Bragg wavelength shifts from each FBG at 1 kHz.

23.2.3 Fatigue Tests

The fatigue tests are performed using a servo-hydraulic Instron® test machine. The displacement is measured with a built-in LVDT and the load with a 2 kN load cell. Each DCB specimens is first ramp loaded under displacement control (2 mm/min) so that the interlaminar crack initiates from the crack starter and propagates approximately for 2 mm. The load reached in the aforementioned crack initiation process is reduced by 20 % and taken as the maximum load level applied in the subsequent cyclic tests. The specimens are then fatigued in load control by applying a sinusoidal waveform with a frequency of 2 Hz and a minimum to maximum load ratio of R = 0.5.

The peak values of displacement and load are recorded at each fatigue cycle. To assess the hysteresis of the load displacement curve, the load and displacement are acquired every 100 cycle for a complete loading cycle with a resolution of 100 points. Similar to the monotonic tests, crack propagation is followed during the fatigue tests using a CCD camera and the energy release rate is determined using the compliance calibration method. Namely, the maximum cyclic energy release rate is calculated using the maximum values of cyclic load and displacement together with the corresponding crack length data. The FBG signals are monitored at a frequency of 100 Hz. The maximum change in Bragg wavelength per cycle is used to determine the corresponding cyclic peak strain.

23.2.4 Strain Measurements

An FBG sensor consists of a periodic modulation of the refractive index made in the core of an optical fiber. Each FBG sensor reflects the broadband light input just over the so called Bragg wavelength λ_B that changes when the sensor is subjected to a strain field. In a homogenously strained optical fiber, where the axial strain ε_z is the dominant strain component with $\varepsilon_x = \varepsilon_y = -\upsilon\varepsilon_z$; ($\upsilon$ is the optical fiber's Poisson ratio), the Bragg wavelength shift $\Delta\lambda_B$ can be expressed by the following equation:

$$\frac{\Delta\lambda_{B,i}}{\lambda_{B0,i}} = (1 - p_e)\varepsilon_{z,i} \tag{23.3}$$

where the index i indicates the FBG sensor along the optical fiber and the elastic optical coefficient p_e is taken equal to 0.215 that can be measured experimentally [19, 20].

Note that, since short gauge length FBG sensors are used, the strain over the length of each FBG is homogenous and consequently the peaks are simply shifted and not split up in multiple peaks as it happens with longer FBGs [11]. As schematically shown in Fig. 23.1, the strain detected by a given FBG sensor is calculated applying the measured Bragg wavelength shift in Eq. 23.3.

23.2.5 Identification of Bridging Traction

The DCB experimental configurations are reproduced in numerical simulation using the commercial software Abaqus® Standard v 6.10. The embedded optical fiber is found to cause a negligible effect on the delamination ERR [21]. Therefore, a two-dimensional plane-strain model is built with the input data taken from the experiment. Note that the crack length analyzed in identification process is chosen so that the fiber bridging zone is completely developed. The materials behave linearly elastic with the properties mentioned in the Sect. 23.2.1. In total, two models corresponding to two different thicknesses of the DCB specimens are built. Due to the symmetry of the DCB specimen and corresponding loading system, only half of the specimen is modeled. The $1/\sqrt{r}$ singularity (r indicates the distance from the crack tip) is fulfilled by

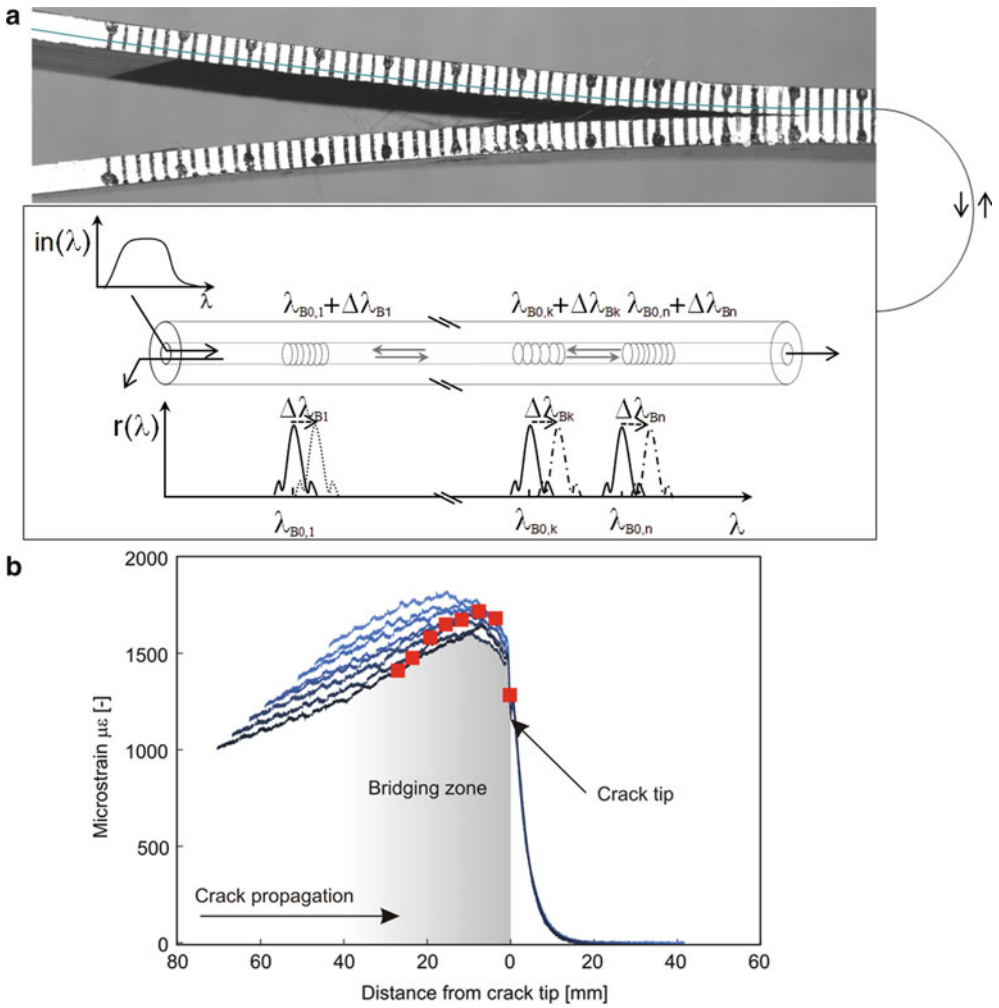

Fig. 23.1 (**a**) The DCB specimen with an embedded optical fiber containing multiplexed FBGs. Also shown are typical reflection spectra of the FBG array. (**b**) Typical strain distribution measured near the crack tip [21]

collapsing the elements at the crack tip to triangles and shifting the mid-nodes of the adjacent element sides to ¼ of the edge. Quadratic quadrilateral elements with reduced integration (Abaqus CPE8R) are used with the mesh radially refined around the crack tip to quadrilateral elements with size of about 20 μm.

The fiber bridging is simulated by applying a parametric exponential surface traction $\sigma_b(z)$ between the crack tip and the initial crack length (see Fig. 23.2). It has been shown in [22] that the bridging traction profile is best described by the following expression:

$$\sigma_b(z) = e^{-\gamma z}\left(\sigma_{\max} - \frac{\sigma_{\max}}{z_{\max}} z\right), \qquad 0 \le z \le z_{\max} \tag{23.4}$$

where σ_{max} is the maximum bridging traction at the crack tip, z_{max} is the length of the bridging zone and γ is a positive modeling parameter that accounts for the extent of non-linearity in the bridging tractions. Employing a Levenberg–-Marquardt least-square optimization algorithm [23, 24], the three parameters in Eq. 23.4 (i.e. σ_{max}, γ, $z_{\max}$) are varied to minimize the difference between the experimentally measured data (i.e. strain and ERR) and corresponding values numerically calculated.

The identified bridging traction function $\sigma_b(z)$ is then combined with the COD values $\delta(z)$ extracted from the optimized FE model to obtain the traction-separation behavior in the fiber bridging zone called "bridging law". The ERR due to fiber bridging is given by the following integral over the whole COD in the bridging zone:

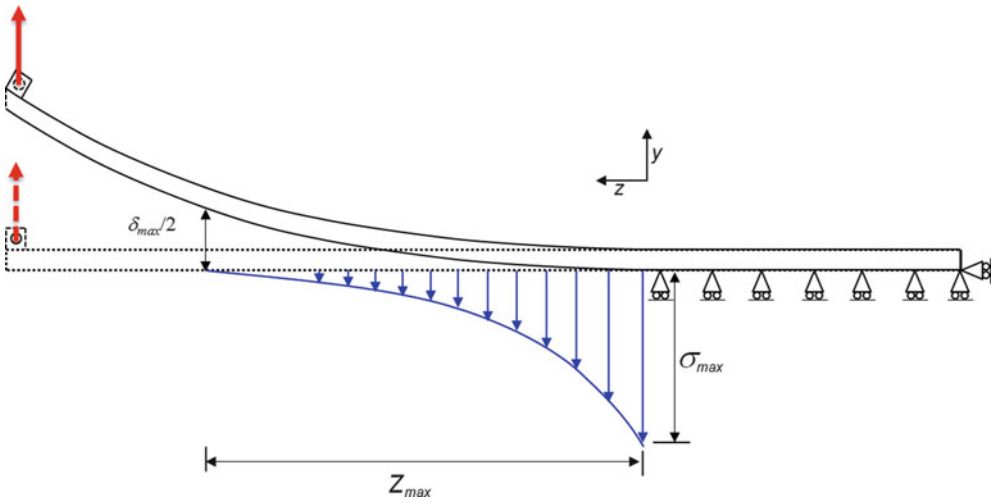

Fig. 23.2 Schematic of the bridging traction profile used in the identification model

$$G_{I,b} = \int_0^{\delta_{max}} \sigma_b(\delta)\, d\delta \tag{23.5}$$

where δ_{max} is the COD at the end of the bridging zone $\delta_{max} = \delta(z = z_{max})$.

23.3 Results and Discussion

Typical load–displacement curves from two monotonic delamination experiments with specimen thicknesses of 4 and 8 mm are shown in Fig. 23.3. Note that difference in the slope of the initial linear part of the curves reflects different flexural stiffness of the two specimens of different thicknesses as it is characteristic for a given specimen geometry. The specimens are unloaded and reloaded after the initial crack jump, thus the onset of nonlinearity at each curve indicates the beginning of crack propagation.

The influence of the specimen thickness on the R-curve is demonstrated in Fig. 23.4, As shown for representative specimens of each thickness, the initiation ERR where the crack has no bridging fibers, is nearly identical (approximately 350 J/m^2) for both specimens, however the thickness has a significant influence on the ERR due to the bridging as it obviously shifts the plateau level in the R-curve.

Following the identification procedure described in Sect. 23.2.5, the traction-opening behavior $\sigma_b(\delta)$ of DCB specimens of both thicknesses are obtained and shown in Fig. 23.5. Note that the identified parameters σ_{max} (the stress right behind the crack tip) and δ_{max} (corresponding to the $\sigma_b(z_{max}) = 0$) are material dominated parameters that do not depend on the specimen thickness. This is based on the fact that both laminates have the same fiber volume fraction and microstructure of the composite around the crack front is similar. The parameter δ_{max} reflects the maximum stretch of the fibers in the bridging zone.

As depicted in Fig. 23.5, the influence of thickness on ERR due to the fiber bridging is attributed to the decrease in the rate of the exponential decay of bridging tractions which is expressed by the parameter γ in Eq. 23.4. Since the thicker specimen is more resistant against deflection, a larger steady state bridging zone, z_{max} develops which is associated with lower values of γ. Based on these results and when the identified material parameters σ_{max} and δ_{max} are provided, the identification of bridging traction function for specimens of different thickness can be carried out with γ as the only variable in Eq. 23.4.

Figure 23.6 shows the evolution of crack growth speed as a function of cyclic ERR in the fatigue delamination of DCB specimens of two different thicknesses. Crack growth speed decreases from a similar value for both specimens but evolves with significantly different rates. Such behavior can be also attributed to the different bridging zones developed in the two specimens for the crack increment range achieved during the fatigue tests (approximately 25 mm).

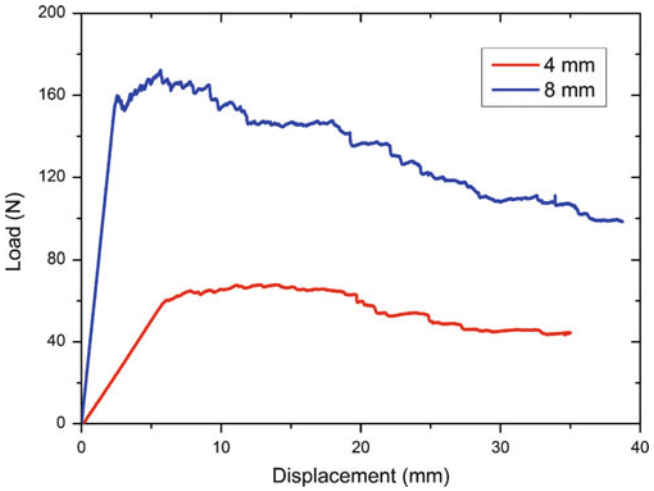

Fig. 23.3 Typical load–displacement curves from DCB specimens with two different thicknesses

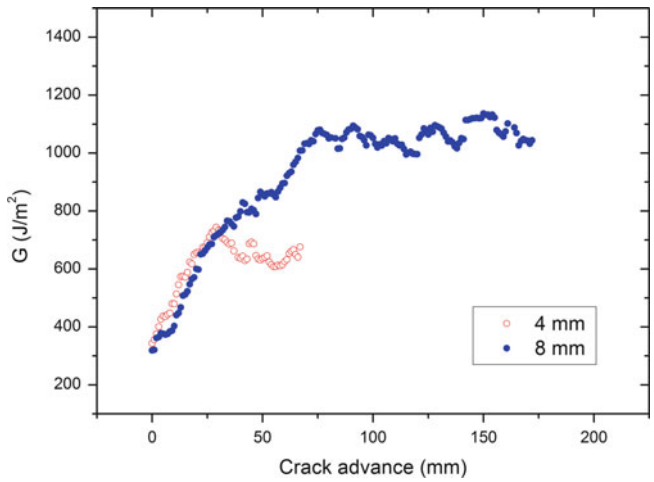

Fig. 23.4 Energy release rate versus crack advance as obtained from the DCB specimens with two different thicknesses

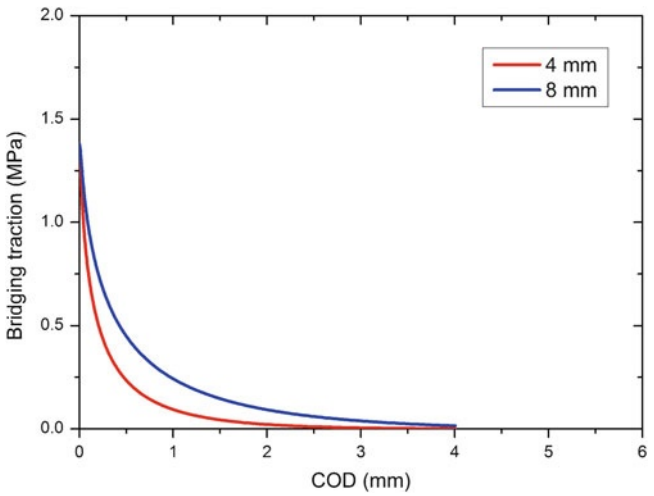

Fig. 23.5 Identified traction-opening relationships for two specimens with different thicknesses. The area under the *curves* represents the energy release rate due to the steady state fiber bridging

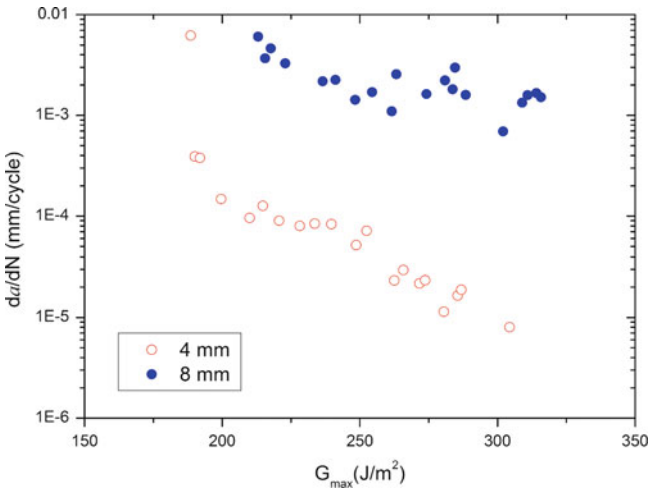

Fig. 23.6 Fatigue crack growth rate as a function of cyclic energy release rate for two specimens with different thicknesses

23.4 Conclusion

The thickness effects on mode I delamination behavior of carbon fiber/epoxy DCB specimens is investigated in monotonic and fatigue experiments. The results indicate that the ERR due to fiber bridging can be affected by the specimens thickness which is reflected in the obtained results.

A semi-experimental method based on parametric FE modeling and internal strain measurements using embedded multiplexed FBG sensors is applied to identify the bridging tractions in delamination of specimens of different thicknesses. The identified bridging law indicates that the maximum bridging traction, and the COD at the end of the bridging zone as material dominated parameters while the change in the rate of bridging traction distribution, γ, can explain the effect of thickness on the ERR due to the fiber bridging.

Acknowledgement The authors acknowledge the financial support from the Swiss National Science Foundation under Grant 200020_137937/1.

References

1. Gibson RF (2011) Principles of composite material mechanics, 3rd edn. CRC Press, Boca Raton
2. RICCIO A (2008) Delamination in the context of composite structural design. In: Sridharan S (ed) Delamination behaviour of composites. Woodhead/Maney, Cambridge, pp 28–60
3. Turon A, Camanho P, Costa J (2008) Delamination in composites: simulation of delamination in composites under static and fatigue loading using cohesive zone models. VDM Verlag Dr. Müller, Berlin
4. Suo Z, Bao G, Fan B (1992) Delamination R-curve phenomena due to damage. J Mech Phys Solids 40(1):1–16
5. Bao G, Suo Z (1992) Remarks on crack-bridging concepts. Appl Mech Re 45(8):355–366
6. Sørensen BF, Jacobsen TK (1998) Large-scale bridging in composites: R-curves and bridging laws. Compos Part A 29(11):1443–1451
7. Jacobsen TK, Sørensen BF (2001) Mode I intra-laminar crack growth in composites-modeling of R-curve from measure bridging laws. Compos Part A 32(1):1–11
8. Brunner AJ, Murphy N, Pinter G (2009) Development of a standardized procedure for the characterization of interlaminar delamination propagation in advanced composites under fatigue mode I loading conditions. Eng Fract Mech 76(18):2678–2689
9. Gregory JR, Spearing SM (2004) A fiber bridging model for fatigue delamination in composite materials. Acta Mater 52(19):5493–5502
10. de Morais AB (2011) A new fibre bridging based analysis of the double cantilever beam (DCB) test. Compos Part A Appl Sci Manuf 42 (10):1361–1368
11. Sorensen L, Botsis J, Gmür T, Cugnoni J (2007) Delamination detection and characterisation of bridging tractions using long FBG optical sensors. Compos Part A 38(10):2087–2096
12. Gowrishankar S, Mei H, Liechti KM, Huang R (2012) A comparison of direct and iterative methods for determining traction-separation relations. Int J Fract 177:109–128
13. Zhu Y, Liechti KM, Ravi-Chandar K (2009) Direct extraction of rate-dependent traction–separation laws for polyurea/steel interfaces. Int J Solids Struct 46(1):31–51
14. Sørensen BF, Jacobsen TK (2003) Determination of cohesive laws by the J integral approach. Eng Fract Mech 70(14):1841–1858
15. Cox BN, Marshall DB (1991) The determination of crack bridging forces. Int J Frac 49(3):159–176
16. Studer M, Peters K, Botsis J (2003) Method for determination of crack bridging parameters using long optical fiber Bragg grating sensors. Compos Part B Eng 34(4):347–359

17. Sorensen L, Botsis J, Gmür T, Humbert L (2008) Bridging tractions in mode I delamination: measurements and simulations. Compos Sci Technol 68(12):2350–2358
18. Bogdanovich A, Pastore CM (1996) Mechanics of textile and laminated composites. Chapman & Hall, London, ref BC: Jd 754
19. Measures RM (2001) Structural monitoring with fiber optic technology. Academic Press, San Diego, USA
20. Botsis J (2012) Fiber Bragg grating applied to in situ characterization of composites. Wiley Encyclopedia of Composites, Second Edition. Edited by Luigi Nicolais and Assunta Borzacchiello. John Wiley & Sons, Inc.
21. Stutz S, Cugnoni J, Botsis J (2011) Studies of mode I delamination in monotonic and fatigue loading using FBG wavelength multiplexing and numerical analysis. Compos Sci Technol 71(4):443–449
22. Stutz S, Cugnoni J, Botsis J (2011) Crack – fiber sensor interaction and characterization of the bridging tractions in mode I delamination. Eng Fract Mech 78:890–900
23. Levenberg K (1944) A method for the solution of certain nonlinear problems in least squares. Quart Appl Math 2(2):164–168
24. Marquardt D (1963) An algorithm for least-squares estimation of nonlinear parameters. SIAM J Appl Math 11:431

Chapter 24
Methodologies for Combined Loads Tests Using a Multi-actuator Test Machine

Marshall Rouse

Abstract The NASA Langley COmbined Loads Test System (COLTS) Facility was designed to accommodate a range of fuselage structures and wing sections and subject them to both quasistatic and cyclic loading conditions. Structural tests have been conducted in COLTS that address structural integrity issues of metallic and fiber reinforced composite aerospace structures in support of NASA Programs (i.e. the Aircraft Structural Integrity (ASIP) Program, High-Speed-Research program and the Supersonic Project, NASA Engineering and Safety Center (NESC) Composite Crew Module Project, and the Environmentally Responsible Aviation Program). This paper presents experimental results for curved panels subjected to mechanical and internal pressure loads using a D-box test fixture. Also, results are presented that describe use of a checkout beam for development of testing procedures for a combined mechanical and pressure loading test of a Multi-bay box. The Multi-bay box test will be used to experimentally verify the structural performance of the Multi-bay box in support of the Environmentally Responsible Aviation Project at NASA Langley.

24.1 Introduction

The ability to subject aerospace structures to combined loads representative of actual operating conditions is an important aspect of aerospace structural design. The standard aerospace industry practice is to design a structure that supports the various loading conditions and to verify the design by structural testing. A test fixture is usually designed to subject the structure to a subset of the loading conditions. The test fixture is often limited to a particular design or single configuration. However, the development of structures technology to be used for future aerospace design requires that full-scale and sub-scale structural concepts be tested with combinations of mechanical and internal pressure loads. Combined-loads testing requires a combined loads test machine with the flexibility to accommodate these structures. The NASA Langley Research Center developed the COmbined Loads Test System (COLTS), which consists of a multi-actuator test machine capable of applying combined loads and internal pressure loading to validate structures technology [1]. Structural tests have been conducted using COLTS to support airframe and space structures technology development. Tests have been conducted for the NASA Aircraft Structural Integrity Program, NASA High-Speed Research program, NASA Engineering and Safety Center (NESC) Composite Crew Module (CCM) Program and Environmentally Responsible Aviation (ERA) Project [2–7].

Three of the tests that were conducted using COLTS are presented in this paper. Experimental results are presented for curved fuselage panels that were tested using a D-box test fixture. Experimental results are presented for a 30-ft checkout beam specimen that is currently being used to develop and verify testing methodology for an ERA composite Multi-bay box test currently being planned for COLTS.

M. Rouse (✉)
NASA Langley Research Center, Structures Testing Branch, Mail Stop 190, Hampton, VA 23681-2199, USA
e-mail: marshall.rouse@nasa.gov

G.P. Tandon et al. (eds.), *Experimental Mechanics of Composite, Hybrid, and Multifunctional Materials, Volume 6*, Conference Proceedings of the Society for Experimental Mechanics Series, DOI 10.1007/978-3-319-00873-8_24,

24.2 Facility Description

24.2.1 Combined Loads Test System

COLTS was designed to accommodate a range of fuselage structures and wing sections and subject them to both quasistatic and cyclic loading conditions. COLTS is capable of testing fuselage barrels up to 4.6 m diameter and 13.7 m long with combined mechanical, internal pressure, and thermal loads. A schematic of COLTS configured with a cylindrical shell mounted between the test machine platens is illustrated in Fig. 24.1a, and a photograph of the facility is shown in Fig. 24.1b. The loading platen is suspended from a gantry that can traverse forward or backward to accommodate test articles of different lengths. Compression and bending loads are applied to the test articles by six 2,001.7-kN hydraulic actuators located perpendicular to and between the loading and reacting platens along the x (longitudinal) axis. Torsion loads are applied to the test articles by two 1,334.5-kN hydraulic actuators located vertically and spaced 7.0 m apart. Shear loads are applied to the test articles by two 1,334.5-kN hydraulic actuators located horizontally and spaced 5.5 m apart. The test machine is located in a steel reinforced concrete pit that is approximately 9.8 m deep, 14.3 m wide, and 22.0 m long. This arrangement is to ensure that pressurized structural testing can be performed safely. The length of the axial actuators is extended by means of tubular extensions to connect the loading platen with the load reacting platen so that test specimens that are longer than 3.05 m can be accommodated.

24.2.2 Mini-COLTS

For development of tests to be conducted in COLTS, an approximately 10 %-scale model of COLTS, called Mini-COLTS, is utilized. Compression and bending, shear, and torsion loads are applied to subscale test models by six 8,896-N hydraulic actuators located perpendicular to and between the loading and reacting platens along the x (longitudinal) axis. Torsion loads are applied to the test articles by two 8,896-N hydraulic actuators located vertically and spaced 81.6 cm inches apart. Shear loads are applied to the test articles by two 8,896-N hydraulic actuators located horizontally and spaced 57.15 cm apart. The length of the axial actuators is fixed with respect to the load reacting platen so that test models that are 139.7 cm can be accommodated. A photograph of the Mini-COLTS is shown in Fig. 24.2. Using the COLTS control system, Mini-COLTS can be used to do operational checkout of the mechanical loading parameters before loading the actual test article. Once the Mini-COLTS loading has been verified, the controls are switched back to the COLTS facility.

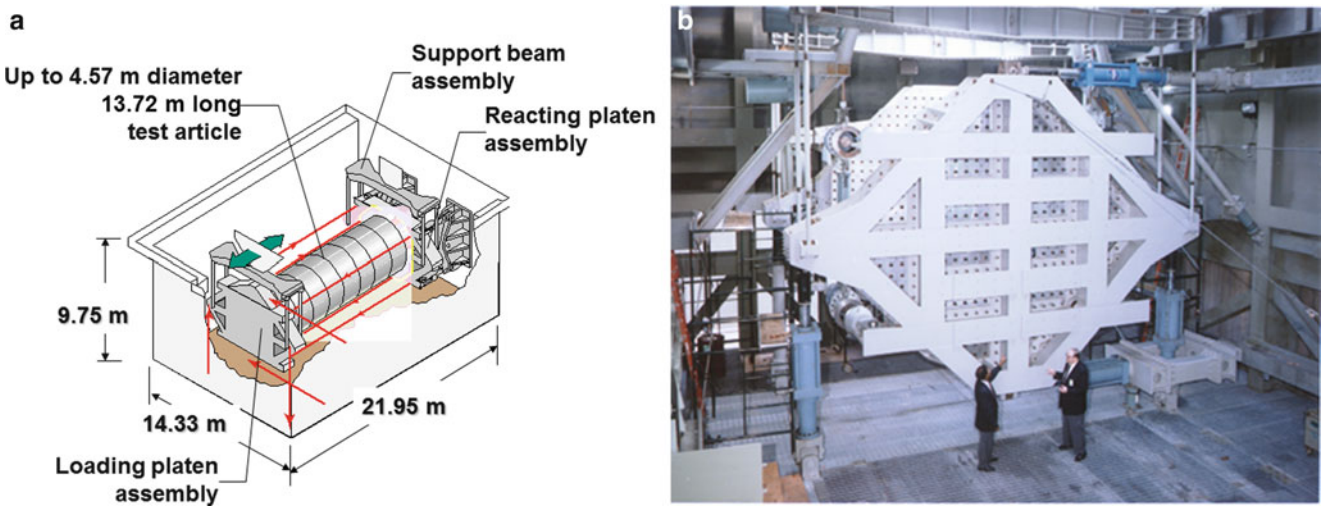

Fig. 24.1 (**a**) Schematic of COLTS configured with a cylindrical shell 37 mounted between the test machine platens. (**b**) Photograph of the COLTS facility

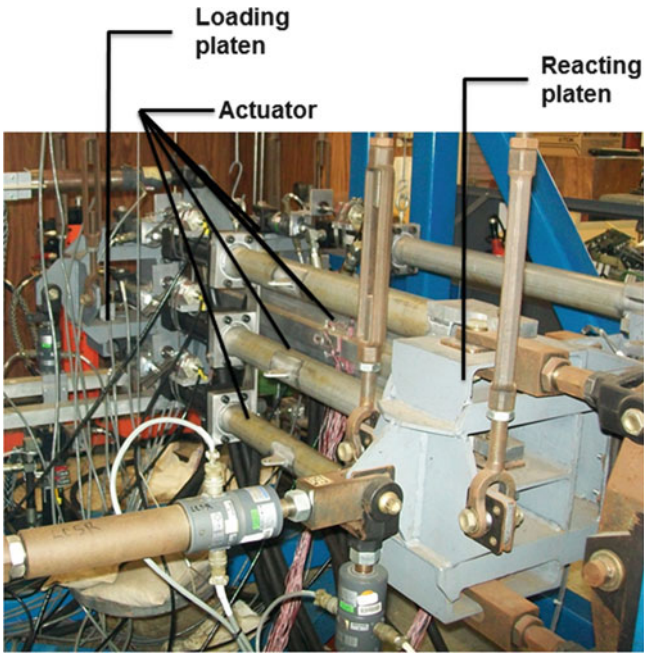

Fig. 24.2 Photograph of the Mini-COLTS

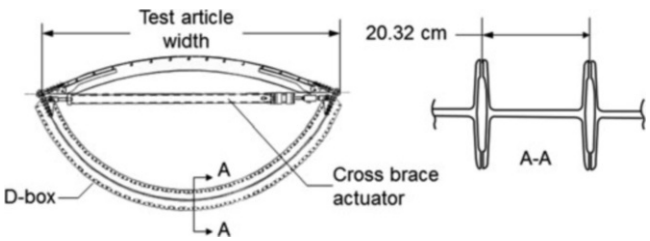

Fig. 24.3 A cross section drawing of the D-box test fixture

24.2.3 D-Box Test Fixture

A cross section drawing of the D-box test fixture is shown in Fig. 24.3. The fixture is used to apply mechanical and internal pressure loads to curved panels. The axial stiffness of the D-box test fixture allows a test panel to experience most of the applied axial load and minimizes the shift in the center-of-pressure of the assembly if the test panel buckles. The low axial stiffness of the D-box test fixture is the result of an assembly of curved I-beams with the cross section shown in the inset of Fig. 24.3. The I-beam sections are 20.32 cm deep and 15 of these sections are used to make the D-box test fixture. This D-box test fixture is designed to test curved panels with 152.4–330.2-cm radii and 50.8–55.9-cm frame spacing. An overhead photo of a panel in the D-box mounted in COLTS and a cabinet view drawing of the D-box test fixture are presented in Fig. 24.4. The drawing shows the hinge fittings attaching the panel to the D-box. Thirteen of these hinge fittings are provided between the I-beams for this purpose. When the D-box assembly is internally pressurized, the assembly expands in a manner that causes the hinge supports to move inward. This deformation would cause the test panel to bend in a way that is not representative of the response of an internally pressurized shell. To prevent this undesirable deformation, cross braces are mounted between the hinge points as shown in Fig. 24.3 such that the distance between the hinge points can be held constant or adjusted as needed to induce the appropriate stress state in the test panel. The D-box test fixture is capable of applying combined axial, shear, and internal pressure loads: 1,751,268 N/m axial load, 525,380.1 N/m shear load, and 137.89 kPa internal pressure.

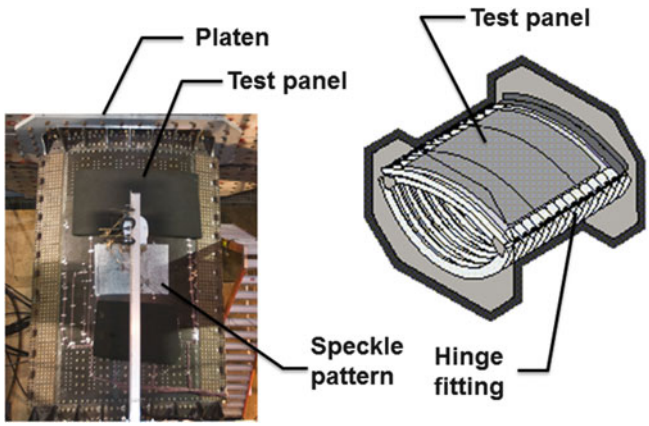

Fig. 24.4 An overhead photo of a panel in the D-box mounted in COLTS and a cabinet view drawing of the D-box test fixture

24.3 Tests Performed

24.3.1 Curved Fuselage Panels

Test result for two curved fuselage graphite-epoxy panels are presented in this paper. Both of the panels were 3.05 m long, 1.83 m arc width and 1.90 m outer mold radius. The test panels were also tested with a 22.86 cm length circumferential notch to simulate discrete source damage. The first panel was a honeycomb sandwiched panel with two frames. The facesheets were fabricated using 28 plies of IM7/PETI-5 graphite-epoxy material titanium honeycomb core. It had two frames mechanically fastened to the skin and spaced 1.02 m apart. The notch was machined into the panel mid-way between the two frames and centered on the longitudinal centerline at the mid-length of the panel. The frames were fabricated from triaxially braided stitched preform and fiber preforms using a resin film infusion process. The second panel was a stiffened graphite-epoxy fuselage side panel design. This panel had eight stringers and four frames. The stringers were spaced equally 17.8 cm apart. The second panel had four frames mechanically fastened to the skin and spaced 0.51 m apart. The notch was machined into this panel mid-way between the two frames and severed an interior stringer. A photograph of the second panel is shown in Fig. 24.5. The skin was fabricated from 34 plies of IM7/PETI-5 graphite-epoxy material. The stringers were fabricated from IM7/PETI-5 graphite-epoxy material and the frames were fabricated from triaxially braided stitched preform and fiber preforms using a resin film infusion process. A detailed description of the curved fuselage panel is given in Reference [3].

The fuselage panels were loaded to 49.12 kPa internal pressure and then axial tension load was applied until failure occurred. A summary of the failure is presented. The experimental axial strain results along a circumferential line located at the mid-length of the first panel are presented in Fig. 24.6. The results indicate that the strain results are uniform across circumference of the panel except at the notch tips. The strains were a maximum of 0.014 m/m near the notch tip and decrease to approximately 0.002 m/m away from the notch tip at a 2,688.8 N axial load and 49.12 kPa internal pressure loading. However, the maximum value of strain at the notch tip varied from 0.008 m/m to 0.012 m/m at the notch tip at an axial load of 4,571.6 N and 49.12 kPa. The lower measured strain value with respect to the previous load condition present in the figure at the notch tip suggests that damage has initiated at the notch tip resulting in a redistribution of loading at the tip. Axial surface strain results measured at the 0.127 cm and 7.188 cm from the notch tip, respectively, are presented in Fig. 24.7. The strain results at 0.127 cm from the notch grew at a higher rate with respect to applied load than the results at 7.188 cm away from the notch. Also, there was a significant reduction in strain at approximately 2,300 N.

A speckle pattern, consisting of black paint dots on a white paint background as seen in Fig. 24.4, was applied to the outer surface of the second panel prior to testing to monitor displacements and strains with a digital image correlation system [7–8]. Axial strain contour results recorded using the digital image correlation system are shown in Fig. 24.8. The full field axial strain gradient at 4,862 kN is presented in Fig. 24.8a. The results presented in Fig. 24.8a indicate that a maximum strain of approximately 0.0075 m/m occurred at the notch tip. The full field axial strain gradient at 5,187 kN is presented in Fig. 24.8b. The results presented in Fig. 24.8b indicate that a maximum strain of approximately 0.015 m/m occurred at the notch tip. However, the area of higher strain gradient is much smaller near the notch tip than the results previously presented. The reduced area of strain gradient suggests that a redistribution of load occurred at the notch tip prior to failure. The results presented suggest that the D-box test fixture can be used to predict response of curved fuselage panels subjected to combined mechanical and internal pressure loading.

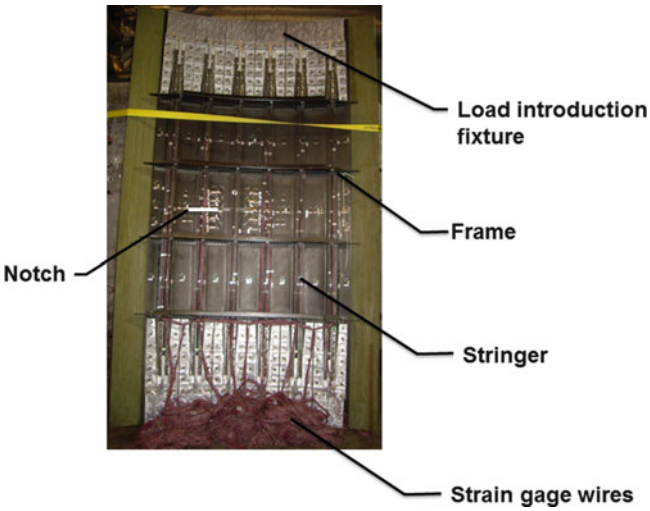

Fig. 24.5 A photograph of the second test panel

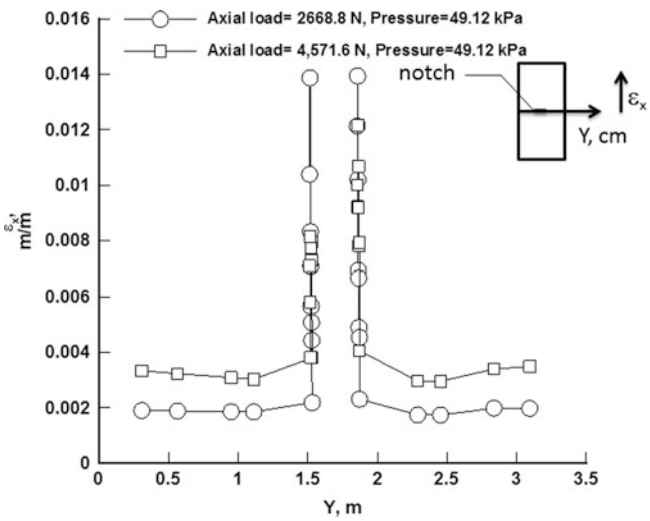

Fig. 24.6 The experimental axial strain results along a circumferential line located at the mid-length of the first panel

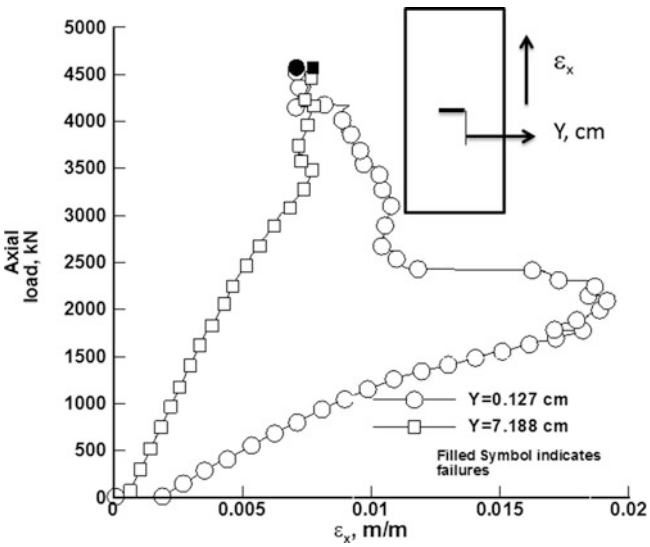

Fig. 24.7 Axial surface strain results measured at the 0.127 cm and 7.188 cm from the notch tip

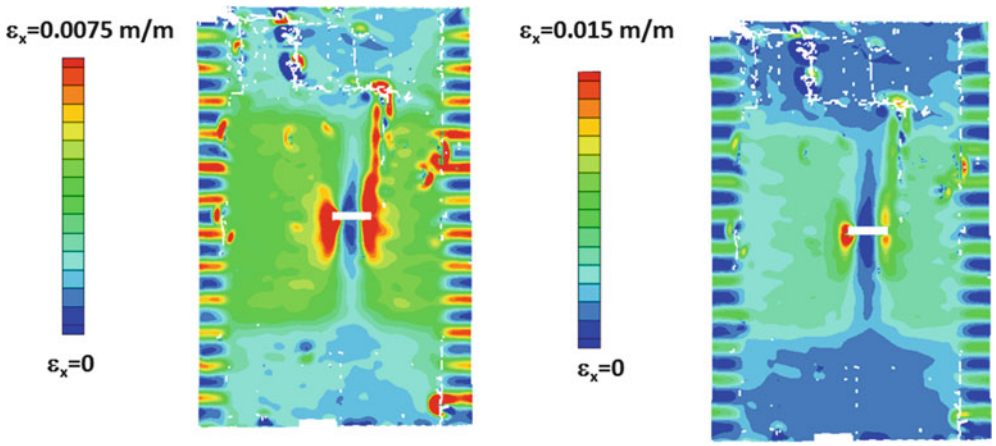

Fig. 24.8 The full field axial strain gradient at 4,862 kN and at 5,187 kN

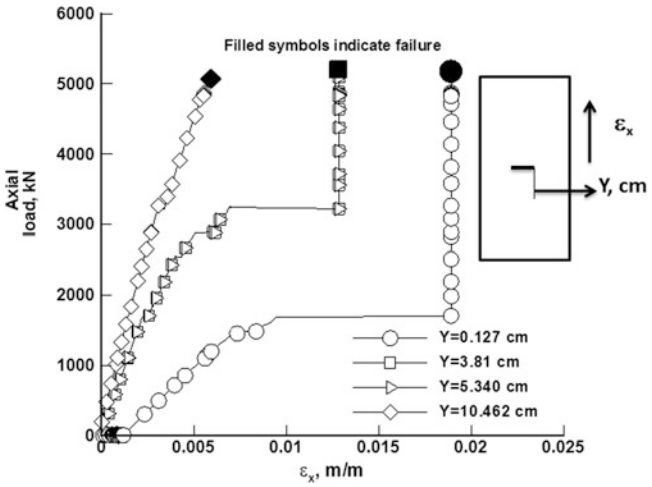

Fig. 24.9 Axial surface strain results

Axial surface strain results measured at the 0.127, 3.81, 5.34, and 10.562 cm from the notch tip, respectively, are presented in Fig. 24.9. The strain results at 0.127 cm from the notch grew at a higher rate with respect to applied load than the results at 3.81 and 5.34 cm away from the notch. Experimental surface strain results at Y = 0.127 cm indicated that maximum strain of approximately 0.018 m/m occurred at approximately 1,500 kN. Also, there was a significant reduction in strain at approximately 1,200 kN. Experimental surface strain results at 3.81 and 5.40 cm indicated that maximum strain of approximately 0.014 m/m occurred at approximately 3,200 kN. At 10.462 cm from the notch tip maximum strain of approximately 0.005 m/m occurred at approximately 5,000 kN just prior to failure of the test panel. A photograph of the failed panel is shown in Fig. 24.10. The photograph indicates that the damage initiated at the notch tip and propagated across the panel to the load introduction structure of the D-box along the hoop edges.

24.3.2 30-Foot Checkout Beam

The 30-ft checkout beam is a structure being used to develop the test operations and procedures for the Environmentally Responsible Aviation Multi-bay test article testing. The Multi-bay test article will be subjected to mechanical loading conditions to simulate flight conditions of the 2.5 and −1.0 g maneuver conditions by applying loads on the end plates of combined loads test machine. In order to achieve the critical 2.5 g maneuver load, the center bay of the crown panel will be loaded to an average compressive running load of 875,634 kN/m across its width. The loading methodology to be used for the future Multi-bay Box test was verified using the 30-ft checkout beam.

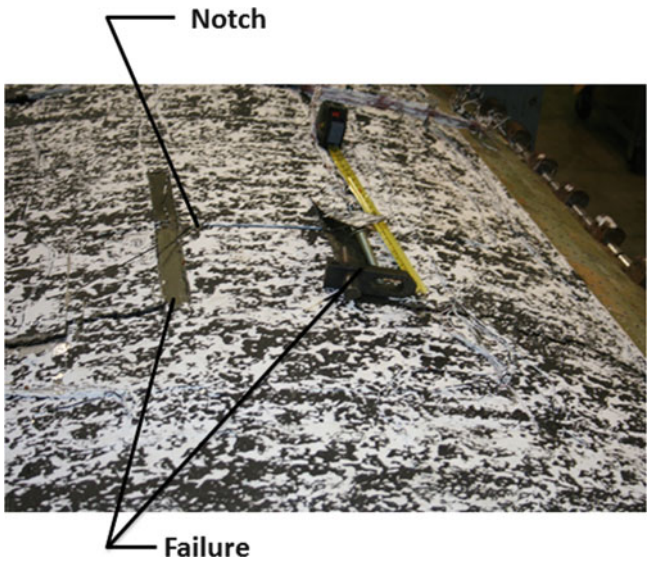

Fig. 24.10 Photograph of the failed panel

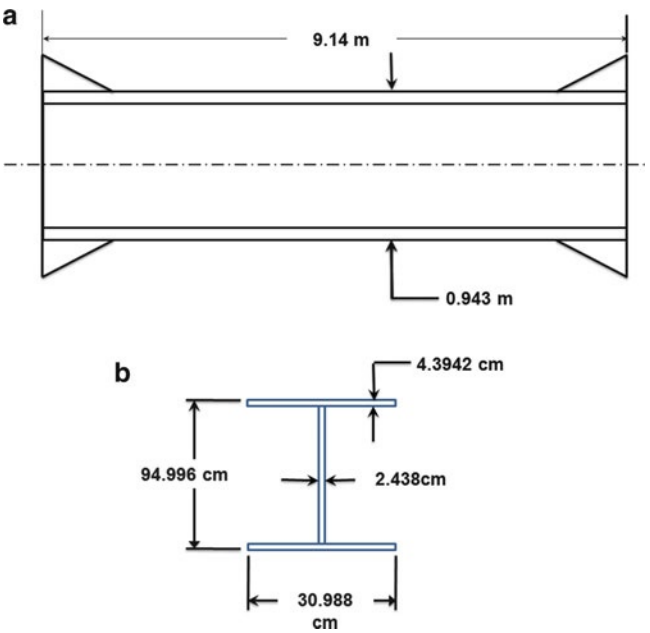

Fig. 24.11 Overall dimensions of the beam (**a**) and the overall cross section of the beam (**b**)

The checkout beam is a W36 × 256, A992 steel I-beam structure reinforced at each end with steel plates to allow load introduction. The overall dimensions of the beam are described in Fig. 24.11a and the overall cross section of the beam is described in Fig. 24.11b. The checkout beam was subject to a maximum applied bending moment 1,346,594 m-N in COLTS in order to verify loading methodologies for the upcoming ERA Multi-bay box test. A photograph of checkout beam installed in COLTS is presented in Fig. 24.12. Strain gages were installed on the upper and lower flange surface at locations A and B as shown in Fig. 24.13. Experimental strain results from the gages are presented in Fig. 24.14. Location A and B are located 0.962 m from the reacting and loading end of the beam, respectively. Experimental strain results at Location A indicate that the top flange was loaded in compression and the bottom flange in loaded in tension with respect to the applied bending moment. Similar results occurred at Location B. Also, the magnitude of the strain was equal at both locations. The results indicate that the beam was subjected to pure bending which is the desirable loading condition for the ERA Multi-bay box.

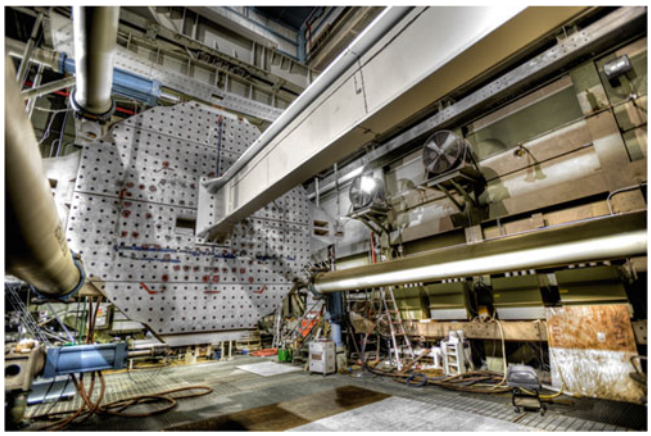

Fig. 24.12 Photograph of checkout beam installed in COLTS

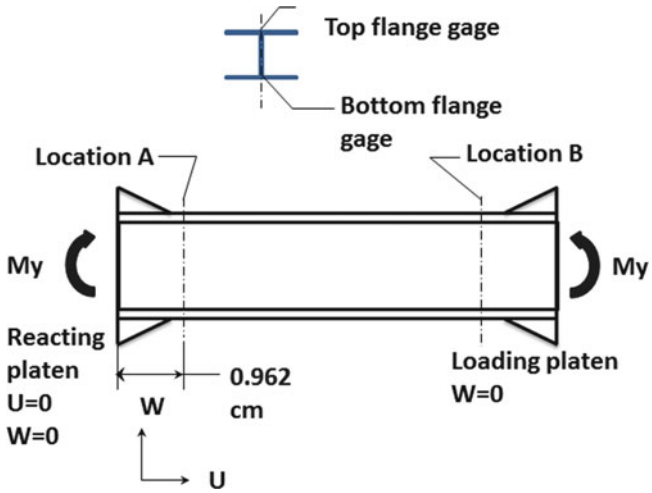

Fig. 24.13 Strain gage locations

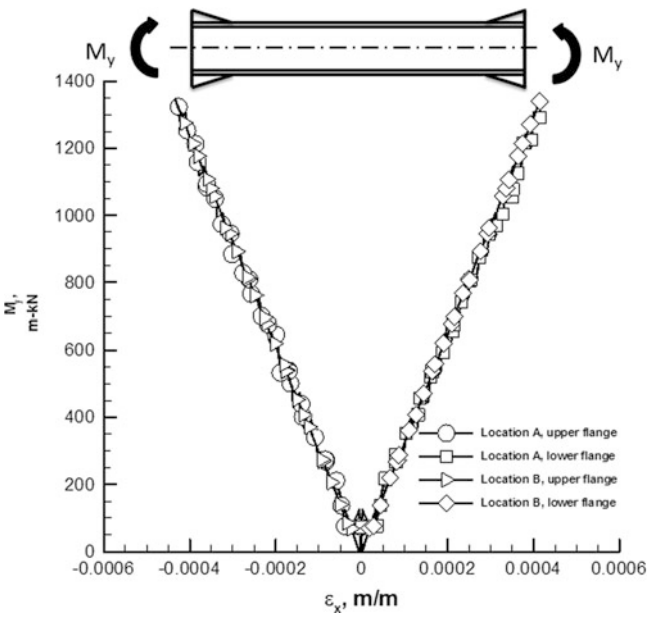

Fig. 24.14 Experimental strain results

24.4 Future Tests

24.4.1 ERA Multi-bay Box

A new structural concept called the Pultruded Rod Stitched Efficient Unitized Structure (PRSEUS) is being developed under the NASA Environmentally Responsible Aviation Project to meet the requirements of unconventional aircraft configurations that have higher lift-to-drag ratios, reduced drag, and lower community noise levels. The PRSEUS concept is being developed and validated through the design, analysis and testing using a building block approach, leading to a 30-ft long multi-bay pressure box test article that represents a portion of the Hybrid Wing Body (HWB) centerbody. The test article is representative of a portion of the center section of a HWB vehicle but addresses the same construction, analysis and pressurization issues that would be encountered on an airframe that has flat pressurized surfaces. These technologies include minimum-gauge design, post-buckled skins, crack arrestment, impact damage, manufacturing scale-up to larger structures, and joining technologies. A sketch of the Multi-bay test article is shown in Fig. 24.15. The Multi-bay test article contains 11 PRSEUS panels (crown, floor, two upper bulkheads, two lower bulkheads, two side rib, two side keels, lower keel), four honeycomb center rib panels, aluminum fittings, access doors, and titanium bolts.

As defined in the 30-ft checkout beam section above, the Multi-bay test article will be subjected to mechanical loads, but it will also be subjected to internal pressure loads. Mechanical and internal pressure loads will be applied simultaneously. The loading conditions will simulate the critical load cases: 2.5 g, 2.5 g plus 63.431 kPa, −1.0 g, and −1.0 g plus 63.431 kPa maneuver conditions, as well as the static 126.863 kPa ground condition that was used to size the overall test article structure. The Multi-bay test article will be subjected to internal pressure loads of 126.863 kPa to simulate a twice static proof condition.

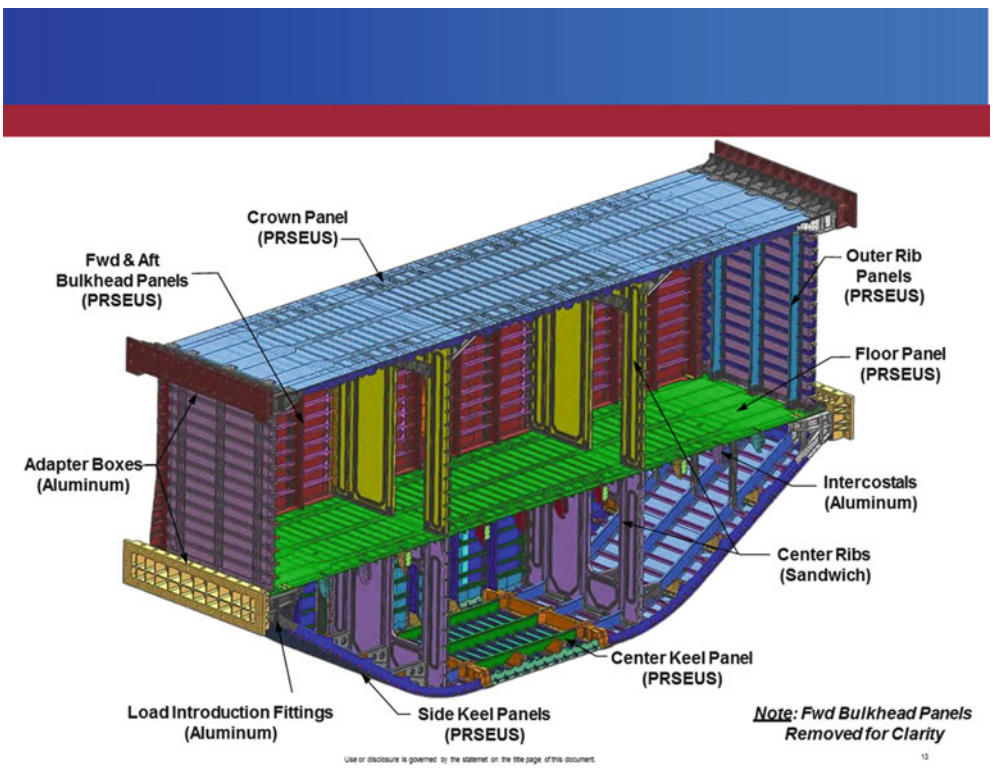

Fig. 24.15 Sketch of the Multi-bay test article

24.5 Concluding Remarks

A combined loads test machine has been demonstrated that is capable of applying combined mechanical, internal pressure loading to various structures. Curved fuselage panel were subjected to axial tension and internal pressure loading with simulated damage. Experimental results from COLTS for a check out beam have been used to verify that the combined loads test machine is capably of applying the proper pure bending loading condition to for the upcoming NASA ERA Multi-bay test article.

References

1. Ambur DR, Rouse M, Starnes JH, Shuart MJ (1994) Facilities for combined loads testing of aircraft structures to satisfy structural technology development requirements. Presented at the 5th annual advanced composites technology conference, Seattle, 22–36 Aug 1994
2. Ambur DR, Rouse M, Young RD, Perez-Ramos C (1999) Evaluation of an aluminum fuselage panel with discrete-source damage and subjected to combined loading conditions, AIAA-99-1382, Apr 1999
3. High Speed Research Program summary report for Task 16 material and structures damage tolerances and 25 fuselage structures, NAA contract NAS1-2020, Sept 1999
4. Ambur DR, Rouse M (2005) Design and evaluation of composite fuselage panels subjected to combined loading conditions. AIAA J Aircraft 42(4):1037–1045
5. Rouse M, Young Richard D, Gehrki RE (2003) Structural stability of a stiffened aluminum fuselage panel subjected to combined mechanical and internal pressure loads. Presented at the 44th AIAA/ASME/ASCE/AHS structures, structural dynamics, and materials conference, Norfolk, 7–10 Apr 2003
6. Composite crew module test NESC-RP-06-019, NASA/TM-211-217190, 2011
7. Jegley DC (2013) Status of advanced stitched unitized composite aircraft structures. Presented at the 51th AIAA aerospace sciences meeting including the New Horizons Forum and Aerospace Exposition, Grapevine, Jan 2013

Chapter 25
Mechanical Characterization and Modeling of Ceramic Foam Materials

I.M. Daniel, J.S. Fenner, and M.-Y. Chen

Abstract The materials investigated were silicon carbide foams of various densities ranging from 7.7 % to 12.3 % of the bulk material density. They were characterized under pure shear and uniaxial compression. Special test procedures were developed for this testing. For shear characterization two pairs of prismatic strips were used in a three-rail fixture. Stress–strain curves to failure were obtained from which the shear modulus, shear strength and ultimate shear strain were determined. A statistical analysis based on the Weibull distribution function was conducted to determine expected differences in results obtained by different test methods, specifically differences between three-rail shear and torsion test results. A power law model was proposed to describe the variation of shear modulus with relative density. It was also shown that the parameters of this model depend on the porosity structure of the foam for the same density. Similar tests were conducted under uniaxial compression. It was found that the Young's modulus varies linearly with the relative density of the foam.

25.1 Introduction

Cellular materials or foams consist of different basic materials, such as metallic, polymeric or ceramic. They afford a means of optimization of mechanical and thermal properties with a minimum weight. They have been extensively discussed and reviewed in the literature. The most widely known and cited treatise on the subject is that by Gibson and Ashby [1]. An erudite review was given by Christensen [2]. Ceramic foams in particular possess a unique set of properties which make them desirable for both structural and functional applications [3–5]. Ceramic foams, such as SiC foams, are of special interest in structures exposed to severe thermal gradients. They are used as core materials in sandwich structures consisting of a ceramic matrix composite (CMC) facesheet on the high temperature side and a polymeric matrix composite (PMC) facesheet on the low temperature side. Although the foam core is primarily intended as a lightweight thermal insulator, it must have adequate stiffness and strength to maintain the integrity of the structure. Of all the factors influencing failure initiation and mode in sandwich structure, the properties of the core material are most important [6].

Open-cell ceramic foams can be produced by pyrolysis, at 1,000–1,200 °C under nitrogen, of a preceramic polymer (a silicone resin) and blown polyurethane. The morphology of the expanded polyurethane is reproduced in the final architecture of the ceramic foam. The foam takes the form of a three-dimensional array of similar size cells, where each cell tends to reach a maximum volume with a minimum surface area and surface energy (Fig. 25.1). It is widely accepted that an optimum cell geometry for low density foams is that of the Kelvin cell. This minimal surface cell proposed by Lord Kelvin is a truncated octahedron or a tetrakaidekahedron, containing 14 faces, 8 hexagons and 6 squares. During the formation of the foam, the thin membranes of each of the 14 facets fall out leaving an open cell reticulated structure consisting of interconnected struts (Figs. 25.1 and 25.2). The physical and mechanical properties of cellular materials are related to their relative density and the morphology, size, and distribution of the holes (cell windows) in the cell walls.

I.M. Daniel (✉) • J.S. Fenner
Northwestern University, Evanston, IL, USA
e-mail: imdaniel@northwestern.edu; JoelFenner2012@u.northwestern.edu

M.-Y. Chen
AFRL, WPAFB, Dayton, OH, USA
e-mail: Ming-Yung.Chen@wpafb.af.mil

G.P. Tandon et al. (eds.), *Experimental Mechanics of Composite, Hybrid, and Multifunctional Materials, Volume 6*, Conference Proceedings of the Society for Experimental Mechanics Series, DOI 10.1007/978-3-319-00873-8_25,

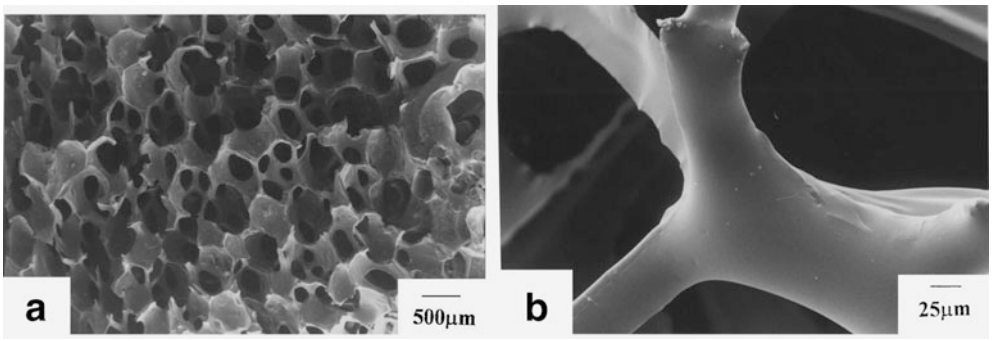

Fig. 25.1 Scanning electron micrographs of a pyrolyzed SiC foam showing (**a**) cell structure, (**b**) strut surface [4]

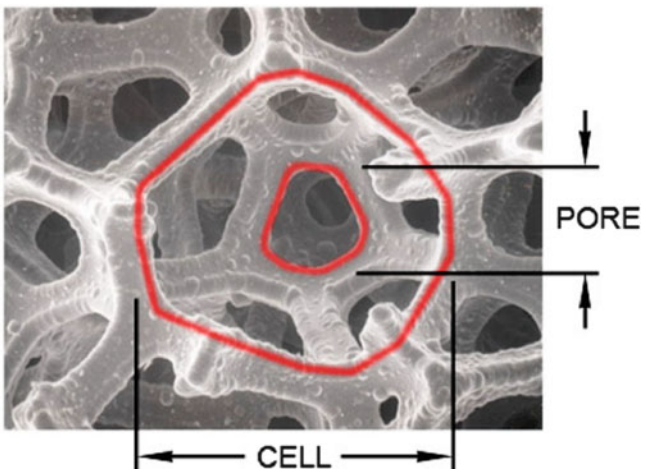

Fig. 25.2 Illustration of pore and cell geometries in a foam [7]

Since the ceramic foams under consideration are brittle materials, they are sensitive to size and stress gradients effects related to statistical distribution of strengths. Careful consideration must be given to the statistical aspects of failure when selecting, testing and designing structures with these materials. Huang and Gibson have proposed an analysis for optimizing the size and density of brittle foams [8].

This study deals with the mechanical characterization under shear and compression and modeling of four silicon carbide (SiC) foams of relative densities ranging from 4 % to 12.3 %.

25.2 Shear Characterization

The materials characterized were:

SiC foam of 7.7 % density and 65 ppi (pores per inch)
SiC foam of 12.3 %density and 65 ppi
SiC foam of 4 % density and 80 ppi
SiC foam of 10 % density and 80 ppi

Shear testing of materials in general is ideally conducted by means of torsion tests of thin wall tubes. Torsion tests of solid rods can provide information for the initial linear range of the stress–strain curve and thereby the value of the shear modulus, if a continuous record is obtained of torque versus angle of twist. However, values of ultimate shear strain and strength are

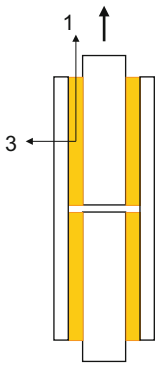

Fig. 25.3 Schematic for pure shear experiments

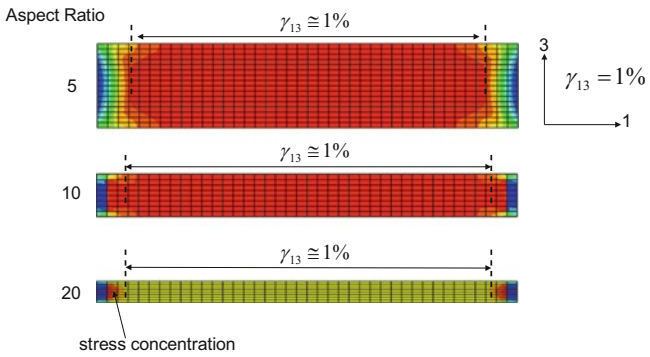

Fig. 25.4 Selection of specimen aspect ratio for shear test

affected by the nonlinear behavior and non-uniform distribution of shear stress across the cross section. An easier approach to getting shear stress–strain curves to failure is the rail shear test, provided the aspect ratio (length to thickness ratio) of specimen is high enough (Fig. 25.3) [9, 10].

An optimum aspect ratio for rail shear specimens can be determined by Finite Element Analysis as shown in Fig. 25.4 for a similar material. In general, it appears that a 10:1 aspect ratio is a reasonable choice.

For the shear test configuration shown in Fig. 25.3, the stresses are

$$\tau_{13} = \frac{P}{2A} \quad \text{and } \sigma_3 = 0 \tag{25.1}$$

and the strains are

$$\gamma_{13} = \sin^{-1}\frac{d}{t} \quad \text{and} \quad \varepsilon_3 = 1 - \cos\gamma_{13} \tag{25.2}$$

In the above, the shear stress and strain are along the loading direction (1-direction) and the normal stress and strain are normal to the loading direction (3-direction); P is the applied load and A is the area of the specimen attached to the rails. The specimens were strips of dimensions: 6 mm thick × 10 mm wide × 60 mm long. They were bonded to the metal rails by means of a room temperature curing epoxy adhesive (Hysol Loctite 9430). Because of the highly brittle nature of the foam materials, a special fixture was built to allow rotation along two axes at one end (Fig. 25.5). The relative displacement was measured with an extensometer mounted on the middle rails. Stress–strain curves to failure were obtained, from which the shear modulus, shear strength, and ultimate shear strain were determined. Typical stress–strain curves are shown in Fig. 25.6 for the four ceramic foams tested.

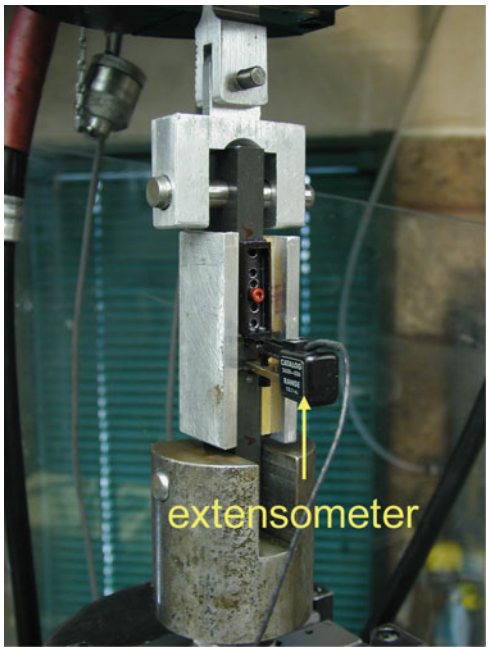

Fig. 25.5 Shear fixture with specimen in testing machine

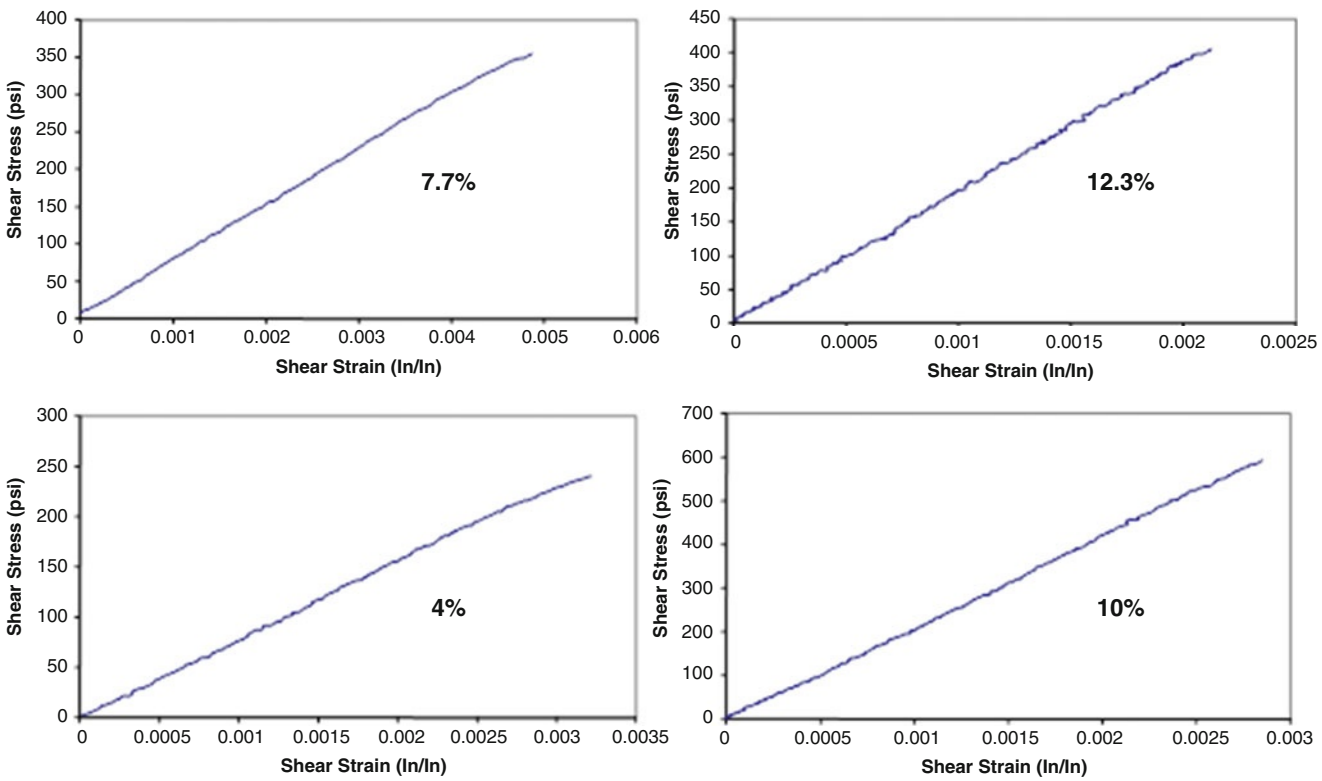

Fig. 25.6 Typical shear stress–strain curves for four ceramic foams tested

25.3 Compression Characterization

Uniaxial compression tests were conducted under stress controlled conditions using prismatic specimens with at least 2:1 aspect ratio. The aspect ratio should not be too low, because that would lead to non uniform and non uniaxial stresses, thus any modulus determination would be erroneous. A high aspect ratio might lead to buckling failure. These tests yield the complete stress–strain behavior including Young's modulus, compressive strength and compressive ultimate strain. Of all the specimen features, the parallelism of the loading faces is the most critical. The specimen dimensions were 25 × 12.5 × 12.5 mm (1 × 0.5 × 0.5 in.).

The loading fixture consists of two flat-ended cylindrical steel rods (platens) machined with ends flat and perpendicular to their axis (Fig. 25.7). The rods were 25 mm (1 in.) in diameter. Because of the high specimen stiffness and the small strains induced, it is necessary to measure accurately the displacement of the fixture platens themselves, not simply the machine crosshead. This was accomplished by using a conventional strain-gage extensometer as a displacement transducer (Fig. 25.7). Typical compressive stress–strain curves are shown in Fig. 25.8.

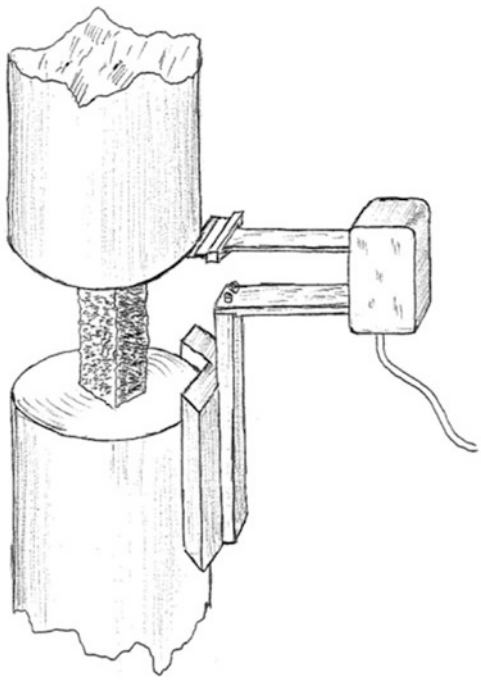

Fig. 25.7 Loading fixture with extensometer

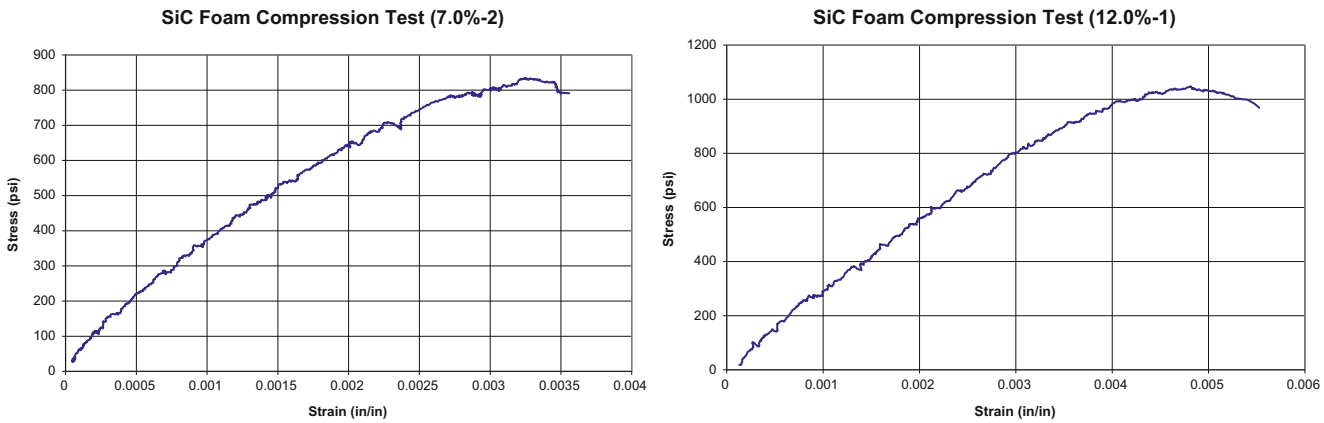

Fig. 25.8 Stress–strain curves under uniaxial compression of SiC foams of two different densities

25.4 Modeling of Elastic Behavior

The measured shear moduli and strengths were summarized in Table 25.1 below for four types of SiC foams of different densities and pores per inch (ppi), which is related to cell wall thickness. In the table below, the foam densities and moduli were normalized by the density and modulus of the bulk material. The properties of the bulk material are as follows:

Density: $\rho_b = 3{,}200$ kg/m^3
Young's modulus: $E_b = 415$ GPa (60×10^6 psi)
Poisson's ratio: $\nu_b = 0.20$
Shear modulus: $G_b = 173$ GPa (25×10^6 psi)

A great deal of research has been reported on modeling of elastic and failure behavior of foams. Simple models for predicting mechanical properties are given in the classical work by Gibson and Ashby [1, 11]. The open cell of a foam is represented as a reticulated structure element (Fig. 25.9).

The relative density is defined in terms of the cell dimensions as

$$\frac{\rho}{\rho_b} = C_1 \left(\frac{t}{l}\right)^2 \tag{25.3}$$

where ρ and ρ_b are the densities of the foam and the bulk solid, respectively, t is the strut or wall thickness, l is the cell size and C_1 a constant. The ratio (t/l) is referred to as the "stockiness" ratio.

For example, a generic model for the elastic modulus in the following form has been found adequate in many cases.

$$\frac{E}{E_b} = C_2 \left(\frac{\rho}{\rho_b}\right)^n \tag{25.4}$$

Table 25.1 Shear modulus and strength of silicon carbide foams

Relative density $\left(\frac{\rho}{\rho_b}\right)$	Pores per inch (ppi)	Relative shear modulus $\left(\frac{G}{G_b}\right)$ average (range)	Average shear strength F_s (psi)
0.077	65	$0.0056 \begin{pmatrix} +0.0003 \\ -0.0004 \end{pmatrix}$	306
0.123	65	$0.0083 \begin{pmatrix} +0.0007 \\ -0.0006 \end{pmatrix}$	418
0.040	80	$0.0037 \begin{pmatrix} +0.0009 \\ -0.0006 \end{pmatrix}$	192
0.100	80	$0.0079 \begin{pmatrix} +0.0015 \\ -0.0021 \end{pmatrix}$	580

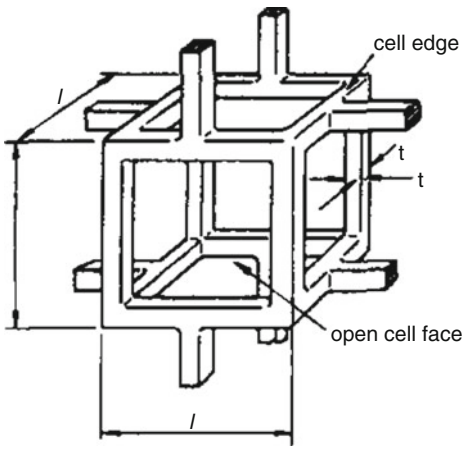

Fig. 25.9 Reticulated structure element representing a foam cell [11]

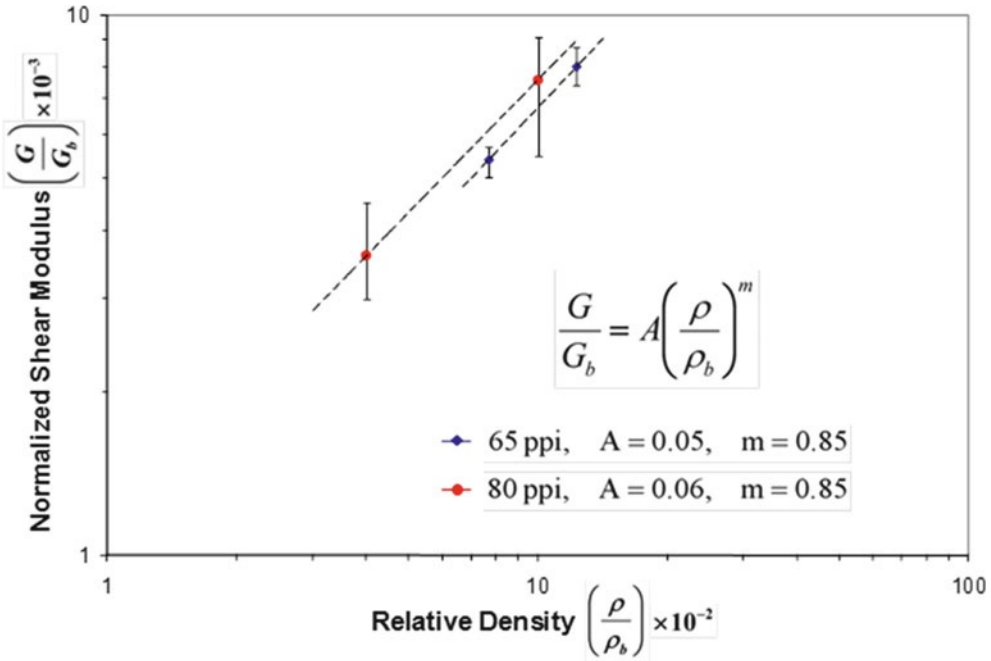

Fig. 25.10 Variation of relative shear modulus with relative density for two SiC foams

where C_2 and n are constants, E is the modulus (shear or Young's modulus of the foam), E_b the modulus of the bulk solid. Similar power law relations were proposed for the elastic collapse.

The shear modulus of the SiC foams tested could be modeled in a similar manner.

$$\frac{G}{G_b} = A\left(\frac{\rho}{\rho_b}\right)^m \tag{25.5}$$

where A and m are constants. Results of Table 25.1 were fitted to relation Eq. 25.5 as shown in Fig. 25.10. The constants obtained are:

Foam A: ppi = 65, $A = 0.05$, $m = 0.85$
Foam B: ppi = 80, $A = 0.06$, $m = 0.85$

It appears that the power exponent m depends only on the foam density regardless of the ppi property. The latter is directly related to and is roughly proportional to the cell wall thickness. It can be shown by analysis that the constant A is related to the ppi value and, thereby, to the cell wall thickness.

The average values of Young's moduli obtained from the compression tests are:

E = 1,725 MPa (250 ksi) and E = 2,760 MPa (400 ksi) for the foams of 7.7 % and 12.3 % relative densities, respectively. It is interesting to note that these moduli are proportional to the densities of the respective materials, 400/250 = 12.3/7.7, i. e., the constants C_2 and n in Eq. 25.4 are equal to unity.

25.5 Stress Gradient Effect on Failure

A statistical analysis was conducted to determine expected differences in results obtained by different test methods, specifically differences between three-rail shear and torsion test results. Failure of brittle materials is initiated by the presence of microscopic flaws, but unlike more ductile materials, failure initiation even on a microscopic scale can be catastrophic. This is measured by the fracture toughness of the material, which is a measure of its sensitivity to defects and their size. Brittle materials such as ceramics and ceramic foams fail by the weakest link principle. Since the existence and

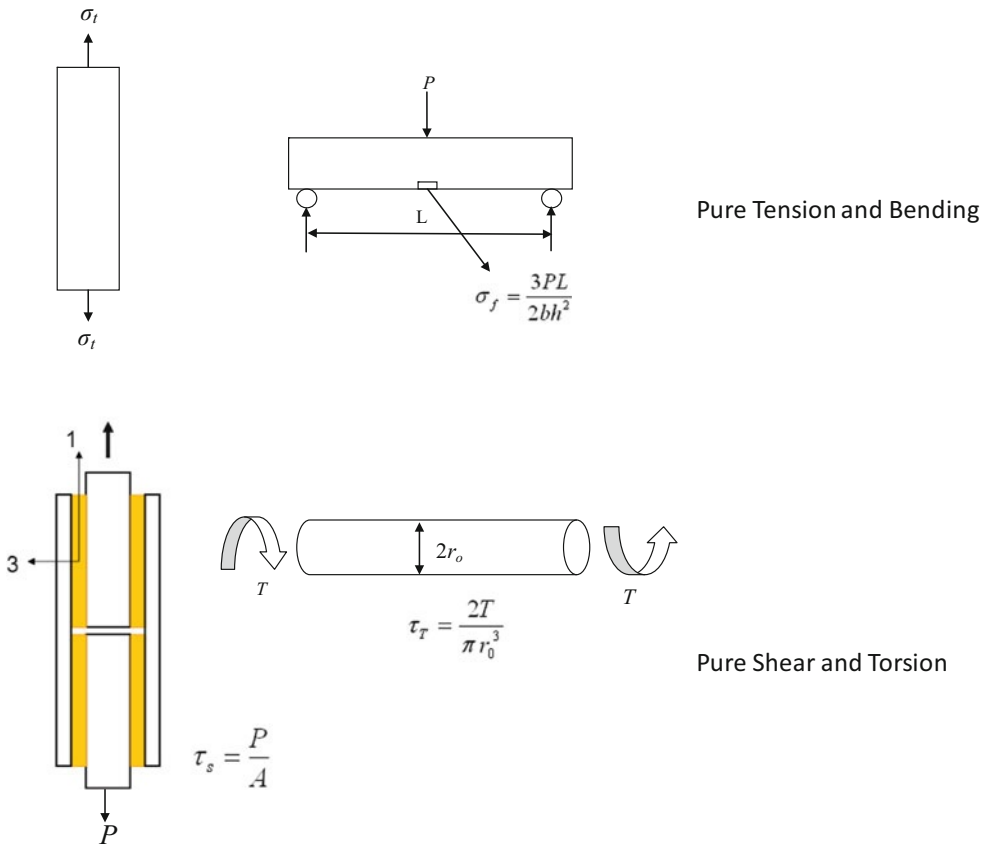

Fig. 25.11 Illustration of failure stresses under pure tension, three-point bending, pure shear, and torsion

distribution of initial defects is random, a statistical description of the scatter in the results is used. This leads to the influence of stress gradient on the failure of brittle materials [12].

The most widely used statistical distribution function is the Weibull one. According to this theory, the probability of failure at a point is given by

$$F = 1 - \exp\left\{-\int_v \left[\frac{\sigma - \sigma_u}{\sigma_o}\right]^m dV\right\} \tag{25.6}$$

where

$F(\sigma)$ = probability of failure of material at stress σ
σ_u = zero probability strength or threshold stress below which the material never fails
σ_o = normalizing scale parameter
m = Weibull modulus or flaw density exponent that characterizes the strength of the material
V = volume of material under stress

One conservative approach is to assume that σ_u is zero. The Weibull modulus is determined by a series of tests, such as tensile, compressive or shear tests. This allows comparison of results from bending and uniaxial tensile or compressive tests and from (rod) torsion and pure shear tests (Fig. 25.11).

Assuming σ_u to be zero, for a uniformly stressed specimen (tension or compression) the probability of failure is expressed as

$$F_t = 1 - \exp\left\{-V_t\left(\frac{\sigma_t}{\sigma_o}\right)^m\right\} \tag{25.7}$$

and, for the non-uniform stress distribution in a beam under three-point bending (assuming the material fails under tension)

$$F_f = 1 - \exp\left\{-V_f \left(\frac{\sigma_f}{\sigma_o}\right)^m \left[\frac{1}{2(m+1)^2}\right]\right\} \tag{25.8}$$

Thus, the ratio of flexural strength to uniform tensile strength (for equal probabilities of failure) is

$$\frac{\sigma_f}{\sigma_t} = \left[2(m+1)^2 \frac{V_t}{V_f}\right]^{\frac{1}{m}} \tag{25.9}$$

If both tension and compression are equally detrimental (as in the case of ceramic foams) the probability of fracture in three-point bending is

$$F'_f = 1 - \exp\left[-V_f \left(\frac{\sigma_f}{\sigma_o}\right)^m \frac{1}{(m+1)^2}\right] \tag{25.10}$$

and then, the ratio between flexural and tensile strengths is

$$\frac{\sigma'_f}{\sigma_t} = \left[(m+1)^2 \frac{V_t}{V_f}\right]^{1/m} \tag{25.11}$$

For pure bending and nearly equal tensile and compressive strengths (ceramic foams) the probability of fracture is

$$F_{pf} = 1 - \exp\left[-V_f \left(\frac{\sigma_f}{\sigma_o}\right)^m \frac{1}{(m+1)}\right] \tag{25.12}$$

and the ratio of bending (pure bending) to tensile strengths is

$$\frac{\sigma_{pf}}{\sigma_t} = \left[(m+1) \frac{V_t}{V_f}\right]^{1/m} \tag{25.13}$$

The Weibull modulus (or shape parameter) m must be determined by conducting a series of tests (tension or compression) and fitting the Weibull distribution function to the cumulative failure probability data to determine the parameters. Low values of m imply high scatter and high values of m low scatter. For example, for a value of $m = 30$ (not very high scatter) and equal volumes, the strength ratios given by Eqs. 25.4, 25.6 and 25.8 are

$$\frac{\sigma_f}{\sigma_t} = 1.29, \frac{\sigma'_f}{\sigma_t} = 1.26, \frac{\sigma_{pf}}{\sigma_t} = 1.12$$

For a low value of $m = 10$ (high scatter)

$$\frac{\sigma_f}{\sigma_t} = 1.73, \frac{\sigma'_f}{\sigma_t} = 1.61, \frac{\sigma_{pf}}{\sigma_t} = 1.27$$

In the case of shear, the probability of failure under pure shear (rail shear test) is

$$F_s = 1 - \exp\left[-V_s \left(\frac{\tau_s}{\tau_o}\right)^m\right] \tag{25.14}$$

τ_s = shear stress
τ_o = scale parameter
M = Weibull modulus in shear
V_s = specimen volume under shear

For a solid rod under torsion the probability of failure is

$$F_T = 1 - \exp\left[-V_T \frac{2}{m+2} \left(\frac{\tau_T}{\tau_o}\right)^m\right] \tag{25.15}$$

The ratio of measured strengths by pure shear and torsion testing is

$$\frac{\tau_T}{\tau_s} = \left[\frac{m+2}{2} \frac{V_s}{V_T}\right]^{1/m} \tag{25.16}$$

The value of m must be obtained from a series of shear tests. It may be assumed equal to the value under tension or compression for quasi-isotropic ceramic foams. If, for example, $m = 30$ (low scatter) or $m = 10$ (high scatter), the strength ratios are

$$\frac{\tau_T}{\tau_s} = 1.10 \quad \frac{\tau_T}{\tau_s} = 1.20$$

25.6 Summary and Conclusions

Ceramic foams of relative densities in the range of 4–12.3 % were tested under uniaxial compression and pure shear. The materials are quasi-isotropic, behaved nearly linearly to failure and failed in a brittle manner. Moduli, strengths and ultimate strains were recorded. The Young's modulus varied linearly with relative density, whereas the shear modulus was related to relative density through a power law with an exponent slightly less than unity. An attempt to extract Poisson's ratio showed that the latter is very low or even negative.

Acknowledgement This work was supported by the Universal Technology Corporation under the US AFRL Rapid Insertion and Development of Hypersonic Materials (RIDHM) program.

References

1. Gibson LJ, Ashby MF (1997) Cellular solids: structure and properties, 2nd edn. Cambridge University Press, Cambridge
2. Christensen RM (2000) Mechanics of cellular and other low density materials. Int J Solid Struct 37:93–104
3. Colombo P, Modesti M (1999) Silicon oxycarbide ceramic foams from a preceramic polymer. J Am Ceram Soc 82(3):573–578
4. Nangrejo MR, Bao X, Edirisinghe MJ (2000) The structue of ceramic foams produced using polymeric precursors. J Mat Sci Lett 19:787–789
5. Bao X, Nangrejo MR, Edirisinghe MJ (2000) Preparation of silicon carbide foams using polymeric precursor solutions. J Mater Sci 35 (17):4365–4372
6. Daniel IM (2009) Influence of core properties on the failure of composite sandwich beams. J Mech Mater Struct 4(7–8):1271–1286
7. ERG (2011) Duocel-reticulated carbon, ceramic and metal foam basics. http://www.ergaerospace.com/Description.htm
8. Huang JS, Gibson LJ (1993) Optimum cell size and density of brittle foams. J Mater Sci Lett 12:602–604
9. Daniel IM, Ishai O (2006) Engineering mechanics of composite materials, 2nd edn. Oxford University Press, New York
10. Daniel IM, Cho J-M (2011) Characterization of anisotropic polymeric foam under static and dynamic loading. Exp Mech 51(8):1395–1403
11. Gibson LJ (1989) Modelling the mechanical behavior of cellular materials. Mater Sci Eng A110:1–36
12. Daniel IM, Weil NA (1963) The influence of stress gradient upon fracture of brittle materials. ASME paper no. 63-WA-228

Chapter 26
Mechanical Characterization for Identifying an Appropriate Thermal Cycle for Curing Ceramic/Glass Composite Seals

Bodhayan Dev and Mark E. Walter

Abstract Solid oxide fuel cells (SOFCs) require seals that can function in severe environments at elevated temperatures. Sealing remains a significant issue for all types of planar SOFCs. In fact seals could be considered the most critical component for commercializing the entire SOFC technology. Not only do inadequate seals present a barrier to commercialization of SOFCs, but there are also significant and interesting fundamental issues in materials selection, characterization, and design. The present research focuses on a novel ceramic/glass composite seal that is produced by roller compaction. It was found that the high heating and cooling rates during binder burnout cycles resulted in seals that were significantly weaker in compression. Post-test analysis showed that the number of micro-voids and other surface anomalies increased significantly with faster heating and cooling rates. By studying the microstructures, surface topography, and mechanical responses of seals cured at different rates, the current research proposes an appropriate thermal cycle for curing the green seals. Seals, thus cured, include minimum micro-voids and surface anomalies and have better compressive mechanical response. These properties would help provide better sealing performance and increased longevity at SOFC operating conditions.

26.1 Introduction

Due to high efficiencies and low emissions, SOFCs have the potential to radically alter the distribution and production of electrical energy. As SOFCs convert chemical energy without any intermediate thermal energy step, their energy limit is not subjected to the Carnot limit. The selections of materials for SOFCs have always been a challenge due to their high operating temperature regime, which ranges from 700 °C to 900 °C. High temperature is preferred for better fuel utilization and high performance. However, it adds to the cost of the materials and the long term stability of the components in SOFC. Planar SOFC designs also require hermetic sealing between each individual cell to avoid intermixing of air-fuel and to avoid any short circuit in the cell. The Seals need to have long-term stability at elevated temperatures and harsh environments.

The two mainstream methods for sealing in SOFCs are compressive sealing and chemical bonding sealing [1, 2]. In compressive sealing, a compliant material is sandwiched between two sealing surfaces and is compressed by an externally applied load. Some of the commonly used compressive seals are mineral-based materials like Thermiculite 866, Statotherm HT, Muscovite, and Phlogopite [2, 3]. The seals can slide across the sealing surface while maintaining the seal [1]. The primary disadvantage of the compressive sealing method is the lack of materials that are compliant at high temperatures and/or remain compliant with thermal cycling [2, 3] and chemical reactions in the aggressive SOFC environment. Furthermore, the compressive seals require complicated infrastructure for providing mechanical loading [2].

The bonding seals approach relies on chemical bonding to provide hermetic sealing. Among the materials which are commonly used in bonding seals, the promising candidates for SOFC applications are glass and glass-ceramics. The primary advantages of bonding seals are a superior chemical stability under reactive atmospheres and not needing an external load frame for effective sealing [4]. The main disadvantages of bonding seals are brittleness at low temperatures, which results in susceptibility to coefficient of thermal expansion (CTE) mismatch [5], softening, and crystallization of the glass phases, which compromises long term durability [5, 6]. True hermetic sealing is difficult, if not impossible, to achieve in an environment where temperatures can change.

B. Dev (✉) • M.E. Walter
Department of Mechanical and Aerospace Engineering, The Ohio State University, Columbus, OH 43210, USA
e-mail: dev.9@osu.edu

G.P. Tandon et al. (eds.), *Experimental Mechanics of Composite, Hybrid, and Multifunctional Materials, Volume 6*, Conference Proceedings of the Society for Experimental Mechanics Series, DOI 10.1007/978-3-319-00873-8_26,

The performance and life span of a seal depends on the degree to which gas flow within the material at the interface is inhibited. Therefore, any macroscopic cracking/damage within the bulk must be avoided and gaps/separation of the interface also leads to failed sealing. With the need to seal against a variety of materials, bonding in the presence of CTE mismatches becomes untenable [7, 8]. For this reason, it is assumed that a successful approach will tailor the CTE [7] and/or rely more on mechanical loading. By working with a composite material, it becomes possible to design the components to affect the macroscopic CTE value. At the same time, it is also critical to select compositions that will maintain some degree of compliance and not crystalize at the desired operating temperatures and during excursions to and from the operating temperature.

Over the past few decades, extensive research has been carried out in selecting an appropriate composition for glass seals for SOFC applications. This follows on a tremendous body of research and product development for sealing glasses in the micro-electronic industries [9] where maximum temperatures are more on the order of 450 °C. Regardless of the application, the results are varying widely, since there are practically unlimited combinations of glass phases and fillers. It is generally accepted that barium or boron-based systems are required in order to mitigate crystallization at these temperatures (e.g., [5]). Within these types of systems, authors have studied crystallization kinetics (e.g., [4, 10–12]), CTE development (e.g., [7, 13]), particle and powder sizes (e.g., [7, 14]), and flow and sintering behavior [5, 15].

The G-18 glass system developed at the Pacific Northwest National Laboratory (PNNL) was designed specifically for SOFCs. As such, this system has been uniquely characterized with measurements of thermal expansion [16, 17], crystallization [18], wetting angle [18], microstructural evolution [19], interaction with interconnect and electrolyte materials [18], mechanical properties [19], and bond strength [17]. The G-18 system has also been modified with different compounds to improve contact angle and thermal expansion characteristics [18]. However G-18 was designed for temperatures up to 700 °C, and when above 700 °C, crystalline phases become unstable and the CTE varies with thermal cycling. G-18 also reacts with other SOFC components to form porous interfaces that are susceptible to fracture.

Rather than using a "pure" glass approach that starts with a single glass that partially crystallizes into a glass-ceramic, the proposed research deals with a two-phase ceramic/glass composite. The ceramic/glass composite approach is an emerging method of high temperature sealing. The processing of the seal begins with a high percentage of Al_2O_3 ceramic powder, an organic binder, and a barium aluminosilicate-based glass powder. The powders are roll-compacted or tape-casted into flat sheets. Binder burn-out and consolidation of the glass powder occurs during a heat treatment at 800 °C for 4 h. The resulting microstructures consist of glass filling voids between Al_20_3 particles. The advantage to this approach is that the alumina provides rigidity that minimizes CTE mismatch issues and allows some degree of resistance against compressive loading in stacks.

However, an appropriate curing cycle is yet to be determined. Most of the past researchers had chosen an arbitrary curing cycle without mentioning the actual reason behind selecting it [5, 12, 16]. However, the current research proposes a rigorous procedure to cure the green seals in an appropriate manner that would expedite the initial binder burnout process without compromising the seal performance. Compression tests on seals, cured at different rates, are initially conducted at room temperature. This is followed by the study of post-test micro structural and stereo optical images of cured seals. These combinations of experiments and microstructural observations are used to identify the appropriate thermal cycle.

26.2 Materials

NexTech Materials, Ltd. (NTM) employs a novel sealing approach of combining mechanical loading with minimum surface bonding to attain the desired seal performance for SOFCs. The seal itself has a ceramic to glass ratio of 60:40, and is processed by either roll-compaction or tape-casting nominally 14 μm glass powder and ~0.5 μm ceramic (alumina) powder mixed with an appropriate organic binder. A typical seal thickness for actual stacks is ~0.25 mm. The glass and alumina phases are shown in the SEM backscatter image provided in Fig. 26.1.

26.3 Seal Cure

The curing process in the present research includes a heating cycle, followed by a dwell a period of 4 h and finally a cooling cycle returning back to room temperature. Smeacetto et al. [21] and Brochu et al. [22] postulated that the micro-voids can originate during the curing process primarily due to entrapment of unwanted gases and also due to differences in the CTE of glassy and ceramic phases. It is anticipated that any void formation would be detrimental to the quality of the seal.

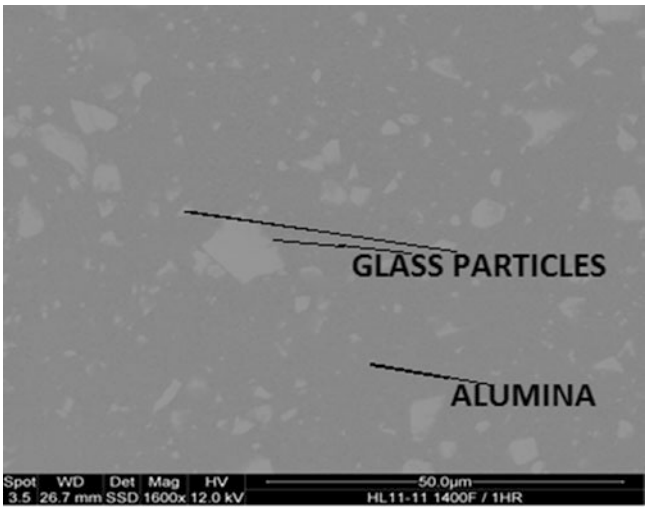

Fig. 26.1 Backscattered image of 0.25 mm green seal

A faster heating and cooling cycle is always preferred to expedite the initial curing process in seals. However, an appropriate curing process should be used for an improved sealing performance. Hence, a tradeoff is required to cure the seals in an appropriate manner without slowing down the process. For this purpose, the mechanical responses of cured seals are obtained using a compression test. The square specimens having a cross sectional area of 12*12 mm^2 and thickness of 1 mm were cut with a razor blade from roll compacted green sheet.

Compression experiments were performed at room temperature, up to a nominal load of 25 N. This load is representative of the pressure applied to a seal in an actual stack. Load and cross-head displacement were recorded throughout the displacement-controlled experiments. Loads and displacements were converted to engineering stress and strain; based on analysis of the load train compliance, strains calculated from cross-head displacement are assumed to be accurate. After obtaining the mechanical response of each seal, the results were correlated with the percentage of voids, and surface anomalies. Based on the above analysis, the appropriate thermal cycle for curing the seal is considered to be the one that results in lower percentages of voids and fewer surface anomalies. A lower compressive stiffness indicates that there are a large number of micro-voids and surface anomalies.

26.4 Results and Discussions

26.4.1 Heating Rate

Green seals are initially heated at the rates of 0.5 °C, 2 °C, 5 °C, 10 °C, 15 °C, 20 °C, and 25 °C per minute until 800 °C, followed by a constant dwell period of 4 h, and finally they are cooled back, at the same rate, to room temperature. Figure 26.2 shows the stress–strain curves of seals cured at different conditions and the mechanical responses of the seals were repeatable. As seen in Fig. 26.2, the seals heated at rates of 15 °C, 20 °C, and 25 °C per minute experienced sudden load drops prior to reaching the maximum load. The aforementioned seals were crushed to several pieces at the completion of the compression test. The seals cured at 5 °C and 10 °C per minute did not fail but their compressive stiffnesses were lower than those cured at 0.5 °C and 2 °C per minute. To further distinguish the 0.5 °C, 2 °C, 5 °C, and 10 °C per minute seals, a microstructural analysis was necessary.

As a next step, voids in the SEM images were manually identified. The MATLAB® is then used to threshold the images and determines void percentage, thus providing an estimate of the evolution of micro-voids with increased heating rates. For each condition, the SEM and the corresponding processed images are provided in Fig. 26.3. In each processed image, the white areas indicate the micro-voids. Experiments with 3 °C and 4 °C per minute heating and cooling were also performed, and although the post-cure stress–strain curves and microstructural images are not presented, the micro-void percentages are included with the other heating rates in Fig. 26.4. The Seals which were cured at 25 °C per minute have the maximum percentage (24.2 %) of micro-voids and heating rates of 0.5 °C and 2 °C per minute have the lowest and nearly identical percentage of micro-voids.

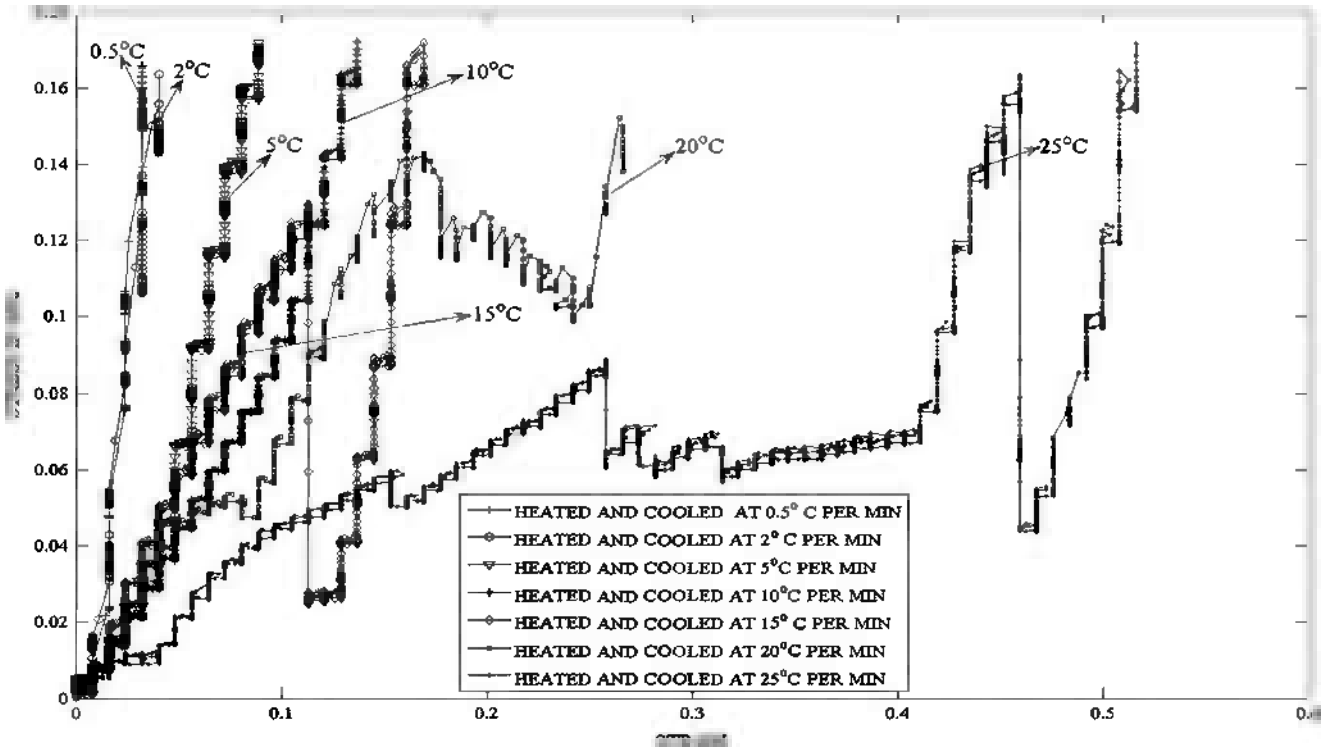

Fig. 26.2 Stress versus strain curves of seals cured at different heating rates

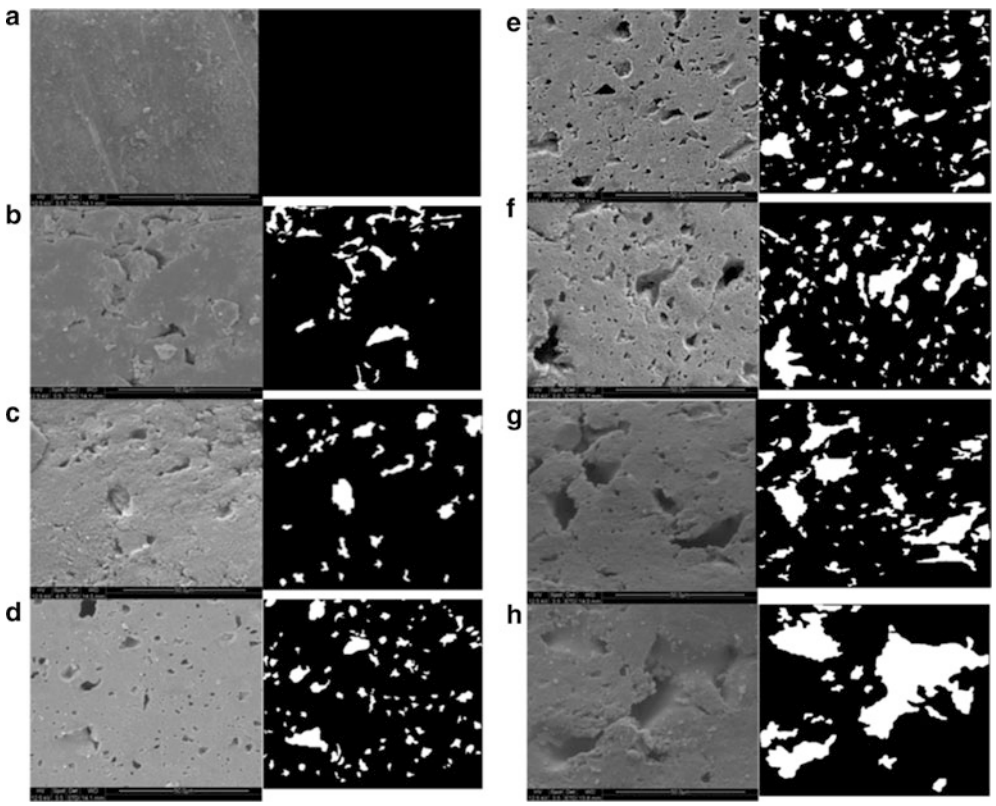

Fig. 26.3 Cross sectional SEM and processed images of (**a**) uncured seal, (**b**) cured at 0.5 °C, (**c**) cured at 2 °C, (**d**) cured at 5 °C, (**e**) cured at 10 °C, (**f**) cured at 15 °C, (**g**) cured at 20 °C, and (**h**) cured at 25 °C per minute

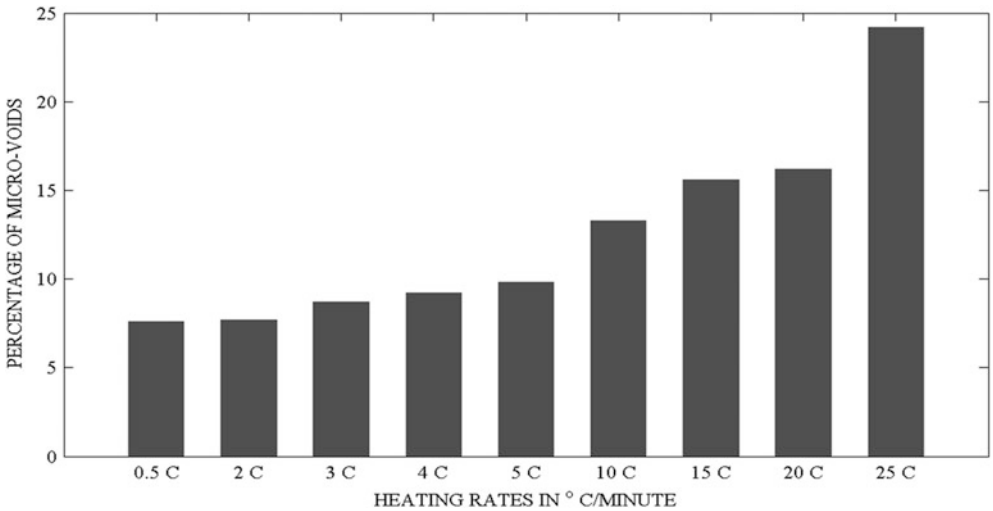

Fig. 26.4 Variation in percentage of voids formed at different heating rates

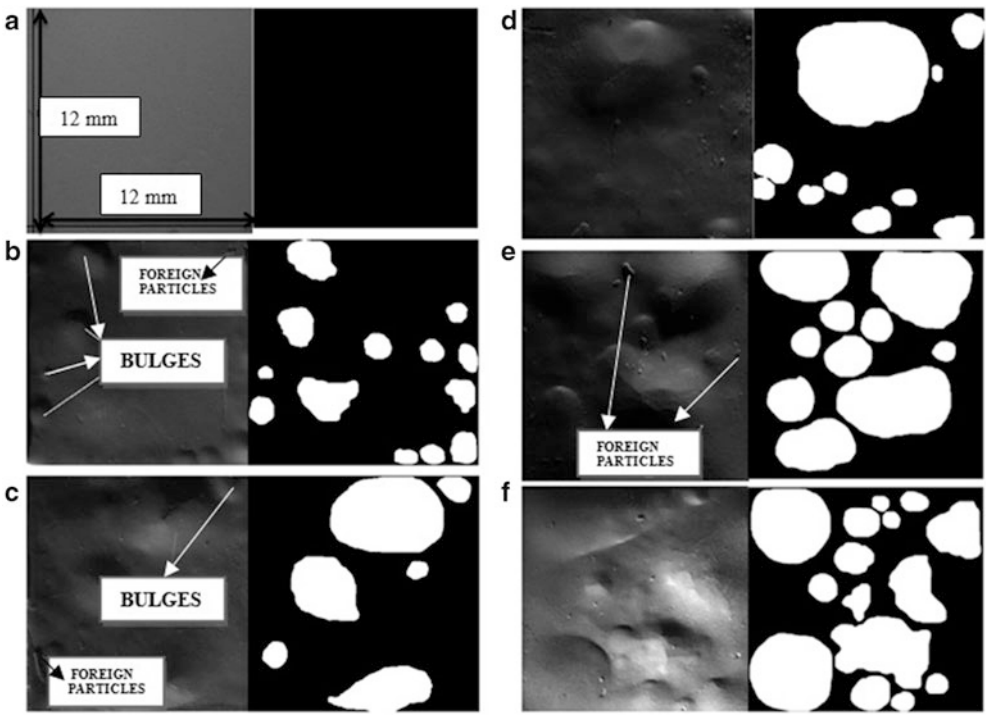

Fig. 26.5 Stereo optical and processed images of surfaces (**a**) cured at 2 °C, (**b**) cured at 5 °C, (**c**) cured at 10 °C, (**d**) cured at 15 °C, (**e**) cured at 20 °C, and (**f**) cured at 25 °C

It was immediately obvious that seals cured at different heating rates also had different surface features. Surface anomalies like bulges, dimples, and undulations are believed to be generated due to the entrapment of residual gases, inherent manufacturing defects and flaws [20] and, in actual applications, could result in leak paths at the interface. The surface topography of each cured seal was studied using a stereo optical microscope images and the same image processing approach was applied. Figure 26.5 presents the percentage evolution of surface anomalies with increased heating rate. From Fig. 26.6 it is clear that the 2 °C per minute heating rate presents a threshold, surpassing above which surface anomalies are occurring.

Referring back to Figs. 26.3, 26.4, and 26.6, it can be observed that there is a strong correlation between mechanical responses, amount of micro-voids, and surface anomalies formed in seals. Thus, it can be concluded that a high percentage of micro-voids and surface anomalies leads to weaker seals.

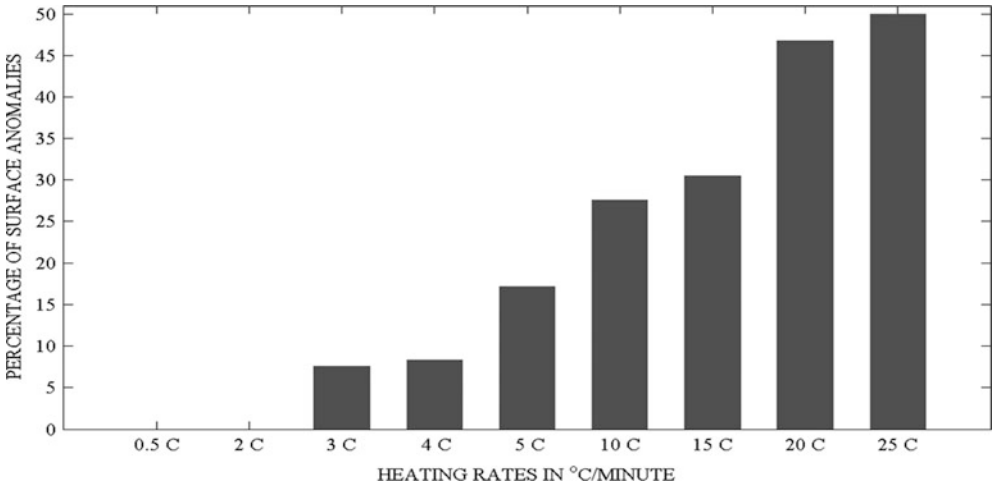

Fig. 26.6 Variation in percentage of micro-voids formed with different heating rates

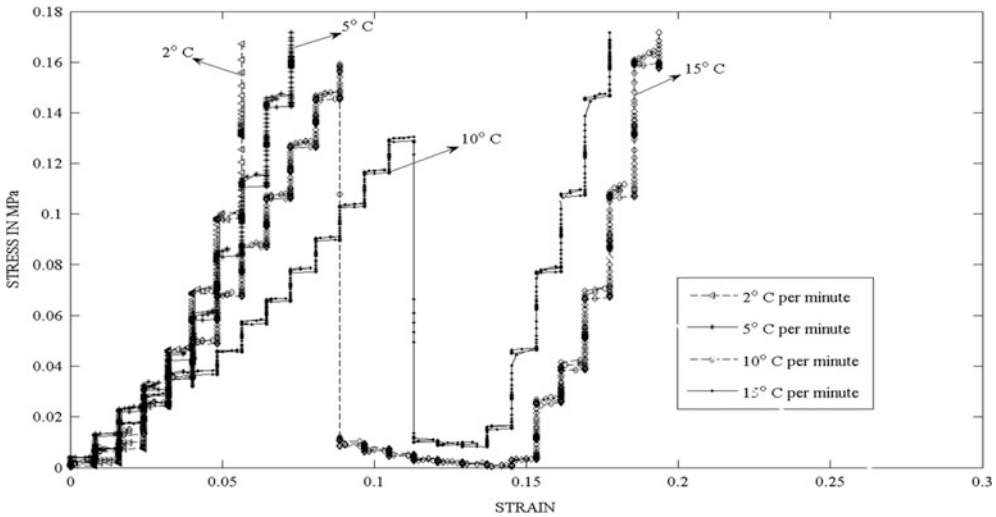

Fig. 26.7 Stress versus strain curves of seals cured at a heating rate of 2 °C per minute but at different cooling rates

The 0.5 °C and 2 °C per minute seals have the highest stiffness and a very similar stress–strain response. In addition, the seals cured at 0.5 °C and 2 °C per minute had essentially the same percentages of micro-voids and zero surface anomalies. Hence, in order to expedite the initial curing process without compromising mechanical properties, a heating rate of 2 °C per minute is chosen.

26.4.2 Cooling Rate

Now that an appropriate heating rate had been chosen, what remained was to find out how the cooling rate influences the microstructure and mechanical response. For determining an appropriate cooling rate, seals were cured at 2 °C per minute, held for 4 h at 800 °C, and then cooled at 2 °C, 5 °C, 10 °C, or 15 °C per minute respectively. It was then observed that the cooling rate practically had no effect on the formation of surface anomalies. Figure 26.7 shows that the compressive stiffnesses of seals cooled at 2 °C and 5 °C per minute are nearly identical, and it was observed that they did not fail during the experiment. However, seals cooled at 10 °C and 15 °C per minute showed spontaneous load drops before reaching the maximum load. These drops are an indication of failure and the specimens were found to be in multiple pieces after the experiment.

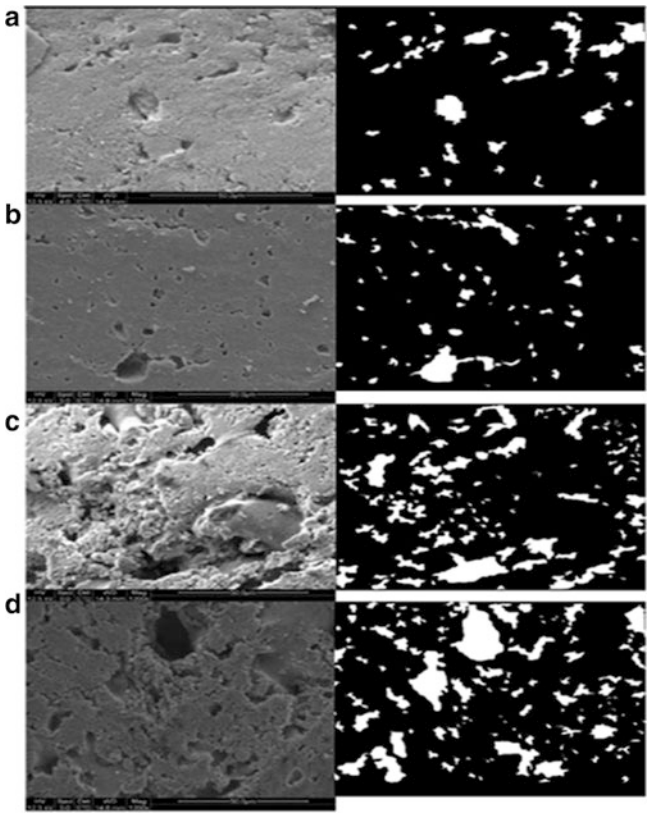

Fig. 26.8 Cross sectional SEM and processed images of seals. (**a**) cooled at 2 °C per minute, (**b**) cooled at 5 °C per minute. (**c**) cooled at 10 °C per minute and (**d**) cooled at 15 °C per minute

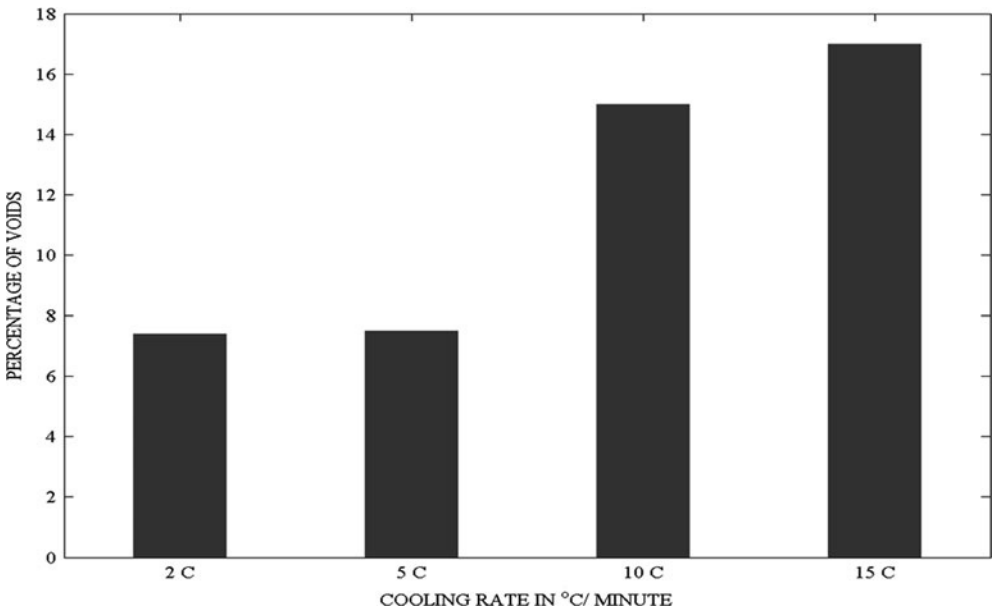

Fig. 26.9 Variation in percentage of micro-voids formed with different cooling rates

Though the current seals were free from surface anomalies, the distribution of micro-voids varied with different cooling rates as shown in Fig. 26.8. The percentages of micro-voids for the four different cooling are presented in Fig. 26.9. The seal cooled at 2 °C per minute was the sample that was previously used in the determination of appropriate heating rate. It is seen that the seals cooled at 2 °C and 5 °C per minute have developed nearly the same percentage of micro-voids and are

consistent with the heat rate studies. As there were no significant differences in the mechanical responses and microstructures of seals cooled at 2 °C and 5 °C per minute, thus, to expedite the initial curing process, a cooling rate of 5 °C per minute was chosen.

26.5 Summary

The present research has successfully identified an appropriate curing cycle for the ceramic/glass composite seals. The appropriate cycle is based on the study of processed scanning electron micrographs, processed stereo optical images, and mechanical responses of seals cured at different rates until 800 °C. It is observed that with a higher heating rate, the percentage of micro-voids and surface anomalies increased and rendered the seals weaker. Based on the above analysis, it is concluded that a heating rate of 2 °C per minute is appropriate for curing the green seals. The next step was to determine the appropriate cooling rate; the seals were heated at 2 °C per minute, held at 800 °C for 4 h, and then cooled at different rates. Using the same methods of analysis, it is concluded that a cooling rate of 5 °C per minute is appropriate for the present ceramic/glass composite seal. Thus the appropriate thermal cycle for curing the green seal consisted of a heating rate of 2 °C per minute, a dwell period of 4 h, and a cooling rate of 5 °C per minute. The seals thus cured in an appropriate way would include minimum defects, micro-voids and surface anomalies. Hence, it will ensure superior sealing under SOFC operating conditions and will eventually lead to an increase in overall power density.

Acknowledgement This work was supported by the Ohio Department of Development's Third Frontier Fuel Cell Program. The authors would also like to thank the staff of NexTech Materials Ltd. for many helpful discussions concerning the SOFC seals

References

1. Chou YS, Stevenson JW, Chick LA (2002) Ultra-low leak rate of hybrid compressive mica seals for solid oxide fuel cells. J Power Source 112:130–136
2. Simner SP, Stevenson JW (2001) Compressive mica seals for SOFC applications. J Power Source 102:310–316
3. Chou Y-S, Stevenson JW (2006) Compressive mica seals for solid oxide fuel cells. J Mater Eng Perform 15:414–421
4. Bansal NP, Gamble EA (2005) Crystallization kinetics of a solid oxide fuel cell seal glass by differential thermal analysis. J Power Source 147:107–115
5. Ghosh S, Dassharma A, Kundu P, Mahanty S, Basu R (2008) Development and characterizations of $BaOCaOAl_2O_3SiO_2$ glass ceramic sealants for intermediate temperature solid oxide fuel cell application. J Non-Cryst Solids 354:4081–4088
6. Weil KS, Deibler JE, Hardy JS, Kim DS, Xia G-G, Chick LA, Coyle CA (2004) Rupture testing as a tool for developing planar solid oxide fuel cell seals. J Mater Eng Perform 13:316–326
7. Ley K, Krumpelt M, Kumar R, Meiser J, Bloom I, Argonne National Laboratory (ANL) (1996) Glass-ceramic sealants for solid oxide fuel cells: part I. Physical properties. J Mater Res 11:1489–1493
8. Le S, Sun K, Zhang N, Shao Y, An M, Fu Q, Zhu X (2007) Comparison of infiltrated ceramic fiber paper and mica base compressive seals for planar solid oxide fuel cells. J Power Source 168:447–452
9. Khanna PK, Bhatnagar SK, Gust W (1999) Analysis of packaging and sealing techniques for microelectronic modules and recent advances. Microelectron Int 16:8–12
10. Lahl N, Bahadur D, Singh K, Singheiser L, Hilpert K (2002) Chemical interactions between aluminosilicate base sealants and the components on the anode side of solid oxide fuel cells. J Electrochem Soc 149:A607–A614
11. Tong J, Han M, Singhal SC, Gong Y (2012) Influence of Al_2O_3 addition on the properties of $Bi_2O_3BaOSiO_2R_xO_y$ (R = K, Zn, etc.) glass sealant. J Non-Cryst Solid 358:4,10–12
12. Arora A, Singh K, Pandey O (2011) Thermal, structural and crystallization kinetics of $SiO_2BaOZnOB_2O_3Al_2O_3$ glass samples as a sealant for SOFC. Int J Hydrog Energy 36:14948–14955
13. Sohn S-B, Choi S-Y, Kim G-H, Song H-S, Kim G-D (2004) Suitable glass-ceramic sealant for planar solid-oxide fuel cells. J Am Soc 87:254–260
14. Wang Y, Walter M, Sabolsky K, Seabaugh M (2006) Effects of powder sizes and reduction parameters on the strength of Ni-YSZ anodes. Solid State Ion 177:1517–1527
15. Hsiu-Tao Chang C-KL (2009) High-temperature mechanical properties of a glass sealant for solid oxide fuel cell. J Power Source 189:1093–1099
16. Stephens E, Vetrano J, Koeppel B, Chou Y, Sun X, Khaleel M (2009) Experimental characterization of glass-ceramic seal properties and their constitutive implementation in solid oxide fuel cell stack models. J Power Source 193:625–631
17. Milhans J, Li DS, Khaleel M, Sun X, Garmestani H (2011) Prediction of the effective coefficient of thermal expansion of heterogeneous media using two-point correlation functions. J Power Source 196:3846–3850

18. Meinhardt K, Kim D-S, Chou Y-S, Weil K (2008) Synthesis and properties of a barium aluminosilicate solid oxide fuel cell glass-ceramic sealant. J Power Source 182
19. Liu WN, Sun X, Khaleel MA (2011) Study of geometric stability and structural integrity of self-healing glass seal system used in solid oxide fuel cells. J Power Source 196:1750–1761
20. Glandus JC, Jouin C (1986) Acoustic detection of artificial internal defects in ceramics. J Mater Sci Lett 5:503–505
21. Smeacetto F, Salvo M, Ferraris M, Cho J, Boccaccini AR (2008) Glass-ceramic seal to join Crofer 22 APU alloy to YSZ ceramic in planar SOFCs. J Eur Ceram Soc 28(1):61–68
22. Brochu M, Gauntt B, Shah R, Miyake G, Loehman R (2006) Comparison between barium and strontium-glass composites for sealing SOFCs. J Eur Ceram Soc 26(15):3307–3313

Chapter 27
Behavior of Bonded Composite Repairs on Dynamically Loaded Pressure Vessels

Matthew Knofczynski and Michael W. Keller

Abstract Bonded composite repairs are increasingly installed on degraded pressure equipment are and frequently treated as permanent repairs. While bonded repairs for these applications have been thoroughly investigated with respect to quasi-static and fatigue performance little research has been done regarding the effectiveness of these repairs under variable dynamic loading and high strain rate conditions. These loading conditions can be found in processing plants, offshore oil platforms, or during short duration events, such as seismic activity. This paper presents experimental results on the response of bonded composite repairs on carbon steel tubing with machined defects in dynamic 4-point bending. Dynamic loading is generated using a hydraulic load system that excites the test specimen near the natural frequency. The impact of reinforcement composition on repair performance is also investigated.

27.1 Introduction

Pipeline and pressure equipment damage due to mechanical, corrosion, or other defects is a significant cost for pipeline and process plant operators. Shutdowns required to repair these issues can cost millions of dollars per day [1]. In recent history, bonded composite repairs have become more common in a variety of industries for the repair of pipework and pressure vessels. Composite repair of metallic structures was first introduced in the aerospace industry to rehabilitate structurally deficient airframes [2]. The approaches developed for these systems were translated to civil structure reinforcement and were recently introduced for the repair of pressure equipment. Composite repairs have several advantages when compared to metallic repairs. Composites are inherently formable and can easily repair complex geometries, composites can be installed in restricted access areas, composites can be installed without the use of welding, and composites offer significant weight to strength benefits when compared to metallic systems. Furthermore, industry analysis has shown that these repairs can be significantly cheaper when compared to replacing the damaged pipe section and compare favorably with welded sleeve repairs (typically 24 % reduction in cost) [1]. Installation of these systems is somewhat different than in the aerospace industry, but consists of essentially the same steps. The repair begins with surface preparation of the substrate, usually grit blasting. The repair system is then prepared by saturating the reinforcement fibers with a resin system, typically epoxies or urethanes, the saturated reinforcement is then applied directly to the prepared substrate by wrapping the material around the damaged section. This repair approach has demonstrated the ability to restore pressure carrying capability of the damaged pipe [3] and even restore the ability of risers to sustain mechanical deformation [4].

While significant research has been devoted to the behavior of the repair systems with respect to environmental conditions [5–7] and the ability to restore pressure carrying capability [3], no information on the effectiveness of these repairs under dynamic loading and high strain conditions exists for this application. Cyclic strain accumulation, or ratcheting, is a common method of failure in dynamically loaded pressure vessels [8–11], especially in conditions operating around the pressure vessel natural frequency. In this paper we investigate the behavior of model piping subjected to cyclic bending at frequencies near the natural frequency of the system. Two specimen types are investigated, a baseline control sample with no bonded repair and a sample with a bonded repair. Results are compared to the static load predictions and initial suggestion for appropriate dynamic loading factors are proposed.

M. Knofczynski (✉) • M.W. Keller
Department of Mechanical Engineering, The University of Tulsa, 800 S. Tucker Dr., Tulsa, OK 74104, USA
e-mail: mknoff@gmail.com

G.P. Tandon et al. (eds.), *Experimental Mechanics of Composite, Hybrid, and Multifunctional Materials, Volume 6*, Conference Proceedings of the Society for Experimental Mechanics Series, DOI 10.1007/978-3-319-00873-8_27,

27.2 Experiment

A dynamic 4-pt bending system was constructed similar to the system described by Yahiaoui, Moffat, and Moreton [11]. Briefly, this system consisted of two articulated clamps that hold the test pipe. Teflon inserts in the clamps allow for some lateral motion of the pipe to reduce any axial constraint that may occur. The articulated clamps were mounted to an aluminum W-flange and then attached to a servohydrualic actuator. A straight pipe specimen extended approximately 3 ft on either side of the articulated clamps. Tuning weights were attached to the extended arms to both generate the dynamic force and to tune the natural frequency of the specimen. A schematic of the setup is shown in Fig. 27.1.

Test pressure vessels were fabricated from 1 in. O.D. carbon steel tubing with a 0.1 in wall thickness. Hemispherical endcaps were welded to the tubing to form a cylindrical pressure vessel. A dimensioned drawing of the test specimen is shown in Fig. 27.2. A simulated axisymmetric corrosion defect was machined into the center of the tubing to a depth approximating 50 % wall loss. This specimen geometry was chosen based on the existence of previous research data for the repair of pressure vessels with axisymmetric defects [12]

All repairs followed the same protocol. Using epoxy putty, the defect was restored back to the undamaged dimensions of the tube. Woven carbon fiber reinforcement was saturated with epoxy and then applied to the damaged region. The specimens were allowed to cure for approximately 48 h at room temp. Samples were put into 4-point bending on the configuration shown in Fig. 27.1 and filled with water until a predetermined pressure was reached. Using a hydraulic cylinder, the sample was excited near the natural frequency of the specimen until failure occurred. Strain of the tubing was measured on both the defect and non-defect sections under the repair, as well as on the non-repaired tubing between the supports. Pressure was also recorded through the duration of the test.

27.3 Model

27.3.1 Natural Frequency

The Natural frequency of the system was determined through an energy method via Eq. 27.1 [13].

$$4\pi^2 f^2 = g\left(\frac{\int mYdx}{\int mY^2dx}\right), \tag{27.1}$$

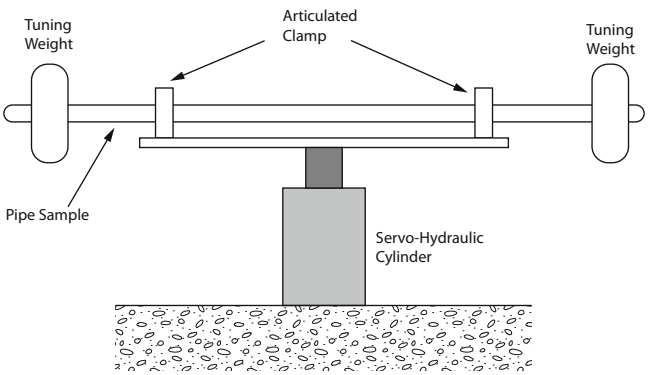

Fig. 27.1 Schematic of the natural frequency testing system used in this research

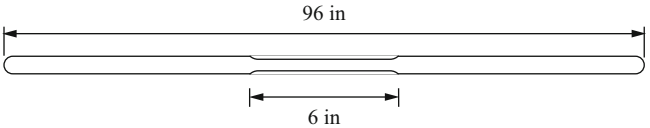

Fig. 27.2 Schematic of specimen, thinned section is 50 % wall loss equating to an outside diameter of approximately 0.9 in. Outer diameter of undamaged region is 1.0 in.

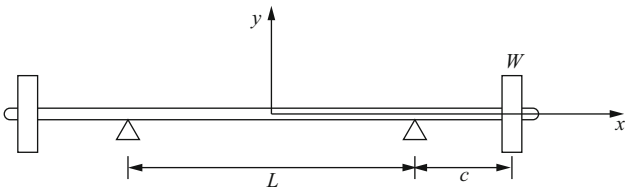

Fig. 27.3 Schematic of the simply supported beam model used to estimate the natural frequencies of the test specimens

Table 27.1 Calculated and experimentally determined natural frequencies for the tested specimens

Overhanging weight (lbs)	Calculated natural frequency (Hz)	Actual natural frequency (Hz)
50	2.5425	2.9
70	2.074495	2.4

where f is the natural frequency, g is the acceleration due to gravity, m is the mass, and Y is the deflection along the x axis. Deflection equation for the simply supported beam with overhanging weights, shown schematically in Fig. 27.3, is given by beam deflection equations for the two regions of the sample. Deflection for the regions between the supports is given by

$$Y = \frac{Wcx(L-x)}{EI}. \tag{27.2}$$

The deflection for the overhang region is given by

$$Y = \frac{Wux\{3c(L-x) - u^2\}}{6EI}. \tag{27.3}$$

For both equations, EI is the smeared properties for the composite beam determined from lamination theory, L is the distance between the supports, c is the overhang distance, W is the overhang weight, and u is the distance through the overhang. The results of this calculation are shown in Table 27.1 and are compared to the apparent natural frequency determined during the experiments.

27.4 Results and Discussion

Two specimen types were examined in this initial study, a non-repaired control specimen and specimens that had been repaired with a bonded composite overwrap. Each specimen behavior will be discussed individually and then compared.

27.4.1 Control Specimens

The unwrapped control specimen was oscillated at 2.9 Hz with amplitude of 0.5 in. and overhanging weight of 50 lbs, which was enough to generate a wall stress of approximately 50 % of yield. Two strain gages were used to monitor the deformation of the specimen, one on the centerline in the damaged region and one on the undamaged section of the tubing. Results of the dynamic oscillation are shown in Fig. 27.4.

From the plots in Fig. 27.4, it is clear that the specimen yielded in the damaged region during testing. The yield was not enough to cause total specimen failure and the test was halted directly after yield was observed.

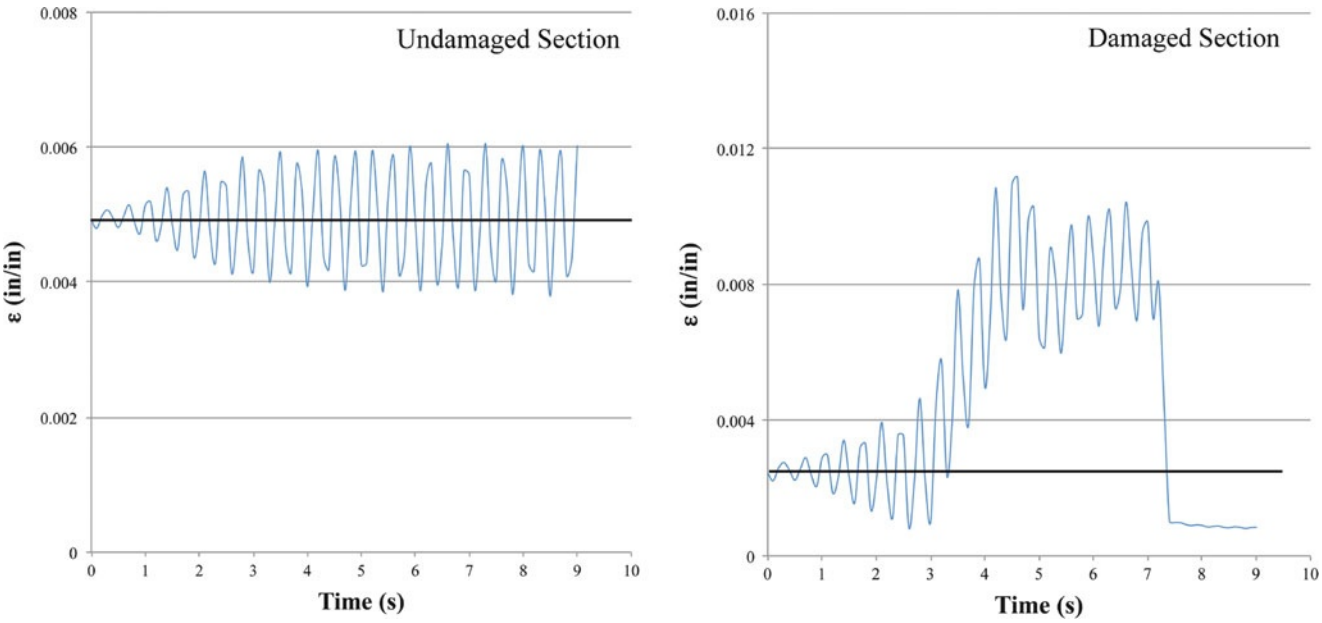

Fig. 27.4 Strain versus time plots for an unrepaired control specimen. The damaged region clearly shows the ratcheting yielding that occurred during the test

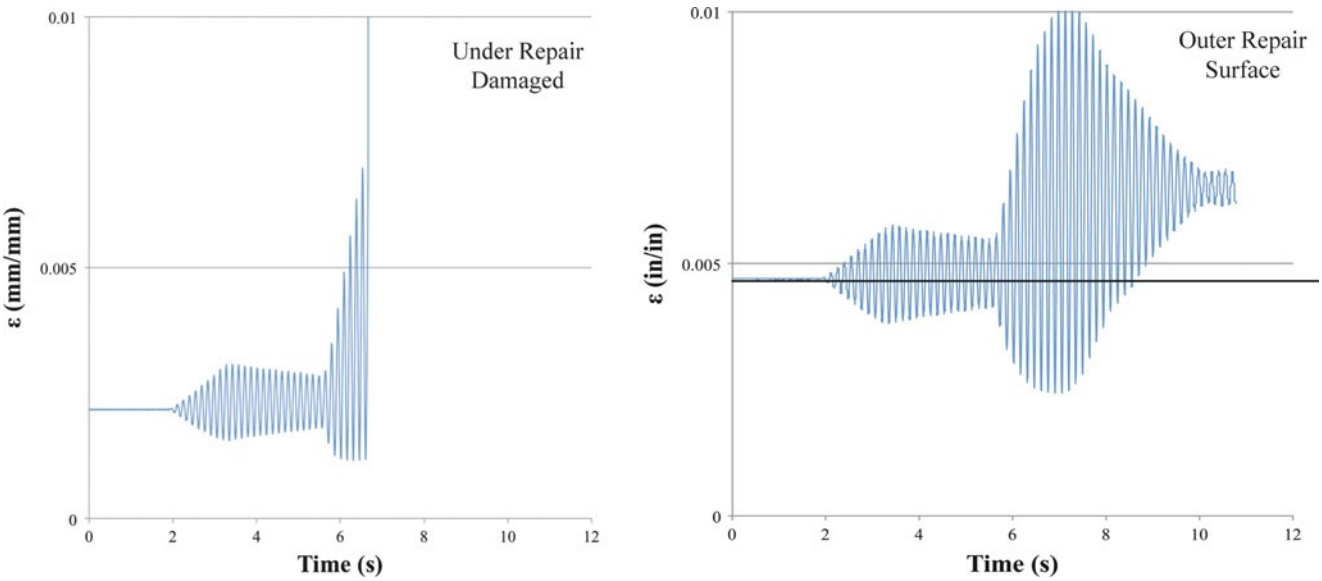

Fig. 27.5 Strain versus time for a specimen that had been repaired with a composite overwrap. Plots are for strain gages under the repair on the surface of the steel and a strain gage on the outer surface of the repair

27.4.2 Repaired Specimens

The second specimen was repaired with two layers of a 12 × 3 K tow carbon fiber/epoxy repair. The overhanging weight was increased to 70 lbs and the oscillation was decreased to 2.5 Hz to accommodate the now lower natural frequency. The increase in overhanging weight was required to induce damage in the repaired tubing. Tests conducted using the same weight as in the control test discussed above did not yield. The new weight was chosen, as it was enough to induce a stress in the undamaged tubing section of approximately 50 %.

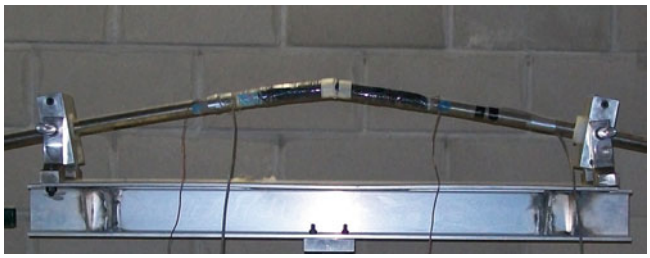

Fig. 27.6 Post-test image showing collapse of test specimen after composite repair failure

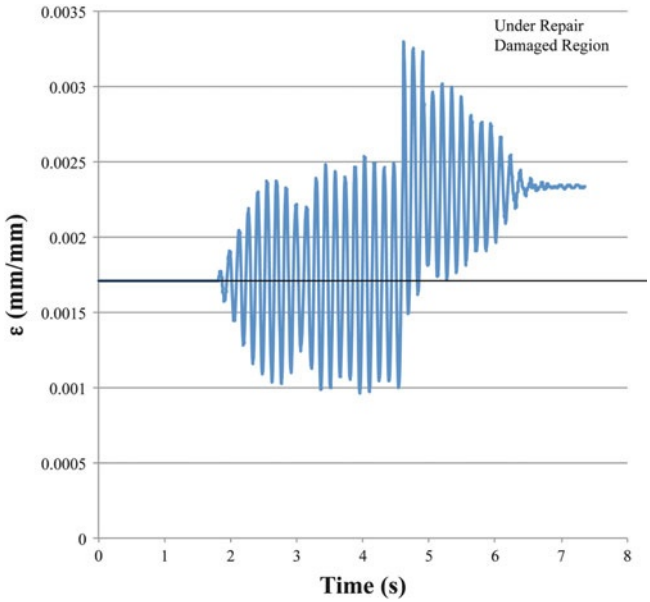

Fig. 27.7 Strain response of specimen repaired with 12 × 6 K composite indicating abrupt failure. Strain gage was located under the repair in the simulated damage region

During the initial repaired test, the composite was not visibly damaged, but cracking was clearly heard at the onset of the largest oscillations. Strain data for the repaired specimen, shown in Fig. 27.5, indicated that the strain gage failed under the wrap. This was correlated to the onset of significant increase in base strain as measured at the top of the repair, indicating yielding of the damaged region. It is likely the repair locally debonded from the repaired tubing, but this has not been confirmed through forensic analysis of the repair. Only a small amount of permanent deformation was noticed at the end of the test. However, the strain gage located outside the repair on an undamaged section did indicate that the tubing underwent net yielding across the entire sample.

The third specimen was repaired with two layers of a 12 × 6 K carbon fiber/epoxy repair. Testing proceeded under the same conditions as for the specimen repaired with a 12 × 3 K composite reinforcement. While this specimen had nominally the same qualitative behavior as the specimen repaired with the 12 × 3 K composite, a complete tensile composite failure occurred during testing, as shown in Fig. 27.6.

Unlike the strain responses in Fig. 27.5, this specimen showed an abrupt change in baseline strain, which was indicative of a single catastrophic failure event. The samples presented above showed a gradual cycle-by-cycle increase in strain consistent with ratcheting-type behavior (Fig. 27.7).

This specimen had higher smeared modulus properties in the axial direction as a result of the higher fiber two count in the 12 × 6 K fibers. Static lamination calculations indicated that the expected max stresses for this specimen would be higher than that of the specimen repaired with the 12 × 3 K composite. This difference is likely the cause of the less dramatic failure of the previous test specimen.

The composite repair was successful in restoring the load carrying capability to that of approximately the native tubing capability based on the required overhanging weight to induce yield. Initial results indicate that a more compliant repair in the axial direction may be beneficiary for reducing the possibility of catastrophic repair failure during a dynamic event. Further testing is required to confirm this initial finding.

27.5 Conclusions

Two composite repairs were applied to a model pipe specimen that contained a simulated corrosion defect. Based on testing performed using a custom-built load frame, one repair system was successful in surviving large amplitude deformations induced by near-natural frequency oscillations. Initial results indicate that a more compliant repair in the direction of axial forces is beneficial for the resistance of the repair to failure.

References

1. Koch G, Brongers M, Tompson N, Virmani Y, Payer J (2001) Corrosion cost and preventive strategies in the united states. Fedral Highway Administration, McLean
2. Baker AA, Rose LRF, Jones R (2003) Advances in the bonded composite repair fo metallic aircraft structures, vol 1. Elsevier Science, Kidlington
3. Duell JM, Wilson JM, Kessler MR (2008) Analysis of a carbon composite overwrap repair system. Int J Press Vessels Piping 85:782–788
4. Alexander C, Ochoa OO (2010) Extending onshore pipeline repair to offshore steel risers with carbon–fiber reinforced composites. Compos Struct 92:499–507
5. Keller MW, Jellison BD, Ellison T (2013) Moisture effects on the thermal and creep performance of carbon fiber/epoxy composites for structural pipeline repair. Compos Part B Eng 45:1173–1180
6. Goertzen W, Kessler M (2006) Creep behavior of carbon fiber/epoxy matrix composites. Mater Sci Eng A 421:217–225
7. Goertzen WK, Kessler MR (2007) Dynamic mechanical analysis of carbon/epoxy composites for structural pipeline repair. Compos Part B Eng 38:1–9
8. Moreton DN, Yahiaoui K, Moffat DG, Machin HC (1994) The behaviour of pressurised plain pipework subjected to simulated seismic loading. Strain 30:63–72
9. Moreton DN, Yahiaoui K, Moffat DG, Zehsaz M (1996) The effect of diameter/thickness ratio on the ratchetting behaviour of pressurised plain pipework subjected to simulated seismic loading. Strain 32:91–96
10. Moreton DN, Zehsaz M, Yahiaoui K, Moffat DG (2005) The ratchetting of plain carbon steel pressurized cylinders subjected to simulated seismic bending: the effect of the D/t ratio and comparison with finite element predictions. J Strain Anal Eng Des 33:39–53
11. Yahuaoui K, Moffat DG, Moreton DN (1992) Techniques for the investigation of the ratchetting behaviour of piping components under internal pressure and simulated seismic loading. Strain 28:53–59
12. Wilson JM (2006) Characterization of a carbon fiber reinforced polymer repair system for structurally deficient steel piping. Ph.D. thesis, The University of Tulsa
13. Blake MP, Mitchell WS (1972) Vibration and acoustic measurement handbook. Spartan, New York

Chapter 28
Fracture Testing of Simulated FRP Repairs II

Tanveer Chawla and M.N. Cavalli

Abstract Fiber-reinforced polymers (FRPs) have excellent strength-to-weight and stiffness-to-weight ratios. This has led to their adoption in a number of weight-critical applications. One example is in the area of wind energy. Most wind turbine blades are fabricated partially or completely out of composite materials. During the manufacturing process, part defects are sometimes observed. The part can either be repaired, typically by removing the defective region and then applying a repair, or the entire part can be scrapped – an expensive option for 40 m + blades. A local repair is a more desirable option. Repairs, however, result in a discontinuity of the reinforcement and the potential for the repaired portion to prematurely fail in service. The current work details an effort to optimize a resin for scarf repair of glass-reinforced polyester composite structures. Results from mixed-mode testing on simulated composite repairs are presented and compared with previous Mode-I and fatigue results.

28.1 Introduction

Delamination and fiber matrix debonding are common forms of damage to composite structures [1]. Cracks may appear in repairs conducted on composite structures due to these forms of damage. Thus measurement of fracture toughness is important in order to test the efficacy of repairs conducted on composite parts. Repaired composite structures are subjected to different modes of loading while in service. Common tests involving Mode I, Mode II and Mixed-Mode loading are double cantilever beam (DCB) test, end notched flexure test (ENF) and mixed-mode bending (MMB) test respectively [2, 3]. Since the onset of crack may be due to cyclic loads, it is required to test the repairs under fatigue too.

As part of previous work, repairs conducted on glass-fiber reinforced polymer composites were tested under Mode I loading [4]. In order to further characterize the repairs they were tested under tension – tension fatigue loading. This was carried out using novel specimens, details of which are listed later. The current paper also includes information on results obtained from testing similar repairs under mixed-mode (Mode I – Mode II) loading. This loading was applied through mixed-mode bending (MMB) test carried out in accordance with ASTM D 6671/D 6671M – 06.

28.2 Mode I Testing

In an effort to improve the performance of repairs on glass fiber reinforced polymer wind turbine blades, Mode I testing was carried out to find an optimum resin out of six shortlisted repair resins (NRR1 to NRR6). Testing was conducted in accordance with ASTM D 5528 [5]. Double Cantilevered Beam (DCB) specimens were manufactured in accordance with ASTM D 5528 and consisted of two separate parts: the lower adherend or parent plate, representing the blade, and the upper adherend or repair plate, simulating the flat part of a one-sided scarf repair. Both adherends consisted of an even number of plies. The specimen configuration, experimental setup and calculations are detailed elsewhere [4]. The fracture toughness values of the new repair resins were compared to those of a base repair resin. This base repair resin (MB-B) was previously

T. Chawla (✉) • M.N. Cavalli
Department of Mechanical Engineering, University of North Dakota, 243 Centennial Drive, Stop 8359, Grand Forks, ND 58202-8359, USA
e-mail: tanveer.chawla@my.und.edu; matthewcavalli@mail.und.nodak.edu

G.P. Tandon et al. (eds.), *Experimental Mechanics of Composite, Hybrid, and Multifunctional Materials, Volume 6*, Conference Proceedings of the Society for Experimental Mechanics Series, DOI 10.1007/978-3-319-00873-8_28,

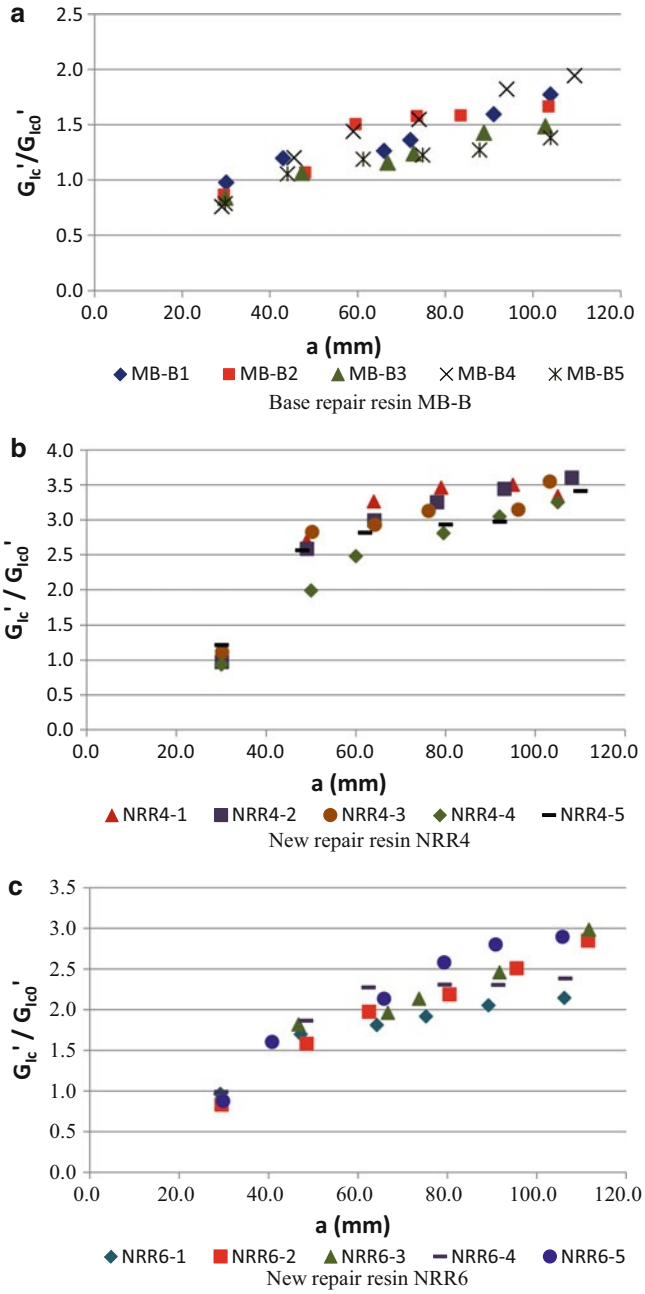

Fig. 28.1 Fracture toughness values from Mode I testing for (**a**) current blade repair resin (**b**) repair resin candidate 4 (**c**) repair resin candidate 6

being used by a wind turbine blade manufacturing company. Some significant results from Mode I testing are given in Fig. 28.1 As seen from the plots, repair resins NRR4 and NRR6 had higher fracture toughness values than those of the base repair resin. The base resin was a polyester resin with moderate styrene content whereas NRR4 and NRR6 were both vinyl-ester resins. NRR4 had high styrene content whereas NRR6 had core shell rubber additive.

28.3 Fatigue Testing

28.3.1 Specimen Details

The top three new repair resins, chosen through Mode I test screening, along with the base repair resin were tested under fatigue tensile loading to choose the final repair resin. The specimen configuration is given in Fig. 28.2.

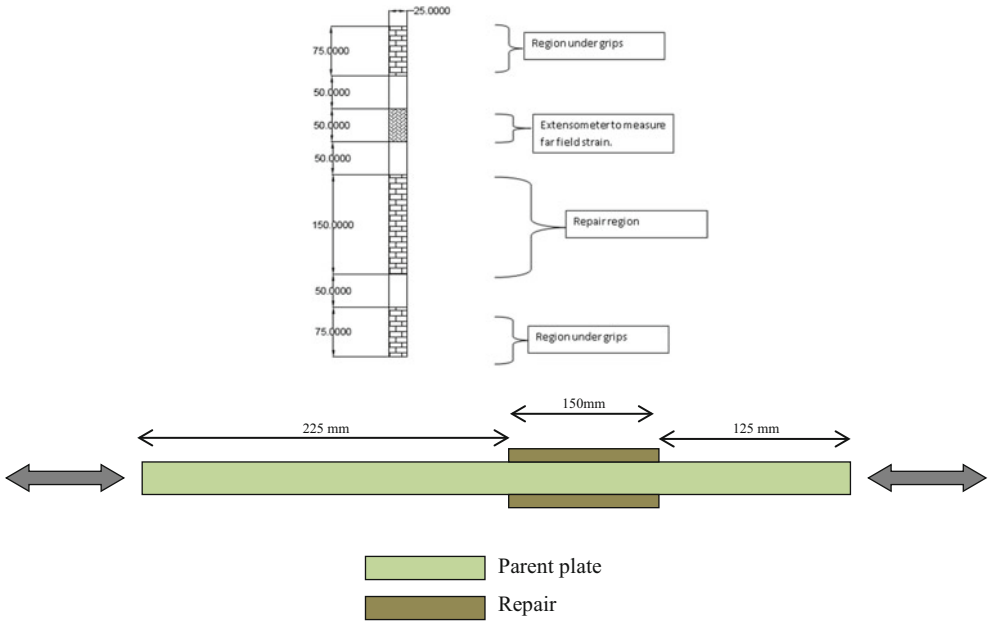

Fig. 28.2 Fatigue tensile test specimen configuration (not to scale)

Table 28.1 Fatigue specimen lay-up and post curing details

1 × Unidirectional ply 1 × Chopped strand mat (CSM)	Repair: hand lay-up	Post curing: 16 h at 40 °C
8 × Unidirectional plies	Parent laminate: vacuum assisted resin transfer molding (VARTM)	Post curing: 16 h at 40 °C
1 × Chopped strand mat (CSM) 1 × Unidirectional ply	Repair: hand lay-up	Post curing: 16 h at 40 °C

28.3.2 Specimen Manufacturing for Fatigue Testing

Specimens for fatigue tensile testing consisted of a parent laminate with a strip of repair on either side. Parent plates (60 cm × 60 cm) were manufactured with the lay-up and post curing details listed in Table 28.1. As the lay-up was symmetric for these parent plates, no warp was observed as opposed to that observed in [4]. Following post curing, surfaces of the parent plates were ground off at the regions where the repair strips were to be laid before conducting the hand lay-up with MB-B and the three chosen candidate repair resins (NRR1, NRR4 and NRR6). Repair was first conducted on one side of the parent plate and left to cure until the gelation of the repair resin and then repair was conducted on the other side. The repairs were left to cure at room temperature for 24 h and then were post cured for 16 h at 40 °C. The post cured sample plates were then cut perpendicular to the repair into 25 cm wide specimens.

28.3.3 Fatigue Testing Results

Results obtained from fatigue testing are depicted in Fig. 28.3. The three selected resins performed better than MB-B under fatigue too. NRR4 was chosen as the final new repair resin based on testing and global availability.

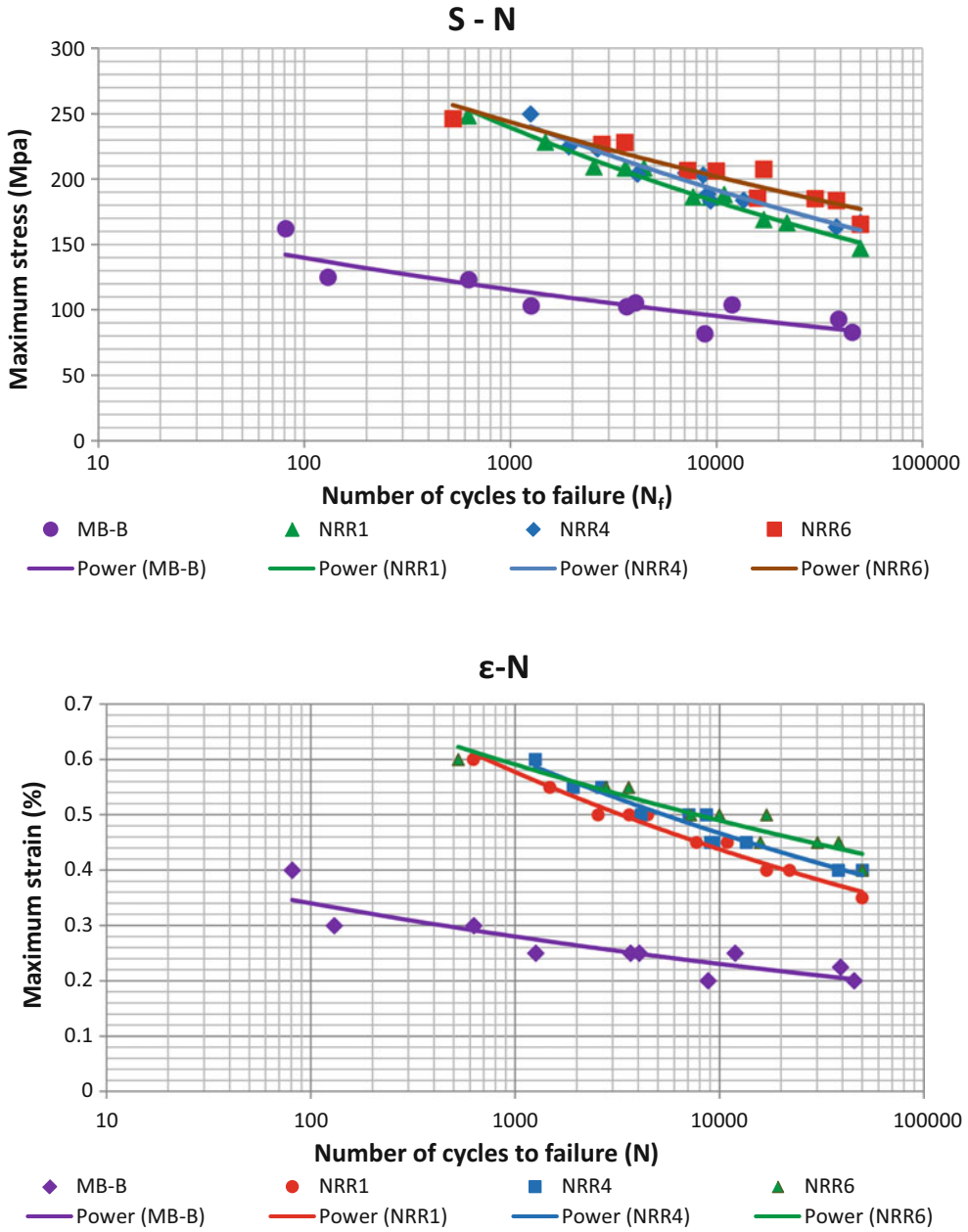

Fig. 28.3 Results from fatigue testing

28.4 Mixed-Mode (Mode I–Mode II) Testing

28.4.1 Specimen Details

Specimens for preliminary mixed mode testing were similar in lay-up to those for Mode I testing but with different dimensions. A description of the lay-up and the materials used is given in Table 28.2.

Table 28.2 Mixed mode specimen lay-up, materials used and curing details

Lay-up	Part	Details
2 × Biaxial plies (±45°) 8 × Unidirectional plies (0°) 1 × Chopped strand mat	Repaired laminate: hand lay-up (upper adherend)	Curing 24 h at room temperature Post curing 16 h at 40 °C
Insert (crack initiator)	Polymer film	Thickness ≤13 μm
8 × Unidirectional plies (0°) 2 × Biaxial plies (±45°)	Parent laminate: VARTM (lower adherend)	Curing 24 h at room temperature Post curing 24 h at 60 °C 3 h at 95 °C

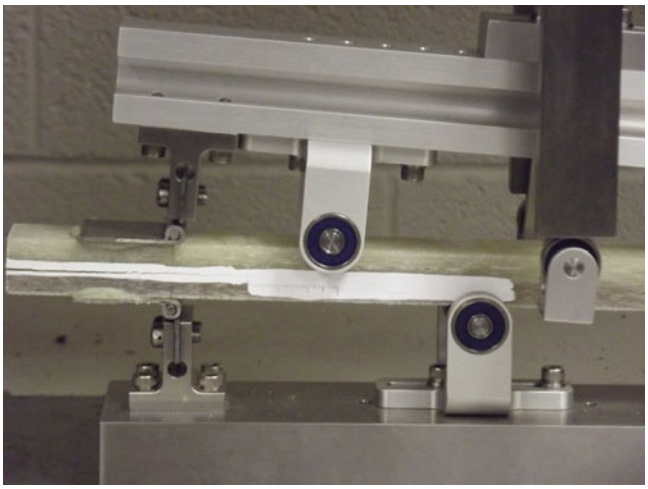

Fig. 28.4 Mixed mode test snapshot

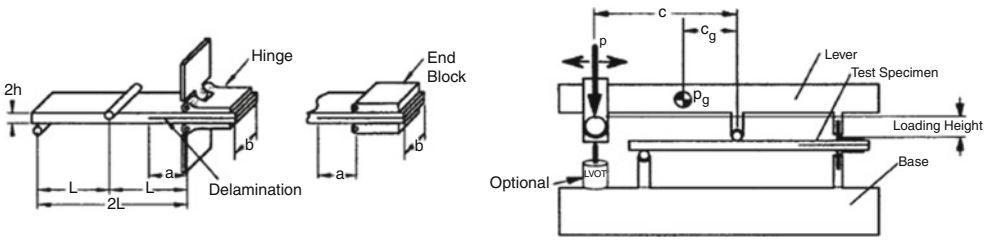

Fig. 28.5 Specimen details, experimental setup and calculation parameters [6]

28.4.2 Mixed Mode Testing

Test method ASTM D 6671 [6] was used to test the fracture toughness of the final new repair resin (NRR4) under mixed mode loading. The testing was conducted on Shimadzu AG-IS Universal Testing Machine under displacement control at a crosshead rate of 0.5 mm/min. A picture of a specimen being tested in the ASTM D 6671 fixture is given in Fig. 28.4.

For preliminary testing, specimens were made with the same thickness as the DCB specimens (h ~ 9 mm) (Fig. 28.5). Mixed-mode ratios (GII/G) of 0.2, 0.5 and 0.8 were used. It was found that the adhesive bond of the piano hinges with the specimen was not able to bear the loads incurred at 0.5 and 0.8 values of GII/G. Therefore the range of the thickness 2 h (Fig. 28.5) was recalculated for the required maximum load, keeping in consideration that the displacements were not large so as to cause geometric nonlinear errors. The final specimen thickness is h ~ 6 mm.

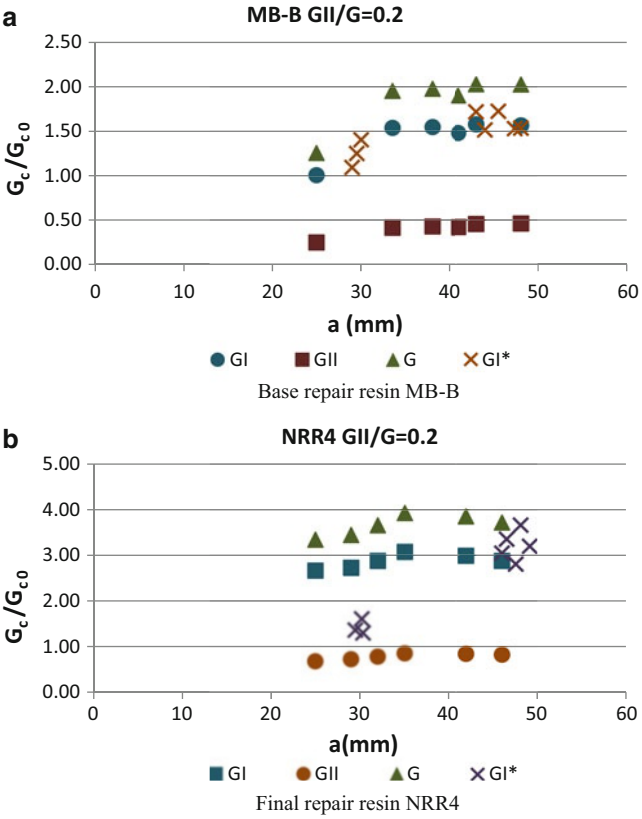

Fig. 28.6 Preliminary mixed mode testing results for (**a**) current blade repair resin and (**b**) repair resin candidate 4

28.4.3 Mixed-Mode Testing Results

Loads were recorded using TRAPEZIUM 2 control software linked to the universal testing machine and images of the loaded samples were captured with a Retiga 1300 camera. These images were analyzed for displacements using Vic-Snap digital image correlation software. Calculations were carried out as detailed in ASTM D 6671. Fracture toughness values normalized with respect to the fracture toughness value for parent plate resin at crack initiation were plotted against crack length. Initial results are plotted in Fig. 28.6. Values from DCB testing (pure Mode I, labeled as GI* in Fig. 28.6) are also plotted for comparison.

Preliminary results show that fracture toughness values obtained with delamination growth in accordance with ASTM D 6671 are higher for NRR4 as compared to MB-B. Testing of specimens with revised dimensions and different mode mixities will further elucidate the performance of new repair resin NRR4 with respect to base resin MB-B.

References

1. Bolotin VV (2001) Mechanics of delaminations in laminate composite structures. Mech Compos Mater 37(5/6):367–380
2. Blake SP, Berube KA, Lopez-Anido RA (2012) Interlaminar fracture toughness of woven E-glass fabric composites. J Compos Mater 46 (13):1583–1592. doi:10.1177/0021998311421221
3. Ducept F, Davies P, Gamby D (2000) Mixed mode failure criteria for a glass/epoxy composite and an adhesively bonded composite/composite joint. Int J Adhes Adhes 20(3):233–244. doi:10.1016/S0143-7496(99)00048-2
4. Chawla T, Cavalli MN (2011) Fracture testing of simulated FRP repairs. Paper presented at the conference proceedings of the society for experimental mechanics series, vol 6. Mohegan Sun, Uncasville, CT, USA, pp 253–258
5. ASTM Standard D5528 – 01(2007) e3 (2007) Standard test method for Mode I interlaminar fracture toughness of unidirectional fiber-reinforced polymer matrix composites. ASTM International, West Conshohocken. doi:10.1520/D5528-01R07E03, www.astm.org
6. ASTM D 6671 – 06 (2006) Standard test method for mixed Mode I – Mode II interlaminar fracture toughness of unidirectional fiber reinforced polymer matrix composites. ASTM International, West Conshohocken. doi:10.1520/D6671M-06, www.astm.org

Chapter 29
An Innovative Measuring Method of Young's Modulus Using Postbuckling Behavior

Atsumi Ohtsuki

Abstract In recent years, flexible materials with very high performance are used widely to establish cost-effective processing with regard to long-term performance and reliability and large deformation analysis is becoming increasingly more important in both analytical and technological interests of structural design (mechanical springs, various thin walled structures). In this study, a new and convenient mechanical testing method (*Compression Column Method*) is provided for measuring the Young's modulus in a flexible multi-layered material. The method is based on a nonlinear deformation theory that takes into account large deformation behaviors (i.e., postbuckling behaviors) of multi-layered materials. Exact analytical solutions are obtained in terms of elliptic integrals. By just measuring the horizontal or the vertical displacement, each Young's modulus in a thin flexible multi-layered material can be easily obtained. Measurements were carried out on a two-layered material (PVC: a high-polymer material + SUS: a stainless steel material). The results confirm that the new method is suitable for flexible multi-layered thin plates/rods. In the meantime, the new method can be applied widely to measure the Young's modulus of thin layers formed by PVD, CVD, Coating (Graphite, Metal Oxide), Paint (Lacquer), Cladding, Lamination, and others.

29.1 Introduction

In recent years, flexible materials with very high performance are used in a wide ranging and diverse applications to establish cost-effective processing with regard to long-term performance and reliability and large deformation analysis is becoming increasingly more important in both analytical and technological interests of structural design (mechanical springs, various thin walled structures). A new bending test method (*Compression Column Method*) is proposed with the nonlinear large deformation theory. By using this method, Young's modulus of each layer in a thin flexible multi-layered material can be easily obtained by just measuring the horizontal displacement or the vertical displacement.

Exact analytical solutions for large deformation are obtained in terms of elliptic integrals under the assumptions that the geometrical nonlinearity arises as a result of large deformation, while the material remains linearly elastic.

In order to assess the applicability of the proposed method, several experiments were carried out using a two- layered material (SWPA: a thin piano wire and Cu: a copper electrodeposition layer). As a result, the new method was found to be suitable for flexible multi-layered materials. Furthermore, the proposed new method is applicable to Young's modulus measurement in a thin layer formed by PVD (Physical Vapor Deposition), CVD (Chemical Vapor Deposition), Electrodeposition, Coating (Graphite, Metal Oxide), Paint (Lacquer), Cladding, Lamination, etc.

Besides the *Compression Column Method* for a flexible multi-layered material studied here, the *Cantilever Method* [1], the *Circular Ring Method* [2, 3], the *Compression Column Method* [4, 5], the Own-weight Cantilever Method [6] for a single-layered material and the *Cantilever Method* [7], the *Compression Column Method* [8], the Own-weight Cantilever Method [9] for a multi-layered material have already been developed and reported, based on the nonlinear large deformation theory. On the other hand, various methods [10–12] have been studied on the basis of the linear small deformation theory for the metallic films and foils in the past.

A. Ohtsuki (✉)
Department of Mechanical Engineering, Fuculty of Science and Technology, Meijo University, 1-501 Shiogamaguchi, Tempaku-ku, Nagoya 468-8502, Japan
e-mail: ohtsuki@meijo-u.ac.jp

G.P. Tandon et al. (eds.), *Experimental Mechanics of Composite, Hybrid, and Multifunctional Materials, Volume 6*, Conference Proceedings of the Society for Experimental Mechanics Series, DOI 10.1007/978-3-319-00873-8_29,

29.2 Theory

The three/four-point bending method and tensile method are commonly used for evaluating mechanical properties (Proportional limit, Elastic limit, Yield point, Ultimate strength, Elastic modulus, Elongation, Contraction, etc.) of various materials. Although these methods are very simple they also have several disadvantages (e.g., a stress concentration around a loading nose, a gripping problem of specimen).

From this point of view, a new testing method (*Compression Column Method*) is devised considering large deformation behaviors of thin flexible materials. The new method can be applied to various multi-layered wires, long fiber materials (Glass fibers, Carbon fibers, Optical fibers, etc.) and multi-layered thin sheet materials.

29.2.1 Basic Equation

Major premises for the analysis are as follows:

1. The scope of the large deformation theory is used within the elastic range.
2. The Euler-Bernoulli's assumption is applicable.
3. Poisson's effect is not considered and shear deformation is neglected.
4. The multi-layered material is considered to be inextensible.

A typical illustration of a load-deflection shape for a columun, compressed between freely pivoted ends, is given in Fig. 29.1. While an ideal straight column is subjected to a small compressive load P, it produces only a deformation slightly shrunk in the longitudinal direction. However, the load P reaches the critical load, the so-called Euler buckling will take place. As an example, a cross section of two-layered plate and rod ($n = 2$) is shown in Fig. 29.2.

Due to the symmetry of the deformed shape, the analysis is carried out for the region AB (only 1/2 of the whole arc length 2 L).

The horizontal displacement is denoted by x, vertical displacement by y, and θ is the deflection angle. Moreover, an arc length is denoted by s, the radius of curvature by R and the bending moment by M. The relationship among R, M, s, x, y and θ are given by:

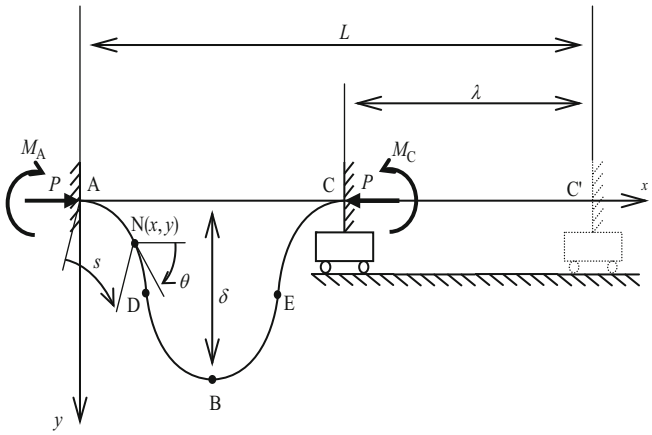

Fig. 29.1 Illustration of a typical load-deflection shape for a multi-layered buckled column

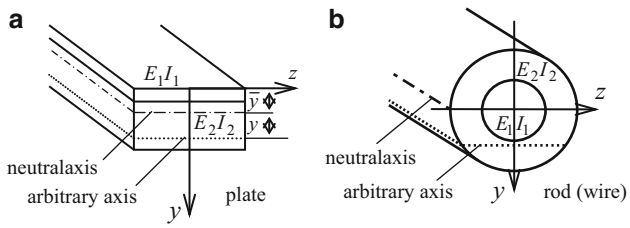

Fig. 29.2 Illustration of cross-section of two-layered material

$$\left.\begin{array}{l} 1/R = -d\theta/ds = M \Big/ \sum_{i=1}^{n} (E_i I_i) \\ dx = ds \cdot \cos\,\theta, dy = ds \cdot \sin\,\theta \end{array}\right\} \tag{29.1}$$

where $E_i I_i$ is the flexural rigidityof ith layer.

The moment applied at an arbitrary position N(x, y) is expressed as

$$M = P \cdot y + M_{\mathrm{A}} \tag{29.2}$$

Introducing the following non-dimensional variables,

$$\left.\begin{array}{l} \xi = x/L,\ \eta = y/L,\ \zeta = s/L,\ \rho = R/L \\ \gamma = PL^2 \Big/ \sum_{i=1}^{n} (E_i I_i),\ \alpha = M_{\mathrm{A}} L \Big/ \sum_{i=1}^{n} (E_i I_i) \end{array}\right\} \tag{29.3}$$

the basic equation of large deformation (: postbuckling behavior) is derived from Eqs. 29.1, 29.2, and 29.3 in the form of:

$$d^2\,\theta/d\zeta^2 + \gamma \cdot \sin\,\theta = 0 \tag{29.4}$$

Considering the boundary condition $(d\theta/d\zeta)|_{\theta=\theta_B} = 0$ $\left(M|_{\theta=\theta_B} = 0\right)$ at the point B, Eq. 29.4 can be integrated to yield the following.

$$d\theta/d\zeta = \pm\sqrt{2\gamma}\,\sqrt{\cos\theta + (\alpha^2 - 2\gamma)/2\gamma} \tag{29.5}$$

Equation 29.5 is the basic equation that determines large deformation behaviors of a compressed column. The double sign ($\pm$) on the right hand side of Eq. 29.5 means that the positive or negative sign is adopted when the deflection angle θ is increasing or decreasing, respectively, with the increase of the non-dimensional arc length ζ. In analysis of the compressed column, only the plus sign (+) is adopted.

In analyzing the nonlinear differential Eq. 29.5 the following formula may be used to transform the variables with respect to angle θ.

$$\left.\begin{array}{l} (\alpha^2 - 2\gamma)/2\gamma = 2k^2 - 1 \\ \cos\theta = 1 - 2k^2 \cdot \sin^2\phi\ (0 \leqq \phi \leqq \pi/2) \end{array}\right\} \tag{29.6}$$

Denoting the half length of a specimen by L and taking into the conditions $\zeta_{\mathrm{AC}}\,(= s_{\mathrm{AC}}/L) = \zeta_{\max} = 1$, $\eta_{\mathrm{AB}} = \eta_{\max} = \delta/L$, $\xi_{\mathrm{AC}} = \xi_{\max} = 1 - \lambda/L$, the maximum non-dimensional arc length ζ_{AC}, the maximum non-dimensional vertical displacement η_{AB} and the maximum non-dimensional horizontal displacement ζ_{AC} are obtained as follows.

$$\zeta_{\mathrm{AC}} = 1 = \left(4/\sqrt{\gamma}\right) \cdot F\,(k,\ \pi/2) \tag{29.7}$$

$$\eta_{\mathrm{AB}} = \delta/L = 4k/\sqrt{\gamma} \tag{29.8}$$

$$\xi_{\mathrm{AC}} = 1 - \lambda/L = \left(4/\sqrt{\gamma}\right) \cdot \{2E\,(k,\ \pi/2) - F\,(k,\ \pi/2)\} \tag{29.9}$$

where $F(k,\pi/2)$ = Legendre − Jacobi's complete elliptic integrals of the first kind

$E(k,\pi/2)$ = Legendre − Jacobi's complete elliptic integrals of the second kind

Moreover, Young's modulus E_i of ith layer can be calculated as in the form of;

$$\sum_{i=1}^{n} (E_i\,I_i) = PL^2/\gamma \tag{29.10}$$

where I_i = second moment of area of the each layer cross section

In the meantime, it is necessary to determine the neutral axis of a multi-layered plate (In case of a multi-layered rod/wire, the cross section is symmetry).

The second moment of area I_i of each cross section for multi-layered plate (thickness h_i, width b: common to all) with respect to the neutral axis is shown as

$$I_i = bh_i^3/12 + bh_i \left(\bar{y} - h_i/2 - \sum_{k=1}^{n} h_{k-1} \right)^2 \qquad (h_0 = 0,\ i \leq n) \tag{29.11}$$

The distance $\overline{y}$ to the neutral axis (see Fig. 29.2) and the relation is obtained as follows.

$$\overline{y} = \sum_{i=1}^{n} E_i \left(S_i\right)_z \Big/ \sum_{i=1}^{n} \left(E_i A_i\right) \tag{29.12}$$

The first moment of area $(S_i)_z$ of each cross section (A_i: the cross-sectional area) with respect to z axis is expressed as

$$\left(S_i\right)_z = bh_i^2/2 + bh_i \left(\sum_{k=1}^{n} h_{k-1} \right) \tag{29.13}$$

The second moment of area I_i of each cross section for multi-layered rods/wires (diameter d_i) with respect to the neutral axis is shown as

$$I_i = \pi \left(d_i^4 - {d_{i-1}}^4 \right)/64 \qquad (d_0 = 0) \tag{29.14}$$

One quantity γ (: the non-dimentional load) is required to calculate Young's modulus E_i from Eq. 29.10. The value of γ is obtained from a chart (: Nonograph) of γ-λ relation (λ: the horizontal displacement) and γ-δ relation (δ: the vertical displacement).

29.2.2 Measuring Techniques

In this paper, representative two methods are introduced in order to measure Young's modulus.

The γ-λ and γ-δ relations are presented in Figs. 29.3 and 29.4 respectively considering user-friendliness. These chsrts are computed previously by using Eqs. 29.7, 29.8, and 29.9. Here, for the sake of simplicity, the usage of the chart is recommend by the author.

As a point to note, for example, a two-step procedure should be done in a measuring experiment, when Young's modulus of each layer in a two-layered material is all unknown (Note that a multi-layered material with number of layers n requires a n- step procedure). In other words, it is possible to reduce a frequency of step in proportion to the number, if the number of layers with known Young's modulus is proven.

As an example to master the thecnique how to use the chart, two measuring processes are shoun below in a two-layered material consisted of a high-polymer material (PVC: Polyvinyl chloride, thickness $h_1 = 0.515$ mm, width $b_1 = 27.0$ mm, length $L_1 = 250.0$ mm) and a stainless steel material (SUS, thickness $h_2 = 0.100$ mm, width $b_2 = 27.0$ mm, length $L_2 = 250.0$ mm).

29.2.2.1 Method 1 (Measurement of λ)

The usage of this method is shown below in a two-layered material. Each Young's modulus E_1, E_2 is obtained for a high-polymer material (PVC: Polyvinyl chloride) (first layer) and a stainless steel material (SUS) (second layer)

[1st Step Procedure] (As a two-layered specimen)

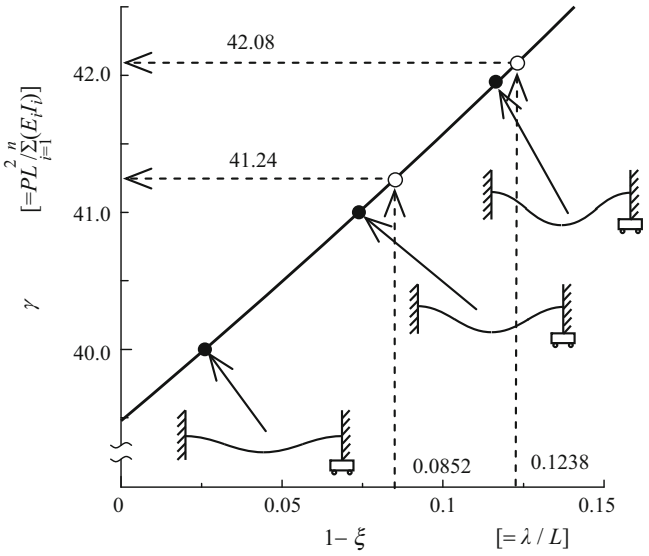

Fig. 29.3 Non-dimensional chart for finding the parameter γ when the parameter λ/L is given

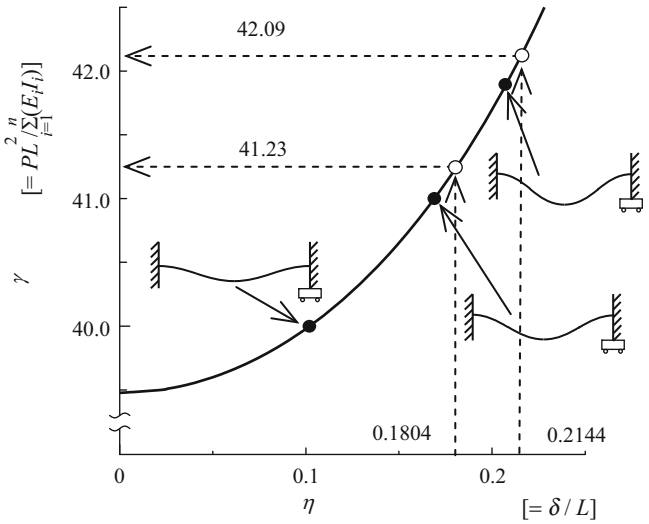

Fig. 29.4 Non-dimensional chart for finding the parameter γ when the parameter δ/L is given

Under the condition of $P = 3.73$ N, $\lambda = 21.3$ mm (i.e., $\lambda/L = 0.0852$) is measured for a double layrer and then the value of γ is taken from Fig. 29.3 ($\gamma = 41.24$). Therefore, from Eq. 29.10, the combined flexural rigidity (I_1, I_2: unknown) is derived as follows.

$$E_1 I_1 + E_2 I_2 = PL^2/\gamma = 3.73 \times (0.25)^2/41.24 \cong 5.643 \times 10^{-3} \tag{29.15}$$

[2nd Step Procedure] (As a single-layered specimen)

Similarly, λ is measured for a single-layer after removing a second layer (SUS). In the condition of $P = 0.706$ N for a PVC single layer, $\lambda = 30.9$ mm (i.e., $\lambda/L = 0.1238$) is measured and γ is taken newly from Fig. 29.3 ($\gamma = 42.084$). Therefore, the flexural rigidity ($I_1 = 3.073 \times 10^{-13}$ m^4 which is not the same value I_1 in Eq. 29.14 because of a difference of the neutral axis, I_2: unknown) can be determined from Eq. 29.10 as follows from Eq. 29.10.

$$E_1 I_1 = PL^2/\gamma = 0.706 \times (0.25)^2/42.084 \cong 1.048 \times 10^{-3} \tag{29.16}$$

Using Eqs. 29.11, 29.12 and the simultaneous Eqs. 29.15 and 29.16, Young's modulus E_1, E_2 of each layer is calculated as $E_1 = 3.41$ GPa for a PVC layer (first layer) and $E_2 = 206.39$ GPa for a SUS layer (second layer).

29.2.2.2 Method 2 (Measurement of δ Only)

Using the chart (Fig. 29.4), each Young's modulus E_1, E_2 is obtained in a two-layered material (first layer: PVC + second layer: SUS).

[1st Step Procedure] (As a two-layered specimen)
Under the condition of $P = 3.73$ N, δ =45.1 mm (i.e., $\delta/L = 0.1804$) is measured and γ is taken from Fig. 29.4 ($\gamma = 41.23$).
Therefore, the combined flexural rigidity is as follows from Eq. 29.10.

$$E_1 I_1 + E_2 I_2 = PL^2/\gamma = 3.73 \times (0.25)^2/41.23 \cong 5.645 \times 10^{-3} \tag{29.17}$$

[2nd Step Procedure] (As a single-layered specimen)
Similarly, δ is measured for a single-layer (PVC) after removing a second layer (SUS) in the condition of $P = 0.706$ N.
$\delta = 53.6$ mm (i.e., $\delta/L = 0.2144$) is measured and γ is taken newly from Fig. 29.4 ($\gamma = 42.084$). Therefore, the flexural rigidity can be determined from Eq. 29.10 as follows.

$$E_1 I_1 = PL^2/\gamma = 0.706 \times (0.25)^2/42.084 \cong 1.048 \times 10^{-3} \tag{29.18}$$

From Eqs. 29.11, 29.12 and the simultaneous Eqs. 29.17 and 29.18, each Young's modulus E_1, E_2 is calculated as $E_1 = 3.41$ GPa for a PVC layer (first layer), $E_2 = 206.39$ GPa for a SUS layer (second layer).

29.3 Experimental Investigation

In order to assess the applicability of the proposed Compression Column Method, several experiments were carried out using a two-layered material (a high-polymer material: PVC + a stainless steel material: SUS).

The experimental set-up is shown in Fig. 29.5 (which shows a thin multi-layered plate, for example).

Since Young's modulus of each layer in the two-layered material is unknown, the measuring experiments were carried out by adopting the two-step procedure. In every step of the procedures, a horizontal displacement λ and a vertical displacement δ are measured for several axial compressive loads P by using a grid paper with 1 mm spacing.

Young's moduli of PVC and SUS obtained by applying the Method 1 and Method 2 are shown in Figs. 29.6 and 29.7, respectively. Here, the influence of a load (P) upon Young's modulus (E) was examined. The figures were described under a two-layered condition (Note that similar figures were describable under a single-layered condition).

In a PVC first layer (see Fig. 29.6), the measured values remain nearly constant for an axial compressive load and the standard deviation is (S.D) very small although every metho has a little scattered values. As a whole, the mean Young's moduli (shown as Av.: Average) deteremined by the two methods are in good agreement with each other. On the other hand,

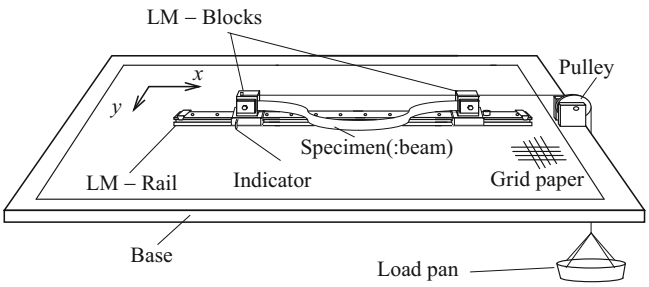

Fig. 29.5 Experimental set-up (as an example, a specimen of multi-layered plate is shown)

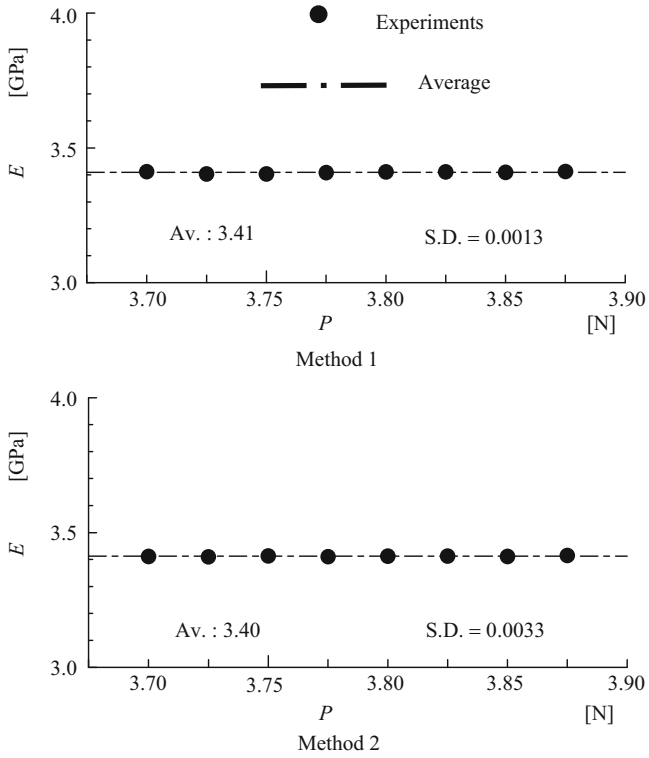

Fig. 29.6 Comparison of Young's moduli of a high-polymer thin plate (PVC:E1) between the two measuring methods for various values of the axial load P (Note: E2 of SUS is known previously)

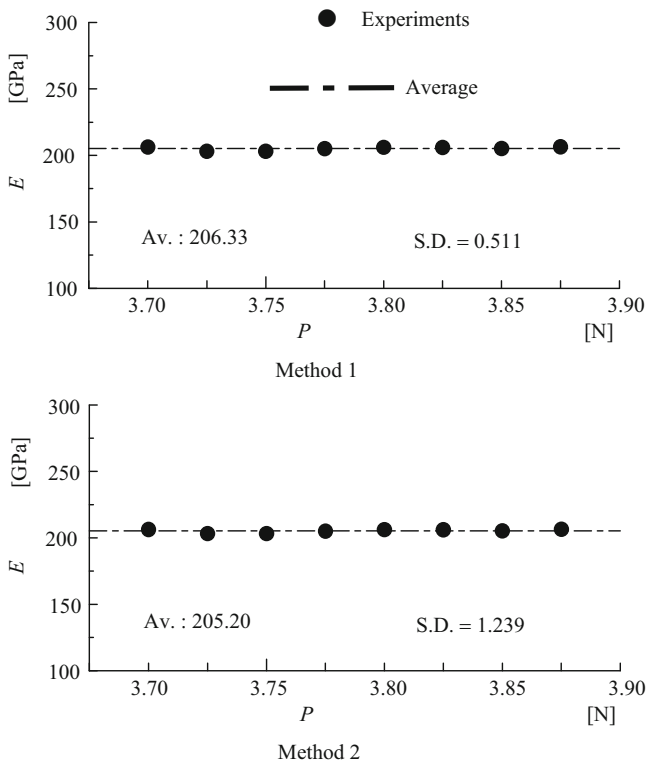

Fig. 29.7 Comparison of Young's moduli of a stainless steel thin plate (SUS:E2) between the two measuring methods for various values of the axial load P (Note: E1 of PVC is known previously)

Trends similar to that of Fig. 29.6 is observed herein for Young's moduli of a SUS second layer (see Fig. 29.7). The measured mean values by two different methods almost agree well.

29.4 Conclusions

The Compression Column Method is analyzed theoretically and proposed as an innovative material testing method for measuring Young's modulus of each layer in a flexible multi-layered material.

The principal conclusions are drawn as follows from the results of theoretical and experimental analyses.

1. The new method is based on the nonlinear large deformation theory. Large deformations are due to a postbuckling of an axial compressed column.
2. Experimental data (horizontal or vertical displacement) can be obtained easily because of a large deformation.
3. For the sake of convenience, two representative charts (: Nomographs) are drawn on the basis of the proposed theory.
4. A two-layered material (a high-polymer material: PVC + astainless steel material: SUS) was tested.
5. Experimental results clarify that the new method is suitable for measuring Young's modulus of each layer in a flexible multi-layered material.
6. Based on the assessments, the proposed method can be applied to multi-layered thin sheets and multi-layered fiber materials (e.g., steel belts, glass fibers, carbon fibers, optical fibers, etc.).
7. Furthermore, the proposed new method is applicable widely to Young's modulus measurement in a thin layer formed, for example, by PVD (Physical Vapor Deposition), CVD (Chemical Vapor Deposition), Electrodeposition, Coating (Graphite, Metal Oxide), Paint (Lacquer), etc.

Acknowledgements The author thanks to Mr. M. Hayashi, Meijo University, Japan, for assistance.

References

1. Ohtsuki A (2005) A new method of measuring Young's modulus for flexible thin materials using a cantilever. In: Proceedings of the 4th international conference on advances in experimental mechanics, vol 3–4, pp 53–58
2. Ohtsuki A, Takada H (2002) A new measuring method of Young's modulus for a thin plate/thin rod using the compressive circular ring. Trans Jpn Soc Spring Res 47:27–31
3. Ohtsuki A (2005) A new measuring method of Young's modulus for flexible materials. In: Proceedings of the 2005 SEM annual conference and exposition on experimental and applied mechanics, Section 72, pp 113(1)–113(8) [CD-ROM]
4. Ohtsuki A (2004) A new Young's modulus measuring method for flexible materials using postbuckling behaviours. In: Fourth international conference on thin-walled structures, pp 233–240
5. Ohtsuki A (2006) A new method of measuring Young's modulus using postbuckling behaviours. In: Proceedings of the 2006 SEM annual conference and exposition on experimental and applied mechanics, Section 78, pp 78(1)–78(4)[CD-ROM]
6. Ohtsuki A (2010) An innovative own-weight cantilever method for measuring Young's modulus in flexible thin materials based on large deflections. Appl Mech Mater 24–25:371–377
7. Ohtsuki A (2008) An innovative cantilever method for measuring Young's modulus of thin flexible multi-layered materials. In: Fifth international conference on thin-walled structures, pp 189–196
8. Ohtsuki A (2011) An innovative method for measuring Young's modulus of multi-layered materials using postbuckling behavior. Procedia Eng 1041–1046
9. Ohtsuki A, Suzuki M (2011) Mechanical testing methods for measuring Young's modulus of thin flexible multi-layered materials (own-weight multi-layered cantilever method). Trans Jpn Soc Spring Res 56:25–31
10. Johansson S, Ericson F, Schweitz JA (1989) Influence of surface coatings on elasticity, residual stress and fracture properties of silicon microelements. J Appl Phys 65:122–128
11. Oda J, Yamada K, Sakamoto J, Kubota T (1991) Three-point tensile test method to evaluate Young's moduli of thin films. Trans Jpn Soc Mech Eng Ser A 57(535):686–691
12. Fukushi M, Miyata H, Murakami A (2006) Development on the tensile apparatus and strength evaluation of thin metal films. Trans Jpn Soc Mech Eng Ser A 72(718):880–885

Chapter 30
On the Use of Ultrasonic Pulse-Echo Immersion Technique for Measuring Real Attenuation

Miguel Goñi and Carl-Ernst Rousseau

Abstract A verification of the fundamental assumption used in ultrasonic pulse echo attenuation measurements through the immersion technique was carried out. The method assumes that a perfectly bonded interface exists between specimen and surrounding liquid. Experiments on hydrophobic polymers show that the assumption is broken and the common procedure to calculate real attenuation is no longer valid since reflection coefficients cannot be determined by means of the basic elastic wave propagation theory. For some cases the technique looses its cogency since no echoes can be received. Available methods using direct contact transducers only offer a partial solution to the problem. For cases where echoes are received, an alternative method of measuring both the reflection and attenuation coefficients is proposed in order to properly apply the immersion technique.

30.1 Fundamentals on the Ultrasonic Pulse-Echo Immersion Technique Regarding Real Attenuation of Solid Materials

The ultrasonic pulse-echo immersion technique consists of sending a mechanical pulse in the ultrasonic frequency range to a material and analyzing several echoes reflected from the material in order to calculate the longitudinal wave speed and attenuation coefficient of the material under test.

The mechanical pulse is created by an ultrasonic transducer that is based on the piezoelectric effect of a crystal. The main characteristic of the immersion technique is that the pulse is not transmitted directly from the transducer to the material but rather through a liquid (water, in the present case) in which the solid material is immersed and that acts as a coupler between transducer and material.

The material sample is immersed in liquid and placed perpendicular to the transducer to facilitate the analysis and calculations. For this same reason, the two main faces of the sample should be parallel to each other.

Figure 30.1 shows the interaction between the ultrasonic pulse, the coupling liquid (water), and the solid material. The arrows represent the ultrasonic pulse traveling through water and arriving at the material (V_0) and the multiple reflections that will travel back to the transducer. V'_0 is called the front wall reflection and V_1 and V_2 are the first and second echo. These echoes are reflections from the back wall of the solid material. Note that the pulse does not reach the sample at an inclination, but at perpendicular.

In the pulse-echo immersion technique, the first and second echoes, V_1 and V_2 are used to calculate the longitudinal wave speed and the attenuation coefficient of the material [6]. The magnitudes of these echoes are, respectively:

$$V'_0 = V_0 R_A D(s'_0) \tag{30.1}$$

$$V_1 = V_0 T_A^2 R_B D(s_1) e^{-\alpha 2h} \tag{30.2}$$

$$V_2 = V_0 T_A^2 R_B^2 R_A D(s_2) e^{-\alpha 4h} \tag{30.3}$$

M. Goñi • C.-E. Rousseau (✉)
University of Rhode Island, Wales Hall, Kingston, RI 02881, USA
e-mail: rousseau@uri.edu

G.P. Tandon et al. (eds.), *Experimental Mechanics of Composite, Hybrid, and Multifunctional Materials, Volume 6*, Conference Proceedings of the Society for Experimental Mechanics Series, DOI 10.1007/978-3-319-00873-8_30,

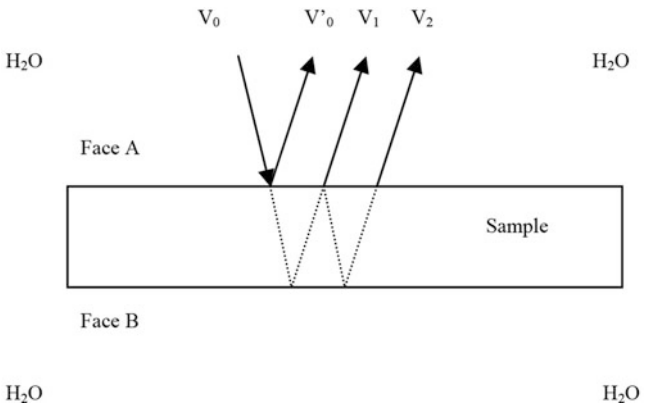

Fig. 30.1 Schematic of interaction of the ultrasonic pulse with the material

In these relations, the following assumptions are made, namely that:

- Reflection and transmission of the pulse occur at the water-sample interface,
- Attenuation of the pulse occurs only within the solid material,
- The beam is spreading.

Also, R_A, R_B, T_A, T_B are the reflection and transmission coefficients of faces A and B, respectively. D(s) is related to the beam spreading of the pulse, α is the attenuation coefficient of the sample, and h is the thickness of the sample. The beam spreading function, $D(s)$ is given by Rogers and Van Buren [5].

In order to calculate the attenuation, Eqs. 30.2 and 30.3 are combined to obtain the following expression:

$$\alpha = \frac{1}{2h} \ln\left(\frac{V_1}{V_2} R_A R_s \frac{D(s_2)}{D(s_1)}\right) \tag{30.4}$$

where V_1 and V_2 are the signals measured with the transducer, R_A and R_B are the reflection coefficients of faces A and B, respectively, and the values for D are calculated using the expressions derived by Rogers and Van Buren [5].

30.2 Deficiencies with Conventional Evaluation of the Attenuation Coefficient

Conventionally, attenuation has been calculated using Eq. 30.4 [2–4], where R_A and R_B are given by:

$$R_A = R_B = \frac{Z_s - Z_w}{Z_s + Z_w} \tag{30.5}$$

where Z_s is the acoustic impedance of the sample and Z_w is the acoustic impedance of the water.

This expression is derived in classical wave propagation, for a plane dilatational wave arriving at a plane interface between two media under the condition of *perfectly bonded interface*.

Recent experiments have shown that in numerous cases this assumption does not hold. Therefore, the use of Eq. 30.5 introduces significant errors in the attenuation coefficient calculation.

These cases refer materials that have low affinity to water, whereby the perfectly bonded interface assumption is broken and Eq. 30.5 can not be used to calculate the reflection coefficients. This is easily demonstrated by measuring the reflection coefficient and comparing them to the theoretical value provided by Eq. 30.5. Evaluation of the reflection coefficient only entail obtaining two signals: one in which the face of interest of the sample is in contact with air and another one with that same face in contact with water, as seen in Fig. 30.2.

For a Teflon specimen, the discrepancy is quite severe, as shown in Fig. 30.3. Moreover, due to the unknown conditions of the water-sample interface, the reflection coefficients of both faces of the same specimen could be different and therefore the method necessitates the measurement of both reflection coefficients prior to calculating the attenuation coefficient using Eq. 30.4.

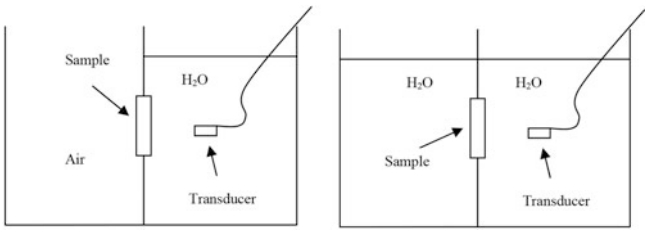

Fig. 30.2 Experimental set up to measure the reflection coefficient of *left* face

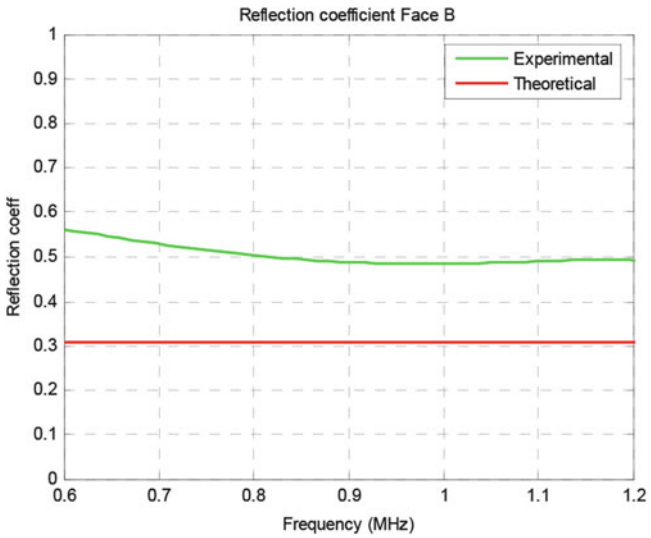

Fig. 30.3 Outcome of an experiment with a mildly hydrophobic Teflon specimen

30.3 New Method Adopted and Conclusions

In order to resolve the problems associated with the traditional ways of calculating the attenuation coefficient of a material [1–4, 7], a new method was developed. This new method considers the reflection coefficients in both faces to be unknown and possibly different. Therefore, it allows measurement of both reflection and attenuation coefficients simultaneously. The method can be extended to any material and guarantees the correct measurement of attenuation.

References

1. He P, Zheng J (2001) Acoustic dispersion and attenuation measurement using both transmitted and reflected pulses. Ultrasonics 39:27–32
2. Kline RA (1984) Measurement of attenuation and dispersion using an ultrasonic spectroscopy technique. J Acoust Soc Am 76(2):498–504
3. McSkimin HJ (1964) In: Mason WP (ed) Physical acoustic, principles and methods, part 1, vol 1. Academic, New York
4. Nolle AW, Mowry SC (1948) Measurement of ultrasonic Bulk-Wave propagation in high polymers. J Acoust Soc Am 20(4):432–439
5. Rogers PH, Van Buren AL (1974) An exact expression for the Lommel diffraction correction integral. J Acoust Soc Am 55:724
6. Treiber M, Kim J-Y, Jacobs L, Qu J (2009) Correction for partial reflection in ultrasonic attenuation measurements using contact transducers. J Acous Soc Am 125(5):2946–2953
7. Umchid S (2008) Frequency dependent ultrasonic attenuation coefficient measurement. In: The 3rd international symposium on biomedical engineering (ISBME), Bangkok, pp 234–238